Distributed, broadband vibration control devices using nonlinear approaches

Bin Bao

N°d'ordre NNT : **2016LYSEI086**

THESE de DOCTORAT DE L'UNIVERSITE DE LYON
opérée au sein de
L'Institut National des Sciences Appliquées de Lyon

Ecole Doctorale 160
ÉLECTRONIQUE, ÉLECTROTECHNIQ37
UE, AUTOMATIQUE

Spécialité de doctorat : Génie Electrique

Soutenue publiquement le 23/09/2016, par :

Bin BAO

Distributed, broadband vibration control devices using nonlinear approaches

-

Systèmes de contrôle de vibrations distribué large bande utilisant des approches non-linéaires

Devant le jury composé de :

BERNARD, Yves	Professeur	Université Paris-Sud	Rapporteur
OUISSE, Morvan	Professeur	ENSMM	Rapporteur
BADEL, Adrien	Maître de Conférences	Univ. Savoie Mont Blanc	Examinateur
MANZONI, Stefano	Associate Professor	Politecnico di Milano	Examinateur
RICHARD, Claude	Professeur	INSA Lyon	Président
GUYOMAR, Daniel	Professeur	INSA Lyon	Directeur
LALLART, Mickaël	Maître de Conférences	INSA Lyon	Co-directeur

Laboratoire de Génie Electrique et Ferroélectricité

Département FEDORA – INSA Lyon - Ecoles Doctorales – Quinquennal 2016-2020

SIGLE	ECOLE DOCTORALE	NOM ET COORDONNEES DU RESPONSABLE
CHIMIE	**CHIMIE DE LYON** **http://www.edchimie-lyon.fr** Sec : Renée EL MELHEM Bat Blaise Pascal 3e etage secretariat@edchimie-lyon.fr Insa : R. GOURDON	M. Stéphane DANIELE Institut de Recherches sur la Catalyse et l'Environnement de Lyon IRCELYON-UMR 5256 Équipe CDFA 2 avenue Albert Einstein 69626 Villeurbanne cedex directeur@edchimie-lyon.fr
E.E.A.	**ELECTRONIQUE, ELECTROTECHNIQUE, AUTOMATIQUE** **http://edeea.ec-lyon.fr** Sec : M.C. HAVGOUDOUKIAN Ecole-Doctorale.eea@ec-lyon.fr	M. Gérard SCORLETTI Ecole Centrale de Lyon 36 avenue Guy de Collongue 69134 ECULLY Tél : 04.72.18 60.97 Fax : 04 78 43 37 17 Gerard.scorletti@ec-lyon.fr
E2M2	**EVOLUTION, ECOSYSTEME, MICROBIOLOGIE, MODELISATION** **http://e2m2.universite-lyon.fr** Sec : Safia AIT CHALAL Bat Darwin - UCB Lyon 1 04.72.43.28.91 Insa : H. CHARLES Safia.ait-chalal@univ-lyon1.fr	Mme Gudrun BORNETTE CNRS UMR 5023 LEHNA Université Claude Bernard Lyon 1 Bât Forel 43 bd du 11 novembre 1918 69622 VILLEURBANNE Cédex Tél : 06.07.53.89.13 e2m2@ univ-lyon1.fr
EDISS	**INTERDISCIPLINAIRE SCIENCES-SANTE** **http://www.ediss-lyon.fr** Sec : Safia AIT CHALAL Hôpital Louis Pradel - Bron 04 72 68 49 09 Insa : M. LAGARDE Safia.ait-chalal@univ-lyon1.fr	Mme Emmanuelle CANET-SOULAS INSERM U1060, CarMeN lab, Univ. Lyon 1 Bâtiment IMBL 11 avenue Jean Capelle INSA de Lyon 696621 Villeurbanne Tél : 04.72.68.49.09 Fax :04 72 68 49 16 Emmanuelle.canet@univ-lyon1.fr
INFOMATHS	**INFORMATIQUE ET MATHEMATIQUES** **http://infomaths.univ-lyon1.fr** Sec :Renée EL MELHEM Bat Blaise Pascal 3e etage infomaths@univ-lyon1.fr	Mme Sylvie CALABRETTO LIRIS – INSA de Lyon Bat Blaise Pascal 7 avenue Jean Capelle 69622 VILLEURBANNE Cedex Tél : 04.72. 43. 80. 46 Fax 04 72 43 16 87 Sylvie.calabretto@insa-lyon.fr
Matériaux	**MATERIAUX DE LYON** **http://ed34.universite-lyon.fr** Sec : M. LABOUNE PM : 71.70 –Fax : 87.12 Bat. Saint Exupéry Ed.materiaux@insa-lyon.fr	M. Jean-Yves BUFFIERE INSA de Lyon MATEIS Bâtiment Saint Exupéry 7 avenue Jean Capelle 69621 VILLEURBANNE Cedex Tél : 04.72.43 71.70 Fax 04 72 43 85 28 Ed.materiaux@insa-lyon.fr
MEGA	**MECANIQUE, ENERGETIQUE, GENIE CIVIL, ACOUSTIQUE** **http://mega.universite-lyon.fr** Sec : M. LABOUNE PM : 71.70 –Fax : 87.12 Bat. Saint Exupéry mega@insa-lyon.fr	M. Philippe BOISSE INSA de Lyon Laboratoire LAMCOS Bâtiment Jacquard 25 bis avenue Jean Capelle 69621 VILLEURBANNE Cedex Tél : 04.72 .43.71.70 Fax : 04 72 43 72 37 Philippe.boisse@insa-lyon.fr
ScSo	**ScSo*** **http://recherche.univ-lyon2.fr/scso/** Sec : Viviane POLSINELLI Brigitte DUBOIS Insa : J.Y. TOUSSAINT viviane.polsinelli@univ-lyon2.fr	Mme Isabelle VON BUELTZINGLOEWEN Université Lyon 2 86 rue Pasteur 69365 LYON Cedex 07 Tél : 04.78.77.23.86 Fax : 04.37.28.04.48

*ScSo : Histoire, Géographie, Aménagement, Urbanisme, Archéologie, Science politique, Sociologie, Anthropologie

Acknowledgements

Firstly, I would like to say that I have been very happy to live here in both daily life and scientific research for the Ph.D. during three years. The LGEF (Laboratoire de Génie Electrique et Ferroélectricité) laboratory really gives me a good impression. When I firstly came alone to France, Ms. Evelyne DORIEUX, the secretary of LGEF, kindly helped me in setting up everything for my good settlement, which was really a great help for me.

After trying several kinds of smart vibration control systems during my Master's Degree in NPU, I found that SSD (Synchronized Switch Damping) family is my favorite. Therefore, I am very lucky that Prof. Daniel GUYOMAR gave me the opportunity to purse my Doctor degree on these techniques in LGEF and let me obtain a further deep understanding on such technique. Herein, I would like to express my deepest appreciation to Prof. Guyomar.

During my daily scientific research life, Dr. Mickaël LALLART provided me the professional academic Ph.D. training and continuous encouragement. He spent a lot of time and effort on training me to be a professional researcher. I really learned a lot from our research discussions and continuous paper modifications. His patient guidance and careful explanation were very helpful for me refining and finishing the Ph.D. work. His meticulous working attitude and his unique analytical method shaped my research style and rectified some drawbacks in my research thinking. Herein, I would like to extend my endless gratitude to Dr. Mickaël LALLART.

For my research topic, I would like to sincerely thank Dr. Linjuan YAN. Without her previous work on smart periodic structures and advices, I will not have had such a good starting research point of the Ph.D. thesis.

I am also very thankful to the committee members who kindly accepted evaluating my work. Their internationally recognized expertise in the field of smart materials, piezoelectric devices and vibration control make me feeling a privileged person and I

am really honored to be able to present them my work. My deepest thanks go to Prof. Yves BERNARD, who accepted to review this thesis and spent time on evaluating my work. My sincere gratitude also goes to Prof. Morvan OUISSE, for his careful readings of this pretty long manuscript and its review. I am also grateful to Dr. Adrien BADEL, expert in the field of SSD techniques, whose presence truly honors me. I also deeply thank Dr. Stefano MANZONI for accepting coming to France for evaluating this work. Finally, I am also very happy that Prof. Claude RICHARD, one of the first SSD investigator, accepted to participate to the committee.

For the financial support, I would like to acknowledge the China Scholarship Council (CSC). In addition, I would like to sincerely thank Dr. Wei TANG. With his encouragement, I gradually earned the courage and confidence to go abroad for pursing a Ph.D. degree.

For the everyday life in LGEF and Lyon, I would like to thank all the colleagues in LGEF, all my friends in Lyon, which is a lovely city especially the ‘Tête d'Or’ park. Also, I would like to sincerely thank Dr. Liuqing WANG. She really gave me great encouragement and support on how to lead an introspective life.

Last but not least, I would like to express my deepest gratitude and love to my parents and younger sister for their endless support and encouragement.

Abstract

Vibrations are a significant and a critical part of our daily life as well as industrial applications, allowing movement of objects, communication (voice) and so on. However, in a large number of cases, vibrations may be undesirable as they raise comfort and even security issues, as large induced strain may lead to failures that can be critical. Hence, ways for limiting such undesirable effects have to be proposed.

For ameliorating vibration reduction systems in engineering applications, miscellaneous vibration control methods, including vibration damping systems, have been developed in recent years. As one of intelligent vibration damping systems, nonlinear electronic damping system using smart materials (*e.g.*, piezoelectric materials), is more likely to achieve multimodal vibration control. With the development of meta-structures (a structure based upon metamaterial concepts), electronic vibration damping shunts, such as linear resonant damping or negative capacitance shunts, have been introduced and integrated abundantly in the electromechanical meta-structure design for wave attenuation and vibration reduction control.

Herein, semi-passive Synchronized Switch Damping on the Inductor (SSDI) technique (which belongs to nonlinear electronic damping techniques), is combined with smart meta-structure (also called smart periodic structure) concept for broadband wave attenuation and vibration reduction control, especially for low frequency applications. More precisely, smart periodic structure with nonlinear SSDI electrical networks is investigated from the following four aspects, including three new techniques for limiting vibrations:

- First, in order to dispose of a tool allowing the evaluation of the proposed approaches, previous finite element (FE) modeling methods for piezoelectric beam structures are summarized and a new voltage-based FE modeling method, based on Timoshenko beam theory, is proposed for investigating smart beam structure with complex interconnected electrical networks.

- Then, the first developed technique lies in smart periodic structure with nonlinear SSDI interconnected electrical networks, which involves wave propagation interaction between continuous mechanical and continuous nonlinear electrical media. Compared with smart periodic structure with nonlinear SSDI independent electrical networks, it exhibits better wave attenuation performance in some specific frequency regions of the primitive pass bands of purely mechanical periodic structures. In addition, two extensions - smart periodic structure with SSDI Hybrid Capacitance-Shunting interconnected electrical networks and smart periodic structure with SSDI Dual-connected electrical networks are proposed:
  - ✧ The additional capacitances in the SSDI Hybrid Capacitance-Shunting interconnected cases can be used to flexibly alter the location of the new generated resonant-type band gap to frequency domains of interest compared with the purely SSDI interconnected cases.
  - ✧ SSDI Dual-connected cases, allowing a trade-off between interconnected and independent approaches, can make good use of less SSDI electronic shunts for achieving relatively broadband and better wave attenuation performance in some specific frequency domains (low-frequency range and the second Bragg-type band gap for the Positive-Negative configuration - opposite polarization direction of the patches, and the first Bragg-type band gap for the Positive-Positive configuration - same polarization direction for the two piezoelectric inserts) compared with the SSDI independent case.
- The second proposed topology lies in smart periodic structures with nonlinear SSDI interleaved / Tri-interleaved electrical networks involving wave propagation interaction between the continuous mechanical medium and the discrete nonlinear electrical medium. Due to unique electrical interleaved configuration and nonlinear SSDI electrical features, electrical irregularities are induced and simultaneously mechanical irregularities are also generated within an investigated periodic cell. Specifically, compared with the SSDI independent case in the investigated frequency domain, the proposed structures require less SSDI electronic shunts and exhibit the following performance differences:

- ✧ SSDI PPPP (all cells have the same polarization direction) / PPNN (the first two and last two cells have opposite polarization direction) interleaved cases have relatively broadband and better attenuation performance in some specific frequency domains (low frequency and primitive pass bands of purely mechanical periodic structures for PPPP configuration, and the two primitive Bragg-type band gaps of purely mechanical periodic structures for PPNN configuration).
- ✧ SSDI PPNP (the third piezoelectric element have opposite polarization direction) interleaved case has globally broadband but relatively limited attenuation performance.
- ✧ SSDI Tri-interleaved (PPPPPP – all the patches have the same polarization direction) case has relatively broadband and better attenuation performance in both low-frequency range and the first primitive Bragg-type band gap of purely mechanical periodic structures.

➢ Finally, the last architecture consists in smart periodic structures with SSDI multilevel interleaved-interconnected electrical networks, involving wave propagation interaction between the continuous mechanical medium and the multilevel continuous nonlinear electrical medium. Compared with the SSDI interconnected case, more resonant-type band gaps in the primitive pass bands of purely mechanical periodic structures can be induced, and the number of such band-gaps are closely related to the interconnection / interleaved level.

Finally, the main works and perspectives of the thesis are summarized in the last chapter.

Keywords: vibration control, piezoelectric damping, nonlinear, periodic structures, wave propagation

Résumé

Les vibrations et systèmes vibratoires sont présents dans de nombreux domaines et applications, tant de la vie courante que dans le domaine industriel (mouvement d'objets, voix, communication etc…). Néanmoins, dans certains cas, ces vibrations sont indésirables voire dangereuses pour la sécurité. Par conséquent, des moyens de limiter ces dernières est une priorité pour assurer non seulement le confort, mais aussi la sécurité des biens et des personnes. C'est dans cette optique que s'inscrivent les travaux de doctorat rapportés dans ce mémoire. Plus particulièrement, l'étude exposée ici s'intéresse aux systèmes de contrôle vibratoire peu consommateurs d'énergie et de faibles dimensions, utilisant des matériaux de conversion d'énergie de type piézoélectrique couplé à des interfaces électriques non-linéaires et distribués de manière périodique. L'originalité du travail exposé tient en la combinaison des avantages des structures périodiques, qui présentent naturellement des bandes fréquentielles de fortes atténuation, avec ceux des approches non-linéaires pour le contrôle de vibrations à l'aide de matériaux actifs.

Ainsi, après une introduction exposant à la fois les motivations pour le développement de techniques de contrôle de vibrations et présentant un état de l'art du domaine (Chapitre 1), le second chapitre s'intéressera à la mise en place d'outil permettant une analyse des techniques proposées dans les chapitres suivants. Plus particulièrement, ce chapitre exposera les méthodes d'éléments finis permettant l'étude des structures périodiques électromécaniques, et mettra en place une analyse basée sur la théorie de Timoshenko pour l'obtention d'une modélisation à éléments finis.

Par la suite, le Chapitre 3 proposera la mise en réseau périodique, incluant le domaine électrique, d'inserts piézoélectriques. Cette interconnexion électrique, étendant la propagation mécanique au domaine électrique, permet ainsi une augmentation des performances d'atténuation pour certaines bandes fréquentielles. Notamment, une extension à des structures périodiques avec des interconnexions électriques deux à deux permet de profiter d'un gain notable en basse fréquence, qui est généralement le

domaine fréquentiel le plus critique et celui ciblé par les approches électromécaniques, tout en permettant une réduction notable du nombre d'interfaces électriques.

Le Chapitre 4 proposera une approche d'entrelacement des réseaux électriques périodique, permettant d'introduire un certain désordre, ou de manière similaire une apériodicité, au niveau local. Cette dernière, par un mécanisme de diffusion des bandes interdites, permet ainsi un élargissement de la bande fréquentielle d'atténuation. En plus de cet élargissement de bande et d'un certain gain en termes d'atténuation, l'entrelacement, comparé à l'approche indépendante, permet également une réduction du nombre de commutateurs dans l'interface électrique, et donc à une meilleure intégration de la méthode.

Fort des approches interconnectées et entrelacées, le Chapitre 5 propose de profiter des avantages des deux techniques via l'élaboration d'une structure interconnectée/entrelacée, dont l'ordre permet un contrôle entre performance et largeur de bande d'atténuation. De plus, une telle méthode, via l'émergence de « méta-cellules » dans le réseau, permet l'apparition de bandes interdites à des fréquences basses, inatteignables dans l'utilisation de structure périodiques classiques.

Enfin, le Chapitre 6 propose une conclusion des travaux, rappelant les avancées majeures des travaux exposés dans ce manuscrit, ainsi que des perspectives de développement des approches proposées.

Mots-clés: vibration, amortissement, piézoélectrique, non-linéaire, structures périodiques, propagation

Table of Contents

Notation and abbreviation

Notation

Greek Characters

Symbol	Signification
ε	Dielectric coefficient
σ	Sign of the piezoelectric constant which depends on the polarization of the material
ω	Angular frequency
ρ	Density
υ_b	Poisson's ratio of the pure beam substructure
γ_0	Transverse shear strain
$\aleph$	Shear coefficient

Alphabetic characters

Symbol	Signification
A_s	Area of PZT electrode
A_c	Cross-section area of beam
A_b	Cross-section area of pure beam
A_p	Cross-section area of piezoelectric material
C	Damping matrix
C_p	Inherent capacitance of a PZT patch at constant strain
d	Generalized nodal displacements
d_{ij}	Piezoelectric charge coefficient
$\boldsymbol{D}$	Vector of electrical displacements (charge/area)
$\boldsymbol{E}$	Vector of electrical field in the material (volts/meter)

E_b	Elastic module of pure beam element (without PZTs)
E_p	Elastic module of piezoelectric element (PZTs)
e_{ij}^T	Dielectric coefficient
EI_s	Bending rigidities
G_b	Shear modulus of pure beam structure
$H(x)$	Hermitian shape functions
I	Electrical current
I_b	Second moment of area of pure beam structure's cross-section
I_p	Second moment of area of piezoelectric element's cross-section
K	Stiffness matrix
l	Length of unit beam element
L_p	Length of PZT patch
M	Mass matrix
Q	Electrical charge quantity
Q_s	Shear force of beam element
S	Vector of material stresses (force/area)
s	Elastic compliance
S_{ij}	Strain coefficients
s_{ij}^E	Elastic compliance constant
T	Vector of material engineering strains (dimensionless parameter)
T_{ij}	Stress coefficients
t_p	Thickness of piezoelectric patch
t_b	Thickness of pure beam element
u	Displacement vector
V_p	Output voltage of piezoelectric patch
w_p	Width of piezoelectric patch
w_b	Width of pure beam element
x_c	Neutral axis of beam element
Y_b	Young modulus of pure beam substructure

Z	Electrical shunting impedance

Subscripts

Symbol	**Signification**
$()_t$	Conventional matrix transpose
$()_{eq}$	Equivalent component
$()_p$	Component related to piezoelectric material
$()_b$	Component related to pure beam element

Superscripts

Symbol	**Signification**
$()^x$	Mechanical or electrical boundary conditions under which the constants are valid
$()^e$	Unit beam element

Abbreviation

Symbol	**Signification**
PZT(s)	Piezoelectric material(s)
SPENs	Semi-Passive Electrical Networks
PEN	Passive Electrical Network
FE	Finite Element
WFE	Wave Finite Element formulation
MWFE	Modified Wave Finite Element formulation

Partie Française

Chapitre FR- 1. Introduction et Etat de l'art

Afin de situer le travail exposé dans cette thèse dans le contexte scientifique et industriel, ce Chapitre propose d'exposer les tenants et aboutissants des techniques de contrôle de vibrations, ainsi que de dresser un état de l'art des différentes techniques disponibles pour atteindre cet objectif. Ainsi, la nécessité de disposer de moyens efficaces permettant de réduire les vibrations sera exposée dans le paragraphe 1.1. Par la suite, les paragraphes 1.2 et 1.3 se focaliseront sur les techniques de contrôle de vibrations standards (avec ou sans l'utilisation de matériaux intelligents). L'utilisation de structures périodiques sera explicitée dans le paragraphe 1.4, avec notamment les applications utilisant des matériaux intelligents qui seront détaillées dans le paragraphe 1.5. Enfin, le paragraphe 1.6 se propose, au vu des approches et dispositifs existants, de situer le travail effectué durant la thèse et de présenter le contenu de ce manuscrit.

1.1 Motivations

Les phénomènes vibratoires font partie des manifestations les plus communes que l'on peut rencontrer dans la nature, et se présentent sous de nombreuses formes (lumière, chaleur, acoustique, mécanique…). Bien que certains de ces phénomènes soient agréable (par exemple la musique) voire indispensable pour la survie, d'autres sont néfastes et peuvent même devenir dangereux, comme par exemple les vibrations donnant lieu à l'endommagement de structures (citons à titre d'illustration l'effondrement du pont de Tacoma Narrows sous l'effet du vent, du pont de la Basse Chaîne sous l'effet d'une troupe militaire marchant au pas ou encore l'arrachement du fuselage de l'avion du vol Aloha 243, expliqué par la corrosion et les nombreux cycles de décollages/.atterrissages de l'appareil, et, dans une optique de systèmes embarqués, le problème de décollement de composants ou d'arrachage de pistes pour les cartes électroniques embarquées - [1]).

Ainsi, être capable de limiter ces vibrations indésirables est un enjeu majeur dans de nombreux domaines, et a été un sujet de recherche appliquée de premier ordre qui a

de tout temps intéressé à la fois les milieux académique et industriel. Le principe de limitation des vibrations peut se décomposer en trois catégories, que ce soit par l'annulation de la source d'excitation (principe qui reste cependant très conceptuel), en isolant la structure à contrôler de la source, ou, dans le cas où l'isolation est délicate, en contrôlant les vibrations en agissant sur la structure.

Cette dernière approche se décline également en trois sous-catégories, via l'absorption (systèmes à masse accordée –[2]), l'amortissement (dissipation de l'énergie mécanique sous forme de chaleur, avec ou sans conversion intermédiaire –[3, 4]) ou la modification des paramètres structuraux (telle que la raideur, afin d'empêcher l'énergie de rentrer dans le système –[5, 6]) ; le domaine principalement visé par cette étude étant l'amortissement.

1.2 Techniques traditionnelles pour le contrôle de vibrations

Classiquement, comme exposé précédemment, les techniques de contrôle de vibrations consistent en la dissipation de l'énergie mécanique présente dans la structure par effet Joule. Ainsi, les méthodes traditionnelles se basent sur une conversion de cette énergie mécanique sous forme de chaleur, possiblement par l'intermédiaire d'une conversion « mécano-mécanique ».

La première technique classique consiste ainsi à utiliser un second résonateur mécanique (Figure FR 1.1), avec un transfert de l'énergie mécanique de la structure à contrôler vers ce sous-système. Ce dernier stocke ainsi l'excédent d'énergie tout en dissipant une plus ou grande partie. Ce concept peut se décliner sous la forme d'amortisseurs à masse accordée ([7, 8]), opérant sur une bande fréquentielle relativement large et de neutralisateurs de vibration accordés ([9]), qui, du fait de la nécessité d'un accordage parfait entre la fréquence de résonance de la structure hôte et de la sous-structure rapportée, ne peut fonctionner que sur une plage fréquentielle réduite.

La seconde approche consiste à directement ajouter des matériaux viscoélastiques sur la structure hôte ; ces derniers accomplissant la fonction d'amortissement en dissipant

une grande partie de l'énergie mécanique stockée sous forme de chaleur. En effet, ces matériaux possédant des caractéristiques à mi-chemin entre les matériaux élastiques purs, qui restituent toute l'énergie emmagasinée lors du relâchement, et les matériaux visqueux purs, dont tout l'énergie fournie est dissipée, leur permettant ainsi d'atténuer les vibrations. Typiquement, les matériaux viscoélastiques peuvent être implémentés directement ou avec une précontrainte, avec le matériau pris en « sandwich » entre deux matériaux élastiques pour cette dernière approche (Figure FR 1.2). On pourra enfin noter la possibilité d'utiliser d'hybrider ces techniques avec l'utilisation d'une masse pour obtenir un système accordé ou de matériaux piézoélectriques afin de disposer d'un système actif.

Enfin, la dernière technique traditionnelle repose sur le transfert et la dissipation d'énergie lors d'un impact (par effet de collision inélastique, de friction et de cisaillement). Ainsi, en utilisant des particules encapsulées dans un réceptacle (dont la dimension principale peut se situer soit dans la direction de vibration soit de manière transverse) avec ce dernier rapporté sur la structure à contrôler. Les particules utilisées, typiquement en acier ou en céramique, peuvent avoir des tailles variables mais généralement dans la plage *[0,05 ; 1]* mm, et chaque réceptacle peut en contenir entre 1 000 et 10 0000.

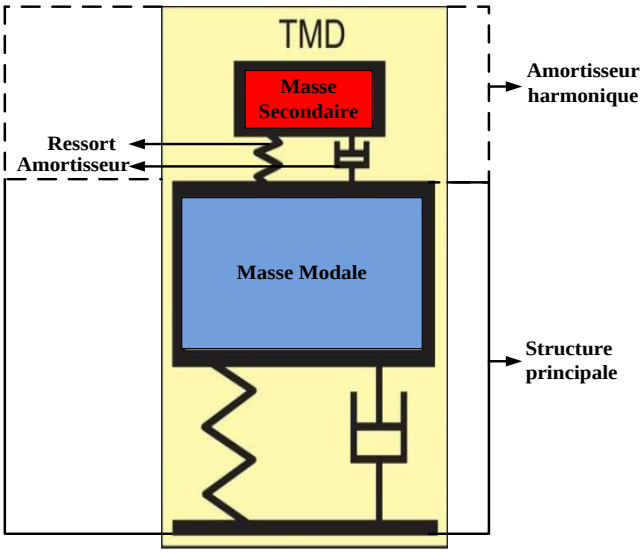

Figure FR 1.1 Principe d'un amortisseur à masse accordée purement mécanique.

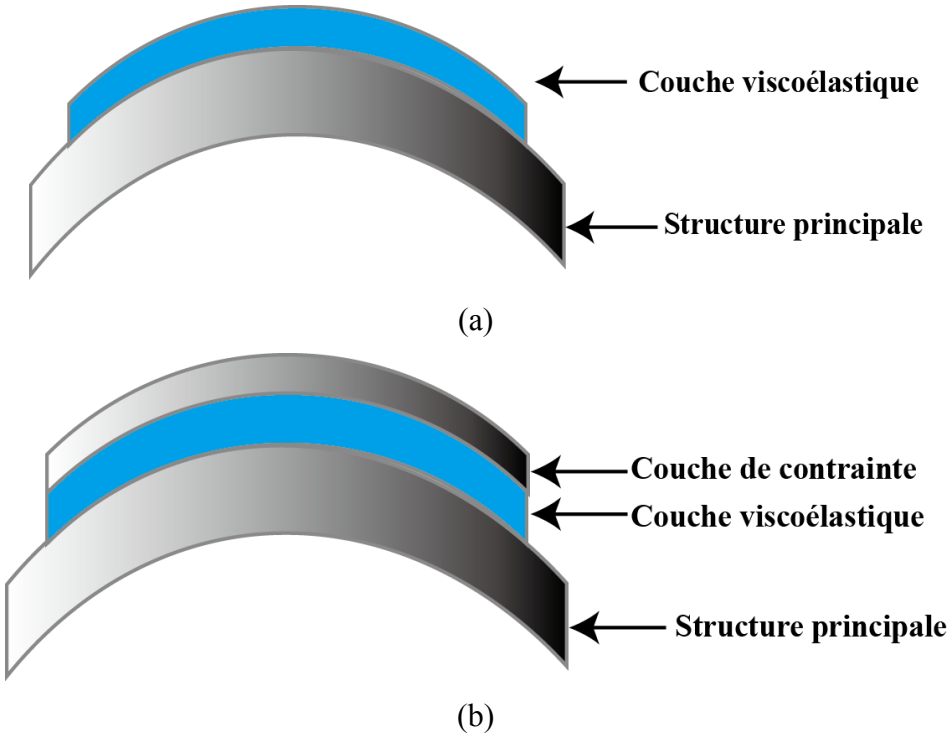

Figure FR 1.2 Amortissement par l'utilisation de matériaux viscoélastiques : (a) matériau libre et (b) matériau précontraint.

1.3 Techniques de contrôle vibratoire électromécanique « intelligent »

Avec l'évènement des matériaux pour la conversion d'énergie, les techniques « traditionnelles » pour le contrôle de vibration, reposant essentiellement sur la dissipation directe de l'énergie mécanique sous forme de chaleur, ont été progressivement complétées par des approches liant d'autres domaines de la Physique. Ainsi, l'utilisation de matériaux électro- ou magnéto-rhéologiques, dont la contrainte de cisaillement peut être contrôlée via l'application d'un champ électrique ou magnétique (conduisant en l'orientation de particules dispersées dans une solution), de matériaux à mémoire de forme (dont le module d'Young champ par une transition de phase induite par une élévation de température suite au passage d'un courant), de

systèmes électromagnétiques (par exemple par les forces de Lorentz ou les courants de Foucault) ou enfin de matériaux piézoélectriques, il est possible de lier le domaine mécanique à un autre domaine (typiquement magnétique ou électrique) pour ensuite stocker et/ou dissiper l'énergie correspondante. Dans le cadre de ce manuscrit, une étude particulière portera sur les éléments piézoélectriques, particulièrement adaptés aux systèmes de faibles dimensions, dont une représentation résumée des différents types de contrôle exposés ci-dessous est donnée en Figure FR 1.3.

1.3.1 Techniques de contrôle de vibrations actives utilisant les matériaux piézoélectriques

L'une des approches les plus directes pour le contrôle de vibrations utilisant des matériaux piézoélectriques consiste à considérer ces derniers comme de simples transducteurs, indépendamment des caractéristiques spécifiques de ces derniers. Ainsi, en insérant ces derniers dans une chaîne complète constituée de capteurs, modules de traitement, amplificateurs de puissance et transducteurs, il est possible d'utiliser les approches de contrôle classiques tels que les systèmes rebouclées de type LQR (*Linear Quadratic Regulator* –[10]) ou LQG (*Linear Quadratic Gaussian*), ou les systèmes à base d'observateurs pour la reconstruction et la prédiction du comportement modal de la structure([11] [12]). Comme mentionné précédemment, les techniques actives peuvent être également combinées de manière hybride avec des approches classiques telle que l'utilisation de matériaux viscoélastiques précontraints.

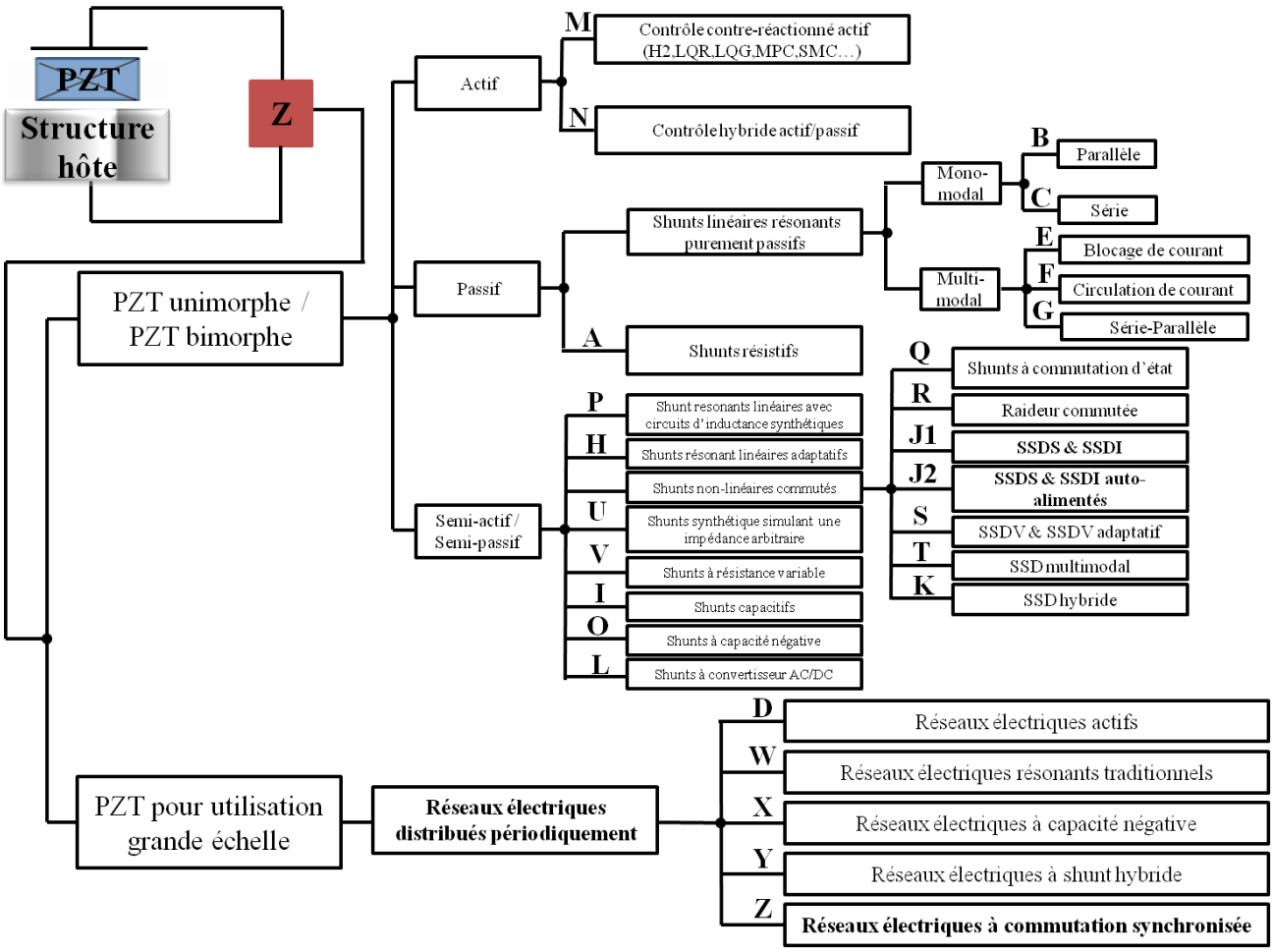

Figure FR 1.3 Résumé des approches typiques pour le contrôle de vibrations à l'aide d'éléments piézoélectriques (**A**: [13-15]; **B**: [15, 16]; **C**: [13]; **D**: [17-19]; **E**: [20]; **F**: [21, 22]; **G**: [23]; **H**: [24-26]; **I**: [27-30]; **J1**: [31, 32]; **J2**: [33, 34]; **K**: [35]; **L**: [5, 36-39]; **M**: [11, 40-53]; **N**: [54, 55]; **O**: [56-60]; **P**: [13, 61-64]; **Q**: [65-67]; **R**: [28, 68-70]; **S**: [71-75]; **T**: [76-82]; **U**: [83, 84]; **V**: [85]; **W**: [86-99]; **X**: [100-105]; **Y**: [106, 107]; **Z**: [108, 109]).

D'un point de vue général, les techniques de contrôle actives présentent d'excellentes performances, qui sont relativement indépendantes du matériau utilisé (bien qu'un couplage soit toujours nécessaire, une faible valeur de ce dernier peut être plus ou moins compensée par l'amplificateur), et peuvent opérer sur une très large bande. Néanmoins, les problèmes de stabilité du contrôle, notamment du fait d'un modèle imprécis (ne prenant par exemple pas en compte les effets des conditions environnementales ou les modes de rang supérieur), et surtout la quantité d'énergie importante requise à la fois pour le calculateur et l'amplificateur[1] et leurs dimensions significatives, limitent l'application de ces techniques dans le cadre de contrôle vibratoire de faibles dimensions et consommation (par exemple dans le cas embarqué).

1.3.2 Techniques de contrôle de vibrations passives utilisant les matériaux piézoélectriques

A la suite de l'utilisation d'éléments piézoélectriques comme simple transducteurs, et pour palier aux inconvénients des approches actives et notamment la forte puissance nécessaire et l'encombrement, le fait de tirer partie des particularités uniques des éléments piézoélectriques, des techniques d'amortissements vibratoires dédiées ont été développées.

Les premières approches proposées dans ce sens ont consisté à directement connecter une charge passive aux électrodes de l'élément piézoélectrique, permettant ainsi un contrôle sans aucun apport d'énergie extérieure ([15]). Du fait de la nature capacitive du matériau, les charges pouvant être envisagées sont résistives ou inductives. La connexion d'une charge résistive adaptée, dont la valeur dépend de l'inverse du produit de la capacité bloquée de l'élément par la pulsation, montre des performances limitées, généralement ciblées sur un mode particulier, mais avec une certaine

[1] Plus précisément, le manque de maîtrise des échanges d'énergies (notamment réactives) nécessitent la mise en place d'amplificateurs surdimensionnés par rapport aux réels besoins de l'application.

robustesse. L'utilisation d'inductance permet de significativement améliorer les performances du système, mais toujours pour une contrôle monomodal, via une adaptation d'impédance complexe en puissance, cependant au prix d'une grande sensibilité par rapport aux variations, du fait cette fois-ci d'une dépendance avec le carrée de la fréquence. De plus, les valeurs d'inductance adaptée sont généralement irréalisables en pratique sans l'utilisation d'inductances synthétiques uniquement obtenues avec des composants actifs, compromettant l'avantage de système énergétiquement fermé. On pourra enfin noter que, bien que les techniques de contrôle de vibration piézoélectriques passives se limitent généralement à un mode en particulier, l'utilisation de branches en parallèle ou en série, bloquant ou laissant passer le courant sauf pour une fréquence (mode) particulière permet, dans une certaine mesure, d'étendre les techniques purement passives à un contrôle multimodal ([20, 22, 23]).

1.3.3 Techniques de contrôle de vibrations semi-passives et semi-actives utilisant les matériaux piézoélectriques

Afin de combiner les avantages du contrôle actif en termes de performance et d'adaptabilité à ceux des circuits passifs en termes de consommation d'énergie et de stabilité, des techniques non-linéaires, généralement basées sur un élément de type interrupteur, ont été proposée. Généralement, ces techniques nécessitent une faible quantité d'énergie pour générer la commande de l'interrupteur, et quelquefois une source d'énergie est également présente dans le circuit de « puissance » incluant l'élément piézoélectrique. Ainsi, bien que la classification des méthodes soit encore sujette à discussion, cette considération énergétique permet de faire un premier tri : les techniques semi-passives ne contiennent aucun élément permettant de fournir de l'énergie à l'élément actif (pas de source dans la partie de « puissance »), mais peuvent nécessiter une quantité d'énergie faible pour le contrôle, alors que pour les techniques semi-actives, un transfert énergétique survient entre une source extérieure et l'élément piézoélectrique. Enfin, l'énergie nécessaire pour le contrôle semi-passif

pouvant être très faible (uniquement génération de la commande), cette dernière peut être directement fournie par l'élément piézoélectrique, conduisant cette fois-ci au concept d' « auto-alimenté ». Egalement, un autre critère à prendre en compte consiste en la nécessiter d'avoir un capteur annexe ou si l'actionneur permettant le contrôle peut être également utilisé en capteur, conduisant à la notion d' « auto-détection ». Ces différentes considérations conduisent ainsi à la classification présentée dans le Tableau FR1-1.

	Source d'énergie dans la branche de puissance	**Aucune source d'énergie dans la branche de puissance et alimentation externe de la commande**	**Aucune source d'énergie dans la branche de puissance et alimentation de la commande directement par l'actionneur**
Signal du capteur issu d'un transducteur externe	Semi-actif	Semi-passif	Semi-passif « auto-alimenté »
Signal du capteur issu du transducteur de contrôle	Semi-actif « auto-détecté »	Semi-passif « auto-détecté »	Semi-passif « auto-alimenté », « auto-détecté »

Tableau FR1-1 Classification des techniques semi-passives et semi-actives.

A partir de ces classifications, il est ainsi possible de voir les travaux proposés consistant en une modification de la raideur par ajout d'un certain nombre d'élément capacitifs ([28]) ou par une commutation synchronisée avec le déplacement ([68]), une commutation basée sur l'état de la vibration (*State Switched Aborber* –[65]) ou une commutation brève conduisant à l'annulation ou l'inversion de la tension ([31, 32]) appartiennent à la catégorie « semi-passif ». La dernière technique est par ailleurs au cœur des recherches exposées dans ce manuscrit. Cette technique, nommée SSDS

(*Synchronized Shunt Damping on Short Circuit*) dans le cas de l'annulation de la tension et SSDI (*Synchronized Shunt Damping on Inductor*) lorsque la tension est inversée, consiste à commuter brièvement, lorsque la tension atteint une valeur maximale ou minimale, l'élément piézoélectrique sur un court-circuit ou une inductance (cette dernière permettant l'inversion). Ceci conduit ainsi à un double effet consistant d'une part à une augmentation significative de la tension par un processus cumulatif et à un décalage temporel de cette dernière, devenant ainsi proche de la vitesse ; ces deux processus dénotant ainsi une augmentation de la conversion et donc à une meilleure extraction de l'énergie mécanique. Par ailleurs, cette technique peut être réalisée de manière totalement auto-alimentée ([33, 34]) , ne nécessitant ainsi aucun apport d'énergie extérieure.

Les performances des techniques semi-passives étant reliées de manière forte au coefficient de couplage électromécanique global, l'augmentation des performances peut se faire en injectant de l'énergie, de manière contrôlée, à l'élément piézoélectrique, rendant les techniques modifiées semi-actives. C'est par exemple le cas pour la technique SSDV (*Synchronized Shunt Damping on Voltage Sources* –[74]) et SSDVa (*adaptive Synchronized Shunt Damping on Voltage Sources* –[75]), où des sources de tension constantes ou lentement variables sont ajoutées dans la branche de commutation afin de compenser un couplage électromécanique faible et ainsi garantir des performances convenables. On pourra aussi noter que les techniques SSD peuvent inclure des traitements locaux simples afin de pouvoir être efficaces même en large bande ([80, 82, 110]), via la définition d'un seuil en deçà duquel la commutation est inhibée ou encore être couplées avec des techniques actives ; ces dernières se focalisant sur les modes peu couplés ([111]). Dans la catégorie de contrôle semi-actif, on peut enfin également inclure les techniques passives incluant des inductances synthétiques (l'utilisation d'amplificateurs opérationnels, via leur alimentation étant l'élément fournissant l'énergie au transducteur piézoélectrique –[37, 83]) ainsi que les méthodes basées sur des capacités négatives afin d'artificiellement améliorer le couplage ([61, 62]).

1.4 Structures périodiques

1.4.1 Généralités

Les structures périodiques, basées sur la répétition d'un motif, trouvent leurs origines dans la conception de guides d'ondes électromagnétiques dans des matériaux tels que les cristaux photoniques ([112-114]), et conduisant au concept de « méta-matériaux » dont les caractéristiques transcendent celles des matériaux constituant la structure. En particulier, de telles structures exhibent des bandes fréquentielles particulières pour lesquelles les ondes sont fortement atténuées. Ceci résulte d'un mécanisme de diffusion de Bragg, où les chemins parcourus par deux rayons, l'un réfléchis en surface et l'autre en profondeur, sont différents, conduisant à un déphasage entre les deux rayons réfléchis. Ainsi, pour certaines fréquences, cette différence de phase est telle que des interférences destructives apparaissent, conduisant ainsi à l'apparition de bandes fréquentielles bloquant les ondes associées.

L'extension de ce principe à d'autres phénomènes de propagation, comme par exemple la propagation d'ondes mécaniques ([115]), toujours via l'utilisation de métamatériaux, est par la suite possible et a fait l'objet de nombreuses études ([116, 117]), portant généralement sur deux catégories distinctes : les métamatériaux acoustiques (propagation dans un gaz ou un liquide) et métamétériaux phononiques (propagation dans un support mécanique). Néanmoins, le contrôle de propoagation utilisant uniquement une diffusion de type Bragg est relativement limitée par les conditions sur les longueurs d'ondes en regard de l'arrangement périodique.

Ainsi, en supplément de ce mécanisme particulier, un autre phénomène, consistant en l'utilisation de résonances locales, peut être exploité ([118, 119]). Comme son nom l'indique, cet effet consiste à utiliser des résonateurs locaux, qui peuvent présenter un phénomène de résonance à des fréquences pouvant être de plusieurs ordres de magnitude inférieures à celle du mécanisme de diffusion de Bragg, ainsi que des effets sous-harmoniques (donc à des fréquences encore plus basses), permettant ainsi la génération de bandes interdites à des fréquences qui sont en meilleure concordance

avec l'application. Enfin, les mécanismes de Bragg et de résonance locale peuvent être combinés ([119-124]), où, lorsque les bandes sont relativement proches, un effet de couplage apparaît conduisant à des performances remarquables sur une bande fréquentielle relativement large.

Enfin, on pourra noter que, dans le cas où une certaine apériodicité est introduite dans la structure, une amélioration des performances peut être observée ([17, 93, 125-127]). Ce phénomène s'explique par une certaine accumulation d'énergie dans des cellules élémentaires particulières, conduisant à un confinement de l'onde qui par conséquent ne se propage presque plus dans les cellules adjacentes.

1.4.2 Application au contrôle vibratoire via l'utilisation de matériaux piézoélectriques

Du fait de leurs caractéristiques uniques, notamment en termes de bandes d'atténuation, l'utilisation de structures périodiques a attiré l'attention de la communauté scientifique dans le cadre du contrôle de vibrations ([128-134]). Cet intérêt a par la suite été étendu à l'inclusion d'éléments électroactifs, tels que les éléments piézoélectriques, dans les cellules élémentaires. Ainsi, l'utilisation de techniques passives, en connectant des éléments résistifs et/ou inductifs à l'insert piézoélectrique a montré une amélioration des performances en termes d'atténuation dans les bandes de coupure ([13, 93]). Notamment, l'utilisation de circuits résonants (composé de la capacité inhérente de l'élément piézoélectrique, d'une inductance – potentiellement synthétisée à l'aide de circuit actifs – et d'une résistance) permet la génération de bandes de coupure du à un effet de résonance locale, pouvant être avantageusement combiné avec une diffusion de Bragg comme précédemment noté. L'extension large bande via l'utilisation de plusieurs branches électriques est également possible avec les structures périodiques ([135]). L'utilisation de circuits actifs comme des montages simulant des capacités négatives, permet également une amélioration significative des performances en augmentant artificiellement le coefficient de couplage électromécanique ([100-105]). Enfin, on pourra noter que

l'inclusion d'élément de conversion d'énergie ajoutant une degré de liberté (domaine électrique) ; il est également possible d'imaginer d'étendre la périodicité dans ce domaine (Figure FR 1.4).

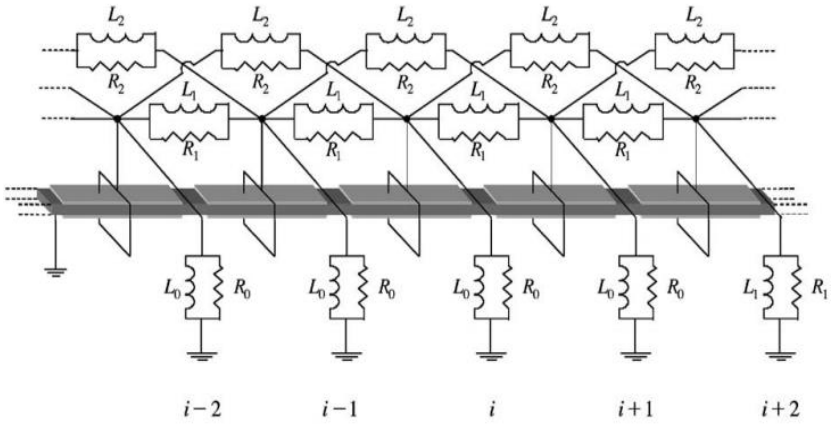

Figure FR 1.4 Exemple d'une structure périodique incluant un élément piézoélectrique avec une technique de contrôle passif et interconnexion électrique ([88]).

Enfin, l'utilisation de techniques semi-passives de type SSDI, où l'élément de commutation est connecté de manière indépendante à chaque élément électroactif d'une cellule, a récemment montré des performances exceptionnelles à la fois en termes d'atténuation mais aussi en termes d'élargissement de la bande passante ([108, 109]). Ceci s'explique du fait de la capacité de la technique à augmenter artificiellement le couplage électromécanique et à son adaptabilité à un changement de fréquence d'excitation.

1.5 Conclusion et présentation du manuscrit

Ce chapitre a montré que les techniques de contrôle de vibrations sont nécessaires dans de nombreuses applications, que ce soit pour le confort de l'utilisateur ou pour la préservation de l'intégrité de la structure hôte. Pour ce faire, les approches classiques, consistant en une dissipation directe de l'énergie mécanique de la structure sous forme de chaleur (avec, potentiellement, un transfert d'énergie mécanique à une structure

secondaire) peuvent être complétées voire étendues à des techniques tirant partie des capacités de conversion d'énergie de certains matériaux. Plus précisément, dans le cadre du travail exposé ici, une attention toute particulière s'est portée sur les éléments piézoélectriques, dont les techniques de contrôle peuvent se décliner sous forme de :

- Méthodes actives : incluant une chaîne complète capteur-traitement-amplification-actionneur, elles présentent d'excellentes performances (également en contrôle multimodal), mais sont gourmandes en place, capacité de calcul et surtout énergie et présentent certains problèmes de stabilité.
- Méthodes passives : tirant avantage des spécificités des éléments piézoélectriques, elles permettent un contrôle sans apport d'énergie extérieur, mais sont généralement limitées à une fréquence ou jeu de fréquences particuliers, ont des performances fortement dépendantes du coefficient de couplage électromécanique, peuvent être limitées en termes de robustesse par rapport à de dérives et sont quelquefois irréalisables de manière réellement passive (valeur d'inductance pouvant atteindre plusieurs centaines d'Henry).
- Méthode semi-passives et semi-actives : poussant plus en avant l'utilisation des propriétés des éléments piézoélectriques, elles consistent en l'ajout d'un élément non-linéaire (typiquement interrupteur) afin de combiner les avantages en termes de performances des techniques actives et ceux en termes de faible consommation des techniques passives. Alors que la génération de la commande de l'interrupteur nécessite une certaine quantité, même faible, d'énergie extérieure (pouvant néanmoins être directement fournie par le transducteur), une source d'énergie extérieure dans la branche de puissance incluant le transducteur peut être adjointe afin d'améliorer les performances, au prix d'un système non autonomes énergétique parlant (auquel cas on parlera de techniques semi-actives, la dénomination « semi-passive » étant réservée au cas où aucune énergie extérieure n'est directement fournie à l'élément piézoélectrique). En particulier, les techniques semi-passives de type

SSD, consistant à commuter l'élément piézoélectrique sur un circuit spécifique quand la tension atteint un extremum, montrent des performances exceptionnelles sans la nécessité d'ajout de sources d'énergie.

Parallèlement, il a été montré que l'utilisation de structures périodiques, conduisant au concept de « métamatériaux » aux propriétés exceptionnelles transcendant les constituant du système, possèdes des facultés exceptionnelles quant au contrôle de la propagation d'ondes, notamment mécaniques. Ceci s'explique par plusieurs effets pouvant être couplés, tels qu'une diffusion de Bragg ou un phénomène de résonance locale. Naturellement, l'incorporation d'éléments de conversion d'énergie dans de telles structures conduit à la possibilité de profiter des avantages inhérents à chaque approche, faisant notamment de l'inclusion de techniques semi-passives dans de tels systèmes une approche séduisante pour l'application au contrôle de vibration.

Ainsi, après un Chapitre d'analyse et de mise en place d'un modèle permettant l'analyse des techniques qui seront proposées par la suite (Chapitre 2), les travaux reportés dans ce manuscrit démarreront dans le Chapitre 3 d'une extension de la combinaison de la technique SSDI et des structures périodiques proposée dans la thèse de L. Yan ([109]), consistant en l'inclusion d'une dimension périodique dans le domaine électrique également, via l'interconnexion des éléments piézoélectrique. A partir de cette analyse, les travaux menés durant la thèse ont ainsi consisté en la conception, analyse et validation expérimentale d'approches interconnectées plus complexes et aux performances améliorés, incluant des entrelacements des connexions électriques (Chapitre 4) et l'hybridation interconnexion/entrelacement (Chapitre 5). Enfin, le Chapitre 6 proposera un résumé des origines et des résultats des voies empruntés, ainsi que des propositions d'extension et une réflexion sur l'applicabilité des techniques proposées.

Chapitre FR- 2. Modélisation des structures périodiques incluant des éléments piézoélectriques

Avant de pouvoir correctement évaluer les performances des techniques de contrôle de vibrations qui seront exposées dans la suite de ce mémoire, il convient d'effectuer une analyse des interactions entre les éléments piézoélectriques et la structure hôte, notamment par l'inclusion du couplage électromécanique de ces premiers. Par la suite, le développement et l'étude des techniques de contrôle de vibrations, exposés dans les Chapitres suivants, pourra être théoriquement analysé en utilisant les modèles exposés ici et en considérant les conditions d'utilisation de ces derniers. Ainsi, ce chapitre propose de discuter des approches et conditions d'application de la méthode des éléments finis (paragraphes 2.1 et 2.2), pour ensuite proposer une approche basée sur la théorie des poutres de Timoshenko pour la modélisation de structures électromécaniques exploitant des matériaux piézoélectriques (paragraphe 2.3) et la proposer à la modélisation basée sur les hypothèses d'Euler-Bernoulli (paragraphe 2.4), pour enfin conclure sur ces modèles dans le paragraphe 2.5.

2.1 Modèle éléments finis de structures piézoélectriques de type poutre avec une approche basée sur l'impédance

La modélisation de structures incluant des éléments piézoélectriques est principalement basée sur l'analyse de systèmes mécaniques multicouches. Plus particulièrement, dans le cas de structures relativement complexes, le recours à des méthodes d'éléments finis est courant car ces dernières permettent une analyse semi-analytique du système.

En particulier, on pourra noter l'analyse numérique des valeurs propres des matrices obtenues permettant d'obtenir les paramètres de propagation des ondes (méthode d'ondes à éléments finis – *Wave Finite Element* – WFE), comme présenté en [136-138]. Cependant cette approche souffre de problèmes de convergence (dus à la

discrétisation du système), qui peuvent néanmoins être adressés en incluant une analyse locale de la propagation, conduisant à la méthode MWFE (*Modified Wave Finite Element* - ondes à éléments finis modifiés –[139, 140]). L'inclusion d'éléments électroactifs tels que des inserts piézoélectriques est également possible, en considérant par exemple ces derniers connectés à une charge linéaire, en prenant en compte le couplage existant entre les domaines électrique et mécanique.

D'un point de vue équationnel, à partir des relations constitutives de la piézoélectricité en prenant le champ électrique E et la contrainte T comme grandeurs indépendantes, et en considérant l'élément piézoélectrique isotrope (symétrie ∞mm) ainsi que les hypothèses d'Euler-Bernoulli (les sections planes restent planes), il est possible de simplifier les relations constitutives, en subdivisant la modélisation selon que la contrainte selon l'axe *2* (largeur) est négligée (cas 1) ou pas (cas 2), tel que :

$$\begin{bmatrix} S_1^p \\ D_3 \end{bmatrix} = \begin{bmatrix} s_{11}^E & \sigma d_{31} \\ \sigma d_{31} & \varepsilon_{33}^T \end{bmatrix} \begin{bmatrix} T_1^p \\ E_3 \end{bmatrix} \quad \text{(cas 1)} \qquad \text{(FR2. 1)}$$

$$\begin{bmatrix} S_1^p \\ S_2^p \\ D_3 \end{bmatrix} = \begin{bmatrix} s_{11}^E & s_{12}^E & \sigma d_{31} \\ s_{21}^E & s_{22}^E & \sigma d_{31} \\ \sigma d_{31} & \sigma d_{31} & \varepsilon_{33}^T \end{bmatrix} \begin{bmatrix} T_1^p \\ T_2^p \\ E_3 \end{bmatrix} \quad \text{(cas 2)} \qquad \text{(FR2. 2)}$$

Ici, les grandeurs S_i et D_j dénotent la déformation et le déplacement électrique selon l'axe respectif i et j, et les paramètres s, ε et d la rigidité, la permittivité et le coefficient de charge piézoélectrique (en utilisant la notation de Voigt, avec l'axe 3 étant l'axe vertical correspondant également à la direction de polarisation). σ est une valeur valant ± 1 selon la direction de la polarisation. Enfin, les exposants sur les grandeurs dénotent les grandeurs associées à l'élément piézoélectrique et sur les paramètres les grandeurs constantes.

Lorsque l'élément piézoélectrique est connecté à une charge électrique passive (Z), il est possible d'exprimer la relation entre la tension et le courant au niveau de cette dernière. En notant que ces grandeurs sont les mêmes que celle au niveau de l'élément piézoélectrique, il est alors possible d'exprimer le champ électrique directement en

fonction de la contrainte ou de la déformation, ce qui permet ainsi que calculer le module d'Young équivalent E_p, donné par :

$$E_p^{Type1} = \frac{T_1^p}{S_1^p} = \frac{1 + j\omega Z C_p}{s_{11}^E + j\omega Z\left(s_{11}^E C_p - \frac{d_{31}^2 A_s}{t_p}\right)} \tag{FR2. 3}$$

$$E_p^{Type2} = \frac{T_1^p}{S_1^p} = \frac{\frac{\omega A_s d_{31}^2}{t_p} Z - \omega s_{11}^E C_p Z + j s_{11}^E}{\frac{2\omega d_{31}^2 A_s \left(s_{11}^E - s_{12}^E\right)}{t_p} Z - \left(\left(s_{11}^E\right)^2 - \left(s_{12}^E\right)^2\right)\omega C_p Z + j\left(\left(s_{11}^E\right)^2 - \left(s_{12}^E\right)^2\right)} \tag{FR2. 4}$$

avec ω la pulsation, A_s la surface de l'insert et t_p son épaisseur, et C_p la capacité bloquée de l'élément piézoélectrique ($C_p = \left(\varepsilon_{33}^T A_s\right)/t_p$). On peut ainsi voir que la connexion d'une charge permet de contrôler les paramètres mécaniques et ainsi de jouer sur la propagation des ondes dans ce domaine physique.

La prise en compte de l'élément actif intégré à la structure se fait en considérant les rigidités de flexion selon trois cas : structure hôte seule, structure hôte avec élément piézoélectrique sur une seule face (unimorphe) et structure hôte avec éléments piézoélectriques sur les deux faces (bimorphe), comme représenté en Figure FR2.1, et conduisant aux expressions des rigidités à la flexion EI_S :

$$\begin{cases} EI_s\big|_B = E_b \dfrac{w_b \left(t_b\right)^3}{12} & \text{pour la structure hôte seule (B)} \\ EI_s\big|_{BP1} = E_b \dfrac{w_b \left(t_b\right)^3}{12} + E_p \dfrac{w_p t_p \left(3\left(t_b\right)^2 + 6 t_b t_p + 4\left(t_p\right)^2\right)}{12} & \text{pour les segments unimorphes (BP1)} \\ EI_s\big|_{BP2} = E_b \dfrac{w_b \left(t_b\right)^3}{12} + 2E_p \dfrac{w_p t_p \left(3\left(t_b\right)^2 + 6 t_b t_p + 4\left(t_p\right)^2\right)}{12} & \text{pour les segments bimorphes (BP1)} \end{cases} \tag{FR2. 5}$$

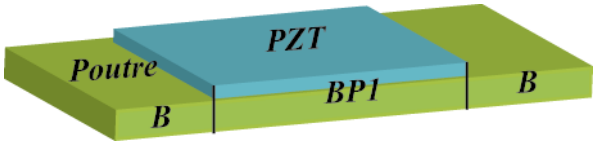

(a)

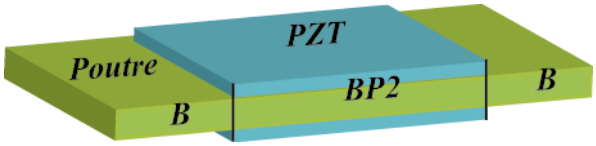

(b)

Figure FR2.1 Cas d'inclusion de l'élément piézoélectrique et découpage des segments : (a) configuration unimorphe ; (b) configuration bimorphe.

A partir des rigidités à la flexion ainsi définies, il est par la suite possible d'appliquer, selon les hypothèses d'Euler-Bernoulli, l'équation de la déformée dynamique selon :

$$\rho A_c \frac{\partial^2 u(x,t)}{\partial t^2} + EI_s \frac{\partial^4 u(x,t)}{\partial x^4} = q(x,t) \qquad \text{(FR2. 6)}$$

où $u(x,t)$ est le déplacement selon l'axe z (axe *3*) à la position x (selon l'axe *1*) et $q(x,t)$ la charge appliquée à la position x. t dénote la variable le de temps. Les grandeurs ρ, A_c et EI_s sont la masse volumique, la section et la rigidité à la flexion pour le segment considéré (Eq. (FR2. 5)). De plus, dans l'optique d'une modélisation par éléments finis, il est considéré que le déplacement de la poutre peut être projeté sur une base de fonctions hermitiennes $[H]$, conduisant ainsi au système matriciel suivant pour un segment :

$$\left[M^e\right]\left\{\ddot{d}^e\right\}+\left[K^e\right]\left\{d^e\right\}=\left\{F^e(t)\right\}$$

$$\begin{cases} \left[M^e\right]=\int_0^l [H]^T \rho A_c [H]dx, \quad \left[K^e\right]=\int_0^l [H'']^T EI_s [H'']dx, \quad \left[F^e(t)\right]=\int_0^l q(x,t)[H]^T dx \\ \left[M^e\right]=\dfrac{\rho A_c l}{420}\begin{bmatrix} 156 & 22l & 54 & -13l \\ 22l & 4l^2 & 13l & -3l^2 \\ 54 & 13l & 156 & -22l \\ -13l & -3l^2 & -22l & 4l^2 \end{bmatrix}, \quad \left[K^e\right]=\dfrac{EI_s}{l^3}\begin{bmatrix} 12 & 6l & -12 & 6l \\ 6l & 4l^2 & -6l & 2l^2 \\ -12 & -6l & 12 & -6l \\ 6l & 2l^2 & -6l & 4l^2 \end{bmatrix} \end{cases} \qquad \text{(FR2. 7)}$$

avec $[M^e]$ la matrice de masse dynamique, $[K^e]$ la matrice de rigidité, $\{d^e\}$ le vecteur de déplacement généralisé (incluant également la pente) et $\{F^e\}$ la matrice de force

généralisée (incluant également les moments). l dénote la longueur du segment. L'obtention du système pour la structure complète s'obtient par l'assemblage des différentes matrices de manière classique (assurance de la continuité du déplacement et de sa dérivée spatiale et identité des forces appliqué au même point de jonction).

Ainsi l'effet de l'élément piézoélectrique, et sa connexion avec une charge électrique linéaire, est pris en compte via la matrice de rigidité $[K^e]$. Néanmoins, cette approche basée sur l'impédance ne permet de considérer que des cas simple de connexion, et plus précisément les cas où la charge est connectée à un seul élément. Ainsi cette méthode ne permet pas de relater le comportement de techniques utilisant des connexions plus complexes ; typiquement des interconnexions comme il sera considéré dans la majeure partie de ce manuscrit. Ainsi, afin de palier à ce problème et pouvoir modéliser le comportement, une autre approche est requise.

2.2 Modèle éléments finis de structures piézoélectriques de type poutre avec une approche basée sur la tension

Afin de pouvoir prendre en considération les cas de connexions électriques plus complexes des éléments piézoélectriques, telles que des interconnexions entre inserts, il est ici proposé de prendre en considération la tension V_p des éléments comme variable plutôt que la charge connectée Z. De plus, il ne sera considéré dans cette partie uniquement le cas *2* de sous-modélisation, celui-ci faisant moins d'hypothèses car ne négligeant pas la contrainte selon l'axe *2*. En considérant que l'épaisseur t_p des matériaux actifs est très faible par rapport aux autres dimensions, il est possible de faire l'hypothèse d'un champ électrique selon l'axe E_3 uniforme selon :

$$E_3 = -\frac{V_p}{t_p} \qquad \text{(FR2. 8)}$$

De plus, selon les hypothèses considérées, il est également possible d'exprimer la déformation longitudinale à partir de la position z selon l'axe *3* et la dérivée spatiale seconde du déplacement :

$$S_1 = -\left(z - x_c\right)\frac{\partial^2 u_3}{\partial x^2} \tag{FR2. 9}$$

En considérant que l'origine de la position verticale *z=0* correspond à la face inférieure de la structure, il est ainsi possible d'obtenir, en combinant l'expression de la déformation longitudinale avec les équations constitutives de la piézoélectricité simplifiées selon les hypothèses considérées, l'expression de la contrainte longitudinale dans la poutre et dans l'élément piézoélectrique:

$$\begin{cases} T_1^b = -\left(z - x_c\right)\dfrac{\partial^2 u_3}{\partial x^2} E_b \\ T_1^p = -\left(z - x_c\right)\dfrac{\partial^2 u_3}{\partial x^2} E_p + \dfrac{\sigma d_{31}}{t_p\left(s_{11}^E + s_{12}^E\right)} V_p \end{cases} \tag{FR2. 10}$$

avec E_b et E_p les modules élastiques donnés par le module d'Young Y et le coefficient de Poisson ν tel que $E_i = Y_i / \left[1 - \left(\nu_i\right)^2\right]$.

A partir de ces équations, le mouvement dynamique est régi par :

$$\rho A_c \frac{\partial^2 u\left(x,t\right)}{\partial t^2} + EI_s \frac{\partial^2 M_{bending}^{Euler-B}}{\partial x^2} = q\left(x,t\right) \tag{FR2. 11}$$

où $M_{bending}^{Euler-B}$ est le moment de flexion du segment considéré :

$$M_{bending}^{Euler-B} = w_b \int T_1\left(z - x_c\right) dz = \begin{cases} E_b I_b \dfrac{\partial^2 u_3}{\partial x^2}, T_1 = T_1^b \\ E_{eq} I_{eq} \dfrac{\partial^2 u_3}{\partial x^2} + b_1 V_p, T_1 = T_1^b + T_1^p \end{cases} \tag{FR2. 12}$$

$$E_{eq} I_{eq} = E_b I_b + E_p I_p$$

$$b_1 = -\frac{\sigma d_{31} w_b}{t_p\left(s_{11}^E + s_{12}^E\right)} \int_{t_b}^{t_b + t_p} (z - x_c) dz$$

Ainsi, en appliquant la méthode des éléments finis de manière similaire au cas basé sur l'impédance, il est possible d'obtenir l'expression matricielle des vecteurs de déplacement et forces généralisés :

$$\begin{cases} \left[M^e\right]\left\{\ddot{d}^e\right\} + \left[K^e\right]\left\{d^e\right\} = \left\{F^e\left(t\right)\right\}, & \text{segment sans insert piézoélectrique} \\ \left[M^e\right]\left\{\ddot{d}^e\right\} + \left[K^e\right]\left\{d^e\right\} + \left[B_1^e\right]\left\{V_p^e\right\} = \left\{F^e\left(t\right)\right\}, & \text{segment avec insert piézoélectrique} \end{cases} \tag{FR2. 13}$$

$$\begin{cases} \left[M^e\right]=\int_0^l [H]^T \rho A_c [H]dx, \quad \left[K^e\right]=\int_0^l [H'']^T EI_s [H'']dx, \\ \left[d^e(t)\right]=\int_0^l u(x,t)[H]^T dx \quad \left[F^e(t)\right]=\int_0^l q(x,t)[H]^T dx \\ \left[B_1^e\right]=\int_0^l b_1 [H'']^T dx, \end{cases}$$

$$\rho A_c = \begin{cases} \rho_b A_b, & \text{segment sans insert piézoélectrique} \\ \rho_b A_b + \rho_p A_p, & \text{segment avec insert piézoélectrique} \end{cases}$$

$$EI_s = \begin{cases} E_b I_b, & \text{segment sans insert piézoélectrique} \\ E_{eq} I_{eq}, & \text{segment avec insert piézoélectrique} \end{cases}$$

Afin de refléter des cas réalistes d'application, il est enfin possible d'adjoindre une matrice *[C^e]* correspondant à un amortissement de type visqueux :

$$\begin{cases} \left[M^e\right]\left\{\ddot{d}^e\right\}+\left[C^e\right]\left\{\dot{d}^e\right\}+\left[K^e\right]\left\{d^e\right\}=\left\{F^e(t)\right\}, & \text{segment sans insert piézoélectrique} \\ \left[M^e\right]\left\{\ddot{d}^e\right\}+\left[C^e\right]\left\{\dot{d}^e\right\}+\left[K^e\right]\left\{d^e\right\}+\left[B_1^e\right]\left\{V_p^e\right\}=\left\{F^e(t)\right\}, & \text{segment avec insert piézoélectrique} \end{cases} \quad \text{(FR2. 14)}$$

qui peut par exemple être obtenue en utilisant un modèle de Rayleigh (*[C^e]=β1[M^e]+β2[K^e]*, avec *β1* et *β2* des coefficients constants).

D'un point de vue électrique, l'équation constitutive de la piézoélectricité peut se réduire selon :

$$D_3 = \frac{-\sigma d_{31} t_p}{\left(s_{11}^E + s_{12}^E\right)} \frac{\partial^2 u_3}{\partial x^2} + \frac{2\left(d_{31}\right)^2 - \varepsilon_{33}^T \left(s_{11}^E + s_{12}^E\right)}{t_p \left(s_{11}^E + s_{12}^E\right)} V_p \quad \text{(FR2. 15)}$$

qui, une fois la méthode des éléments finis appliquée, devient :

$$\begin{cases} \left\{Q^e\right\}=\left[B_2^e\right]\left\{d^e\right\}+\left[B_3^e\right]\left\{V_p^e\right\} \\ \left[B_2^e\right]=\dfrac{-[\sigma] w_b d_{31} t_p}{\left(s_{11}^E + s_{12}^E\right)} \int_0^l [H'']dx \\ \left[B_3^e\right]=\dfrac{w_b \left[2{d_{31}}^2 - \varepsilon_{33}^T \left(s_{11}^E + s_{12}^E\right)\right]}{t_p \left(s_{11}^E + s_{12}^E\right)} \left[L_p\right] \end{cases} \quad \text{(FR2. 16)}$$

avec *{Q^e}* le vecteur de charge électrique au niveau de l'insert piézoélectrique du segment considéré et *[σ]* et *[Lp]* les matrices dénotant la direction de polarisation et la longueur de l'élément piézoélectrique.

Ainsi, comparé à l'approche précédente par impédance, la méthode exposée ici basée sur la tension ne fait aucune présupposition concernant le réseau électrique connecté,

conduisant ainsi à un jeu de deux équations faisant explicitement apparaître les grandeurs électriques de tension et de charge :

$$\begin{cases} \left[M^e\right]\left\{\ddot{d}^e\right\}+\left[C^e\right]\left\{\dot{d}^e\right\}+\left[K^e\right]\left\{d^e\right\}+\left[B_1^e\right]\left\{V_p^e\right\}=\left\{F^e(t)\right\} \\ \left\{Q^e\right\}=\left[B_2^e\right]\left\{d^e\right\}+\left[B_3^e\right]\left\{V_p^e\right\} \end{cases} \quad \text{(FR2. 17)}$$

le comportement global du système étant obtenu en combinant ce jeu d'équation avec les conditions fixées par le réseau électrique connecté.

2.3 Modèle éléments finis utilisant la théorie de Timoshenko

Les précédentes modélisations se sont attachées à décrire le comportement du système en utilisant les hypothèses d'Euler-Bernoulli, conduisant à des contraintes sur l'épaisseur, qui doit rester très faible par rapport aux autres dimensions. Dans le cas de structures avec des épaisseurs plus importantes (mais toujours relativement faibles), ce modèle peut conduire à des résultats aberrants par rapport aux observations expérimentales. Dans ce cas, il convient de relâcher des contraintes sur les hypothèses.

Ainsi, dans ce paragraphe, un modèle sera développé de manière analogue au cas précédent (avec la tension comme variable), mais en utilisant les hypothèses, moins fortes, de la théorie des poutres de Timoshenko, qui inclut en plus une contrainte et une déformation de cisaillement, cette dernière étant considérée constante ($S_5=\gamma_0$, où γ_0 est une constante) :

$$\begin{bmatrix} S_1^p \\ S_2^p \\ S_5^p \\ D_3 \end{bmatrix} = \begin{bmatrix} s_{11}^E & s_{12}^E & 0 & \sigma d_{31} \\ s_{12}^E & s_{11}^E & 0 & \sigma d_{31} \\ 0 & 0 & s_{55}^E & 0 \\ \sigma d_{31} & \sigma d_{31} & 0 & \varepsilon_{33}^T \end{bmatrix} \begin{bmatrix} T_1^p \\ T_2^p \\ T_5^p \\ E_3 \end{bmatrix} \quad \text{(FR2. 18)}$$

De plus, l'expression de la déformation longitudinale en fonction de la position selon la verticale est cette fois-ci dépendante de la rotation et donc du cisaillement :

$$S_1 = -(z-x_c)\frac{\partial\varphi(x)}{\partial x} = -(z-x_c)\frac{\partial\left(\frac{\partial u_3}{\partial x}-\gamma_0\right)}{\partial x} \quad \text{(FR2. 19)}$$

En considérant l'expression de la contrainte de cisaillement dans la structure hôte telle que :

$$T_5^b = \aleph G_b \gamma_0,\ G_b = \frac{Y_b}{2(1+\nu_b)} \text{ et } \aleph = \frac{6+12\nu_b+6(\nu_b)^2}{7+12\nu_b+4(\nu_b)^2} \tag{FR2. 20}$$

la force de cisaillement Q_s est donnée par :

$$Q_s = \aleph G A_c^b \gamma_0 \text{ avec } G = \begin{cases} G_b, & \text{segment sans insert piézoélectrique} \\ G_{eq} = \left(G_b + \dfrac{A_c^p}{\aleph A_c^b s_{55}^E} \right), & \text{segment avec insert piézoélectrique} \end{cases} \tag{FR2. 21}$$

L'expression du moment de flexion peut également être obtenue selon :

$$M_{bending}^{Timo} = \begin{cases} M_{bending}^{Timo-b} = E_b I_b \dfrac{\partial \varphi(x)}{\partial x} & \text{segment sans insert piézoélectrique} \\ M_{bending}^{Timo-eq} = E_{eq} I_{eq} \dfrac{\partial \varphi(x)}{\partial x} + b_1 V_p & \text{segment avec insert piézoélectrique} \end{cases} \tag{FR2. 22}$$

$$E_{eq} I_{eq} = E_b I_b + E_p I_p$$

Par la suite, l'équation du mouvement de la structure peut être obtenue par le principe d'Hamilton, qui, par un bilan des variations d'énergies potentielle, cinétique et transférée par la charge, conduit à :

$$\begin{cases} \rho A_c \left(\dfrac{\partial u_3}{\partial t} \right)^2 - \dfrac{\partial Q_s}{\partial x} = q, \\ \rho I_s \left(\dfrac{\partial \varphi(x)}{\partial t} \right)^2 + Q_s - \dfrac{\partial M_{bending}^{Timo}}{\partial x} = m \end{cases} \tag{FR2. 23}$$

où q et m dénote la force et le moment distribués le long du segment considéré. En affectant au déplacement et à la rotation un jeu de fonctions de forme $N(x)^2$:

$$\begin{bmatrix} u(x,t) \\ \varphi(x,t) \end{bmatrix} = N(x) d^e = \begin{bmatrix} [N_u(x)] \\ [N_\varphi(x)] \end{bmatrix} d^e \tag{FR2. 24}$$

l'équation mécanique matricielle est donnée par :

$$\begin{cases} [M^e]\{\ddot{d}^e\} + [K^e]\{d^e\} = \{F^e(t)\}, & \text{segment sans insert piézoélectrique} \\ [M^e]\{\ddot{d}^e\} + [K^e]\{d^e\} + [B_1^e]\{V_p^e\} = \{F^e(t)\}, & \text{segment avec insert piézoélectrique} \end{cases} \tag{FR2. 25}$$

[2] avec l'ordre polynomial de la fonction de forme du déplacement d'un degré plus que celle de la rotation pour assurer la convergence.

$$\left[M^e\right]=\int_0^l\begin{bmatrix}\left[N_u(x)\right]\\ \left[N_\varphi(x)\right]\end{bmatrix}^T\begin{bmatrix}\rho A_c & 0\\ 0 & \rho I_{ts}\end{bmatrix}\begin{bmatrix}\left[N_u(x)\right]\\ \left[N_\varphi(x)\right]\end{bmatrix}dx$$

$$\left[K^e\right]=\int_0^l\begin{bmatrix}\dfrac{\partial\left[N_\varphi(x)\right]}{\partial x}\\ \left[N_\varphi(x)\right]+\dfrac{\partial\left[N_u(x)\right]}{\partial x}\end{bmatrix}^T\begin{bmatrix}EI_s & 0\\ 0 & \aleph GA_c^b\end{bmatrix}\begin{bmatrix}\dfrac{\partial\left[N_\varphi(x)\right]}{\partial x}\\ \left[N_\varphi(x)\right]+\dfrac{\partial\left[N_u(x)\right]}{\partial x}\end{bmatrix}dx$$

$$\left[B_1\right]=b_1\int_0^l\frac{\partial\left[N_\varphi(x)\right]^T}{\partial x}dx$$

$$\rho A_c=\begin{cases}\rho_b A_c^b, & \text{segment sans insert piézoélectrique}\\ \rho_b A_c^b+\rho_p A_c^p, & \text{segment avec insert piézoélectrique}\end{cases}$$

$$\rho I_{ts}=\begin{cases}\rho_b I_b, & \text{segment sans insert piézoélectrique}\\ \rho_b I_b+\rho_p I_p, & \text{segment avec insert piézoélectrique}\end{cases}$$

$$EI_s=\begin{cases}E_b I_b, & \text{segment sans insert piézoélectrique}\\ E_{eq} I_{eq}, & \text{segment avec insert piézoélectrique}\end{cases}$$

$$\aleph GA_c^b=\begin{cases}\aleph G_b A_c^b, & \text{segment sans insert piézoélectrique}\\ \aleph G_{eq} A_c^b, & \text{segment avec insert piézoélectrique}\end{cases}$$

où l'expression de la charge appliquée se calcule selon :

$$\left\{F^e\right\}=\int_0^l\begin{bmatrix}\left[N_u(x)\right]\\ \left[N_\varphi(x)\right]\end{bmatrix}^T\begin{Bmatrix}q\\ m\end{Bmatrix}dx \qquad \text{(FR2. 26)}$$

Il est également possible, de manière analogue au paragraphe précédent, d'introduire une matrice dénotant d'un amortissement (par exemple, sous la forme d'un amortisseur de Rayleigh).

D'un point de vue électrique, l'induction électrique s'obtient à partir de la rotation selon :

$$D_3=\frac{-\sigma d_{31} t_p}{\left(s_{11}^E+s_{12}^E\right)}\frac{\partial\varphi(x)}{\partial x}+\frac{2\left(\sigma d_{31}\right)^2-\varepsilon_{33}^T\left(s_{11}^E+s_{12}^E\right)}{t_p\left(s_{11}^E+s_{12}^E\right)}V_p \qquad \text{(FR2. 27)}$$

conduisant à l'expression de la charge Q :

$$Q = \frac{-\sigma w_b d_{31} t_p}{\left(s_{11}^E + s_{12}^E\right)} \varphi(x) \Big|_{x_{k0}}^{\left(x_{k0}+L_p\right)} + \frac{w_b L_p \left[2{d_{31}}^2 - \varepsilon_{33}^T \left(s_{11}^E + s_{12}^E\right)\right]}{t_p \left(s_{11}^E + s_{12}^E\right)} V_p \qquad \text{(FR2. 28)}$$

où x_{k0} est la position du $k^{\text{ème}}$ élément. Ceci conduit ainsi à l'équation électrique :

$$\begin{aligned} \left\{Q^e\right\} &= \left[B_2^e\right]\left\{d^e\right\} + \left[B_3^e\right]\left\{V_p^e\right\} \\ \left[B_2^e\right] &= \frac{-\left[\sigma\right] w_b d_{31} t_p}{\left(s_{11}^E + s_{12}^E\right)} \int_0^l \frac{\partial\left[N_\varphi(x)\right]}{\partial x} dx \\ \left[B_3^e\right] &= \frac{w_b \left[2{d_{31}}^2 - \varepsilon_{33}^T \left(s_{11}^E + s_{12}^E\right)\right]}{t_p \left(s_{11}^E + s_{12}^E\right)} \left[L_p\right] \end{aligned} \qquad \text{(FR2. 29)}$$

Ainsi, le jeu d'équation pour un élément s'exprime de manière similaire au cas d'une poutre d'Euler-Bernoulli, mais avec des matrices se calculant de manière différentes :

$$\begin{cases} \left[M^e\right]\left\{\ddot{d}^e\right\} + \left[C^e\right]\left\{\dot{d}^e\right\} + \left[K^e\right]\left\{d^e\right\} + \left[B_1^e\right]\left\{V_p^e\right\} = \left\{F^e\right\} \\ \left\{Q^e\right\} = \left[B_2^e\right]\left\{d^e\right\} + \left[B_3^e\right]\left\{V_p^e\right\} \end{cases} \qquad \text{(FR2. 30)}$$

2.4 Comparaison des modèles basés sur les hypothèses d'Euler-Bernoulli et de Timoshenko

Le but de ce paragraphe consiste à comparer les hypothèses de chaque modèle exposé ici ainsi que, en utilisant les résultats des Chapitres suivants, montrer l'impact des différentes hypothèses dans une étude de cas.

Alors que les jeux d'équations finaux de tous les modèles sont similaires, les hypothèses de départ diffèrent, comme montré dans le Tableau FR2-1, conduisant ainsi des expressions des matrices constitutives également différentes (Tableau FR2-2). On pourra de plus remarque que les matrices de couplage *B* sont absentes lorsque l'approche basée sur l'impédance est considérée ; l'effet du couplage et de la connexion particulière étant exprimée de manière implicite dans la matrice de raideur. Enfin, dans le cas où les connexions électriques ne sont à priori pas définies (approche basée sur la tension), on remarquera l'égalité de ces matrices de couplage dans tous les modèles considérés.

Un exemple de résolution numérique dans le cas où les éléments actifs sont laissés en circuit ouvert ou connectés indépendamment à une charge formée d'une résistance et d'une inductance est donné en Figure FR2.2. Dans ce cas, l'épaisseur de la structure étant relativement faible, l'effet de rotation est relativement négligeable, conduisant à des résultats similaires entre les différents modèles. On remarquera cependant quelques différences entre les bandes interdites purement induites par les propriétés mécaniques (bandes de Bragg aux alentours de [7,200 ; 8] kHz), alors que les bandes induites par la résonance électrique sont superposées, ce qui s'explique par l'équivalence des matrices de couplage.

	Euler-Bernoulli Type1	Euler-Bernoulli Type2	Timoshenko
$=0$	$T_2^{b,p}, S_2^{b,p}, T_3^{b,p}, S_3^{b,p}, T_4^{b,p}, S_4^{b,p},$ $T_5^{b,p}, S_5^{b,p}, T_6^{b,p}, S_6^{b,p}, E_1, E_2.$	$S_2^{b,p}, T_3^{b,p}, S_3^{b,p}, T_4^{b,p}, S_4^{b,p},$ $T_5^{b,p}, S_5^{b,p}, T_6^{b,p}, S_6^{b,p}, E_1, E_2.$	$S_2^{b,p}, T_3^{b,p}, S_3^{b,p}, T_4^{b,p},$ $S_4^{b,p}, T_6^{b,p}, S_6^{b,p}, E_1, E_2.$
$\neq 0$	$T_1^{b,p}, S_1^{b,p},$ $E_3.$	$T_1^{b,p}, S_1^{b,p},$ $T_2^{b,p}, E_3.$	$T_1^{b,p}, S_1^{b,p}, T_2^{b,p},$ $T_5^{b,p}, S_5^{b,p}, E_3.$

Tableau FR2-1 Comparaison des hypothèses des différents modèles.

Euler-Bernoulli Type 1	M^e	K^e	B_1^e, B_2^e, B_3^e
Euler-Bernoulli Type 2	$M_{Euler-B}^e$	$K_{Euler-B}^e$	$\left(B_1^e, B_2^e, B_3^e\right)_{Euler-B}$
Timoshenko	M_{Timo}^e	K_{Timo}^e	$\left(B_1^e, B_2^e, B_3^e\right)_{Timo}$

Tableau FR2-2 Expressions des matrices constitutives des modèles.

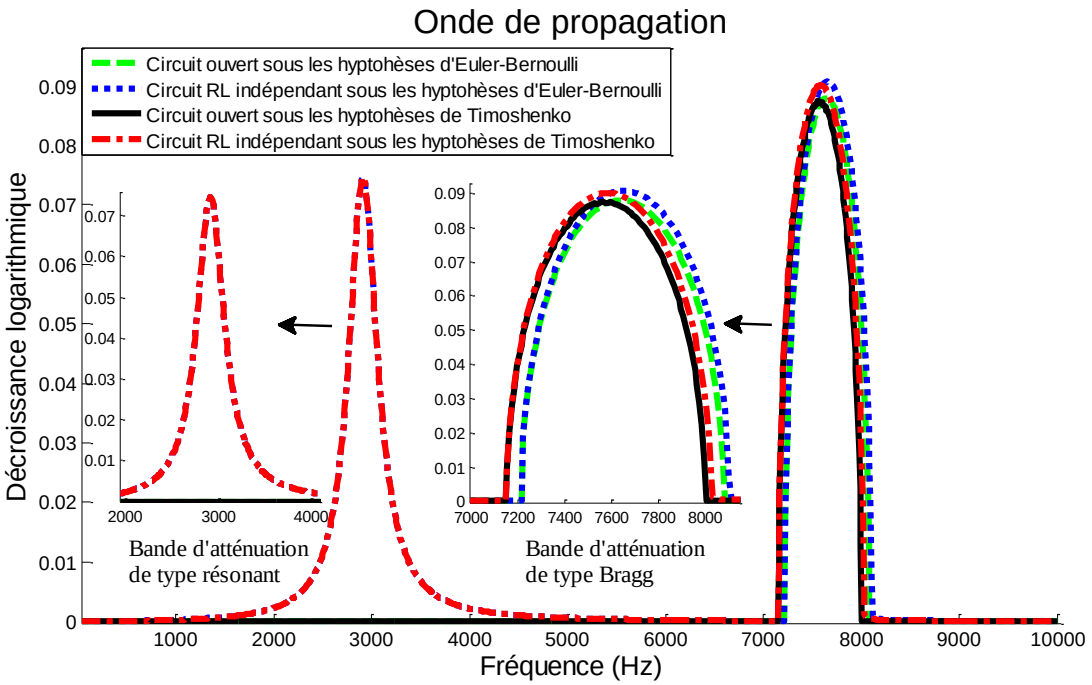

Figure FR2.2 Comparaison des résultats numériques dans le cas circuit ouvert et connexion résistive-inductive indépendante selon la modélisation.

2.5 Conclusion

Avant d'exposer les différentes techniques de contrôle de vibrations qui seront exposées dans les Chapitres suivants, ce Chapitre s'est intéressé à la modélisation des structures électromécaniques en vue de l'estimation semi-analytique des performances des méthodes étudiées dans ce manuscrit, avec une maîtrise du compromis entre simplicité et précision selon les caractéristiques de la structure étudiées. Ainsi, deux types d'approches, soit basée sur l'impédance soit sur la tension, ont été étudiées ; la dernière étant privilégiée car permettant de mettre en œuvre des connexions électriques plus complexes. De plus, trois types d'hypothèses ont été considérés, de la plus simple et la plus rapide à une plus complexe basée sur la théorie des poutres de Timoshenko prenant en compte la rotation. Ainsi, à partir des caractéristiques de la structure, le modèle le plus approprié, en termes de fidélité et de simplicité/rapidité de résolution, pourra être utilisé.

Chapitre FR- 3. Structures périodiques intelligentes avec réseaux électriques non-linéaires interconnectés

L'objectif de ce Chapitre est de donner une première architecture de structure périodique exploitant les matériaux piézoélectriques pour le contrôle de vibrations. Plus particulièrement, il est ici considéré un couplage électrique, en plus de celui mécanique, entre les cellules unitaires, ainsi que proposé dans la thèse de Linjuan YAN ([109]). Ainsi, à partir de la définition de la structure et des principes de fonctionnement dans le paragraphe 3.1, une étude de son fonctionnement théoriques sera entreprise d'un point de vue électrique dans le paragraphe 3.2 et mécanique et électromécanique dans le paragraphe 3.3. A partir de cette modélisation, les performances théoriques en terme de propagation et d'atténuation seront discutées dans le paragraphe 3.4. Dans l'optique de l'application de cette technique à des structures réelles, le paragraphe 3.5 propose d'étudier le cas d'une structure finie sous des conditions aux limites définies (encastrement ici) implémentant l'approche proposée, cette analyse étant par la suite validée par des mesures expérimentales exposées dans le paragraphe 3.6. Avant une conclusion générale sur ce Chapitre en paragraphe 3.7, des extensions possibles de l'approche seront proposées dans le paragraphe 3.6.

3.1 Principes

A partir du concept de structures périodiques combinant des matériaux de conversion électroactifs et plus particulièrement des éléments piézoélectriques ([109]), il est ici proposé d'étudier plus en avant le concept de structures périodiques avec interconnexions électriques. Un exemple de structure pouvant être envisagée est représentée en Figure FR3.1, faisant apparaître l'architecture électrique générale (vie une impédance Z) ainsi que le cas particulier de l'utilisation du SSDI.

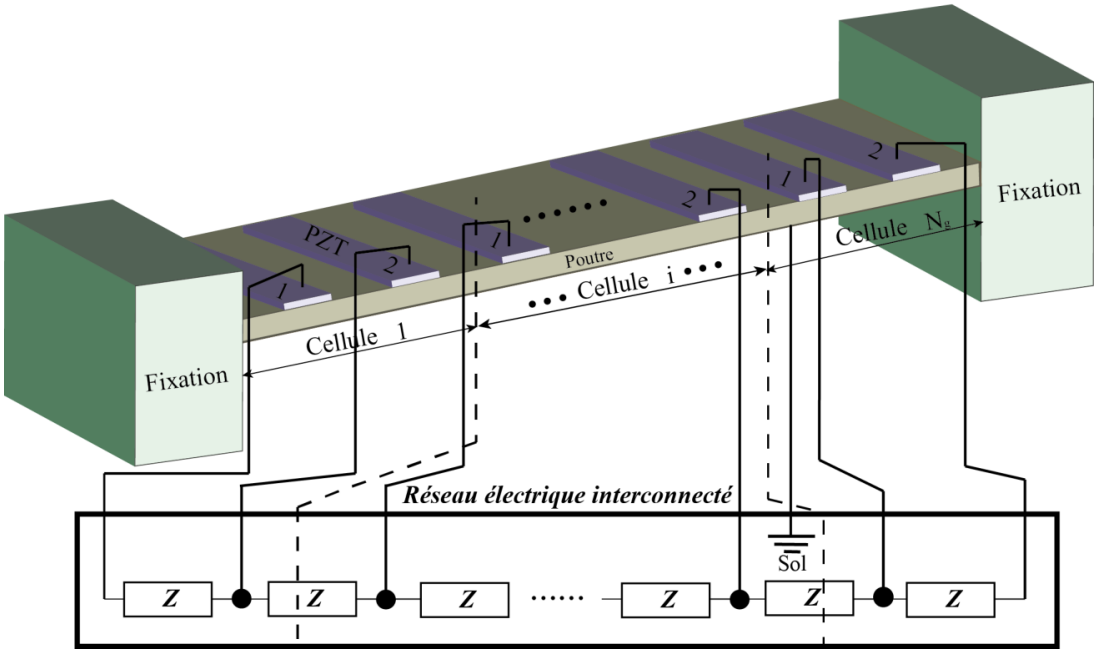

(a)

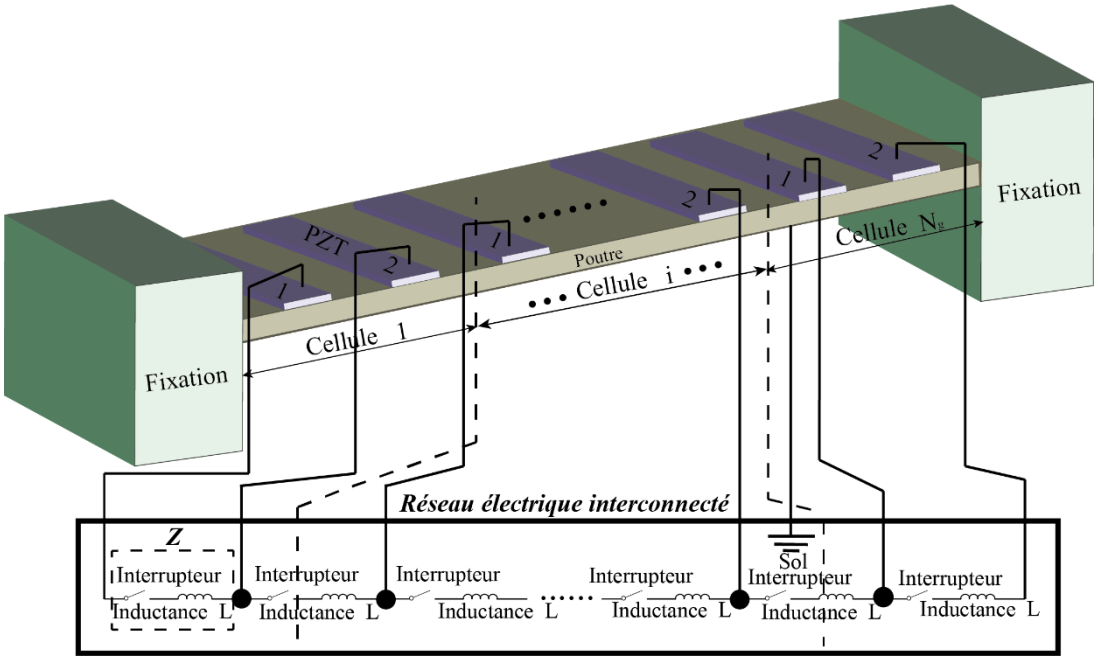

(b)

Figure FR3.1. Exemple de structures périodiques électriquement interconnectées.

A partir de cet exemple, on voit ainsi apparaître des cellules minimales composées de deux éléments piézoélectriques. En effet, ces éléments étant interconnectés, il est possible de modifier les polarités d'un élément à l'autre, conduisant à la Figure FR3.2.

Cette dernière montre ainsi différents cas d'opérations, mais toujours avec un principe de transfert énergétique dans le domaine électrique entre les éléments actifs, alors que les structures périodiques à réseau électrique indépendant ([108, 109]) ne permettent de transmission d'énergie que sous forme mécanique. A partir de la Figure FR3.2, on peut également remarquer les différences en termes d'opération selon la fréquence considérée. Ainsi, à basse fréquence, la déformation des deux éléments étant similaire, la différence de tension maximale entre les matériaux est obtenue dans le cas de polarisation inversée (nommée PN pour « *Positif-Négatif* »), conduisant à de meilleurs échanges énergétiques et donc à des performances accrues. Dans le cas hautes fréquences, les déformations sont à peu près opposées, et la structure avec même polarisation (nommée PP pour « *Positif-Positif*») est à priori plus intéressante du fait de la plus grande différence de potentiel entre les éléments.

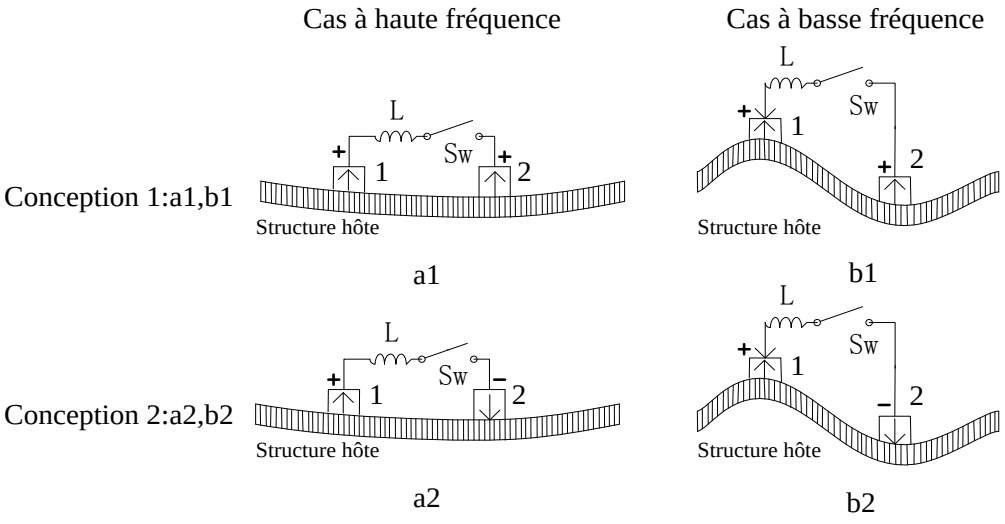

Figure FR3.2. Cellule minimale et polarisation des éléments piézoélectriques.

3.2 Modélisation

3.2.1 Comportement électrique

Il est ici proposé d'étudier le comportement électrique des structures périodiques, électriquement indépendantes ou interconnectées. Plus précisément, cette partie propose d'exprimer l'impédance linéaire ramenée par la technique SSDI lorsqu'elle est utilisée de manière indépendante ou entre deux éléments actifs (Figure FR3.3). Le principe de la technique SSDI consiste à inverser rapidement et de manière imparfaite (caractérisé par le coefficient d'inversion γ) la tension aux bornes d'un élément piézoélectrique, et, par extension, la différence de tension entre deux éléments dans le cas interconnecté. Ceci permet à la fois une augmentation importante de l'amplitude de la tension ainsi qu'un décalage temporel de celle-ci, qui devient mieux synchronisée avec la vitesse ; les deux effets dénotant d'un meilleur processus de conversion d'énergie électromécanique.

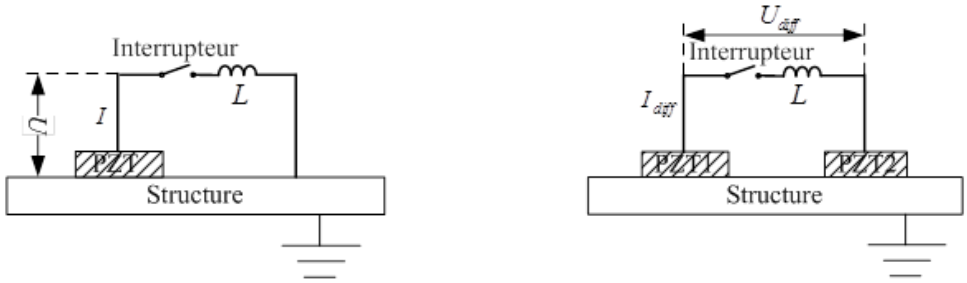

(a) Un élément *(b) Deux éléments*

Figure FR3.3. Structure piézoélectrique implémentant la technique SSDI.

En considérant qu'un élément piézoélectrique peut, d'un point de vue électrique, être modélisé comme une source de courant contrôlée par la vitesse avec une impédance de sortie capacitive, il est alors possible d'appliquer le théorème de Norton pour avoir la source équivalente, conduisant à la représentation de la Figure FR3.4, où la tension équivalente est donnée par la différence des tensions à vide de chaque élément (selon la convention choisie), et la capacité équivalente par la moitié de la capacité bloquée (en considérant les éléments piézoélectriques identiques).

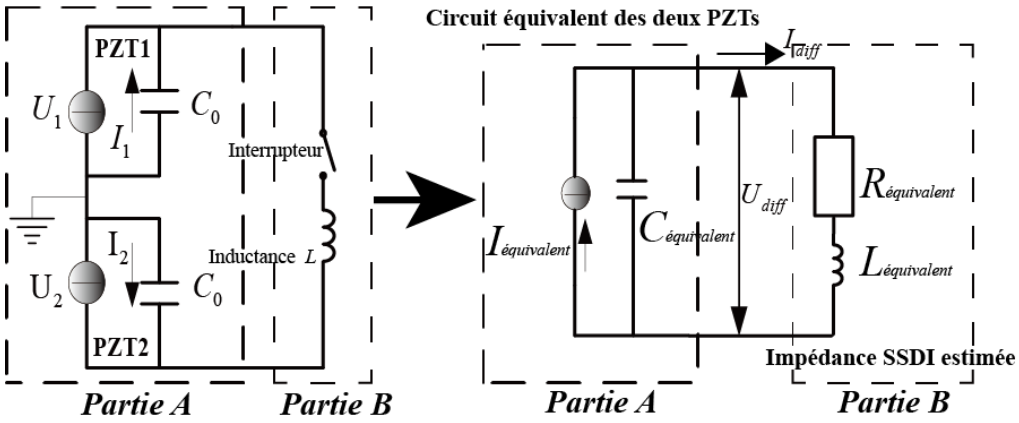

Figure FR3.4. Représentation électrique équivalente de l'interconnexion.

Concernant plus particulièrement la technique SSDI, il est proposé ici, afin de pouvoir ultérieurement évaluer les performances de la méthode, de la représenter par son impédance équivalente via la méthode du premier harmonique. Ainsi, en considérant une excitation monochromatique, en décomposant la tension sous la forme d'une tension proportionnelle au déplacement et une tension constante par morceaux dont le signe est donné par le signe de la vitesse, et en considérant le courant comme impulsionnel, on obtient l'impédance équivalente dans le cas indépendant et interconnecté (respectivement notés Z_{ind}^{SSDI} et Z_{int}^{SSDI}) :

$$Z_{ind}^{SSDI}(\omega) = \frac{\pi(1-\gamma_{ind})}{4\omega C_0(1+\gamma_{ind})} + \frac{j}{\omega C_0}$$
$$Z_{\text{int}}^{SSDI}(\omega) = \frac{\pi(1-\gamma_{\text{int}})}{2\omega C_0(1+\gamma_{\text{int}})} + \frac{2j}{\omega C_0} \quad \text{(FR3.1)}$$

pour lesquelles il est intéressant de noter que la partie imaginaires correspond exactement à la partie imaginaire de l'impédance adaptée, dénotant de la propriété d' « auto-adaptation » de la technique SSDI (tout en utilisant une inductance de faible valeur).

3.2.2 Comportement mécanique

Une fois l'impédance équivalente de la technique SSDI estimée, il est possible de mener une modélisation commune à toutes les techniques (par exemple résistive ou non-linéaire) du comportement mécanique de la structure considérée. Plus particulièrement, le principe de l'analyse menée ici consiste à étudier en premier lieu une seule cellule, en décomposant cette dernière par la technique des éléments finis, puis de tirer de cette analyse la relation globale entre les nœuds extrêmes, permettant de mettre en place la matrice de transfert à partir de laquelle les propriétés de propagation d'ondes pourront être tirées.

Modélisation par éléments finis d'une cellule

La modélisation menée ici sera basée sur les hypothèse d'Euler-Bernoulli exposées dans le Chapitre 2. Sous ces hypothèses, le comportement de chaque élément de la cellule peut être donné par :

$$\begin{cases} \left[M^e\right]\left\{\ddot{d}^i\right\}+\left[C^e\right]\left\{\dot{d}^i\right\}+\left[K^e\right]\left\{d^i\right\}+\left[B_1^e\right]\left\{V_p^i\right\}=\left\{P^i\right\} \\ \left\{Q^i\right\}=\left[B_2^e\right]\left\{d^i\right\}+\left[B_3^e\right]\left\{V_p^i\right\} \end{cases} \quad \text{(FR3.2)}$$

avec M^e, K^e and C^e les matrices de masse dynamique, de raideur en court-circuit et d'amortissement structurel, B_3 la matrice de capacité, et B_1 et B_2 les matrices de couplage. Les grandeurs d, P, Q et V représentent les vecteurs de déplacement et force généralisés (déplacement/pente et force/moment), ainsi que les charges et les tensions au niveau des inserts piézoélectriques. L'exposant i dénote de la $i^{ème}$ cellule périodique et e de l'élément unitaire au sein de celle-ci.

L'expression des matrices de capacité et de couplage peuvent s'obtenir par l'application de la méthode des éléments finis, conduisant à :

$$B_1^e=\begin{bmatrix}B_{11} & B_{12}\end{bmatrix},\ \begin{cases}B_{11}=b_{11}\int_0^l\left[H''\right]^T dx, \quad b_{11}=-\dfrac{p_1 d_{31} w_b}{t_p\left(s_{11}^E+s_{12}^E\right)}\int_{t_b}^{t_b+t_p}\left(u_3-x_c\right)dx_3\\ B_{12}=b_{12}\int_0^l\left[H''\right]^T dx, \quad b_{12}=-\dfrac{p_2 d_{31} w_b}{t_p\left(s_{11}^E+s_{12}^E\right)}\int_{t_b}^{t_b+t_p}\left(u_3-x_c\right)dx_3\end{cases}$$

$$B_2^e=\begin{bmatrix}B_{21}\\ B_{22}\end{bmatrix},\ \begin{cases}B_{21}=b_{21}\int_0^l\left[H''\right]dx, \quad b_{21}=-\dfrac{p_1 d_{31} t_p}{\left(s_{11}^E+s_{12}^E\right)}\\ B_{22}=b_{22}\int_0^l\left[H''\right]dx, \quad b_{22}=-\dfrac{p_2 d_{31} t_p}{\left(s_{11}^E+s_{12}^E\right)}\end{cases} \qquad \text{(FR3.3)}$$

$$B_3^e=\begin{bmatrix}B_{31} & 0\\ 0 & \mathrm{B}_{32}\end{bmatrix},\quad B_{31}=B_{32}=\frac{w_b L_p\left[\varepsilon_{33}^T\left(s_{11}^E+s_{12}^E\right)-2d_{31}^2\right]}{t_p\left(s_{11}^E+s_{12}^E\right)}$$

où p est la direction de polarisation (conventionnellement choisie à 1 pour positif et -1 pour négatif), d le coefficient piézoélectrique, s les compliances, ε la permittivité, w_b, t_p et L_p la largeur de la structure, et l'épaisseur et la longueur de l'insert. Enfin, u_3 représente le déplacement en flexion et x_c la position de la fibre neutre.

A partir de ces relations, il est possible de réarranger l'équation du mouvement sous la forme fréquentielle, en fonction de la pulsation ω :

$$\begin{cases}P^i=A^e\cdot d^i+B_1^e\cdot V_p^i\\ I_p^i=j\omega B_2^e\cdot d^i+j\omega B_3^e\cdot V_p^i\end{cases} \qquad \text{(FR3.4)}$$

Où I est le courant et A représente la matrice de raideur dynamique, définie selon le type de connexion (*cc* pour court-circuit, *co* pour circuit ouvert, *ind* pour indépendant, et *pass* pour passif) :

$$A_{cc}=A^e;$$

$$A_{co}=A^e+B_1^e\cdot B_4^e,\quad B_4^e=\begin{bmatrix}B_{41}\\ B_{42}\end{bmatrix},\quad B_{41,42}=b_{41,42}\int_0^l\left[H''\right]dx,\quad b_{41,42}=\frac{d_{31}{t_p}^2}{L_p\left[\grave{o}_{33}^T\left(s_{11}^E+s_{12}^E\right)-2d_{31}^2\right]};$$

$$A_{ind}^{pass}=A^e+B_1^e\cdot B_5^e,\quad B_5^e=\begin{bmatrix}B_{51}\\ B_{52}\end{bmatrix},\quad B_{51,52}=\frac{j\omega Z_{ind}^{passive}\cdot B_{21,22}}{\left(1-j\omega Z_{ind}^{passive}\cdot B_{31,32}\right)}; \qquad \text{(FR3.5)}$$

$$A_{ind}^{SSDI}=A^e+B_1^e\cdot B_6^e,\quad B_6^e=B_4^e\left(1+\frac{1+\gamma_{ind}}{1-\gamma_{ind}}\cdot\frac{4j}{\pi}\right)\ \ or\ \ \frac{j\omega Z_{ind}^{SSDI}\cdot B_{21,22}}{\left(1-j\omega Z_{ind}^{SSDI}\cdot B_{31,32}\right)}.$$

Dans le cas interconnecté cependant, il convient de d'abord étudier l'effet des échanges énergétiques entre les inserts et de prendre en compte ces échanges dans l'expression matricielle. Ainsi, en considérant les relations électriques entre les éléments (p_1 et p_2 représentant les inserts) :

$$V_i - \frac{Z}{2}\cdot I_i = V_{p1} \;;\; V_{p1} - Z\cdot I_m = V_{p2} \;;\; I_i + I_{p1} = I_m \;;\; V_{p2} - \frac{Z}{2}\cdot I_{i+1} = V_{i+1} \;;$$
$$I_{p2} + I_m = I_{i+1} \;;\; P^i = A^e\cdot d^i + B_1^e\cdot V_p \;;\; I_p = B_2^e\cdot \dot{d}^i + B_3^e\cdot \dot{V}_p\,, \tag{FR3.6}$$

l'équation donnant les relations entre deux cellules adjacentes fait apparaître des termes électriques :

$$\begin{Bmatrix} P^i \\ V_{i+1} \\ I_{i+1} \end{Bmatrix} = A_{\mathrm{int}erconnected}\cdot \begin{Bmatrix} d^i \\ V_i \\ I_i \end{Bmatrix} = \begin{bmatrix} A_{11} & A_{12} & A_{13} \\ A_{21} & A_{22} & A_{23} \\ A_{31} & A_{32} & A_{33} \end{bmatrix}\cdot \begin{Bmatrix} d^i \\ V_i \\ I_i \end{Bmatrix}$$

$$\begin{aligned}
A_{11} &= A^e - Z\cdot B_{21}\cdot B_{12}\cdot j\omega; \\
A_{12} &= B_{11} + B_{12} - Z\cdot B_{12}\cdot B_{31}\cdot j\omega; \\
A_{13} &= -\left(\frac{Z}{2}\cdot B_{11} + \frac{3Z}{2}\cdot B_{12}\right) + \frac{Z^2}{2}\cdot B_{12}\cdot B_{31}\cdot j\omega; \\
A_{21} &= -\omega^2\cdot\frac{Z^2}{2}\cdot B_{31}\cdot B_{21} - \frac{Z}{2}\cdot B_{22}\cdot j\omega - \frac{3}{2}Z\cdot B_{21}\cdot j\omega; \\
A_{22} &= 1 - \frac{Z^2}{2}\cdot B_{31}^2\cdot\omega^2 - 2Z\cdot B_{31}\cdot j\omega; \\
A_{23} &= \frac{3}{2}Z^2\cdot B_{31}\cdot j\omega - 2Z + \frac{Z^3}{4}\cdot B_{31}^2\cdot\omega^2; \\
A_{31} &= \omega^2\cdot Z\cdot B_{32}\cdot B_{21} + B_{22}\cdot j\omega + B_{21}\cdot j\omega; \\
A_{32} &= Z\cdot B_{31}^2\cdot\omega^2 + 2B_{31}\cdot j\omega; \\
A_{33} &= 1 - 2Z\cdot B_{31}\cdot j\omega - \frac{Z^2}{2}\cdot B_{31}^2\cdot\omega^2.
\end{aligned} \tag{FR3.7}$$

avec Z l'impédance (éventuellement équivalente, comme pour le SSDI) connectée entre les éléments.

Matrice de transfert

A partir de l'analyse d'une cellule à l'aide de la technique des éléments finis exposée dans la partie précédente, il est possible de tirer le lien entre cellules adjacentes et

d'obtenir ainsi le comportement global de la structure. Cette relation est obtenue en isolant les nœuds extrêmes dans la matrice de raideur dynamique :

$$\begin{Bmatrix} P_0^i \\ P_j^i \\ P_n^i \end{Bmatrix} = \left[A_{ind}\right] \cdot \begin{Bmatrix} d_0^i \\ d_j^i \\ d_n^i \end{Bmatrix} = \begin{bmatrix} a_{00} & a_{0j} & a_{0n} \\ a_{j0} & a_{jj} & a_{jn} \\ a_{n0} & a_{nj} & a_{nn} \end{bmatrix} \cdot \begin{Bmatrix} d_0^i \\ d_j^i \\ d_n^i \end{Bmatrix}, A_{ind} = A_{case}^e$$

$$\begin{Bmatrix} P_0^i \\ P_j^i \\ P_n^i \\ U_{i+1} \end{Bmatrix} = \left[A_{\text{int}}\right] \cdot \begin{Bmatrix} d_0^i \\ d_j^i \\ d_n^i \\ U_i \end{Bmatrix} = \begin{bmatrix} a_{00} & a_{0j} & a_{0n} & c_{00} \\ a_{j0} & a_{jj} & a_{jn} & c_{j0} \\ a_{n0} & a_{nj} & a_{nn} & c_{n0} \\ b_{00} & b_{0j} & b_{0n} & d_{00} \end{bmatrix} \cdot \begin{Bmatrix} d_0^i \\ d_j^i \\ d_n^i \\ U_i \end{Bmatrix} = \begin{bmatrix} AA_{11} & AA_{12} \\ AA_{21} & AA_{22} \end{bmatrix} \begin{Bmatrix} d_0^i \\ d_j^i \\ d_n^i \\ U_i \end{Bmatrix} \quad \text{(FR3.8)}$$

avec U le vecteur électrique généralisé (tension et courant) et en considérant aucune excitation au sein même des cellules (uniquement sur les extrémités), ce qui permet d'utiliser la réduction de Guyan conduisant aux matrices de transfert :

$$\begin{Bmatrix} d_n^i \\ P_n^i \end{Bmatrix} = T \cdot \begin{Bmatrix} d_0^i \\ P_0^i \end{Bmatrix} = \begin{bmatrix} t_{11} & t_{12} \\ t_{21} & t_{22} \end{bmatrix} \cdot \begin{Bmatrix} d_0^i \\ P_0^i \end{Bmatrix}$$

$$t_{11} = -\alpha_{12}^{-1}\alpha_{11}, \quad t_{12} = \alpha_{12}^{-1}, \quad t_{21} = -\alpha_{21} + \alpha_{22}\alpha_{12}^{-1}\alpha_{11}, \quad t_{22} = -\alpha_{22}\alpha_{12}^{-1}. \quad \text{(FR3.9)}$$

$$\alpha_{11} = a_{00} - a_{0j}a_{jj}^{-1}a_{j0}; \quad \alpha_{12} = a_{0n} - a_{0j}a_{jj}^{-1}a_{jn};$$
$$\alpha_{21} = a_{n0} - a_{nj}a_{jj}^{-1}a_{j0}; \quad \alpha_{22} = a_{nn} - a_{nj}a_{jj}^{-1}a_{jn}.$$

dans le cas indépendant et

$$\begin{Bmatrix} d_n^i \\ P_n^i \\ U_{i+1} \end{Bmatrix} = T \begin{Bmatrix} d_0^i \\ P_0^i \\ U_i \end{Bmatrix}, T = \begin{bmatrix} -K_{12}^{-1} \cdot K_{11} & K_{12}^{-1} & -K_{12}^{-1} \cdot K_{13} \\ -K_{21} + K_{22} \cdot K_{12}^{-1} \cdot K_{11} & -K_{22} \cdot K_{12}^{-1} & -K_{23} + K_{22} \cdot K_{12}^{-1} \cdot K_{13} \\ K_{31} - K_{32} \cdot K_{12}^{-1} \cdot K_{11} & K_{32} \cdot K_{12}^{-1} & K_{33} - K_{32} \cdot K_{12}^{-1} \cdot K_{13} \end{bmatrix} \quad \text{(FR3.10)}$$

$$K_{11} = a_{00} - a_{0j}a_{jj}^{-1}a_{j0}; \quad K_{12} = a_{0n} - a_{0j}a_{jj}^{-1}a_{jn}; \quad K_{13} = c_{00} - a_{0j}a_{jj}^{-1}c_{j0};$$
$$K_{21} = a_{n0} - a_{nj}a_{jj}^{-1}a_{j0}; \quad K_{22} = a_{nn} - a_{nj}a_{jj}^{-1}a_{jn}; \quad K_{23} = c_{n0} - a_{nj}a_{jj}^{-1}c_{j0};$$
$$K_{31} = b_{00} - b_{0j}a_{jj}^{-1}a_{j0}; \quad K_{32} = b_{0n} - b_{0j}a_{jj}^{-1}a_{jn}; \quad K_{33} = d_{00} - b_{0j}a_{jj}^{-1}c_{j0}.$$

dans le cas interconnecté. L'analyse des valeurs propres de ces matrices de transfert permet ainsi de remonter aux caractéristiques (nombre d'onde et atténuation) des ondes mécaniques (propagative ou évanescentes) ainsi que, dans le cas interconnecté, des ondes électriques.

3.3 Résultats théoriques de la propagation

L'objectif de cette partie est, à partir des développements théoriques effectués précédemment et en considérant les paramètres et dimensions donnés dans le Tableau FR3-1 tirés de la structure expérimentale étudiée dans le paragraphe 3.5, de discuter des capacités d'amortissement des différentes techniques par l'analyse des caractéristiques des ondes (notamment de propagation).

Structure hôte

Module d'Young	$Y_b = 190\times10^9\, Pa$	Coefficient de Poisson	$v_b = 0.21$	Densité	$\rho_b = 7875 kg/m^3$
Longueur	$L_b = 176\times10^{-3} m$	Largeur	$w_b = 35\times10^{-3} m$	Epaisseur	$t_b = 1.5\times10^{-3} m$

Inserts piézoélectriques

Compliance en circuit ouvert	$s_{11}^E = 10.66\times10^{-12} m^2/N$ $s_{12}^E = -3.34\times10^{-12} m^2/N$	Densité	$\rho_p = 7650 kg/m^3$
Permittivité relative	$\frac{\varepsilon^T}{\varepsilon_0} = 1150$	Coefficient de charge	$d_{31} = -108\times10^{-12} m/V$
Longueur	$L_p = 10\times10^{-3} m$	Epaisseur	$t_p = 0.5\times10^{-3} m$

Tableau FR3-1. Caractéristiques et dimensions de la structure.

3.3.1 Cas résistif

Dans un premier temps, il est proposé d'évaluer les performances d'amortissement lors de l'utilisation d'une charge résistive pure. Les facteurs d'atténuation, obtenus à partir des valeurs propres de la matrice de transfert, sont donné pour les cas indépendants et interconnectés, ainsi que pour le cas en circuit ouvert pour comparaison, en Figure FR3.5. Par ailleurs, il est considéré ici que la résistance utilisé

est adaptée pour chaque fréquence considérée. On voit ainsi l'apparition en circuit ouvert de bande interdites avec un fort potentiel d'amortissement, caractéristique typique des structures périodiques. L'hybridation de cette méthode avec des matériaux de conversion d'énergie électromécanique (éléments piézoélectriques ici) permet une amélioration du potentiel d'amortissement par l'apparition de valeurs non nulles du facteur d'atténuation hors des bandes interdites originales.

Néanmoins, on remarquera dans ces zones que les structures de type interconnectées présentent des performances moindres que le cas indépendant. Cependant, ce dernier voit son facteur d'amortissement diminuer dans les bandes interdites originales, alors que l'interconnexion électrique permet de ne pas modifier l'amortissement de ces zones, dans les bandes fréquentielles basses pour les structures de type PN et haute pour le type PP, ce qui est en accord avec la description qualitative du paragraphe 3.1. Ainsi l'utilisation des structures interconnectées purement résistives permet un bon compromis entre structures périodiques purement mécanique (équivalent du cas en circuit ouvert) et les structures périodiques électromécaniques à connexion électrique indépendante.

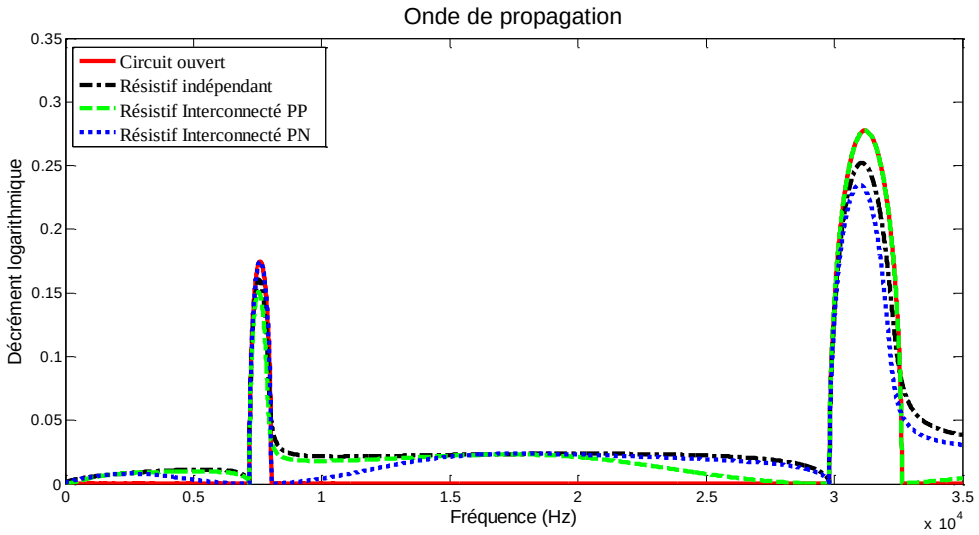

Figure FR3.5. Constantes d'atténuation de l'onde mécanique de propagation dans le cas résistif.

3.3.2 SSDI

Alors que dans le cas résistif les performances hors des bandes interdites originales sont toujours favorables au cas indépendant, il est intéressant de noter que l'utilisation de l'interface SSDI dépend du facteur d'inversion. Ainsi, outre le fait de l'augmentation des capacités d'amortissement par rapport au cas résistif, on peut voir, à partir de la Figure FR3.6, l'apparition de zones de plus forte atténuation (par rapport au cas indépendant) entre les bandes interdites originales par l'utilisation de structures interconnectées. Néanmoins, la bande fréquentielle de ces zones est fortement dépendante du facteur d'inversion, et diminue avec celui-ci, alors que l'amplitude du facteur d'atténuation connaît une variation dépendante de la bande fréquentielle considérée (augmentation relative - par rapport au cas indépendant - du pouvoir d'amortissement en basse fréquence mais diminution relative de celui-ci pour les moyennes fréquence dans l'exemple de la Figure FR3.6). Ceci peut être notamment attribué au fait que l'interconnexion permet une diminution significative des pertes lors de la commutation et ainsi à un meilleur échange d'énergie entre les inserts. Néanmoins, on pourra noter que pour des applications très intégrées, la difficulté d'implémentation d'inductances à faibles pertes peut fortement diminuer le facteur d'inversion, et ainsi donner un avantage conséquent aux structures électriquement interconnectées en terme d'amortissement large bande efficace. Egalement, on peut remarquer que ces nouvelles bandes d'atténuation correspondent aux extrema de l'atténuation des ondes électriques (Figure FR3.7), dénotant une interaction particulière, où, aux fréquences considérées, l'onde électrique agit de manière destructive avec l'onde de propagation mécanique.

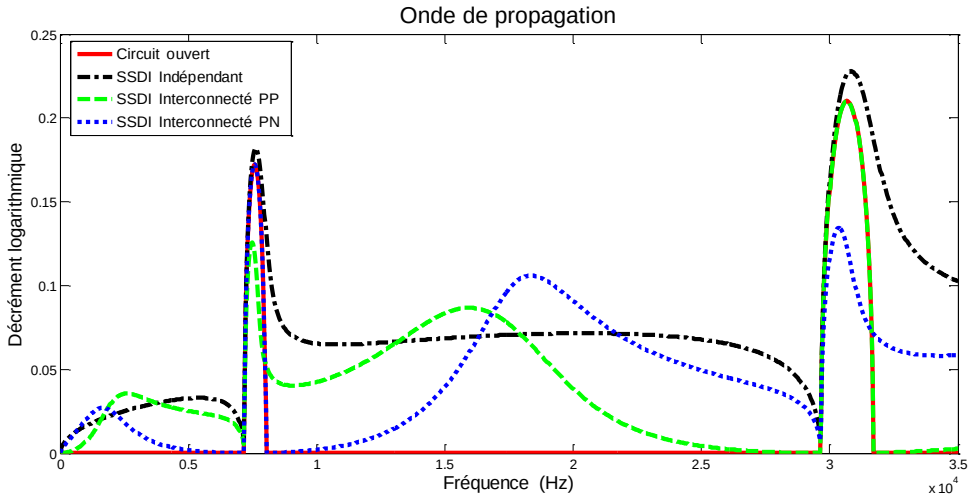

(b) γ_{ind}=0.1, γ_{int}=0.2

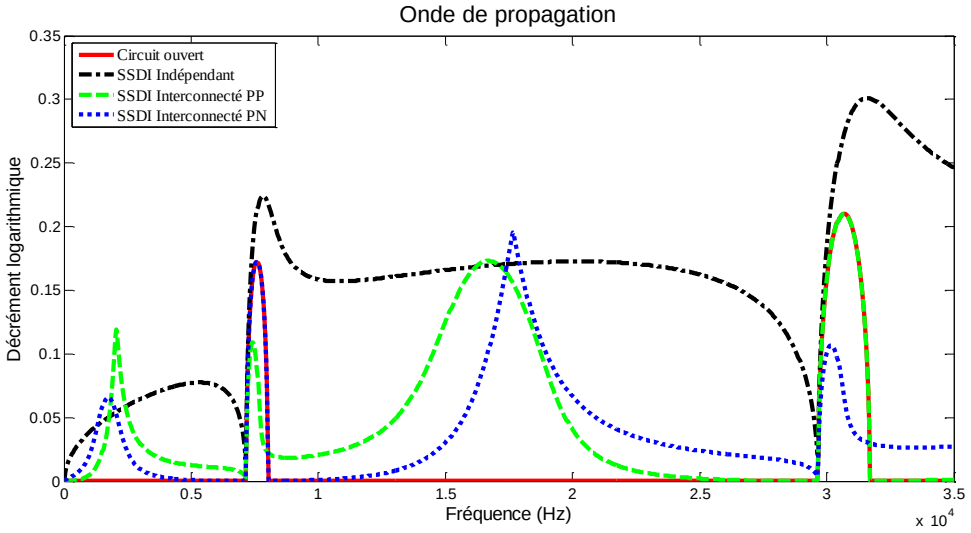

(b) γ_{ind}=0.5, γ_{int}=0.6

Figure FR3.6. Constantes d'atténuation de l'onde mécanique de propagation avec la technique SSDI pour plusieurs valeurs du coefficient d'inversion.

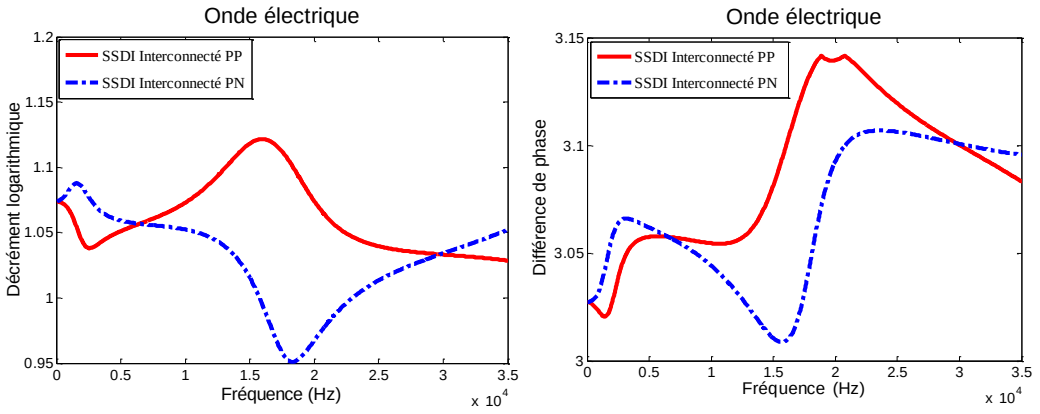

(a) γ_{ind}=0.1, γ_{int}=0.2

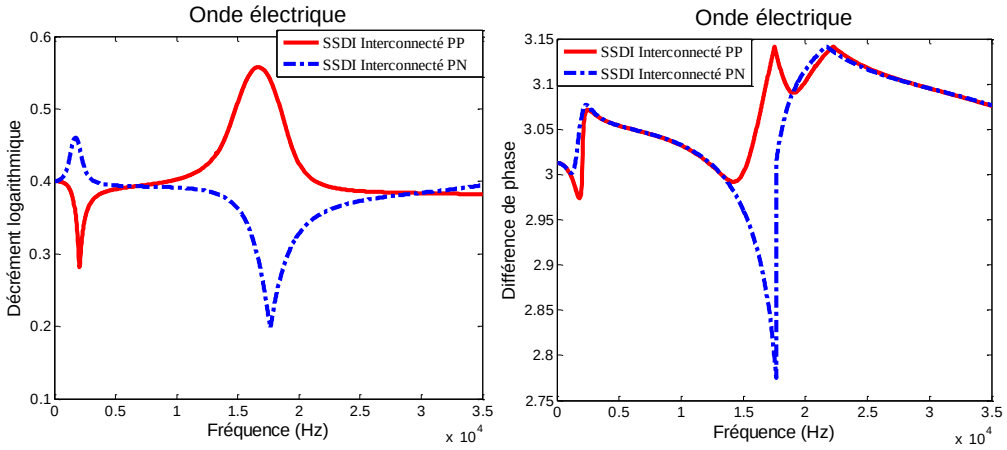

(b) γ_{ind}=0.5, γ_{int}=0.6

Figure FR3.7. Constantes d'atténuation des ondes électriques avec la technique SSDI pour plusieurs valeurs du coefficient d'inversion.

3.4 Application à des structures finies

Dans la continuité de la démarche précédente, ce paragraphe propose d'étudier le comportement d'une structure périodique dont les conditions aux limites sont fixées, reflétant ainsi des cas réalistes. Ainsi, à partir de la modélisation par éléments finis obtenue par le découpage d'une cellule, puis de la mise en place de la matrice de transfert de la cellule complète, il est possible d'établir la réponse pour une structure composée de plusieurs cellules avec celles extrêmes soumises à des conditions aux limites particulières. De plus, en considérant une force extérieure appliquée entre les $nf^{ème}$ et $(nf+1)^{ème}$ cellules et en appliquant le principe de superposition, on peut ainsi obtenir le comportement global de la structure en tout point.

Plus particulièrement, en considérant à titre d'exemple une structure encastrée-encastrée composée de N_g cellules (dont les vecteurs extrêmes de déplacement généralisé sont nuls mais avec une réaction en terme de force et moment des encastrements) dont les terminaisons sont en circuit ouvert dans le cas interconnecté, on obtient la réponse entre toute cellule $i^{ème}$ et $(i+1)^{ème}$ cellules :

$$\begin{Bmatrix} d^i \\ P^i \end{Bmatrix} = [T]^i \begin{Bmatrix} 0 \\ P_0^0 \end{Bmatrix} + [T]^{(i-nf)} \begin{Bmatrix} 0 \\ P_{ex}^{nf} \end{Bmatrix}$$

$$P_{ex}^{nf} = \begin{bmatrix} F^{ex} & 0 \end{bmatrix}^t$$

$$P_0^0 = -\left(t_{12}^{\{N_g\}}\right)^{-1} t_{12}^{\{N_g-nf\}} P_{ex}^{nf} \qquad \text{(FR3.11)}$$

$$\begin{cases} [T]^{N_g} = \begin{pmatrix} t_{11}^{\{N_g\}} & t_{12}^{\{N_g\}} \\ t_{21}^{\{N_g\}} & t_{22}^{\{N_g\}} \end{pmatrix} \\ [T]^{(N_g-nf)} = \begin{pmatrix} t_{11}^{\{N_g-nf\}} & t_{12}^{\{N_g-nf\}} \\ t_{21}^{\{N_g-nf\}} & t_{22}^{\{N_g-nf\}} \end{pmatrix} \end{cases}$$

pour le cas indépendant et

$$\begin{Bmatrix} d_i \\ P_i \\ U_i \end{Bmatrix} = [T]^i \begin{Bmatrix} 0 \\ P_0^0 \\ U_0 \end{Bmatrix} + [T]^{(i-nf)} \begin{Bmatrix} 0 \\ P_{ex}^{nf} \\ 0 \end{Bmatrix}$$

$$P_{ex}^{nf} = \begin{bmatrix} F^{ex} & 0 \end{bmatrix}^t$$

$$P_0^0 = \left(t_{12}^{\{N_g\}}\right)^{-1} \left(-t_{13}^{\{N_g\}} V_0 - t_{12}^{\{N_g-nf\}} P_{ex}^{nf}\right)$$

$$V_0 = \left(t_{42}^{\{N_g\}} \left(t_{12}^{\{N_g\}}\right)^{-1} t_{13}^{\{N_g\}} - t_{43}^{\{N_g\}}\right)^{-1} \left(t_{42}^{\{N_g-nf\}} - t_{42}^{\{N_g\}} \left(t_{12}^{\{N_g\}}\right)^{-1} t_{12}^{\{N_g-nf\}}\right) P_{ex}^{nf} \qquad \text{(FR3.12)}$$

$$T^{\{N_g\}} = \begin{bmatrix} t_{11}^{\{N_g\}} & t_{12}^{\{N_g\}} & t_{13}^{\{N_g\}} & t_{14}^{\{N_g\}} \\ t_{21}^{\{N_g\}} & t_{22}^{\{N_g\}} & t_{23}^{\{N_g\}} & t_{24}^{\{N_g\}} \\ t_{31}^{\{N_g\}} & t_{32}^{\{N_g\}} & t_{33}^{\{N_g\}} & t_{34}^{\{N_g\}} \\ t_{41}^{\{N_g\}} & t_{42}^{\{N_g\}} & t_{43}^{\{N_g\}} & t_{44}^{\{N_g\}} \end{bmatrix}, \quad T^{\{N_g-nf\}} = \begin{bmatrix} t_{11}^{\{N_g-nf\}} & t_{12}^{\{N_g-nf\}} & t_{13}^{\{N_g-nf\}} & t_{14}^{\{N_g-nf\}} \\ t_{21}^{\{N_g-nf\}} & t_{22}^{\{N_g-nf\}} & t_{23}^{\{N_g-nf\}} & t_{24}^{\{N_g-nf\}} \\ t_{31}^{\{N_g-nf\}} & t_{32}^{\{N_g-nf\}} & t_{33}^{\{N_g-nf\}} & t_{34}^{\{N_g-nf\}} \\ t_{41}^{\{N_g-nf\}} & t_{42}^{\{N_g-nf\}} & t_{43}^{\{N_g-nf\}} & t_{44}^{\{N_g-nf\}} \end{bmatrix}$$

pour le cas interconnecté

3.5 Validation expérimentale

Afin de valider les résultats théoriques, à la fois de manière qualitative et quantitative, il est ici proposé d'étudier le comportement expérimental d'une structure électromécanique périodique composée de 8 cellules unitaires. Les résultats, représentés en Figure FR3.8 pour les cas résistifs (où les résistances sont adaptées par rapport à chaque mode) et en Figure FR3.9 pour les techniques SSDI, montrent tout d'abord une supériorité de ces dernières en termes de capacité d'amortissement, permettant un gain jusqu'à 3 dB dans le cas expérimental considéré.

Egalement, ainsi que précédemment prévu qualitativement et quantitativement, on note une meilleure atténuation en basse fréquence de la structure PN par rapport à la configuration PP, et l'inverse dans les hautes fréquences.

En comparant avec la structure indépendante, alors que la structure PP montre un meilleur amortissement en haute fréquence par rapport au cas indépendant, les meilleures performances en basses fréquences restent obtenues avec la connexion indépendante. Ceci peut être attribué au fait que la structure n'a pas été totalement optimisée afin de s'assurer que la distribution des inserts permette un accord en fréquence de résonance de la structure globale et optima du facteur d'amortissement d'une cellule seule.

Enfin, on pourra noter quelques différences entre prévisions théoriques et résultats expérimentaux, qui peuvent être attribuées à une certaine apériodicité expérimentale ainsi que par le fait que deux structures différentes ont été utilisées entre le cas PP et PN.

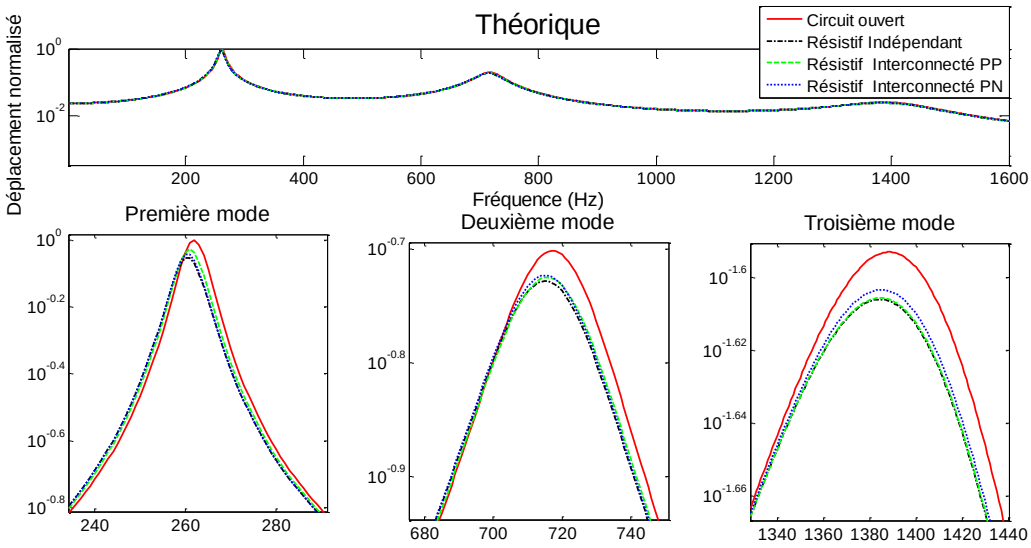

(a) Résultats théoriques

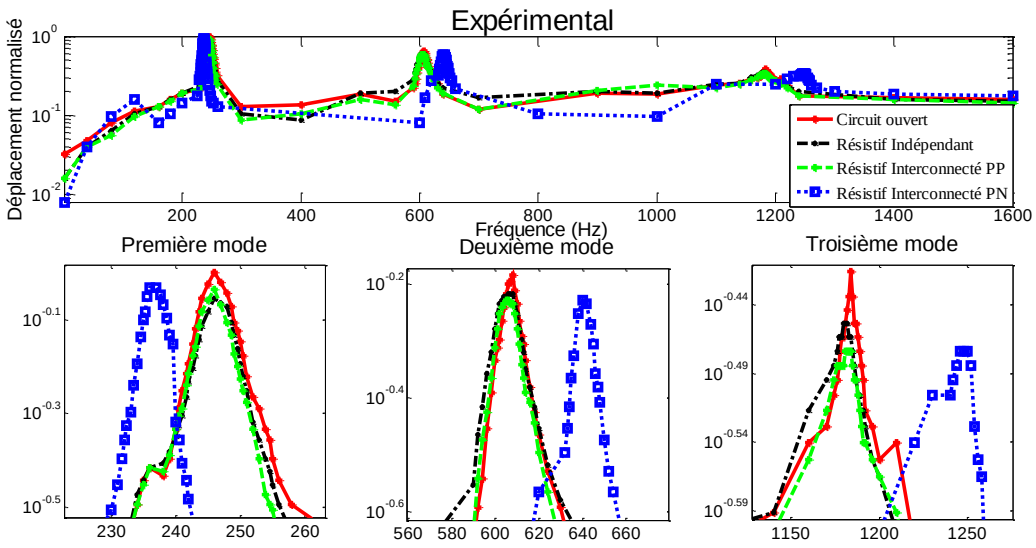

(b) Résultats expérimentaux

Figure FR3.8. Résultats théoriques et expérimentaux pour les cas résistifs.

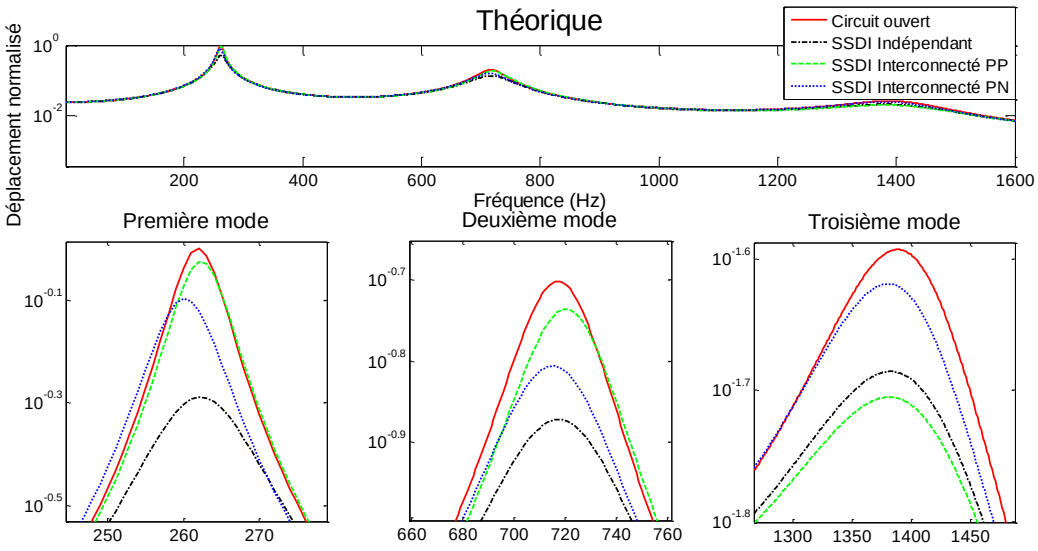

(a) Résultats théoriques

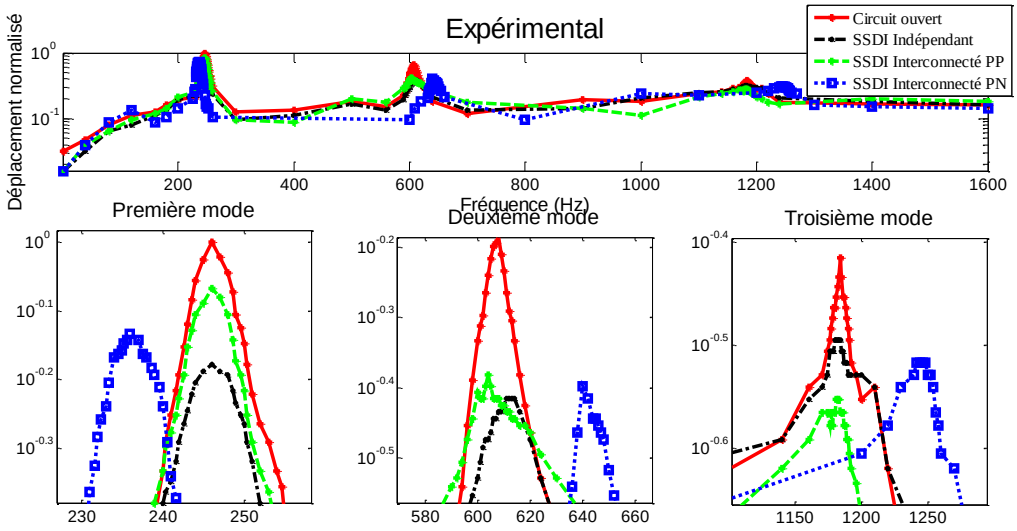

(b) Résultats expérimentaux

Figure FR3.9. Résultats théoriques et expérimentaux pour les cas SSDI.

3.6 Conclusion et extensions

Dans la continuité des travaux initiés dans la thèse de Linjuan Yan, et basé sur leurs perspectives, ce Chapitre a proposé l'étude de structures périodiques utilisant des matériaux électroactifs interfacés de manière non-linéaire, en y incorporant en plus un aspect de propagation électrique due à l'interconnexion des éléments dans le domaine électrique. A partir de ce principe, deux sous-catégories ont été proposées, selon la polarisation de deux inserts électroactifs adjacent.

Ainsi, à partir d'analyses théoriques allant de la décomposition en éléments finis d'une cellule unitaire jusqu'à la structure globale, il a été montré qu'une telle interconnexion permet la génération de nouvelles bandes interdites, dont la bande passante dépend du facteur d'amélioration de la conversion du au processus de traitement non-linéaire (facteur d'inversion). Egalement, les bandes fréquentielles ciblées selon le type de configuration (polarisée identique ou alternée) sont différentes, avec un contrôle plutôt basse fréquence pour les cellules à polarisation alternée et haute fréquence pour les polarisations identiques.

Néanmoins, les résultats obtenus ne montrent que peu d'amélioration voire une dégradation des performances par rapport au cas indépendant. Cependant, le principe d'interconnexion est néanmoins une piste à creuser. Notamment, l'hybridation de cellules interconnectés formant des métacellules indépendantes, utilisant par exemple la structure représentée en Figure FR3.10(a), peut s'avérer intéressante. Les résultats (obtenus par une démarche identique à celle utilisée dans ce Chapitre) utilisant une telle configuration montrent ainsi des capacité d'atténuation similaire au cas indépendant, mais avec moitié moins de commutateurs électroniques, facilitant ainsi l'intégration et la consommation (Figure FR3.10(b)). Ainsi, le contrôle de la granularité du nombre de métacellules et du nombre de cellules interconnectées les composant, peut permettre un contrôle efficace du compromis en performance et simplicité.

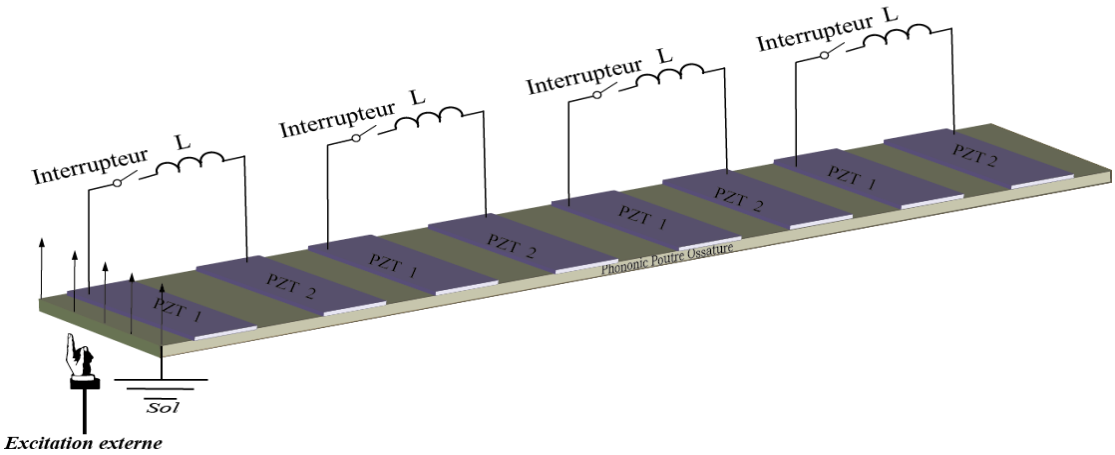

(a)

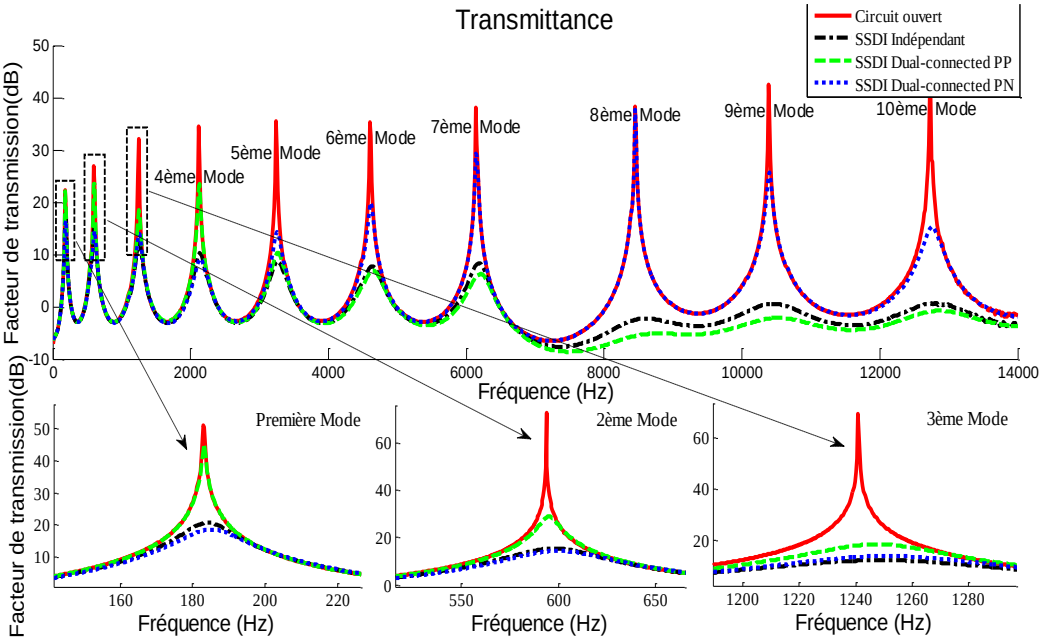

(b)

Figure FR3.10. Structure périodique avec bi-interconnexion électrique : (a) Principes ; (b) Résultats théoriques pour une poutre encastrée-encastrée.

Chapitre FR- 4. Structure périodiques intelligentes avec réseaux électriques non-linéaires entrelacés

Alors que le Chapitre précédent a montré que l'avantage de l'interconnexion électrique des cellules composant la structure périodique tient plus à la simplicité de mise en œuvre (moins de commutateurs) que des performances en termes d'amortissement, ce Chapitre se propose d'utiliser des entrelacements des interconnexions électriques, conduisant à l'apparition de metacellules et d'une certaine apériodicité permettant une augmentation des performances d'atténuation. De manière similaire au cas précédent, ce Chapitre se compose d'une exposition des principes qualitatifs de fonctionnement de la technique (paragraphe 4.1), suivi de la modélisation théorique (paragraphe 4.2) permettant une discussion des performances en termes d'atténuation d'ondes (paragraphe 4.3), puis de l'application expérimentale à une structure de type poutre encastrée-encastrée (paragraphe 4.5), et enfin, avant la conclusion récapitulant les avancées et proposant des extensions de la méthode (paragraphe 4.6), une extension utilisant un réseau tri-entrelacé (paragraphe 4.5).

4.1 Principes

Le principe de la structure entrelacée consiste à confiner l'interconnexion entre cellule à un groupe de cellule donné (4), conduisant à la création d'une méta-cellule, comme représenté en Figure FR4. 1. Du fait de l'utilisation de 4 cellules unitaires, trois cas peuvent être considérés selon la direction de polarisation des éléments piézoélectriques d'une méta-cellule (« P » dénotant « positif » et « N » « négatif » : PPPP (toutes les directions de polarisation sont les mêmes), PPNN (les deux premières cellules ont une direction de polarisation identique et opposée au deux dernières cellules) et PPNP (la troisième cellule a une direction de polarisation différentes).

4.2 Modélisation

Cette partie propose, en vue d'une étude théorique de la propagation, de mettre en place un modèle de manière similaire au Chapitre précédent, en s'intéressant d'abord à la modélisation d'une méta-cellule sous la forme de l'assemblage d'éléments finis, puis d'en dériver la matrice de transfert caractérisant la méta-cellule. Cette dernière ne sera néanmoins pas détaillée ici car son obtention est strictement identique à l'analyse menée dans le chapitre précédent.

Dans le cas entrelacé, une méta-cellule est composée de quatre cellules élémentaires électriquement interconnectées. En utilisant le modèle basé sur la théorie de Timoshenko, il a été établi dans le Chapitre 2 le comportement électromécanique de chaque élément suivant :

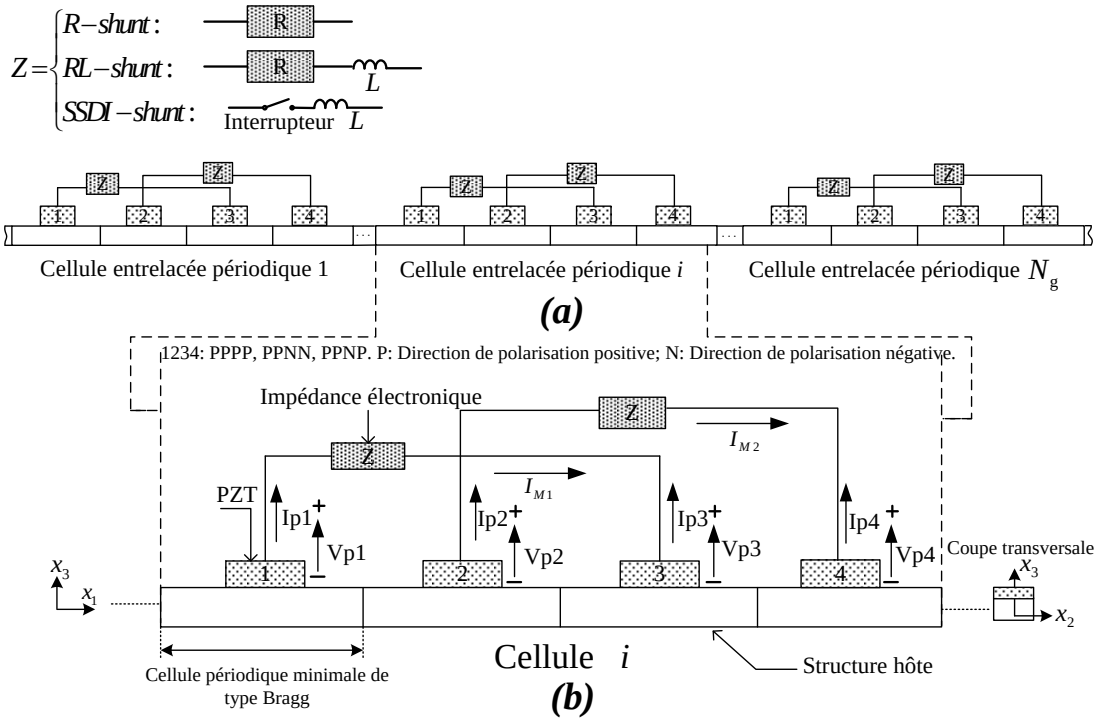

Figure FR4. 1. Structure périodique avec connexion électrique entrelacée : (a) Vue générale ; (b) Détail d'une méta-cellule.

$$\begin{cases} \left[M^e\right]\left\{\ddot{d}^i\right\}+\left[C^e\right]\left\{\dot{d}^i\right\}+\left[K^e\right]\left\{d^i\right\}+\left[B_1^e\right]\left\{V_p^i\right\}=\left\{P^i\right\} \\ \left\{Q^i\right\}=\left[B_2^e\right]\left\{d^i\right\}+\left[B_3^e\right]\left\{V_p^i\right\} \end{cases} \tag{FR4.1}$$

où d, P, V et Q sont les vecteurs de déplacement généralisé (déplacement et rotation), de force généralisée (force et moment), de tension et de charge sur l'élément piézoélectrique ; l'exposant i référant à la $i^{ème}$ méta-cellule. Les paramètres M^e, C^e et K^e sont les matrices de masse dynamique, d'amortissement structurel et de raideur, B_1^e et B_2^e les matrices électromécaniques et B_3^e la matrice de capacité bloquée :

$$B_1^e=\begin{bmatrix} B_{11} & B_{12} & B_{13} & B_{14} \end{bmatrix}$$

$$\begin{cases} B_{11}=b_{11}\int_0^l \dfrac{\partial\left[N_\varphi(x)\right]^T}{\partial x}dx, \quad b_{11}=-\dfrac{p_1 d_{31} w_b}{t_p\left(s_{11}^E+s_{12}^E\right)}\int_{t_b}^{t_b+t_p}\left(u_3-x_c\right)dx_3 \\ B_{12}=b_{12}\int_0^l \dfrac{\partial\left[N_\varphi(x)\right]^T}{\partial x}dx, \quad b_{12}=-\dfrac{p_2 d_{31} w_b}{t_p\left(s_{11}^E+s_{12}^E\right)}\int_{t_b}^{t_b+t_p}\left(u_3-x_c\right)dx_3 \\ B_{13}=b_{13}\int_0^l \dfrac{\partial\left[N_\varphi(x)\right]^T}{\partial x}dx, \quad b_{13}=-\dfrac{p_3 d_{31} w_b}{t_p\left(s_{11}^E+s_{12}^E\right)}\int_{t_b}^{t_b+t_p}\left(u_3-x_c\right)dx_3 \\ B_{14}=b_{14}\int_0^l \dfrac{\partial\left[N_\varphi(x)\right]^T}{\partial x}dx, \quad b_{14}=-\dfrac{p_4 d_{31} w_b}{t_p\left(s_{11}^E+s_{12}^E\right)}\int_{t_b}^{t_b+t_p}\left(u_3-x_c\right)dx_3 \end{cases} \tag{FR4.2}$$

$$B_2^e=\begin{bmatrix} B_{21} \\ B_{22} \\ B_{23} \\ B_{24} \end{bmatrix}, \quad \begin{cases} B_{21}=b_{21}\int_0^l \dfrac{\partial\left[N_\varphi(x)\right]}{\partial x}dx, \quad b_{21}=-\dfrac{p_1 d_{31} t_p}{\left(s_{11}^E+s_{12}^E\right)} \\ B_{22}=b_{22}\int_0^l \dfrac{\partial\left[N_\varphi(x)\right]}{\partial x}dx, \quad b_{22}=-\dfrac{p_2 d_{31} t_p}{\left(s_{11}^E+s_{12}^E\right)} \\ B_{23}=b_{23}\int_0^l \dfrac{\partial\left[N_\varphi(x)\right]}{\partial x}dx, \quad b_{23}=-\dfrac{p_3 d_{31} t_p}{\left(s_{11}^E+s_{12}^E\right)} \\ B_{24}=b_{24}\int_0^l \dfrac{\partial\left[N_\varphi(x)\right]}{\partial x}dx, \quad b_{24}=-\dfrac{p_4 d_{31} t_p}{\left(s_{11}^E+s_{12}^E\right)} \end{cases}$$

$$B_3^e=\begin{bmatrix} B_{31} & 0 & 0 & 0 \\ 0 & B_{32} & 0 & 0 \\ 0 & 0 & B_{33} & 0 \\ 0 & 0 & 0 & B_{34} \end{bmatrix}, \quad B_{31}=B_{32}=B_{33}=B_{34}=\frac{w_b L_p\left[2{d_{31}}^2-\varepsilon_{33}^T\left(s_{11}^E+s_{12}^E\right)\right]}{t_p\left(s_{11}^E+s_{12}^E\right)}$$

Le jeu d'équation électromécanique peut être réécrit dans le domaine fréquentiel selon :

$$\begin{cases} \left\{P^i\right\} = \left[A^e\right]\left\{d^i\right\} + \left[B_1^e\right]\left\{V_p^i\right\} \\ \left\{I_p^i\right\} = \left[j\omega B_2^e\right]\left\{d^i\right\} + \left[j\omega B_3^e\right]\left\{V_p^i\right\} \end{cases} \tag{FR4.3}$$

avec I_p le courant sortant de l'élément piézoélectrique et A^e la matrice de raideur dynamique purement mécanique $\left(A^e = -\omega^2 M^e + j\omega C^e + K^e\right)$ et ω la pulsation. En considérant une connexion indépendante, la tension s'écrit sous la forme :

$$\left\{V_p^{\ i}\right\} = \begin{cases} \left[B_4^e\right]\left\{d^i\right\}, & \text{en circuit ouvert;} \\ \left[B_5^e\right]\left\{d^i\right\}, & \text{pour une connexion résisitive ou inductive-résistive;} \\ \left[B_6^e\right]\left\{d^i\right\}, & \text{pour une connexion SSDI.} \end{cases} \tag{FR4.4}$$

avec :

$$B_4^e = \begin{bmatrix} B_{41} \\ B_{42} \\ B_{43} \\ B_{44} \end{bmatrix}, \quad B_5^e = \begin{bmatrix} B_{51} \\ B_{52} \\ B_{53} \\ B_{54} \end{bmatrix}, \quad B_6^e = \begin{bmatrix} B_{61} \\ B_{62} \\ B_{63} \\ B_{64} \end{bmatrix}$$

$$\begin{cases} B_{41} = b_{41}\int_0^l \dfrac{\partial\left[N_\varphi(x)\right]}{\partial x}dx, \quad b_{41} = \dfrac{d_{31}{t_p}^2}{L_p\left[\varepsilon_{33}^T\left(s_{11}^E + s_{12}^E\right) - 2d_{31}^2\right]}; \\ B_{42} = b_{42}\int_0^l \dfrac{\partial\left[N_\varphi(x)\right]}{\partial x}dx, \quad b_{42} = \dfrac{d_{31}{t_p}^2}{L_p\left[\varepsilon_{33}^T\left(s_{11}^E + s_{12}^E\right) - 2d_{31}^2\right]}; \\ B_{43} = b_{43}\int_0^l \dfrac{\partial\left[N_\varphi(x)\right]}{\partial x}dx, \quad b_{43} = \dfrac{d_{31}{t_p}^2}{L_p\left[\varepsilon_{33}^T\left(s_{11}^E + s_{12}^E\right) - 2d_{31}^2\right]}; \\ B_{44} = b_{44}\int_0^l \dfrac{\partial\left[N_\varphi(x)\right]}{\partial x}dx, \quad b_{44} = \dfrac{d_{31}{t_p}^2}{L_p\left[\varepsilon_{33}^T\left(s_{11}^E + s_{12}^E\right) - 2d_{31}^2\right]}. \end{cases} \tag{FR4.5}$$

$$\begin{cases} B_{51} = \dfrac{j\omega Z_{ind}^{passive} \cdot B_{21}}{\left(1 - j\omega Z_{ind}^{passive} \cdot B_{31}\right)} \\ B_{52} = \dfrac{j\omega Z_{ind}^{passive} \cdot B_{22}}{\left(1 - j\omega Z_{ind}^{passive} \cdot B_{32}\right)} \\ B_{53} = \dfrac{j\omega Z_{ind}^{passive} \cdot B_{23}}{\left(1 - j\omega Z_{ind}^{passive} \cdot B_{33}\right)} \\ B_{54} = \dfrac{j\omega Z_{ind}^{passive} \cdot B_{24}}{\left(1 - j\omega Z_{ind}^{passive} \cdot B_{34}\right)} \end{cases}, \quad \begin{cases} B_{61} = \dfrac{j\omega Z_{ind}^{SSDI} \cdot B_{21}}{\left(1 - j\omega Z_{ind}^{SSDI} \cdot B_{31}\right)} \\ B_{62} = \dfrac{j\omega Z_{ind}^{SSDI} \cdot B_{22}}{\left(1 - j\omega Z_{ind}^{SSDI} \cdot B_{32}\right)} \\ B_{63} = \dfrac{j\omega Z_{ind}^{SSDI} \cdot B_{23}}{\left(1 - j\omega Z_{ind}^{SSDI} \cdot B_{33}\right)} \\ B_{64} = \dfrac{j\omega Z_{ind}^{SSDI} \cdot B_{24}}{\left(1 - j\omega Z_{ind}^{SSDI} \cdot B_{34}\right)} \end{cases}$$

$Z_{ind}^{passive}$ et Z_{ind}^{SSDI} dénotant respectivement de l'impédance (équivalente) dans le cas linéaire (résistif ou inductif-résistif) et SSDI. Dès lors, il est possible de décrire le comportement électromécanique d'un point de vue purement mécanique, avec la matrice de raideur globale A_{EC} :

$$\left\{P^i\right\} = \begin{cases} \left[A^e\right]\left\{d^i\right\}, & \text{en court-ciruit} \\ \left[A_{EC}\right]\left\{d^i\right\}, & \text{pour les autres types de connexion} \end{cases}$$

$$A_{EC} = \begin{cases} A_{open} = A^e + B_1^e \cdot B_4^e \\ A_{ind}^{passive} = A^e + B_1^e \cdot B_5^e \\ A_{ind}^{SSDI} = A^e + B_1^e \cdot B_6^e \end{cases} \tag{FR4.6}$$

avec $A_{open}, A_{ind}^{passive}$ et A_{ind}^{SSDI} dénotant des matrices de raideurs équivalentes en circuit ouvert, en connexion linéaire et en connexion SSDI.

Pour la structure entrelacée considérée, les relations internes entre les tension et courants sont nécessaires afin de pouvoir en déduire la matrice de raideur équivalente de la méta-cellule. Ces relations électriques sont données par :

$$\begin{cases} V_{p1}^i - I_{M1} Z_{\text{int}} = V_{p3}^i \\ I_{p1}^i = -I_{p3}^i = I_{M1} \\ V_{p2}^i - I_{M2} Z_{\text{int}} = V_{p4}^i \\ I_{p2}^i = -I_{p4}^i = I_{M2} \\ \left\{P^i\right\} = \left[A^e\right]\left\{d^i\right\} + \left[B_1^e\right]\left\{V_p^i\right\} \\ \left\{I_p^i\right\} = \left[j\omega B_2^e\right]\left\{d^i\right\} + \left[j\omega B_3^e\right]\left\{V_p^i\right\} \end{cases}, \quad I_p^i = \begin{bmatrix} I_{p1}^i \\ I_{p2}^i \\ I_{p3}^i \\ I_{p4}^i \end{bmatrix}, \quad V_p^i = \begin{bmatrix} V_{p1}^i \\ V_{p2}^i \\ V_{p3}^i \\ V_{p4}^i \end{bmatrix} \tag{FR4.7}$$

avec *pj* dénotant du *j*^{ème} insert de la méta-cellule (*j=1…4*). Par conséquent, la relation entre tension et vecteur de déplacement généralisé s'obtient par :

$$\left\{V_p^i\right\} = \left[B_8^e\right]\left\{d^i\right\}$$

$$B_8^e = \begin{bmatrix} \dfrac{-\left(\dfrac{B_{21}+B_{23}}{B_{31}}\right) + j\omega Z_{\text{int}} B_{21}}{2 - j\omega Z_{\text{int}} B_{31}} \\ \dfrac{-\left(\dfrac{B_{22}+B_{24}}{B_{31}}\right) + j\omega Z_{\text{int}} B_{22}}{2 - j\omega Z_{\text{int}} B_{31}} \\ -\left(\dfrac{B_{21}+B_{23}}{B_{31}}\right) - \dfrac{-\left(\dfrac{B_{21}+B_{23}}{B_{31}}\right) + j\omega Z_{\text{int}} B_{21}}{2 - j\omega Z_{\text{int}} B_{31}} \\ -\left(\dfrac{B_{22}+B_{24}}{B_{31}}\right) - \dfrac{-\left(\dfrac{B_{22}+B_{24}}{B_{31}}\right) + j\omega Z_{\text{int}} B_{22}}{2 - j\omega Z_{\text{int}} B_{31}} \end{bmatrix} \tag{FR4.8}$$

permettant d'exprimer la matrice de raideur dynamique équivalente :

$$\left\{P^i\right\} = \left[A_{\text{int}erleaved}\right]\left\{d^i\right\} = \left[A^e + B_1^e B_8^e\right]\left\{d^i\right\} \tag{FR4.9}$$

4.3 Résultats théorique de la propagation

Cette partie se propose d'évaluer les performances en termes d'atténuation d'onde de propagation dans une méta-cellule entrelacée, représentée en Figure FR4. 2. Les paramètres des constituants sont les mêmes que ceux du Chapitre précédent (Tableau FR3-1), excepté que l'utilisation de la théorie de Timoshenko nécessite l'utilisation de la compliance de cisaillement $s_{55}^{E} = 21.77 \times 10^{-12} m^2 / N$. Pour une comparaison équitable, une méta-cellule entrelacée est comparée à quatre cellules indépendantes.

Dans les cas linéaires et en considérant une valeur de composants optimale, représentés en Figure FR4.3, on voit ainsi que la technique indépendante reste la plus large bande. Cependant, dans le cas purement résistif, l'entrelacement, et plus spécifiquement la connexion PPPP, permet de disposer de bandes d'atténuation relativement larges, tout en n'affectant pas les bandes interdites originales.

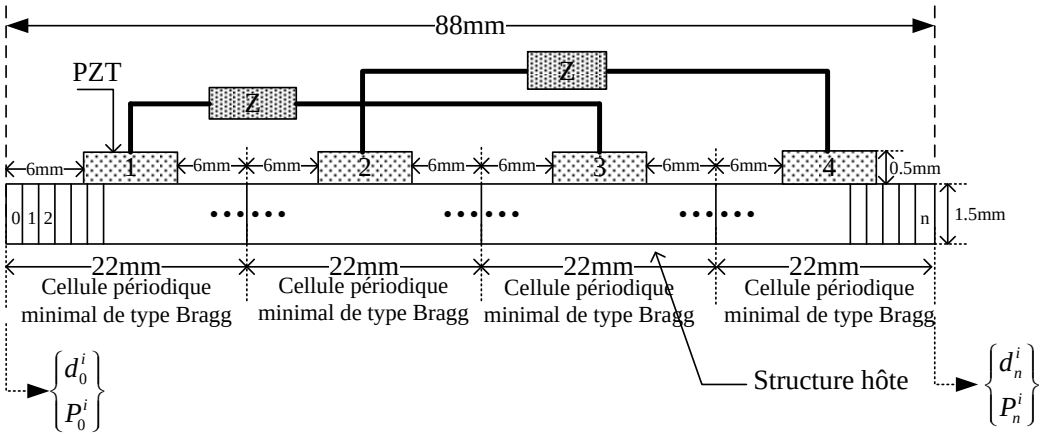

Figure FR4. 2. Meta-cellule entrelacée.

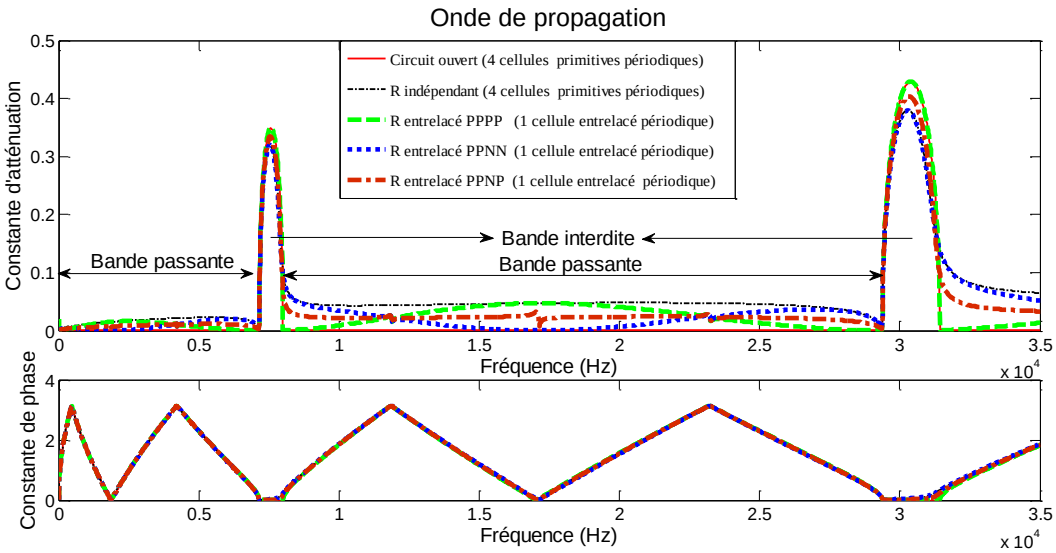

(a)

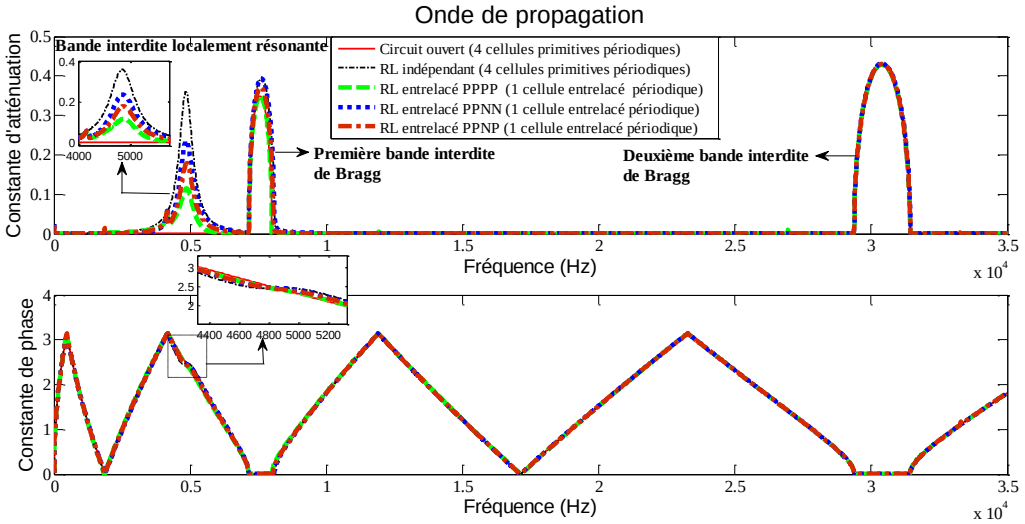

(b)

Figure FR4.3. Constantes d'atténuation dans le cas linéaire : (a) Résistif ; (b) Inductif-résistif.

Cependant, lors de l'utilisation de la technique SSDI (Figure FR4.4), il est des plus intéressant de noter des bande fréquentielles dans les bandes passantes originales où l'utilisation de l'entrelacement permet une augmentation significative des performances (connexion PPPP) comparé au cas SSDI indépendant, sans être toutefois aussi large bande. Une autre propriété remarquable tient au fait que dans certaines configurations (PPNN), l'entrelacement permet une forte augmentation du facteur d'atténuation dans les bandes interdites originales. Ces caractéristiques remarquables, non présentes dans le cas linéaires, tiennent à la particularité du SSDI à permettre des échanges énergétiques impulsionnels et efficaces, avec une auto-adaptation naturelle du fait du principe de détection des extrema. De plus, ce transfert énergétique se fait via la connexion électrique, dont la propagation est généralement bien plus rapide que dans le domaine mécanique. Ainsi, bien que le compromis entre bande passante et amplitude d'atténuation soit plus en faveur du dernier critère dans le cas de l'entrelacement, le dimensionnement de la structure de telle sorte que les bandes de forte atténuation correspondent aux modes naturels de la structure, permettrait de disposer de structures et techniques à fort pouvoir d'atténuation.

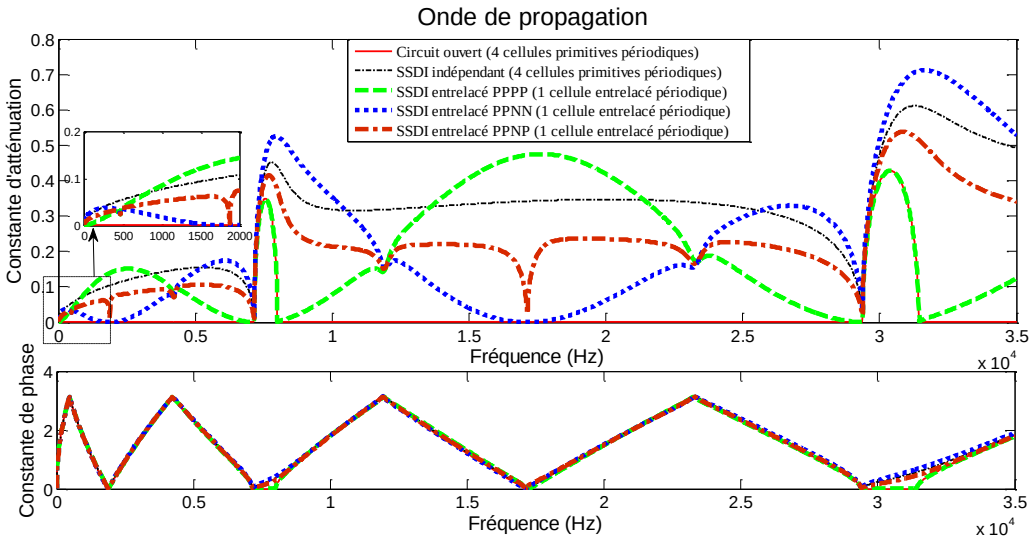

Figure FR4.4. Constantes d'atténuation dans le cas SSDI.

4.4 Validation expérimentale

Afin de confirmer les résultats obtenus théoriquement, il est ici proposé de vérifier expérimentalement les performances d'atténuation sur une structure périodique finie (poutre encastrée-encastrée) identique à celle exposée dans le chapitre précédent.

La structure étant composée de 8 cellules élémentaires, différentes connexions sont possibles, et peuvent considérer par exemple de travailler à nombre constant de cellules dont les terminaux électriques sont connectés (de manière indépendante ou entrelacée), ou encore à nombre de commutateur SSDI constant. Les différentes configurations envisagées ici sont représentées en Figure FR4.5.

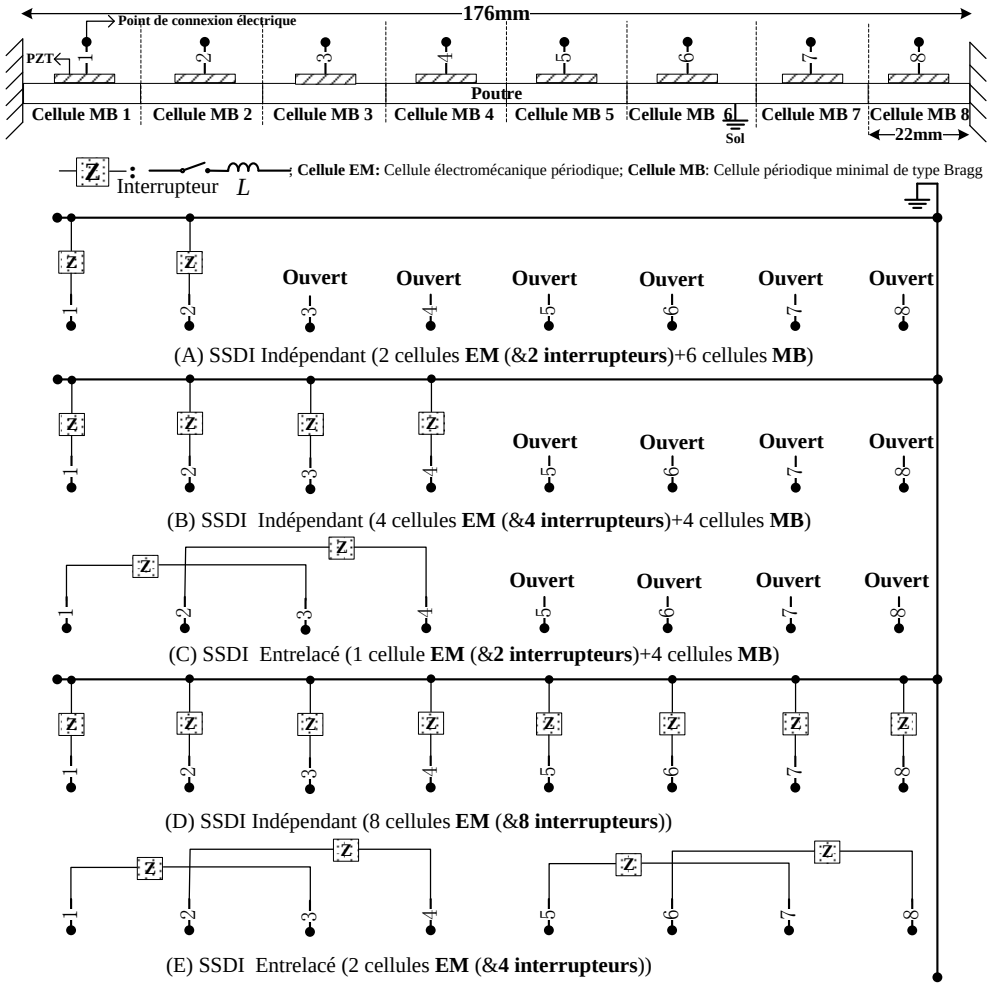

Figure FR4.5. Configurations expérimentales.

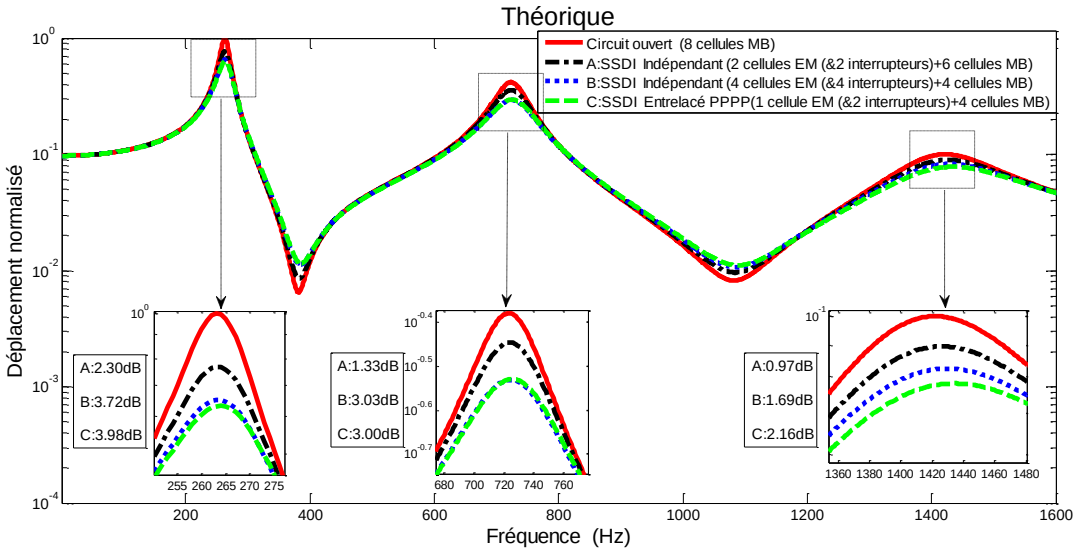

(a)

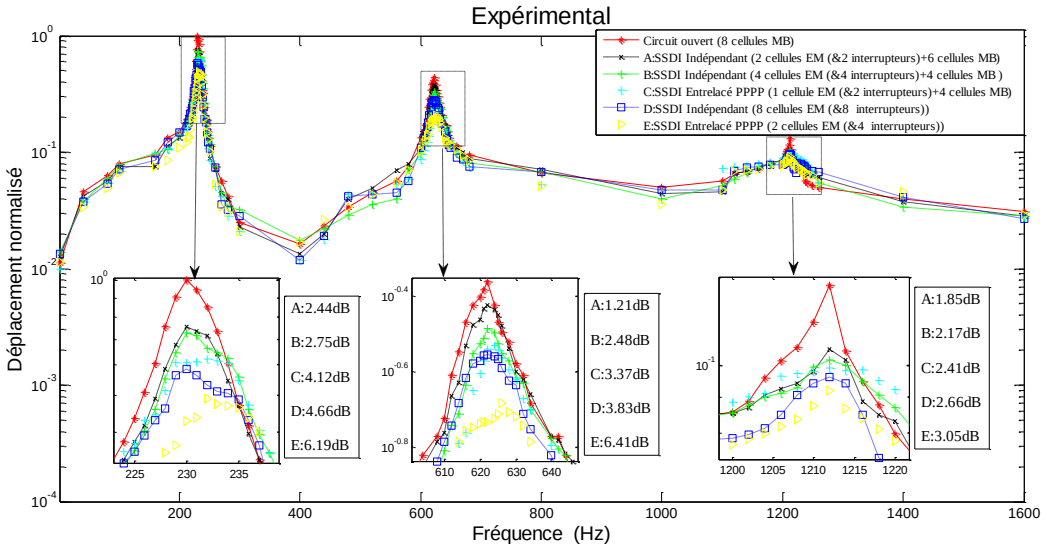

(b)

Figure FR4.6. Résultats : (a) théoriques et (b) expérimentaux pour les structures entrelacées.

Les résultats, présentés en Figure FR4.6, montrent une bonne concordance entre prédictions théoriques, obtenues à partir des matrices de transfert et l'application des conditions aux limites, et relevés expérimentaux. On remarque tout d'abord, de manière tout à fait logique, une augmentation des performances avec le nombre de commutateur. Néanmoins, et plus important encore, à nombre de commutateurs constant, on voit que les techniques entrelacées permettent un gain en termes

d'amortissement, allant jusqu'à 3 dB supplémentaires dans le cas considéré. On remarque même que la technique entrelacée utilisant toutes les cellules avec 4 commutateurs permet une atténuation plus importante que la technique indépendante utilisant 8 commutateurs. Une telle augmentation des performances pour un nombre réduit de circuit peut s'expliquer par le fait que les structures entrelacées, bien qu'étant périodiques à haut niveau, introduisent localement un certain niveau de désordre ; cette certaine apériodicité permettant une meilleure atténuation grâce à un phénomène d'étalement spectral ([93]).

4.5 Structures tri-entrelacées

Le principe exposé dans les parties précédentes de ce chapitre pour 2 entrelacements pouvant être étendu à plusieurs entrelacements, il est proposé dans cette partie d'évaluer les performances de structure tri-entrelacées tel que représenté en Figure FR4.7. Dans ce cas, chaque méta-cellule est composée de 6 cellules unitaires, les interconnexions consistant à connecter le premier élément piézoélectrique au quatrième, le second au cinquième, et le troisième au sixième.

En menant une analyse similaire au cas précédent (en considérant cependant les hypothèses d'Euler-Bernoulli), on obtient les résultats en termes de factor de localisation (représentant l'atténuation moyenne d'une cellule unitaire) représentés en Figure FR4.8. On remarque ainsi des plages de meilleure atténuation que la configuration indépendante, notamment autour de la bande interdite originale (du fait de l'hybridation de bandes interdites dû à la périodicité et au mécanisme de conversion d'énergie), et ce sur des plages fréquentielles relativement étendues.

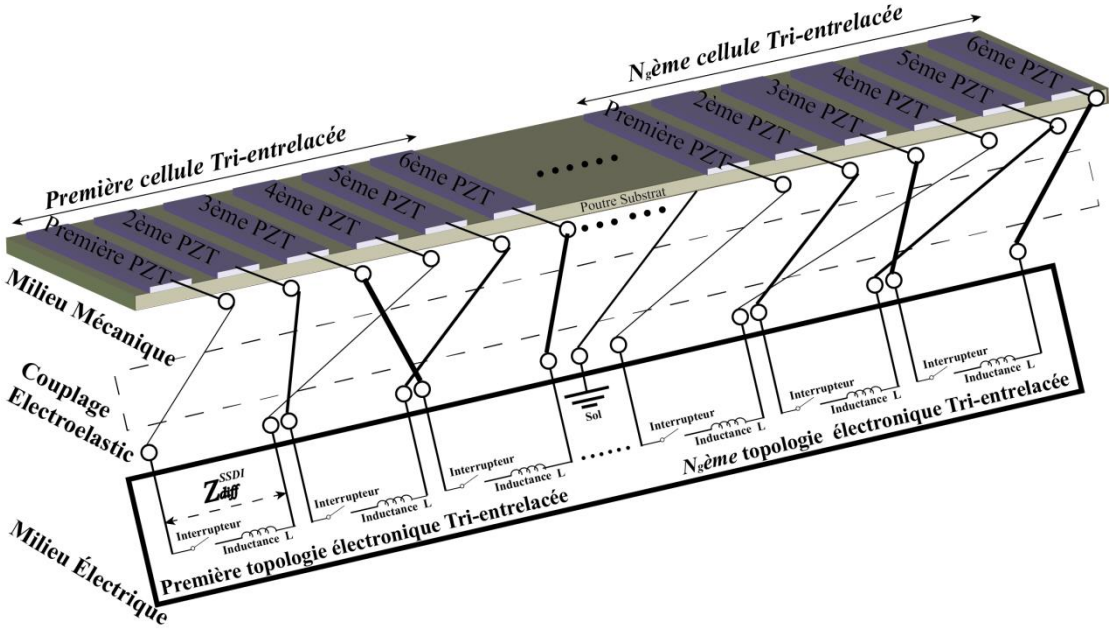

Figure FR4.7. Structures tri-entrelacée.

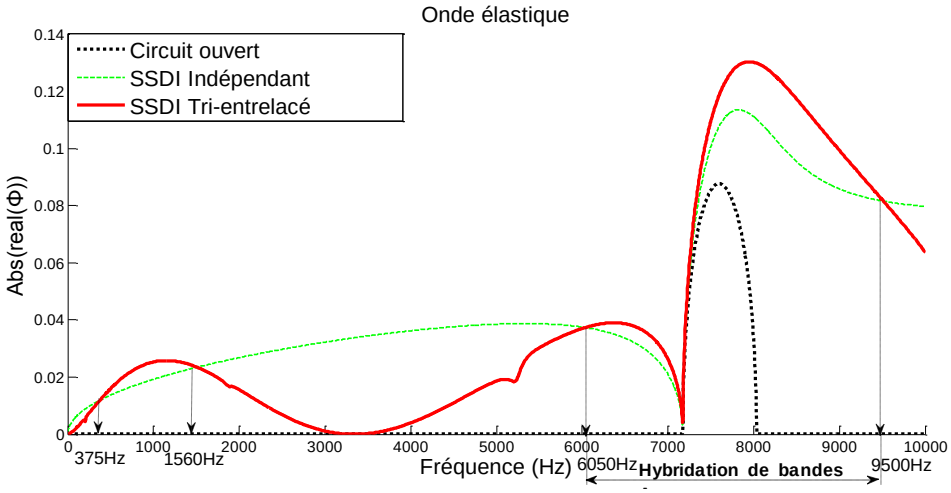

Figure FR4.8. Facteur de localisation d'une cellule tri-entrelacée et comparison avec la configuration SSDI indépendant.

La validation expérimentale, en considérant différentes configuration (Figure FR4.9), conduit aux résultats de la Figure FR4.10, qui montrent que les meilleures performances sont obtenues lors de l'utilisation de l'approche tri-entrelacée. Un résultat des plus intéressant consiste à combiner des cellules avec une configuration

de type SSDI indépendant avec des méta-cellules formant une structure tri-entrelacée. Une telle approche, utilisant une apériodicité au niveau du réseau électrique et des interconnexions, permet ainsi, en exploitant justement ce niveau contrôlé de désordre, d'obtenir les meilleures performances en termes de contrôle de vibrations.

4.6 Conclusion

Dans la continuité des études de ce doctorat, ce Chapitre a proposé une approche de type entrelacée pour le contrôle de vibrations à l'aide de structures périodiques. Combinant à la fois une structure indépendante au niveau de l'association des méta-cellules et interconnectée au sein de celles-ci, la configuration entrelacée permet donc de bénéficier des avantages des deux approches, ou du mois de contrôler le compromis entre performances en termes d'atténuation et largeur de bande. Plus particulièrement, l'apériodicitié (ou le désordre) engendrée par cette mixité permet ainsi un meilleur étalement des fréquences interdites, notamment par l'hybridation de fréquences interdites. Enfin, on pourra noter que l'utilisation simultanée de différents types de configurations (indépendantes, interconnectées, entrelacées, tri-entrelacées etc…) permet l'introduction d'une apériodicité au niveau électrique qui présente un impact mécanique des plus intéressants pour l'amortissement vibratoire.

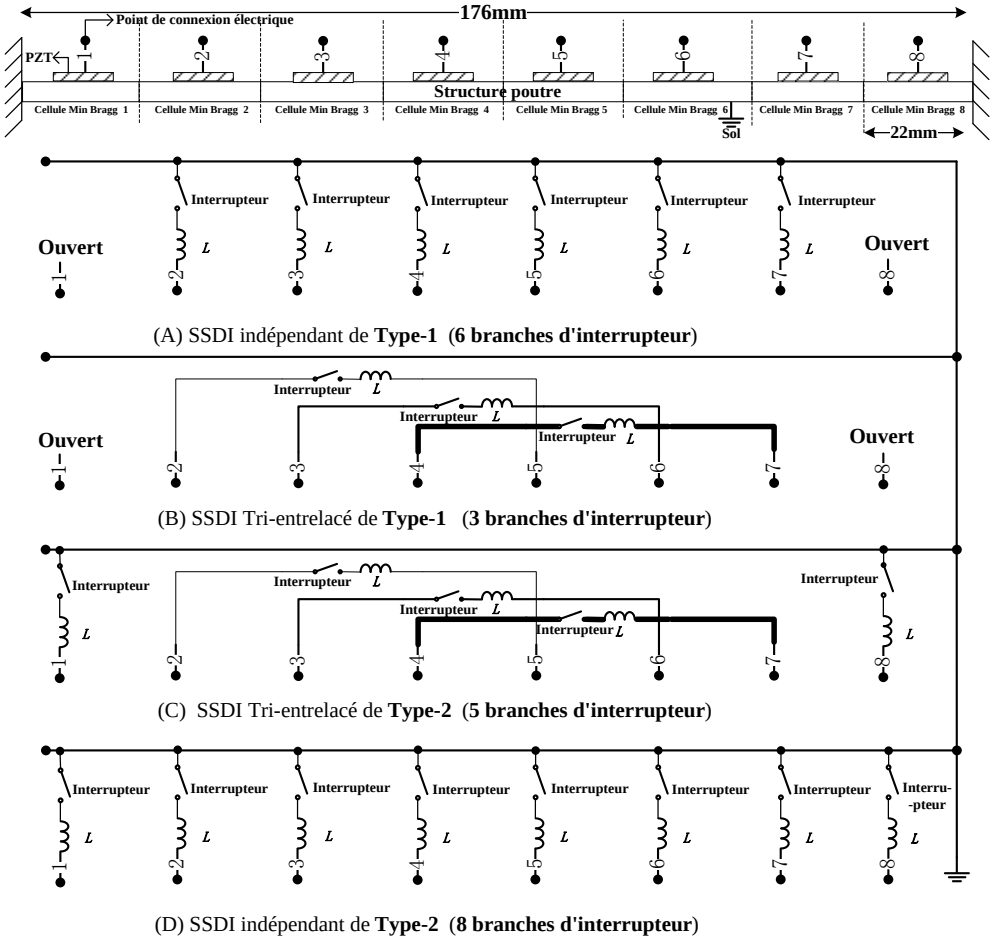

Figure FR4.9. Configurations expérimentales pour l'évaluation de la configuration tri-entrelacée.

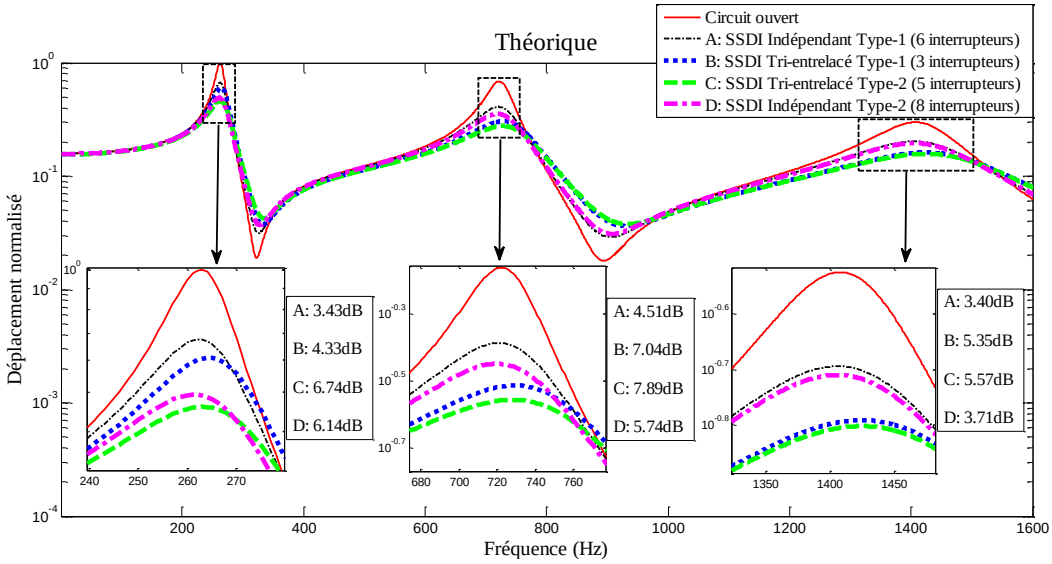

(a)

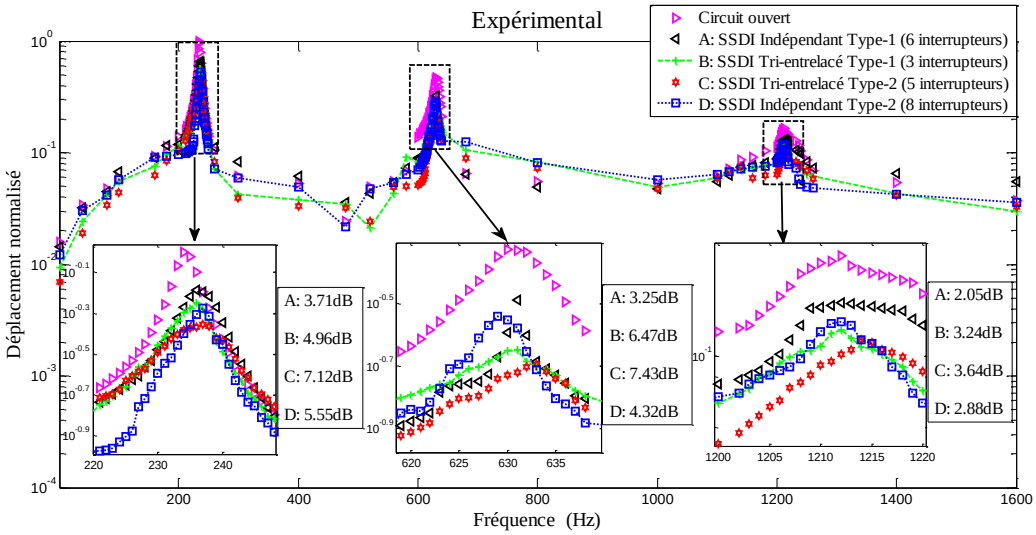

(b)

Figure FR4.10. Résultats : (a) Théoriques et (b) Expérimentaux pour l'évaluation de la configuration tri-entrelacée.

Chapitre FR- 5. Structure périodiques intelligentes avec réseaux électriques non-linéaires interconnectés/entrelacés

Ce Chapitre propose d'unifier les structures présentées précédemment (interconnectées et entrelacées) afin de proposer une approche hybride permettant de profiter des avantages des deux approches et ainsi d'obtenir un meilleur contrôle du compromis entre performances et largeur de bande. Ainsi, une structure à l'architecture interconnectée/entrelacée est présentée et discutée. Après l'introduction du principe (paragraphe 5.1) et de la modélisation associée (paragraphe 5.2), l'étude en termes de la propagation et des caractéristiques associées sera menée dans le paragraphe 5.3. Ensuite, dans l'optique d'une application réaliste aux structures fines, le paragraphe 5.4 établira l'obtention de la fonction de transfert, qui sera expérimentalement validée et discutée dans le paragraphe 5.5. Enfin, le paragraphe 5.6 donnera une conclusion générale au concept exposé dans ce chapitre.

5.1 Principes

Le principe de l'hybridation de l'interconnexion et de l'entrelacement consiste à interconnecter chaque $i^{ème}$ cellule avec la $(i+k)^{ème}$ cellule, avec k l'ordre d'entrelacement. Plus particulièrement, il sera considéré dans ce chapitre les ordres 1 (Figure FR5.1 – dont on pourra noter la similitude avec le configuration d'interconnexion pure), 2 (Figure FR5.2) et 3 (Figure FR5.3). Une telle configuration du réseau électrique permet ainsi des échanges particuliers en termes d'énergie et donc une propagation de l'onde électrique permettant de cibler des modes bien particuliers dans l'optique du contrôle de vibrations, correspondant à un multiple de la période d'interconnexion.

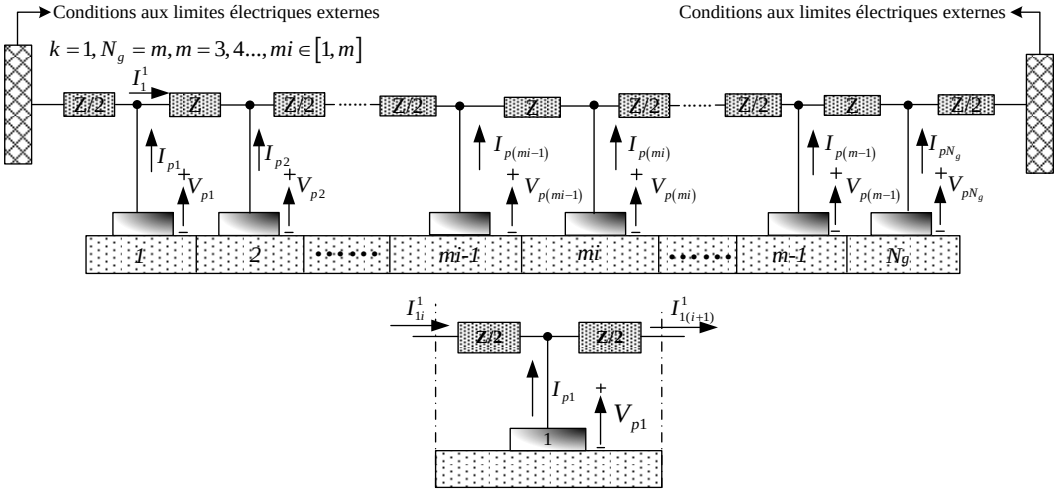

Figure FR5.1. Structure interconnectée/entrelacée d'ordre 1 et méta-cellule unitaire.

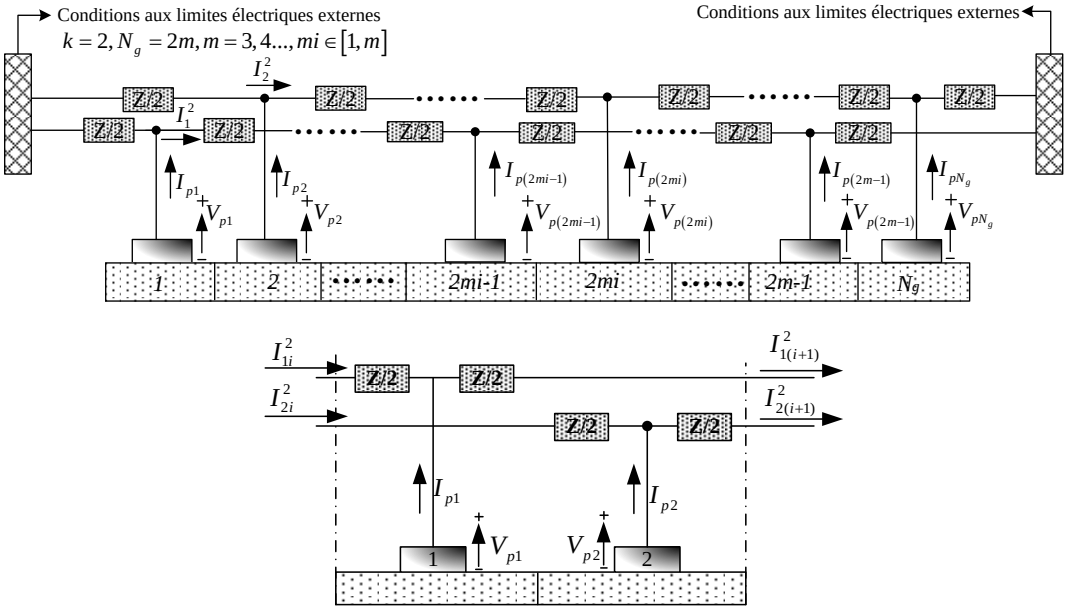

Figure FR5.2. Structure interconnectée/entrelacée d'ordre 2 et méta-cellule unitaire.

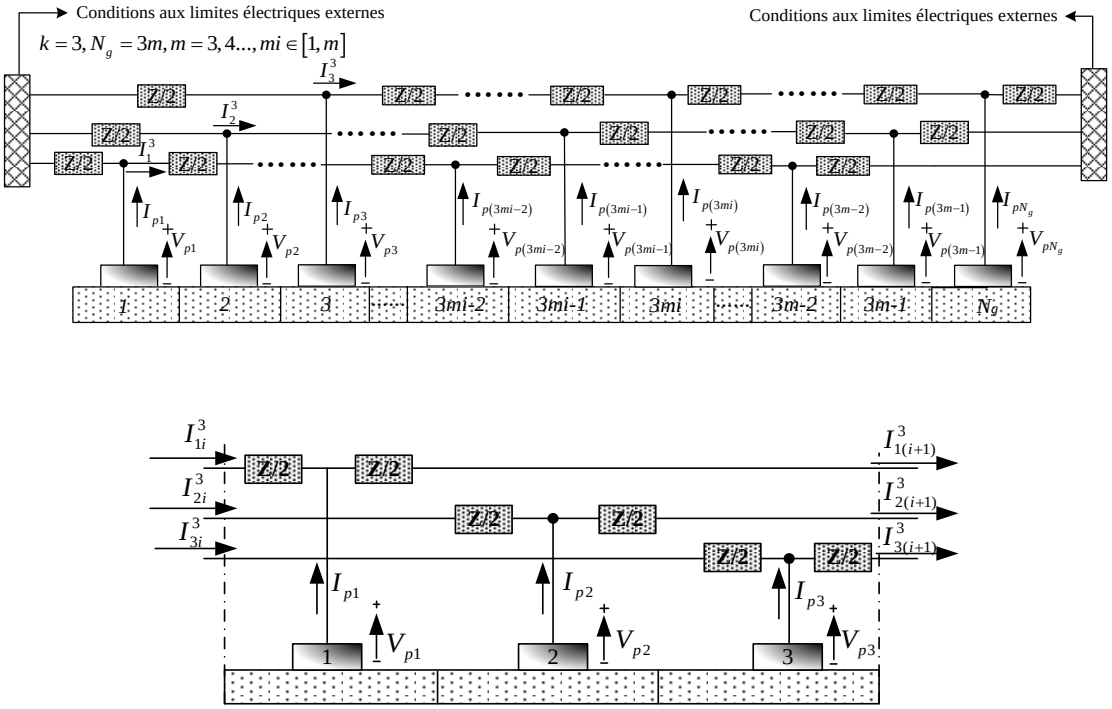

Figure FR5.3. Structure interconnectée/entrelacée d'ordre 3 et méta-cellule unitaire.

5.2 Analyse théorique

De manière analogue aux chapitres précédents, l'analyse théorique des structures interconnectées/entrelacées se décomposent en une étude par éléments finis d'une méta-cellule en particulier, permettant la mise en place d'une formulation par matrice de transfert conduisant aux caractéristiques de propagation des ondes mécaniques et électriques.

5.2.1 Analyse par éléments finis d'une méta-cellule

L'étude repose ici sur les hypothèses d'Euler-Bernoulli dont le jeu d'équations électromécaniques a été démontré dans le chapitre FR2, conduisant ici à :

$$\begin{cases} \left[-\omega^2 M^e\right]\left\{d^i\right\}+\left[j\omega C^e\right]\left\{d^i\right\}+\left[K^e\right]\left\{d^i\right\}+\left[B_1^{k-level}\right]\left\{V_p^i\right\}=\left\{P^i\right\} \\ \left\{I_p^i\right\}=\left[j\omega B_2^{k-level}\right]\left\{d^i\right\}+\left[j\omega B_3^{k-level}\right]\left\{V_p^i\right\} \end{cases} \quad \text{(FR5.1)}$$

avec *d*, *P*, *V* et *I* les vecteurs de déplacement généralisé (déplacement et pente), de force généralisée (force et moment), de tension piézoélectrique et de courant sortant

de l'élément piézoélectrique ; l'exposant i référant à la $i^{ème}$ méta-cellule. Les paramètres M^e, C^e et K^e sont les matrices de masse dynamique, d'amortissement structurel et de raideur. En menant une analyse analogue aux travaux précédents, les matrices électromécaniques et électriques sont données par :

$$\begin{aligned}
&\left[B_1^{1-level}\right]=\left[B_1\right]\\
&\left[B_2^{1-level}\right]=\left[B_2\right]\\
&\left[B_3^{1-level}\right]=\left[B_3\right]\\
&\left[B_4^{1-level}\right]=\left[B_4\right]
\end{aligned}
\qquad
\begin{cases}
\left[B_1^{2-level}\right]=\left[B_1 \quad B_1\right], \quad \left[B_2^{2-level}\right]=\begin{bmatrix}B_2\\B_2\end{bmatrix}\\
\left[B_3^{2-level}\right]=\begin{bmatrix}B_3 & 0\\0 & B_3\end{bmatrix}, \quad \left[B_4^{2-level}\right]=\begin{bmatrix}B_4\\B_4\end{bmatrix}
\end{cases}$$

$$\begin{cases}
\left[B_1^{3-level}\right]=\left[B_1 \quad B_1 \quad B_1\right], \quad \left[B_2^{3-level}\right]=\begin{bmatrix}B_2\\B_2\\B_2\end{bmatrix}\\
\left[B_3^{3-level}\right]=\begin{bmatrix}B_3 & 0 & 0\\0 & B_3 & 0\\0 & 0 & B_3\end{bmatrix}, \quad \left[B_4^{3-level}\right]=\begin{bmatrix}B_4\\B_4\\B_4\end{bmatrix}
\end{cases} \tag{FR5.2}$$

avec :

$$\begin{aligned}
B_1 &= \left(-\frac{d_{31}w_b}{t_p\left(s_{11}^E+s_{12}^E\right)}\int_{t_b}^{t_b+t_p}\left(u_3-x_c\right)dx_3\right)\int_0^l\left[H''\right]^T dx\\
B_2 &= -\frac{d_{31}t_p}{\left(s_{11}^E+s_{12}^E\right)}\int_0^l\left[H''\right]dx\\
B_3 &= \frac{w_b L_p\left[2{d_{31}}^2-\varepsilon_{33}^T\left(s_{11}^E+s_{12}^E\right)\right]}{t_p\left(s_{11}^E+s_{12}^E\right)}\\
B_4 &= \frac{d_{31}{t_p}^2}{L_p\left[\varepsilon_{33}^T\left(s_{11}^E+s_{12}^E\right)-2d_{31}^2\right]}\int_0^l\left[H''\right]dx
\end{aligned} \tag{FR5.3}$$

A partir de l'analyse des connexions électriques dans le cas considéré d'interconnexion/entrelacement, la relation entre les nœuds de la méta-cellule considérée, pour un ordre k d'interconnexion/entrelacement, est donnée par, en notant

A^e_{mec} la matrice de raideur dynamique purement mécanique $\left(A^e_{mec} = \left[-\omega^2 M^e\right] + \left[j\omega C^e\right] + \left[K^e\right]\right)$:

$$k\text{-}level : \begin{Bmatrix} P^i \\ V^k_{k(i+1)} \\ I^k_{k(i+1)} \\ \dots \\ V^k_{jj(i+1)} \\ I^k_{jj(i+1)} \\ \dots \\ V^k_{1(i+1)} \\ I^k_{1(i+1)} \end{Bmatrix} = \begin{bmatrix} A^e_{mec} & B_1 & -\frac{Z}{2}B_1 & \dots & B_1 & -\frac{Z}{2}B_1 & \dots & B_1 & -\frac{Z}{2}B_1 \\ -j\omega\frac{Z}{2}B_2 & 1-j\omega\frac{Z}{2}B_3 & j\omega\frac{Z^2}{4}B_3 - Z & \dots & 0 & 0 & \dots & 0 & 0 \\ j\omega B_2 & j\omega B_3 & 1-j\omega\frac{Z}{2}B_3 & \dots & 0 & 0 & \dots & 0 & 0 \\ \dots & \dots & \dots & \dots & \dots & \dots & \dots & \dots & \dots \\ -j\omega\frac{Z}{2}B_1 & 0 & 0 & \dots & 1-j\omega\frac{Z}{2}B_3 & j\omega\frac{Z^2}{4}B_3 - Z & \dots & 0 & 0 \\ j\omega B_2 & 0 & 0 & \dots & j\omega B_3 & 1-j\omega\frac{Z}{2}B_3 & \dots & 0 & 0 \\ \dots & \dots & \dots & \dots & \dots & \dots & \dots & \dots & \dots \\ -j\omega\frac{Z}{2}B_1 & 0 & 0 & \dots & 0 & 0 & \dots & 1-j\omega\frac{Z}{2}B_3 & j\omega\frac{Z^2}{4}B_3 - Z \\ j\omega B_2 & 0 & 0 & \dots & 0 & 0 & \dots & j\omega B_3 & 1-j\omega\frac{Z}{2}B_3 \end{bmatrix} \begin{Bmatrix} d^i \\ V^k_{ki} \\ I^k_{ki} \\ \dots \\ V^k_{jji} \\ I^k_{jji} \\ \dots \\ V^k_{1i} \\ I^k_{1i} \end{Bmatrix} \tag{FR5.4}$$

5.2.2 Matrice de transfert

L'obtention de la matrice de transfert dans la configuration proposée s'obtient en réarrangeant les termes de l'équation (FR5.1) afin de faire apparaître les nœuds extrêmes de la méta-cellule :

$$\begin{Bmatrix} P^i_0 \\ P^i_J \\ P^i_n \\ U^k_{i+1} \end{Bmatrix} = \begin{bmatrix} a_{00} & a_{0J} & a_{0n} & c_{00} \\ a_{J0} & a_{JJ} & a_{Jn} & c_{J0} \\ a_{n0} & a_{nJ} & a_{nn} & c_{n0} \\ b_{00} & b_{0J} & b_{0n} & d_{00} \end{bmatrix} \begin{Bmatrix} d^i_0 \\ d^i_J \\ d^i_n \\ U^k_i \end{Bmatrix} \tag{FR5.5}$$

avec J le nombre d'éléments de la méta-cellules et U^k_{i+1} le vecteur des tensions et courants :

$$\left\{U^k_i\right\} = \begin{Bmatrix} V^k_{ki} \\ I^k_{ki} \\ \dots \\ V^k_{1i} \\ I^k_{1i} \end{Bmatrix} \tag{FR5.6}$$

Ainsi, en considérant aucun force et moment extérieurs, il est possible d'appliquer le principe de réduction de Guyan conduisant à la matrice de transfert *T* (en considérant la continuité des déplacements/pentes et l'inversion des forces/moments du fait de la réaction de la méta-cellule suivante) :

$$\begin{Bmatrix} d_n^i \\ P_n^i \\ U_{i+1}^k \end{Bmatrix} = T \begin{Bmatrix} d_0^i \\ P_0^i \\ U_i^k \end{Bmatrix}, \quad T = \begin{bmatrix} -S_{12}^{-1} \cdot S_{11} & S_{12}^{-1} & -S_{12}^{-1} \cdot S_{13} \\ -S_{21} + S_{22} \cdot S_{12}^{-1} \cdot S_{11} & -S_{22} \cdot S_{12}^{-1} & -S_{23} + S_{22} \cdot S_{12}^{-1} \cdot S_{13} \\ S_{31} - S_{32} \cdot S_{12}^{-1} \cdot S_{11} & S_{32} \cdot S_{12}^{-1} & S_{33} - S_{22} \cdot S_{12}^{-1} \cdot S_{13} \end{bmatrix} \quad \text{(FR5.7)}$$

où les paramètres *S* sont donnés par :

$$\begin{cases} S_{11} = a_{00} - a_{0J} a_{JJ}^{-1} a_{J0}, & S_{12} = a_{0n} - a_{0J} a_{JJ}^{-1} a_{Jn}, & S_{13} = c_{00} - a_{0J} a_{JJ}^{-1} c_{J0} \\ S_{21} = a_{n0} - a_{nJ} a_{JJ}^{-1} a_{J0}, & S_{22} = a_{nn} - a_{nJ} a_{JJ}^{-1} a_{Jn}, & S_{23} = c_{n0} - a_{nJ} a_{JJ}^{-1} c_{J0} \\ S_{31} = b_{00} - b_{0J} a_{JJ}^{-1} a_{J0}, & S_{32} = b_{0n} - b_{0J} a_{JJ}^{-1} a_{Jn}, & S_{33} = d_{00} - b_{0J} a_{JJ}^{-1} c_{J0} \end{cases} \quad \text{(FR5.8)}$$

5.3 Discussion théorique

A partir de l'expression de la matrice de transfert, il est possible d'évaluer les caractéristiques entre termes de capacités d'atténuation des techniques envisagées. Dans le cas de structures dont la cellule élémentaire est similaire aux chapitres précédents, les résultats en termes de facteur de localisation sont présentés en Figure FR5.4. Cette figure montre l'apparition de nouvelles bandes interdites, filtrant les ondes associées à ces fréquences, due à l'interaction et à la propagation particulière de l'onde électrique. Néanmoins, et concordant avec le compromis entre bande passante et performance, l'amplitude de la constante d'atténuation de ces bandes décroît avec leur nombre. On remarque également que les ordres impairs (1 et 3) présentent une dégradation de l'atténuation dans la bande interdite originale.

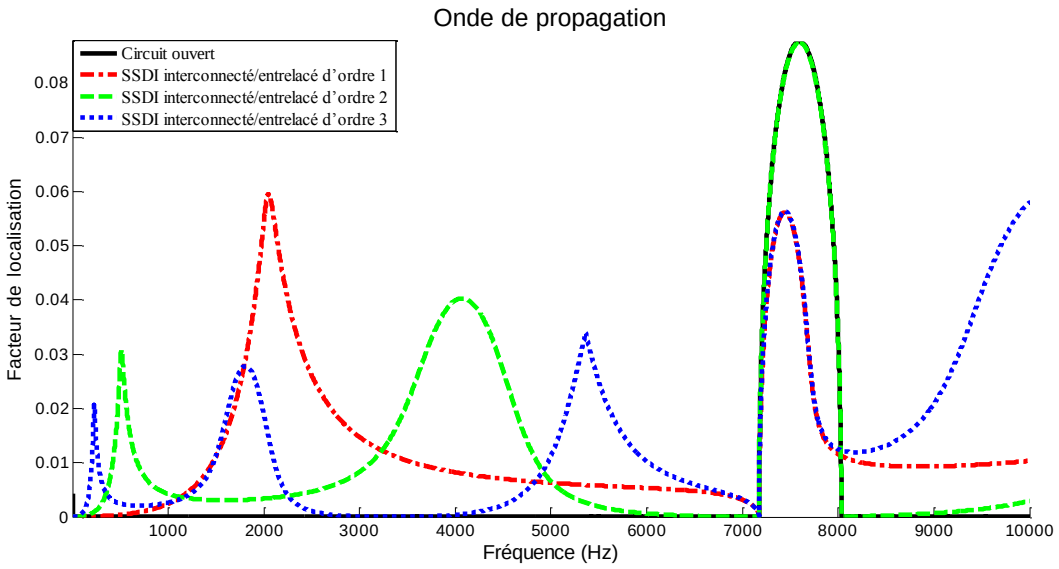

Figure FR5.4. Facteur de localisation dans le cas de structures interconnectées/entrelacées.

Néanmoins, la multiplication des bandes avec l'ordre d'interconnexion/entrelacement, notamment vers les basses fréquences, permet une meilleure atténuation des premiers modes de vibrations, comme indiqué dans la Figure FR5.5 qui considère une poutre avec des conditions aux limites libre.

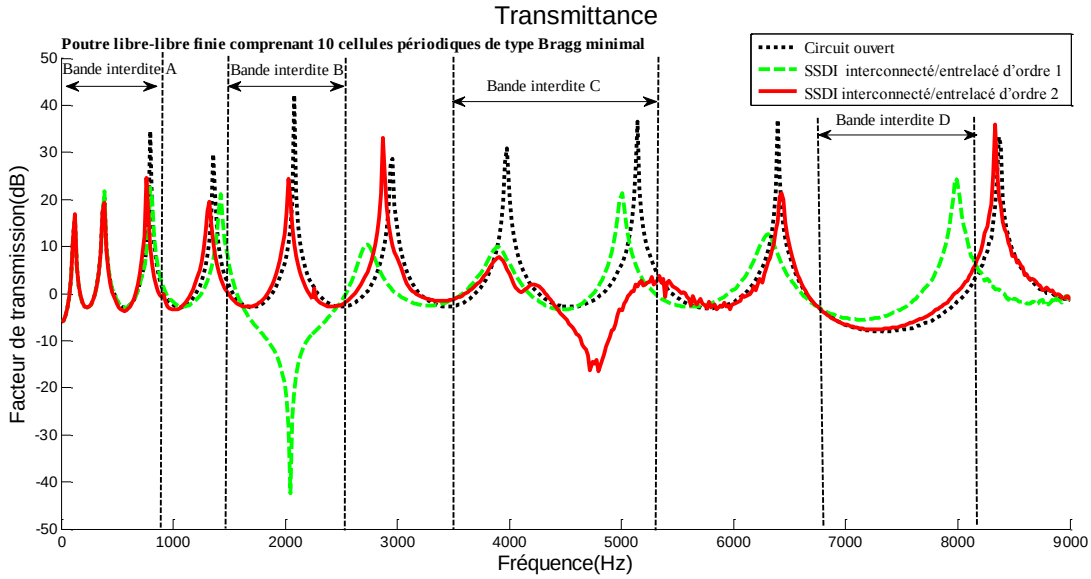

Figure FR5.5. Facteur de transmission pour une structure périodique de type poutre libre-libre avec 10 cellules élémentaires.

5.4 Application aux poutre finies – cas encastré-encastré

Avant de pouvoir valider le principe des structure interconnectée/entrelacées dans le cas réaliste, il convient de pouvoir obtenir la réponse en fréquence théorique d'une structure donnée. En considérant une structure encastrée-encastrée, les encastrements imposent un déplacement et sa dérivée spatiale nuls, tout en appliquant des forces et des moments aux nœuds extrêmes. De même, d'un point de vue électrique, il est considéré que les éléments piézoélectriques extrêmes (première et dernière méta-cellules – soit *2k* éléments piézoélectriques avec *k* l'ordre d'interconnexion/entrelacement) sont en circuit ouvert, imposant un courant nul et une tension non nulle. En appliquant ces principes pour N_g méta-cellules avec une force extérieure *F* appliquée entre les $nf^{ème}$ et $(nf+1)^{ème}$ méta-cellules, on obtient la réponse en tout nœuds *i* de la structure :

$$\begin{Bmatrix} d_i \\ P_i \\ Uc_i^k \end{Bmatrix} = [Tc]^i \begin{Bmatrix} 0 \\ P_0^0 \\ Uc_0^k \end{Bmatrix} + [Tc]^{(i-nf)} \begin{Bmatrix} 0 \\ P_{ex}^{nf} \\ 0 \end{Bmatrix} \quad \text{(FR5.9)}$$

avec $[Tc]$ la matrice de transfert obtenue en utilisant un vecteur de tension/courant Uc_i^k séparant chacune des grandeurs (tensions suivies des courants) :

$$\begin{Bmatrix} d_n^i \\ P_n^i \\ Uc_{i+1}^k \end{Bmatrix} = Tc \begin{Bmatrix} d_0^i \\ P_0^i \\ Uc_i^k \end{Bmatrix}, \quad \left\{Uc_i^k\right\} = \begin{Bmatrix} V_{ki}^k \\ \cdots \\ V_{1i}^k \\ I_{ki}^k \\ \cdots \\ I_{1i}^k \end{Bmatrix} \quad \text{(FR5.10)}$$

et où P_0^0 est la réaction de l'encastrement de gauche, Uc_0^k le vecteur de tension/courant de la première méta-cellule et P_{ex}^{nf} le vecteur de force généralisé appliqué :

$$P_{ex}^{nf} = [F \quad 0] \quad \text{(FR5.11)}$$

$$V_0^k = \left(t_{42}^{\{N_g\}} \left(t_{12}^{\{N_g\}} \right)^{-1} t_{13}^{\{N_g\}} - t_{43}^{\{N_g\}} \right)^{-1} \left(t_{42}^{\{N_g - nf\}} - t_{42}^{\{N_g\}} \left(t_{12}^{\{N_g\}} \right)^{-1} t_{12}^{\{N_g - nf\}} \right) P_{ex}^{nf}$$

$$P_0^0 = \left(t_{12}^{\{N_g\}} \right)^{-1} \left(-t_{13}^{\{N_g\}} V_0^k - t_{12}^{\{N_g - nf\}} P_{ex}^{nf} \right)$$

$$Uc_0^k = \begin{Bmatrix} V_{k0}^k \\ \dots \\ V_{10}^k \\ I_{k0}^k \\ \dots \\ I_{10}^k \end{Bmatrix} = \begin{Bmatrix} V_{k0}^k \\ \dots \\ V_{10}^k \\ 0 \\ \dots \\ 0 \end{Bmatrix} = \begin{Bmatrix} V_0^k \\ I_0^k \end{Bmatrix}, \quad \begin{cases} V_0^k = \begin{Bmatrix} V_{k0}^k \\ \dots \\ V_{10}^k \end{Bmatrix} \\ I_0^k = \begin{Bmatrix} I_{k0}^k \\ \dots \\ I_{10}^k \end{Bmatrix} = \begin{Bmatrix} 0 \\ \dots \\ 0 \end{Bmatrix} \end{cases}$$

5.5 Validation expérimentale

Les concepts précédemment exposés ont été expérimentalement appliqués sur une poutre encastrée-encastrée identique aux chapitres précédents. Néanmoins, on pourra noter que le nombre limité de cellules élémentaires ne permet ici que d'évaluer les ordres 1 et 2 d'interconnexion/entrelacement. Les résultats, présentés en Figure FR5.6, montrent une prépondérance de l'ordre 2 d'interconnexion/entrelacement sur l'ordre 1 en termes d'atténuation basse fréquence (1er et 2nd modes), expliqué par la plus grande longueur de la méta-cellule et la création de bandes interdites dans les basses fréquences, comportement qui se trouve inversé pour le 3ème mode.

Comparé au SSDI utilisé de manière indépendante, on remarque que l'interconnexion/entrelacement d'ordre 1 est (très) légèrement plus performant en basse fréquence (1er mode), alors qu'en haute fréquence, la structure d'ordre 2 est plus intéressante que le SSDI indépendant. Néanmoins, bien que les différences soient relativement faibles, il convient de noter la plus grande simplicité d'implémentation des structures interconnectées/entrelacées, car elles nécessitent moins de commutateurs (dans ce cas 8 pour la technique indépendante, 7 pour l'interconnexion/entrelacement d'ordre 1 et 6 pour l'interconnexion/entrelacement d'ordre 2).

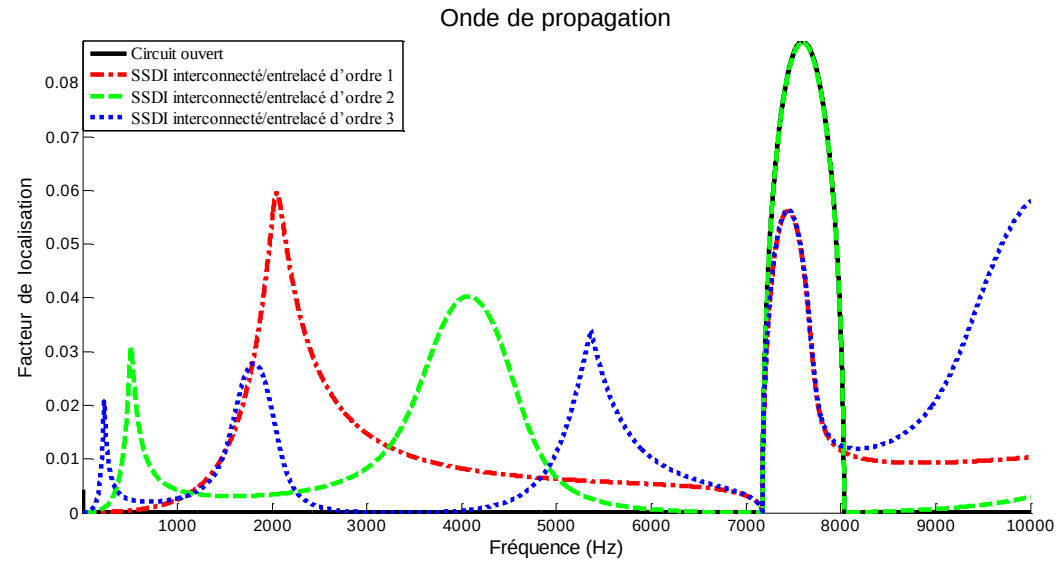

(a)

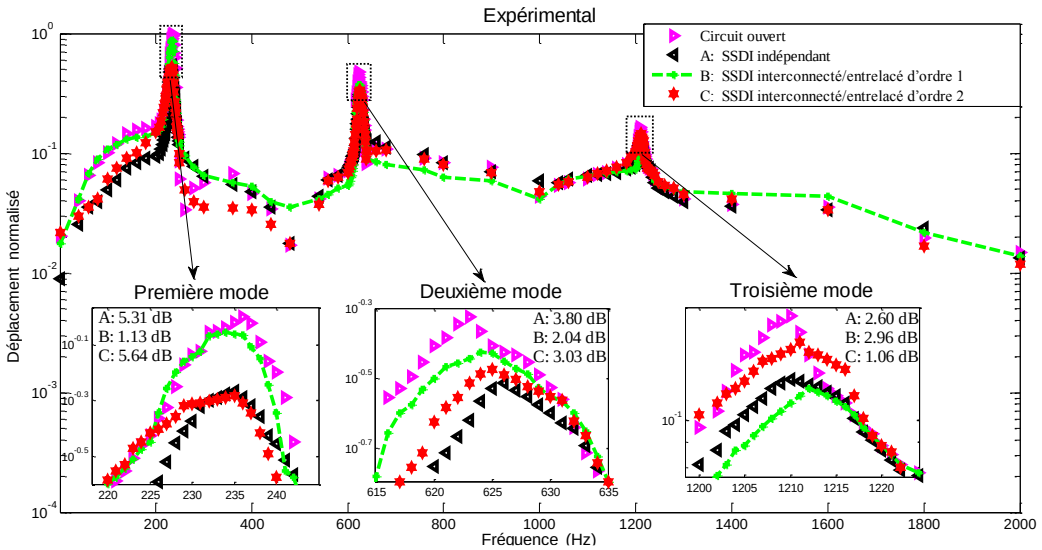

(b)

Figure FR5.6. Résultats sur une poutre encastrée-encastrée : (a) théoriques ; (b) expérimentaux.

5.6 Conclusion

En guise de dernier chapitre, les travaux exposés ici ont proposé une combinaison des approches présentées dans les précédents chapitres du mémoire, en proposant une hybridation entre la méthode d'interconnexion et celle d'entrelacement. Une telle méthode, en permettant des échanges énergétiques dans le domaine électrique sur la globalité de la structure (interconnexion) tout en introduisant localement un désordre

(entrelacement) permet ainsi, selon l'ordre choisi, de contrôler le compromis entre performance et bande passante, notamment en générant des bandes interdites à des fréquences inférieures à celle de la première bande interdite originale ; le nombre de ces bandes étant étroitement lié à l'ordre d'interconnexion/entrelacement. De plus, l'utilisation d'une telle approche, permettant des performances similaires au cas indépendant en basse fréquence, nécessite l'utilisation d'un nombre de commutateurs électriques réduit.

Chapitre FR- 6. Conclusion et Perspectives

Les travaux retranscrits dans ce mémoire ont pour objet le contrôle de vibration utilisant des structures périodiques équipées d'éléments piézoélectriques interfacés en réseau, s'inscrivant ainsi dans le cadre de l'application de structures distribuées.

Ainsi, un état de l'art exposant les motivations pour le contrôle vibratoire et allant des concepts généraux au cas spécifique des structures périodiques utilisant des matériaux intelligents a permis la mise en place progressive de l'originalité et l'essence même de cette thèse.

Avant l'exposition des techniques envisagée lors du doctorat, le second chapitre s'est quant à lui intéressé à la mise en place d'outils, notamment par l'exposition et le développement de modèles à éléments finis, pour la formalisation théorique et l'analyse des techniques exposées dans les chapitres suivants.

Le troisième chapitre a ensuite exposé une première technique s'inscrivant dans le sujet du travail de doctorat, en proposant et analysant les performances en termes de contrôle vibratoire de structure périodique avec des éléments piézoélectriques interconnectés de manière non-linéaire. Ce chapitre a également permis de démontrer, via une analyse de l'impédance équivalente, de la capacité du SSDI à s'adapter à des changements de fréquences d'excitation. Concernant la technique envisagée, il a été montré que la technique d'interconnexion non-linéaire ne permet pas forcément d'atteindre la largeur de bande de l'approche où les éléments piézoélectriques sont interfacés de manière indépendante, mais conduit à l'apparition de bandes spécifiques de forte atténuation. A partir de ces principes, des extensions ont pu être proposées, notamment l'utilisation de l'interconnexion de manière localisée, permettant un bon

compromis entre la largeur de bande de la connexion indépendante et les performances de la technique d'interconnexion.

Le prolongement de cette approche a ensuite été proposé dans le quatrième chapitre, consistant en l'entrelacement des connexions électriques. L'intérêt d'une telle approche est qu'elle permet de combiner une périodicité haut niveau, par l'assemblage de méta-cellules composées de cellules unitaires entrelacées, tout en exhibant au niveau local une irrégularité permet un étalement de la bande passante et donc une atténuation large bande et conduisant à une combinaison de bandes interdites de type de Bragg et dues au couplage électromécanique et la propagation de l'onde acoustique. L'entrelacement peut être ensuite entendu à plusieurs cellules, par exemple via un tri-entrelacement, permettant de mieux cibler les modes basse fréquence.

Enfin, afin de profiter de leurs avantages respectifs, le dernier chapitre a consisté à combiner ces deux dernières approches, conduisant au concept de structures interconnectées/entrelacées, permettant à la fois d'introduire une certaine apériodicité au niveau locale tout en assurant une distribution électrique globale au niveau de la structure, et donc à une propagation de l'onde électrique sur sa totalité. De plus, l'augmentation de l'ordre d'interconnexion/entrelacement permet l'apparition de plus en plus de bandes interdites en basse fréquence, permettant ainsi de cibler les premiers modes, qui sont généralement les plus critiques, pour le contrôle de vibration.

Ainsi, ces travaux ont permis de mettre en évidence l'intérêt de l'utilisation de structures périodiques distribuées dans le cadre du contrôle de vibrations. Certaines questions restent cependant ouvertes et méritent un travail plus poussé, telles que la compréhension précises des phénomènes physiques liés à l'interconnexion pour le contrôle vibratoire, permettant ainsi d'envisager la conception rationnelle de nouvelles approches, ou encore l'hybridation avec d'autres approches pour le contrôle de vibrations, comme par exemple la distribution de systèmes à masse accordée

électromécaniques et interconnectés électrique. Enfin, l'extension des méthodes exposées ici, dont l'analyse et la validation s'est cantonnée au cas de poutres, à des plaques permettrait une applicabilité accrue (par exemple contrôle acoustique).

English Part

Chapter 1 Background and Literatures Review

Abstract

In order to introduce the research background of the dissertation, this chapter reviews most of literatures on vibration control approaches. Through the comparison among different vibration control methods, the academic merit of the dissertation gradually emerges. Specifically, motivation of the dissertation is interpreted in section 1.1. Traditional and smart vibration control systems are summarized in sections 1.2 and 1.3. In order to better understand the vibration control methodology using periodic structures and aperiodic structures, band gaps generation mechanisms in periodic structures and wave localization in aperiodic structures are introduced in section 1.4. Section 1.5 summarizes smart periodic structures with different electrical networks and their application in vibration control systems. Finally, conclusion and outline of the thesis are given in section 1.6.

1.1 Motivation

Being one of common natural phenomena in the world, vibration exists in miscellaneous forms of physical phenomena, including light, heat, sound, elastic medium and so on. People even cannot live without vibration since vibrations of the heart, the eardrum and vocal cords are indispensable body functions. In the engineering field, scientists and engineers have great interest in investigating different kinds of vibration propagation mechanisms and further controlling them for facilitating people's life. According to different vibration propagation mechanisms, the wave, which denotes the propagation of vibration, can be divided into two kinds: mechanical wave (such as sound, elastic and heat waves) which propagates through physical media, electro-magnetic wave (such as radio, *X*-ray and optical waves) whose propagation does not rely on any physical medium. Normally, vibration control engineering can be divided into two kinds according to the purpose of practical

applications: vibration utilization (such as energy harvesting [141]) and vibration suppression/attenuation (such as harmful noise elimination [142] - some practical vibration damage accidents are depicted in Figure 1.1 and Figure 1.2).

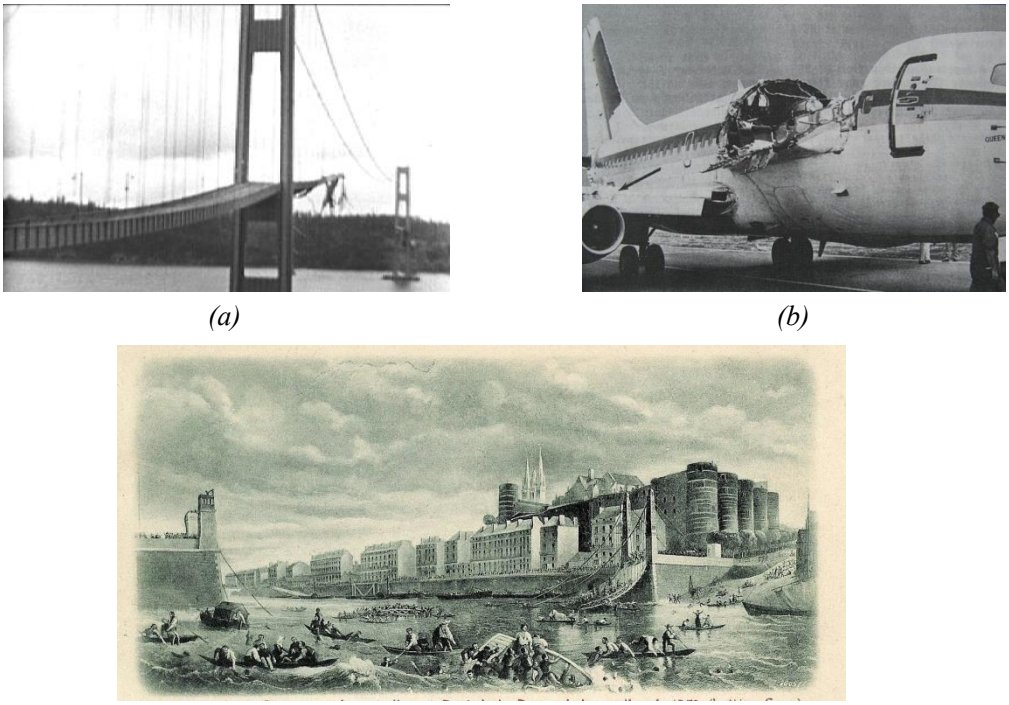

(a) *(b)*

(c)

Figure 1.1 (a) Tacoma Narrows Bridge collapse because of aero-elastic flutter (from https://en.wikipedia.org/wiki/Tacoma_Narrows_Bridge); (b) Fuselage of Aloha Airlines Flight 243 after the explosive decompression (from https://en. wikipedia.org/wiki/Aloha_Airlines_Flight_243); (c) Angers Bridge collapse attributed to dynamic load due to the storm and the soldiers, particularly as they seem to have been somewhat in step, combined with corrosion of the anchors for the main cables (from https://en.wikipedia.org /wiki/Angers_Bridge).

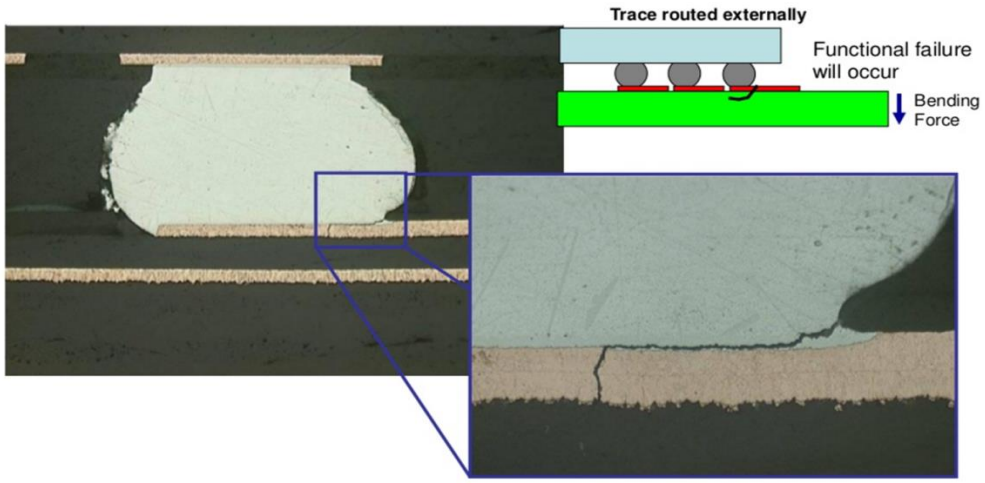

Figure 1.2 Microcracks in a Printed Circuit Board as a result of vibration [1].

In this dissertation, vibration control device design only refers to vibration attenuation of elastic structures. Figure 1.3 shows different kinds of vibration control methods exerted on different sections of a general mechanical system. Specifically, cancelling the vibration of the excitation source [143] is the most effective way for vibration reduction, but there have been not many mature methods for source vibration cancellation. The secondary effective approach is vibration isolation [144, 145] which adds vibration isolators between the excitation source and the controlled object for reducing the vibration transmission. Vibration isolators could lower the natural frequency of a mechanical system below the excitation frequency. This keeps the natural frequency and the excitation frequency 'out of sync' which in turn reduces the amount of vibration and potential problems. However, if both of the source vibration cancellation and the vibration isolation cannot satisfy the vibration control requirements for practical applications, there are three kinds of vibration control methodologies which can be directly applied to the controlled object: vibration absorption, vibration damping and structural modification. In the vibration absorption method, dynamic vibration absorbers (tuned spring-mass systems) [2] are attached to the controlled object for reducing the vibration of a harmonically excited system. In terms of vibration damping systems which dissipate the vibration energy of the controlled object through different kinds of energy conversion, the approaches can be

divided into two kinds: purely mechanical damping systems (mechanical to mechanical energy transmission and mechanical to heat energy conversion through viscous effects or friction) [3, 4] and smart damping systems (mechanical to electrical / magnetic / thermal *etc.* energy conversion through smart materials [5, 6]).

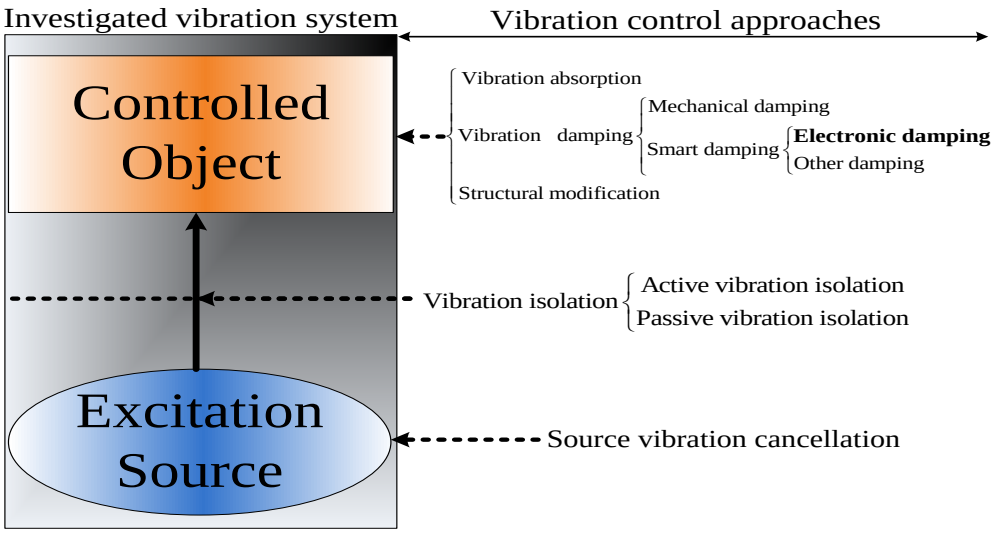

Figure 1.3 A diagram of different vibration control approaches.

As for structural modification [146, 147], for structural designers, optimal structural modification represents the structural parameter alteration for minimizing the structural mass and improving the dynamic characteristics in order to reduce the dynamic response from some disturbances. For control designers, sizing and placement of actuators and sensors on the host structure are taken into consideration for optimal structural modification so that a specified performance index is minimized. Among the structural modification methodologies, periodic structures for mechanical wave propagation control (phononic metamaterials [148]), composed of an assembly of identical elements connected in a repeating pattern, have attracted more and more attention in recent years. Actually, the concept of metamaterials stemmed from the field of electromagnetic wave tailoring (photonic crystals [149]). Within the bandgaps generated by electromagnetic metamaterials, electromagnetic wave can be prohibited at desired frequencies. Similarly, due to the periodic nature created by the artificial

structural design, mechanical periodic structures also exhibit similar particular dynamic characteristics of filtering mechanical wave.

Recently, smart periodic structures with linear electrical networks [150] have become new effective structural ideologies for designing distributed, broadband vibration control devices. Such structure can generate not only Bragg-type phononic bandgaps by virtue of the characteristics of mechanical periodic structures from the point of view of structure designers, but also, from the perspective of control designers, resonant-type phononic bandgaps through the merits of smart damping systems. In addition, wave localization of aperiodic structures also has the potential of enhancing vibration control in some particular frequency ranges. Several smart periodic structures with nonlinear electrical networks are proposed and investigated in this dissertation for integrating the following features into the distributed broadband vibration control device design: broadband low-frequency vibration control potentials of nonlinear electronic damping systems, elastic wave attenuation abilities of mechanical periodic structures and wave localization capabilities of aperiodic structures.

1.2 Traditional damping vibration control systems

Normally, vibration damping means dissipating the vibration energy of the mechanical vibration system. Herein, traditional vibration damping control systems denote mechanical damping control systems (mechanical to mechanical energy transmission and / or mechanical to heat energy conversion through viscous / viscoelastic /frictional / hydraulic effects). Three different kinds of mechanical damping control systems are introduced in the following section: tuned dynamic vibration damping control systems, viscoelastic vibration damping control systems and particles vibration damping control systems.

1.2.1 Tuned dynamic damping vibration control systems

A tuned dynamic vibration reduction system [151], in its most generic form, consisting of a mass, a spring and an energy dissipater (damper / neutralizer), is an auxiliary system whose parameters can be tuned to reduce the vibration of a host structure. Specifically, it suppresses the vibration at its point of attachment to the host structure through the application of an interface force. According to the effective frequency bandwidth of the tuned dynamic vibration reduction system, it can be divided into two kinds [152, 153], resulting in:

- Tuned mass damper (TMD - Figure 1.4) [7, 8] which dampens the modal contribution from a specific troublesome natural frequency of the host structure over a wide range of excitation frequencies.
- Tuned vibration neutralizer (TVN) [9, 154, 155] which neutralizes the vibration at a specific troublesome excitation frequency over a very narrow bandwidth centered at the tuned frequency.

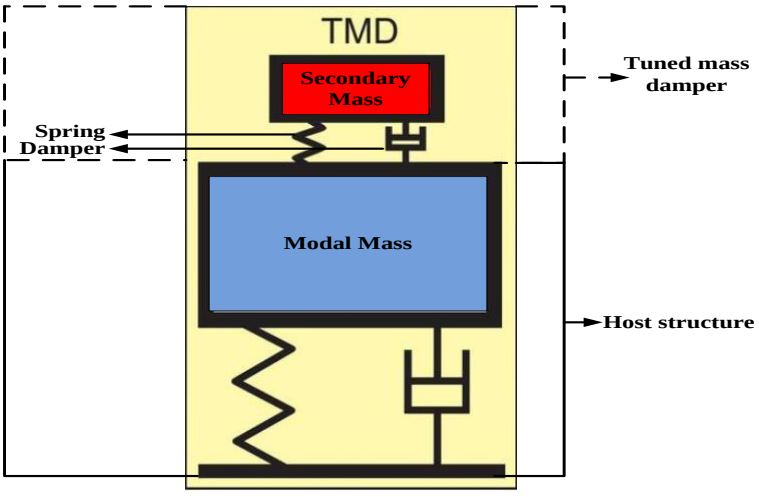

Figure 1.4 Operating principle of a purely mechanical TMD.

As for the tuned mass damper, its tuning frequency is optimally tuned to a value slightly lower than that of the targeted modal frequency, and an optimal level of damping also needs to be designed into the system. In 1909, Frahm [156] firstly applied the TMD concept for reducing the rolling motion of ships as well as ship hull vibrations. Later, atheoretical theory for the TMD methodology was presented by Ormondroyd and Den Hartog in 1928 [157], followed by a detailed discussion of optimal tuning and damping parameters in DenHartog's book on mechanical vibrations in 1940 [158]. Since then, TMDs have been widely used in many engineering applications such as wide span structures (bridges, spectator stands, large stairs, stadium roofs) as well as slender tall structures (high rises) which tend to be easily excited to high vibration amplitudes in one of their basic mode shapes (for instance, by wind or marching and jumping people). In order to better understand the TMD approaches, Figure 1.5 shows two specific examples of practical TMD applications: Figure 1.5 (a) shows one type of vertical TMD installed below a bridge; Figure 1.5 (b) shows one kind of pendulum TMD installed in a high rises.

In terms of a tuned vibration neutralizer (TVN) (or undamped tuned vibration absorber) [155, 159]. The optimal tuning condition is that the tuned frequency is equal to the specific troublesome excitation frequency. The method can only reduce the vibration over a very narrow bandwidth centered at the tuned frequency. Total suppression of the vibration at this frequency is achieved on the condition that there is no damping in the TVN.

However, if the tuned dynamic vibration control systems become mistuned due to a drift in the excitation frequency or a drift in the tuned frequency caused by environmental variation (*e.g.*, temperature change), the vibration control performance of the systems would deteriorate. Especially, a mistuned TVN actually increases the vibration of the host structure [155]. To avoid mistuning, robust or adaptive tunable dynamic vibration control systems have been developed, and are capable of improving the stability of vibration control performance or retuning themselves in real

time. For convenience, adaptive tunable dynamic vibration control methods using smart materials are also included in this section.

(a)

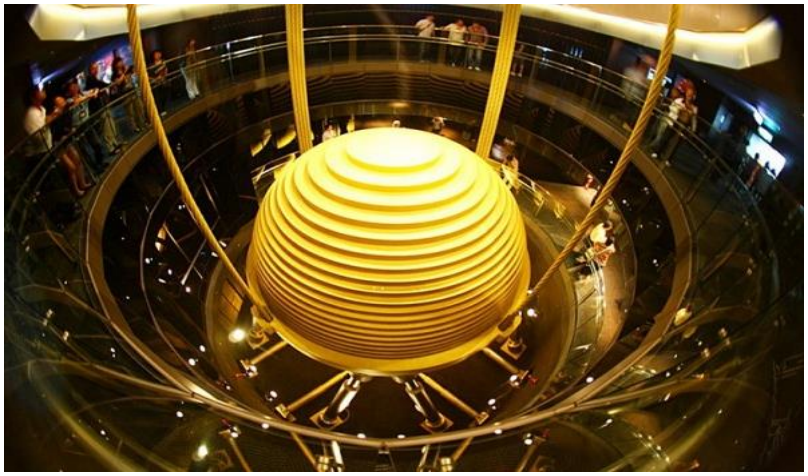

(b)

Figure 1.5 (a) vertical TMD installed below a bridge (from http://www.gerbusa.com); (b) pendulum TMD installed in a tall buildings (from http://www.sourceable.net).

In order to enhance the robustness and vibration reduction performance of the tuned dynamic vibration control systems, many different design criteria [160-164] were proposed for optimizing the system parameters including mass, stiffness and damping. Marano *et al.* [165] proposed a system design criterion which firstly adopted the optimization for the tuned mass ratio. Compared with the previous optimal methods only considering the optimization for the TMD stiffness and the damping ratio, such criterion has better vibration control performance. Hoang *et al.* [166] proposed an optimal TMD for a SDOF (single-degree of freedom) structure under seismic loads. It was shown that the vibration control performance becomes more robust by using large mass ratio. Bekdas and Nigdeli [167] proposed a revised metaheurestic optimization approach (harmony search) to optimize the TMD parameters.

In addition, miscellaneous types of multiple and adaptive TMDs [168-174] were proposed for adjusting the tuned dynamic vibration control systems in real time over a broadband frequency range. Kareem and Kline [175] investigated the dynamic characteristics of multiple mass dampers (MMDs) with distributed natural frequencies under random loading. Bonello *et al.* [176] proposed an adaptive tuned vibration absorber (ATVA) with variable stiffness (by adapting the curvature of piezoelectric actuated parallel curved beams). Weber *et al.* [177] proposed an adaptive tuned mass damper whose stiffness and damping can be tuned in real-time. It consists of a tuned mass, a tuned passive spring and a magneto-rheological (MR) damper. Cunefare *et al.* [66] proposed a state switched absorber with the ability of adapting the resonant frequencies automatically. Davis and Lesieutre [28] proposed a piezoelectric-based vibration absorber which tunes its resonant frequencies by virtue of a ladder of external capacitive shunt circuits.

1.2.2 Viscoelastic damping vibration control systems

Viscoelasticity can be defined as viscoelastic material response which exhibits characteristics of both viscous fluid and elastic solid. In a purely elastic material, all the mechanical energy is stored in the material sample during loading, but is returned

when the load is removed. For elastic materials, the stress and strain curves move completely in phase as shown in Figure 1.6 (a). According to Hooke's Law, the stress is proportional to the strain, and the modulus is defined at the ratio of stress to strain. Conversely, a purely viscous material does not return any of the energy stored during loading. All the mechanical energy is lost once the load is removed. For viscous materials, the stress is proportional to the rate of the strain as shown in Figure 1.6 (b), and the ratio of stress to strain rate is known as viscosity. Different from the previous two materials, a viscoelastic material possesses both elastic and viscous behavior, which is illustrated in Figure 1.6 (c). In a viscoelastic material, some of the mechanical energy stored in the material is recovered after removing the load, and the remaining mechanical energy is dissipated into heat. The stress at a loading frequency is out-of-phase with the strain by the phase shift $\theta\,(0<\theta<\frac{\pi}{2})$ which is a damping measure of the materials. The larger the phase shift θ, the greater the viscoelastic damping. The modulus of a viscoelastic material can be represented as:

$$E_{ve} = E_e + iE_v = \frac{\sigma_{PP}}{\varepsilon_{PP}} e^{i\theta} \tag{1.1}$$

where E_e is the real component of this complex term (storage modulus) which relates to the elastic behavior of the material, E_v is the imaginary component (loss modulus) which relates to the viscous behavior of the material.

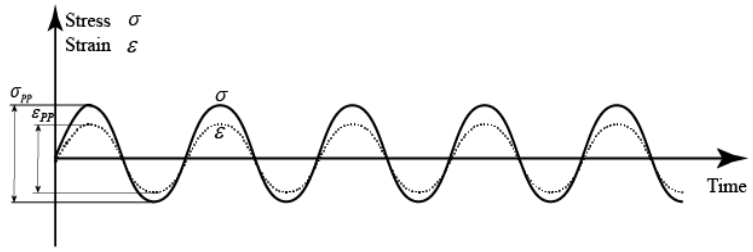

(a)

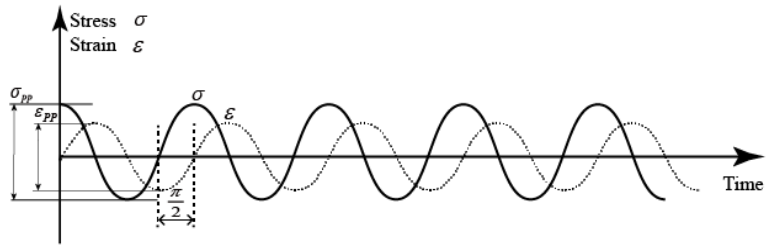

(b)

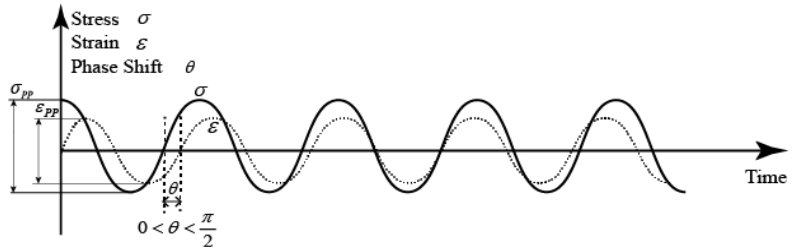

(c)

Figure 1.6 (a) elastic material; (b) viscous material; (c) viscoelastic material.

Traditionally, there are two different viscoelastic damping treatments [178-184] for viscoelastic damping implementation as shown in Figure 1.7: unconstrained (free) layer damping treatment, and constrained (sandwich) layer damping treatment. In the configuration of unconstrained layer damping (Figure 1.7 (a)), the viscoelastic material is either sprayed or bonded on the host structure using a pressure-sensitive adhesive. When the host structure undergoes bending vibration, the viscoelastic layer deforms greatly in extension and compression in planes parallel to the host structure. The hysteresis loop of the cyclic stress and strain dissipates the mechanical energy, and the damping performance of the unconstrained layer system is independent of the mode shape of vibration for full coverage by the viscoelastic layer. Furthermore, the

system loss factor of an unconstrained layer system increases with the thickness, storage modulus, and loss factor of the viscoelastic layer. As for the configuration of constrained layer damping (Figure 1.7 (b)), it consists of two outer elastic layers (the constraining layer and the host structure) and one core viscoelastic layer. Such configuration is more effective than the unconstrained configuration since more energy is dissipated into heat within the core viscoelastic layer when the host structure is in bending vibration state. Kerwin [178] firstly analyzed the vibration of a beam with a viscoelastic layer. The damping factor of the viscoelastic material was modelled through a complex shear modulus approach. The imaginary part of shear modulus is assigned to the damping layer, where the energy is dissipated. Results demonstrated that the shear mechanism is the predominating viscoelastic damping mechanism. Lall *et al.* [180] developed two formulations based on simplified methods and one based on an exact method for damping analysis of a partially covered sandwich beam. In the first formulation, an expression for the modal system loss factor is derived as the ratio of energy dissipated per cycle to the maximum strain energy during a cycle of harmonic motion. In the second formulation, the analysis is carried out by a Rayleigh-Ritz method. Kung *et al.* [181] proposed a new analytical, energy based approach for predicting the harmonic vibration response of a damped beam with multiple viscoelastic patches (each damping patch is composed of a metallic constrained layer and an adhesive viscoelastic layer). Huang *et al.* [184] derived general differential equations of motion for a three-layer sandwich structure with viscoelastic core through the Hamilton's principle and Donnell-Mushtari-Vlasov simplification.

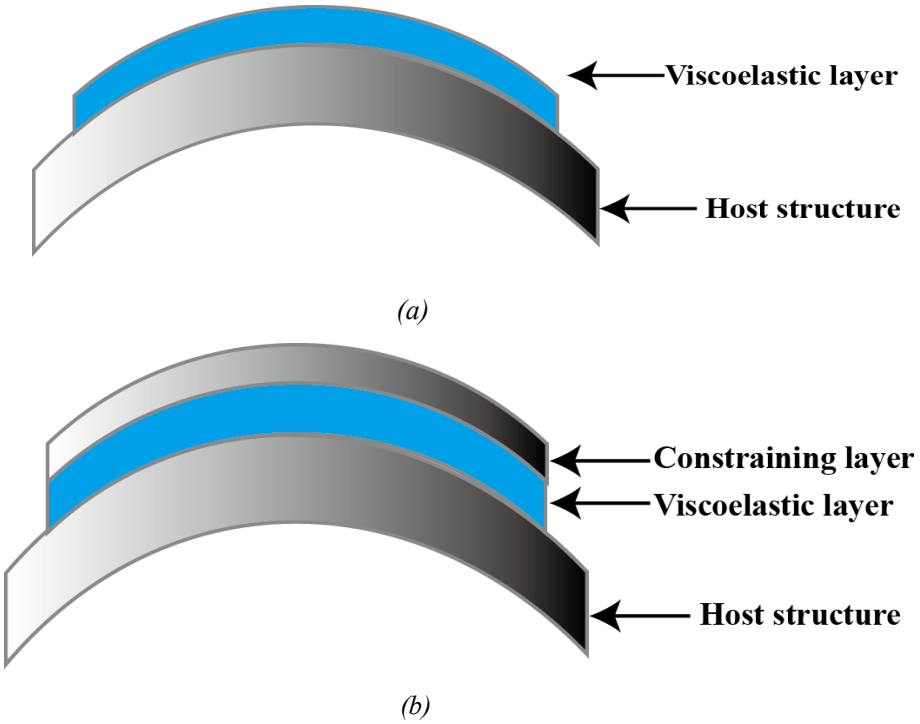

Figure 1.7 (a) unconstrained (free) layer viscoelastic damping; (b) constrained (sandwich) layer viscoelastic damping.

Additionally, another two hybrid viscoelastic damping treatments for viscoelastic damping implementation are introduced in this section as shown in Figure 1.8: tuned viscoelastic damper [185-187] (Figure 1.8 (a)), and active constrained layer damping treatment [188-191] (Figure 1.8 (b)). Specifically, the tuned viscoelastic dampers are generally applicable to suppress the vibration associated with a single frequency or a narrow band of frequencies. The original unwanted resonance peak will be split into two resonance frequencies (one below and one above the original resonance frequency of the original system). In the active constrained layer damping treatment, the conventional passive constrained layer damping is enhanced by active control schemes for controlling the strain of the constrained layer. The shear in the core viscoelastic layer (sandwiched between two piezoelectric layers) can be controlled by the piezoelectric actuators (layers).

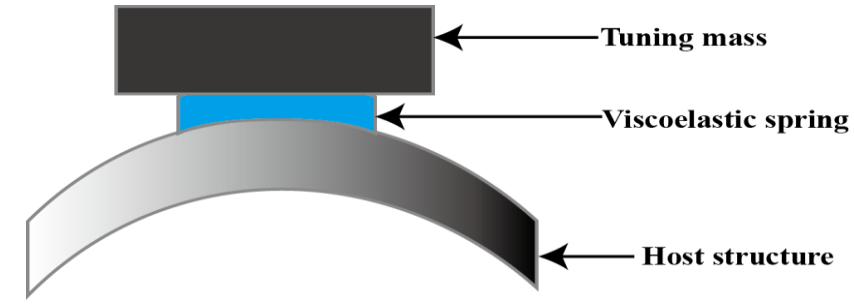

(a)

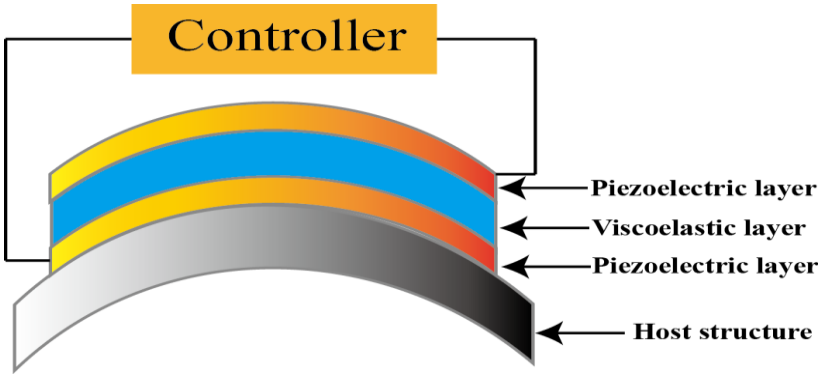

(b)

Figure 1.8 (a) tuned viscoelastic damper; (b) active constrained layer viscoelastic damping.

1.2.3 Particles damping vibration control systems

The particle impact damper is a passive vibration damping control device using metal or ceramic particles or powders of small size which are inserted in an enclosure attached to a vibrating structure. Specifically, metal or ceramic particles or powders of small size are directly placed inside the containing holes with the holes partially or fully filled. Usually, the size of the particles is in the range of 0.05-1 *mm* in diameter (*e.g.*, lead or tungsten steel as shown in Figure 1.9 [192]), and a large number of particles (in the order of 1,000 or even 10,000) are contained in a single hole. Within such particle size range, the particles are considered non-cohesive.

(a) *(b)*

Figure 1.9 (a) Lead particles; (b) tungsten carbide particles [192].

In contrast to the principle of stored elastic energy dissipation of viscoelastic materials, particle damping treatment focuses on energy dissipation through a combination of inelastic collision, friction and shear damping. Specifically, the kinetic energy of the particle impact damping system is absorbed or dissipated into heat through the momentum exchange (between solid moving particles and the enclosure), friction, impact restitution and shear deformations. Many theoretical and experimental researches [193-200], classified by the direction of excitation either in the vertical (direction of gravity) or horizontal (normal to gravity) plane (*e.g.*, transverse particle beam dampers and longitudinal particle beam dampers as illustrated schematically in Figure 1.10 [192]), have been proposed.

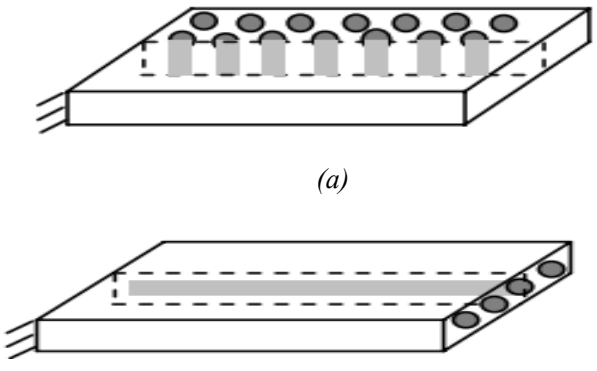

(a)

(b)

Figure 1.10 (a) Transverse particle beam dampers; (b) longitudinal particle beam dampers [192].

Friend and Kinra [201] experimentally investigated a cantilever beam vibrating freely in the vertical plane with a particle damper attached to the free end. High damping performance is achieved with a small weight penalty. In addition, the effect of particle clearance and displacement amplitude on the specific damping capacity is also investigated. Masri [202] proposed an exact solution of the general steady-state response of a forced steady-state horizontally excited system with an impact damper. By taking the motion of the system as a piecewise linear process, a stability analysis of the solution is performed. Saluena *et al.* [203] mathematically evaluated the dissipative properties of granular materials using the particle dynamics method which is a methodology where individual particles are modeled and their motions tracked in time. They showed the pattern of the analysis in terms of energy-loss rate displaying different damping regimes in the amplitude-frequency plane of the excitation force. Papalou and Masri [204] investigated the mechanism of particle impact dampers in a horizontally vibrating single degree of freedom (SDOF) system under random base excitation. They studied the influence of mass ratio, container dimensions, and excitation levels using tungsten powder, and provided optimum design of particle damper based upon reduction in system response. Palazzolo and Kascak [205] theoretically modeled impact dampers applied to multiple degrees of freedom (MDOF) structures with 3-D beam finite elements. Through conducting simulations in the modal subspace rather than full DOF physical coordinate space, good accuracy and substantial savings in computational time were demonstrated. Popplewell and Semercigil [206] investigated the performance of a particle filled bean bag impact damper. Their experimental setup simulated a SDOF structure vibrating horizontally due to sinusoidal excitation. Cempel *et al.* [207] presented a simplified energy approach for measuring the influence of various particle-filling configurations on the damping loss factor of a SDOF system under horizontal forced vibration. Mao *et al.* [208] utilized the discrete element method (DEM) to simulate particle damping for a cantilever beam vibrating vertically.

1.3 Smart damping vibration control systems

Different from the traditional mechanical damping systems previously exposed (except active constrained damping system), smart damping systems attenuate mechanical vibration by converting energy between the mechanical and another physical domain (*e.g.,* electrical or magnetic) through smart materials (electrorheological (ER) fluids [209-213], magnetorheological (MR) fluids [214-218], electrostrictive materials [219-224], shape memory alloys (SMA) [225-230], electromagnetic materials, piezoelectric materials and so on). Generally, an electro-rheological fluid is obtained through a dispersion of solid particles within an insulating oil [231]. The application of an electric field results in the orientation of the particles yielding an increase of the shear stress developed within the fluid and generally in the development of a static yield stress. The change in stress levels is rapid after applying the electric field (response times are often quoted in milliseconds), and the corresponding relaxation time is on a comparable scale upon removal of the field [211]. A magneto-rheological fluid is one kind of smart fluid in a carrier fluid, usually a type of oil. When subjected to a magnetic field, the fluid greatly increases its apparent viscosity, to the point of becoming a viscoelastic solid. When in its active state, the yield stress of the fluid can be controlled by varying the magnetic field intensity. A shape memory alloy is an alloy which 'remembers' its original shape and that deformed returns to its pre-deformed shape when heated.

Electromagnetic materials or dampers dissipate the mechanical energy mainly through Lenz's law [109, 232-237]. For example, loops of electrical current (Foucault currents [238]), generated in a conductor in a time-varying magnetic field, are induced either by movement of the conductor in a stationary magnetic field or by the varying reluctivity of a magnetic circuit whose flux is linked to the conductor, initiating 'Lorentz' (or 'motional') and 'reluctance' (or 'transformer') electromotive forces, respectively. Such induced currents will be dissipated into heat at the rate of I^2R and the forces will disappear because of the electrical resistance R of the conductor.

Therefore, electromagnetic current dampers can be divided into two main types: 'Lorentz' [239] and 'reluctance' [240] types.

For piezoelectric and electrostrictive materials, both of piezoelectric and electrostrictive effects can be described as the link between electrostatics and mechanics: piezoelectric effect describes the first order (linear) coupling between dielectric and elastic phenomena, while electrostrictive effect describes the second order (nonlinear) coupling between dielectric and elastic phenomena [219].

In this dissertation, smart materials mainly refer to piezoelectric materials (PZTs). In order to apply the electromechanical ability of PZTs [241, 242] for damping purposes, piezoelectric patches are commonly attached to the targeted mechanical structure, which forms a smart mechanical structure. As shown in Figure 1.11, piezoelectric shunt damping techniques can be categorized by two kinds: smart damping techniques for enhancing damping capability of a single PZT (or collocated PZT pairs) bonded on the host structure; and smart damping electronic networks for enhancing damping capability of several PZTs bonded on the host structure.

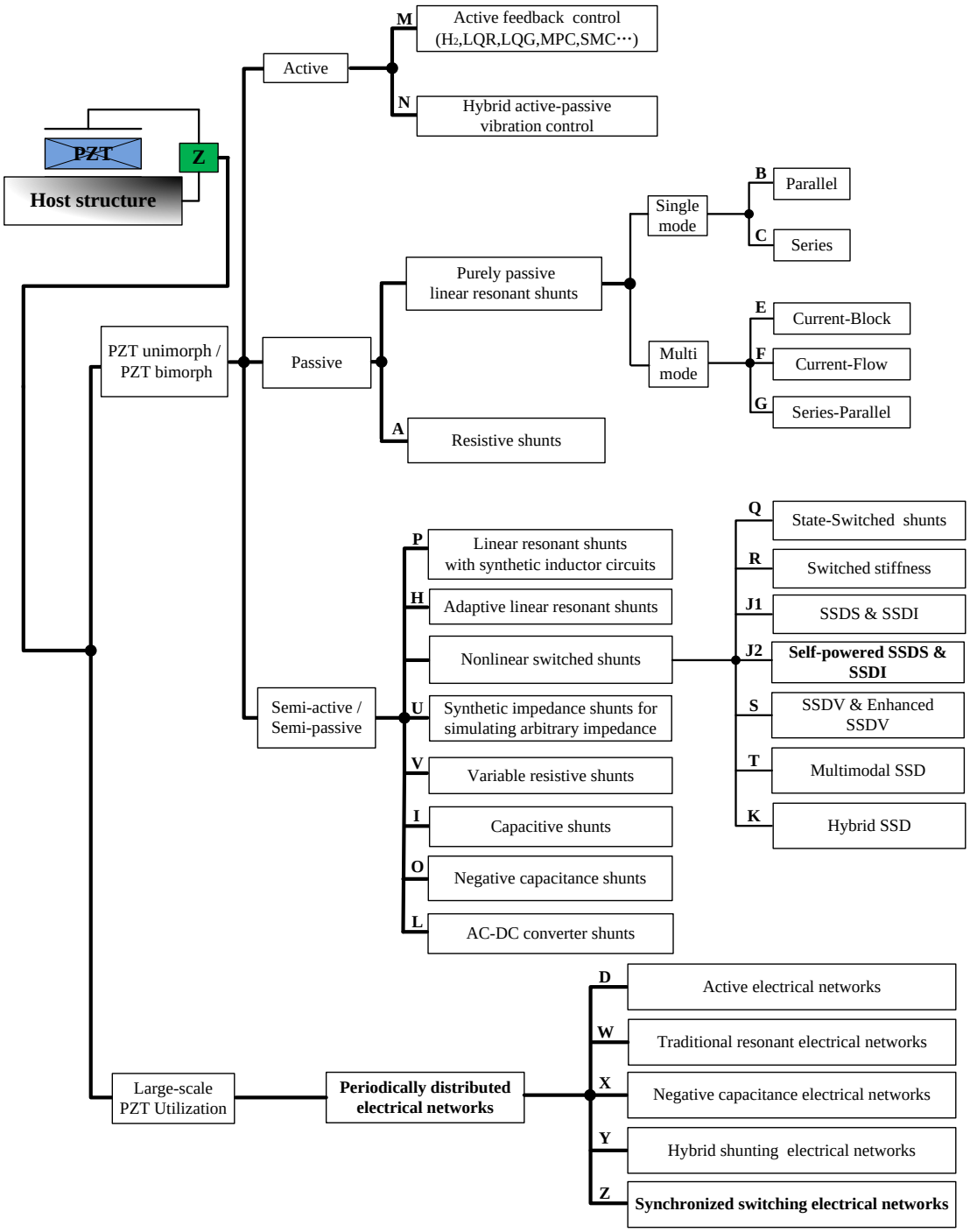

Figure 1.11 Different smart shunt damping techniques (**A**: [13-15]; **B**: [15, 16]; **C**: [13]; **D**: [17-19]; **E**: [20]; **F**: [21, 22]; **G**: [23]; **H**: [24-26]; **I**: [27-30]; **J1**: [31, 32]; **J2**: [33, 34]; **K**: [35]; **L**: [5, 36-39]; **M**: [11, 40-53]; **N**: [54, 55]; **O**: [56-60]; **P**: [13, 61-64]; **Q**: [65-67]; **R**: [28, 68-70]; **S**: [71-75]; **T**: [76-82]; **U**: [83, 84]; **V**: [85]; **W**: [86-99]; **X**: [100-105]; **Y**: [106, 107]; **Z**: [108, 109]).

For smart damping techniques for enhancing damping capability of a single PZT (or collocated PZT pairs) bonded on the host structure, according to whether the external energy is introduced into the investigated vibration system or not, smart damping techniques for enhancing damping capability of single PZT can be categorized by three main types: active vibration control (significant amount of external energy is added to neutralize the energy of the system for vibration reduction), passive vibration control (no external energy is directly added to neutralize the energy of the system for vibration reduction) and semi-active / semi-passive vibration control (when a small amount of external energy is added to neutralize the energy of the system for vibration reduction, semi-active type denoting that part of the energy is directly transferred to the PZT, while in semi-passive type, energy is only used for generating command signals):

- ✧ Active vibration control includes:

  Active feedback control algorithms (*e.g.*, H_2, *LQR*, *LQG*, *MPC* and *SMC*) [11, 40-53] and hybrid active control methodologies [54, 55].

- ✧ Passive vibration control includes:

  Resistive shunts [13-15]; purely passive linear resonant shunts (for single-mode (Parallel [15, 16], Series [13]) and multi-mode (Current-block [20], Current-flow [21, 22] and Series-Parallel [23])) and so on.

- ✧ Semi-active / semi-passive vibration control includes:

  Linear resonant shunts with synthetic inductor circuits [13, 61-64]; adaptive linear resonant shunts [24-26]; nonlinear switched shunts (Stated-Switched shunts [65-67], Switched stiffness [28, 68-70], SSDS & SSDI [31, 32], Self-powered SSDS & SSDI [33, 34], SSDV and Enhanced SSDV [71-75], multimodal SSD [76-82] and Hybrid SSD [35]); synthetic impedance shunts for simulating arbitrary impedance [83, 84]; variable resistive shunts [85]; capacitive shunts [27-30]; negative capacitance shunts [56-60]; AC-DC converter shunts [5, 36-39] and so on.

1.3.1 Active smart damping vibration control systems

In 1956, Olsen [243] firstly discussed an active electronic control application which refers to a electronic vibration reducer consisting of a sensor, amplifier, and driver connected either in negative or positive feedback configuration. For active smart damping methodology, smart materials (*e.g.*, piezoelectric materials) used as sensors and actuators (the both being separated), are indispensable media for implementing active vibration control algorithms. According to different digital active control algorithms, external energy is regularly added to the damping system for vibration reduction. In addition, the energy exchange, and more specifically the reactive part that yields the need of bulky amplifier, is not as controlled as in semi-passive and semi-active approaches.

- Active---LQR / LQG feedback control

Normally, according to the principle of optimal control separation, a classical feedback LQR (linear-quadratic-regulator) controller design can be divided into two parts: one part representing optimal controller design, and the other part representing the state observer design. However, the sensor measuring system may measure the noise signal which would decrease the robustness of the LQR controller. In order to improve the robustness of the LQR controller, the LQG (Linear-Quadratic-Gaussian) controller was proposed which also has two similar parts. The optimal controller design is same as the LQR controller design. However, in the part of the state observer design, Kalman filter is used to filter out the noise (the default is white noise signal) impact on the estimated state, so that the estimated state is more accurate, while LQR does not consider this factor in this part.

Zhang *et al.* [10] proposed a LQR controller based on the independent mode space control techniques to suppress the first two vibration modes of the system, where the curves of state variables and output variables are given. The simulation results proved the effectiveness of theoretical analysis and achieved good performance. Fleming *et al.* [40] proposed an active feedback control technique where electrical impedance is

connected to the terminals of an electromagnetic actuator for reducing vibration in the host structure. The coupled mechanical system can be controlled by measuring the coil terminal voltage and controlling the resultant current. The regular LQR or H_2 controller in the technique is used to facilitate automatic tuning of the electrical impedance.

- Active---MPC feedback control

Regardless of the algorithm forms of MPC (model predictive control), the later should have three features: prediction model, receding horizon optimization and feedback correction. Specifically, the function of prediction model is based on the object's history information and future input to predict future output, and the MPC is optimized in a receding horizon controlling way during a limited period of time. As for the feedback correction, if the model is accurate and not affected by experimental disturbance, the algorithm will not need feedback, and is equivalent to an open loop control algorithm. However, if the model is mismatched, feedback control will begin playing the role of correction.

Wills *et al.* [11] proposed a new active vibration control approach employing model predictive control (MPC), which can reduce high computational requirements of MPC. Specifically, the proposed method advances in three aspects: previous results on constraint handling for active structures are extended; MPC offers improved dynamic performance in the presence of actuator limitations; MPC can be implemented on inexpensive hardware at high sampling rates using traditional online quadratic programming methods for nontrivial models and with significant control performance achievements.

- Active---SMC feedback control

SMC (Sliding Mode Control) is a nonlinear control method that alters the dynamics of a nonlinear system by application of a discontinuous control signal that forces the system to "slide" along a cross-section of the system's normal behavior. It can also be regarded as a variable structure control method since the state-feedback control law of

SMC can switch from one continuous structure to another based on the current position in the state space.

Wang *et al.* [12] presented an experimental study of an adaptive robust sliding mode control scheme based on the Lyapunov's direct method for active vibration control of a flexible beam using PZT sensor and actuator. Two adaptive robust sliding mode controllers for vibration suppression are designed: a discontinuous bang-bang robust compensator and a smooth compensator with a hyperbolic tangent function. Both controllers guarantee asymptotic stability, as proved by the Lyapunov's direct method. Experimental results demonstrated the effectiveness and the robustness of both adaptive sliding mode controllers.

- Active---Hybrid active-passive vibration control

Some researchers also investigated the hybrid vibration control treatments in which the passive and active vibration control methods are organically integrated for vibration damping. Trindade *et al.* [55] provided a review of the open literature concerning geometric configurations, modeling approaches and control algorithms for hybrid active (piezoelectric)-passive (viscoelastic) damping treatments of beams. Specifically, using a unified finite element model able to represent sandwich damped beams with piezoelectric laminated faces and an optimal control algorithm, the geometric optimization of four hybrid treatments (Active Constrained Layer (ACL) [244], Active-Passive Constrained Layer (APCL) [245], separated Active (AC) and Passive (PCL) treatments (AC / PCL) [246], Active (AC) and Passive Stand-Off Layer (PSOL) (AC / PSOL) [247]) was studied through treatment length and viscoelastic material thickness parametric analyses. The configurations of these treatments are clearly depicted in Figure 1.12. A comparison of the performances of these hybrid damping treatments was carried out and the advantages of each treatment were identified. Globally, AC / PCL and AC / PSOL hybrid treatments are much more effective than the other (ACL and APCL) treatments. The AC / PSOL hybrid damping performance is generally worse than that of AC / PCL, but more effective than that of AC / PCL for relatively thick viscoelastic layers. In addition, the drawbacks of each

treatment compared with passive or active treatments were also investigated. For instance, the performance of ACL hybrid treatment can be increased only by reducing significantly the thickness of the viscoelastic layer compared with the passive treatment.

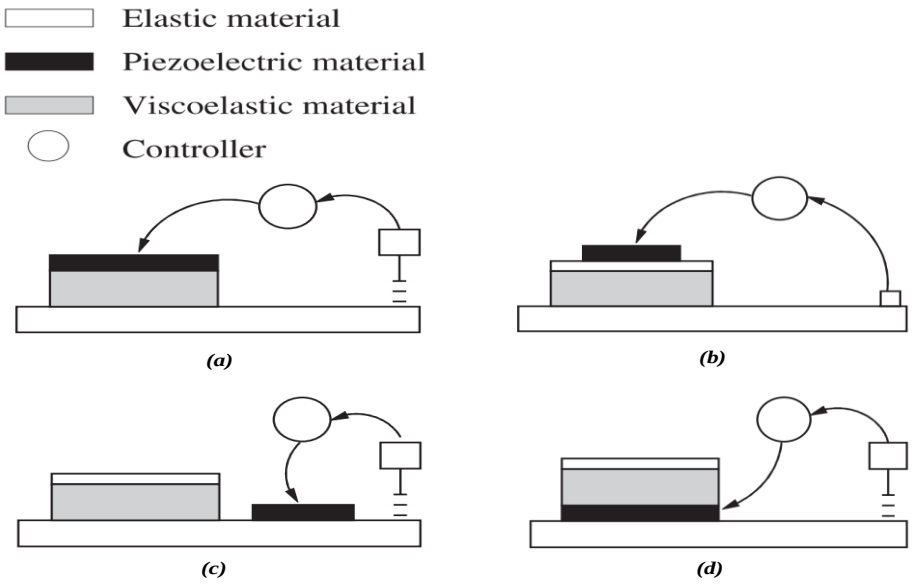

Figure 1.12 (a) Active Constrained Layer (ACL); (b) Active-Passive Constrained Layer (APCL); (c) separated Active (AC) and Passive (PCL) treatments (AC / PCL); (d) Active (AC) and Passive Stand-Off Layer (PSOL) (AC / PSOL) [55].

1.3.2 Passive smart damping vibration control systems

In 1979, Forward [15] firstly proposed a passive smart damping concept, namely 'electronic damping': a set of piezoelectric devices is placed on a host structure to sense and control the mechanical vibrations. The key to achieve electronic control in a mechanical system is the appropriate use of electrical-to-mechanical energy conversion transducers with electric resonant circuits that would provide efficient coupling between the electronics and the mechanical system. Since then, more and more passive smart damping vibration control approaches have emerged:

- Passive---Resistive shunts

Normally, resistive shunts reduce the vibration by virtue of partially dissipating electrical energy (converted from mechanics) of the smart damping system into heat

energy through the connected resistors. Ishii [14] fabricated an electromechanical damper using piezoelectric materials connected to an external resistance. Experimental results showed that mechanical energy generated by vibration noise can be transformed into electrical energy through the piezoelectric effect, and then dissipated into heat energy through the external resistance. The dissipated energy is maximized when the connected resistor Z equals the modulus of the impedance of the piezoelectric material:

$$Z = \frac{1}{\omega C_0} \tag{1.2}$$

where ω is the angular frequency, and C_0 denotes the inherent capacitance of the piezoelectric material.

- Passive---Purely passive linear resonant shunts--Single mode

As for single-mode resonant shunts, Hagood and Flotow [13] provided the first analytical analysis of vibration damping through passive shunting. The study showed how a piezoelectric patch shunted through a single-modal resistive-inductive (*RL*) circuit exhibits a behavior equivalent to a mechanical vibration absorber. A resonant shunt is simple to design and offers effective damping at the vicinity of a selected mode of the underlying structure.

Wu [16] investigated vibration control performance of the piezoelectric shunts with a parallel *RL* circuit. Results showed that both of the inductance and resistance values affect the vibration damping performance: the peak amplitude of the displacement versus frequency curve of a structural mode decreases with the increase of the shunt resistance under the optimum tuning condition, and becomes a plateau at the optimum resistance. When the resistance increases further, the middle of the plateau continues to decrease, but two humps appear around the plateau shoulders.

- Passive --- Purely passive linear resonant shunts -- Multi mode

Wu [20] presented a passive multiple-mode shunt-damping method using a single PZT for vibration reduction. A ‘blocking’ circuit which consists of one parallel *LC* anti-resonant circuit or a series of them, in series with each parallel *RL* shunt circuit

designed for one structural mode, is employed in the proposed method. The number of the structural modes for shunt-damping is determined by the number of anti-resonant circuits in each branch circuit. These anti-resonant circuits are designed to produce infinite electrical anti-resonant impedance at the natural frequencies of all other *RL* shunt circuits. Each branch circuit is functional only at its own targeted mode but is open-circuited at all other frequencies. Therefore, they do not interfere with each other when all shunt branches are connected to the PZT terminals. Experimental results showed that modified multi-mode shunt circuits have excellent vibration reduction performance for two and three structural modes using a single PZT transducer bonded on a two-wing aluminum cantilever beam.

Behrens *et al.* [22] introduced a current flowing controller for multimode vibration control. Different from the current blocking technique which prevents the current from flowing at a specific frequency, the current flowing controller allows the current to flow through using a series *LC* circuit for a specific anti-resonance frequency. The series LC circuit appears to be a short circuit at the specific frequency and approximately open circuit for all the other frequencies. The passive control strategy is validated through experimentation on two piezoelectric laminated structures.

Fleming *et al.* [23] presented a new multimode piezoelectric shunt damping structure using the series-parallel impedance. Such series-parallel impedance contains fewer components, and contains smaller inductors than most previous circuit designs. Experimental results demonstrate that a series-parallel shunt circuit connected to two terminals of a PZT bonded on a simply supported beam has better multi-mode damping performance.

Furthermore, the required value for the inductors (that are very large) cannot be realized unless using synthetic inductors considered as semi-active type, and are discussed in detail in section 1.3.3.

1.3.3 Semi-active / semi-passive smart damping vibration control systems

Different from the passive or active vibration control systems, semi-active and semi-passive approaches consider that a small amount of energy is used for neutralizing vibrations (either through the command of nonlinear components and/or energy transfer to the piezoelectric element). Semi-active smart vibration control will transfer part of the external energy directly to the PZT while semi-passive smart vibration control only uses the external energy for generating command signals. In addition, some of semi-passive smart vibration types have self-powered versions which require no external energy and only use the internal energy (*i.e.*, from the PZT) for command signal generation, and can be therefore considered as passive to some extent.

- Semi-active --- Linear resonant shunts with synthetic inductor circuits

Normally, the inherent capacitance of PZTs is quite small as well as the target mode frequency, and thus the inductance in the linear resonant shunts needs to very large (even up to hundreds of Henries) for low-frequency vibration control. However, in many practical applications, such large inductance values cannot be implemented with a coil inductor but only through synthetic circuit designs for virtual inductors, such as Antoniou gyrators [62] or Riodan virtual inductors [61]. Specifically, operational amplifiers which require external power supplies are indispensable components for such virtual inductors. Most researchers [26, 135, 248] have adopted such virtual inductors for single-mode or multi-mode vibration control in a low frequency range. Park [248] developed a general modeling of the tuned electrical absorber for describing an additional damping which is implemented in the equation of motion of the piezo / beam system. Using assumed series displacement shape functions, a mathematical model is also developed to describe the flexural vibrations of the cantilevered piezo / beam system. The effectiveness of a series *RL* and parallel *RL* resonant shunt circuit was demonstrated theoretically and experimentally. In the experiment, active filters [249] were used as virtual inductors in the shunt circuits.

- Semi-active --- Adaptive linear resonant shunts

Hollkamp *et al.* [26] presented a self-tuning piezoelectric vibration damper which consists of a pair of PZT attached to the structure and shunted by an resistor-inductor (*R*-*L*) circuit. It tunes itself to a particular mode and tracks that mode if it varies in frequency through producing an electrical resonance which can be tuned to the desired structural mode by a simple control system. The damping performance of the damper is experimentally demonstrated on a cantilevered beam.

Niederberger *et al.* [24] proposed a new technique for the online adaptation of multi-mode resonant shunts. Parameters of the circuit components can be optimally tuned online through minimizing the relative phase difference between a vibration reference signal and the shunt current. The damping performance of the proposed technique is experimentally validated on a cantilever beam. During the experiments, the adaptive law converges quickly and maintains optimal performance in the presence of environmental uncertainties.

- Semi-active --- Synthetic impedance shunts for simulating arbitrary impedance

Fleming *et al.* [37, 83] proposed a method for implementing an impedance of arbitrary order and complexity using a current source and digital signal processor (DSP) for piezoelectric shunting damping. Such synthetic impedance can be used in place of shunt damping networks to provide effective structural damping without the problems associated with direct circuit implementations such as the requirement of a large number of operational amplifiers in the linear resonant shunts for low-frequency multimode vibration control.

- Semi-passive---Variable resistive shunts

Warkentin *et al.* [85] proposed a variable resistive shunt-damping concept. Such shunt-damping circuit consists of a rectified DC voltage source and a time-varying resistor. A 1D electromechanical circuit model is used to evaluate the performance of the shunt-damping circuit (effective material loss factor). The resistor connected to two electrical terminals of the PZT varies freely over time. In order to find the 'ideal' periodic resistance time history, each half-cycle is divided into a number of equal intervals, and the resistance is assumed to vary linearly with time between the values

at the endpoints of each interval. The varying resistance is determined by maximizing the loss factor of the shunted composite system. The behavior of the rectified DC voltage source shunting scheme is also investigated to determine the achievable damping levels and potential undesirable motions induced at higher harmonics of resonance or disturbance frequencies by the electrical nonlinearities.

- Semi-active --- Negative capacitance shunts

In 1979, Forward [56] firstly proposed a multimode vibration suppression method with piezoelectric elements connected to negative capacitance shunts. Such negative capacitance can be realized by an operational amplifier [57, 250]. Most of past researches [56-60] placed attention on negative capacitances as they allow 'cancelling' or 'compensating' the capacitive nature of the piezoelectric element (PZT), or, more or less equivalently, provide an artificial enhancement of the electromechanical coupling. The resistance in the negative capacitance shunt could dissipate energy over a greater frequency range due to the "cancellation" of the PZT capacitance. Park *et al.* [58] developed a mathematical model for describing the flexural vibration of beams with the electromechanical interactions of an IDE (inter-digital electrode) PZT which is shunted with a synthesized negative capacitance circuit. The ability of the IDE PZT and the negative capacitive shunt damper in reducing multiple vibration modes is demonstrated theoretically and experimentally. Results showed that effective attenuations of vibration amplitudes achieved with the increase of the shunt resistance, with good agreement between the theory and the experiment.

Berardengo *et al.* [251] proposed a new negative capacitance (NC) shunt layout using a pair of NCs in Series-Parallel (SP) configuration (Figure 1.13(c)) based on a new refined model of the capacitance of the piezoelectric patch. The proposed model of piezo-capacitance showed that the capacitance value at the considered resonant mode does not depend on the modes of the structure at lower frequency, but just on those at higher frequency. The attenuation performance of the proposed NC shunt layout is improved compared with traditional (in Series (Figure 1.13(b)) and in Parallel (Figure

1.13(a))) NC layouts. The stabilities of ideal NC circuit layouts in Series, in Parallel and in Series-Parallel are also deeply investigated and compared.

Marneffe *et al.* [60] presented a detailed theoretical analysis of the negative capacitance shunt technique. It was shown that the system 'piezo stack + negative capacitance' can be seen as an equivalent transducer with enhanced electromechanical coupling factor *k* and equivalent formulas were also presented. Stability was deduced on an undamped structure from a single admittance curve as well as performance. Two different implementations (series versus parallel) were compared, and the lack of robustness of the parallel implementation was demonstrated. All the analytical results were validated experimentally on a truss structure. Experiments showed that the negative capacitance shunt behaves as expected.

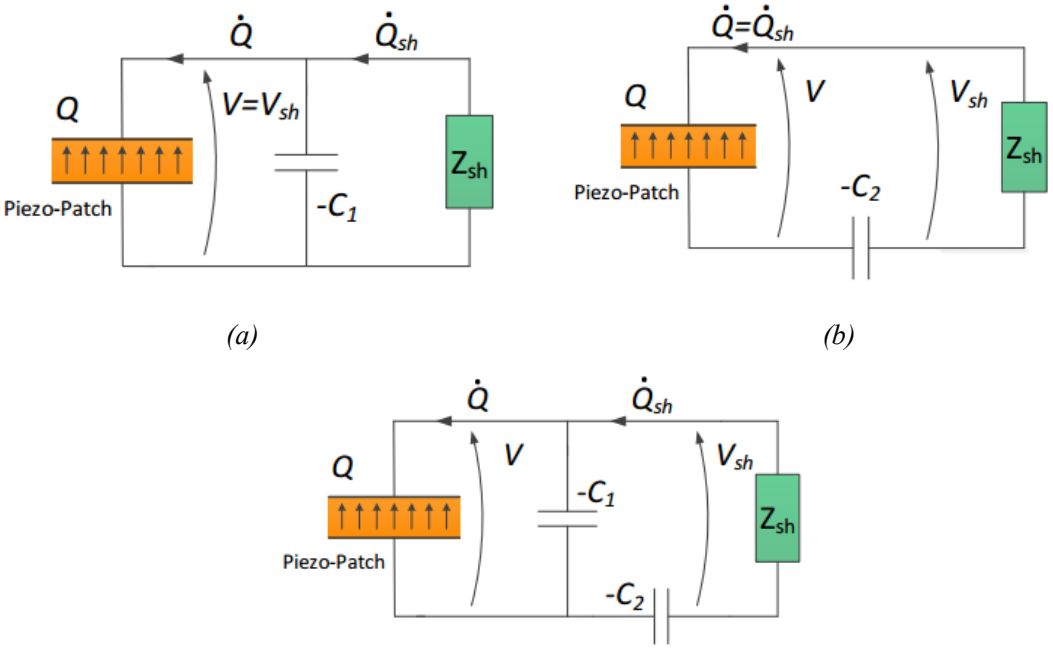

Figure 1.13 (a) Circuit layout based on one NC in Parallel; (b) circuit layout based on one NC in Series; (c) proposed circuit layout based on two NCs: Series + Parallel (SP) [251].

➢ Semi-passive --- AC-DC converter shunts

Lesieutre *et al.* [39] investigated the damping capability of a piezoelectric energy harvesting system composed of a full-bridge rectifier, a filtering capacitor, a switching DC–DC step-down converter, and a battery. Under conditions of harmonic excitation,

the electromechanical coupling coefficient of the piezoelectric system, and the ratio of the rectifier output voltage during operation to its maximum open circuit value are the determinant factors of effective modal loss. Experiments on a base-driven piezoelectric cantilever with a system coupling coefficient of 26% yielded an effective loss factor for the fundamental vibration mode of 2.2%, in excellent agreement with theoretical predictions.

- Semi-passive --- Nonlinear switched circuits -- State-Switched shunts

Clark [65] proposed a state-switched vibration control method to switch the electrical shunt circuit of a PZT for dissipating energy in a simple mechanical system. Specifically, switching is carried out between open-circuit (high stiffness) and short- or resistive-circuit (low stiffness) states. The approach keeps the PZT in each of the high- and low-stiffness states for one quarter-cycle increments. In order to achieve vibration reduction, the PZT actuator stores energy in the high-stiffness state and dissipates that energy in the low-stiffness state. Numerical results showed that the method has the potential of state-switching the piezoelectric actuator for vibration control.

- Semi-passive---Capacitive shunts

Davis *et al.* [28] proposed a solid-state tunable semi-active piezoelectric vibration damper. Such damper has two significant characteristics: One feature is the use of piezoelectric elements as part of the investigated device stiffness. The effective stiffnesses of these elements were adjusted electrically, using a passive capacitive shunt circuit, to tune the resonance frequency of the investigated device and ensure that this frequency is not excited. The tuning range of the damper is thus bounded by its short-circuit and open-circuit resonance frequencies, hence requiring high coupling coefficient to be effective. Another feature is the ability to use the piezoelectric elements as sensors. A control scheme was developed to estimate the desired tuning frequency from the sensor signals, to determine the appropriate shunt capacitance value.

- Semi-active --- Nonlinear switched circuits -- Switched stiffness

The switched stiffness method leads to change in the stored potential energy, which results in the decrease of total energy of the system. In order to reduce the total energy of the system, the stiffness of the spring is switched according to a heuristic control law based on the position and velocity feedback. The spring should possess two distinct stiffness values: high stiffness (for the higher value) and low stiffness (for the lower value). When the system is moving away from its equilibrium state, the stiffness of the system is set to the higher value, and when it returns to its equilibrium, it is set to the lower value. Such vibration control method can change the stored potential energy of the system through the use of a bi-stiffness spring set with the resulting relay-type control logic based on the position and velocity feedback, which actually reduces the total energy of the system. Ramaratnam *et al.* [69] proposed a simple semi-active structural vibration control based on switching the system equivalent stiffness between two distinct values. In the proposed method, a new robust output feedback variable structure observer is used to estimate the required velocity signal for implementing the control law without velocity sensors. The effectiveness of the vibration suppression of the method was demonstrated by numerical and experimental results. Guyomar *et al.* [252] proposed a synchronized switch stiffness control (SSSC) method, which relies on connecting the piezoelectric element to an electrical network when the displacement (or equivalently the strain) crosses a zero value. Such a nonlinear treatment allows an effective control of the stiffness, while requiring less power than the classical methods. In the case of a monochromatic excitation on a cantilever beam, theoretical predictions showed good agreement with experimental measurements.

- Semi-passive --- Nonlinear switched circuits -- SSDS & SSDI

In 1999, Richard *et al.* [31] firstly proposed a nonlinear technique called Synchronized Switch Damping on Short circuit (SSDS) which can realize broadband vibration control without relying on any tuned electric load. In the proposed technique, the PZT is simply continuously switched from open-circuit to short-circuit synchronously to the mechanical strain. Specifically, the PZT stays in the high-stiffness (open-circuit) state for most of the vibration cycle, and is momentarily

pulsed to the low-stiffness (short-circuit) state to dissipate stored energy. There is no need for external power supply unless for the low power circuitry of the switching device. However, micro-controllers or other active components for implementing the switching device also require external low power supplies. Further on, in 2000, Richard *et al.* [32] proposed another important Synchronized Switching Damping (SSD) technique, namely Synchronized Switching Damping on Inductor (SSDI). Instead of discharging the PZT during a brief short circuit in the SSDS technique, the PZT in the SSDI technique is connected to a small inductor, which allows the inversion of the voltage and then released to open circuit. Due to the switching mechanism, the amplitude of piezoelectric voltage is magnified and shifted out of phase with the motion thus enhancing the damping mechanism, which is the same case as in the SSDS technique. However, the enlargement of the amplitude is greater than that in the SSDS technique because of additional inversion effect.

- Semi-passive --- Nonlinear switched circuits -- Self-powered SSDS & SSDI

In addition, semi-passive SSDS & SSDI techniques have self-powered capabilities. In 2007, Richard *et al.* took out a patent [33] for self-powered electronic breaker with automatic switching. Since such electronic breaker (Figure 1.14) has the capability of detecting maxima or minima of potential difference between its power electrodes without external energies (except a few percentage – less than 5% - of the electrostatic energy available on the piezoelectric element itself), the SSDS technique can be implemented in a self-powered (and self-sensing) way through the circuit proposed in the patent. Furthermore, the SSDI technique can also be realized in a self-powered way through the above patent as shown in Figure 1.15. Based on such self-powered SSDI technique, Lallart *et al.* [34] proposed a self-powered adaptive SSDI technique (Figure 1.16), which offers a disabling capability based on a comparison between the actual piezoelectric voltage and its history. Such capability allows the damping of the most energetic mode at a given instant. Experimental results showed that a beam impulse response, considering the first two modes, exhibits better damping performance.

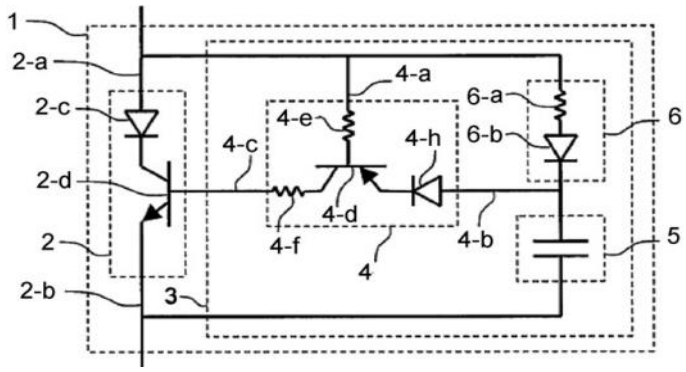

Figure 1.14 Implementation for maximum or minimum detection [33].

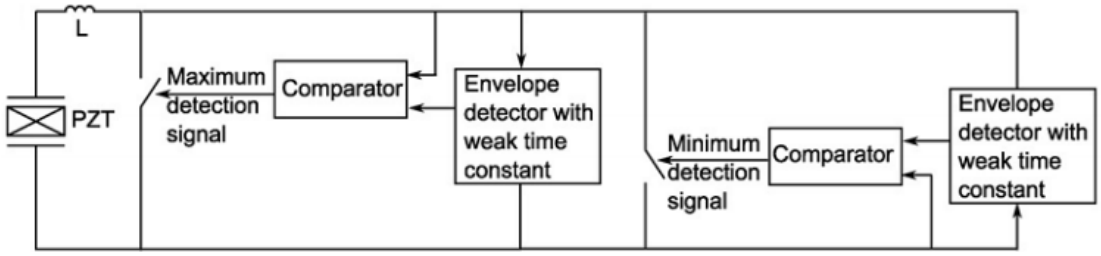

Figure 1.15 Original self-powered SSDI control block diagram [34].

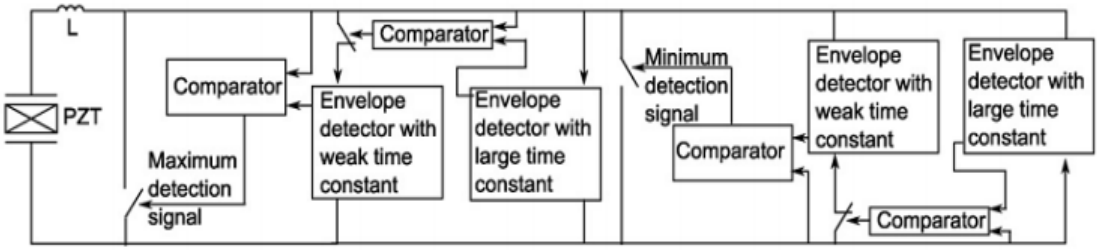

Figure 1.16 Self-powered adaptive SSDI control block diagram [34].

- Semi-active ---Nonlinear switched circuit -- SSDV

Among the synchronized switching damping techniques, external voltage sources in the SSDV (Synchronized Switching Damping on Voltage Sources) technique, are not

only used as low-power supplies for active components (such as operational amplifiers and DSP), but also directly used for enhancing the SSD damping performance. Specifically, the values of external voltage sources can be integrated into the theoretical value of SSDV damping. Lefeuvre *et al.* [74] firstly proposed a semi-passive SSDV technique. The difference between such a technique and the SSDI technique is that the PZT is switched on a positive or a negative voltage source across the inductive shunt circuit. Furthermore, dissipated energy of the system particularly depends on the voltage amplitude across the electrodes of PZTs. These additional constant voltage sources will increase the amplitude of piezoelectric voltage, and thus increasing the damping effect. Badel *et al.* [75] proposed an enhanced SSDV technique, which can tune the mechanical force resulting from the SSDV process to the vibration level since the original SSDV technique uses a constant continuous voltage source whereas the proposed enhancement uses an adaptive continuous voltage source. Normally, with the original SSDV technique, the absolute value of the continuous voltage remains constant which induces stability problems when the vibration amplitude tends to zero. However, these stability problems can be bypassed using the enhanced SSDV technique [253].

- Semi-active --- Nonlinear switched circuits -- Multimodal SSD

Except a few self-powered switched methods [33, 34, 254], in most of switched shunting control methods [76-79], implementation of switching devices is active and has to rely on low-power components (such as operational amplifiers) [71], DSP (digital signal processor) [37], or real time platforms (such as *dSpace* or an *xpc-target* system from MATLAB) [76, 80, 81, 110, 111, 255]) in order to obtain better multimodal control. Guyomar *et al.* [110] proposed a nonlinear semi-passive multimodal vibration law for the SSD technique, based on a probabilistic description of the piezoelectric voltage, and resulting in an optimization of the energy dissipated in the nonlinear device connected to the PZTs. Such control law can simultaneously optimize both displacement-based and energy-based vibration control criteria, which is much more effective than the original control law consisting of processing the

piezoelectric voltage on each strain extrema. In addition, they also [82] proposed another semi-passive random vibration control based on statistics. In the proposed method, the voltage or displacement signal is analyzed during a given time window. The statistically probable displacement or voltage-level threshold is determined from both the average and standard deviation of the signal during the observation period. The voltage step occurs on a local maximum of the signal but only above the statistically defined threshold. Experimental and theoretical results showed that a significant decrease in vibration energy is obtained in the case of a clamped beam excited by random noise. Lallart *et al.* [80] proposed a self-adaptive semi-active damping technique: Blind switch damping (BSD). Such technique is independent from the electromechanical structure characteristics, and thus allows a large frequency band operation and a good robustness facing environmental drifts. The control law of the technique presents a simple command that can be easily implemented. As well, the technique can rely on an energy injection / recovery basis which can make the system requiring relatively low power. Ji *et al.* [81] proposed a switch control strategy based on an energy threshold for the synchronized switch damping (SSD) techniques in multimode control. Such strategy, derived from the total converted energy of a SSD system in a given time window, can be used in both the Synchronized Switch Damping on the Inductor (SSDI) technique and the Synchronized Switch Damping on the Voltage source (SSDV) technique. Experimental results showed that voltage inversion is prevented at some of the displacement extrema to increase the total converted energy, and exhibits better global damping effect than classical SSDI and classical SSDV, respectively.

- Semi-active --- Nonlinear switched circuits -- Hybrid SSD

Ji *et al.* [35] proposed a semi-active SSDNC (Synchronized Switching Damping on Negative Capacitances) technique. Specifically, the variation of the voltage on the piezoelectric element and the current in the circuit are analyzed, and the damping effect using the SSDNC is deduced. In addition, the energy balance and stability of the system are also investigated analytically. In order to validate the theoretical developments, the method is applied to the single-mode and two-mode control of a

composite beam. Its control performance was confirmed by experimental results: for the first mode in single-mode control, the SSDNC is much more effective than SSDI, while in other cases, the SSDNC is also more effective than SSDI, although not significantly while requiring external power supply.

1.4 Band gap generation mechanisms in periodic structures and wave localization in aperiodic structures

1.4.1 Bragg scattering mechanism

Strictly speaking, smart periodic structures with distributed electrical shunt-damping networks can be regarded as electromechanical metamaterials. Metamaterial application design, originally developed for electromagnetic wave (*e.g.,* radio waves, optical waves and *X*-rays) propagation control (photonic crystals) [112-114], are viewed at the intersection of two classical categories-materials and devices - since the characteristics of metamaterials is that their remarkable properties not only arise from the behavior of the bulk materials that form them, but more from their deliberate structuring arrangement. In recent years, the metamaterial concept has been extended to many other features including extraordinary properties such as negative dynamic modulus and/or density, superior thermoelectric characteristics, and phononic bandgaps (PBGs). Among metamaterials, mechanical metamaterials [116, 117], used for generating PBGs (ranges of wavelength or frequency within which waves cannot propagate through the structure), can be divided into two categories: acoustic metamaterials (mechanical waves passing through a gas or a liquid) [118, 256, 257] and phononic metamaterials (mechanical waves passing through a solid) [258]. According to the types of energy flow carried by phonons, phononic metamaterials can be classified as two kinds: phononic crystals (PCs, manipulating elastic waves - [98, 259]) and thermocrystals (manipulating heat waves - [260, 261]).

Therefore, electromechanical metamaterial is one kind of phononic crystals (PCs). The earliest investigations of PCs [262-264] are commonly based on the Bragg

scattering mechanism [265]. Assuming that a crystal is comprised of parallel planes of atoms (called Bragg planes) that reflect the *X*-rays, spaced a distance *d* apart, the conditions for a sharp peak in the intensity of the scattered radiation are as follows:

- ✧ The *X*-rays should be specularly reflected by the ions in any Bragg plane;
- ✧ The reflected *X*-rays from successive planes should interfere constructively.

As shown in Figure 1.17, path difference between two *X*-rays reflected from adjoining planes equals *2dsin(θ)*, where θ is the scattering angle. For the rays to interfere constructively, this path difference should be a positive integral number of wavelength λ, which leads to Bragg's law describing the Bragg condition on θ for the constructive interference to be at its strongest:

$$2d\sin(\theta) = n\lambda, n = 1, 2, 3, \ldots \tag{1.3}$$

As can be seen from the above equation, an observable reflected diffraction pattern only occurs for wavelengths that are on the same scale as the atomic spacing *d* in the material.

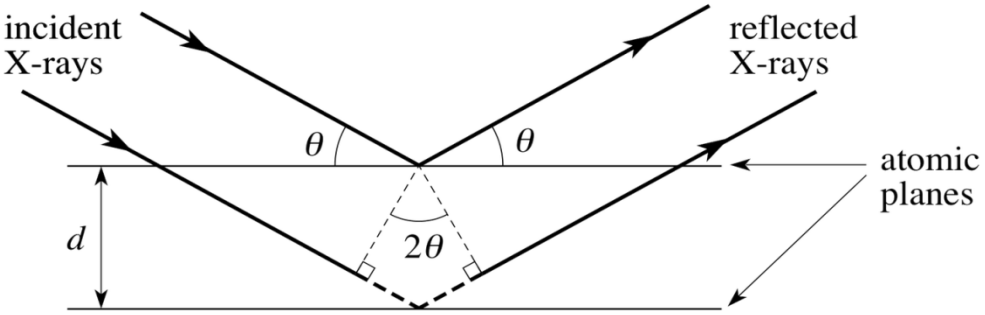

Figure 1.17 Schematic diagram of Bragg diffraction: two monochromatic beams with identical wavelength approach a crystalline solid and are scattered off two different atoms (from http://www.physics.brocku.ca/PPLATO).

Specifically for periodic structures or PCs, the dispersion property of PCs is a common research topic in solid state physics. The essence of mechanical periodicity of elastic wave propagation has been demonstrated in detail in Brillouin's eminent work [115]. Due to Bragg scattering, bandgaps representing frequency intervals in which wave propagation is not allowed or attenuated, are generated at wavelengths comparable to the spatial scale of the periodicities in the periodic structures or PCs.

Such band gaps are called Bragg-type bandgaps, whose central frequencies are determined by the Bragg condition $L = n\left(\frac{\lambda}{2}\right)\left(n = 1, 2, 3, ...\right)$. Herein, L is the lattice constant of the periodic system and λ is the wavelength of elastic waves in the host material.

Kushwaha *et al.* [256] firstly proposed the full band-structure calculations for periodic, elastic PCs. For transverse polarization of vibrations, a 'phononic' band gap which extends throughout the Brillouin zone, is obtained. A complete acoustic gap or a low density of states should have important consequences for the suppression of zero-point motion and for the localization of phonons, and may lead to better vibration reduction performance.

Martinez-sala *et al.* [257] reported sound attenuation experiments performed on a sculpture. As shown in Figure 1.18 (a), the sculpture consists of a periodic distribution of hollow stainless-steel cylinders, which a diameter of 2.9 *cm*, simple cubic symmetry and a unit cell of 10 *cm*. The cylinders are fixed on a circular, *4-m*-diameter platform that can rotate around a vertical axis. Such periodic distribution of wave scatters can induce severe sound attenuations in some spectral regions. The Bragg sound attenuation peak at 1.67 kHz could be attributed to the formation of the first gap in this sculpture as shown in the Figure 1.18 (b).

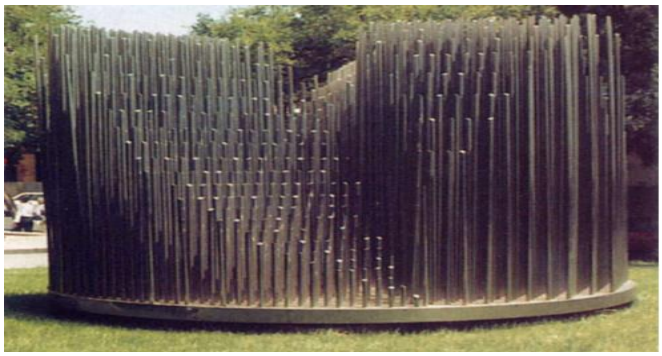

(a)

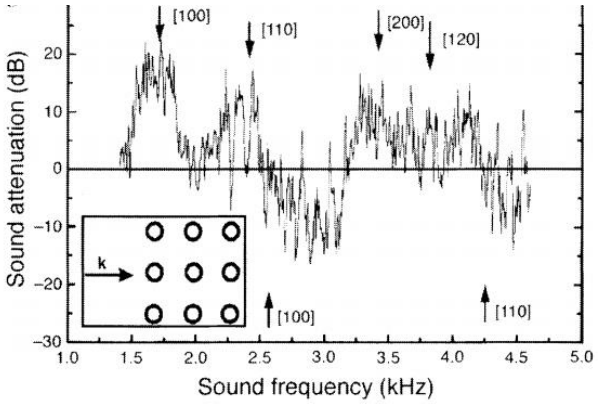

(b)

Figure 1.18 (a) Kinematic sculpture by Eusebio Sempere; (b) sound attenuation results as a function of the sound frequency. The wave vector is along the (100) direction as shown in the inset. Arrows indicate the calculated maxima and minima due to interference from the different crystal planes of the sculpture [257].

In order to further investigate PCs, a series of study mainly relied on experimental tests of 1D-3D problems and researches are still performed. Commonly, theoretical methods include transfer matrix method [266], plane wave expansion method [256], multiple scattering theory [267], finite difference time domain method [268] and finite element method [269].

However, the Bragg condition implies that Bragg-type bandgaps are not suitable for filtering elastic waves in the low-frequency range because the lattice constant must be of the same order as the relevant wavelength. In other words, low-frequency Bragg-type bandgaps probably appears in large-scale PCs, while PCs with conventionally small dimensions cannot bring low-frequency Bragg-type band gaps for many practical applications, such as low-frequency vibration reduction.

1.4.2 Local resonance mechanism

In order to overcome the drawback of the application struggle of small-scale PCs in the low-frequency range, Liu *et al.* [118] firstly proposed a type of locally resonant (*RL*) band gap mechanism in their research on 3D PCs composed of cubic arrays of

coated spheres immersed in an epoxy matrix as shown in the Figure 1.19. Such locally resonant-type bandgaps were obtained in a frequency region two orders of magnitude lower than that given by the Bragg limit. Compared with the Bragg-type PCs, the locally resonant-type PCs consisting of periodic arrays of oscillators embedded in the host structure are most likely to generate low-frequency PBGs with small dimensions.

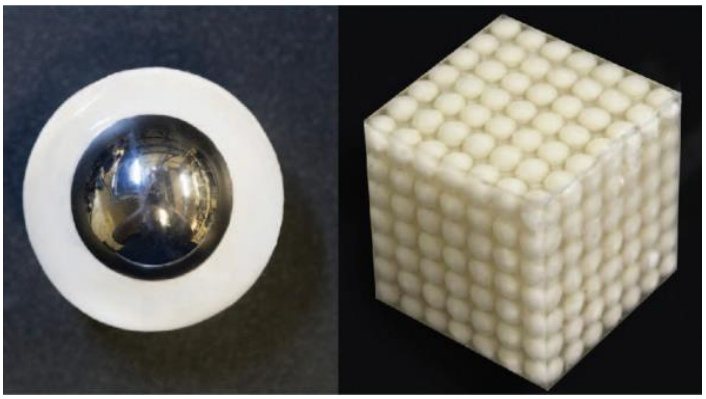

Figure 1.19 Images of the sample that first realized a local resonance-induced anomalous mass effect. Left: The cut-away view of a sample unit cell consisting of a small metallic sphere coated by a thin uniform layer of silicone rubber. Right: The sample made by using epoxy to glue together the units shown on the left. The effective frequencies for total reflection by the sample were shown to correspond to a wavelength that is between one and two orders of magnitude larger than the size of the lattice constant, which is 1.55 cm [118, 119].

Wang *et al.* [270] investigated the two dimensional binary locally resonant phononic crystals, which are composed of periodic soft rubber cylinders immersed in epoxy host. Numerical simulations showed that sub-frequency gaps appear due to the high contrast of mass density and elastic constant of the soft rubber. The locally resonant mechanism in generating the sub-frequency gaps is thoroughly analyzed by studying the two-dimensional model and its quasi-one-dimensional mechanical equivalent. However, traditional oscillators [270-272] or stiffer oscillators [273] in locally

resonant-type PCs are very heavy, and their locally resonant-type bandgaps are not only too narrow to be implemented for many potential applications, but also unchangeable since it is difficult to modify the mechanical structure of such locally resonant-type PCs after molding.

Furthermore, active PCs [17-19] can provide more flexible elastic wave propagation control on generating the low-frequency PBGs. Reynolds *et al.* [19] proposed a new type of active viscoelastic metamaterial, which achieves double negativity (bulk modulus and density) and could be employed as a high-performance vibration isolator at low frequencies. A mathematical method for manipulating the band gap profile is developed and a prototype is produced. Through applying active control using optimized feedback filters, the region at which attenuation occurs around the original Bragg-type PBG could be greatly enhanced while retaining the peak of passive band gap performance. The proposed active metamaterial demonstrated that a unified design philosophy matching the best features of active and passive functionality has the capability of achieving high levels of attenuation over wide frequency bands. However, the active resonant oscillators requiring external energies still cannot be applied in potential applications with low power supplies or completely without external energies. The literatures of smart periodic structures with electrical shunt-damping networks requiring low or no power supplies will be reviewed in detail in section *1.5*.

1.4.3 Hybridization mechanism (near coupling between Bragg scattering and local resonance)

Interaction between the local resonance and Bragg PBGs in PCs is also investigated by some researchers [119-124]. Sharma *et al.* [119] studied the low frequency wave propagation behavior of sandwich beams containing periodically embedded internal resonators. Local resonance and Bragg bandgaps coexist in such a system and the width of both bandgaps is a function of the resonator parameters as well as their periodicity. The interaction between the two bandgaps is investigated by changing the

local resonance frequency. Results showed that a single combined band gap does not exist for this system and that the Bragg bandgaps transition into sub-wavelength bandgaps when the local resonance frequency is above their associated classical Bragg frequency. Xiao *et al.* [121] presented a design of locally resonant (*RL*) beams using periodic arrays of beam-like resonators attached to a thin homogeneous beam, which provided experimental evidence of the associated band gap properties, especially the coexistence of *RL* and Bragg band gaps, and their evolution with tuned local resonance. In order to experimentally validate the concept, several *RL* beam specimens were achieved by mounting 16 equally spaced resonators onto a free-free host beam, which use the same host beam. The resonance frequencies of the resonators on each beam are different. The measured vibration transmittances of these specimens give evidence of three interesting band gap phenomena: transition between *RL* and Bragg bandgaps, near-coupling effect of the local resonance and Bragg scattering, and resonance frequency of local resonators outside of the *RL* bandgaps.

1.4.4 Wave localization in aperiodic structures

The possibility of localization or confinement of vibration modes and waves in aperiodic structures is also investigated by researchers [17, 93, 125-127]. On one hand, when localization occurs, the modal amplitude of a global mode becomes confined to a local region of the structure, and thus produces energy accumulation which may lead to structural fatigue damage [127]. On the other hand, wave localization may also have good effects on practical applications such as vibration reduction [93] or energy harvesting. Baz [17] investigated the aperiodicity effect in active periodic structures. In his study, the aperiodicity is intentionally introduced by proper tuning of controllers for individual substructure or cell. In order to illustrate their tunable filtering and localization characteristics, the theory governing the operation of the active periodic structures is introduced and numerical examples are also presented. The considered examples include periodic/aperiodic spring-mass systems controlled by piezoelectric actuators. The presented results emphasized the unique potential of

active periodic structures in controlling the wave propagation both in the spectral and spatial domains in an attempt to stop/confine the propagation of undesirable disturbances.

1.5 Elastic wave propagation in smart periodic structures and its applications in vibration control systems

In order to enhance the damping performance of smart structures, various shunt strategies (passive / active / semi-active / semi-passive shunts) were proposed, which have already been introduced in the above section *1.3*. Before choosing an optimal electrical shunt, the optimization of the geometry and the placement of the piezoelectric patch on the host structure are of prior importance for avoiding charge cancellation and vibration node locations. However, because of these difficulties, a single piezoelectric patch cannot consistently achieve multimodal vibration control. Hereof, through the distribution of several piezoelectric patches all over the structure [86-90, 274], it is possible to sense and control wavelength being large enough compared with the length of the piezoelectric patches and thus improve the multimodal damping performance.

In terms of smart vibration control systems, active vibration control with smart structures [17, 275-279] may bring excellent vibration damping performance, but its implementation (*e.g.*, for driving PZT actuators) is complex, including high-voltage power amplifiers and high hardware requirements. Moreover, its close-loop feedback control algorithms [280, 281] are more likely to exhibit instability because of spillover effects [49] of un-modelled modes of the control system. By comparison, passive or semi-active / semi-passive vibration control techniques with smart structures only requires a simple passive electrical network (PEN) or a semi-active / semi-passive electrical network (SAEN / SPEN) and its stability can be guaranteed easily, but their ability for multimodal control is still an open issue. This section aims at reviewing the literatures on smart periodic structures with passive or semi-active / semi-passive electrical networks (PENs or SAENs / SPENs) in recent years.

1.5.1 Smart periodic structures with traditional resonant electrical networks

Ruzzene and Baz [92] firstly utilized the inherent particularities of smart materials to design electromechanical metamaterials. Specifically, they introduced shape memory inserts acting as sources of impedance mismatch with tunable characteristics in rod PCs. With inherent controllable capability of the inserts whose elastic modulus can be varied up to three times as the alloy undergoes phase transformation from martensite to austenite, proper impedance mismatch for limiting elastic wave propagation along rod PCs is introduced.

As for smart periodic structures with single-mode resonant electrical networks [92-99] , Thorp *et al.* [93] firstly used single-mode *RL* resonant oscillators [13] in his investigation on the elastic wave attenuation and localization of the piezoelectric rod PCs. Locally resonant band gaps are produced centered at the tuning frequencies of the single-mode *RL* resonant shunts. Bergamini *et al.* [98] adopted single-mode *RL* resonant shunts in his proposed PC with adaptive connectivity (Figure 1.20) for generating a pass band within primitive Bragg-type band gaps (Figure 1.21). Both of theoretical and experimental results showed that the location and bandwidth of the pass band are determined by the *RL* resonant shunts.

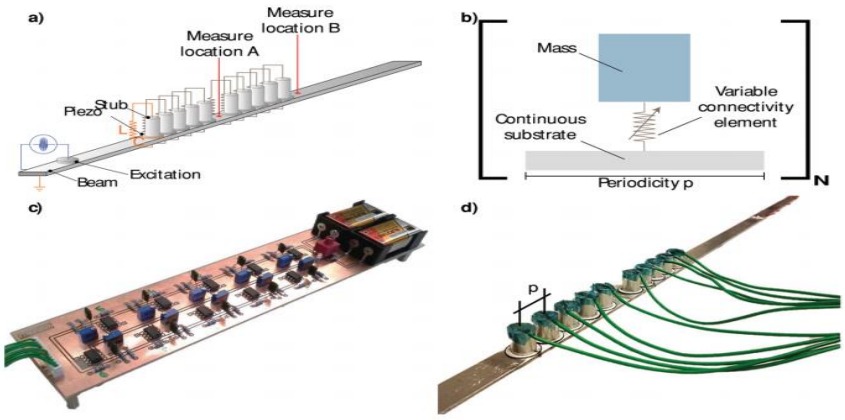

Figure 1.20 A new class of PCs with tunable (frequency-dependent) connectivity: a) Schematic views of the considered phononic crystal with cylindrical stubs and piezoelectric discs. Each transducer is shunted through an inductive circuit in order to

obtain frequency dependent stiffness elements between the substrate and the stubs; b) Unit cell of the PC: the variable stiffness element changes the mechanical connectivity of the unit cell from a periodic structure to a simple continuous substrate; c), d) Photographs of the semi-active circuit for the implementation of the shunting inductors and the investigated PC [98].

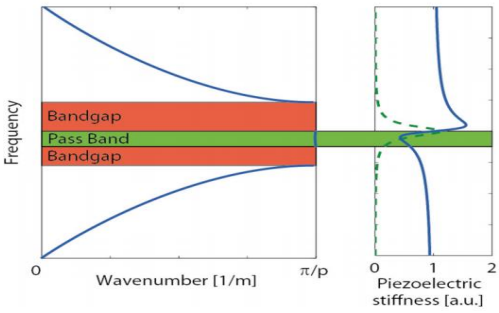

Figure 1.21 Qualitative representation of the effect of frequency dependent stiffness elements on the band structure of the phononic crystal: The diagram on the left reports the dispersion relation of the phononic crystal: the Bragg-type PBG occurs at a wavenumber related to the lattice periodicity *p*, as defined in Figure 1.20 (b). The diagram on the right represents the real (solid line) and the imaginary (dashed line) parts of the complex stiffness of a piezoelectric disc shunted through an inductive circuit. Just below the resonance frequency, the real part is strongly reduced and isolates the stubs responsible for the band gap, creating therefore a neat pass band [98].

Wang *et al.* [99] investigated a smart metamaterial structure composed of an aluminum alloy beam and periodic arrays of PZT patches shunted by *A-R* (amplifier-resonator) circuits, as shown in Figure 1.22. Influences of circuital parameters on attenuation factors and the equivalent Young's modulus are studied. It is shown that *A-R* shunting circuits can evidently increase resonant-type PBG attenuation compared with passive *RSCs* (resonant shunting circuits) [13] and *R-A* (resonator-amplifier) [96] shunting circuits. Due to the negative equivalent elastic modulus of piezoelectric patches at frequencies lower than the resonance, the central

frequency of attenuations is lower than the resonant frequency. Wider attenuation frequency ranges can be gained by a combination of smart metamaterial cells with different circuital parameters (in a similar way than aperiodic structures). Resonant-type PBG frequency can be far lower than the Bragg-type PBG frequency (Figure 1.23). Theoretical results have good agreements with experimental results, which validates the effectiveness of the proposed strategy.

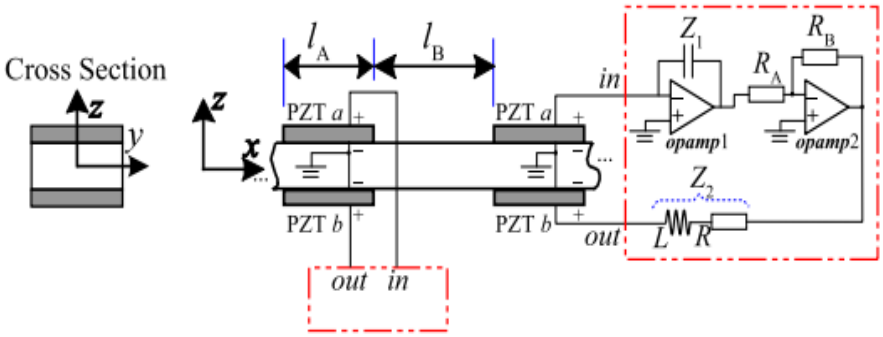

Figure 1.22 Periodic arrays of amplifier-resonator (*A*-*R*) piezoelectric shunting on a beam [99].

.

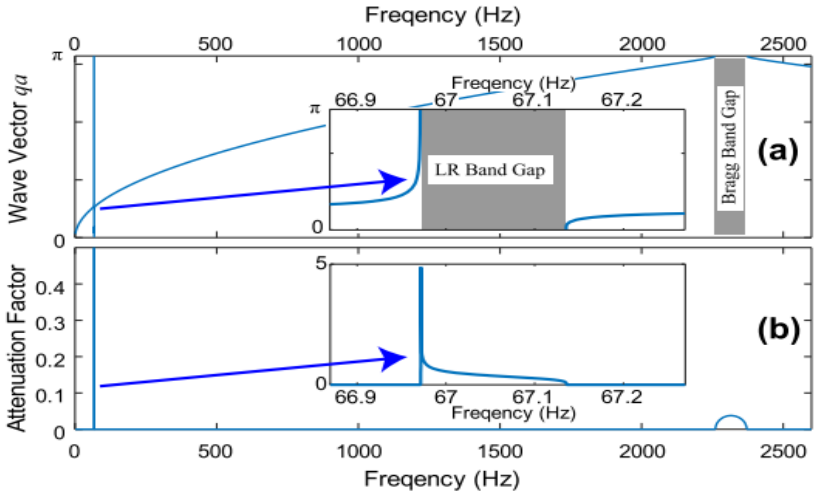

Figure 1.23 Calculated (a) phase constants and (b) attenuation constants of a 1D piezoelectric metamaterial. The inner subfigures are zoom-in views of the locally resonant band gap [99].

Concerning smart periodic structures with multi-mode resonant electrical networks, Dell'Isola *et al.* [87] investigated smart structures with passive distributed electrical networks. Specifically, an array of uniformly distributed piezoelectric elements is positioned on a host beam and their terminals are interconnected by a passive electric network. Two different electric interconnections were theoretically and experimentally examined: *R* network (resistive connection of adjacent PZTs) and *RL* network (resistive–inductive connection of adjacent PZTs). The proposed approach advances in the three following points: multimode vibration damping, reduction of the optimal inductance with respect to classical passive resonant piezoelectric shunting, decrease of the optimal inductance for increased number of piezoelectric elements. Maurini *et al.* [88] investigated and compared five different electrical topologies connected to a piezoelectric beam. Their optimal parameters are found by adopting a criterion for critical damping of $\bar{k}$-waves (a particular standing wave as defined by Courant and Hilbert [282]): the parameters are suitably chosen to have the quickest temporal vibration decay for a single wave number $\bar{k}$. The analysis is based on homogenized models of the modular piezo-electromechanical systems (one of modular piezo-electromechanical systems is shown in Figure 1.24 as an example). Bisegna *et al.* [89] investigated the multimodal damping performance of an elastic beam equipped with multiple piezoelectric actuators connected to an electrical network. Two analytical models of the electromechanically coupled structure are considered: a homogenized one, that is accurate when a large number of actuators is employed, is used to derive simple design criteria for the electric network; and a discrete one, able to face real situations when few actuators are employed, which is adopted to test the network performance, defined as the exponential time-decay rate of the free vibrations of the controlled structure.

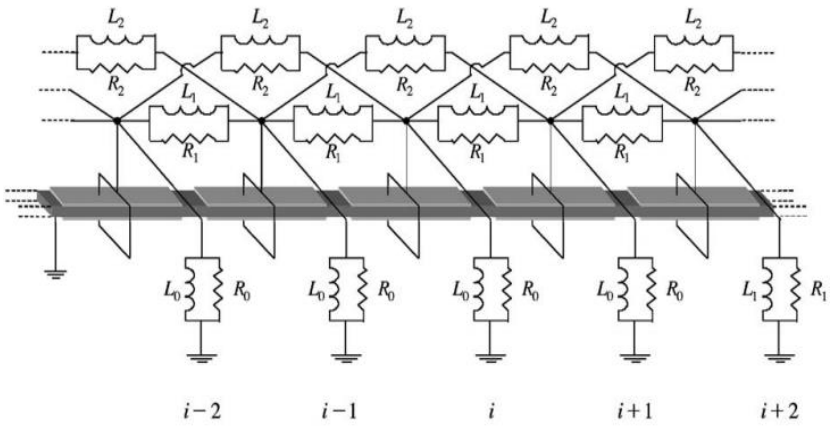

Figure 1.24 Generic modular PEM beam [88].

Airoldi *et al.* [135] proposed the method of generating multiple locally resonant band gaps in a beam by using multi-resonant shunts [20], and the generated multiple PBGs can be tuned to target several structural modes of the beam PC. Zhou *et al.* [150] proposed more easy-operating high-order resonant circuits connected to a periodic piezoelectric array for efficiently generating two separate resonant-type PBGs.

In addition, some researchers are more focused on the theoretical investigations and their representativeness in real structure for the electromechanical metamaterials for wave propagation and / or electromechanical coupling [128-134]. Collet *et al.* [283] proposed a wave-based criterion to evaluate the coupling factor of the piezoelectric composite. Enhanced Wave and Finite Element Method (WFEM) [139] is employed for obtaining the dispersion relations and the shapes of the waves. Then, the factor can be calculated in three different but equivalent formulas. Results showed that the coupling factor is frequency-dependent and it is strongly related to the geometric parameters, so it can significantly change the optimal performance of the piezoelectric waveguide and its ability to dampen vibrations. Huang *et al.* [284] provided effective numerical prediction tools for wave propagation characteristics and dynamic behavior of smart structures equipped with shunted PZTs, which enable the evaluation of the performance of shunted PZT patches on the control of flexural wave propagation, and facilitate design modifications and systematic investigations of geometric and electric

parameters of beam structures with shunted PZT patches. Wen *et al.* [285] proposed an analytical method for evaluating the propagation constant in arbitrary direction in the plate with periodic piezoelectric arrays (Figure 1.25), which can avoid the complicated transcendental eigenvalue problem. Based on the proposed method, the directionality of waves propagating or decaying in the plate with arrays of single-mode resonant shunts is investigated including directionality of attenuation constant, location of band gaps, and group velocity in pass band. Moreover, theoretical results are verified by simulation using COMSOL finite element software as shown in Figure 1.26, Figure 1.27 and Figure 1.28.

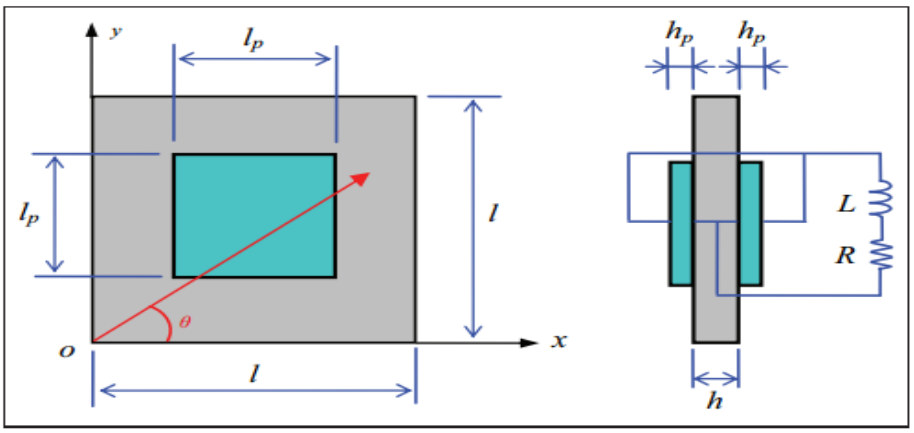

Figure 1.25 Sketch of the unit periodic cell [285].

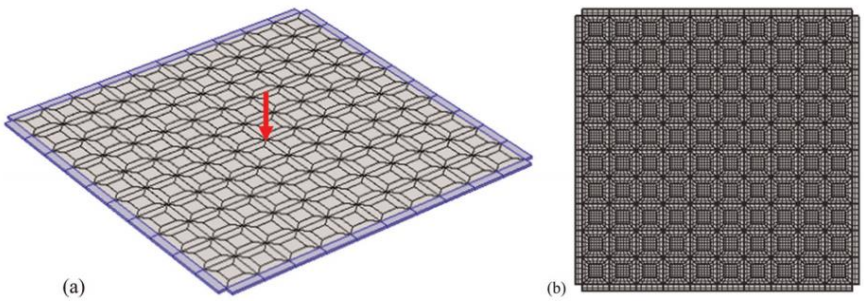

Figure 1.26 Finite-cell model in COMSOL: (a) isometric view; (b) top view [285].

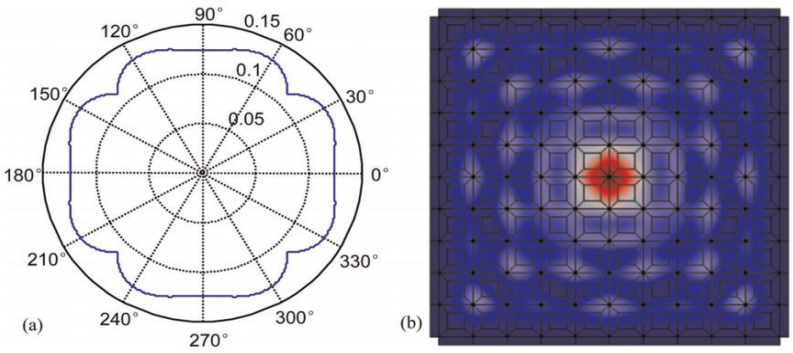

Figure 1.27 Wave propagation in the resonant-type PBG: (a) directional attenuation constant; (b) simulated wave field. Depth of red color spectrum represents amplitude of displacement [285].

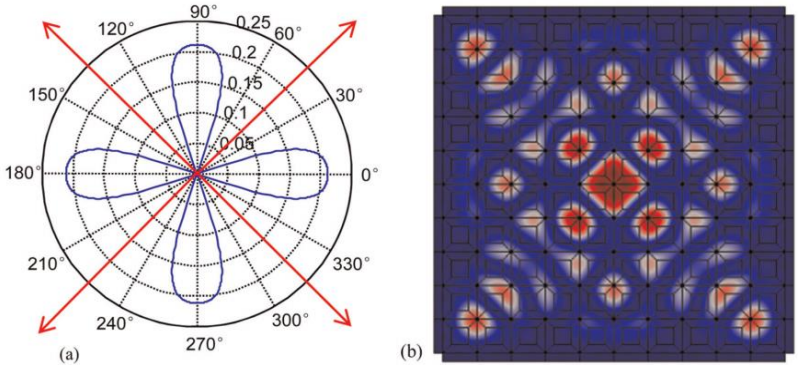

Figure 1.28 Wave propagation in the Bragg-type PBG: (a) directional attenuation constant; (b) simulated wave field. Red arrows denote the pass band direction. The depth of red color spectrum represents amplitude of displacement [285].

Recently, some research interest has been placed on the investigation of wave propagation properties of complex distributed interconnected resonant electrical networks onto a smart periodic structure [286-288]. In the previous distributed electrical networks onto a smart periodic structure, electrical relationships induced by each electrical shunt-damping branch are enclosed in each minimal Bragg unit cell, while in the complex distributed interconnected electrical networks, electrical relationships induced by each electrical shunt-damping branch may involve more than one minimal Bragg unit cell. Typically, Bergamini *et al.* [286] investigated the wave transmission characteristics of a hybrid one dimensional (1D) electromechanical

metamaterial as shown in Figure 1.29 (a). In the presented metamaterial, a resistor and an analog circuit composed of a synthetic inductor (Figure 1.29 (b)), connected between adjacent PZTs, can be regarded as an integral part of a material. The hybrid characteristic is the result of the coupling between a 1D mechanical waveguide in the form of an elastic beam (supporting the propagation of transverse waves) and a discrete electrical transmission line (consisting of a series of inductors connected to ground through capacitors).

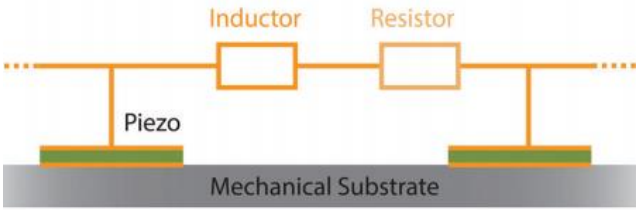

(a)

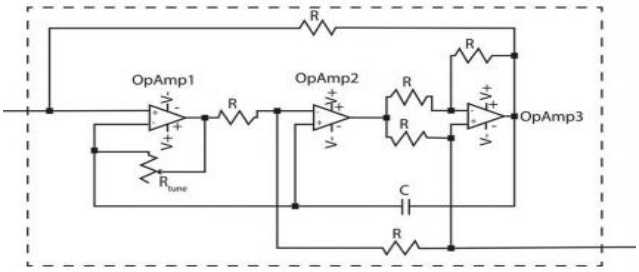

(b)

Figure 1.29 (a) Hybrid electromechanical PC; (b) circuit used to synthesize the inductors [286].

1.5.2 Smart periodic structures with negative capacitance electrical networks

In terms of the usage of negative capacitance shunts in resonant-type PCs [100-105], Beck *et al.* [101] experimentally investigated a piezoelectric cantilever beam PC. The results demonstrated that a negative capacitance piezoelectric periodic array enabled the PC to have the abilities of effective global vibration reduction and energy localization near the forcing of a structure. Huang *et al.* [103] theoretically studied the wave propagation properties and wave energy diffusion of the piezoelectric beam PC with a negative capacitance periodic array based on Wave Finite Element (WFE) method and Diffusion Matrix Model (DMM) approach. Electrical and geometrical

parameters in the coupled system have been optimized, and maximal effect of the shunted piezoelectric patches on wave propagation control is also obtained.

1.5.3 Smart periodic structures with hybrid shunting (negative capacitance shunt + resonant shunt) electrical networks

Some researchers also adopted both *RL* resonant shunts and negative capacitance shunts in the resonant-type PC design [106, 107]. Casadei *et al.* [106] used a periodic array of hybrid-shunted piezoelectric patches for vibration reduction of a PC plate over broad frequency ranges. In the proposed periodic cell, two adjacent primordial periodic cells compose one novel unit periodic cell, both of them being independently shunted with *RL* resonant circuits and negative capacitance circuits (Figure 1.30). *RL* resonant shunts are used for individual mode control over medium-high frequency bands, and negative capacitance shunts aim at broadband vibration reduction over low-frequency bands.

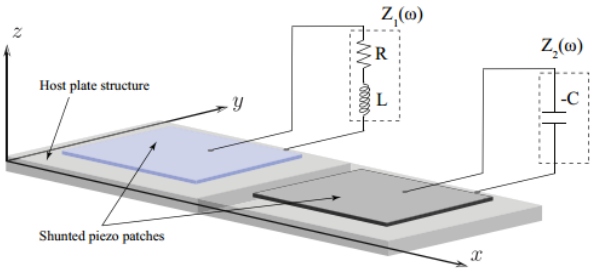

Figure 1.30 Plate with surface-bonded piezoelectric patches independently shunted with *RL* and negative capacitance circuits [106].

Zhang *et al.* [107] investigated the flexural wave band gaps in PC beam with hybrid shunting circuits. In the hybrid shunting circuit configuration, a negative capacitance shunt and a single-mode *RL* resonant shunt are connected in parallel to the same piezoelectric patch in one primitive periodic cell (Figure 1.31). Theoretical

predictions demonstrated that the generated resonant-type PBGs can be made wider through appropriately setting the electrical parameters of the hybrid shunting circuits

.

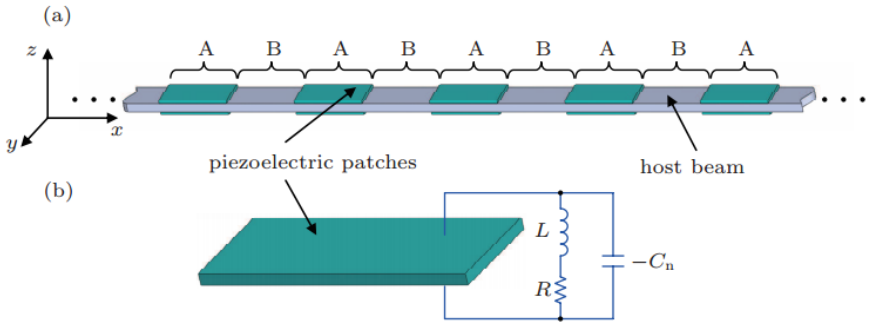

Figure 1.31 (a) Phononic metamaterial beam; (b) piezoelectric patch with hybrid shunts ($-C_n$ denotes negative capacitance shunt) [107].

1.5.4 Smart periodic structures with synchronized switching electrical networks

Recently, nonlinear electronic resonant oscillators have also been applied in the electromechanical PC design. Lallart *et al.* [108] proposed a piezoelectric PC beam carrying independent nonlinear SSDI (Synchronized Switching Damping on Inductor) electrical networks (Figure 1.32). In the configuration of electronic networks, each SSDI shunt is independently connected to the piezoelectric patch. Numerical results show that broadly resonant-type bandgaps can be obtained, especially broadband low-frequency bandgaps that can be used for low-frequency multimodal vibration reduction even without external power supplies. In addition, a smart periodic structure with nonlinear interconnected SSDI networks is also proposed as future work in Yan's PHD dissertation [109].

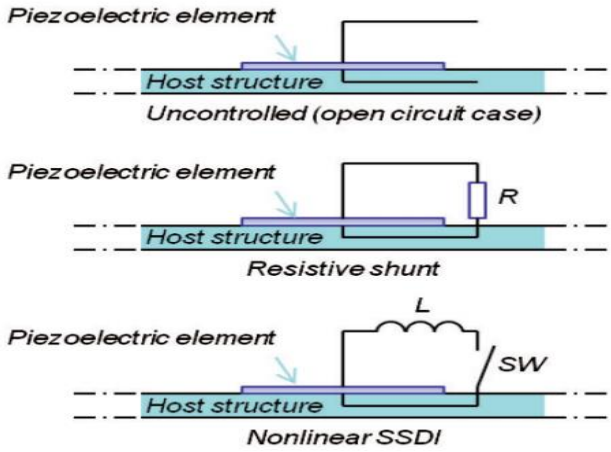

Figure 1.32 Investigated control cases for a single periodic cell [108].

1.6 Conclusion and outline of the thesis

As can be seen from the above research background for the dissertation, there have been many research activities on vibration control and smart periodic structures, and numerous researches have been conducted. In order to design better distributed broadband vibration control devices, the dissertation will start from the initial study of a smart periodic structure with nonlinear interconnected electrical networks as proposed in Yan's PHD dissertation [109], and then will take advantage of smart periodic structures with distributed electrical networks, by conducting theoretical and experimental researches through considering the following challenging ideas: (1) complex distributed interconnected electrical networks onto a smart periodic structure (*e.g.*, [286]), that have the potential of more flexibly manipulating or even tailoring elastic wave propagation, and thus improve the vibration control performance, especially in the low-frequency region (little research has been conducted on resonant-type PBG generation using complex distributed interconnected electrical networks); (2) nonlinear electrical shunts that are rarely used in researches on smart periodic structures with distributed electrical networks, in spite of the nonlinear resonant shunts advancing the linear resonant shunts in some aspects (*e.g.*, [108]); (3) while many researchers have already investigated the irregularities in various aperiodic structures for decreasing the fatigue damage or achieving localized vibration

control, such researches on the irregularities mainly involve the purely mechanical localization capabilities, so that for electromechanical structures, irregularities should involve both of mechanical and electrical irregularities.

The dissertation consists of six chapters. Except Chapter 1, Chapter 2 introduces the previous finite element methods for modeling the smart periodic beam structures with passive / semi-passive electrical networks, and then proposes a new finite element method for modeling the smart periodic beam structures based on the Timoshenko theory, which fits the modeling of smart periodic beam structures with complex interconnected electrical networks.

Chapter 3 further investigates the smart periodic structure with nonlinear interconnected electrical networks, which involves wave propagation interaction between the continuous mechanical medium and the continuous nonlinear electrical medium. Nonlinear SSDI shunts are applied to the interconnected electrical networks. Based on the finite element modeling for the proposed structure, its electro-elastic coupling between elastic wave (propagating through purely mechanical part of the structure) and electrical wave (propagating through the nonlinear interconnected electronic network) is investigated. Experimental results on low-frequency vibration control validated the theoretical predictions for the existence of the low-frequency resonant-type PBG generated by the proposed structure.

Chapter 4 proposes a smart periodic structure with nonlinear interleaved-switched electrical networks, which involves wave propagation interaction between the continuous mechanical medium and the discrete nonlinear electrical medium. In the proposed structure, an interleaved periodic cell is composed of several primitive Bragg periodic cells because of the interleaved-switched electrical interconnection. The primitive Bragg periodic cells are disordered and aperiodic within an interleaved periodic cell, while such interleaved periodic cells are periodic throughout the global smart periodic structure. Experimental and theoretical results showed that such structure exhibits excellent low-frequency vibration control performance.

Chapter 5 proposes a smart periodic structure with more complex interconnected electrical networks using nonlinear interleaved-interconnected interconnections. It

involves electro-elastic coupling between elastic wave (propagating through purely mechanical part of the structure) and multilevel electrical waves (propagating through the nonlinear interleaved-interconnected electronic network). Normally, distributed multimodal resonant (*RL*) shunt damping can be used to achieve several separate resonant-type PBGs for elastic wave propagation control. While using the proposed method, resonant-type PBGs can be induced by the peaks and valleys of multilevel electrical waves. Numerical results showed that the number of resonant-type PBGs over the primitive pass band between adjacent primitive Bragg-type PBGs is determined by levels of the nonlinear interleaved-interconnected electronic network. Compared with broadband elastic wave propagation control realized by independent nonlinear electrical networks, the proposed method is more flexible, and easily targets several discrete frequency range of interest without affecting other frequency domains, or with limited effect on it.

Chapter 6 summarizes the main conclusions obtained from the present work, and further investigations are also proposed and discussed.

Chapter 2 Electro-elastic modeling of smart periodic structures with semi-passive electrical networks

Abstract

In accordance with the proliferation of smart structures for vibration damping purposes (due to their significant advantages compared to traditional vibration reduction techniques), this chapter proposes to investigate the interactions between active materials and mechanical part of such smart beam structures. Such a study is motivated by the fact of disposing of a reliable model for assessing the performances of the techniques exposed in the following chapters. More specifically, previous finite element modeling methods of smart beams with SPENs that are presented in sections 2.1 and 2.2, a new finite element modeling of such structures is proposed based on the Timoshenko beam theory in the section 2.3 and compared and discussed with respect to the previous approaches in the section 2.4. Finally, section 2.5 summarizes the work of this chapter.

2.1 Impedance-based FE modeling of piezoelectric beam structures with semi-passive electrical networks

2.1.1 Brief literature review

Modeling semi-passive/passive vibration electronic damping systems belongs to the generalized research topic of elastic multi-layered systems (Figure 2.1). As for modeling methods of common elastic multi-layered systems, the finite element (FE) modeling method, as one kind of discretization algorithms, is more attractive in the engineering applications than semi-analytical/analytical algorithms based on strain energy approaches including a large number of dynamic equations. Stiffening and

added-mass effects induced by the piezoelectric patches can be conveniently applied in the FE-based semi-passive damping analysis (Figure 2.2).

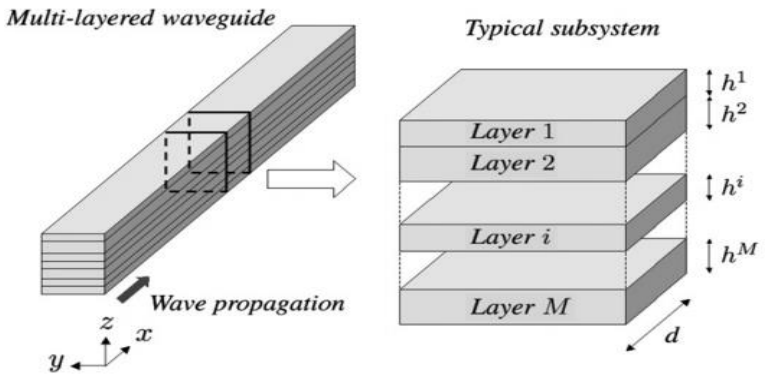

Figure 2.1 Illustration of an elastic multi-layered system [289].

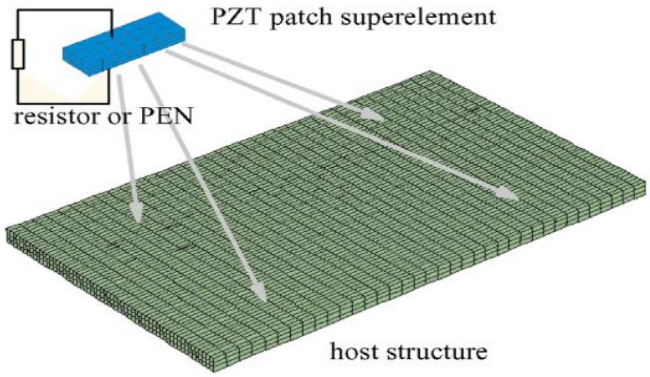

Figure 2.2 Integration of a piezoelectric patch as superelement attached to the structural FE model at multiple locations. The PEN is included afterwards in the dynamic equations [290].

In the early investigations of FE modeling on elastic periodic structures, Mead [291, 292] proposed an numerical technique based on the classic 3D finite element frameworks, converting the problem of evaluating wave characteristics of periodic systems into the problem of solving linear eigenvalues. It has simple numerical

implementation since the wave properties of the given periodic structure are derived from the classic finite element representation of unit cell of the periodic structure, which greatly simplifies the evaluation of elastic multi-layered structures. Based on a state vector representation of the kinematic variables of systems (displacement, forces), Zhong and Williams [293] formulated another effective FE modeling approach for periodic structures. Symplectic orthogonality properties are obtained for capturing the frequency evolution of the wave modes. Such numerical techniques are generally called Wave Finite Element (WFE) formulation [136-138].

However, the standard WFE formulations [136] exhibit some application problems such as a lack of convergence- directly related to the discretization of wave solution $\exp(-ikd)$ (where d denotes the length of unit periodic cell). In order to solve the issues in WFE, Mencik and Ichchou [289] proposed a dynamic sub-structuring technique, termed Modified Wave Finite Element (MWFE) formulation [139, 140]. The technique allows the dynamics of each layer cross-section to be projected on a local wave mode basis with appropriate dimension, and thus enhances the convergence of the wave mode expansion used for global wave mode construction and the well-conditioning of the associated eigenvalue problem. Furthermore, through the diffusion matrix model (DMM) [139], the MWFE approach can be extended to take shunted piezoelectric elements into consideration. With these numerical techniques, the influence of the shunted piezoelectric patches on wave propagation can be carefully investigated. Reflection and transmission coefficients of propagating waves in structures with shunted piezoelectric patches, and forced response of the smart structure can be calculated based on the time response of the structure which can be obtained via an inverse discrete Fourier transform (IDFT) approach. These general formulations can be applied to all types of slender structures [131, 132, 283, 284].

In this section, a classical FE modeling of piezoelectric beam structure is introduced, which is frequently used in the existing literature on wave propagation control of smart periodic beams with SPENs [96, 99, 102, 135, 150, 294-298], and will be at the root of the analysis of the control techniques proposed in the next chapters.

2.1.2 Constitutive electromechanical relationships of a linear piezoelectric material

A typical piezoelectric patch is shown in Figure 2.3. In order to model the piezoelectric material with electronic shunts, internal electromechanical relationships of a linear piezoelectric material should be firstly clarified. The general electromechanical equations for a linear PZT can be written as [13, 242]:

$$\begin{bmatrix} D \\ S \end{bmatrix} = \begin{bmatrix} \varepsilon^T & d \\ d_t & s^E \end{bmatrix} \begin{bmatrix} E \\ T \end{bmatrix} \tag{2.1}$$

Where D denotes the vector of electrical displacements (charge/area), E the vector of electrical field in the material (volts/meter), S the vector of strains (dimensionless parameter), and T the vector of stresses (force/area). ε is the dielectric coefficient (the superscript $(\ )^T$ on material properties denotes that the parameter is taken at constant stress), d the piezoelectric charge coefficient (the subscript $(\ )_t$ denotes the conventional matrix transpose), s the elastic compliance (the superscript $(\ )^E$ signifies that the values are measured at constant electrical field (*e.g.*, short circuit)):

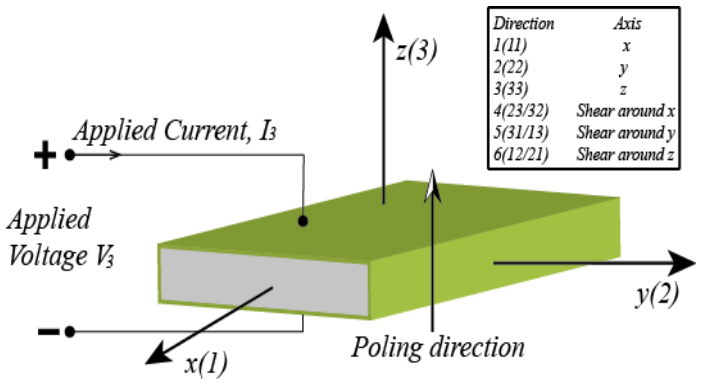

Figure 2.3 A typical piezoelectric material with the top and bottom surfaces electrodes and z(3) aligned with the polarization direction of the piezoelectric material.

$$\begin{cases} D=\begin{bmatrix} D_1 \\ D_2 \\ D_3 \end{bmatrix}, \quad E=\begin{bmatrix} E_1 \\ E_2 \\ E_3 \end{bmatrix}, \quad S=\begin{bmatrix} S_{11} \\ S_{22} \\ S_{33} \\ 2S_{23} \\ 2S_{31} \\ 2S_{12} \end{bmatrix}=\begin{bmatrix} S_1 \\ S_2 \\ S_3 \\ S_4 \\ S_5 \\ S_6 \end{bmatrix}, \quad T=\begin{bmatrix} T_{11} \\ T_{22} \\ T_{33} \\ T_{23} \\ T_{31} \\ T_{12} \end{bmatrix}=\begin{bmatrix} T_1 \\ T_2 \\ T_3 \\ T_4 \\ T_5 \\ T_6 \end{bmatrix} \\ \varepsilon^T=\begin{bmatrix} \varepsilon_{11}^T & \varepsilon_{12}^T & \varepsilon_{13}^T \\ \varepsilon_{21}^T & \varepsilon_{22}^T & \varepsilon_{23}^T \\ \varepsilon_{31}^T & \varepsilon_{32}^T & \varepsilon_{33}^T \end{bmatrix}, \quad d_t=\begin{bmatrix} d_{11} & d_{21} & d_{31} \\ d_{12} & d_{22} & d_{32} \\ d_{13} & d_{23} & d_{33} \\ d_{14} & d_{24} & d_{34} \\ d_{15} & d_{25} & d_{35} \\ d_{16} & d_{26} & d_{36} \end{bmatrix}, \quad s^E=\begin{bmatrix} s_{11}^E & s_{12}^E & s_{13}^E & s_{14}^E & s_{15}^E & s_{16}^E \\ s_{21}^E & s_{22}^E & s_{23}^E & s_{24}^E & s_{25}^E & s_{26}^E \\ s_{31}^E & s_{32}^E & s_{33}^E & s_{34}^E & s_{35}^E & s_{36}^E \\ s_{41}^E & s_{42}^E & s_{43}^E & s_{44}^E & s_{45}^E & s_{46}^E \\ s_{51}^E & s_{52}^E & s_{53}^E & s_{54}^E & s_{55}^E & s_{56}^E \\ s_{61}^E & s_{62}^E & s_{63}^E & s_{64}^E & s_{65}^E & s_{66}^E \end{bmatrix} \end{cases} \tag{2.2}$$

The axis nomenclature is also shown in Figure 2.3. *1* refers to the *x* axis (longitudinal axis), *2* corresponds to the *y* axis and *3* corresponds to the *z*(vertical) axis. Axis *3* is assigned to the direction of the initial polarization of the piezoelectric element, and axes *1* and *2* lie in the plane perpendicular to axis *3*. The strain coefficients S_{ij} define the deformation of the piezoelectric lattice and are dimensionless. For a general varying strain, the strain tensor may be written as:

$$S_{i,j}=\frac{\partial u_i}{\partial x_j} \tag{2.3}$$

where $\begin{cases} u_i=u_x,u_y,u_z; & i=x,y,z(1,2,3) \\ x_j=x_x,x_y,x_z; & j=x,y,z(1,2,3) \end{cases}$, and u_i is the displacement of lattice point under study along x_j.

A strain tensor is symmetric, *i.e.*,

$$S_{i,j}=S_{j,i}\,(i\neq j) \tag{2.4}$$

The strain components $S_1(S_{11}), S_2(S_{22}), S_3(S_{33})$ are used to describe the infinitesimal distortions associated with a change in volume along the directions *x,y* and *z,* respectively. The other strain components S_4, S_5, S_6 are defined in terms of changes of angle between the basis vectors (shear):

$$\begin{cases} S_4 = S_{23} + S_{32} = 2S_{23} \\ S_5 = S_{13} + S_{31} = 2S_{31} \\ S_6 = S_{21} + S_{12} = 2S_{12} \end{cases} \tag{2.5}$$

The stress component $T_{i,j}$ represents a force applied in the *i*-direction to a unit area of the plane whose outward-drawn normal lies in the *j*-direction. The stress tensor is symmetric just as the strain tensor. The dielectric coefficient ε_{ij}^T determines the charge per unit area in the *i*-axis due to an electric field applied in the *j*-axis. The piezoelectric coefficient d_{ij} is the ratio of the strain in the *j*-axis to the electric field applied along the *i*-axis, when all external stresses are held constant. The elastic compliance constant s_{ij}^E is the ratio of the strain in *i*-direction to the stress in the *j*-direction, given that there is no change of stress along the other two directions.

Assuming that the PZT is poled along the *3*-axis (the PZT is vibrating in the (*3, 1*)-mode) as shown in Figure 2.3, and viewing the piezoelectric material as a transversely isotropic material, many of the parameters in the above matrices (2.2) will be either zero, or can be expressed in terms of other parameters. In particular, the non-zero compliance coefficients are:

$$\begin{cases} s_{11}^E = s_{22}^E \\ s_{13}^E = s_{31}^E = s_{23}^E = s_{32}^E \\ s_{12}^E = s_{21}^E \\ s_{44}^E = s_{55}^E \\ s_{66}^E = 2\left(s_{11}^E - s_{12}^E\right) \\ d_{31} = d_{32} \\ d_{15} = d_{24} \\ \varepsilon_{11}^T = \varepsilon_{22}^T \end{cases} \tag{2.6}$$

Subsequently, equations (2.2) can be simplified using:

$$\varepsilon^T = \begin{bmatrix} \varepsilon_{11}^T & 0 & 0 \\ 0 & \varepsilon_{11}^T & 0 \\ 0 & 0 & \varepsilon_{33}^T \end{bmatrix}, \quad d_t = \begin{bmatrix} 0 & 0 & d_{31} \\ 0 & 0 & d_{31} \\ 0 & 0 & d_{33} \\ 0 & d_{15} & 0 \\ d_{15} & 0 & 0 \\ 0 & 0 & 0 \end{bmatrix}, \quad s^E = \begin{bmatrix} s_{11}^E & s_{12}^E & s_{13}^E & 0 & 0 & 0 \\ s_{21}^E & s_{22}^E & s_{23}^E & 0 & 0 & 0 \\ s_{31}^E & s_{32}^E & s_{33}^E & 0 & 0 & 0 \\ 0 & 0 & 0 & s_{44}^E & 0 & 0 \\ 0 & 0 & 0 & 0 & s_{55}^E & 0 \\ 0 & 0 & 0 & 0 & 0 & s_{66}^E \end{bmatrix} \tag{2.7}$$

2.1.3 Bending rigidity calculation of the piezoelectric beam based on reduced piezoelectric equations

Under the Euler-Bernoulli assumptions, the constitutive piezoelectric equations can be further reduced as two types. In the Type-1 of constitutive piezoelectric equations, all faces of each PZT patch are supposed to be free of constraints except for surfaces along the *x*-*y* plane:

$$\begin{cases} T_2^p = T_3^p = T_4^p = T_5^p = T_6^p = 0 \\ S_2^p = S_3^p = S_4^p = S_5^p = S_6^p = 0 \end{cases} \tag{2.8}$$

In the Type-2 of constitutive piezoelectric equations, assumptions of the stress/strain components are made:

$$\begin{cases} T_3^p = T_4^p = T_5^p = T_6^p = 0 \\ S_2^p = S_3^p = S_4^p = S_5^p = S_6^p = 0 \end{cases} \tag{2.9}$$

This therefore yields:

$$Piezo-Equations\ Type\text{-}1: \quad \begin{bmatrix} S_1^p \\ D_3 \end{bmatrix} = \begin{bmatrix} s_{11}^E & \sigma d_{31} \\ \sigma d_{31} & \varepsilon_{33}^T \end{bmatrix} \begin{bmatrix} T_1^p \\ E_3 \end{bmatrix} \tag{2.10}$$

$$Piezo-Equations\ Type\text{-}2: \quad \begin{bmatrix} S_1^p \\ S_2^p \\ D_3 \end{bmatrix} = \begin{bmatrix} s_{11}^E & s_{12}^E & \sigma d_{31} \\ s_{21}^E & s_{22}^E & \sigma d_{31} \\ \sigma d_{31} & \sigma d_{31} & \varepsilon_{33}^T \end{bmatrix} \begin{bmatrix} T_1^p \\ T_2^p \\ E_3 \end{bmatrix} \tag{2.11}$$

where σ is the sign of the piezoelectric constant which depends on the polarization of the material.

When the PZT patch, independently connected to an electrical circuit shunt, experiences vibrations, electromechanical coupling occurs between both of the

mechanical and electrical domains. The electrical relationships of the electrical circuit can be given as:

$$\begin{cases} I_p = \dfrac{U_p}{Z} = \dfrac{t_p E_3}{Z} \\ I_p = -\dfrac{dQ^e}{dt} = -j\omega A_s D_3 \end{cases} \tag{2.12}$$

where I_p ,U_p and Q^e respectively denote the piezoelectric voltage, the output current and the electric charge quantity of the PZT patch, t_p is the thickness of the piezoelectric patch, ω the angular frequency, A_s the area of the PZT electrode, Z the complex impedance of the electrical circuit shunt.

Therefore,

$$D_3 = \frac{jt_p}{\omega A_s Z} E_3 = \sigma d_{31} T_1^p + \varepsilon_{33}^T E_3 \tag{2.13}$$

As for the Type-1 of constitutive piezoelectric equations, applying the equation (2.13) in (2.10)，the stress component T_1^p and the strain component S_1^p can be obtained as:

$$\begin{cases} S_1^p = \dfrac{E_3}{\sigma d_{31}}\left[d_{31}^2 - \dfrac{t_p s_{11}^E}{A_s}\left(C_p - j\dfrac{1}{Z\omega} \right) \right], C_p = \dfrac{\varepsilon_{33}^T A_s}{t_p} \\ T_1^p = \dfrac{E_3}{\sigma d_{31}}\left[-\dfrac{t_p}{A_s}\left(C_p - j\dfrac{1}{Z\omega} \right) \right] \end{cases} \tag{2.14}$$

where C_p is the inherent capacitance of a PZT patch at constant stress.

When harmonic vibration is assumed, the equivalent elastic modules of the PZT patch, E_p^{Type1}, can be obtained according to the equation (2.14):

$$E_p^{Type1} = \frac{T_1^p}{S_1^p} = \frac{1 + j\omega Z C_p}{s_{11}^E + j\omega Z\left(s_{11}^E C_p - \dfrac{d_{31}^2 A_s}{t_p} \right)} \tag{2.15}$$

Similarly, as for Type-1 of constitutive piezoelectric equations, applying Eq. (2.13) in Eq. (2.11)，the strain component S_1^p and the stress components T_1^p, T_2^p yield:

$$\begin{cases} T_1^p = \dfrac{s_{11}^E}{\left(s_{11}^E\right)^2 - \left(s_{12}^E\right)^2} S_1^p - \dfrac{\sigma d_{31}}{s_{11}^E + s_{12}^E} E_3 \\ T_2^p = -\dfrac{s_{12}^E}{\left(s_{11}^E\right)^2 - \left(s_{12}^E\right)^2} S_1^p + \left(\dfrac{\sigma d_{31} s_{12}^E}{s_{11}^E \left(s_{11}^E + s_{12}^E\right)} - \dfrac{\sigma d_{31}}{s_{11}^E} \right) E_3 \end{cases} \tag{2.16}$$

And the electric displacement D_3 can also be given as:

$$\begin{aligned} D_3 &= \sigma d_{31} T_1^p + \sigma d_{31} T_2^p + \varepsilon_{33}^T E_3 \\ &= \frac{\sigma d_{31}}{s_{11}^E + s_{12}^E} S_1^p + \left(\varepsilon_{33}^T - \frac{2 d_{31}^2}{s_{11}^E + s_{12}^E} \right) E_3 \end{aligned} \tag{2.17}$$

According to equations (2.13) and (2.17), the strain component S_1^p, T_1^p can also be written as:

$$S_1^p = \left(\frac{j t_p}{\sigma d_{31} \omega A_s Z} \left(s_{11}^E + s_{12}^E\right) - \frac{\varepsilon_{33}^T}{\sigma d_{31}} \left(s_{11}^E + s_{12}^E\right) + 2\sigma d_{31} \right) E_3 \tag{2.18}$$

$$T_1^p = \left(\frac{j t_p s_{11}^E}{\sigma d_{31} w A_s Z \left(s_{11}^E - s_{12}^E\right)} - \frac{s_{11}^E \varepsilon_{33}^T}{\sigma d_{31} \left(s_{11}^E - s_{12}^E\right)} + \frac{\sigma d_{31}}{s_{11}^E - s_{12}^E} \right) E_3 \tag{2.19}$$

Therefore, when harmonic vibration is assumed, the equivalent elastic modulus E_p^{Type2} of the PZT patch including the effects of the external electrical impedance Z, can be obtained as:

$$E_p^{Type2} = \frac{T_1^p}{S_1^p} = \frac{\dfrac{\omega A_s d_{31}^2}{t_p} Z - \omega s_{11}^E C_p Z + j s_{11}^E}{\dfrac{2\omega d_{31}^2 A_s \left(s_{11}^E - s_{12}^E\right)}{t_p} Z - \left(\left(s_{11}^E\right)^2 - \left(s_{12}^E\right)^2 \right) \omega C_p Z + j \left(\left(s_{11}^E\right)^2 - \left(s_{12}^E\right)^2 \right)} \tag{2.20}$$

As shown in the Figure 2.4, there are mainly two kinds of unit piezoelectric beam elements commonly used in the smart periodic beam structures, namely unimorph and bimorph structures, which have different moments of inertia in the beam segment with PZT patches. The bending rigidities EI_s of the different elements can be given by:

$$\begin{cases} EI_s\big|_B = E_b \dfrac{w_b (t_b)^3}{12} & \text{for the beam segment B} \\ EI_s\big|_{BP1} = E_b \dfrac{w_b (t_b)^3}{12} + E_p \dfrac{w_p t_p \left(3(t_b)^2 + 6t_b t_p + 4(t_p)^2\right)}{12} & \text{for the beam segment BP1 (unimorph)} \\ EI_s\big|_{BP2} = E_b \dfrac{w_b (t_b)^3}{12} + 2E_p \dfrac{w_p t_p \left(3(t_b)^2 + 6t_b t_p + 4(t_p)^2\right)}{12} & \text{for the beam segment BP2 (bimorph)} \end{cases}$$

(2.21)

Where E_b is the elastic modulus of the pure beam element (without PZTs), w_b, t_b the width and thickness of the pure beam element, and w_p, t_p the width and thickness of the PZT patch, $E_p = E_p^{type1} or\ E_p^{type2}$.

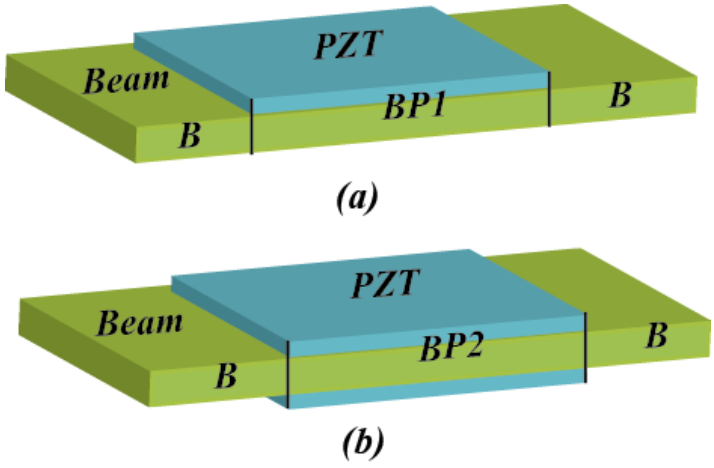

Figure 2.4 (a) Unit beam element of a piezoelectric beam carrying identical PZT patches periodically-unsymmetrically bonded to only one surface of the beam (unimorph); (b) Unit beam element of a piezoelectric beam carrying a pair of identical PZT patches periodically-symmetrically bonded to both surfaces of the beam (bimorph).

2.1.4 Dynamics of the piezoelectric beam carrying SPENs

Based on the finite element method, a beam structure can be divided into several identical sections and each section can be regarded as unit beam element. Since each segment B, BP1 or BP2 of the piezoelectric beam is considered as an Euler-Bernoulli beam as shown in Figure 2.4, the elastic waves in the beam are thus governed by the following differential equations:

$$\rho A_c \frac{\partial^2 u(x,t)}{\partial t^2} + EI_s \frac{\partial^4 u(x,t)}{\partial x^4} = q(x,t) \tag{2.22}$$

where $u(x,t)$ denotes the displacement of the beam along the *z*-axis, $q(x,t)$ the external applied load. *x* and *t* indicate spatial and time axes. EI_s, ρ, A_c are, respectively, the bending rigidity, density and cross-section area of the beam, differing for different beam segments (Eq.(2.21)).

It is also considered that the unit beam element can be expressed by Hermitian shape functions $H(x)$, which is a shape function of a two-node Euler-Bernoulli beam element as follows:

$$\begin{aligned} H(x) &= \begin{bmatrix} H_1(x) & H_2(x) & H_3(x) & H_4(x) \end{bmatrix} \\ H_1(x) &= 1 - \frac{3x^2}{l^2} + \frac{2x^3}{l^3}, \quad H_3(x) = \frac{3x^2}{l^2} - \frac{2x^3}{l^3} \\ H_2(x) &= x - \frac{2x^2}{l} + \frac{x^3}{l^2}, \quad H_4(x) = -\frac{x^2}{l} + \frac{x^3}{l^2} \end{aligned} \tag{2.23}$$

where *l* is the length of unit beam element.

Therefore,

$$u^e = H(x) d^e \tag{2.24}$$

where *u* is the displacement vector, *d* generalized nodal displacements, and the subscript *e* representing the unit beam element.

After the application of the Hermitian shape functions and Galerkin's method [299, 300], the dynamical equations of the unit beam element can be obtained as:

$$\left[M^e\right]\left\{\ddot{d}^e\right\} + \left[K^e\right]\left\{d^e\right\} = \left\{F^e(t)\right\} \tag{2.25}$$

$$\begin{cases} \left[M^e\right]=\int_0^l [H]^T \rho A_c [H]dx, \quad \left[K^e\right]=\int_0^l [H'']^T EI_s [H'']dx, \quad \left[F^e(t)\right]=\int_0^l q(x,t)[H]^T dx \\ \left[M^e\right]=\dfrac{\rho A_c l}{420}\begin{bmatrix} 156 & 22l & 54 & -13l \\ 22l & 4l^2 & 13l & -3l^2 \\ 54 & 13l & 156 & -22l \\ -13l & -3l^2 & -22l & 4l^2 \end{bmatrix}, \quad \left[K^e\right]=\dfrac{EI_s}{l^3}\begin{bmatrix} 12 & 6l & -12 & 6l \\ 6l & 4l^2 & -6l & 2l^2 \\ -12 & -6l & 12 & -6l \\ 6l & 2l^2 & -6l & 4l^2 \end{bmatrix} \end{cases}$$

As can be seen from the above FE modeling on the piezoelectric beam with SPENs, the external electrical impedance *Z* connected to the PZT patch is perfectly taken into consideration through the element stiffness matrix K^e, which is frequently used in the dynamic analysis of smart periodic beam structures. In this dissertation, such FE modeling of smart structures with SPENs in consideration of the electrical impedance *Z* (independently connected to one PZT patch), will be named *Z*-determined FE modeling of smart structures with SPENs.

However, such *Z*-determined FE modeling of smart structures with SPENs only fits piezoelectric structures with independent shunting SPENs, where each electrical circuit shunt is independently connected to the PZT patch. Thus the electrical impedance *Z* is distinct and can be easily obtained. However, in smart structures with complex SPENs, electrical shunts may be applied between two PZT patches, so that the electrical relation of each PZT patch is no more simply affected by external electrical impedance *Z*, but by the complex interconnected electrical relationships with other PZT patches. Therefore, such FE modeling of piezoelectric structures with SPENs including independent external impedance *Z* is adaptable for independent SPENs with different electrical shunts, but not for complex SPENs.

2.2 Voltage-based FE modeling of piezoelectric beam structures with semi-passive electrical networks

As shown from the above analysis, *Z*-determined FE modeling can be used to describe the electromechanical relationships of the piezoelectric structure with independent shunting SPENs as shown in the Figure 2.5 (a), but is impotent to the internal electromechanical relationships in smart structures with complex SPENs because of the complex impedance components (composed of the impedance Z and the unknown piezoelectric networks) as shown in the Figure 2.5 (b).

In this section, another class of FE modeling of smart structures with SPENs based on the Euler-Bernoulli theory, which is named as *V*-determined FE modeling of smart structures with SPENs for convenience in the dissertation, is introduced. The significant feature of *V*-determined FE modeling of smart structures with SPENs [106, 108, 128, 135, 290, 301-305] is that, the piezoelectric voltage V_p of the PZT patch, which replaces the external impedance *Z* as a variable compared to the *Z*-determined FE modeling of smart structures with SPENs, is used for the FE modeling of smart structures with SPENs. Through such variable feature, the *V*-determined FE modeling of smart structures with SPENs has the potential to describe complex electrical relationships in both kinds of piezoelectric structures as shown in the Figure 2.5.

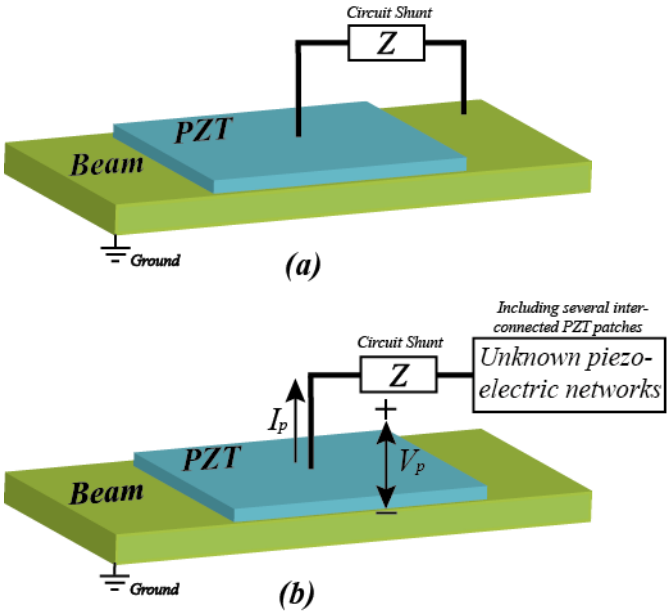

Figure 2.5 (a) A beam element of the piezoelectric beam with independent shunting SPENs; (b) a beam element of the piezoelectric beam carrying complex piezoelectric SPENs.

2.2.1 Bending moment description using the piezoelectric voltage

Since the piezoelectric equation Type-2 (Eq.(2.11)) is directly adopted in the following chapters, and the procedure of obtaining Type-1 for *V*-determined FE modeling method is similar with that of Type-2 for *V*-determined FE modeling method, herein for avoiding redundancy, the piezoelectric equation Type-2 is only chosen for introducing the *V*-determined FE modeling method of smart structures with SPENs under the Euler-Bernoulli assumption, and is also adopted in the following chapters. As known from Eq.(2.16), the longitudinal stress of the PZT patch can be given as:

$$T_1^p = \frac{s_{11}^E}{\left(s_{11}^E\right)^2 - \left(s_{12}^E\right)^2} S_1^p - \frac{\sigma d_{31}}{s_{11}^E + s_{12}^E} E_3 \tag{2.26}$$

Different from the electrical field description in Eq.(2.13), the electrical field is expressed as a function of piezoelectric voltage V_p instead of a function of the external impedance:

$$E_3 = -\frac{V_p}{t_p} \tag{2.27}$$

Where t_p is the thickness of the PZT patch.

Therefore, the stress T_1^p of Eq.(2.26) can be further rewritten as:

$$T_1^p = E_p S_1^p + \frac{\sigma d_{31}}{t_p\left(s_{11}^E + s_{12}^E\right)} V_p, E_p = \frac{s_{11}^E}{\left(s_{11}^E\right)^2 - \left(s_{12}^E\right)^2} \tag{2.28}$$

where E_p denotes elastic rigidity of the PZT patch in-plane strain.

Normally, the longitudinal strain is defined as the distance from the second spatial derivative of the deflection u_3 and the neutral axis x_c. Based on the Euler-Bernoulli beam theory, the strain along axis *x*, as shown in the Figure 2.3, has the following form:

$$S_1 = -\left(z - x_c\right)\frac{\partial^2 u_3}{\partial x^2} \tag{2.29}$$

Assuming that $z = 0$ is the lower surface of the beam, the neutral axis x_c of the beam element without PZT patches can be given by:

$$x_c = \frac{t_b}{2} \tag{2.30}$$

where t_b is the thickness of the pure beam without PZT patches.

The neutral axes of different beam elements as shown in the Figure 2.4, can also be written as:

$$\begin{cases} x_c = \dfrac{E_b t_b^2 + E_p t_p^2 + 2 t_b t_p E_p}{2\left(E_b t_b + E_p t_p\right)}, \text{ PZT patches cover one surface (Figure 2.4(a))} \\ x_c = \dfrac{t_b}{2}, \text{ PZT patches cover both surfaces (Figure 2.4(b))} \end{cases} \tag{2.31}$$

where E_b denotes the elastic modulus of the pure beam without PZT patches - $E_b = \dfrac{Y_b}{1-(\nu_b)^2}$: Y_b and ν_b respectively refer to the Young modulus and Poisson's ratio of the pure beam substructure.

Thus,

$$\begin{cases} T_1^b = -(z-x_c)\dfrac{\partial^2 u_3}{\partial x^2} E_b \\ T_1^p = -(z-x_c)\dfrac{\partial^2 u_3}{\partial x^2} E_p + \dfrac{\sigma d_{31}}{t_p\left(s_{11}^E + s_{12}^E\right)} V_p \end{cases} \tag{2.32}$$

where T_1^b denotes the stress of the pure beam structure along *x*-axis.

Therefore, the bending moment of the piezoelectric beam $M_{bending}^{Euler-B}$ can be given as:

$$M_{bending}^{Euler-B} = w_b \int T_1 (z-x_c)\, dz = \begin{cases} E_b I_b \dfrac{\partial^2 u_3}{\partial x^2}, T_1 = T_1^b \\ E_{eq} I_{eq} \dfrac{\partial^2 u_3}{\partial x^2} + b_1 V_p, T_1 = T_1^b + T_1^p \end{cases} \tag{2.33}$$

Where w_b is the width of the pure beam (the PZT patch is assumed to have the same width as the pure beam structure), T_1 is the strain of the piezoelectric beam along *x*-axis. $E_{eq} I_{eq} = E_b I_b + E_p I_p$ (I_b and I_p are respectively the second moment of area of the pure beam structure's cross-section and the second moment of area of the piezoelectric element's cross-section), and $b_1 = -\dfrac{\sigma d_{31} w_b}{t_p\left(s_{11}^E + s_{12}^E\right)} \int_{t_b}^{t_b+t_p} (z-x_c) dz$.

2.2.2 Dynamical equations of the piezoelectric beam in the mechanical domain

Similarly to the *Z*-determined FE modeling methodology of smart structures with SPENs (*i.e.*, Eq.(2.22)), the elastic waves in the piezoelectric beam are governed by the following same differential equations:

$$\rho A_c \frac{\partial^2 u(x,t)}{\partial t^2} + EI_s \frac{\partial^2 M_{bending}^{Euler-B}}{\partial x^2} = q(x,t) \tag{2.34}$$

Thus, the mechanical equations of unit FE beam element can be given with Hermitian shape functions $H(x)$ as:

$$\begin{cases} \left[M^e\right]\left\{\ddot{d}^e\right\} + \left[K^e\right]\left\{d^e\right\} = \left\{F^e(t)\right\}, & \text{beam element without PZTs} \\ \left[M^e\right]\left\{\ddot{d}^e\right\} + \left[K^e\right]\left\{d^e\right\} + \left[B_1^e\right]\left\{V_p^e\right\} = \left\{F^e(t)\right\}, & \text{beam element with PZTs} \end{cases} \tag{2.35}$$

$$\begin{cases} \left[M^e\right] = \int_0^l [H]^T \rho A_c [H] dx, \quad \left[K^e\right] = \int_0^l [H'']^T EI_s [H''] dx, \quad \left[F^e(t)\right] = \int_0^l q(x,t)[H]^T dx \\ \left[B_1^e\right] = \int_0^l b_1 [H'']^T dx, \end{cases}$$

$$\rho A_c = \begin{cases} \rho_b A_b, & \text{beam element without PZTs} \\ \rho_b A_b + \rho_p A_p, & \text{beam element with PZTs} \end{cases}$$

$$EI_s = \begin{cases} E_b I_b, & \text{beam element without PZTs} \\ E_{eq} I_{eq}, & \text{beam element with PZTs} \end{cases}$$

In actual applications, a damping matrix should also be is added in the mechanical equations to relate losses in experimental structures, which can be for example modeled as Rayleigh damping, yielding:

$$\begin{cases} \left[M^e\right]\left\{\ddot{d}^e\right\} + \left[C^e\right]\left\{\dot{d}^e\right\} + \left[K^e\right]\left\{d^e\right\} = \left\{F^e(t)\right\}, & \text{beam element without PZTs} \\ \left[M^e\right]\left\{\ddot{d}^e\right\} + \left[C^e\right]\left\{\dot{d}^e\right\} + \left[K^e\right]\left\{d^e\right\} + \left[B_1^e\right]\left\{V_p^e\right\} = \left\{F^e(t)\right\}, & \text{beam element with PZTs} \\ \left[C^e\right] = \beta_1\left[M^e\right] + \beta_2\left[K^e\right], & \beta_1 \text{ and } \beta_2 \text{ are constant coefficients} \end{cases} \tag{2.36}$$

2.2.3 Dynamical equations of the piezoelectric beam in the electrical domain

As demonstrated from Eqs.(2.17), (2.27) and (2.29), the electrical relationships between the electrical displacement and the piezoelectric voltage can be summarized as:

$$D_3 = \frac{-\sigma d_{31} t_p}{\left(s_{11}^E + s_{12}^E\right)} \frac{\partial^2 u_3}{\partial x^2} + \frac{2\left(d_{31}\right)^2 - \varepsilon_{33}^T \left(s_{11}^E + s_{12}^E\right)}{t_p \left(s_{11}^E + s_{12}^E\right)} V_p \tag{2.37}$$

Then, by integrating the electrical displacement over the length L_p of the PZT patch, the electric charge quantity Q^e of one PZT patch can be given in matrix-vector notation:

$$\left\{Q^e\right\} = \left[B_2^e\right]\left\{d^e\right\} + \left[B_3^e\right]\left\{V_p^e\right\} \tag{2.38}$$

$$\left[B_2^e\right] = \frac{-\left[\sigma\right] w_b d_{31} t_p}{\left(s_{11}^E + s_{12}^E\right)} \int_0^l \left[H''\right] dx$$

$$\left[B_3^e\right] = \frac{w_b \left[2{d_{31}}^2 - \varepsilon_{33}^T \left(s_{11}^E + s_{12}^E\right)\right]}{t_p \left(s_{11}^E + s_{12}^E\right)} \left[L_p\right]$$

where $\left[\sigma\right]$ and $\left[L_p\right]$ denote diagonal matrices which respectively depend on the sign of polarization direction of the bonded PZT patches and the length of the bonded PZT patches.

As shown by Eq.(2.38), dynamic equations of the bonded PZT patch in the electrical domain are described by the electric charge quantity and the piezoelectric voltage of the PZT patch under vibration, and do not involve external shunting circuitries, so it will be convenient for coupling the effects of the external complex SPENs with the dynamic electrical Eq.(2.38) of the bonded PZT patch after the electrical equations of the SPENs are built. Furthermore, the dynamical electrical relationships of the bonded PZT patches with SPENs can be easily incorporated into the dynamically mechanical equations of the piezoelectric beam (2.36) through the use of the piezoelectric voltage V_p.

Thus, the electro-elastic relationships of *V*-determined FE modeling methodology of smart structures with SPENs based on the Euler-Bernoulli beam theory can be summarized as:

$$\begin{cases} \left[M^e\right]\left\{\ddot{d}^e\right\} + \left[C^e\right]\left\{\dot{d}^e\right\} + \left[K^e\right]\left\{d^e\right\} + \left[B_1^e\right]\left\{V_p^e\right\} = \left\{F^e(t)\right\} \\ \left\{Q^e\right\} = \left[B_2^e\right]\left\{d^e\right\} + \left[B_3^e\right]\left\{V_p^e\right\} \end{cases} \tag{2.39}$$

2.3 FE modeling of piezoelectric beam structures with semi-passive electrical networks based on the Timoshenko beam theory

In view of the superiority of the *V*-determined FE modeling of smart structures with SPENs, a *V*-determined FE modeling method of smart structures with SPENs based on the Timoshenko beam theory is proposed in the section, which fits two-node Timoshenko beam FE theories integrated into the FE modeling of smart beam structures. Mechanical as well as electrical relationships of a smart Timoshenko beam structure with SPENs are then discussed in detail.

2.3.1 Hypotheses

Herein, the piezoelectric beam is modeled as a moderately thick beam based on the Timoshenko beam theory. Axes *x*, *y* and *z* (or *1*, *2* and *3* respectively) are defined along the length, width and thickness of the beam (Figure 2.6), respectively. Considering Voigt's notation (11→1, 22→2, 33→3, 23→4, 13→5, 12→6), the following assumptions are made: the stress components other than T_1 and T_2 (stress components in the axial direction) and T_5 (transverse shear stress) are negligible so that $T_3 = T_4 = T_6 = 0$; no torsion is considered, the strain components except S_1 (strain component in the axial direction) and S_5 (transverse shear strain) are negligible, with the transverse shear strain having a constant value γ_0, so that $S_2 = S_3 = S_4 = S_6 = 0$; the piezoelectric materials are viewed as transverse isotropic material (∞mm symmetry) with a polarization axis along *z*.

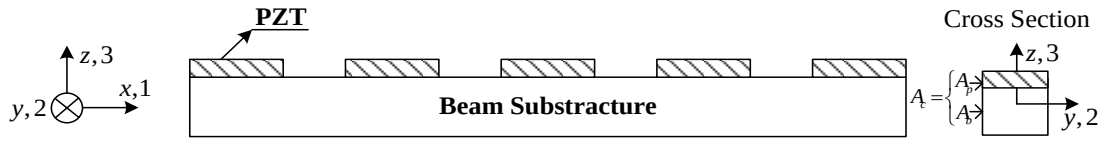

Figure 2.6 Schematic of bending beam with distributed PZTs.

For the isotropic piezoelectric materials, reduced constitutive piezoelectric equations based on the Timoshenko theory can be given as:

$$\begin{bmatrix} S_1^p \\ S_2^p \\ S_5^p \\ D_3 \end{bmatrix} = \begin{bmatrix} s_{11}^E & s_{12}^E & 0 & \sigma d_{31} \\ s_{12}^E & s_{11}^E & 0 & \sigma d_{31} \\ 0 & 0 & s_{55}^E & 0 \\ \sigma d_{31} & \sigma d_{31} & 0 & \varepsilon_{33}^T \end{bmatrix} \begin{bmatrix} T_1^p \\ T_2^p \\ T_5^p \\ E_3 \end{bmatrix} \tag{2.40}$$

where s^E $\left(s_{11}^E,\ s_{12}^E,\ s_{55}^E\right)$ corresponds to the mechanical compliance tensor of the piezoelectric material under constant electric field and ε^T to the electrical permittivity under constant stress. d_{31} is the piezoelectric charge constant. E_3 and D_3 are given as the electric field intensity and electrical displacement along *z* direction, respectively. σ is the sign of the piezoelectric constant which depends on the polarization direction of the material.

2.3.2 Mechanical perspective

For the pure beam substructures, under the previous assumptions and according to Hooke's law, the relationship between the stress T_1^b along *x*-axis and strain S_1^b along the same axis of the substrate structure is given by:

$$T_1^b = E_b S_1^b \tag{2.41}$$

with $E_b = \dfrac{Y_b}{1-\nu_b^{\,2}}$, and Y_b and ν_b respectively referring to the Young modulus and Poisson's ratio of the substrate structure.

For the piezoelectric materials, according to the above hypotheses, the strain along the length (*x*-axis) and the width (*y*-axis) in Eq.(2.40) can be rewritten as follows:

$$\begin{cases} S_1^p = s_{11}^E T_1^p + s_{12}^E T_2^p + \sigma d_{31} E_3 \neq 0 \\ S_2^p = s_{12}^E T_1^p + s_{11}^E T_2^p + \sigma d_{31} E_3 = 0 \end{cases} \tag{2.42}$$

Therefore, the stress along *x*-axis can be obtained as:

$$T_1^p = \frac{s_{11}^E}{\left(s_{11}^E\right)^2 - \left(s_{12}^E\right)^2} S_1^p - \frac{\sigma d_{31}}{s_{11}^E + s_{12}^E} E_3 \tag{2.43}$$

According to the above *V*-determined FE modeling method of smart structures, the stress along *x*-axis can also be written as:

$$T_1^p = E_p S_1^p + \frac{\sigma d_{31}}{t_p \left(s_{11}^E + s_{12}^E\right)} V_p, E_p = \frac{s_{11}^E}{\left(s_{11}^E\right)^2 - \left(s_{12}^E\right)^2} \tag{2.44}$$

Then the strain along *x*-axis $S_1\left(S_1^b, S_1^p\right)$ has the following form based on the Timoshenko beam theory:

$$S_1 = -\left(z - x_c\right)\frac{\partial \varphi(x)}{\partial x} = -\left(z - x_c\right)\frac{\partial\left(\frac{\partial u_3}{\partial x} - \gamma_0\right)}{\partial x},\ \gamma_0 = \frac{\partial u_3}{\partial x} - \varphi(x) \tag{2.45}$$

where u_3 is the vertical deflection of the neutral axis in the x_3 direction, and γ_0 is the transverse shear strain.

According to Eq.(2.31), the neutral axis x_c has different values in the different cases, so there are different strain values S_1 along *x*-axis in different beam elements.

As discussed in the literature [306], the shear coefficient of the Timoshenko beam, which is used to define the transverse shear strain γ_0, can be determined by:

$$\aleph = \frac{6 + 12\nu_b + 6\left(\nu_b\right)^2}{7 + 12\nu_b + 4\left(\nu_b\right)^2} \tag{2.46}$$

Thus, the transverse shear stress of the pure beam structure T_5^b can be defined as:

$$T_5^b = \aleph G_b \gamma_0,\ G_b = \frac{Y_b}{2\left(1 + \nu_b\right)} \tag{2.47}$$

where G_b is the shear modulus of the pure beam structure.

According to Eq.(2.40), the transverse shear stress of the bonded piezoelectric material T_5^p can be expressed as:

$$T_5^p = \frac{S_5^p}{s_{55}^E} = \frac{\gamma_0}{s_{55}^E} \tag{2.48}$$

Therefore, the shear force Q_s of the beam can be obtained as:

$$Q_s = \begin{cases} Q_s^b = \int_{A_c} T_5^b dA_c = \int_{A_c} \aleph G_b \gamma_0 dA_c = \aleph G_b A_c^b \gamma_0 \\ Q_s^{eq} = \int_{A_c} T_5^b dA_c + \int_{A_c} T_5^p dA_c = \aleph G_{eq} A_c^b \gamma_0, G_{eq} = \left(G_b + \frac{A_c^p}{\aleph A_c^b s_{55}^E} \right) \\ = \aleph G A_c^b \gamma_0, G = \begin{cases} G_b, & \text{for the pure beam element} \\ G_{eq}, & \text{for the beam element with PZTs} \end{cases} \end{cases} \tag{2.49}$$

where A_c is the cross-sectional area of the beam, A_c^b denotes the cross-sectional area of the pure beam element, A_c^p denotes the cross-sectional area of the piezoelectric material in the beam element with PZT patches as shown in Figure 2.6, Q_s^b is the shear force of the pure beam element and Q_s^{eq} the shear force of the beam element with PZT patches.

In addition, the bending moment of the Timoshenko piezoelectric beam structure $M_{bending}^{Timo}$ is equal to:

$$M_{bending}^{Timo} = \begin{cases} M_{bending}^{Timo-b} = -w_b \int T_1^b \left(z - x_c \right) dz = -w_b \int E_b S_1^b \left(z - x_c \right) dz = E_b I_b \frac{\partial \varphi(x)}{\partial x} \\ M_{bending}^{Timo-eq} = -w_b \int T_1^b \left(z - x_c \right) dz - w_b \int T_1^p \left(z - x_c \right) dz = E_{eq} I_{eq} \frac{\partial \varphi(x)}{\partial x} + b_1 V_p \end{cases} \tag{2.50}$$

where $M_{bending}^{Timo-b}$ denotes the bending moment of the pure beam element without PZT patches and $M_{bending}^{Timo-eq}$ the bending moment of the beam element with PZT patches (the PZT patch has the same width of the pure beam substructure). w_b, I_b and I_p

are respectively the second moment of area of the pure beam element's cross-section and that of the piezoelectric element's cross-section, $E_{eq}I_{eq} = E_b I_b + E_p I_p$.

According to the finite element method, a structure can be divided into several identical sections and each section can be regarded as an element according to the finite element method. The equation of a Timoshenko beam element for the beam bending can be derived through Hamilton's principle:

$$\delta\Pi = \int_{t_1}^{t_2} \left(\delta U_s - \delta T_k + \delta W_{ex} \right) dt = 0 \tag{2.51}$$

where Π denotes the potential energy, δU_s, δT_k and δW_{ex} are the variation of the strain energy, the variation of the kinetic energy and the work produced by the external transversal load, respectively. The strain energy is given as:

$$U_s = \frac{1}{2}\int \left(M_{bending}^{Timo} \frac{\partial \varphi(x)}{\partial x} + Q_s \left(\frac{\partial u_3}{\partial x} - \varphi(x) \right) \right) dx \tag{2.52}$$

By assuming free harmonic motion and including the effect of rotary inertia, the kinetic energy is given as:

$$T_k = \frac{1}{2}\int_0^l \left(\rho A_c \left(\frac{\partial u_3}{\partial t} \right)^2 + \rho I_{ts} \left(\frac{\partial \varphi(x)}{\partial t} \right)^2 \right) dx \tag{2.53}$$

$$\rho A_c = \begin{cases} \rho_b A_c^b, & \text{for the pure beam element} \\ \rho_b A_c^b + \rho_p A_c^p, & \text{for the beam element with PZTs} \end{cases}$$

$$\rho I_{ts} = \begin{cases} \rho_b I_b, & \text{for the pure beam element} \\ \rho_b I_b + \rho_p I_p, & \text{for the beam element with PZTs} \end{cases}$$

where ρ is the mass density of the beam, ρ_b the mass density of the pure beam element and ρ_p the mass density of the piezoelectric material.

Finally, the work of the external forces is given as:

$$W_{ex} = \int_0^l \begin{Bmatrix} u_3 \\ \varphi \end{Bmatrix}^T \begin{Bmatrix} q \\ m \end{Bmatrix} dx \tag{2.54}$$

where q and m are the distributed forces and moments along the length of the beam element.

The two differential equations of motion and associated boundary conditions are obtained by substituting equations of U_s, T_k and W_{ex} into the Hamilton principle equation and integrating by parts:

$$\begin{aligned}\delta\Pi = &\int_{t_1}^{t_2}\left[\int_0^l\left(M_{bending}^{Timo}\frac{\partial\delta\varphi(x)}{\partial x}+Q_s\left(\frac{\partial\delta u_3}{\partial x}-\delta\varphi(x)\right)-\rho A_c\left(\frac{\partial u_3}{\partial t}\right)^2\delta u_3-\right.\right.\\ &\left.\left.-\rho I_s\left(\frac{\partial\varphi(x)}{\partial t}\right)^2\delta\varphi(x)+q\delta u_3+m\delta\varphi(x)\right)dx\right]dt\\ =&\int_{t_1}^{t_2}\left\{\int_0^l\left[\left(\frac{\partial M_{bending}^{Timo}}{\partial x}-Q_s-\rho I_s\left(\frac{\partial\varphi(x)}{\partial t}\right)^2+m\right)\delta\varphi(x)+\left(\frac{\partial Q_s}{\partial x}-\rho A_c\left(\frac{\partial u_3}{\partial t}\right)^2+q\right)\delta u_3\right]dx\right.\\ &\left.-\left[M_{bending}^{Timo}\delta\varphi(x)\right]_0^l-\left[Q_s\delta u_3\right]_0^l\right\}dt\end{aligned} \tag{2.55}$$

Therefore,

$$\begin{cases}\rho A_c\left(\frac{\partial u_3}{\partial t}\right)^2-\frac{\partial Q_s}{\partial x}=q,\\ \rho I_s\left(\frac{\partial\varphi(x)}{\partial t}\right)^2+Q_s-\frac{\partial M_{bending}^{Timo}}{\partial x}=m\end{cases} \tag{2.56}$$

According to Hamilton's principle, the shape functions for u_3 and φ exactly satisfy the homogeneous form of the static equations of equilibrium for a uniform Timoshenko beam:

$$\frac{\partial Q_s}{\partial x}=0 \tag{2.57}$$

$$Q_s-\frac{\partial M_{bending}^{Timo}}{\partial x}=0 \tag{2.58}$$

From the previous equations, avoiding shear locking phenomenon can only be satisfied if the polynomial order for (u_3) is selected one order higher than the polynomial order for (φ). Assuming that the shape function $N(x)$ of the two-node Timoshenko beam element can be given as:

$$N(x)=\begin{bmatrix}\left[N_u(x)\right]\\ \left[N_\varphi(x)\right]\end{bmatrix} \tag{2.59}$$

then,

$$\begin{bmatrix}u(x,t)\\ \varphi(x,t)\end{bmatrix}=N(x)d^e,\ u(x,t)=N_u(x)d^e,\varphi(x,t)=N_\varphi(x)d^e. \tag{2.60}$$

where $d^e=\{u_1 \quad \varphi_1 \quad u_2 \quad \varphi_2\}^T$ is the array of nodal displacements and rotations of the beam element, and $u(x,t)$ and $\varphi(x,t)$ are the deflection and the rotation of the points on the beam element.

Finally, the finite element representation of the equations of motion can be developed by substituting the displacement distribution into Hamilton's principle equation, and carrying out the integration over the beam length:

$$\begin{cases}\left[M^e\right]\left\{\ddot{d}^e\right\}+\left[K^e\right]\left\{d^e\right\}=\left\{F^e\right\}, & \text{the beam element without PZTs}\\ \left[M^e\right]\left\{\ddot{d}^e\right\}+\left[K^e\right]\left\{d^e\right\}+\left[B_1^e\right]\left\{V_p^e\right\}=\left\{F^e\right\}, & \text{the beam element with PZTs}\end{cases} \tag{2.61}$$

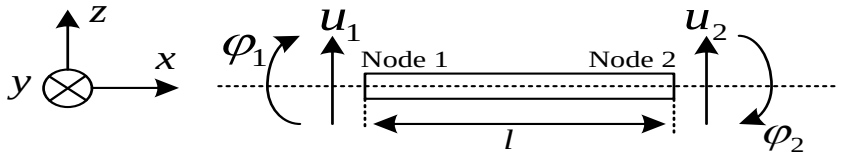

Figure 2.7 Beam element with two nodes: each node has two coordinates.

$$\left[M^e\right]=\int_0^l\begin{bmatrix}\left[N_u(x)\right]\\ \left[N_\varphi(x)\right]\end{bmatrix}^T\begin{bmatrix}\rho A_c & 0\\ 0 & \rho I_{ts}\end{bmatrix}\begin{bmatrix}\left[N_u(x)\right]\\ \left[N_\varphi(x)\right]\end{bmatrix}dx$$

$$\rho A_c=\begin{cases}\rho_b A_c^b, & \text{for the pure beam element}\\ \rho_b A_c^b+\rho_p A_c^p, & \text{for the beam element with PZTs}\end{cases}$$

$$\rho I_{ts} = \begin{cases} \rho_b I_b, & \text{for the pure beam element} \\ \rho_b I_b + \rho_p I_p, & \text{for the beam element with PZTs} \end{cases}$$

$$\left[K^e\right] = \int_0^l \begin{bmatrix} \dfrac{\partial\left[N_\varphi(x)\right]}{\partial x} \\ \left[N_\varphi(x)\right] + \dfrac{\partial\left[N_u(x)\right]}{\partial x} \end{bmatrix}^T \begin{bmatrix} EI_s & 0 \\ 0 & \aleph GA_c^b \end{bmatrix} \begin{bmatrix} \dfrac{\partial\left[N_\varphi(x)\right]}{\partial x} \\ \left[N_\varphi(x)\right] + \dfrac{\partial\left[N_u(x)\right]}{\partial x} \end{bmatrix} dx$$

$$EI_s = \begin{cases} E_b I_b, & \text{for the pure beam element} \\ E_{eq} I_{eq}, & \text{for the beam element with PZTs} \end{cases}$$

$$\aleph GA_c^b = \begin{cases} \aleph G_b A_c^b, & \text{for the pure beam element} \\ \aleph G_{eq} A_c^b, & \text{for the beam element with PZTs} \end{cases}$$

$$\left[B_1\right] = b_1 \int_0^l \frac{\partial\left[N_\varphi(x)\right]^T}{\partial x} dx$$

and the consistent force array is given as:

$$\left\{F^e\right\} = \int_0^l \begin{bmatrix} \left[N_u(x)\right] \\ \left[N_\varphi(x)\right] \end{bmatrix}^T \begin{Bmatrix} q \\ m \end{Bmatrix} dx$$

If the Rayleigh damping matrix C^e is introduced, the global motion equation holds the following form:

$$\left[M^e\right]\left\{\ddot{d}^e\right\} + \left[C^e\right]\left\{\dot{d}\right\} + \left[K^e\right]\left\{d^e\right\} + \left[B_1^e\right]\left\{V_p^e\right\} = \left\{F^e\right\} \tag{2.62}$$

Herein, the shape functions satisfying the above two constrain equations for the Timoshenko beam in the literature [307] are adopted in this dissertation, and can be found in appendix A.

2.3.3 Electrical perspective

For the PZT patch, the electrical displacement can be calculated from Eq.(2.40):

$$D_3 = \frac{-\sigma d_{31} t_p}{\left(s_{11}^E + s_{12}^E\right)} \frac{\partial\varphi(x)}{\partial x} + \frac{2\left(\sigma d_{31}\right)^2 - \varepsilon_{33}^T \left(s_{11}^E + s_{12}^E\right)}{t_p \left(s_{11}^E + s_{12}^E\right)} V_p \tag{2.63}$$

Then, the electrical charge quantity Q of one piezoelectric patch can be expressed by integrating the electrical displacement over the width and overall length of the piezoelectric patch:

$$Q = w_b \int D_3 dx \tag{2.64}$$

Assuming that the piezoelectric patches are identical and the k^{th} beam element with piezoelectric patches is bonded at the position $x_{k0} \le x_1 \le x_{k0} + L_p$ of the bending beam, the expression of the electrical charge Q yields:

$$Q = \frac{-\sigma w_b d_{31} t_p}{\left(s_{11}^E + s_{12}^E\right)} \varphi(x) \Bigg|_{x_{k0}}^{\left(x_{k0} + L_p\right)} + \frac{w_b L_p \left[2{d_{31}}^2 - \varepsilon_{33}^T \left(s_{11}^E + s_{12}^E\right)\right]}{t_p \left(s_{11}^E + s_{12}^E\right)} V_p \tag{2.65}$$

where x_{k0} is the beginning position of the k^{th} beam element and L_p is the length of piezoelectric beam element. Herein, the width of the PZT patch is assumed equal to the width of the pure beam structure w_b.

Then, the electrical equation can be given in matrix-vector notation:

$$\left\{Q^e\right\} = \left[B_2^e\right]\left\{d^e\right\} + \left[B_3^e\right]\left\{V_p^e\right\} \tag{2.66}$$

with

$$\left[B_2^e\right] = \frac{-\left[\sigma\right] w_b d_{31} t_p}{\left(s_{11}^E + s_{12}^E\right)} \int_0^l \frac{\partial\left[N_\varphi(x)\right]}{\partial x} dx$$

$$\left[B_3^e\right] = \frac{w_b \left[2{d_{31}}^2 - \varepsilon_{33}^T \left(s_{11}^E + s_{12}^E\right)\right]}{t_p \left(s_{11}^E + s_{12}^E\right)} \left[L_p\right]$$

where $\left[\sigma\right]$ and $\left[L_p\right]$ are diagonal matrices which respectively depend on the polarization and length of the bonded piezoelectric patches.

Such electrical equations can be easily applied to any electrical boundary condition of the SPENs of piezoelectric structures.

In summary, from the previous analysis, a *V*-determined FE modeling of smart structures with SPENs based on the Timoshenko beam theory is established, and the electro-elastic relationships of the modeling can be generalized as:

$$\begin{cases} \left[M^e\right]\left\{\ddot{d}^e\right\} + \left[C^e\right]\left\{\dot{d}^e\right\} + \left[K^e\right]\left\{d^e\right\} + \left[B_1^e\right]\left\{V_p^e\right\} = \left\{F^e\right\} \\ \left\{Q^e\right\} = \left[B_2^e\right]\left\{d^e\right\} + \left[B_3^e\right]\left\{V_p^e\right\} \end{cases} \tag{2.67}$$

2.4 Comparison between Euler-Bernoulli and Timoshenko models

In order to further understand the electromechanical relationships of the proposed modeling, the previous FE methods for piezoelectric beam structures with SPENs using Euler-Bernoulli and Timoshenko beam theories are compared in this section.

Table 2.1 shows the hypotheses comparison between Euler-Bernoulli and Timoshenko theories for modeling piezoelectric beam structures with SPENs. The difference in the assumptions between Euler-Bernoulli type1 and Euler-Bernoulli type2 given is as follows:

$$\begin{cases} T_2^{b,p} = 0, \text{in Euler-Bernoulli type1} \\ T_2^{b,p} \neq 0, \text{in Euler-Bernoulli type2} \end{cases} \tag{2.68}$$

and the difference in the assumptions between Euler-Bernoulli and Timoshenko approach is:

$$\begin{cases} T_5^{b,p} = 0, S_5^{b,p} = 0, \text{in Euler-Bernoulli} \\ T_5^{b,p} \neq 0, S_5^{b,p} \neq 0, \quad \text{in Timoshenko} \end{cases} \tag{2.69}$$

Table 2.1 Assumption comparison between Euler-Bernoulli and Timoshenko beam theories.

	Euler-BernoulliType1	Euler-BernoulliType2	Timoshenko
$=0$	$T_2^{b,p}, S_2^{b,p}, T_3^{b,p}, S_3^{b,p}, T_4^{b,p}, S_4^{b,p},$ $T_5^{b,p}, S_5^{b,p}, T_6^{b,p}, S_6^{b,p}, E_1, E_2.$	$S_2^{b,p}, T_3^{b,p}, S_3^{b,p}, T_4^{b,p}, S_4^{b,p},$ $T_5^{b,p}, S_5^{b,p}, T_6^{b,p}, S_6^{b,p}, E_1, E_2.$	$S_2^{b,p}, T_3^{b,p}, S_3^{b,p}, T_4^{b,p},$ $S_4^{b,p}, T_6^{b,p}, S_6^{b,p}, E_1, E_2.$
$\neq 0$	$T_1^{b,p}, S_1^{b,p},$ $E_3.$	$T_1^{b,p}, S_1^{b,p},$ $T_2^{b,p}, E_3.$	$T_1^{b,p}, S_1^{b,p}, T_2^{b,p},$ $T_5^{b,p}, S_5^{b,p}, E_3.$

Based on the above-mentioned different assumptions, the electromechanical relationships of different FE modeling approaches for piezoelectric beam structures are obtained as shown by Eqs.(2.25), (2.39) and (2.67). The electromechanical relationships of FE modeling for piezoelectric beam structures based on the Euler-Bernoulli type1 assumption only include the mechanical equations without the

electrical equations since the external electrical impedance Z is imbedded in the mechanical equations (impedance-based approach). By comparison, electrical equations are obtained using the voltage-based approach with the Euler-Bernoulli type 2 and Timoshenko beam theories as shown in Eqs.(2.39) and (2.67).The mass matrix M^e, stiffness matrix K^e, and electrical matrices B_1^e, B_2^e, B_3^e of the electromechanical equations of the FE modeling for piezoelectric beam structures based on Euler-Bernoulli type 2 and Timoshenko beam theories are compared in Table 2.2. Different from the mass matrix $M_{Euler-B}^e$, stiffness matrix $K_{Euler-B}^e$, and electrical matrices $B_{1Euler-B}^e, B_{2Euler-B}^e, B_{3Euler-B}^e$ in Eq.(2.39) based on the Euler-Bernoulli type 2 assumption, the transverse shear strain and stress are considered in the mass matrix M_{Timo}^e, stiffness matrix K_{Timo}^e, and electrical matrices $B_{1Timo}^e, B_{2Timo}^e, B_{3Timo}^e$ using Timoshenko approach as show in Eq.(2.67). However, it is interesting to find the following relationships of electrical matrices:

$$\begin{cases} B_{1Euler-B}^e = \int_0^l b_1 \left[H''\right]^T dx = b_1 \int_0^l \dfrac{\partial \left[N_\varphi(x)\right]^T}{\partial x} dx = B_{1Timo}^e \\ B_{2Euler-B}^e = \dfrac{-\left[\sigma\right] w_b d_{31} t_p}{\left(s_{11}^E + s_{12}^E\right)} \int_0^l \left[H''\right] dx = \dfrac{-\left[\sigma\right] w_b d_{31} t_p}{\left(s_{11}^E + s_{12}^E\right)} \int_0^l \dfrac{\partial \left[N_\varphi(x)\right]}{\partial x} dx = B_{2Timo}^e \\ B_{3Euler-B}^e = \dfrac{w_b \left[2{d_{31}}^2 - \varepsilon_{33}^T \left(s_{11}^E + s_{12}^E\right)\right]}{t_p \left(s_{11}^E + s_{12}^E\right)} \left[L_p\right] = B_{3Timo}^e \end{cases} \quad (2.70)$$

Table 2.2 A comparison of the terms of electromechanical relationships of different FE modeling methods.

	M^e	K^e	B_1^e, B_2^e, B_3^e
Euler-BernoulliType2	$M_{Euler-B}^e$	$K_{Euler-B}^e$	$\left(B_1^e, B_2^e, B_3^e\right)_{Euler-B}$
Timoshenko	M_{Timo}^e	K_{Timo}^e	$\left(B_1^e, B_2^e, B_3^e\right)_{Timo}$

Therefore, consideration of the transverse shear strain and stress affects the mass and stiffness matrices of the FE modeling of piezoelectric beam structures, but cannot

affect the electrical relationships of the piezoelectric beam structures along the electrical field E_3. Actually, the transverse shear strain and stress have the relationships of the electrical parameters along electrical field E_1, as shown in Eq.(2.7) ($S_5^p = d_{15}E_1 + s_{55}^E T_5^p$). However, E_1 is assumed to be equal to *0* in the above FE modeling approaches.

In order to further investigate the difference between wave propagation properties of smart periodic structures under Euler-Bernoulli and Timoshenko beam assumptions, piezoelectric periodic structures without electrical networks / with independent RL-resonant shunting electrical networks (both ends of each PZT connected to the Resistance-Inductance shunt circuit) are taken as an example for comparing logarithmic decay of propagative wave under different beam assumptions and results are shown in Figure 2.8. Based on the parameters of the piezoelectric periodic beam sample used in the experimental sections of the undermentioned chapters, logarithmic decay curves of propagative wave in different electrical boundary conditions under different assumptions are plotted in Figure 2.9. It can be seen that there is a little difference in the Bragg-type stop bands ([7 kHz, 8 kHz] around) of propagative wave of the structure in the open circuit condition under Euler-Bernoulli and Timoshenko beam assumptions, since the piezoelectric periodic beam sample used in the experimental section of the following chapters can be reasonably simplified as a Euler-Bernoulli beam, the transverse shear strain and stress have less effects on the mechanical characterization of such piezoelectric beam structures using the FE modeling. But when a smart periodic beam is not fit for being assumed as a Euler-Bernoulli beam but only a Timoshenko beam (moderate thickness), the proposed FE method based on the Timoshenko beam assumption will show better accuracy in modeling such smart periodic beam structure. Resonant-type stop bands (centered around 3 kHz) of propagative wave of the structure with independent RL-resonant shunting electrical networks under the two assumptions are almost the

same since the electrical relationships of the piezoelectric beam structures along the electrical field E_3 are less affected by the transverse shear strain and stress.

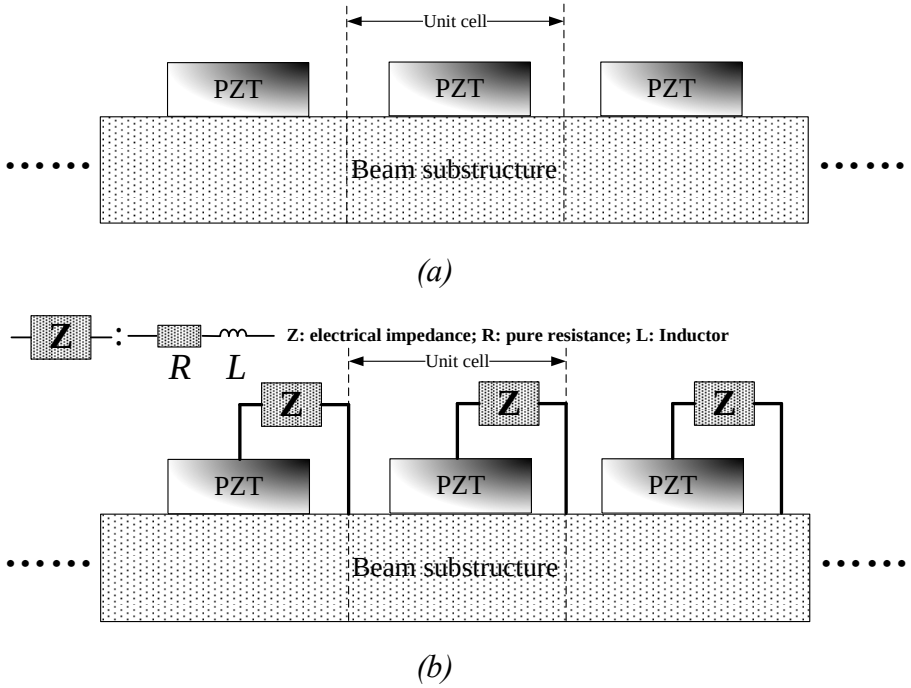

Figure 2.8 (a) Piezoelectric periodic structure without electrical networks (in open circuit condition); (b) piezoelectric periodic structure with independent *RL*-resonant shunting electrical networks.

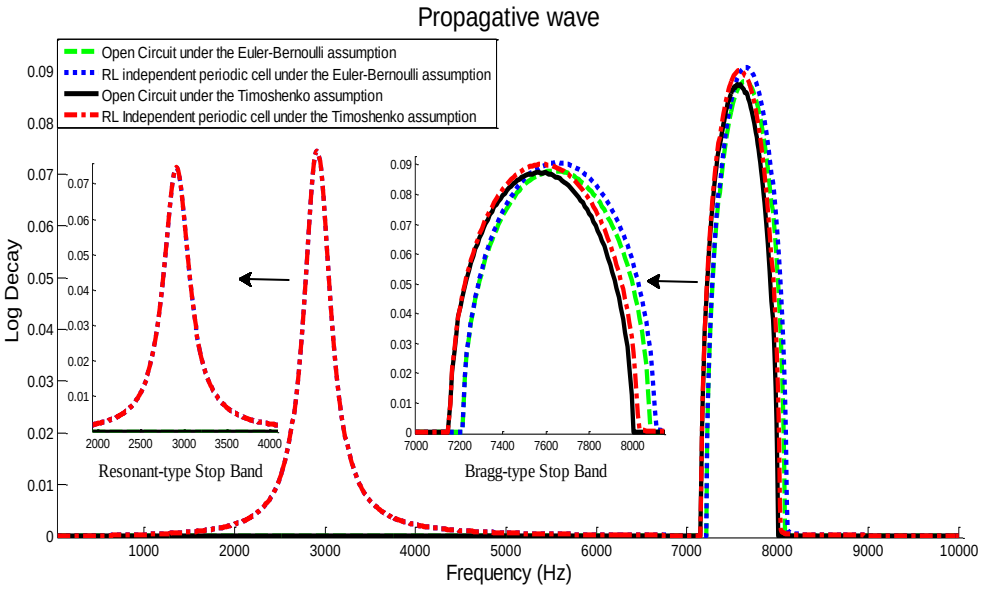

Figure 2.9 A comparison of logarithmic decay of propagative wave in open circuit and RL independent cases under Euler-Bernoulli / Timoshenko beam assumptions.

2.5 Conclusion

In this section, existing FE modeling methodologies of the smart beam structures with SPENs are discussed and divided into two categories: *Z*-determined (impedance-based) FE modeling of smart structures with SPENs and *V*-determined (voltage -based) FE modeling of smart structures with SPENs. The *Z*-determined FE modeling is commonly used for the smart structures with independent shunting SPENs (each PZT is independently connected to a dedicated shunting circuit) since the modeling method can incorporate the effects of external electrical impedances into the calculation of the equivalent modulus of the smart structure component. But this approach is not suitable for taking into account the effects of external interconnected electrical SPENs into the consideration, since the electrical impedances in external complex electrical SPENs may simultaneously affect more than one bonded smart vibrating patch. By comparison, the *V*-determined FE modeling method, which is characterized by the considering the voltage as variable, is more likely able to include the electrical relationships of complex SPENs in the dynamic mechanical equations of

smart structures through the medium of the dynamic electrical equations of smart structures. In addition, a *V*-determined FE modeling method of smart beam structures based on the Timoshenko beam theory is proposed, which is established from two aspects of mechanical and electrical domains. The comparison of this approach with the previously used Euler-Bernoulli assumptions shows that additional assumptions of the transverse shear strain and stress for the FE modeling of smart beam structures benefit the mechanical domain representation, but have no effects on the electrical quantities.

With the development of smart structures with SPENs, especially smart periodic structures, the modeling methods will be more and more diversified not only because of the requirements in terms of characterization of the complexity of multi-layered elastic systems in the mechanical domain, but also due to the requirements of characterizing the electromechanical coupling complexity of the smart structures coupled with multi-layered electrical circuitries in the electric domain. Hence, proper model, chosen in accordance with the computational requirements, complexity and representativeness under the working conditions, is a critical step in the analysis of a given system. Hence, in this chapter, such approaches are reviewed and new ones proposed, with the most proper ones selected as a basis of modeling in the next chapters.

Chapter 3 Smart periodic structure with nonlinear interconnected electrical networks

Abstract

The purpose of this chapter is to give a first architecture of the smart periodic structure with nonlinear interconnected electrical networks. In the investigated electromechanical metamaterial, smart materials offer an interface between the continuous mechanical medium in the form of the purely mechanical part of the structure, and continuous electrical medium in the form of the interconnected nonlinear electrical networks onto the structure. Specifically, section 3.1 introduces the overview of the investigated smart periodic structure. Fundamentals for investigating the structure are provided in section 3.2. By virtue of section 3.2 and chapter 2, finite element modeling for the structure is established in the section 3.3. Then, theoretical discussions on wave propagation properties of the structure are given in the section 3.4 based on the established finite element modeling. Section 3.5 provides the global relationship under given boundary conditions, taking clamped-clamped configuration as a case study, for theoretical frequency response predictions which are validated by experiments in section 3.6. In addition, some extensions of the proposed structure are introduced in section 3.7. Finally, section 3.8 summarizes the obtained results of this chapter.

3.1 Overview of the investigated structure

Based on the initial research on smart periodic structure with nonlinear SSDI interconnected electrical networks which is firstly introduced in Yan's PHD dissertation [109], the structure is further investigated in this chapter. Figure 3.1 (a) shows a beam example of the investigated structure under clamped-clamped boundary condition, in which the electrical load Z represents purely resistive or resonant electronic shunt.

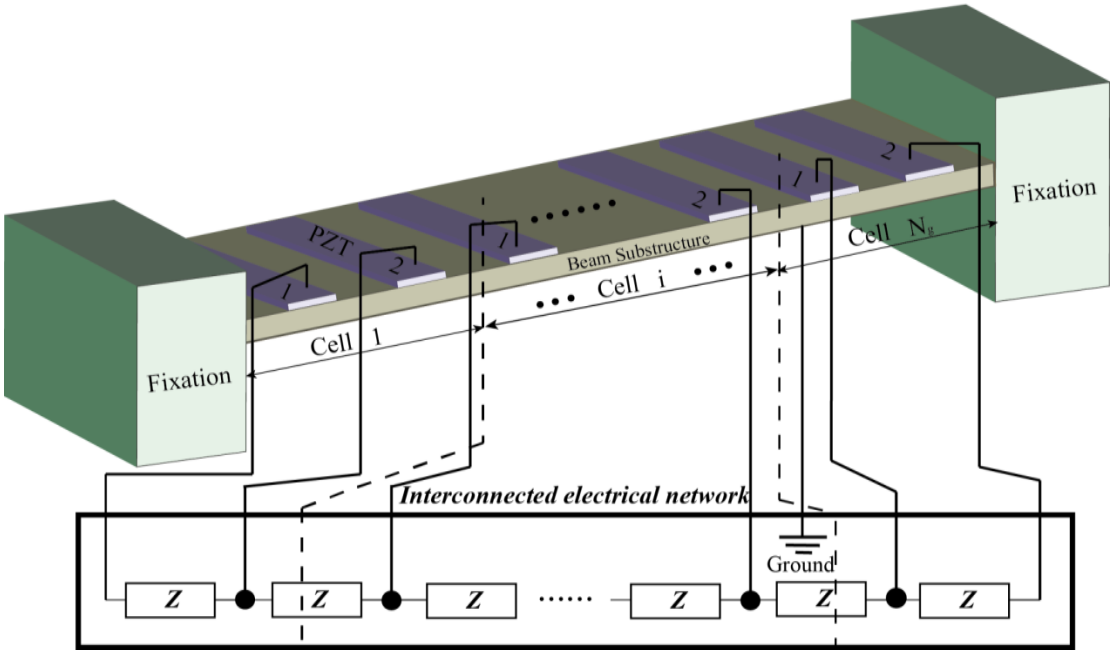

(a)

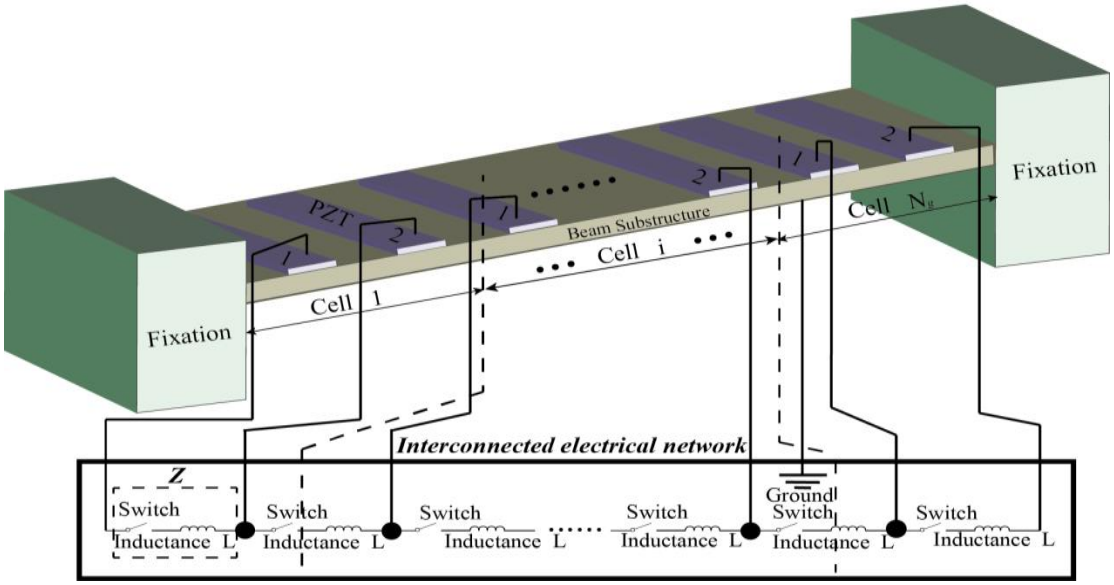

(b)

Figure 3.1 (a) Investigated structure with electrical interconnected networks; (b) Investigated structure with electrical interconnected networks using nonlinear SSDI shunts.

Within a minimal interconnected periodic cell, two PZTs marked 1 and 2 are bonded at different positions, and interconnected with the nonlinear SSDI shunt. Adjacent minimal interconnected periodic cells are also interconnected with the nonlinear SSDI shunt. The deformations and piezoelectric voltages of two PZTs in the minimal interconnected periodic cell are different during the vibration process because of the position difference. Based on the polarization directions of two adjacent PZTs, two configurations of the interconnected periodic cell are proposed, and so-called 'positive-positive (PP)' and 'positive-negative (PN)' configuration. In the PP or PN designs, the polarizations of two adjacent PZTs have same or opposite direction, respectively. Figure 3.1 (b) shows a beam example of the investigated structure using nonlinear SSDI shunts as electrical loads.

3.2 Fundamentals

3.2.1 Principles of the SSDI technique

Two kinds of piezoelectric structures with SSDI shunt damping device are shown in Figure 3.2 (Figure 3.2 (a) for independent connection with a single PZT and Figure 3.2 (b) for interconnected connection with two identical PZTs). The entire SSDI control device is represented schematically in Figure 3.3, which is composed of a switching control module (*e.g.*, self-powered circuit board [34] or semi-active control techniques [32, 308]) and an inductor L connected to one or two PZTs.

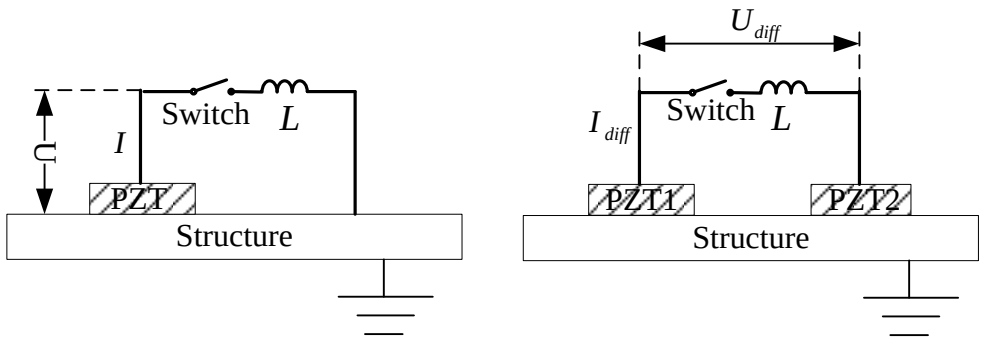

(a) one PZT *(b)* Two PZTs

Figure 3.2 Piezoelectric structures with SSDI control device

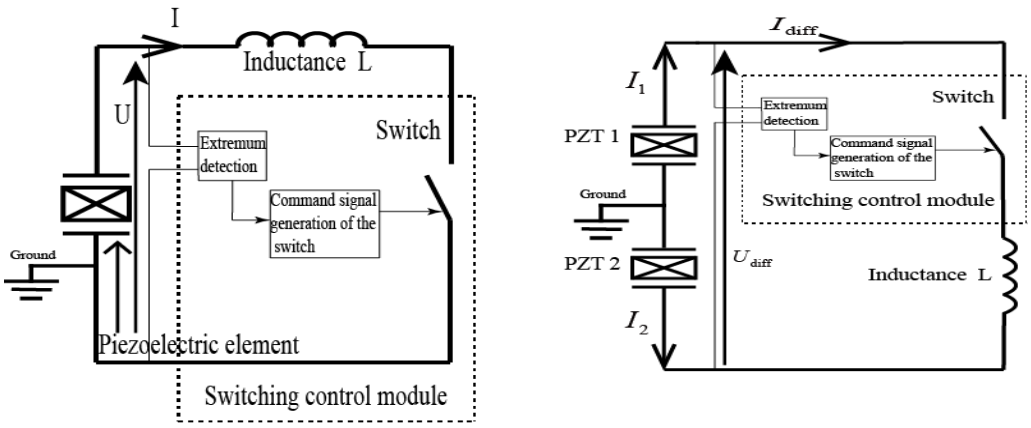

(a) one PZT *(b)* Two PZTs

Figure 3.3 Schematic diagram of the SSDI technique

When a voltage extremum between both ends of the switching interface occurs, the switch will be closed. The inductance L and the capacitance C_0 of the piezoelectric elements then compose an oscillator. The switch is kept closed until the voltage U on the piezoelectric element or the voltage difference U_{diff} between two piezoelectric elements has been reversed. However, the closing duration of the switch is very short compared with the open time of the switch in one mechanical vibration period.

In the case of the piezoelectric structure with independent SSDI control (one PZT) as shown in Figure 3.2 (a), the duration of the closed state t_i is half of the pseudo-period of the *L*-*C* resonant circuit:

$$t_i = \pi\sqrt{LC_0} \tag{3.1}$$

During the closed time of the switch, the voltage between both ends of the switch interface is inverted imperfectly, since the switching network (electronic switch + inductance) dissipates a portion of the energy stored on the inherent capacitance of the piezoelectric element. The energy losses can be characterized by an electrical quality factor Q_e, as follows:

$$Q_e = \frac{1}{r}\sqrt{\frac{L}{C_0}} \tag{3.2}$$

The absolute PZT voltage V_M before the inversion process and the absolute PZT voltage V_m after the inversion process (Figure 3.4(a)) thus have the following relationships:

$$V_m = \gamma_{ind} V_M = V_M e^{-\frac{\pi}{2Q_e}} \tag{3.3}$$

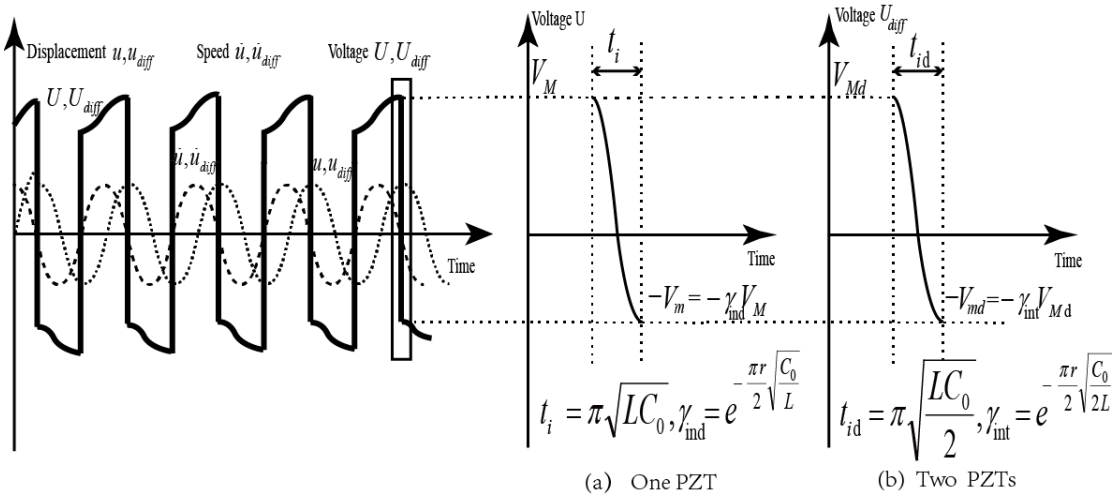

Figure 3.4 Typical waveforms of displacement, speed and voltage in the SSDI control

where γ_{ind} denotes the inversion coefficient for independent SSDI shunt connected to a single PZT and *r* the total resistance of the switching network.

In terms of energy conversion, when the PZT is in open circuit condition, the outgoing piezoelectric current of the PZT is null and the piezoelectric voltage varies proportionally with the displacement as shown in Figure 3.5. Hence, part of the mechanical energy is converted to electrical energy during half a periodic motion, but the electrical energy is then totally converted back to mechanical energy during another half the periodic cycle. Therefore, the total mechanical energy of the electromechanical structure is not decreased and the net converted energy is zero.

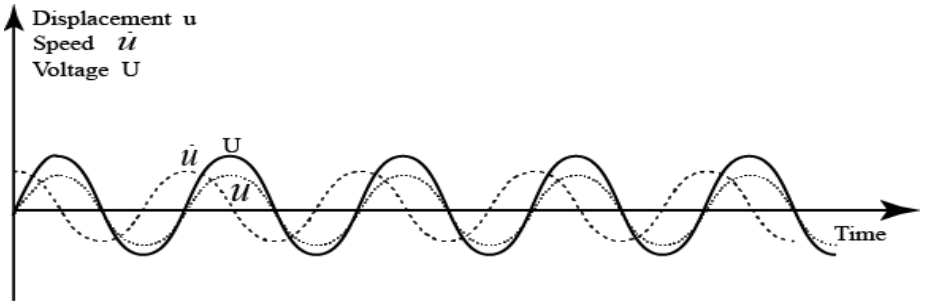

Figure 3.5 Typical waveforms of the electromechanical structure in the open circuit condition.

However, when using the SSDI technique, amplitude amplification and phase shift of the piezoelectric voltage can be realized by the nonlinear process, which results in irreversible energy conversion from mechanical to electrical domain during a periodic motion. More precisely, for a comprehensive understanding, from the aspect of a SDOF spring-mass-damper system, the energy equation of a piezoelectric structure can be obtained over a time window [0, *T*]:

$$\underbrace{\left[\frac{1}{2}M_K\dot{u}^2\right]_{\dot{u}(0)}^{\dot{u}(T)}}_{\text{Kinetic Energy}} + \underbrace{\left[\frac{1}{2}K_E u^2\right]_{u(0)}^{u(T)}}_{\text{Elastic Energy}} + \underbrace{\int_0^T \alpha U\dot{u}dt}_{\text{Converted Energy}} + \underbrace{\int_0^T C_L\dot{u}^2dt}_{\text{Mechanical Losses}} = \underbrace{\int_0^T F\dot{u}dt}_{\text{External Energy}} \tag{3.4}$$

where M_K, K_E and C_L denote the dynamic mass, short-circuit stiffness and structural damping, respectively. α is the force factor and U the piezoelectric voltage. F refers to the external force, u the displacement of the structure, and $\dot{u}$ is the time domain derivative of the displacement (velocity).

As shown in Eq.(3.4), the item entitled 'converted energy' can be modified by external electrical shunts (*e.g.*, purely resistive shunt (*R* shunt), linear resonant shunt (*RL* shunt) or nonlinear SSDI shunt). For the SSDI shunt, the piezoelectric voltage is almost in phase with the velocity, so the integral of the product of the voltage by the velocity is greatly magnified as shown in Eq.(3.4). In other words, during the whole vibration cycle, a part of the mechanical energy is converted into electrical energy in a continuous way.

3.2.2 Electrical synchronized switch impedance estimation

- SSDI impedance estimation for piezoelectric structure with one PZT independently connected to one SSDI control device.

For the structure with one PZT independently connected to one SSDI control device as shown in the Figure 3.2 (a), assuming that the displacement is purely sinusoidal when the SSDI technique is operating in steady state, and the excitation force has an angular frequency ω, the displacement *u(t)* can be expressed by:

$$u(t) = u_M \sin(\omega t + \varphi) \tag{3.5}$$

where u_M is the displacement amplitude.

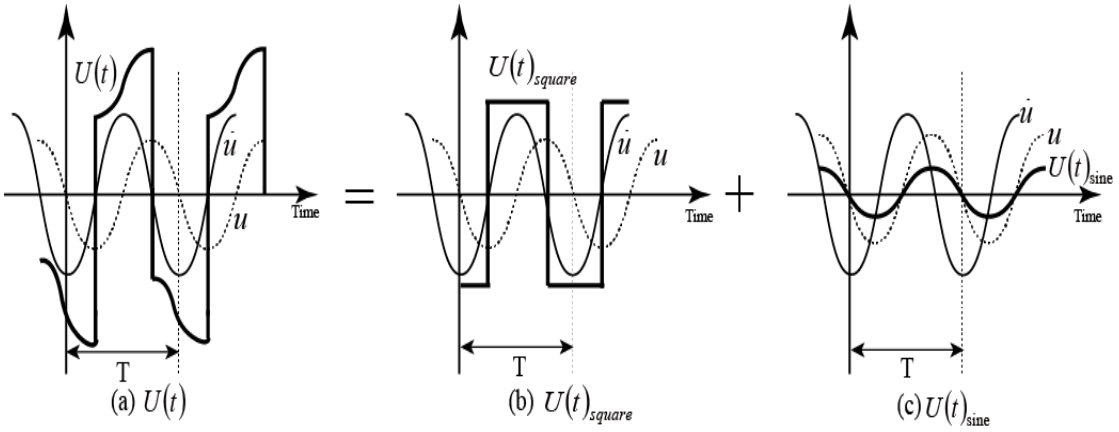

Figure 3.6 Schematic decomposition of the piezoelectric voltage *U(t)* as the sum of two functions $U(t)_{square}$ and $U(t)_{\sin e}$ for the SSDI switch control.

As shown in Figure 3.6, the piezoelectric voltage $U(t)$ can be decomposed into two components $U(t)_{square}$ and $U(t)_{sine}$ which respectively denote a square signal proportional to the sign of the velocity $\dot{u}$ and a sinusoidal signal proportional to the displacement. Specifically, such discontinuous piezoelectric voltage can be expressed as the sum of two functions [75] (the first term is an image of displacement, and the second term is a crenel function):

$$U(t)=U(t)_{sine}+U(t)_{square}=\frac{\alpha}{C_0}u(t)+\frac{\alpha}{C_0}h(t) \tag{3.6}$$

$$h(t)=u_M\frac{1+\gamma_{ind}}{1-\gamma_{ind}}sign(\dot{u}(t)) \tag{3.7}$$

where *h(t)* is the crenel function.

In a periodic motion, the crenel function *h(t)* with the same sign than the velocity, is periodic and can be expressed as Fourier series:

$$h(t)_{Fourier}=u_M\frac{1+\gamma_{ind}}{1-\gamma_{ind}}\sum_{n=0}^{\infty}\left(\frac{4}{\pi(2n+1)}cos\left((2n+1)\omega t+\varphi\right)\right) \tag{3.8}$$

Additionally, the piezoelectric voltage V_M before the switching action and piezoelectric voltage V_m after the switching action have the following relationships:

$$V_M = V_m + \frac{2\alpha}{C_0} u_M \tag{3.9}$$

Furthermore, $h(t)_{Fourier}$ can be simplified with the first harmonic approximation, on the condition that the displacement is assumed to remain sinusoidal. Hence the piezoelectric voltage can be given by:

$$U(t)_{Fourier} = \frac{\alpha}{C_0} u_M \left(\sin(\omega t + \varphi) + \frac{1+\gamma_{ind}}{1-\gamma_{ind}} \frac{4}{\pi} \cos(\omega t + \varphi) \right) \tag{3.10}$$

Since the switch closed time t_i is much smaller than the structural vibration period T_{period} (normally it is roughly between 1/20 and 1/50 of T_{period} [110]), when the switch is closed, the displacement and velocity of the structure can be considered as constant during the period. Therefore, the periodic discontinuous current flowing through the closed switch can be written as:

$$I(t) = -C_0 \frac{dU(t)}{dt} = C_0 (V_m + V_M) \sum_{n=-\infty}^{\infty} \delta\left(t - \frac{T_{period}}{4} - n\frac{T_{period}}{2} \right) \tag{3.11}$$

with $\delta(x)$ referring to the Delta function of the variable x. If Eq.(3.3) and Eq.(3.9) are inserted into Eq.(3.11), the later can also be written as:

$$I(t) = 2\alpha u_M \frac{1+\gamma_{ind}}{1-\gamma_{ind}} \sum_{n=-\infty}^{\infty} \delta\left(t - \frac{T_{period}}{4} - n\frac{T_{period}}{2} \right) \tag{3.12}$$

Then, the current $I(t)$ can be approximated by its first harmonic:

$$I(t)_{Fourier} = 2\alpha u_M \frac{1+\gamma_{ind}}{1-\gamma_{ind}} \frac{2\omega}{\pi} \cos\left(\omega t - \frac{\pi}{2} \right) = 4\alpha u_M \frac{1+\gamma_{ind}}{1-\gamma_{ind}} \frac{\omega}{\pi} \sin(\omega t) \tag{3.13}$$

Furthermore, assuming that the functions $\sin(\omega t)$, $\cos(\omega t)$ in the frequency domain can respectively be given by $g(\omega)$ and $jg(\omega)$, the piezoelectric voltage $U(t)_{Fourier}$ and piezoelectric current $I(t)_{Fourier}$ in the frequency domain can thus respectively be written as:

$$U(\omega) = \frac{\alpha}{C_0} u_M \left(1 + \frac{1+\gamma_{ind}}{1-\gamma_{ind}} \frac{4j}{\pi} \right) g(\omega) \tag{3.14}$$

$$I(\omega) = 4\alpha u_M \frac{1+\gamma_{ind}}{1-\gamma_{ind}} \frac{\omega}{\pi} g(\omega) \tag{3.15}$$

Therefore, the equivalent electrical impedance of an independent SSDI control device connected to a single PZT on the structure yields:

$$Z_{ind}^{SSDI}(\omega) = \frac{U(\omega)}{I(\omega)} = \frac{\pi(1-\gamma_{ind})}{4\omega C_0(1+\gamma_{ind})} + \frac{j}{\omega C_0} \tag{3.16}$$

- Equivalent circuit of the piezoelectric structure with two PZTs connected to one SSDI control

In the case of the structure with two PZTs connected to one SSDI control device as shown in Figure 3.4 (b), the two inserts and the associated circuit can be equivalently seen as an independent current source in parallel with an equivalent impedance according to Norton's theorem in the closed state depicted in Figure 3.7. By removing the current sources and replacing them with open circuit state, the equivalent capacitance of the two PZTs is obtained as:

$$C_{equivalent} = \frac{C_0}{2} \tag{3.17}$$

Therefore, similarly, the duration of the switching event t_{id} can be given by:

$$t_{id} = \pi\sqrt{LC_{equivalent}} = \pi\sqrt{L\frac{C_0}{2}} \tag{3.18}$$

The relationship between the equivalent factor Q_d and the voltage difference of two PZTs before (V_{Md}) and after (V_{md}) the inversion process can also be given by:

$$Q_d = \frac{1}{r}\sqrt{\frac{L}{C_{equivalent}}} \tag{3.19}$$

$$V_{md} = \gamma_{\text{int}} V_{Md} = V_{Md} e^{-\frac{\pi}{2Q_d}} \tag{3.20}$$

where γ_{int} denotes the inversion coefficient for the SSDI shunt connected between two PZTs.

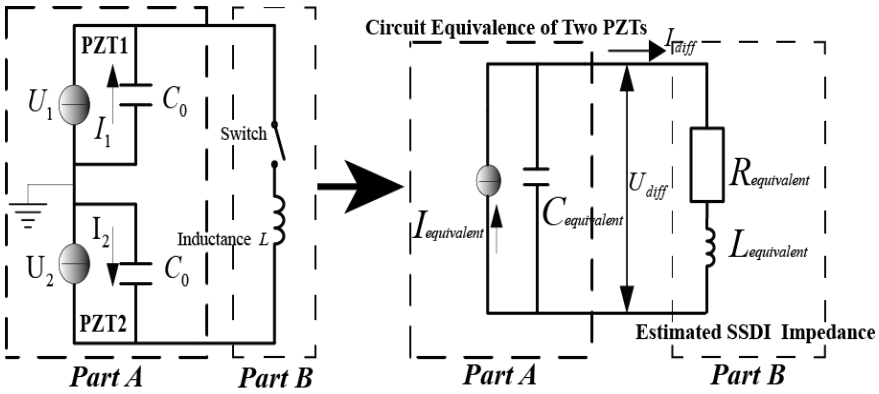

Figure 3.7 Equivalent circuit of two PZTs with SSDI control device on the piezoelectric structure.

- SSDI impedance estimation for piezoelectric structure with two PZTs connected to one SSDI control device.

For the structure with two PZTs connected through one SSDI control device as shown in Figure 3.2 (b), the displacement difference u_d between the displacement u_1 of one PZT and the displacement u_2 of the other one can be expressed by:

$$u_d(\mathrm{t}) = u_1(t) - u_2(t) = u_{Md}\sin(\omega t + \theta) \tag{3.21}$$

where u_{Md} denotes the amplitude of the displacement difference.

When the switch is open, the voltages $U_1(t), U_2(t)$ of two PZTs are given by:

$$U_1(t) = \frac{\alpha}{C_0}u_1(t), U_2(t) = \frac{\alpha}{C_0}u_2(t) \tag{3.22}$$

Hence, the voltage difference $U_{diff}(t)$ can be obtained as:

$$U_{diff}(t) = U_1(t) - U_2(t) = \frac{\alpha}{C_0}u_d(t) = \frac{\alpha}{C_0}u_{Md}\sin(\omega t + \theta) \tag{3.23}$$

When the SSDI control device is operating in steady state, the voltage difference $U_{diff}(t)$ and the current $I_{diff}(t)$ flowing through the closed switch, can be obtained as:

$$U_{diff}(t) = \frac{\alpha}{C_0}u_d(\mathrm{t}) + \frac{\alpha}{C_0}h_d(t) \tag{3.24}$$

$$h_d(t) = u_{Md} \frac{1+\gamma_{\text{int}}}{1-\gamma_{\text{int}}} sign\left(\dot{u}_d(t)\right) \tag{3.25}$$

$$I_{diff}(t) = -C_{equivalent} \frac{dU_{diff}(t)}{dt} \tag{3.26}$$

The relationships between the piezoelectric voltage V_{Md} before the switching action and the piezoelectric voltage V_{md} after the switching action, as shown in Figure 3.4 (b), can be given as:

$$V_{Md} = V_{md} + \frac{2\alpha}{C_0} u_{Md} \tag{3.27}$$

The function $h_d(t)$ can then be expressed as Fourier series:

$$h_d(t)_{Fourier} = u_{Md} \frac{1+\gamma_{\text{int}}}{1-\gamma_{\text{int}}} \sum_{n=0}^{\infty} \left(\frac{4}{\pi(2n+1)} cos\left((2n+1)\omega t + \theta\right) \right) \tag{3.28}$$

Similarly, according to first harmonic approximation, voltage difference $U_{diff}(t)$ and current $I_{diff}(t)$ after simplification can be written in the frequency domain as:

$$U_{diff}(\omega) = \frac{\alpha}{C_0} u_{Md} \left(1 + \frac{1+\gamma_{\text{int}}}{1-\gamma_{\text{int}}} \frac{4j}{\pi} \right) g(\omega) \tag{3.29}$$

$$I_{diff}(\omega) = 2\alpha u_{Md} \frac{1+\gamma_{\text{int}}}{1-\gamma_{\text{int}}} \frac{\omega}{\pi} g(\omega) \tag{3.30}$$

The equivalent electrical impedance Z_{int}^{SSDI} of the SSDI shunt between two PZTs on the structure can then be obtained as:

$$Z_{\text{int}}^{SSDI}(\omega) = \frac{U_{diff}(\omega)}{I_{diff}(\omega)} = \frac{\pi(1-\gamma_{\text{int}})}{2\omega C_0(1+\gamma_{\text{int}})} + \frac{2j}{\omega C_0} \tag{3.31}$$

Since the second items $\frac{j}{\omega C_0}$ (in Eq.(3.16)) and $\frac{2j}{\omega C_0}$ (in Eq.(3.31)) correspond to optimized inductance values for each angular frequency ω [94], the SSDI shunt has an interesting talent of automatic impedance adaptation with a small inductance, which provides a semi-passive technique [34] for avoiding the utilization of active synthetic

inductors to realize large inductance for low-frequency resonant vibration control and automatic modal adaptation. Furthermore, the real parts of the equivalent impedances only depend on frequency, clamped capacitance and inversion coefficient in both cases.

Similarly, the inversion coefficient γ_{int} can be given as:

$$\gamma_{\text{int}} = e^{-\frac{\pi}{2Q}} = e^{-\frac{r\pi}{2}\sqrt{\frac{C_{equivalent}}{L}}} \tag{3.32}$$

where *r* is the resistance of the switching network.

Thus, the relationship between γ_{ind} and γ_{int} holds:

$$\gamma_{\text{int}} = e^{-\frac{r\pi}{2}\sqrt{\frac{C_0}{2L}}} = \gamma_{ind}^{\sqrt{\frac{1}{2}}} > \gamma_{ind} \tag{3.33}$$

Therefore, since the equivalent capacitance in the interconnected SSDI case is less than that in the independent case, the corresponding inversion coefficient γ_{int} is greater than γ_{Ind}.

For piezoelectric structures, the physical properties of a vibration control system can be modified by the use of arbitrary electrical impedance connected across two electrodes of PZTs [15]. For instance, the effect of external electrical network on the elastic modulus of the shunted patch E_p^{SU} can be simplified as [309]:

$$E_p^{SU} = \frac{E_p^E\left(j\omega C_0 + Y^{SU}\right)}{j\omega C_0\left(1-k_{31}^2\right)+Y^{SU}} \tag{3.34}$$

where E_p^E is the elastic modulus of the PZT in short circuit, $Y^{SU} = \frac{1}{Z}$, with *Z* the electrical impedance of the shunt branch in the electrical damping networks, and k_{31} is the electromechanical coupling coefficient for transverse operation [13].

As it can be seen from Eq.(3.34), electrical impedance affects the elastic modulus of the PZT. Since the elastic modulus ratio between the structure's segments with PZTs and the structure's segments without PZTs in a periodic cell influences the bandwidth and location of band gaps of periodic structures, different electrical impedances will induce various band gaps. Therefore, the SSDI electrical synchronized switch

impedances applied to periodic structures may contribute to band gaps tuning for low-frequency efficient vibration reduction.

3.2.3 Stability analysis of electrical SSDI shunts

As for smart periodic structures with electrical shunting networks, stability of electrical networks is significant for achieving wave propagation control. Some unwanted aperiodicities induced by the instabilities of electrical networks can easily lower the control performance unless some aperiodicities are intentionally induced by electrical networks for improving the control performance. Compared with active control strategies, the stability of passive or semi-passive shunting circuits is more easily guaranteed since no energy is externally provided to the piezoelectric element. Nevertheless, there are still risks leading to system instability in some semi-passive / semi-active shunting techniques such as negative capacitance.

Herein, the nonlinear SSDI shunt independently connected to one PZT can be simply treated as a linear series *RLC* circuit ($R_{independent}$, $L_{independent}$, $C_{independent}$) in the frequency domain under the condition of the first harmonic approximation, as follows:

$$\begin{cases} C_{independent} = C_0, L_{independent} = \dfrac{1}{\omega^2 C_0} \\ R_{independent} = \dfrac{\pi\left(1-\gamma_{ind}\right)}{4\omega C_0\left(1+\gamma_{ind}\right)} \end{cases} \tag{3.35}$$

Similarly, the nonlinear SSDI shunt between two PZTs can be simply regarded as a linear series *RLC* circuit ($R_{equivalent}$, $L_{equivalent}$, $C_{equivalent}$, as shown in the Part B of Figure 3.7), as follows:

$$\begin{cases} C_{equivalent} = \dfrac{C_0}{2}, L_{equivalent} = \dfrac{2}{\omega^2 C_0} \\ R_{equivalent} = \dfrac{\pi\left(1-\gamma_{\text{int}}\right)}{2\omega C_0\left(1+\gamma_{\text{int}}\right)} \end{cases} \tag{3.36}$$

Therefore, the equivalent damping ratio of above-mentioned simplified resonant circuit systems can be respectively given as:

$$\begin{cases} \zeta_{independent} = \dfrac{R_{independent}}{2}\sqrt{\dfrac{C_{independent}}{L_{independent}}} = \dfrac{\pi(1-\gamma_{ind})}{8(1+\gamma_{ind})} & (0 \le \gamma_{ind} < 1) \\ \zeta_{equivalent} = \dfrac{R_{equivalent}}{2}\sqrt{\dfrac{C_{equivalent}}{L_{equivalent}}} = \dfrac{\pi(1-\gamma_{\mathrm{int}})}{8(1+\gamma_{\mathrm{int}})} & (0 \le \gamma_{\mathrm{int}} < 1) \end{cases} \tag{3.37}$$

According to the above equation, the equivalent damping ratio $\zeta_{equivalent}$ of the SSDI shunt between two PZTs and the equivalent damping ratio $\zeta_{independent}$ of the SSDI shunt independently connected to one PZT are located in the value domain: $\zeta_{equivalent}, \zeta_{independent} \in \left[0,\ \dfrac{\pi}{8}\right]$, and therewith such electronic SSDI nonlinear resonant systems are underdamped and have high stabilities.

3.2.4 Physical principles of the investigated structure

Figure 3.8 depicts a bending beam periodic cell of a smart periodic structure with interconnected electrical networks in different vibration frequency ranges. Specifically, when the structure vibrates in the low frequency domain, the voltage difference between the two PZTs with the PN interconnection is greater than that with the PP interconnection due to opposite polarization directions and same strain directions of the two PZTs (Figure 3.8.a1 and Figure 3.8.a2), while when the structure vibrates in a high frequency domain, the voltage difference with the PP interconnection is higher than that with the PN interconnection (Figure 3.8.b1 and Figure 3.8.b2), since polarization directions are the same while the strain directions are opposite.

On the basis of the previous periodic beam cell bending description and Eq.(3.4), it can be seen that the greater voltage difference between two PZTs, the better wave attenuation performance of the nonlinear SSDI process. Hence, performance of PN interconnection and PP interconnection is expected to be different according to the wavelength (and thus excitation frequency). More particularly, in the case of large

wavelengths, PN method is expected to show better wave attenuation than PP method, while the latter is expected to have higher damping capabilities in the case of short wavelengths.

Therefore, both of interconnected methods are suitable for vibration reduction, but aim at different frequency ranges. A 'critical frequency point' may also be expected between low frequency domain and high frequency domain where the same wave attenuation performance is achieved by using PP interconnected method and PN interconnected method.

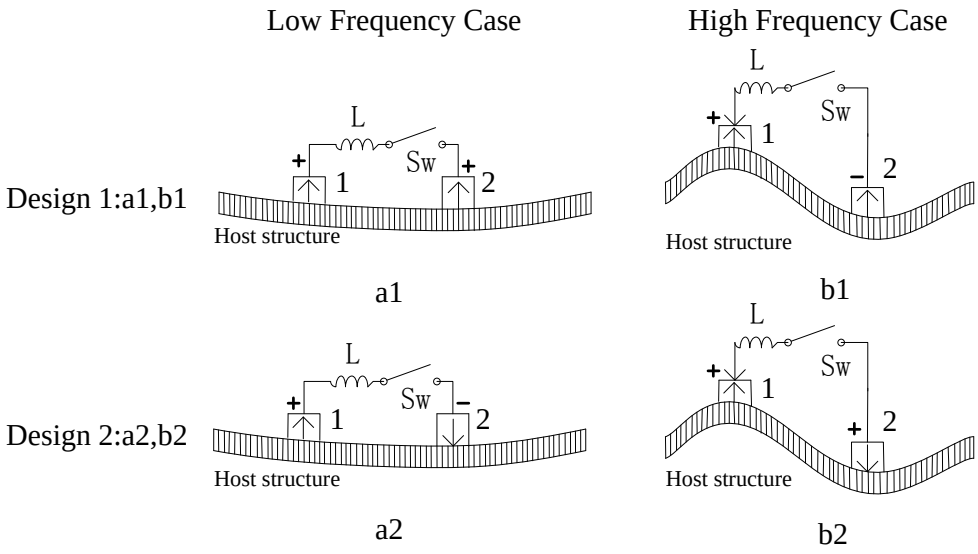

Figure 3.8 Periodic bending beam cell in different frequency cases.

Herein, performance of the investigated structure arises from two effects: the first one lies in the SSDI technique, which allows a much better mechanical to electrical energy conversion (then dissipated in the switching shunt branches) equivalent to an additional damping from a mechanical point of view. The second origin lies in the

unique characteristics of periodic structures, where the periodic arrangement allows the appearance of band gaps where energy is prevented from entering into the structure. Therefore, two vibration reduction mechanisms of PP / PN interconnections benefit from the interaction of above damping effects.

3.3 Modeling of the investigated structure based on Euler-Bernoulli beam theory

3.3.1 Electromechanical relationships of an interconnected periodic cell

The dynamic behavior of each periodic cell (Figure 3.9) and global transfer matrix of the investigated periodic structure (Figure 3.1) are modeled and established using finite element (FE) method in this subsection. Global frequency responses of the structure are finally obtained by combination of the transfer matrices.

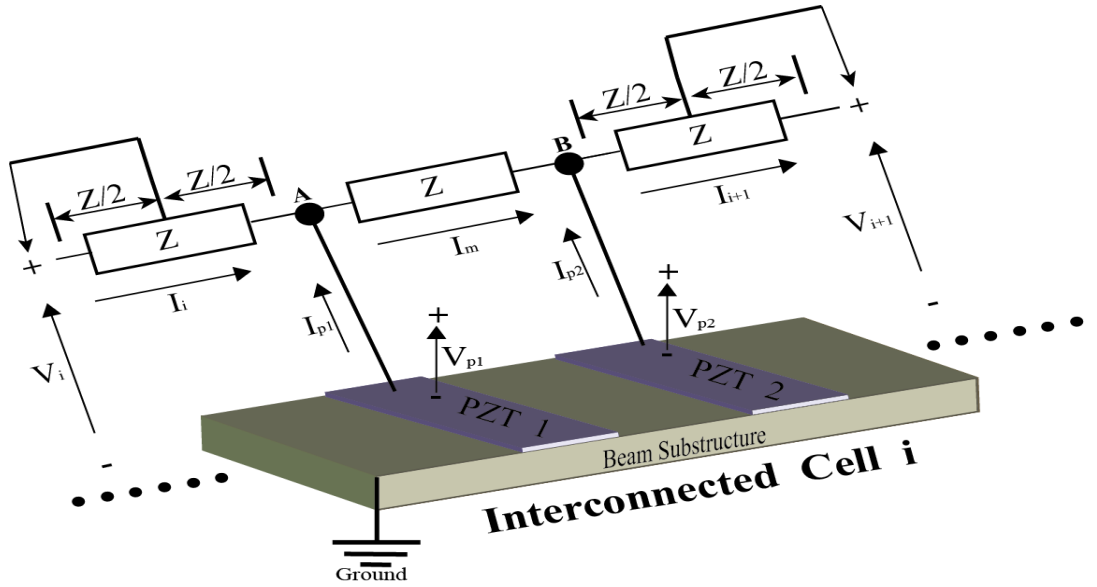

(a)

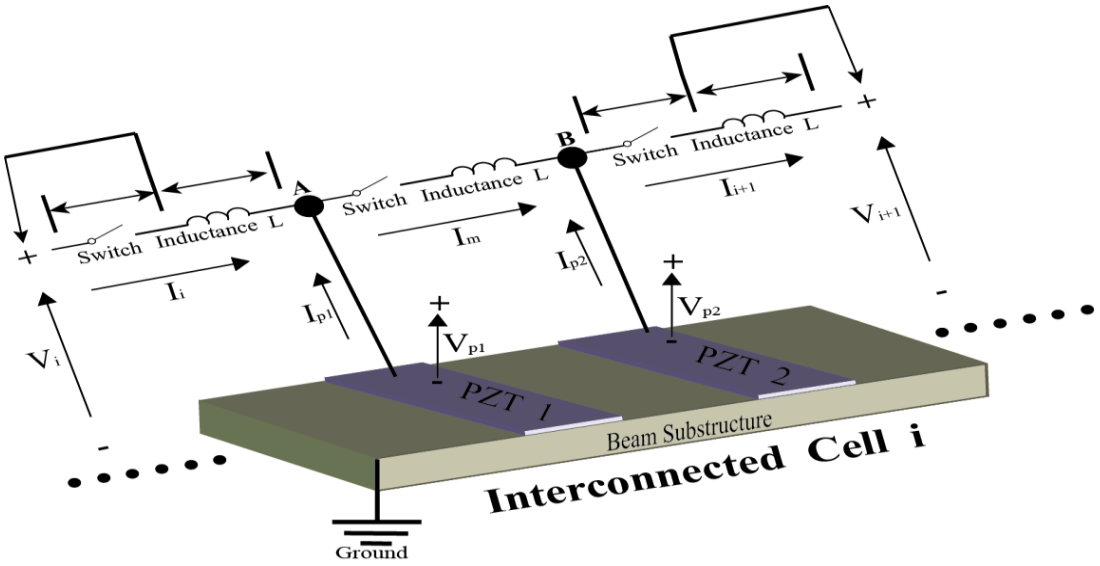

(b)

Figure 3.9 (a) A periodic cell in the investigated structure, *Z* denotes the electrical impedance; (b) application to the SSDI interconnection.

Supposing the investigated periodic structure satisfies Euler-Bernoulli beam assumptions and is composed of N_g cells, each periodic cell of the investigated

structure can be divided into *n* Euler-Bernoulli elements modeled by a two-node beam element. Two PZTs are implemented in the interconnected periodic cell.

According to FE modeling considering Euler-Bernoulli beam introduced in the section 2.2 of Chapter 2, the electro-elastic relationships of a smart bending beam under external excitation can be summarized as:

$$\begin{cases} \left[M^e\right]\left\{\ddot{d}^i\right\}+\left[C^e\right]\left\{\dot{d}^i\right\}+\left[K^e\right]\left\{d^i\right\}+\left[B_1^e\right]\left\{V_p^i\right\}=\left\{P^i\right\} \\ \left\{Q^i\right\}=\left[B_2^e\right]\left\{d^i\right\}+\left[B_3^e\right]\left\{V_p^i\right\} \end{cases} \tag{3.38}$$

with dynamic matrices M^e, K^e and C^e representing the mass, short-circuit stiffness and structural damping (*e.g*, Rayleigh damping with $C^e=\beta_1 M^e+\beta_2 K^e$). Superscript i denotes the i^{th} periodic cell and e denotes the unit beam element. d^i and P^i are $2(n+1)$ by 1 matrices which respectively refer to displacement, slope vector, and force, moment vector of all the nodes. V_p^i and Q^i with size of 2 by 1 denote the output voltage and electrical charge of two PZTs. B_1^e is a $2(n+1)$ by 2 matrix relating to the electromechanical conversion, obtained by:

$$B_1^e=\left[B_{11}\ B_{12}\right],$$

$$\begin{cases} B_{11}=b_{11}\int_0^l\left[H''\right]^T dx, \quad b_{11}=-\dfrac{p_1 d_{31} w_b}{t_p\left(s_{11}^E+s_{12}^E\right)}\int_{t_b}^{t_b+t_p}\left(u_3-x_c\right)dx_3 \\ B_{12}=b_{12}\int_0^l\left[H''\right]^T dx, \quad b_{12}=-\dfrac{p_2 d_{31} w_b}{t_p\left(s_{11}^E+s_{12}^E\right)}\int_{t_b}^{t_b+t_p}\left(u_3-x_c\right)dx_3 \end{cases}$$

where H'' is the second order derivative of Hermitian shape functions. $p_{1,2}$ are the signs of piezoelectric constant depending on the direction of polarization of two PZTs 1, 2 in the interconnected periodic cell. Specifically, it is assumed equal to 1 when the direction is positive (P) and -1 when it is negative (N). d_{31} is given as the piezoelectric charge coefficient and s_{ij}^E are the elastic constants under constant electric field. w_b, t_b and t_p respectively refer to the width and thickness of the

structure, and thickness of the PZT. Finally, u_3 denotes the displacement along the axis 3 and x_c the neutral axis position. The other electromechanical coupling matrix B_2^e, with size 2 by $2(n+1)$ and representing the mechanical to electrical energy conversion, can be expressed by:

$$B_2^e = \begin{bmatrix} B_{21} \\ B_{22} \end{bmatrix}, \quad \begin{cases} B_{21} = b_{21} \int_0^l [H''] dx, \quad b_{21} = -\dfrac{p_1 d_{31} t_p}{\left(s_{11}^E + s_{12}^E\right)} \\ B_{22} = b_{22} \int_0^l [H''] dx, \quad b_{22} = -\dfrac{p_2 d_{31} t_p}{\left(s_{11}^E + s_{12}^E\right)} \end{cases}$$

Finally, B_3^e denotes the inherent capacitance of the PZTs and can be calculated in the following forms:

$$B_3^e = \begin{bmatrix} B_{31} & 0 \\ 0 & B_{32} \end{bmatrix}, \quad B_{31} = B_{32} = \frac{w_b L_p \left[\varepsilon_{33}^T \left(s_{11}^E + s_{12}^E\right) - 2d_{31}^2 \right]}{t_p \left(s_{11}^E + s_{12}^E\right)}$$

with ε_{33}^T the electrical permittivity under constant stress and L_p the length of a piezoelectric patch.

Rearranging the equations, the electrical relationship and the dynamical motion relationship of one smart periodic cell can also be obtained in frequency domain as:

$$\begin{cases} P^i = A^e \cdot d^i + B_1^e \cdot V_p^i \\ I_p^i = j\omega B_2^e \cdot d^i + j\omega B_3^e \cdot V_p^i \end{cases} \tag{3.39}$$

with A^e ($A^e = -\omega^2 M^e + j\omega C^e + K^e$) the dynamic stiffness matrix of the system and ω the angular frequency. I_p denotes the output current of the PZTs in the periodic cell.

Simplifying the dynamical relationships of the electromechanical periodic cell, the voltage equation of the piezoelectric element can be written as:

$$\left[A_{case}^e\right]\left\{d^i\right\} = \left\{P^i\right\} \tag{3.40}$$

where $\left[A_{case}^e\right]$ is equal to $[A_{short}], [A_{open}], \left[A_{ind}^{passive}\right], \left[A_{ind}^{SSDI}\right]$ (respectively denoting

short circuit condition, open circuit condition, purely resistive (or linear resonant) shunt control and independent SSDI interface), according to the following electrical conditions:

$$A_{short} = A^e;$$

$$A_{open} = A^e + B_1^e \cdot B_4^e, \quad B_4^e = \begin{bmatrix} B_{41} \\ B_{42} \end{bmatrix}, \quad B_{41,42} = b_{41,42} \int_0^l [H''] dx, \quad b_{41,42} = \frac{d_{31} t_p^{\,2}}{L_p \left[\dot{o}_{33}^T \left(s_{11}^E + s_{12}^E \right) - 2 d_{31}^2 \right]};$$

$$A_{ind}^{passive} = A^e + B_1^e \cdot B_5^e, \quad B_5^e = \begin{bmatrix} B_{51} \\ B_{52} \end{bmatrix}, \quad B_{51,52} = \frac{j\omega Z_{ind}^{passive} \cdot B_{21,22}}{\left(1 - j\omega Z_{ind}^{passive} \cdot B_{31,32} \right)};$$

$$A_{ind}^{SSDI} = A^e + B_1^e \cdot B_6^e, \quad B_6^e = B_4^e \left(1 + \frac{1+\gamma_{ind}}{1-\gamma_{ind}} \cdot \frac{4j}{\pi} \right) \quad or \quad \frac{j\omega Z_{ind}^{SSDI} \cdot B_{21,22}}{\left(1 - j\omega Z_{ind}^{SSDI} \cdot B_{31,32} \right)}.$$

For the interconnected case (Figure 3.9) in the i^{th} periodic cell, $V_{p1,p2}$ and $I_{p1,p2}$ are the output voltages and currents of piezoelectric patches *1, 2* which are connected through the electrical load *Z*. I_m is the current through the load *Z*. $V_{i,i+1}$ and $I_{i,i+1}$ are the voltages and currents of the two-port network of the interconnected periodic cell. Then the following relationships of the periodic cell can be established:

$$V_i - \frac{Z}{2} \cdot I_i = V_{p1} \tag{3.41}$$

$$V_{p1} - Z \cdot I_m = V_{p2} \tag{3.42}$$

$$I_i + I_{p1} = I_m \tag{3.43}$$

$$V_{p2} - \frac{Z}{2} \cdot I_{i+1} = V_{i+1} \tag{3.44}$$

$$I_{p2} + I_m = I_{i+1} \tag{3.45}$$

$$P^i = A^e \cdot d^i + B_1^e \cdot V_p \tag{3.46}$$

$$I_p = B_2^e \cdot \dot{d}^i + B_3^e \cdot \dot{V}_p \tag{3.47}$$

$$I_p = \begin{bmatrix} I_{p1} \\ I_{p2} \end{bmatrix}; V_p = \begin{bmatrix} V_{p1} \\ V_{p2} \end{bmatrix}, Z = \begin{cases} Z_{\text{int}}^{passive}, & \text{for the purely resistive or linear resonant shunt;} \\ Z_{\text{int}}^{SSDI}, & \text{for the nonlinear SSDI shunt.} \end{cases}$$

Considering similar PZTs (so that $B_{31}=B_{32}$), dynamical responses for the interconnected periodic cells can be summarized as:

$$\begin{Bmatrix} P^i \\ V_{i+1} \\ I_{i+1} \end{Bmatrix} = A_{\text{interconnected}} \cdot \begin{Bmatrix} d^i \\ V_i \\ I_i \end{Bmatrix} = \begin{bmatrix} A_{11} & A_{12} & A_{13} \\ A_{21} & A_{22} & A_{23} \\ A_{31} & A_{32} & A_{33} \end{bmatrix} \cdot \begin{Bmatrix} d^i \\ V_i \\ I_i \end{Bmatrix} \tag{3.48}$$

$$\begin{aligned}
A_{11} &= A^e - Z \cdot B_{21} \cdot B_{12} \cdot j\omega; \\
A_{12} &= B_{11} + B_{12} - Z \cdot B_{12} \cdot B_{31} \cdot j\omega; \\
A_{13} &= -\left(\frac{Z}{2} \cdot B_{11} + \frac{3Z}{2} \cdot B_{12} \right) + \frac{Z^2}{2} \cdot B_{12} \cdot B_{31} \cdot j\omega; \\
A_{21} &= -\omega^2 \cdot \frac{Z^2}{2} \cdot B_{31} \cdot B_{21} - \frac{Z}{2} \cdot B_{22} \cdot j\omega - \frac{3}{2} Z \cdot B_{21} \cdot j\omega; \\
A_{22} &= 1 - \frac{Z^2}{2} \cdot B_{31}^2 \cdot \omega^2 - 2Z \cdot B_{31} \cdot j\omega; \\
A_{23} &= \frac{3}{2} Z^2 \cdot B_{31} \cdot j\omega - 2Z + \frac{Z^3}{4} \cdot B_{31}^2 \cdot \omega^2; \\
A_{31} &= \omega^2 \cdot Z \cdot B_{32} \cdot B_{21} + B_{22} \cdot j\omega + B_{21} \cdot j\omega; \\
A_{32} &= Z \cdot B_{31}^2 \cdot \omega^2 + 2B_{31} \cdot j\omega; \\
A_{33} &= 1 - 2Z \cdot B_{31} \cdot j\omega - \frac{Z^2}{2} \cdot B_{31}^2 \cdot \omega^2.
\end{aligned}$$

Compared to Eq.(3.40), there are another two parameters in Eq.(3.48), namely the voltage and current, from which it can be inferred that the dynamical responses in the interconnected case can be controlled by using an electrical method.

3.3.2 Transfer matrix formulations between periodic cells

The transfer matrix linking the displacements and forces on both sides of a periodic cell based on its dynamical relationships is introduced in this subsection. According to electrical boundary conditions of the periodic cell, two kinds of transfer matrix formulations are discussed as follows.

- Transfer matrix formulations between independent periodic cells.

For transfer matrix formulations between independent periodic cells, schematics of purely mechanical beam structure and smart periodic beam structure with independent electrical networks (electrical boundary conditions are closed in the periodic cell) are shown in Figure 3.10. The generalized nodal displacement vectors (the displacement

and rotation vectors in the frequency domain) $\left\{d^i\right\}$ and generalized nodal forces vectors (the force and moment vectors in the frequency domain) $\left\{P^i\right\}$ are propagated among adjacent periodic cells. $d_L^i\left(=d_0^i\right), P_L^i\left(=P_0^i\right), d_R^i\left(=d_n^i\right), P_R^i\left(=P_n^i\right)$ are respectively the generalized displacements and generalized forces vectors at the left-end node and the right-end node of any mechanical periodic cell *i*. According to the vibration propagation direction as shown in Figure 3.10, $d_n^i = d_0^{i+1}, P_n^i = -P_0^{i+1}$.

The form of Eq.(3.40) can be rearranged by separation of extreme vectors from internal vectors of a periodic cell:

$$\begin{Bmatrix} P_0^i \\ P_j^i \\ P_n^i \end{Bmatrix} = \left[A_{ind}\right] \cdot \begin{Bmatrix} d_0^i \\ d_j^i \\ d_n^i \end{Bmatrix} = \begin{bmatrix} a_{00} & a_{0j} & a_{0n} \\ a_{j0} & a_{jj} & a_{jn} \\ a_{n0} & a_{nj} & a_{nn} \end{bmatrix} \cdot \begin{Bmatrix} d_0^i \\ d_j^i \\ d_n^i \end{Bmatrix}, A_{ind} = A_{case}^e \tag{3.49}$$

Supposing there is no external load (moment and force) applied within the cell, according to Guyan's reduction, expressions of the dynamic response of one electromechanical periodic cell can be simplified as:

$$\begin{Bmatrix} P_0^i \\ P_n^i \end{Bmatrix} = \begin{bmatrix} \alpha_{11} & \alpha_{12} \\ \alpha_{21} & \alpha_{22} \end{bmatrix} \cdot \begin{Bmatrix} d_0^i \\ d_n^i \end{Bmatrix} \tag{3.50}$$

where

$$\alpha_{11} = a_{00} - a_{0j}a_{jj}^{-1}a_{j0}; \quad \alpha_{12} = a_{0n} - a_{0j}a_{jj}^{-1}a_{jn};$$
$$\alpha_{21} = a_{n0} - a_{nj}a_{jj}^{-1}a_{j0}; \quad \alpha_{22} = a_{nn} - a_{nj}a_{jj}^{-1}a_{jn}.$$

Therefore, the transfer matrix of the periodic cell *T* can be written as [108]:

$$\begin{Bmatrix} d_n^i \\ P_n^i \end{Bmatrix} = T \cdot \begin{Bmatrix} d_0^i \\ P_0^i \end{Bmatrix} = \begin{bmatrix} t_{11} & t_{12} \\ t_{21} & t_{22} \end{bmatrix} \cdot \begin{Bmatrix} d_0^i \\ P_0^i \end{Bmatrix} \tag{3.51}$$

$$t_{11} = -\alpha_{12}^{-1}\alpha_{11}, \quad t_{12} = \alpha_{12}^{-1}, \quad t_{21} = -\alpha_{21} + \alpha_{22}\alpha_{12}^{-1}\alpha_{11}, \quad t_{22} = -\alpha_{22}\alpha_{12}^{-1}.$$

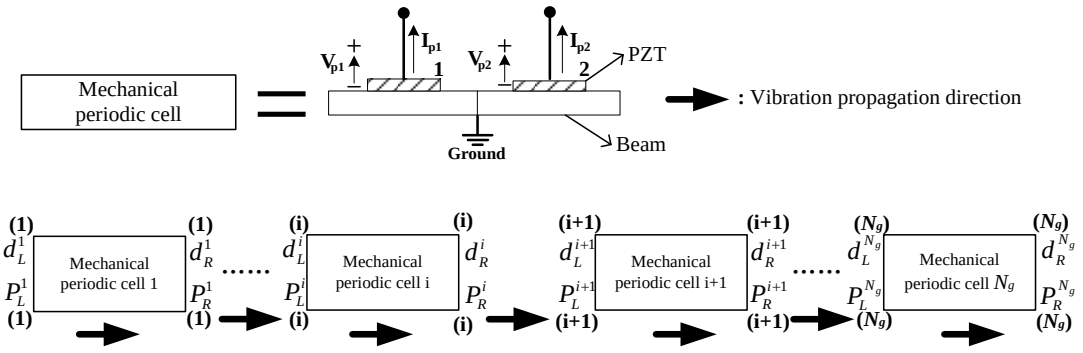

(a)

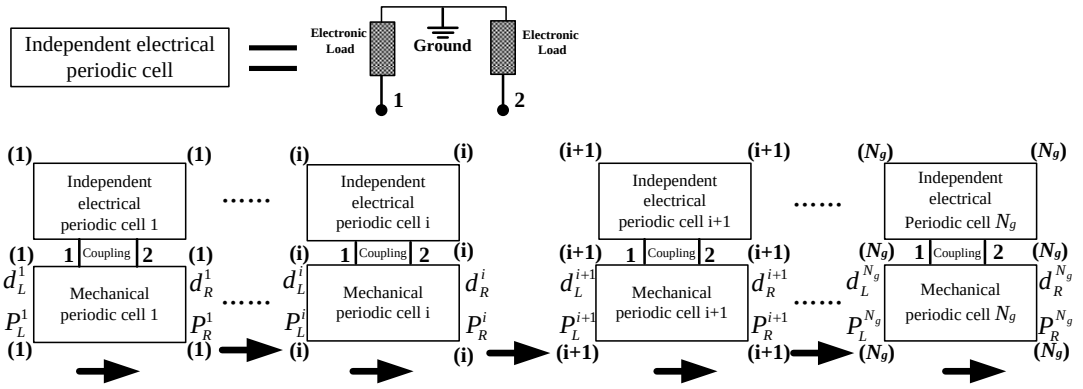

(b)

Figure 3.10 (a) Schematic representation of purely mechanical beam structure composed of N_g periodic cells; (b) Schematic representation of smart beam structure with independent electrical networks composed of N_g periodic cells.

The propagation constants are obtained with the calculation of eigenvalues $eig(T)_i\ (i=1,2,3,4)$ of the transfer matrix T:

$$eig(T)_i = e^{jk_iL} = e^{\mu} = e^{\alpha+j\beta} \tag{3.52}$$

Where k_i is the complex wavenumber, L is the length of a periodic cell, μ is a complex number, called 'propagation constant', α denotes the logarithmic decay of the vibration amplitude of a wave propagating from one cell to the next one, called 'attenuation constant', and β represents the phase difference between the wave in two adjacent cells, called 'phase constant'. The real part and imaginary part of the propagation constant define the frequency bands where energy is transmitted or attenuated along the length of the considered structure.

Traditionally, from the propagation aspect within the medium, two kinds of mechanical waves (propagating wave and evanescent wave) can be identified as follows according to the values of propagation constants:

- Evanescent wave traveling to the left (resp. right) direction ($\beta=0$, $\alpha<0$ $(resp.>0)$);
- Propagative wave traveling to the left (resp. right) direction ($\beta<0$ $(resp.>0)$).

Furthermore, the equivalent condition for the pass and stop bands of propagating wave can be written as follows:

- If $\alpha=0$, then we have "Pass band" as there is no amplitude attenuation.
- If $\alpha\neq 0$, then we have "Stop band" as there is amplitude attenuation.

The association of the propagation element can be illustrated in Figure 3.11.

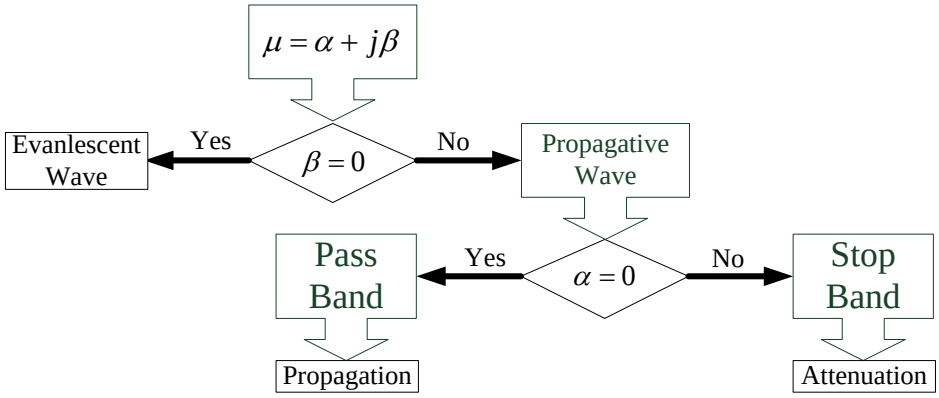

Figure 3.11 Propagation element block diagram of purely mechanical periodic structure / smart periodic structure with independent electrical networks.

- Transfer matrix formulations between interconnected periodic cells.

For transfer matrix formulations between interconnected periodic cells, schematics of smart periodic beam structure with interconnected electrical networks are shown in Figure 3.12. Similarly, in terms of the interconnected methods defining $U_i = \begin{Bmatrix} V_i \\ I_i \end{Bmatrix}$, the following equation is obtained as:

$$\begin{Bmatrix} P_0^i \\ P_j^i \\ P_n^i \\ U_{i+1} \end{Bmatrix} = \left[A_{\text{int}}\right] \cdot \begin{Bmatrix} d_0^i \\ d_j^i \\ d_n^i \\ U_i \end{Bmatrix} = \begin{bmatrix} a_{00} & a_{0j} & a_{0n} & c_{00} \\ a_{j0} & a_{jj} & a_{jn} & c_{j0} \\ a_{n0} & a_{nj} & a_{nn} & c_{n0} \\ b_{00} & b_{0j} & b_{0n} & d_{00} \end{bmatrix} \cdot \begin{Bmatrix} d_0^i \\ d_j^i \\ d_n^i \\ U_i \end{Bmatrix} = \begin{bmatrix} AA_{11} & AA_{12} \\ AA_{21} & AA_{22} \end{bmatrix} \begin{Bmatrix} d_0^i \\ d_j^i \\ d_n^i \\ U_i \end{Bmatrix} \tag{3.53}$$

with

$$A_{\text{int}} = A_{\text{int}erconnected} = \begin{bmatrix} A_{11} & A_{12} & A_{13} \\ A_{21} & A_{22} & A_{23} \\ A_{31} & A_{32} & A_{33} \end{bmatrix}$$

$$AA_{11} = \begin{bmatrix} a_{00} & a_{0j} & a_{0n} \\ a_{j0} & a_{jj} & a_{jn} \\ a_{n0} & a_{nj} & a_{nn} \end{bmatrix} = A_{11}, \quad AA_{12} = \begin{bmatrix} c_{00} \\ c_{j0} \\ c_{n0} \end{bmatrix} = \begin{bmatrix} A_{12} & A_{13} \end{bmatrix}$$

$$AA_{21} = \begin{bmatrix} b_{00} & b_{0j} & b_{0n} \end{bmatrix} = \begin{bmatrix} A_{21} \\ A_{31} \end{bmatrix}, \quad AA_{22} = \begin{bmatrix} d_{00} \end{bmatrix} = \begin{bmatrix} A_{22} & A_{23} \\ A_{32} & A_{33} \end{bmatrix}$$

$$Z=\begin{cases} Z_{\text{int}}^{passive}, & \text{for the purely resistive or linear resonant shunt;} \\ Z_{\text{int}}^{SSDI}, & \text{for the nonlinear SSDI shunt.} \end{cases}$$

Therefore, according to Guyan's reduction, the transfer matrix T of the periodic cell can be further simplified as:

$$\begin{Bmatrix} P_0^i \\ P_n^i \\ U_{i+1} \end{Bmatrix} = K \begin{Bmatrix} d_0^i \\ d_n^i \\ U_i \end{Bmatrix}, K = AA_{11} - AA_{12} \cdot AA_{22}^{-1} \cdot AA_{21} = \begin{bmatrix} K_{11} & K_{12} & K_{13} \\ K_{21} & K_{22} & K_{23} \\ K_{31} & K_{32} & K_{33} \end{bmatrix} \tag{3.54}$$

$$\begin{aligned} &K_{11} = a_{00} - a_{0j}a_{jj}^{-1}a_{j0}; \quad K_{12} = a_{0n} - a_{0j}a_{jj}^{-1}a_{jn}; \quad K_{13} = c_{00} - a_{0j}a_{jj}^{-1}c_{j0}; \\ &K_{21} = a_{n0} - a_{nj}a_{jj}^{-1}a_{j0}; \quad K_{22} = a_{nn} - a_{nj}a_{jj}^{-1}a_{jn}; \quad K_{23} = c_{n0} - a_{nj}a_{jj}^{-1}c_{j0}; \\ &K_{31} = b_{00} - b_{0j}a_{jj}^{-1}a_{j0}; \quad K_{32} = b_{0n} - b_{0j}a_{jj}^{-1}a_{jn}; \quad K_{33} = d_{00} - b_{0j}a_{jj}^{-1}c_{j0}. \end{aligned}$$

The matrix can also be translated into:

$$\begin{Bmatrix} d_n^i \\ P_n^i \\ U_{i+1} \end{Bmatrix} = \begin{bmatrix} -K_{12}^{-1} \cdot K_{11} & K_{12}^{-1} & -K_{12}^{-1} \cdot K_{13} \\ K_{21} - K_{22} \cdot K_{12}^{-1} \cdot K_{11} & K_{22} \cdot K_{12}^{-1} & K_{23} - K_{22} \cdot K_{12}^{-1} \cdot K_{13} \\ K_{31} - K_{32} \cdot K_{12}^{-1} \cdot K_{11} & K_{32} \cdot K_{12}^{-1} & K_{33} - K_{32} \cdot K_{12}^{-1} \cdot K_{13} \end{bmatrix} \begin{Bmatrix} d_0^i \\ P_0^i \\ U_i \end{Bmatrix} \tag{3.55}$$

Since d^i (the displacement and slope vectors) are continuous between finite beam elements in a periodic cell, and P_n^i the force and moment exerted on the right side of the i^{th} electromechanical periodic cell) is opposite to P_0^{i+1} (those exerted on the left side of the $(i+1)^{th}$ electromechanical periodic cell), the transfer matrix T between periodic cells can thus be given as:

$$\begin{Bmatrix} d_n^i \\ P_n^i \\ U_{i+1} \end{Bmatrix} = T \begin{Bmatrix} d_0^i \\ P_0^i \\ U_i \end{Bmatrix}, T = \begin{bmatrix} -K_{12}^{-1} \cdot K_{11} & K_{12}^{-1} & -K_{12}^{-1} \cdot K_{13} \\ -K_{21} + K_{22} \cdot K_{12}^{-1} \cdot K_{11} & -K_{22} \cdot K_{12}^{-1} & -K_{23} + K_{22} \cdot K_{12}^{-1} \cdot K_{13} \\ K_{31} - K_{32} \cdot K_{12}^{-1} \cdot K_{11} & K_{32} \cdot K_{12}^{-1} & K_{33} - K_{32} \cdot K_{12}^{-1} \cdot K_{13} \end{bmatrix} \tag{3.56}$$

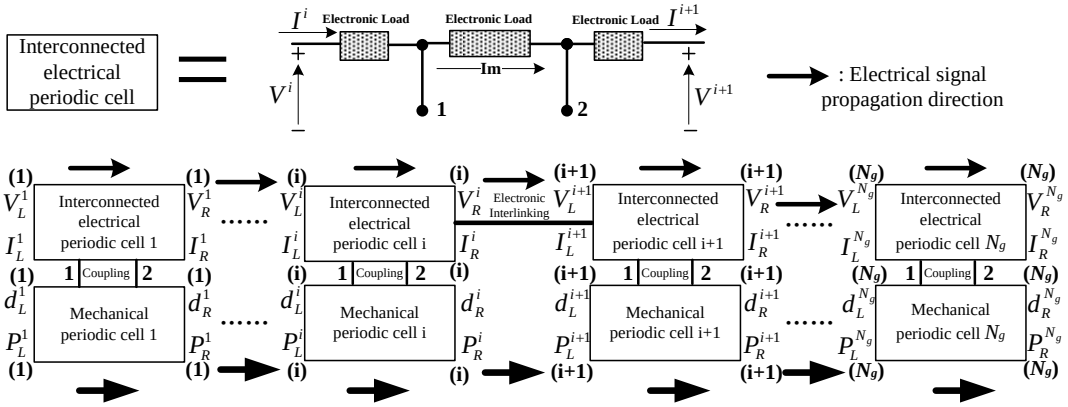

Figure 3.12 Schematic representation of smart beam structure with interconnected electrical networks composed of N_g periodic cells.

For periodic structure with independent electrical networks (each PZT is connected to independent electrical shunt), electrical boundary conditions are closed in an independent smart periodic cell. Since there is no continuous electrical relationship between adjacent smart periodic cells, similar with the purely mechanical periodic cell, wave propagation properties of unit smart periodic cell can be analyzed through traditional transfer matrix method like Eq.(3.51). However, electrical relationships of an interconnected periodic cell are interrelated in piezoelectric periodic structure with interconnected electrical networks. Through the proposed transfer matrix method (Eq.(3.53)), a pair of electrical parameters U_i is introduced to explicate the electrical relationships between adjacent interconnected periodic cells. Furthermore, the concept of electrical wave is proposed to represent the eigenvalue arising from the electrical interconnection between adjacent interconnected periodic cells, and can be identified according to the value continuity of the eigenvalues of the transfer matrix method excluding the eigenvalues of propagative and evanescent waves. Propagation element block diagram of smart periodic beam with interconnected electrical networks is shown in Figure 3.13.

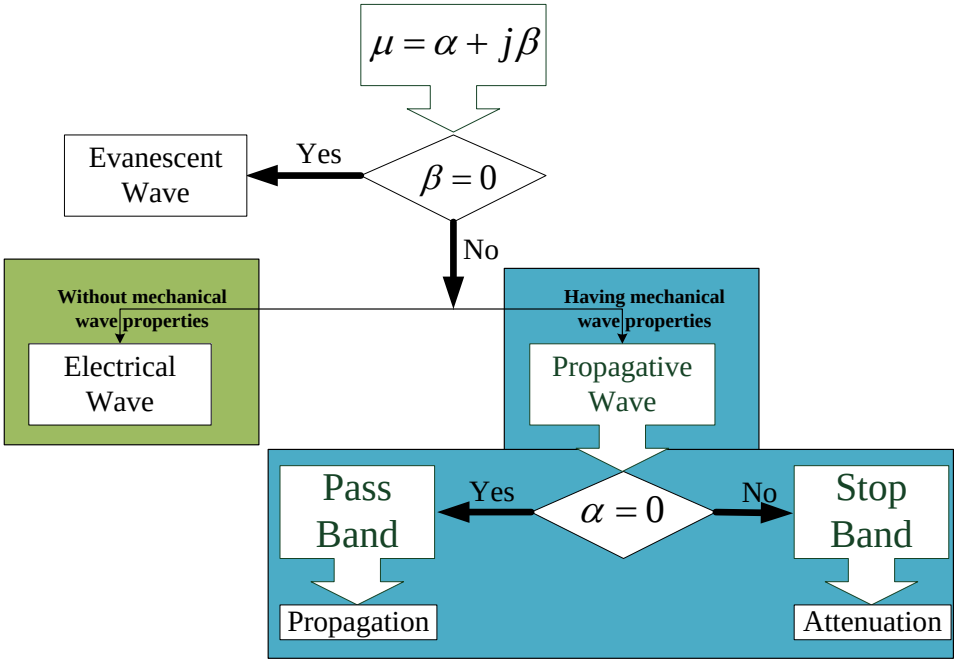

Figure 3.13 Propagation element block diagram of smart periodic structure with interconnected electrical networks.

3.4 Theoretical discussion of wave attenuation performance

Wave attenuation properties of investigated periodic structure are theoretically compared and discussed in this section based on the experimental sample whose parameters are listed in Table 3.1 and Table 3.2. In order to make fair comparison on wave attenuation performance between the independent and interconnected cases, the investigated periodic cell includes two PZTs bonded symmetrically on the beam, as shown in Figure 3.14. The dimension of the cell is 44 mm. Each PZT is 10 mm long. Actually, the investigated periodic cell is considered as two adjacent minimal periodic cells in purely mechanical periodic structure or smart periodic structure with independent electrical networks. PP and PN PZT configurations make difference on wave attenuation capabilities only in smart periodic structure with interconnected electrical networks. According to FEM analysis, the investigated cell is decomposed into several FE elements. In order to obtain propagation constant of the investigated periodic cell under different electrical boundary conditions, transfer matrix for the

whole cell is then derived. Only positive direction is taken into account in following wave attenuation analysis and no structural damping is considered ($\mathbf{C}^e$= [0]).

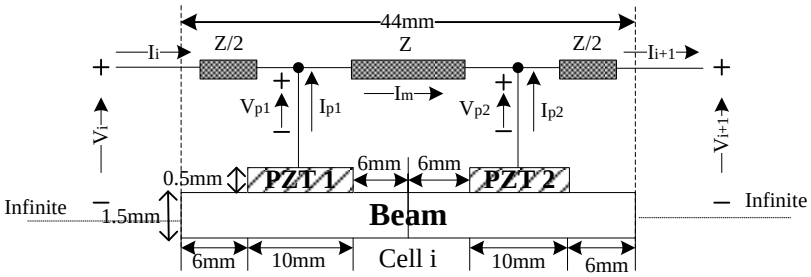

Figure 3.14 An interconnected periodic cell in the investigated structure.

Table 3.1 Dimensional and material properties of the beam

Young's modulus	$Y_b = 190\times10^9\, Pa$	Poisson's ratio	$v_b = 0.21$	Density	$\rho_b = 7875 kg/m^3$
length	$L_b = 176\times10^{-3} m$	Width	$w_b = 35\times10^{-3} m$	Thickness	$t_b = 1.5\times10^{-3} m$

Table 3.2 Dimensional and material properties of the piezoelectric patch

Compliance in short circuit	$s_{11}^E = 10.66\times10^{-12} m^2/N$ $s_{12}^E = -3.34\times10^{-12} m^2/N$	Length	$L_p = 10\times10^{-3} m$
Charge coefficient	$d_{31} = -108\times10^{-12} m/V$	Thickness	$t_p = 0.5\times10^{-3} m$
Relative dielectric constant	$\frac{\varepsilon^T}{\varepsilon_0} = 1150$	Density	$\rho_p = 7650 kg/m^3$

3.4.1 Purely resistive case

Curves of real ('Log Decay') and imaginary ('Phase difference') parts of propagation constant of the investigated periodic cell with different electrical connections using purely resistive shunts are plotted in Figure 3.15-Figure 3.17, as well as the case without any electrical connections (open circuit) for comparison. The applied resistances used in different electrical connections are all optimal and equal to $\frac{1}{2\pi fC_0}$ and $\frac{1}{\pi fC_0}$, respectively, and thus adjusted to the structural frequency f.

As shown in the logarithmic decay curve of propagative wave in purely resistive and open-circuit cases (Figure 3.15), periodic structure filters elastic wave in some frequency ranges corresponding to stop bands (band gaps). Stop bands do not appear over a very wide frequency band in open-circuit condition, but in purely resistive cases some attenuation occurs in the original pass bands. More specifically, logarithmic decay of propagative wave in the independent case outperforms those in the PP / PN interconnected cases in original pass bands of the investigated frequency domain, therefore elastic wave attenuation capability using purely resistive shunts in electrical independent connection is superior compared with other electrical interconnected cases. In terms of interconnected cases, PP / PN interconnections exhibit better and different wave attenuation performance in original pass bands (Bragg-type band gaps [7.2 kHz, 8.1 kHz] and [29 kHz, 32 kHz]) compared with open-circuit condition. Specifically, wave attenuation performance in the PP case is better than that in the PN case around the first Bragg-type band gap [7.2 kHz, 8.1 kHz]. While around the second Bragg-type band gap [29 kHz, 32 kHz], the wave attenuation capability in the PN case becomes better.

For two Bragg-type band gaps, PN interconnection shows similar performance than open circuit case and better performance than independent case within the first Bragg-type band gap, but shows the worst attenuation performance in the second Bragg-type band gap. On the contrary, within the second Bragg-type band gap, performance of PP interconnection is better than that of PN interconnection and is

similar than open circuit case, but shows the worst performance in the first Bragg-type band gap. Therefore, it can be concluded that electrical interconnected configurations can enhance the attenuation performance of mechanical periodic structure, and also have the abilities to weaken the performance of Bragg-type band gaps. In other words, performance of interconnected configurations closely relates to different frequency domains of interest.

Phase differences of propagative wave in different cases are almost the same as shown in Figure 3.16 (a). Two main plateau inflexion areas (0 or π) correspond to two Bragg-type band gaps. However, dispersive differences of propagative wave among different cases can hardly be distinguished. Therefore, herein, group velocities for different cases are illustrated in Figure 3.16 (b) for further investigating the dispersion properties. Group velocities from phase difference curves of propagative wave, yielded by the *h-p* version of the FE method, can be expressed as [310]:

$$V_g = L_{unit} \left| \frac{d\omega}{d\beta} \right| \tag{3.57}$$

where L_{unit} is the length of unit periodic cell.

Within primitive stop bands ([7.2 kHz, 8.1kHz] and [29 kHz, 32 kHz]), group velocity for open circuit case equals zero, since phase differences of propagative wave are equal to a plateau constant (0 or π). Figure 3.16 (b) shows group velocities in different cases: band gaps begin to increase from 0 m/s at the beginning of primitive stop bands, and the maximum group velocities are all above 5000 m/s, but when the frequency approaches the end of primitive stop bands, group velocities are all dropped back to 0 m/s. Specifically, dropping rates for independent and PP interconnected cases are slower than the dropping rate of the PN interconnected case within the first primitive stop band ([7.2 kHz, 8.1 kHz]). In the second primitive stop band ([29 kHz, 32 kHz]), the independent case and the PN interconnected case have slower dropping rate than the PP interconnected case. Actually, such abrupt alteration can be illustrated by wave propagation velocity difference between mechanical medium with low velocities and electrical medium with high velocities. In addition, two narrow frequency areas ([1.85

kHz, 1.95 kHz] and [17.1 kHz, 17.4 kHz]) in which group velocities vary abruptly, correspond to two small inflexion areas (π) of phase difference of propagative wave in open circuit case. Compared with open circuit case, group velocities in other cases are increased in the first small inflexion area ([1.85 kHz, 1.95 kHz]) due to electrical network influence. In the second small inflexion area ([17.1 kHz, 17.4 kHz]), maximum group velocities in other cases are lowered from about 2300 m/s (at 17.25 kHz) to about 1500 m/s (at 17.15 kHz).

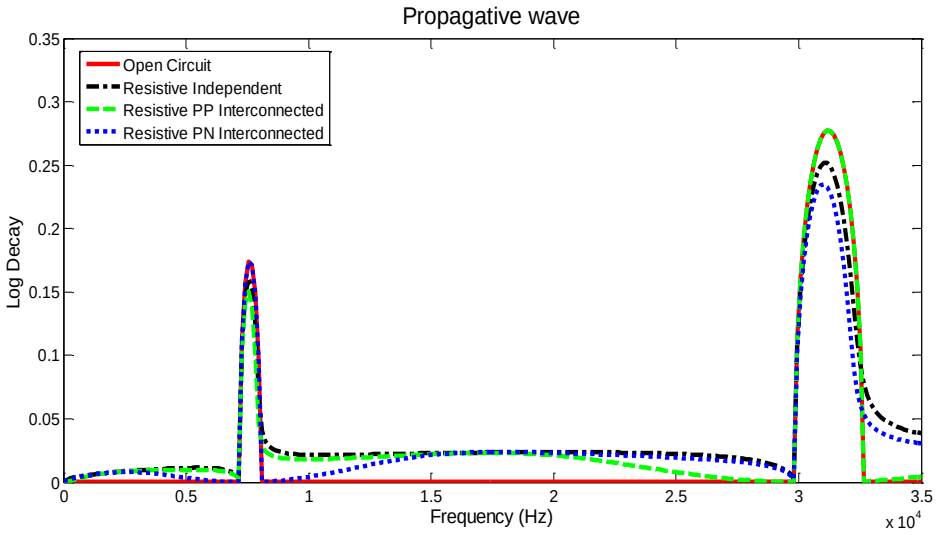

Figure 3.15 Logarithmic decay of propagative wave in resistive and open circuit cases.

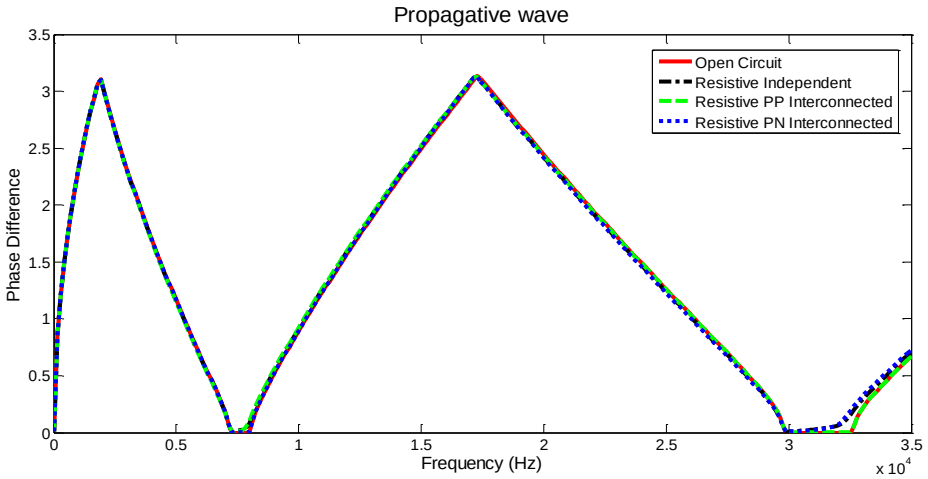

(a)

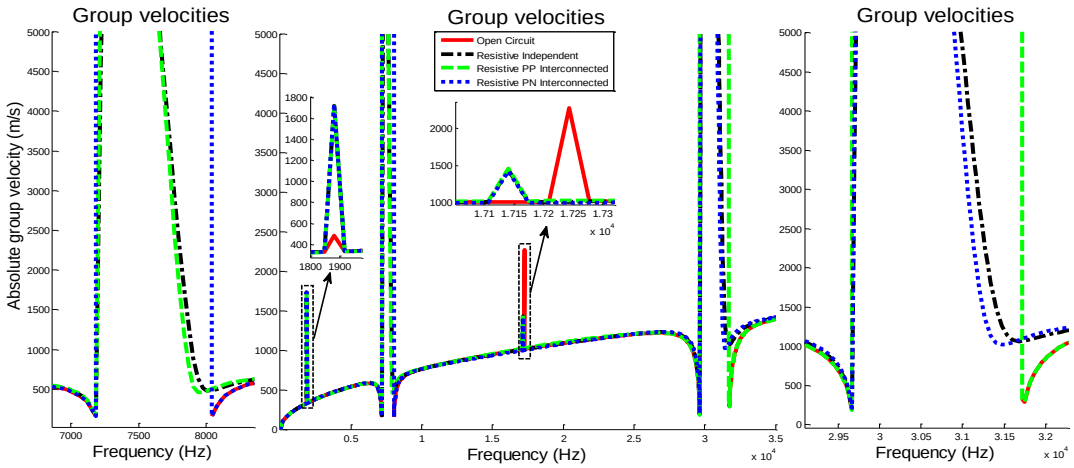

(b)

Figure 3.16 (a) Phase difference and (b) group velocities of propagative wave in resistive and open circuit cases.

Evanescent wave characteristics in different cases are shown in Figure 3.17. The logarithmic decay of evanescent wave starts to increase gradually from a non-zero propagation constant with the increase of the frequency due to the abrupt change of mechanical impedance. It reflects the interface between non-piezoelectric and piezoelectric beam sections. For electrical wave in different conditions (Figure 3.17), variation of electrical wave curves does not change significantly over the frequency domain.

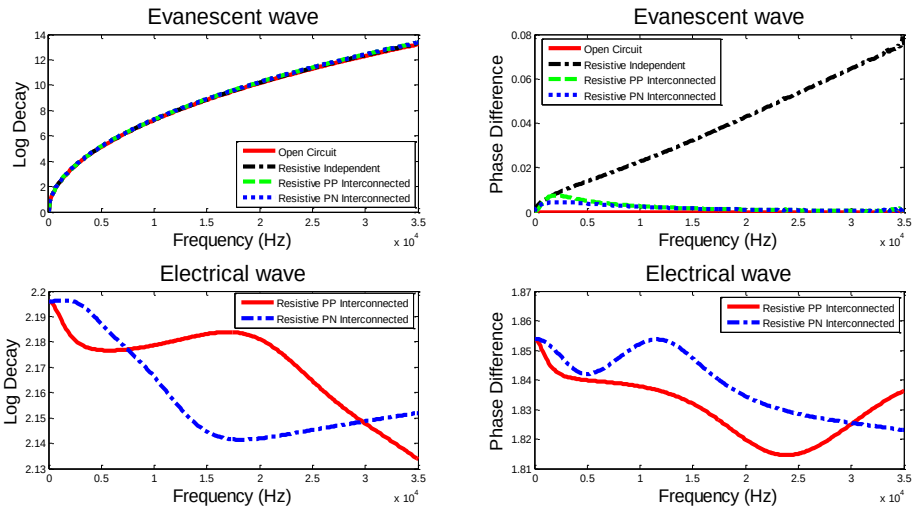

Figure 3.17 Evanescent and electrical waves in different cases.

3.4.2 Nonlinear switched cases

Wave attenuation performance of smart periodic structure featuring nonlinear SSDI technique (interconnected and independent cases) with different inversion coefficients are given in Figure 3.18-Figure 3.26. Similar curves of evanescent wave are obtained in the investigated cases (Figure 3.20, Figure 3.23 and Figure 3.26) except in the independent case, in which phase difference of evanescent wave increases with the frequency.

As shown in Figure 3.18, Figure 3.21 and Figure 3.24, SSDI cases achieved much better wave attenuation performance than resistive cases. With the increase of the inversion coefficient, wave attenuation properties of periodic structures with SSDI independent / interconnected electrical networks are enhanced. Globally speaking however, the SSDI independent case outperforms the interconnected case on wave attenuation performance over the whole investigated frequency domain, especially in the SSDI independent case with relatively high value inversion coefficient (Figure 3.21), excluding some frequency ranges where new stop bands arise in the SSDI interconnected cases. These new band gaps induced by SSDI interconnected methods match the frequencies where peaks and troughs of electrical wave appear (Figure 3.20, Figure 3.23 and Figure 3.26). Such electrical wave influence allows the increase of

propagative wave attenuation with SSDI interconnected methods, outperforming the SSDI independent method in some specific frequency ranges (low and medium (<5 kHz) and high ([12 kHz, 24 kHz]) frequency bands in the given analyses). Specifically, with the increase of the voltage inversion coefficient from $\gamma_{ind} = 0.1$ (and $\gamma_{int} = 0.2$) to $\gamma_{ind} = 0.5$ (and $\gamma_{int} = 0.6$), the frequency ranges in which periodic structure with SSDI interconnected electrical network shows better elastic wave attenuation performance than periodic structure with SSDI independent electrical network, are narrowed as listed in Table 3.3:

Table 3.3 The frequency domains in which SSDI independent case outperforms SSDI interconnected cases.

	SSDI PP interconnected		SSDI PN interconnected	
$\gamma_{ind} = 0.1, \gamma_{int} = 0.2$	$[1.6\ kHz,\ 3.7\ kHz]$	$[13.2\ kHz, 18\ kHz]$	$[640\ Hz,\ 2.2\ kHz]$	$[16.3\ kHz,\ 21.8\ kHz]$
……	↓ *Narrowed*	↓ *Narrowed*	↓ *Narrowed*	↓ *Narrowed*
$\gamma_{ind} = 0.5, \gamma_{int} = 0.6$	$[1.8\ kHz,\ 2.4\ kHz]$	$[17\ kHz,\ 18\ kHz]$	$[1.3\ kHz,\ 2\ kHz]$	$[16\ kHz,\ 17.5\ kHz]$

Phase differences of propagative wave in SSDI / SSDS cases are respectively shown in Figure 3.19 (a), Figure 3.22 (a) and Figure 3.25 (a). Specifically, influence of different SSDI / SSDS networks on the phase difference curves is diminutive and cannot be observed obviously except two main plateau areas corresponding to two Bragg-type band gaps. Similarly, dispersion properties of propagative wave in different SSDI / SSDS cases can be investigated by comparing their group velocities (Figure 3.19 (b), Figure 3.22 (b) and Figure 3.25 (b)). As shown in Figure 3.19 (b), within the first Bragg-type band gap, maximum group velocity of the SSDI PP interconnected case (approximately 3700 m/s) is higher than that of the SSDI independent case (3300 m/s), and the SSDI PN interconnected case has the highest group velocity which is above 5000 m/s. By comparison, within the second

Bragg-type band gap, maximum group velocity of the PN interconnected case (around 5000 m/s) is higher than that of the SSDI independent case (4700 m/s), and the PP interconnected case has the highest group velocity which is above 5000 m/s among all the cases. When inversion coefficients increase, maximum group velocities of the PP / PN interconnected cases are increased above 5000 m/s while maximum group velocities of SSDI independent case go down within the two Bragg-type band gaps as shown in Figure 3.22 (b). On the contrary, when inversion coefficients decrease, maximum group velocities of PP / PN interconnected cases are lowered while maximum group velocities of the SSDI independent case increase above 5000 m/s in the Bragg-type band gaps as shown in Figure 3.25 (b).

When it comes to the first small inflexion area ([1.85 kHz, 1.95 kHz]), maximum group velocities of all the SSDI / SSDS cases with low inversion coefficients are lower than maximum group velocity in open circuit case as shown in Figure 3.19 (b) and Figure 3.22 (b). While when the SSDI independent case and SSDI PP interconnected case feature high inversion coefficients as shown in Figure 3.25 (b), their maximum group velocities are higher than maximum group velocity of open circuit case, and group velocity of SSDI PP interconnected case with high inversion coefficients firstly goes down to 200 m/s and then increases back to group velocity of open circuit case. For group velocities around the second small inflexion area (Figure 3.19 (b), Figure 3.22 (b) and Figure 3.25 (b)), with the inversion coefficient increasing, group velocity curves of all SSDI cases become to fluctuate more and more violently around group velocity curve of open circuit case.

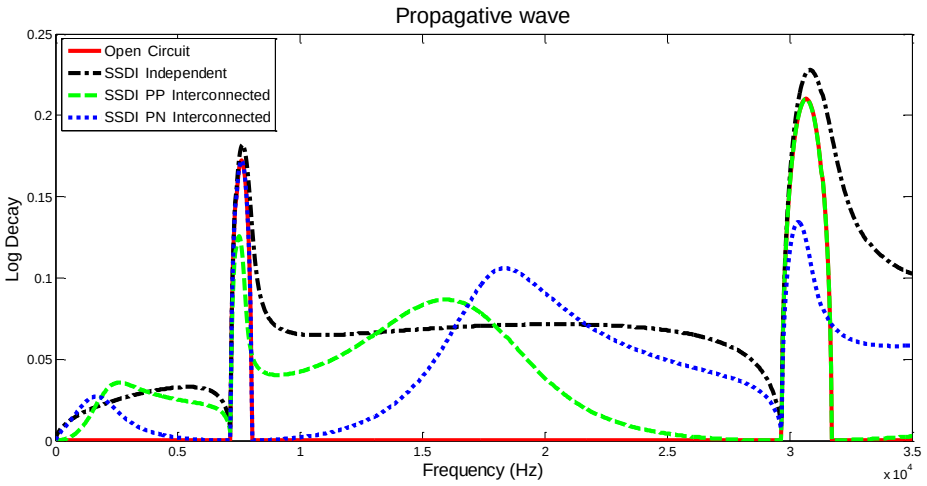

Figure 3.18 Logarithmic decay of propagative wave in SSDI cases and comparison with open circuit ($\gamma_{ind} = 0.1, \gamma_{int} = 0.2$).

Therefore, the bandwidth of these specific frequency domains, affected by electrical wave in SSDI interconnected cases, could be adjusted by the proper choice of inversion coefficient. Furthermore, in the periodic structure with SSDI interconnected electrical networks where the voltage inversion coefficient equals zero, namely the SSDS (Synchronized Switch Damping on the Short circuit) technique [31] in which no inductor is required, better wave attenuation performance than that in SSDS independent case, can be found in relatively broad frequency ranges ([300 Hz, 1.85 kHz] and [17 kHz, 24 kHz] for SSDS PN interconnected case, and [1.85 kHz, 5 kHz] and [12 kHz, 17 kHz] for SSDS PP Interconnected case). The appearance of new stop bands can be attributed to the interplay between mechanical and electrical wave propagation mechanisms. As electrical wave propagates with a higher velocity than that of elastic wave, particular interaction between them arises for specific frequencies where additive vibration damping performance occurs. Electrical wave peaks and troughs are determined by mutual interaction between mechanical and electrical sections. Specifically, SSDI impedance in the electrical section of the structure is automatically adapted to vibration of mechanical section of the structure. Apparently, such mutual interaction is different from the electrical resonance mechanism of periodic structure with linear resonant electrical networks. Electrical wave modes in

the electrical section of periodic structure with linear resonant electrical networks may be manually targeted. Locations of elastic wave band gaps induced by linear electrical resonance can be predicted from the electrical domain since linear resonance will cause the mechanical impedance mismatch during the same frequency range where specific electrical resonance occurs. However, mutual interaction between electrical and mechanical sections in the investigated structure is complicated, and thus locations of band gaps cannot be easily predicted from the electrical domain.

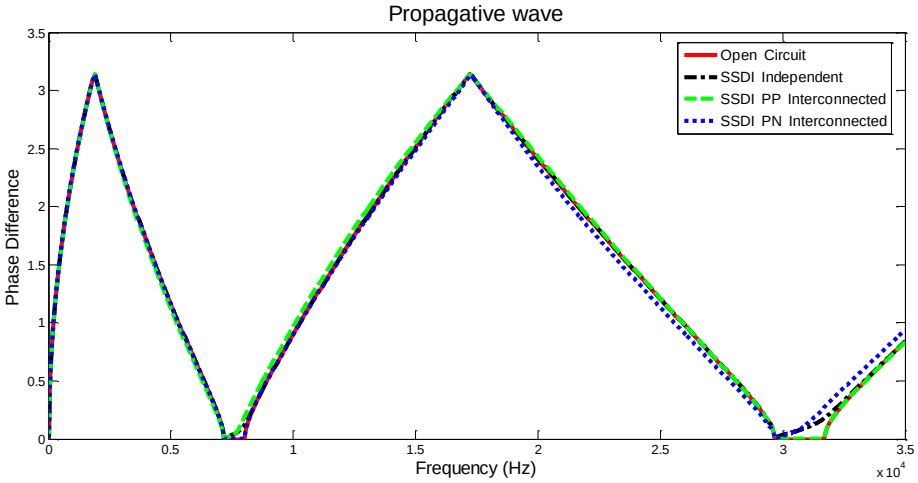

(a)

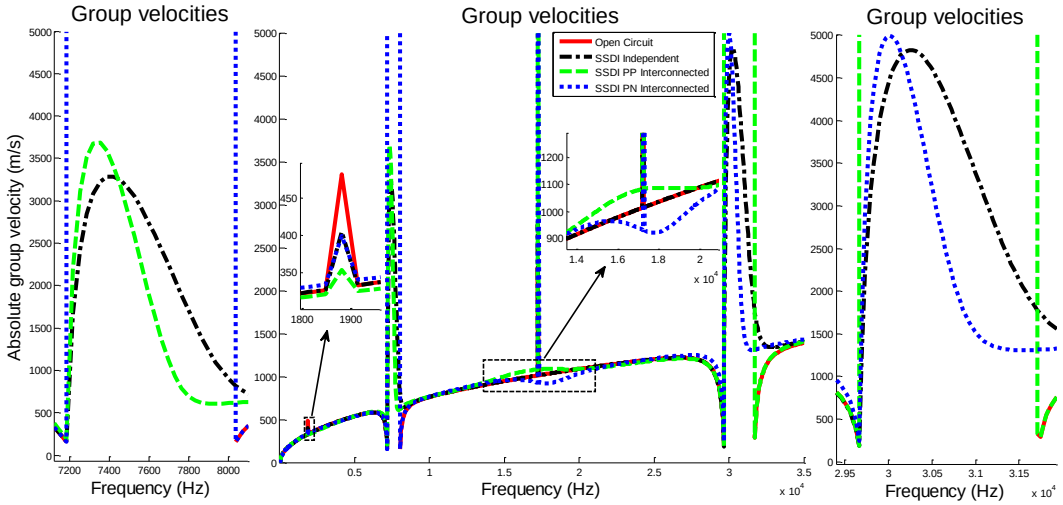

(b)

Figure 3.19 (a) Phase difference and (b) group velocities of propagative wave in SSDI cases ($\gamma_{ind} = 0.1, \gamma_{int} = 0.2$).

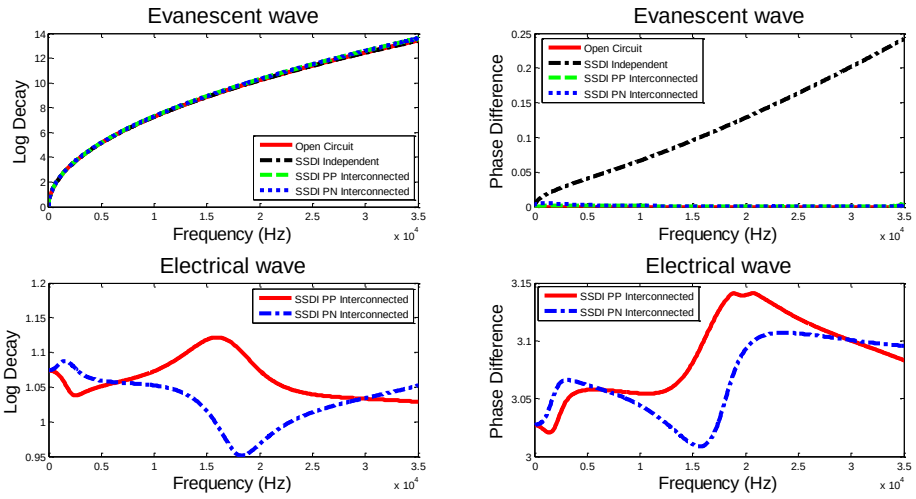

Figure 3.20 Evanescent and electrical waves in SSDI cases ($\gamma_{ind} = 0.1, \gamma_{int} = 0.2$).

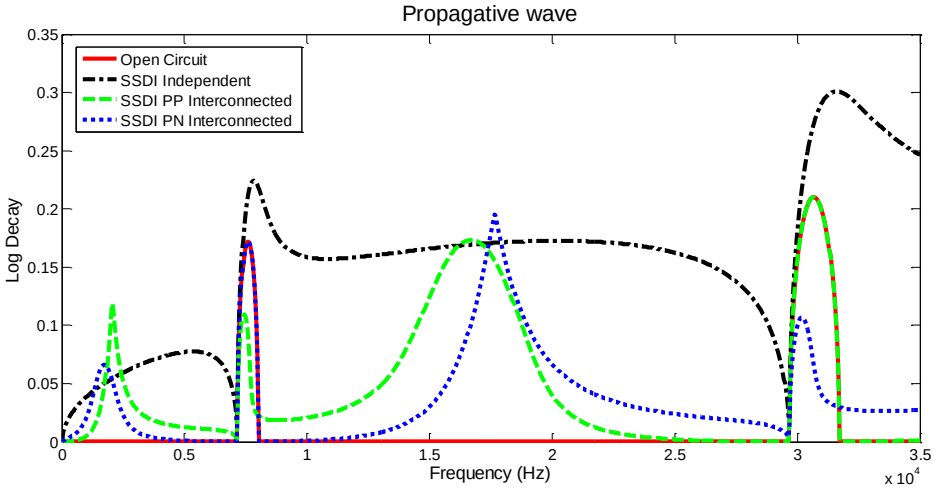

Figure 3.21 Logarithmic decay of propagative wave in SSDI cases ($\gamma_{ind} = 0.5$, $\gamma_{int} = 0.6$).

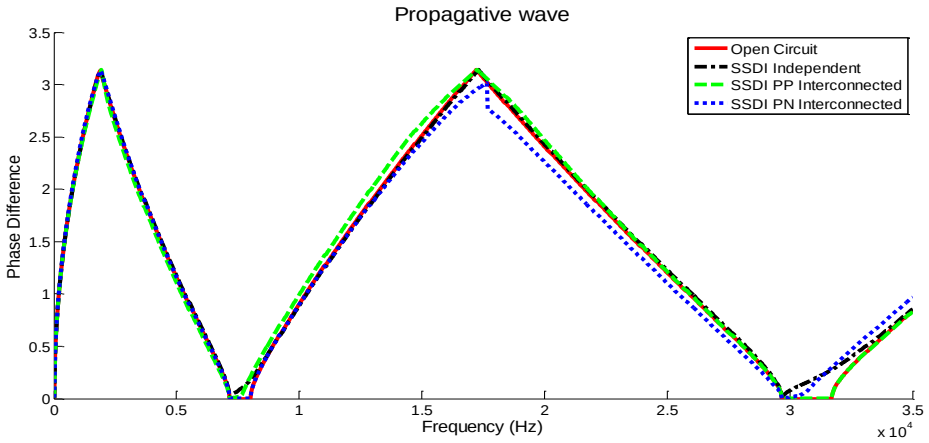

(a)

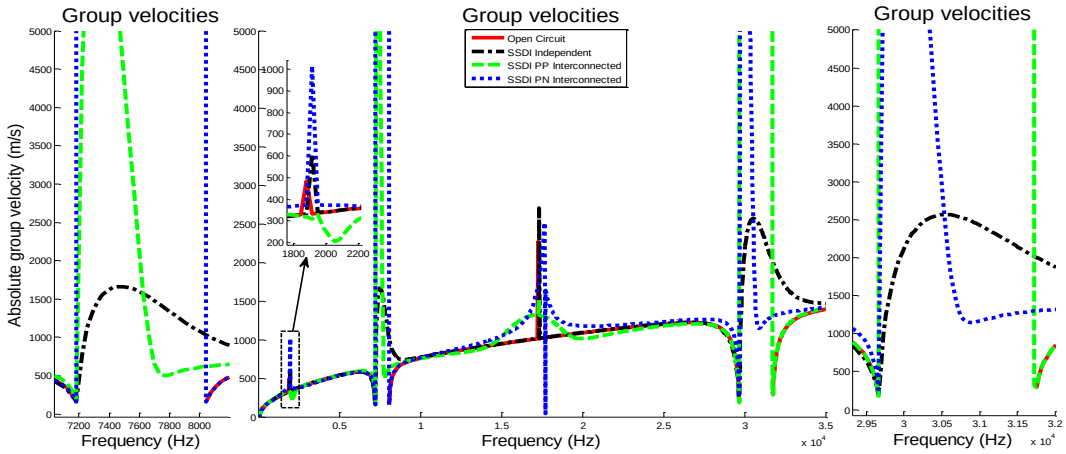

(b)

Figure 3.22 (a) Phase difference and (b) group velocities of propagative wave in SSDI cases ($\gamma_{ind} = 0.5, \gamma_{\text{int}} = 0.6$).

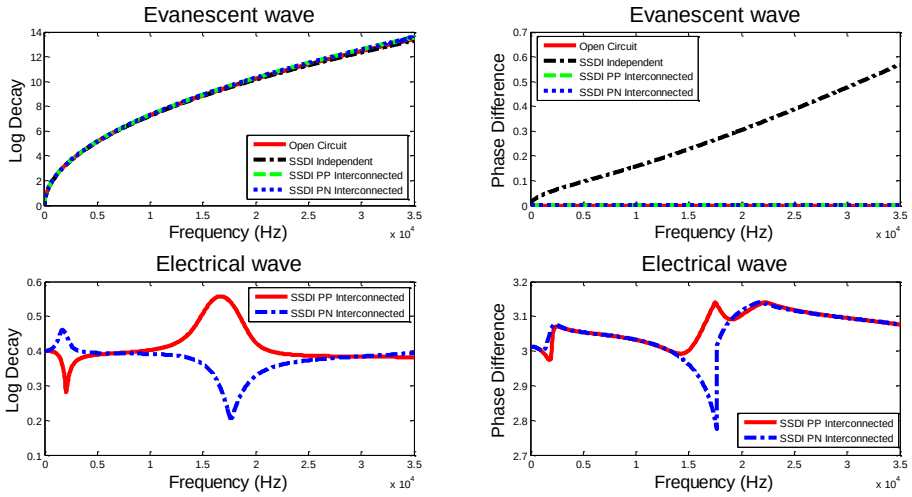

Figure 3.23 Evanescent and electrical waves in SSDI cases ($\gamma_{ind} = 0.5, \gamma_{\text{int}} = 0.6$).

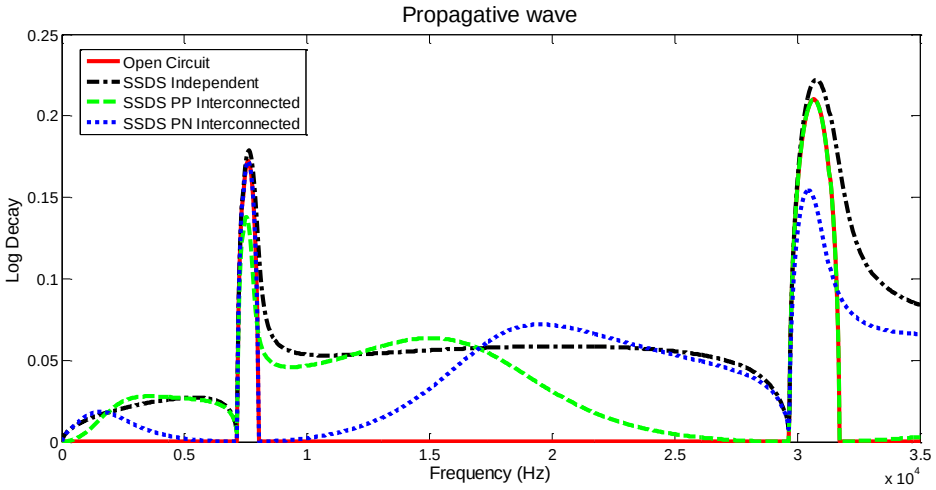

Figure 3.24 Logarithmic decay of propagative wave in SSDS case.

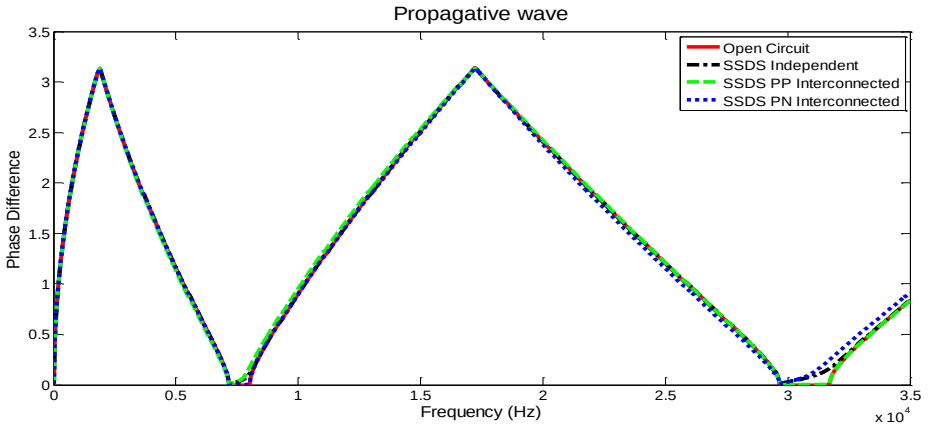

(a)

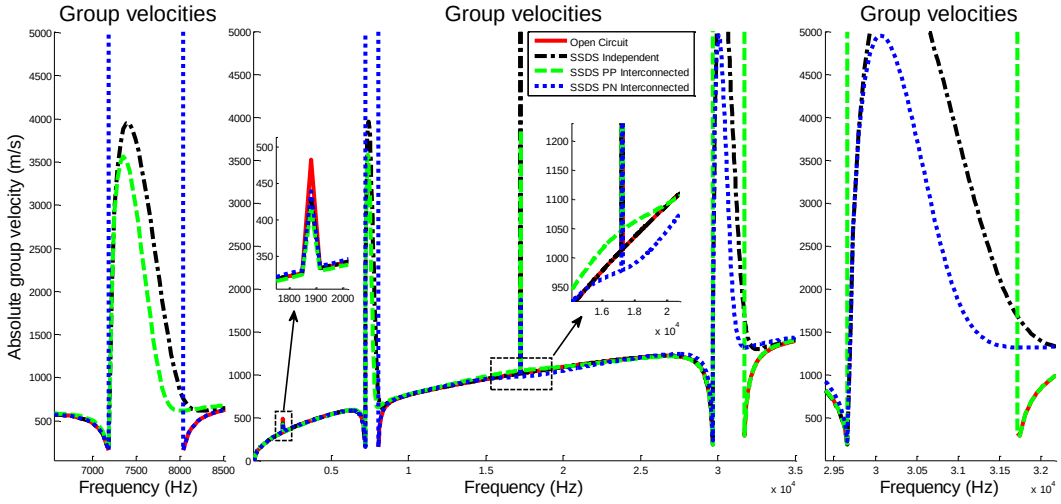

(b)

Figure 3.25 (a) Phase difference and (b) group velocities of propagative wave in SSDS case.

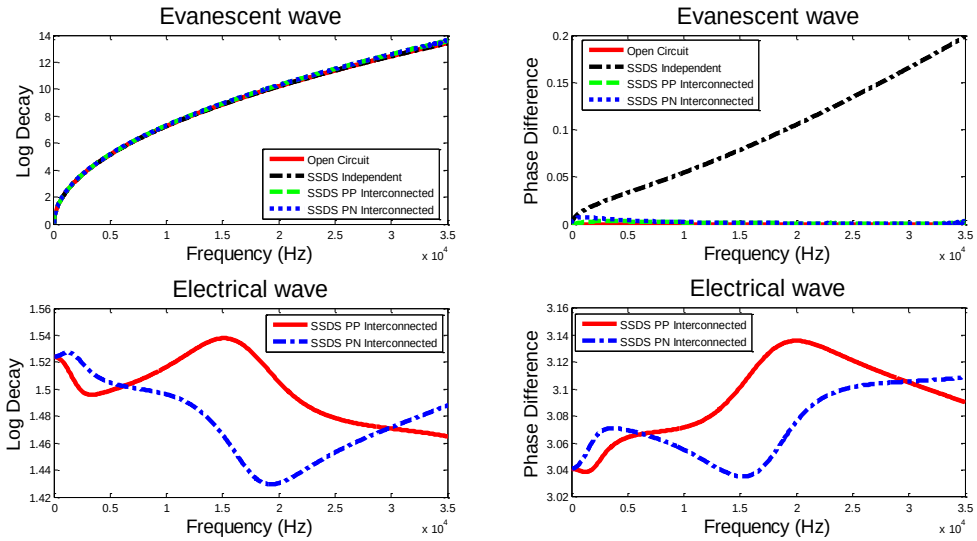

Figure 3.26 Evanescent and electrical waves in SSDS case.

Furthermore, wave attenuation performance differences can be observed between SSDI PP interconnected method and SSDI PN interconnected method (Figure 3.18， Figure 3.21 and Figure 3.24), since trends of logarithmic decays of electrical wave in the SSDI PP and PN interconnected cases are nearly opposite (Figure 3.20, Figure 3.23 and Figure 3.26). Better attenuation performance is obtained in the first Bragg-type stop band for the SSDI PN interconnected approach, and in the second Bragg-type stop band for the SSDI PP interconnected approach, which can be explained by principles of the interconnection methods introduced in section 3.2.2. Specifically, for an example of logarithmic decay comparison when $\gamma_{ind} = 0.1, \gamma_{int} = 0.2$, smart periodic structure using the SSDI PN interconnected method shows better attenuation performance in the relatively low frequency spectrum (before the first Bragg-type stop band (<2 kHz)) and relatively medium frequency spectrum ([17 kHz, 29 kHz]). Meanwhile, wave attenuation performance of smart periodic structure using the SSDI PP interconnected method is better in the frequency spectra close to the first Bragg-type stop band ([2 kHz, 7 kHz] and [8 kHz, 17 kHz]). Supplementary resonant-type stop bands can be generated by implementing SSDI interconnected methods, allowing the design of band characteristics of periodic structure to match the

resonance frequency of the targeted structure, therefore allowing high vibration damping performance.

Figure 3.27-Figure 3.30 show the 3D views and contours of logarithm decay of propagative wave versus the inversion coefficient with nonlinear PN / PP interconnections. For the contour of switched PN interconnected case, the second Bragg-type stop band ([29 kHz, 31 kHz]) is extended to 35 kHz, and two new resonant-type stop bands are generated. The first new resonant-type stop band ([1.4 kHz, 2.3 kHz]) appears on condition that the range of inversion coefficient is about [0.5, 0.9]. In the second new resonant-type stop band ([16 kHz, 26 kHz]), attenuation performance is the best on condition that the range of inversion coefficient is about [0.4, 0.6] and the excitation frequency range is about [17 kHz, 19 kHz].

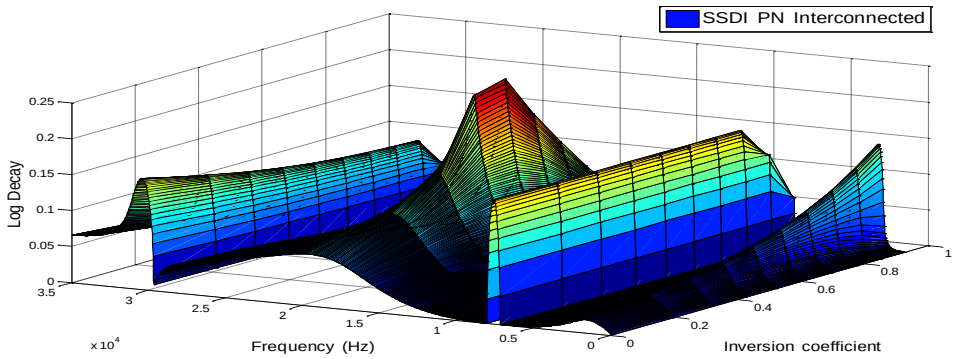

Figure 3.27 3D view of logarithm decay of propagative wave versus the inversion coefficient with PN switching interconnection.

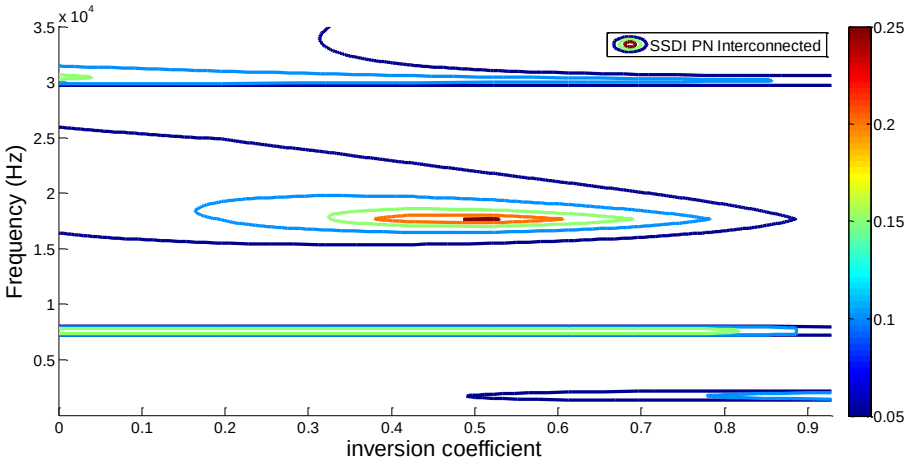

Figure 3.28 Contour of logarithm decay of propagative wave versus the inversion coefficient with PN switching interconnection.

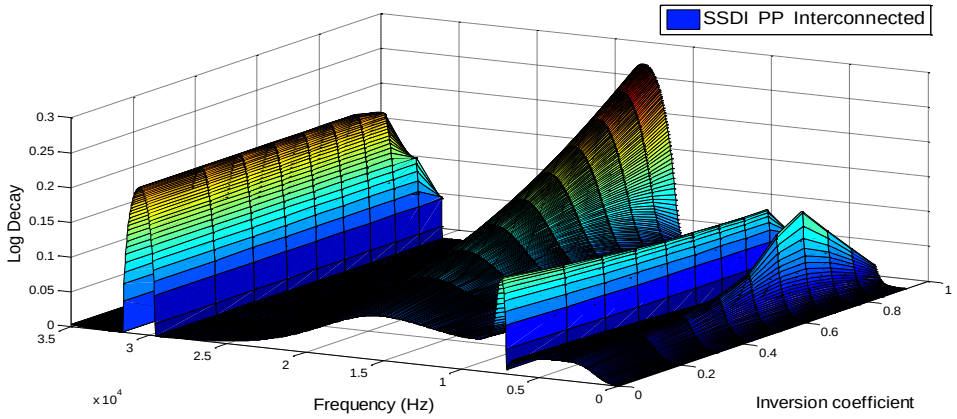

Figure 3.29 3D view of logarithm decay of propagative wave versus the inversion coefficient with PP switching interconnection.

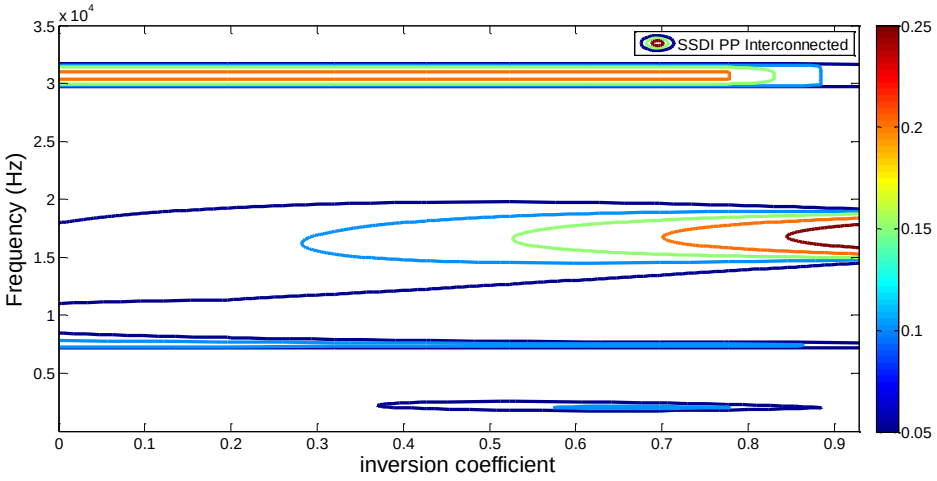

Figure 3.30 Contour of logarithm decay of propagative wave versus the inversion coefficient with PP switching interconnection.

For the contour of switched PP interconnected case, except the Bragg-type stop bands ([7 kHz, 8 kHz] and [29 kHz, 31 kHz]), there are two new resonant-type stop bands induced by nonlinear PP interconnected method. The first resonant-type stop band appears at the frequency range [2 kHz, 2.5 kHz] on condition that the inversion coefficient has a value between 0.4 and 0.9. With the increase of inversion coefficient, wave attenuation performance is better and better within the second resonant-type stop band ([11 kHz, 18 kHz]).

Moreover, electrical losses would increase when dealing with high frequency devices, yielding a dramatic drop of inversion coefficient. Utilization of SSDI interconnected methods allows better attenuation performance of frequency ranges of interest under such conditions. Furthermore, SSDS PP / PN interconnected method is a premium choice for significantly absorbing mechanical vibrations in inductance-free integration (*i.e.*, the inversion coefficient is zero, *e.g.*, Figure 3.24).

3.5 Global relationship under the clamped-clamped case

The transfer matrix formulation presented in section 3.3.2 can be applied to obtain the frequency response along the periodic beam structure for harmonic excitation.

➢ Periodic structure consisting of independent periodic cells

For periodic structure composed of independent periodic cells, state vectors at the beginning and end of the i^{th} periodic cell can be represented by the transfer matrix T:

$$\begin{Bmatrix} d_n^i \\ P_n^i \end{Bmatrix} = T \cdot \begin{Bmatrix} d_0^i \\ P_0^i \end{Bmatrix} = \begin{pmatrix} t_{11} & t_{12} \\ t_{21} & t_{22} \end{pmatrix} \cdot \begin{Bmatrix} d_0^i \\ P_0^i \end{Bmatrix} \tag{3.58}$$

where $i \in \left[1, \quad N_g\right]$; N_g is the number of equivalently independent periodic cells of the investigated periodic structure. $d_0^i, P_0^i, d_n^i, P_n^i$ respectively denote the generalized displacements and generalized forces vectors at the left-end node and right-end node of the i^{th} equivalently independent periodic cell. Therefore, the global transfer matrix of the investigated structure composed of equivalently independent periodic cells can be given as:

$$T_g = \left[T\right]^{N_g} \tag{3.59}$$

Assuming that the considered structure is a clamped-clamped beam, and the external force F is applied to the node between the nf^{th} and $\left(nf+1\right)^{th}$ minimal Bragg periodic cells, the fixed ends which feature a zero vector of displacement and slope, are under external force and moment exerted by the clamps, respectively noted as:

$$P_0^0 = \left[F^0 \quad M^0\right]^t, \quad P_n^{N_g} = \left[F^{N_g} \quad M^{N_g}\right]^t$$

with the vector P_0^0 $(resp.\, P_n^{N_g})$ denoting the force F^0 $(resp.\, F^{N_g})$ and moment M^0 $(resp.\, M^{N_g})$ applied by the clamp to the left (*resp.* right) end of the structure.

Thus, the clamped-clamped boundary condition can be expressed as follows:

$$\begin{cases} d_0^0 = 0 \\ d_n^{N_g} = 0 \end{cases} \text{ and } \begin{cases} P_0^0 \neq 0 \\ P_n^{N_g} \neq 0 \end{cases} \tag{3.60}$$

where d_0^0, P_0^0 and $d_n^{N_g}, P_n^{N_g}$ respectively denote the generalized displacement and force vectors at the left end of the 1^{st} periodic cell and at the right end of the N_g^{th} periodic cell.

According to the linearity of the system [311], state vectors at any intermediate nodal point can be obtained by considering the boundary conditions and the sum of the responses from the left end and external excitations, yielding:

$$\begin{Bmatrix} d^i \\ P^i \end{Bmatrix} = [T]^i \begin{Bmatrix} 0 \\ P_0^0 \end{Bmatrix} + [T]^{(i-nf)} \begin{Bmatrix} 0 \\ P_{ex}^{nf} \end{Bmatrix} \tag{3.61}$$

with $P_{ex}^{nf} = \begin{bmatrix} F^{ex} & 0 \end{bmatrix}^t$ the external excitation vector (F^{ex} is the applied force and no external moment is exerted on the smart periodic beam). d^i, P^i respectively denote the generalized displacement and force vectors at the node point between the i^{th} periodic cell and the $(i+1)^{th}$ periodic cell.

The generalized force vectors of left fixed-end and right fixed-end of the beam can be obtained as:

$$\begin{cases} P_0^0 = -\left(t_{12}^{\{N_g\}}\right)^{-1} t_{12}^{\{N_g-nf\}} P_{ex}^{nf} \\ P_n^{N_g} = \left[-t_{22}^{\{N_g\}} \left(t_{12}^{\{N_g\}}\right)^{-1} t_{12}^{\{N_g-nf\}} + t_{22}^{\{N_g-nf\}} \right] P_{ex}^{nf} \end{cases} \tag{3.62}$$

where the matrices $t_{ij}^{\{N_g\}}$ and $t_{ij}^{\{N_g-nf\}}$ are the 2 by 2 constitutive matrices of $[T]^{N_g}$ and $[T]^{N_g-nf}$, respectively:

$$\begin{cases} [T]^{N_g} = \begin{pmatrix} t_{11}^{\{N_g\}} & t_{12}^{\{N_g\}} \\ t_{21}^{\{N_g\}} & t_{22}^{\{N_g\}} \end{pmatrix} \\ [T]^{(N_g-nf)} = \begin{pmatrix} t_{11}^{\{N_g-nf\}} & t_{12}^{\{N_g-nf\}} \\ t_{21}^{\{N_g-nf\}} & t_{22}^{\{N_g-nf\}} \end{pmatrix} \end{cases} \tag{3.63}$$

- Periodic structure composed of interconnected periodic cells

Both ends of interconnected electrical circuits are open, and thus currents I_0 (*resp.* I_{N_g}) of both ends are equal to zero for smart periodic structures with interconnected electrical networks under clamped-clamped boundary condition. Assuming that V_0

(*resp.* V_{N_g}) are the voltages of both ends of circuits, the following equation may be established, considering open circuit condition for the extreme electrical nodes:

$$\begin{Bmatrix} 0 \\ P_n^{N_g} \\ U_{N_g} \end{Bmatrix} = [T]^{N_g} \begin{Bmatrix} 0 \\ P_0^0 \\ U_0 \end{Bmatrix} + [T]^{(N_g - nf)} \begin{Bmatrix} 0 \\ P_{ex}^{nf} \\ 0 \end{Bmatrix} \tag{3.64}$$

$$U_{N_g} = \begin{Bmatrix} V_{N_g} \\ I_{N_g} \end{Bmatrix} = \begin{Bmatrix} V_{N_g} \\ 0 \end{Bmatrix}, \quad U_0 = \begin{Bmatrix} V_0 \\ I_0 \end{Bmatrix} = \begin{Bmatrix} V_0 \\ 0 \end{Bmatrix}$$

Solving the above equations, dynamic responses based on transfer matrix method under clamped-clamped condition can be obtained as:

$$V_0 = \left(t_{42}^{\{N_g\}} \left(t_{12}^{\{N_g\}} \right)^{-1} t_{13}^{\{N_g\}} - t_{43}^{\{N_g\}} \right)^{-1} \left(t_{42}^{\{N_g - nf\}} - t_{42}^{\{N_g\}} \left(t_{12}^{\{N_g\}} \right)^{-1} t_{12}^{\{N_g - nf\}} \right) P_{ex}^{nf}$$

$$P_0^0 = \left(t_{12}^{\{N_g\}} \right)^{-1} \left(-t_{13}^{\{N_g\}} V_0 - t_{12}^{\{N_g - nf\}} P_{ex}^{nf} \right)$$

$$V_{N_g} = t_{32}^{\{N_g\}} P_0^0 + t_{33}^{\{N_g\}} V_0 + t_{32}^{\{N_g - nf\}} P_{ex}^{nf}$$

$$P_n^{N_g} = t_{22}^{\{N_g\}} P_0^0 + t_{23}^{\{N_g\}} V_0 + t_{22}^{\{N_g - nf\}} P_{ex}^{nf}$$

$$T^{\{N_g\}} = \begin{bmatrix} t_{11}^{\{N_g\}} & t_{12}^{\{N_g\}} & t_{13}^{\{N_g\}} & t_{14}^{\{N_g\}} \\ t_{21}^{\{N_g\}} & t_{22}^{\{N_g\}} & t_{23}^{\{N_g\}} & t_{24}^{\{N_g\}} \\ t_{31}^{\{N_g\}} & t_{32}^{\{N_g\}} & t_{33}^{\{N_g\}} & t_{34}^{\{N_g\}} \\ t_{41}^{\{N_g\}} & t_{42}^{\{N_g\}} & t_{43}^{\{N_g\}} & t_{44}^{\{N_g\}} \end{bmatrix}, \quad T^{\{N_g - nf\}} = \begin{bmatrix} t_{11}^{\{N_g - nf\}} & t_{12}^{\{N_g - nf\}} & t_{13}^{\{N_g - nf\}} & t_{14}^{\{N_g - nf\}} \\ t_{21}^{\{N_g - nf\}} & t_{22}^{\{N_g - nf\}} & t_{23}^{\{N_g - nf\}} & t_{24}^{\{N_g - nf\}} \\ t_{31}^{\{N_g - nf\}} & t_{32}^{\{N_g - nf\}} & t_{33}^{\{N_g - nf\}} & t_{34}^{\{N_g - nf\}} \\ t_{41}^{\{N_g - nf\}} & t_{42}^{\{N_g - nf\}} & t_{43}^{\{N_g - nf\}} & t_{44}^{\{N_g - nf\}} \end{bmatrix}$$

Therefore, the displacement, slope, force, moment, voltage and current vectors at any node *i* may be obtained from:

$$\begin{Bmatrix} d_i \\ P_i \\ U_i \end{Bmatrix} = [T]^i \begin{Bmatrix} 0 \\ P_0^0 \\ U_0 \end{Bmatrix} + [T]^{(i - nf)} \begin{Bmatrix} 0 \\ P_{ex}^{nf} \\ 0 \end{Bmatrix} \tag{3.65}$$

3.6 Experimental setup for low-frequency vibration damping validation

Following the previous analysis, frequency responses of the clamped-clamped piezoelectric periodic beam are compared and discussed theoretically and experimentally in this section for validating damping performance on smart periodic structure with different electrical networks.

The beam sample given in Figure 3.31 is composed of four interconnected periodic cells and the length of each interconnected cell is 44 mm. Parameters of the beam substructure and PZTs are listed in Table 3.1 and Table 3.2. The experimental setup is depicted in Figure 3.32. There are five nodal points in the clamped-clamped beam sample. The nodal point between the 1st interconnected periodic cell and the 2nd interconnected periodic cell, and the nodal point between the 3rd interconnected periodic cell and the 4th interconnected periodic cell can be used to achieve numerical frequency response curves for the interconnected case, except two fixed end points and the middle nodal point between the 2nd and 3rd interconnected periodic cells. Therefore, four interconnected periodic cells are enough for comparing attenuation performance between the SSDI interconnected methods and the SSDI independent method through observing the difference of frequency response curves. An external force, applied to the node between the 1st interconnected periodic cell and the 2nd interconnected periodic cell, is generated by an electromagnet driven by an amplifier with the signal delivered by a function generator. Herein, the switching command is produced by a dSpace system which controls dedicated switching circuits for obtaining more precise experimental results. However, it might be convenient to replace the dSpace system by integrated self-powered SSDI circuits [33, 34] as the switching control device in practical applications. An inductive displacement sensor is used for monitoring the displacement of the node between the 3rd interconnected periodic cell and the 4th interconnected periodic cell. The displacement in the steady state is ensured to remain sinusoidal for each measured point for validating the first

harmonic approximation. Such approximation is further enforced by the fact that the resonant nature of the structure actually filters high-order harmonics, while for off-resonance excitation, the magnitude of the voltage (including the nonlinear part whose amplitude relies on the displacement) is too small to induce significant response. Herein, the steady state of flexural response is observed through the displacement of a single nodal point, thus only stationary waves can be considered, which is consistent with the flexural nature of the vibration. Therefore, no phase delay for each considered mode appears.

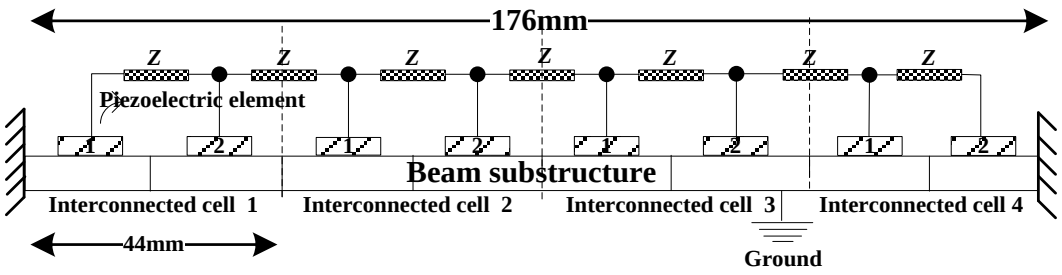

Figure 3.31 Clamped-clamped piezoelectric periodic beam.

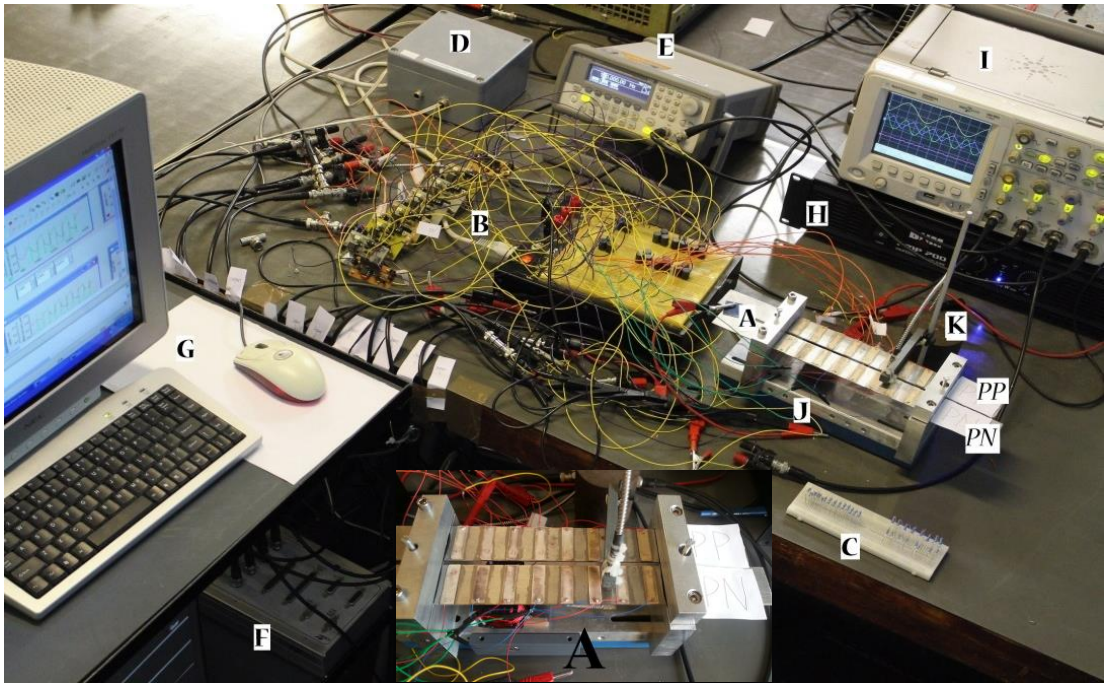

Figure 3.32 Experimental Setup: A: Host piezoelectric beams including the PP interconnected and the PN interconnected; B: SSDI switching circuits; C: optimal resistance arrays for different modes; D: displacement signal conditioner; E: function generator; F: dSpace system; G: computer; H: power amplifier; I: oscilloscope; J: electromagnet; K: inductive vibrometer; *PP*: PP interconnected configuration; *PN*: PN interconnected configuration.

3.7 Theoretical and experimental results

Structural damping is considered in the following analysis to reflect experimental behavior. More precisely, Rayleigh damping, defining the damping matrix C^e of one element as a function of mass and stiffness matrices of a single element (respectively given as M^e and K^e) such as $C^e = \beta_1 M^e + \beta_2 K^e$, is introduced in the frequency response analysis. According to preliminary experimental measurements, the coefficients β_1 and β_2 have been determined to be equal to:

$$\begin{cases} \beta_1 = 20 s^{-1} \\ \beta_2 = 13 \times 10^{-6} s \end{cases}$$

In experiments, the inversion coefficients in SSDI independent and interconnected cases are equal to 0.5 and 0.6 ($\gamma_{ind} = 0.5, \gamma_{\text{int}} = 0.6$), respectively. Two types of damping techniques (resistive shunts and SSDI shunts with different inversion coefficients) are experimentally implemented with independent or (PP / PN) interconnected methods in periodic structures. Measured results in different cases are compared with theoretical displacement predictions as depicted in Figure 3.33 - Figure 3.38. Table 3.4 summarizes theoretical and experimental damping performance of resistive, SSDS and SSDI techniques for each mode.

Considering that it is difficult to implement automatic resistance adaptation practically for each frequency in resistive cases, three different fixed optimized resistances are adopted for the three vibration mode in experiments (each resistance corresponding to the frequency range around the mode of interest). Since the two beam samples used for PP / PN interconnected methods are not exactly the same in practical implementation, slight differences between theoretical and experimental modes appear between the two configurations. However, these errors are allowable for the conclusive results. In addition, since higher mode displacements (2nd mode and 3rd mode) are too small to be sensed in experiments, larger force for beam excitation was applied for these modes, and then normalized with respect to the 1st mode excitation.

Globally, according to the comparison among logarithmic decays of propagative wave, normalized theoretical and experimental displacement responses in different cases (resistive cases: Figure 3.33 for theoretical results, Figure 3.34 for experimental results; SSDS cases: Figure 3.35 for theoretical results, Figure 3.36 for experimental results; SSDI cases: Figure 3.37 for theoretical results, Figure 3.38 for experimental results), smart periodic structures with SSDI electrical networks have the best attenuation performance in the whole investigated frequency spectrum. In resistive cases, as shown in Table 3.4, damping performance of 1.06 dB for theoretical results and 1.11 dB for experimental results is obtained in the independent case for the first modal vibration control, which is slightly better than that of the interconnected cases.

For the 2nd modal control and the 3rd modal control, theoretical predictions are close in each mode of independent and interconnected cases, while in comparison of experimental results, interconnected approaches achieve better damping performance (0.89 dB for the 2nd mode and 1.16 dB for the 3rd mode) than the independent method.

In terms of smart periodic structure with SSDS electrical networks, theoretical predictions of independent and PN interconnected cases are better than that of the PP interconnected case for the first two modes, and in the third mode, theoretical predictions are close in independent and interconnected cases. Experimentally, the PN interconnected case exhibits better damping performance than the other SSDS cases in the whole investigated frequency spectrum. Additionally, the PP interconnected case shows similar damping performance with the PN interconnected case in the 3rd mode, although it shows the worst damping performance in the 1st and 2nd modes among all the SSDS cases. Such performance difference between the PP interconnected case and the PN interconnected case can be explained by PP / PN connection configurations introduced in Section 3.2.

For smart periodic structure with SSDI electrical networks, damping performance is enhanced with the increased inversion coefficient since more structural energy is converted to electrical energy by the artificially nonlinear voltage inversion process. According to theoretical results and experimental measurements, damping performance of the SSDI independent case is superior to the other two SSDI (PN and PP) interconnected cases for vibration reduction of the first two modes. However, for suppressing the third mode, SSDI PP interconnected network shows the best damping performance among all the SSDI cases, which is also attributed to the work principle demonstrated in Section 3.2.

As shown in results (Figure 3.33 - Figure 3.38 and Table 3.4), some small discrepancies appear between theoretical results and experimental results, which may be caused by several factors: theoretical results are based on the simplified Euler-Bernoulli beam theory; Rayleigh damping used in the FE modeling is determined manually according to the experimental measurement. In addition, there

are mode shifts between theoretical modes and experimental modes, between the piezoelectric PP beam sample and the piezoelectric PN beam sample. Part of reason for mode shifts is explained by different piezoelectric beam samples with the same theoretical parameters, but with some discrepancies in experiments. Furthermore, with the increase of inversion coefficient, the mode shifts between the PP beam sample and the PN beam sample become larger as shown in the comparison between Figure 3.35 and Figure 3.37. The main cause of mode shifts is that dispersion curves of a PP interconnected periodic cell are different from the curves of a PN interconnected periodic cell. Such dispersive difference becomes more evident with the increase of inversion coefficient. Another aspect lies in some aperiodicity in the experimental implementations, yielding better performance than theoretically predicted [93, 312]. Despite these differences, change trends in the damping performance of interconnected methods can be well explained by the general principle of interconnected methods since the investigated frequency range is before the first Bragg-type stop band and thus is immune to Bragg scattering mechanism. In addition, theoretical predictions for attenuation performance of the interconnected cases, under first harmonic approximation of SSDI impedance estimation, are in good agreement with experimental results. The critical frequency point, from which PP interconnected method becomes having better wave attenuation performance than PN interconnected method, may exist between the 2nd mode and the 3rd mode.

Although theoretical results are obtained based on simplified linearization of SSDI electrical damping system, experimental results match well with theoretical predictions on the damping performance difference between the PP interconnected configuration and the PN interconnected configuration. Mutual validation between theoretical and experimental results is established in the low frequency domain including the first three modes. Therefore, the linearization of the SSDI electrical system is valid in characterizing smart periodic structure with SSDI interconnected / independent electrical networks, since it is implemented by considering the nonlinear piecewise voltage (and thus taking phase shift and amplitude magnification of the voltage into account).

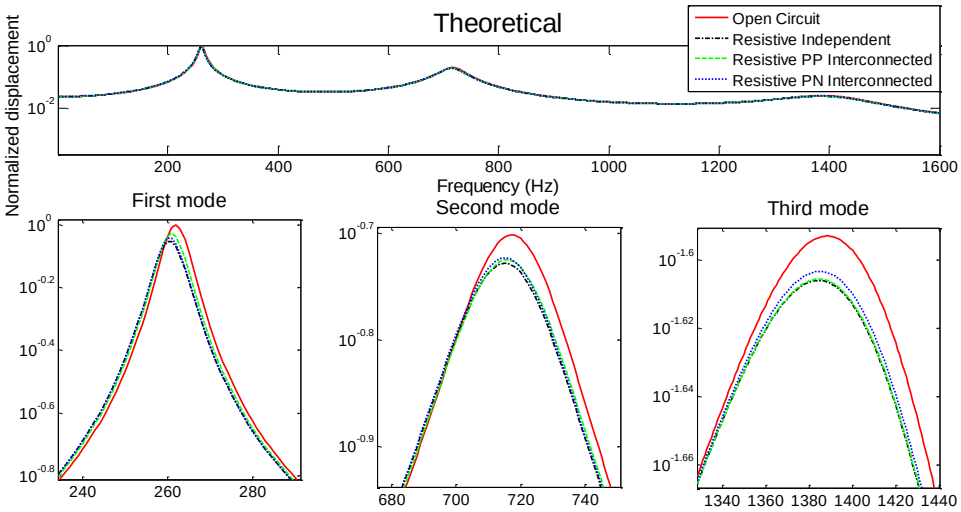

Figure 3.33 Normalized theoretical displacement of clamped-clamped beam in resistive cases.

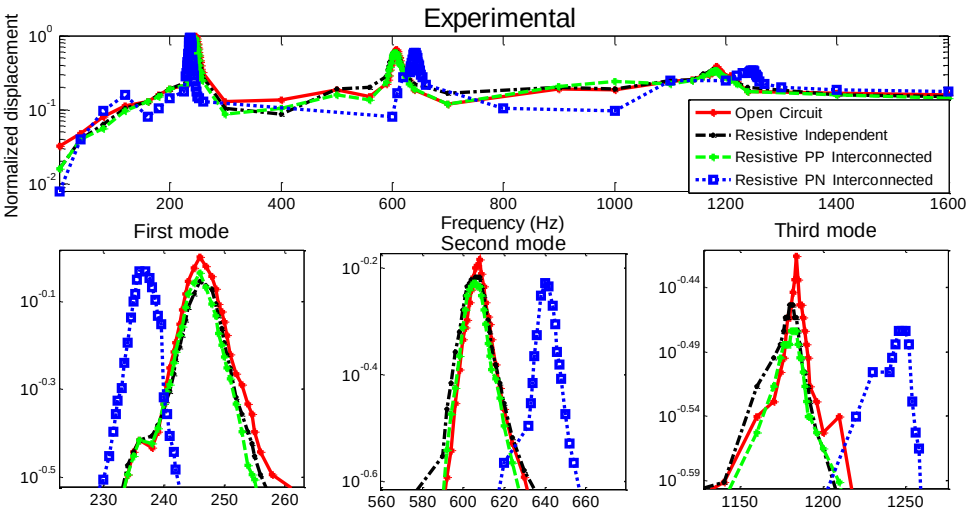

Figure 3.34 Normalized experimental displacement of clamped-clamped beam in resistive cases.

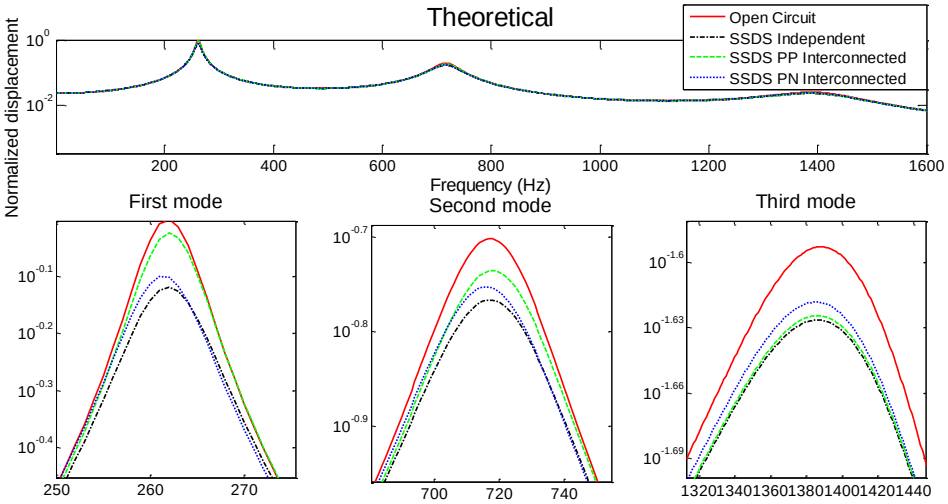

Figure 3.35 Normalized theoretical displacement of clamped-clamped beam in SSDS cases.

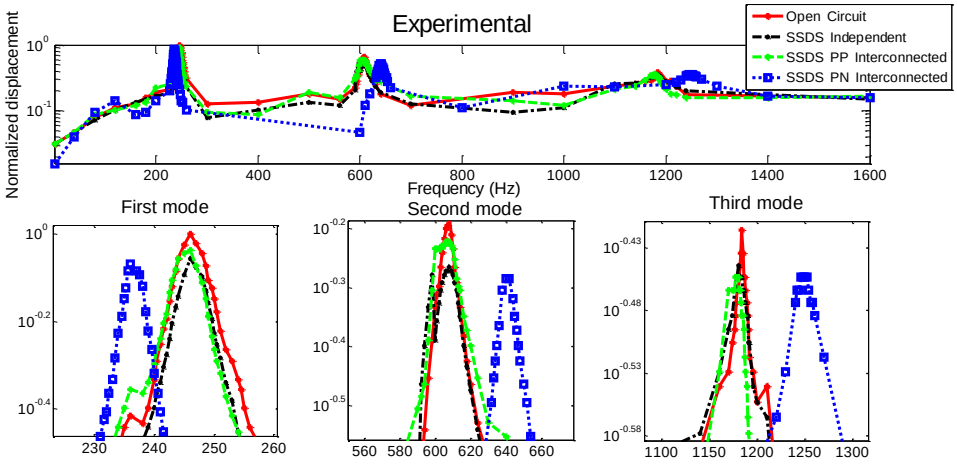

Figure 3.36 Normalized experimental displacement of clamped-clamped beam in SSDS cases.

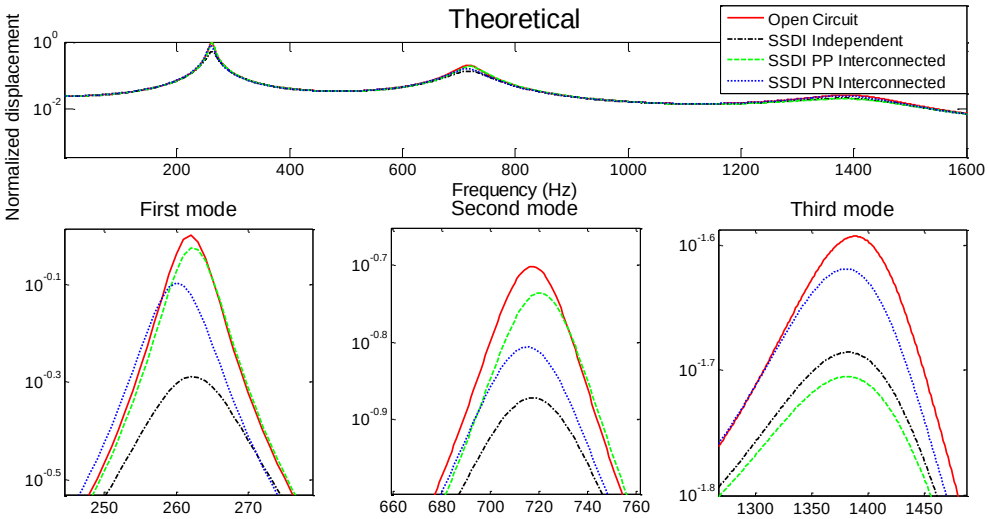

Figure 3.37 Normalized theoretical displacement of clamped-clamped beam in SSDI cases.

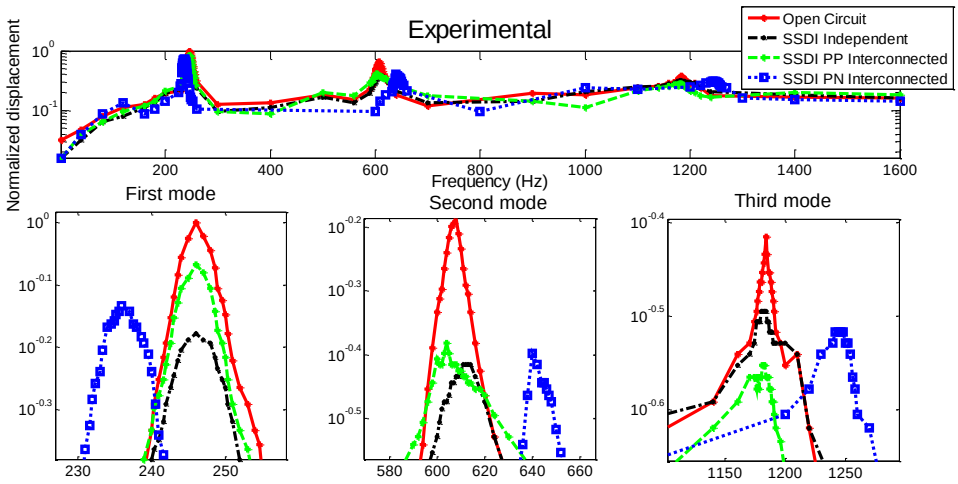

Figure 3.38 Normalized experimental displacement of clamped-clamped beam in SSDI cases.

Table 3.4 Attenuation of normalized displacement under different techniques.

		1st Mode	2nd Mode	3rd Mode
Resistive Independent (dB)	Theoretical	1.06	0.53	0.27
	Experimental	1.11	0.66	0.76
Resistive Interconnect PP (dB)	Theoretical	0.57	0.46	0.25
	Experimental	0.72	0.89	1.16
Resistive Interconnect PN (dB)	Theoretical	0.88	0.43	0.21
	Experimental	0.65	0.89	1.16
SSDS Independent (dB)	Theoretical	2.38	1.29	0.67
	Experimental	1.11	1.63	0.56
SSDS Interconnect PP (dB)	Theoretical	0.49	0.68	0.63
	Experimental	0.72	0.78	0.76
SSDS Interconnect PN (dB)	Theoretical	2.01	1.02	0.51
	Experimental	1.35	2.01	0.76
SSDI Independent (dB)	Theoretical	5.78	3.41	1.86
	Experimental	3.56	4.65	1.58
SSDI Interconnect PP (dB)	Theoretical	0.50	0.68	2.25
	Experimental	1.35	3.95	2.74
SSDI Interconnect PN (dB)	Theoretical	1.94	2.09	0.52
	Experimental	2.66	4.30	2.03

3.8 Extensions

Although the core of this chapter lies in the presentation and analysis of interconnected periodic structures, this section proposes to discuss possible extensions of the exposed principles that may provide some enhancement of the damping performance.

3.8.1 Smart periodic structure with SSDI Hybrid Capacitance-Shunting interconnected electrical networks

A new smart periodic structure with SSDI Hybrid Capacitance (HC)-Shunting interconnected electrical networks is proposed in this section, which can alter locations of new generated resonant-type PBG (Phononic Band Gap) between Bragg-type PBGs through changing values of the external capacitances. As shown in Figure 3.39, identical external capacitances (C) are respectively connected to each

PZT of a PP / PN interconnected SSDI periodic cell, which composes a SSDI HC-shunting PP / PN interconnected periodic cell of the proposed structure.

The equivalent capacitance of each PZT in the proposed structure is equal to:

$$C_{equ} = C_0 + C \tag{3.66}$$

Therefore,

$$Z_{\text{int}-C} = \frac{\pi\left(1-\gamma_{\text{int}-C}\right)}{2\omega\left(1+\gamma_{\text{int}-C}\right)C_{equ}} + \frac{2j}{\omega C_{equ}} \tag{3.67}$$

In addition, it should be noted that,

$$\gamma_{\text{int}-C} = e^{-\frac{r\pi}{2}\sqrt{\frac{C_{equ}}{2L}}} = \gamma_{ind}^{\sqrt{\frac{C_{equ}}{2C_0}}} \tag{3.68}$$

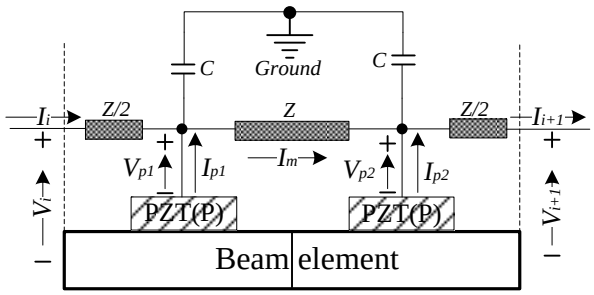

(a)

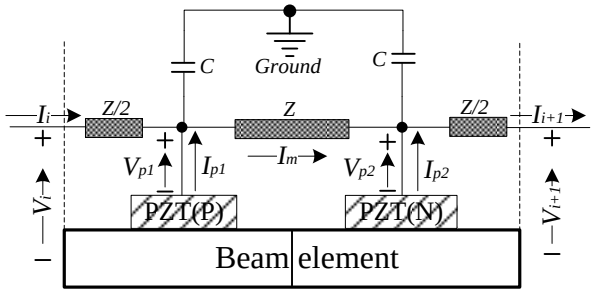

(b)

Figure 3.39 (a) Hybrid-Capacitance interconnected periodic cell *i* with PP configuration; (b) Hybrid-Capacitance interconnected periodic cell *i* with PN configuration. *Z* is the SSDI impedance.

Similarly, dynamical response relationships for the HC-Shunting PP / PN interconnected periodic cell can be summarized as:

$$\begin{Bmatrix} P^i \\ V_{i+1} \\ I_{i+1} \end{Bmatrix} = A_{\text{int}erconnected-C} \begin{Bmatrix} d^i \\ V_i \\ I_i \end{Bmatrix} = \begin{bmatrix} A_{11} & A_{12} & A_{13} \\ A_{21} & A_{22} & A_{23} \\ A_{31} & A_{32} & A_{33} \end{bmatrix} \cdot \begin{Bmatrix} d^i \\ V_i \\ I_i \end{Bmatrix} \tag{3.69}$$

$$A_{11} = A^e - Z_{\text{int}-C} \cdot B_{21} \cdot B_{12} \cdot j\omega;$$

$$A_{12} = B_{11} + B_{12} - Z_{\text{int}-C} \cdot B_{12} \cdot B_{31} \cdot j\omega;$$

$$A_{13} = -\left(\frac{Z_{\text{int}-C}}{2} \cdot B_{11} + \frac{3Z_{\text{int}-C}}{2} \cdot B_{12} \right) + \frac{Z_{\text{int}-C}^2}{2} \cdot B_{12} \cdot B_{31} \cdot j\omega;$$

$$A_{21} = -\omega^2 \cdot \frac{Z_{\text{int}-C}^2}{2} \cdot B_{31} \cdot B_{21} - \frac{Z_{\text{int}-C}}{2} \cdot B_{22} \cdot j\omega - \frac{3}{2} Z_{\text{int}-C} \cdot B_{21} \cdot j\omega;$$

$$A_{22} = 1 - \frac{Z_{\text{int}-C}^2}{2} \cdot B_{31}^2 \cdot \omega^2 - 2Z_{\text{int}-C} \cdot B_{31} \cdot j\omega;$$

$$A_{23} = \frac{3}{2} Z_{\text{int}-C}^2 \cdot B_{31} \cdot j\omega - 2Z_{\text{int}-C} + \frac{Z_{\text{int}-C}^3}{4} \cdot B_{31}^2 \cdot \omega^2;$$

$$A_{31} = \omega^2 \cdot Z_{\text{int}-C} \cdot B_{32} \cdot B_{21} + B_{22} \cdot j\omega + B_{21} \cdot j\omega;$$

$$A_{32} = Z_{\text{int}-C} \cdot B_{31}^2 \cdot \omega^2 + 2 \cdot B_{31} \cdot j\omega;$$

$$A_{33} = 1 - 2Z_{\text{int}-C} \cdot B_{31} \cdot j\omega - \frac{Z_{\text{int}-C}^2}{2} \cdot B_{31}^2 \cdot \omega^2.$$

Based on the above relationships and transfer matrix method, numerical results are presented using the experimental parameters listed in Table 3.1 and Table 3.2. Figure 3.40 shows logarithmic decay curves of propagative wave in smart periodic structures with the SSDI HC-Shunting PP / PN interconnected networks under different values of external capacitances ($C=(0,\ 0.25,\ 0.5,\ 0.75,\ 6) \times C_0$). With the increase of the external capacitances, the location of the peak of the first resonant-type band gap in the SSDI HC-Shunting PP interconnected network is gradually close to 0 Hz, and the peak of the second resonant-type band gap approaches the location of the second Bragg-type band gap in the SSDI HC-Shunting PP interconnected case. At the same time, the peaks of two new resonant-type band gaps are gradually close to the first Bragg-type band gap in the SSDI HC-Shunting PN interconnected case. In addition, it should be noted that the frequency regions in which the attenuation performance of SSDI HC-Shunting PN interconnected network outperforms that of SSDI independent network, are getting narrower and narrower when the external capacitance increases.

Especially, when the capacitance value is close to or larger than the inherent capacitance of the piezoelectric element, such frequency regions even disappear.

Therefore, above theoretical comparisons demonstrated that introducing external capacitances with proper values into SSDI interconnected networks can improve the application flexibility by changing the location of the resonant-type band gaps, but introducing external capacitances with large values may greatly weaken the attenuation performance of the structures, as they yield reduced electromechanical coupling. This is also similar with the research of Fleming *et al* [23], stating that placing an external capacitance across the two terminals of a piezoelectric element, the inductance requirements of piezoelectric shunt damping systems can be greatly reduced, and better damping performance was experimentally validated through the comparison with the damping systems without additional capacitances, but additional capacitance with too large values will lead to poor damping performance.

Phase difference curves of propagative wave in the SSDI HC-Shunting PP / PN interconnected case under different values of external capacitances are shown in Figure 3.41. Curve changes of the phase difference corresponding to the peaks of resonant-type band gaps in different cases are small except the phase difference change corresponding to the peak of second resonant-type band gap in the SSDI HC-Shunting PN interconnected case. It can be seen that such phase difference change gradually approaches the location of the first Bragg-type band gap with the increase of the additional capacitance values.

Figure 3.42 shows evanescent and electrical waves in the SSDI HC-Shunting PP / PN interconnected cases using different values of external capacitances. It can be seen that logarithmic decay and phase difference curves of evanescent wave are similar in different cases. The peaks and valleys of electrical wave are closely related to the locations of new resonant-type band gaps. It shows that additional capacitances can indirectly alter the properties of propagative wave by virtue of the wave propagation interaction between the electrical and mechanical media of smart periodic structures.

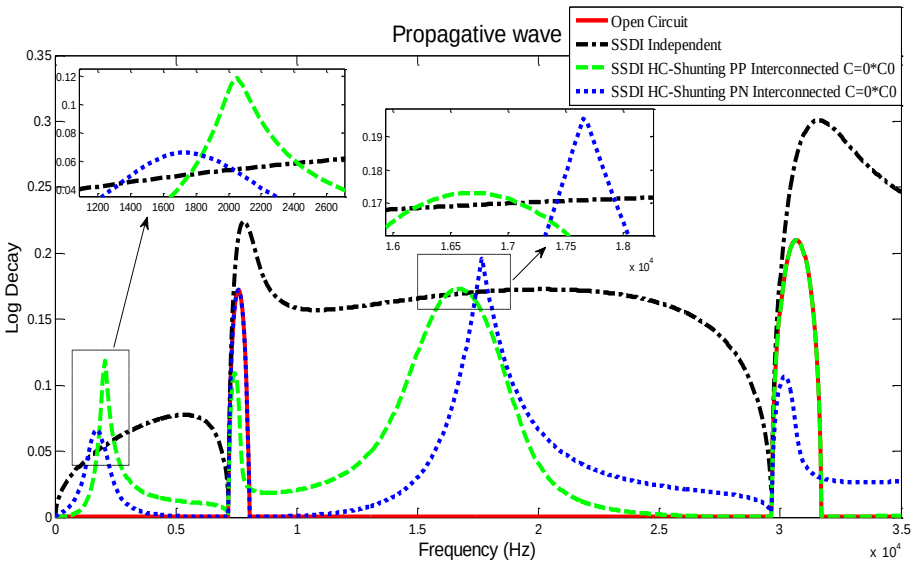

(a)

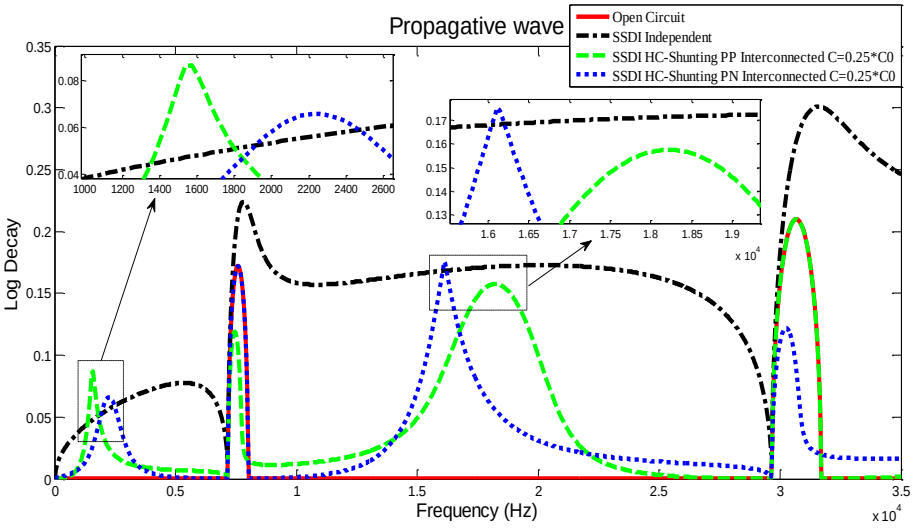

(b)

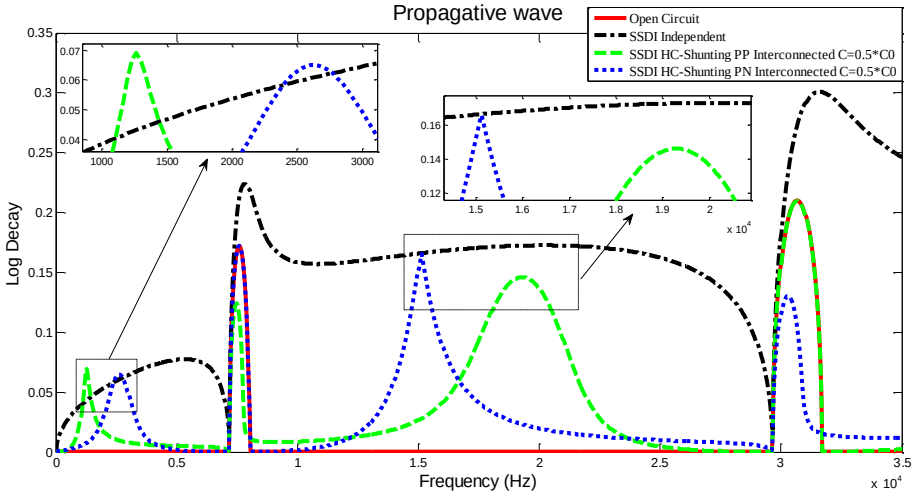

(c)

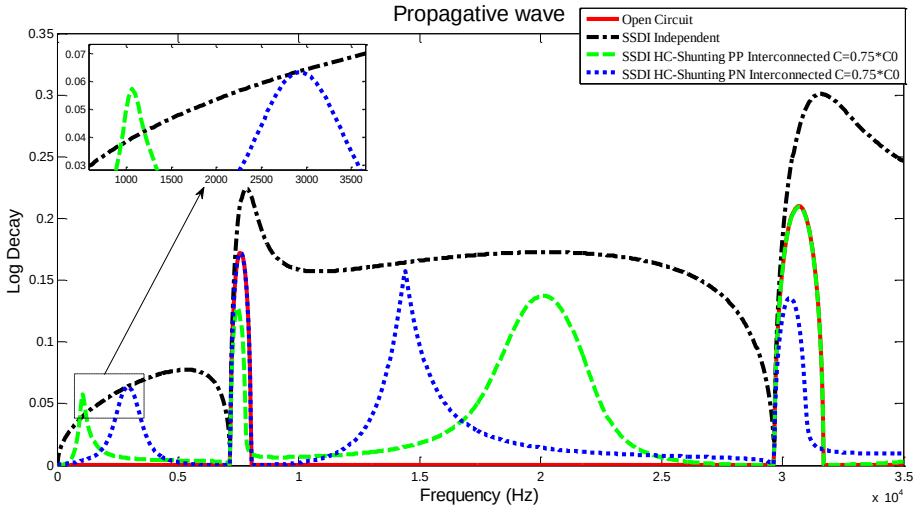

(d)

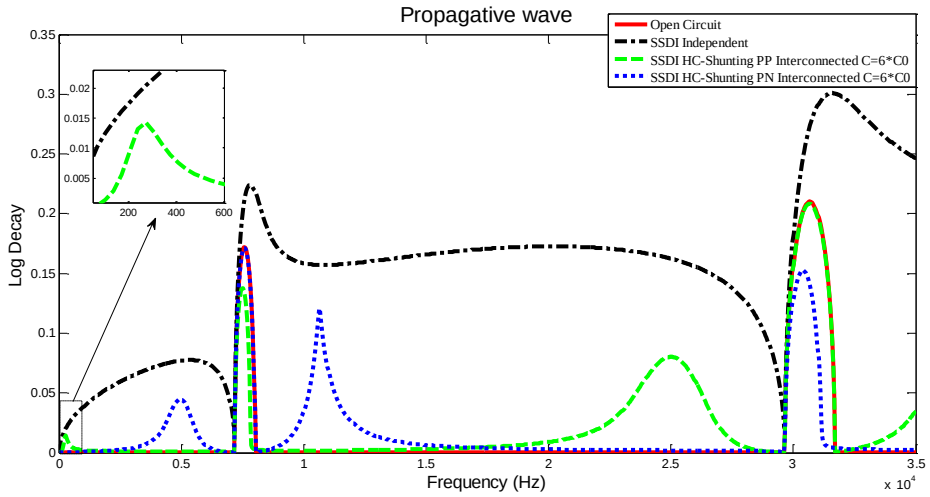

(e)

Figure 3.40 (a) Logarithmic decay of propagative wave in SSDI HC-Shunting PP interconnected case ($C=0*C_0$); (b) Logarithmic decay of propagative wave in SSDI HC-Shunting PN interconnected case ($C=0.25*C_0$); (c) Logarithmic decay of propagative wave in SSDI HC-Shunting PN interconnected case ($C=0.5*C_0$); (d) Logarithmic decay of propagative wave in SSDI HC-Shunting PN interconnected case ($C=0.75*C_0$); (e) Logarithmic decay of propagative wave in SSDI HC-Shunting PN interconnected case ($C=6*C_0$). $\gamma_{ind}=0.5$, $\gamma_{\mathrm{int}-C}=\gamma_{ind}^{\sqrt{\frac{C_0+C}{2C_0}}}$.

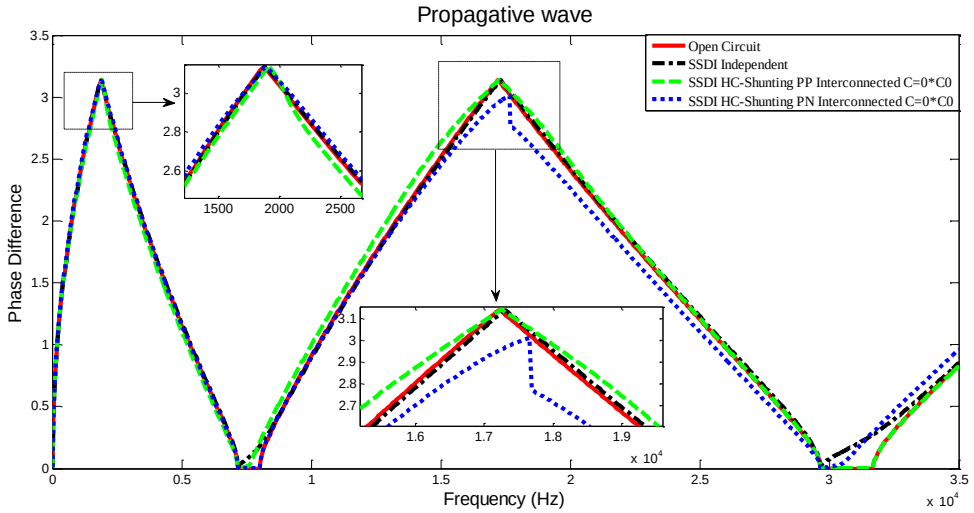

(a)

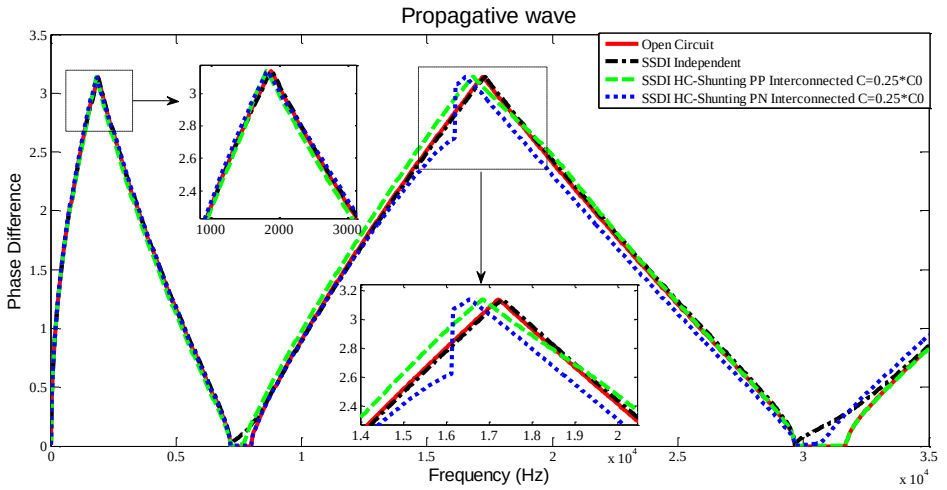

(b)

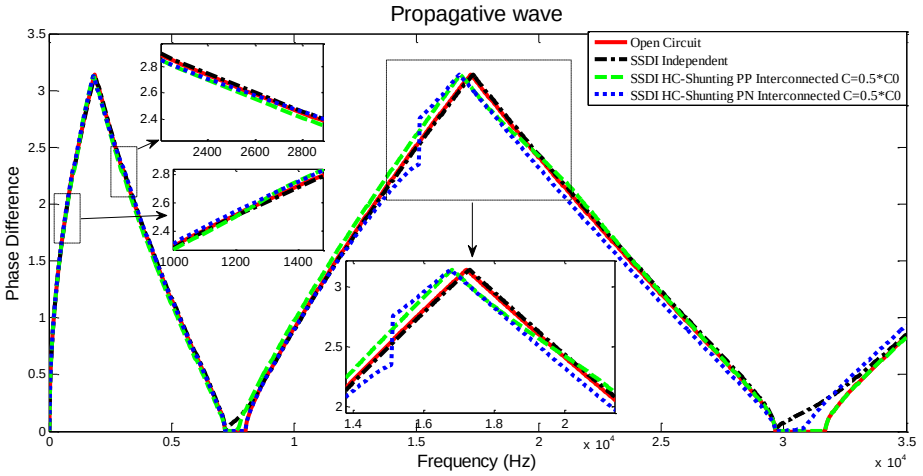

(c)

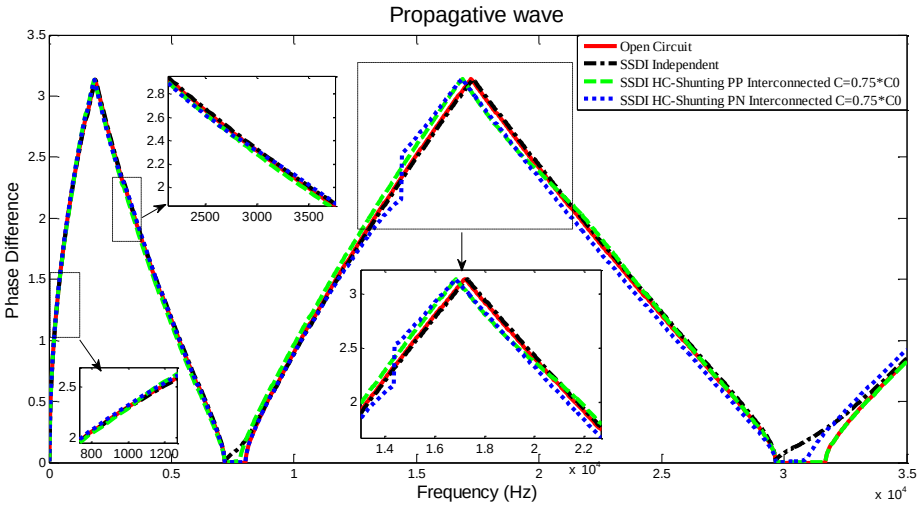

(d)

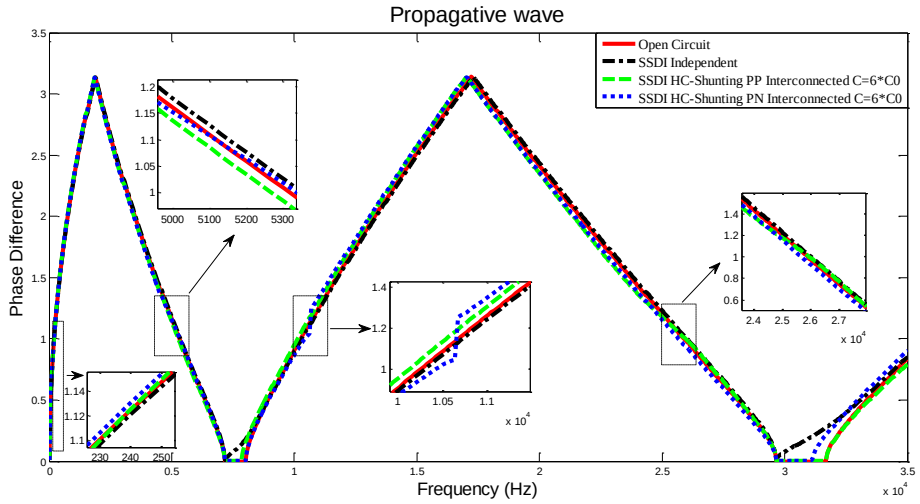

(e)

Figure 3.41 (a) Logarithmic decay of propagative wave in SSDI HC-Shunting PP interconnected case ($C=0*C_0$); (b) Logarithmic decay of propagative wave in SSDI HC-Shunting PN interconnected case ($C=0.25*C_0$); (c) Logarithmic decay of propagative wave in SSDI HC-Shunting PN interconnected case ($C=0.5*C_0$); (d) Logarithmic decay of propagative wave in SSDI HC-Shunting PN interconnected case ($C=0.75*C_0$); (e) Logarithmic decay of propagative wave in SSDI HC-Shunting PN interconnected case ($C=6*C_0$). $\gamma_{ind}=0.5$, $\gamma_{\mathrm{int}-C}=\gamma_{ind}^{\sqrt{\frac{C_0+C}{2C_0}}}$.

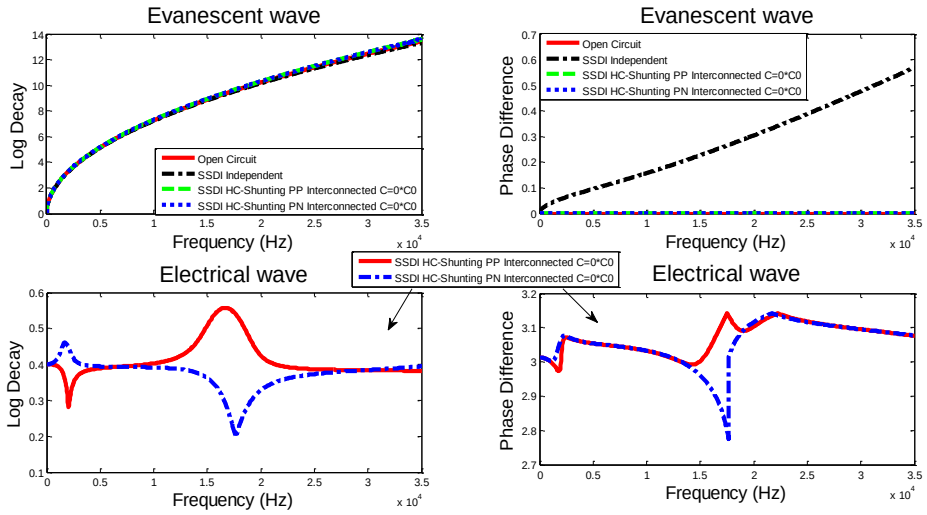

(a)

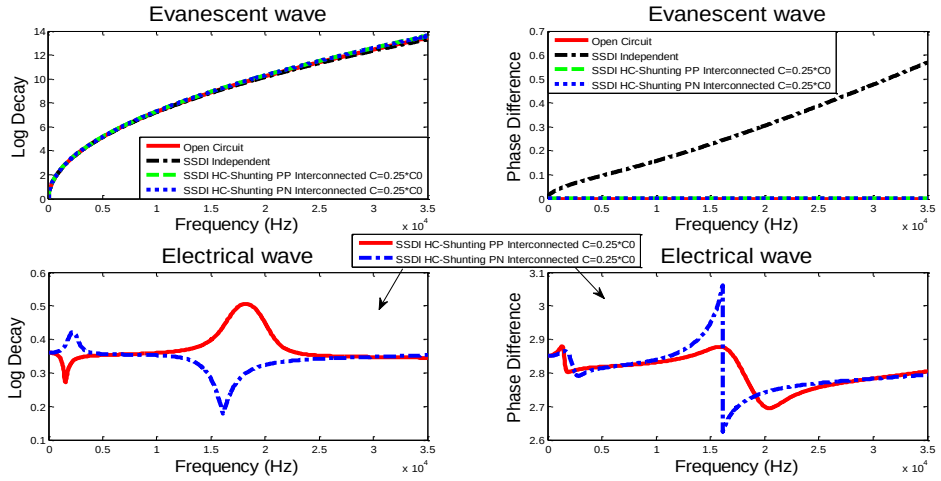

(b)

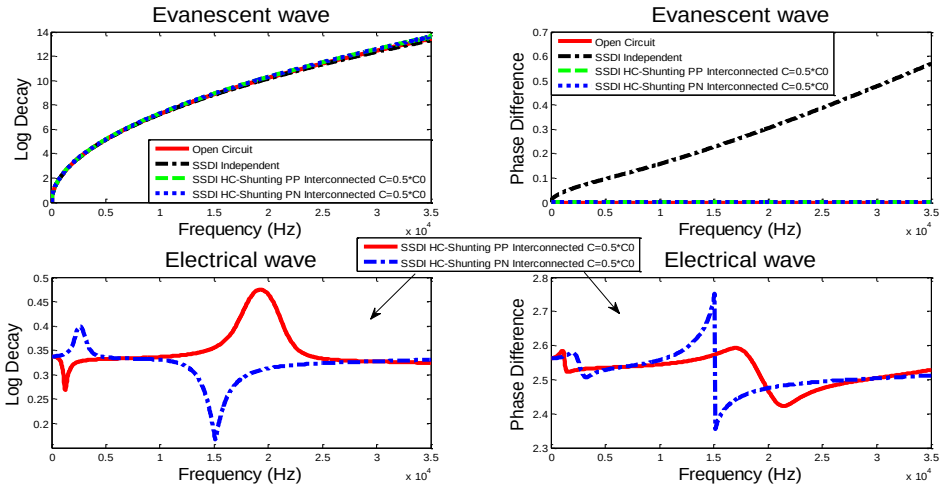

(c)

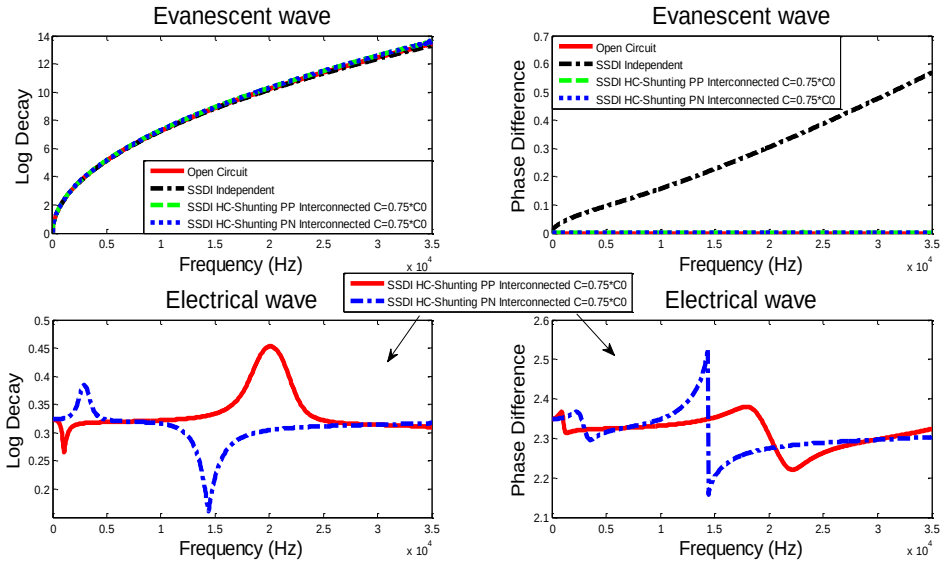

(d)

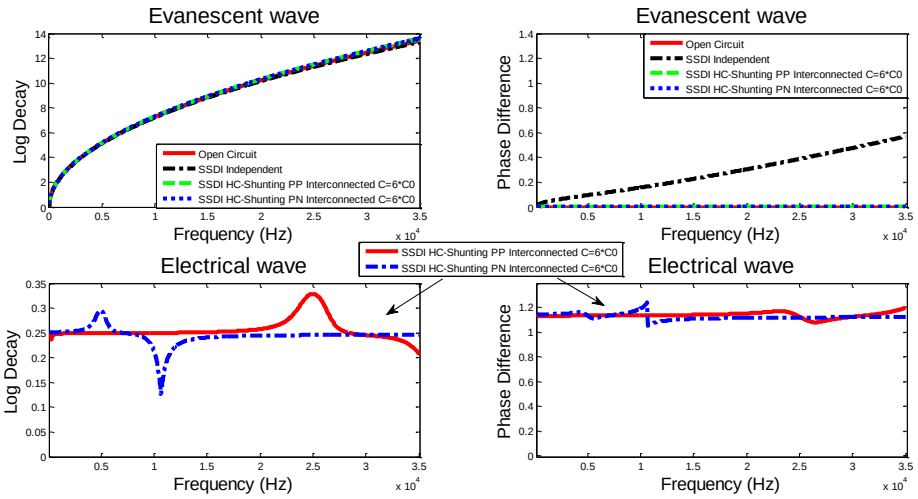

(e)

Figure 3.42 (a) Evanescent and electrical waves in SSDI HC-Shunting PP interconnected case ($C=0*C_0$); (b) evanescent and electrical waves in SSDI HC-Shunting PN interconnected case ($C=0.25*C_0$); (c) evanescent and electrical waves in SSDI HC-Shunting PN interconnected case ($C=0.5*C_0$); (d) evanescent and electrical waves in SSDI HC-Shunting PN interconnected case ($C=0.75*C_0$); (e) evanescent and electrical waves in SSDI HC-Shunting PN interconnected case ($C=6*C_0$). $\gamma_{ind}=0.5$, $\gamma_{\mathrm{int}-C}=\gamma_{ind}^{\sqrt{\frac{C_0+C}{2C_0}}}$.

3.8.2 Smart periodic structure with SSDI Dual-connected electrical networks

A new smart periodic structure with SSDI PP / PN Dual-connected electrical networks is proposed in this section. Two kinds of SSDI PP / PN Dual-connected periodic cells are depicted in Figure 3.43.

Similarly, for a PP / PN Dual-connected periodic cell, $V_{p1,p2}$ and $I_{p1,p2}$ are the output voltages and currents of piezoelectric patches 1, 2 which are connected across the electronic load *Z*. The signs of piezoelectric constant depend on the direction of polarization of the piezoelectric patches 1, 2: when the direction is positive (*P*), it is assumed equal to 1, and when negative (*N*), it is assumed equal to -1. I_m is the current through the load *Z*. Then the periodic cell holds the following relationships:

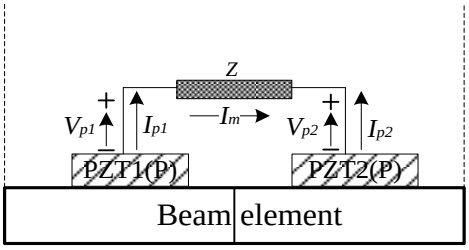

(a)

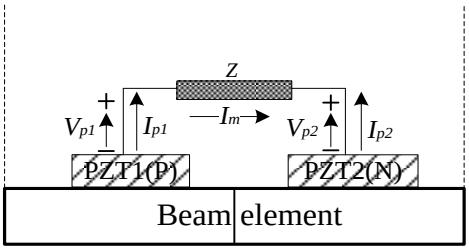

(b)

Figure 3.43 (a) Dual-connected periodic cell *i* with PP configuration; (b) Dual-connected periodic cell *i* with PN configuration. *Z* is the SSDI impedance.

$$\begin{cases} P^i = A^e d^i + B_1^e V_p \\ I_{p1} = B_{21}\dot{d}^i + B_{31}\dot{V}_{p1} \\ I_{p2} = B_{22}\dot{d}^i + B_{32}\dot{V}_{p1} \\ I_{p1} = I_m, I_{p2} = -I_m \qquad , I_p = \begin{bmatrix} I_{p1} \\ I_{p2} \end{bmatrix}, V_p = \begin{bmatrix} V_{p1} \\ V_{p2} \end{bmatrix} \\ V_{p1} - I_m Z = V_{p2} \\ Z = \dfrac{\pi\left(1-\gamma_{\text{int}}\right)}{2\omega\left(1+\gamma_{\text{int}}\right)C_0} + \dfrac{2j}{\omega C_0} \end{cases} \tag{3.70}$$

Therefore, the piezoelectric voltages of the PZTs in the periodic cell can be obtained as:

$$V_p = B_5^e d^i, B_5^e = \begin{bmatrix} \dfrac{-\left(\dfrac{B_{21}+B_{22}}{B_{31}}\right) + j\omega Z B_{21}}{2 - j\omega Z B_{31}} \\ -\left(\dfrac{B_{21}+B_{22}}{B_{31}}\right) - \dfrac{-\left(\dfrac{B_{21}+B_{22}}{B_{31}}\right) + j\omega Z B_{21}}{2 - j\omega Z B_{31}} \end{bmatrix} \tag{3.71}$$

And the dynamical relationships of the SSDI PP / PN Dual-connected periodic cell can be given by:

$$\left\{P^i\right\} = A^e_{Dual-connected} \cdot d^i = \left(A^e + B_1^e B_5^e\right) \cdot d^i \tag{3.72}$$

Through transfer matrix analysis based on the experimental parameters listed in Table 3.1 and Table 3.2, Figure 3.44 shows logarithmic decay and phase difference curves of propagative wave in smart periodic structures with the SSDI PP / PN Dual-connected networks. For equitable attenuation performance comparison, two minimal independent periodic cells with two identical SSDI shunts are compared with one minimal PP / PN Dual-connected periodic cell with one same SSDI shunt. Compared with the SSDI independent case having good attenuation performance in the whole investigated frequency band, better attenuation performance is exhibited in some stop bands, more particularly the frequency range [3.35 kHz, 13.9 kHz] for SSDI PP Dual-connected case, and the frequency ranges [0 Hz, 840 Hz] ∪ [21.2 kHz, 35 kHz] for SSDI PN Dual-connected case. Therefore, the SSDI PP / PN Dual-connected cases indeed do not have broader attenuation performance than the SSDI independent case, but they have the ability of using less SSDI shunts to achieve

better attenuation performance in some relatively broad frequency ranges close to stop bands.

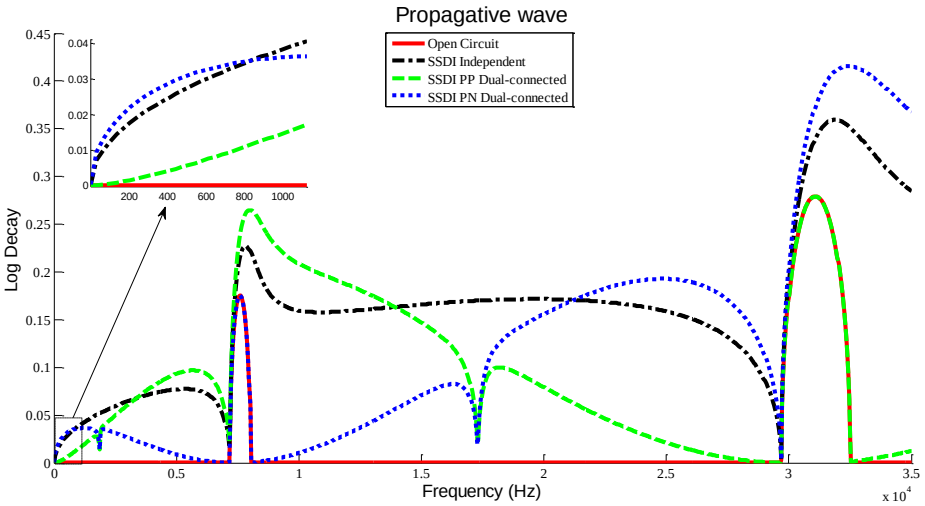

(a)

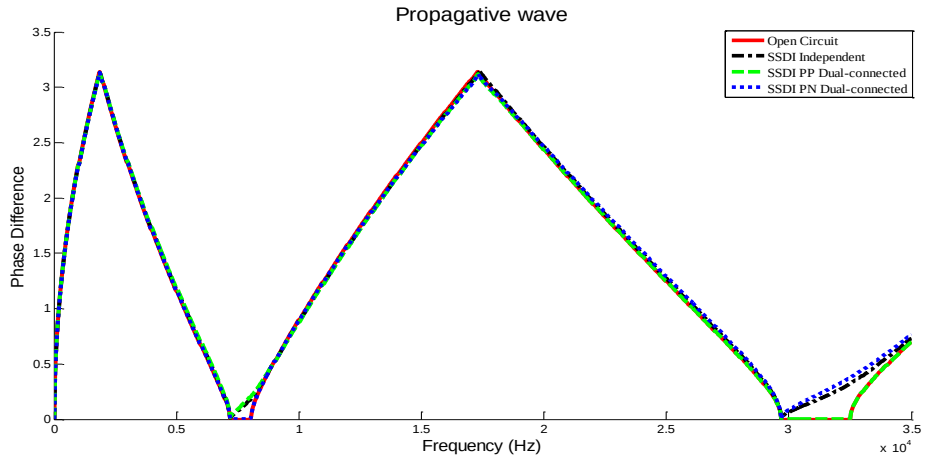

(b)

Figure 3.44 (a) logarithmic decay curves and (b) phase difference curves of propagative wave in smart periodic structures with the SSDI PP / PN Dual-connected networks. $\gamma_{ind} = 0.5$, $\gamma_{int} = 0.6$.

Figure 3.45 shows logarithmic decay and phase difference curves of evanescent wave in smart periodic structures with the SSDI PP / PN Dual-connected networks. Compared with the logarithmic decay curve of evanescent wave in the SSDI independent case, logarithmic decay curves of evanescent wave in the SSDI PP / PN Dual-connected cases are increasing in a similar rate before 5.7 kHz around, and in a slower rate in the following frequency range [5.7 kHz, 35 kHz]. In addition, phase

difference curves of evanescent wave in the SSDI PP / PN Dual-connected cases are increasing at a higher rate than the curve of evanescent wave in the SSDI independent case within the whole investigated frequency range.

Figure 3.46 shows the 3D plots of logarithmic decay of elastic wave for the SSDI PP / PN Dual-connected cases versus the voltage inversion coefficient compared with the SSDI independent case. With the increase of inversion coefficient, all the attenuation performances are enhanced in different cases. Although the SSDI independent case have globally better attenuation performance than the SSDI PP / PN Dual-connected cases, locally compared with the SSDI independent case, the SSDI PP Dual-connected case has better attenuation performance at the vicinity of the first resonant-type band gap, while the SSDI PN Dual-connected case exhibits better attenuation performance near 0 Hz and the second resonant-type band gap.

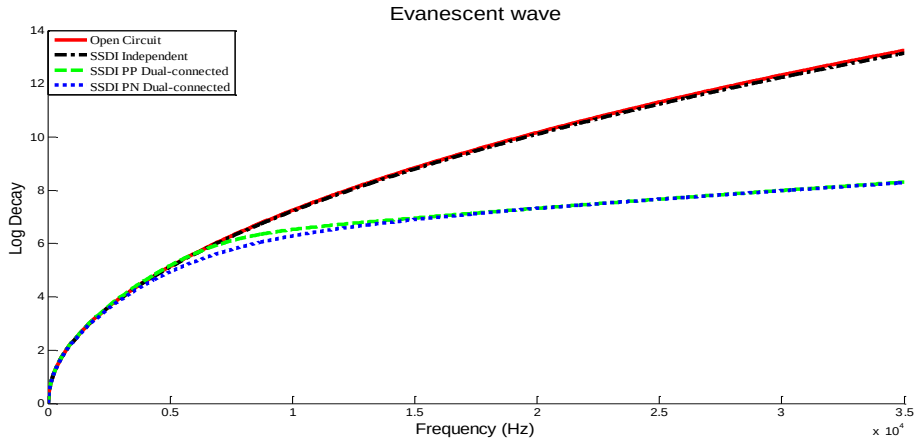

(a)

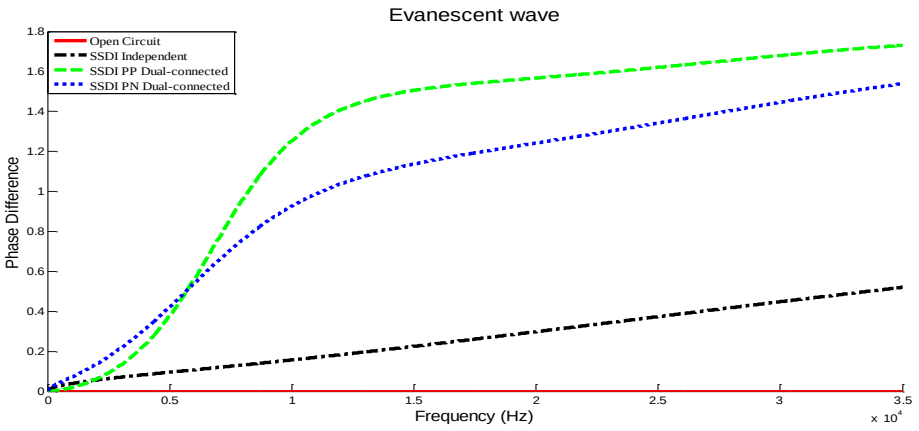

(b)

Figure 3.45 (a) logarithmic decay curves and (b) phase difference curves of evanescent wave in smart periodic structures with the SSDI PP / PN Dual-connected networks. $\gamma_{ind} = 0.5$, $\gamma_{int} = 0.6$.

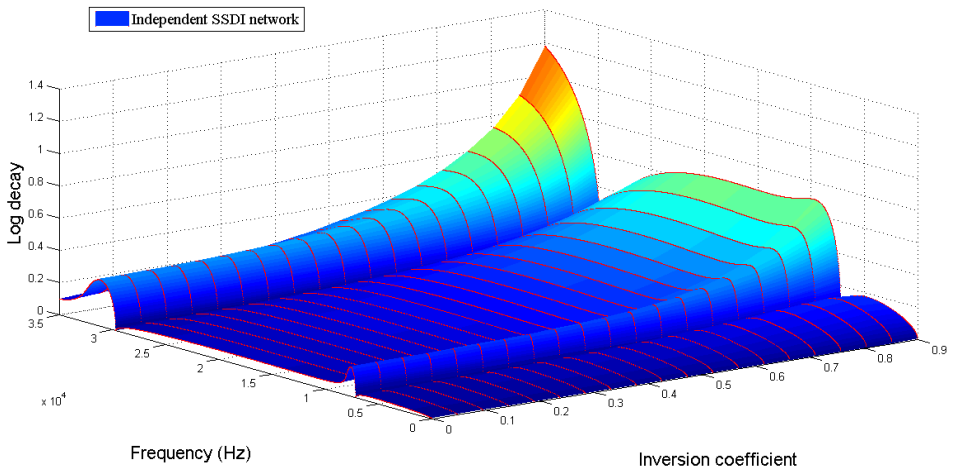

(a)

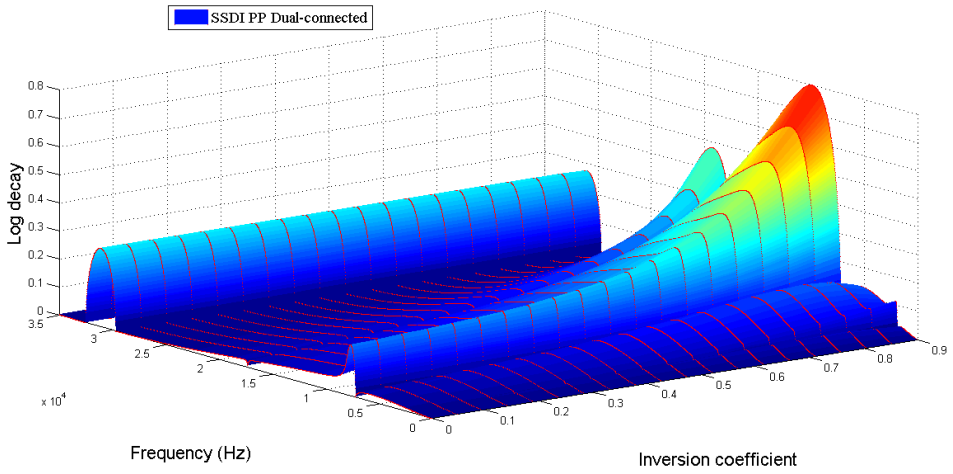

(b)

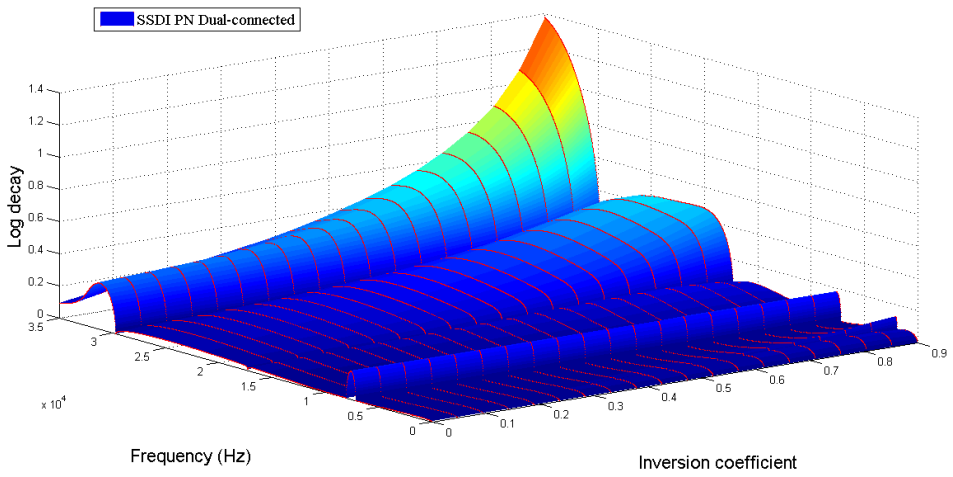

(c)

Figure 3.46 (a) 3D plot of logarithmic decay of elastic wave for the SSDI independent case versus the voltage inversion coefficient; (b) 3D plot of logarithmic decay of elastic wave for the SSDI PP Dual-connected case versus the voltage inversion coefficient; (c) 3D plot of logarithmic decay of elastic wave for the SSDI PN Dual-connected case versus the voltage inversion coefficient (for equitable comparison, the axis of inversion coefficient used in the above 3D plots for the SSDI PP / PN Dual-connected case adopts the inversion coefficient value for the SSDI independent case since $\gamma_{int} = \gamma_{ind}^{\sqrt{\frac{1}{2}}}$).

In addition, in order to further demonstrate the damping effect and attenuation capability of the SSDI PP / PN Dual-connected cases, transmission factors of propagative wave in finite smart structures with above different SSDI connection configurations under free-free boundary condition are calculated and compared. Herein, the finite smart beam used in the previous experiments for the SSDI PP / PN interconnected case, is adopted as a sample as shown in Figure 3.47 (a). It is composed of 8 minimal Bragg-type periodic cells. Figure 3.47 (b) and (c) respectively show the smart beam sample with the SSDI independent networks and with the SSDI PP / PN Dual-connected networks. The external force is placed on one side of the beam whose amplitude of the displacement is assumed to be equal to D_0, and the amplitude of the other side of the beam is equal to D_8. Therefore, the transmission

factor K_{Trans} [298] of the chosen finite beam structure under different SSDI electrical boundary conditions can be obtained through the following equation:

$$K_{trans} = 20\log_{10}\left(\frac{D_8}{D_0}\right) \tag{3.73}$$

Figure 3.47 (d) shows transmission factor of finite free-free smart beam with different electrical boundary conditions. Specifically, all the SSDI cases have good damping performance in the whole investigated frequency range compared with open circuit case. The SSDI PN Dual-connected case exhibits the best damping performance in the first two modes (the 1st and the 2nd). The SSDI independent case shows the best damping performance from the 3rd mode to the 6th mode. From the 7th mode to the 10th mode, the SSDI PP Dual-connected case has the best damping performance. Therefore, it can be seen that in some relatively broadband frequency ranges, the SSDI PP / PN Dual-connected methods indeed can be applied to improve the damping performance using less SSDI shunt branches than the SSDI independent method.

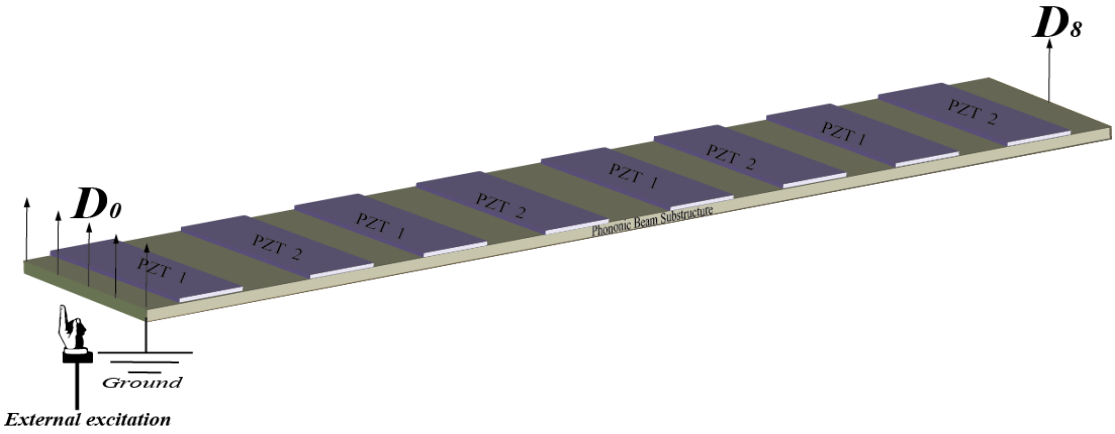

(a)

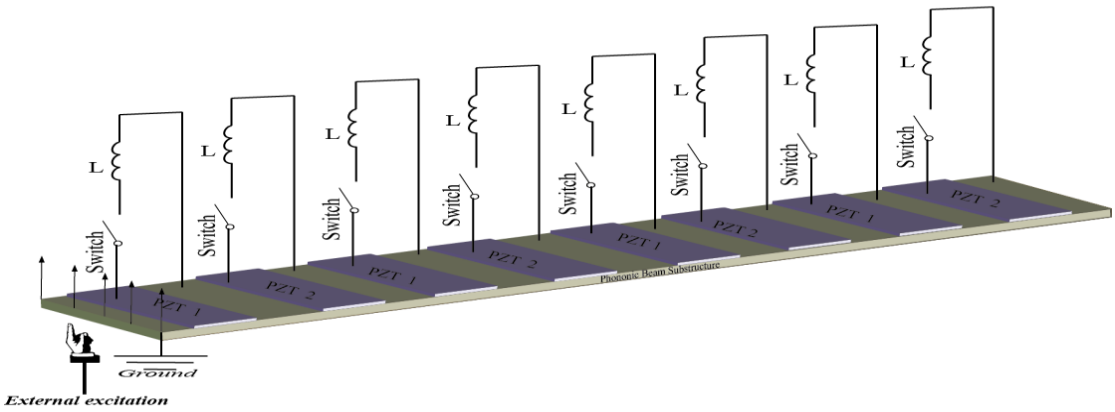

(b)

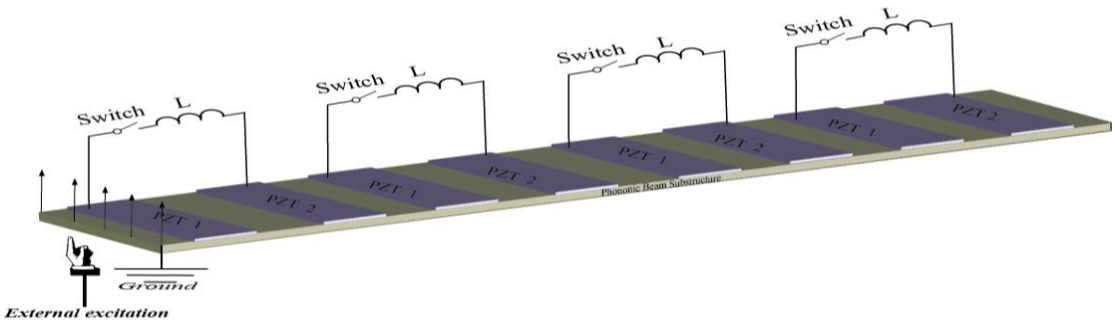

(c)

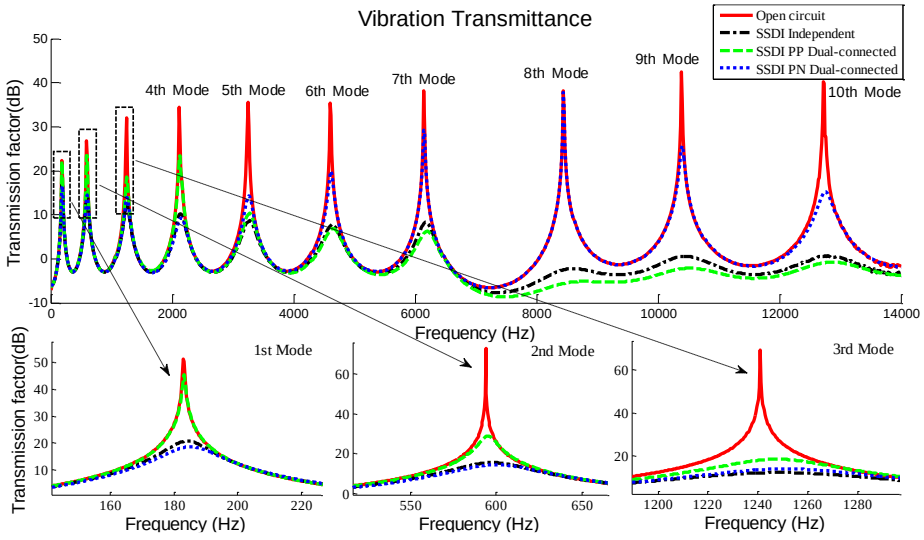

(d)

Figure 3.47 (a) Free-free piezoelectric beam without electrical shunting networks; (b) free-free piezoelectric beam with SSDI independent networks; (c) free-free piezoelectric beam with SSDI PP / PN Dual-connected networks; (d) transmission factor of finite free-free smart beam with different electrical boundary conditions. $\gamma_{ind} = 0.5$, $\gamma_{int} = 0.6$.

3.9 Conclusion

Smart periodic structure with SSDI interconnected electrical networks is further investigated and demonstrated theoretically and experimentally based on FE modeling and wave propagation theory in this chapter. Furthermore, smart periodic structure with SSDI PP / PN Hybrid Capacitance-shunting interconnected electrical networks and smart periodic structure with SSDI PP / PN Dual-connected electrical networks are proposed as possible extensions. Specifically, a periodic array of uniformly distributed PZTs is positioned on a clamped-clamped beam, and their PZT terminals are connected by three different electrical networks which have been studied theoretically and experimentally:

A. Resistive or SSDI PP / PN interconnected electrical networks;
B. SSDI PP / PN Hybrid Capacitance-shunting interconnected electrical networks;
C. SSDI PP / PN Dual-connected electrical networks.

For analyzing the nonlinear SSDI relationship in an interconnected periodic cell, the SSDI shunt is estimated using first harmonic approximation. SSDI shunt utilization in the interconnected electrical networks not only has better attenuation performance and higher damping efficiency than purely resistive shunts, but also has the talent of automatic impedance adaptation according to SSDI impedance estimation.

Hence, with the increase of resonant modes, linear resonant circuit device for multi-mode is more and more complicated while the SSDI shunt, especially the self-powered version, has simple implementation and its electronic impedance is naturally optimized in each frequency point including all the natural frequencies of the structure. Therefore, smart periodic structure with one type of piezoelectric electrical network using nonlinear SSDI shunts, is more likely to have better broadband attenuation performance than smart periodic structure with the same type of piezoelectric electrical network using linear resonant shunts where wave attenuation performance (frequency bandwidth and attenuation amplitude) mainly depends on the damping ratio related to two variables (resistance and inductance).

In addition, from the aspect of active / passive vibration control, smart periodic structure with linear resonant electrical networks needs external energy for large inductance emulation typically reaching hundreds of Henry in the low frequency range, while periodic structure with nonlinear resonant electrical networks can be self-powered in the whole frequency range. Based on the application assumption of requiring no external energy for low-frequency vibration reduction, the investigated SSDI interconnected method can be considered as a better and personalized SSDI network compared with the periodic structures with independent SSDI electrical networks. In order to fairly compare wave attenuation performance of the independent and interconnected systems using SSDI shunts, the interconnected system used the same SSDI switching control devices as the independent system.

Although the performance of SSDI interconnected methods is more localized, if the interested vibration modes of structure are limited to specific frequencies (especially the low-frequency band which needs external energy for linear electrical shunts) and external energy cannot be provided, the SSDI interconnected methods will be the best way among the SSDI independent / interconnected methods and the independent / interconnected linear *RL* resonant methods. Furthermore, smart periodic structure with SSDS interconnected electrical networks is more suitable for highly integrated solutions to better absorb mechanical vibration energy than the structure with SSDS independent electrical networks in the low frequency range.

Although there are some objective factors which result in small discrepancies between the theoretical and experimental results, the present analysis proves the effectiveness and technical feasibility of designing new electromechanical multimodal damping devices via piezoelectric periodic structure with SSDI interconnected electrical networks.

Furthermore, two extension works are proposed in this chapter: smart periodic structure with SSDI Hybrid Capacitance-Shunting interconnected electrical networks and smart periodic structure with SSDI Dual-connected electrical networks. Through the additional capacitance effect, the location of the new generated resonant-type band

gap can be altered flexibly to frequency ranges of interest in the smart periodic structure with SSDI HC-Shunting interconnected electrical networks. Compared with the SSDI independent configuration, SSDI PP / PN Dual-connected electrical configurations have the ability of using less SSDI switching devices but still obtaining better attenuation performance near the Bragg-type band gaps. In addition, SSDI PN Dual-connected electrical configuration also exhibits better attenuation performance in the low frequency band (close to 0 Hz).

Chapter 4 Smart periodic structure with nonlinear interleaved electrical networks

Abstract

This chapter proposes a novel smart periodic structure with nonlinear interleaved electrical networks. Continuous mechanical (in the form of the purely mechanical part of the structure) medium and discrete electrical (in the form of nonlinear interleaved electrical networks) medium are electromechanically coupled via smart materials in the proposed structure. Such electro-elastic coupling configuration is different from the previous investigated structure with nonlinear interconnected electrical networks, but similar with the previous proposed structure with nonlinear Dual-connected electrical networks in Chapter 3. Specifically, section 4.1 introduces the overview of the proposed structure. Finite element modeling of the proposed structure is given in section 4.2 based on Timoshenko beam theory and the other theoretical investigations (e.g., electrical consumption analysis of the electronic impedance in the proposed structure). Section 4.3 gives theoretical discussions on the dispersion properties of the proposed structure based on the established modeling. Section 4.4 estimates the group velocity of the proposed structure under different electrical boundary conditions. Section 4.5 experimentally investigates the proposed structure through comparing the frequency response between theoretical predictions and experimental measurements in the low frequency range. Section 4.6 introduces the extension structure of the proposed structure-smart periodic structure with nonlinear Tri-interleaved electrical topologies. Finally, section 4.7 summarizes the conclusions of this chapter.

4.1 Overview of the proposed structure

Smart periodic structure with nonlinear interleaved-switched electronic networks, is proposed and investigated for vibration reduction and elastic wave attenuation in this chapter. Figure 4.1 (a) shows a schematic diagram of the investigated structure in which the electronic load Z can be either linear electrical shunt or nonlinear electrical

shunt (*R*-shunt, *RL*-shunt and SSDI-shunt). Figure 4.1 (b) exhibits a single interleaved periodic cell of the investigated structure. It is composed of four adjacent minimal Bragg-type periodic cells which are regarded as an integral periodic cell due to the internal interleaved electrical connection. N_g is the total number of interleaved periodic cells in the investigated structure. According to different polarization directions of four identical PZTs in four adjacent minimal Bragg-type periodic cells (1, 2, 3, 4), the interleaved periodic cell can be divided into three types: $P_1P_2P_3P_4$ (PPPP), $P_1P_2N_3N_4$ (PPNN) and $P_1P_2N_3P_4$ (PPNP), as shown in Figure 4.1 (b). P_{dp} and N_{dp} denote that the $dp^{th}(dp^{th}=1^{st},2^{nd},3^{rd},4^{th})$ PZT in the interleaved periodic cell has the positive polarization direction and the negative polarization direction, respectively.

Contrary to the interconnected case, the interleaved approach differs on several aspects:

1. The electrical propagation is confined, *i.e.* no electrical energy is exchanged between macrocells.
2. Within an interleaved cell, there is an interleaved electrical energy exchange.
3. The interleaved method allows introducing some controlled disorder with a certain level of local aperiodicity, but with a high-level periodicity.

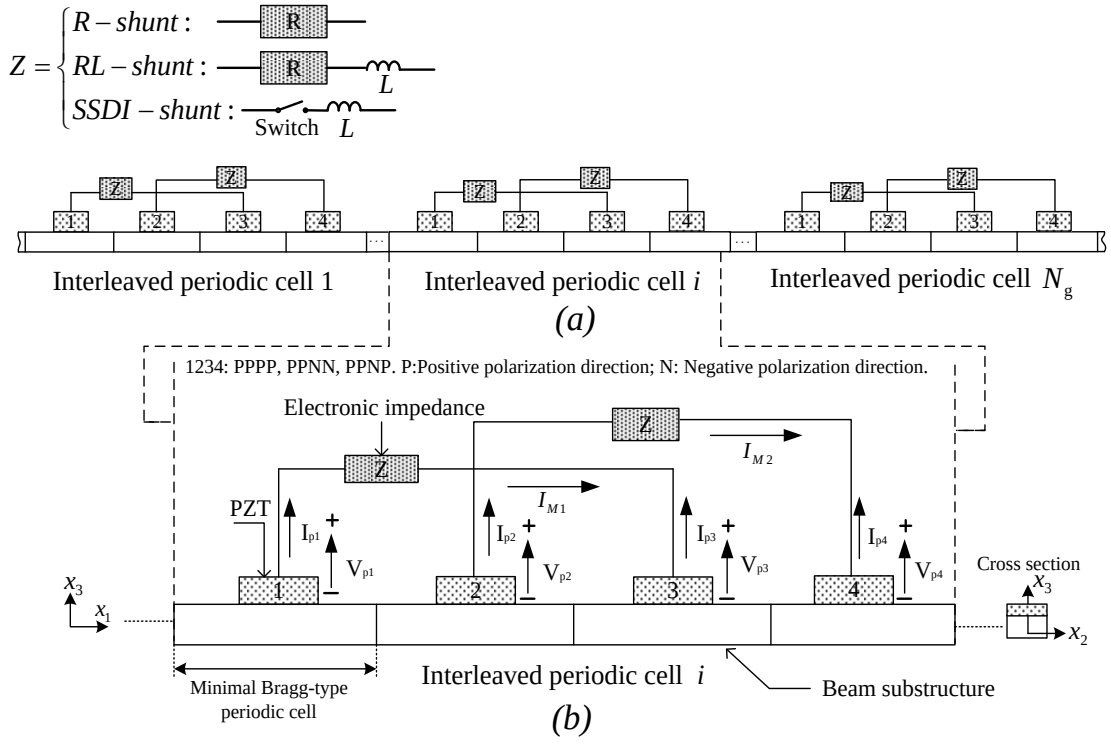

Figure 4.1 (a) Smart periodic beam with interleaved electrical networks using different electrical shunts; (b) an interleaved periodic cell.

4.2 Modeling of the proposed structure based on Timoshenko beam theory

4.2.1 Electro-elastic relationships of the interleaved periodic cell

Four minimal Bragg-type periodic cells with interleaved interconnection compose an interleaved periodic cell in the investigated structure. The total number of interleaved periodic cells in the investigated structure is N_g (the total number of minimal Bragg-type cells is $N_T=4N_g$). According to the previous analysis in Chapter 2, a finite element (FE) modeling of piezoelectric beam is established based on Timoshenko beam theory, and can be applied to any boundary condition. The i^{th} interleaved periodic cell ($1 \le i \le N_g$) can be divided into n finite elements. Electrical boundary

condition of each unitary interleaved network is closed in its interleaved periodic cell. The electro-elastic relationships in the investigated periodic cell can be summarized as:

$$\begin{cases} \left[M^e\right]\left\{\ddot{d}^i\right\}+\left[C^e\right]\left\{\dot{d}^i\right\}+\left[K^e\right]\left\{d^i\right\}+\left[B_1^e\right]\left\{V_p^i\right\}=\left\{P^i\right\} \\ \left\{Q^i\right\}=\left[B_2^e\right]\left\{d^i\right\}+\left[B_3^e\right]\left\{V_p^i\right\} \end{cases} \tag{4.1}$$

where d^i and P^i are $2(n+1)$ by 1 matrices relating the displacement, slope vector, and the force, moment vector of all the nodes of the i^{th} periodic cell. V_p^i and Q^i with matrix size of 4 by 1 denote the voltage and electrical charge of the four PZTs in the investigated periodic cell. B_1^e is a $2(n+1)$ by 4 matrix relating to the electromechanical conversion, given by:

$$B_1^e=\begin{bmatrix} B_{11} & B_{12} & B_{13} & B_{14} \end{bmatrix}$$

$$\begin{cases} B_{11}=b_{11}\int_0^l \dfrac{\partial\left[N_\varphi(x)\right]^T}{\partial x}dx, \quad b_{11}=-\dfrac{p_1 d_{31} w_b}{t_p\left(s_{11}^E+s_{12}^E\right)}\int_{t_b}^{t_b+t_p}\left(u_3-x_c\right)dx_3 \\ B_{12}=b_{12}\int_0^l \dfrac{\partial\left[N_\varphi(x)\right]^T}{\partial x}dx, \quad b_{12}=-\dfrac{p_2 d_{31} w_b}{t_p\left(s_{11}^E+s_{12}^E\right)}\int_{t_b}^{t_b+t_p}\left(u_3-x_c\right)dx_3 \\ B_{13}=b_{13}\int_0^l \dfrac{\partial\left[N_\varphi(x)\right]^T}{\partial x}dx, \quad b_{13}=-\dfrac{p_3 d_{31} w_b}{t_p\left(s_{11}^E+s_{12}^E\right)}\int_{t_b}^{t_b+t_p}\left(u_3-x_c\right)dx_3 \\ B_{14}=b_{14}\int_0^l \dfrac{\partial\left[N_\varphi(x)\right]^T}{\partial x}dx, \quad b_{14}=-\dfrac{p_4 d_{31} w_b}{t_p\left(s_{11}^E+s_{12}^E\right)}\int_{t_b}^{t_b+t_p}\left(u_3-x_c\right)dx_3 \end{cases}$$

p_1, p_2, p_3, p_4 are the signs of piezoelectric constant which depend on the direction of polarization of the four PZTs (1,2,3,4) in the investigated periodic cell. Herein, it is assumed equal to 1 when the direction is positive and -1 when it is negative.

The electromechanical coupling matrix B_2^e with size 4 by $2(n+1)$ is given by:

$$B_2^e=\begin{bmatrix}B_{21}\\B_{22}\\B_{23}\\B_{24}\end{bmatrix},\quad\begin{cases}B_{21}=b_{21}\int_0^l\dfrac{\partial\left[N_\varphi(x)\right]}{\partial x}dx, & b_{21}=-\dfrac{p_1d_{31}t_p}{\left(s_{11}^E+s_{12}^E\right)}\\[2ex] B_{22}=b_{22}\int_0^l\dfrac{\partial\left[N_\varphi(x)\right]}{\partial x}dx, & b_{22}=-\dfrac{p_2d_{31}t_p}{\left(s_{11}^E+s_{12}^E\right)}\\[2ex] B_{23}=b_{23}\int_0^l\dfrac{\partial\left[N_\varphi(x)\right]}{\partial x}dx, & b_{23}=-\dfrac{p_3d_{31}t_p}{\left(s_{11}^E+s_{12}^E\right)}\\[2ex] B_{24}=b_{24}\int_0^l\dfrac{\partial\left[N_\varphi(x)\right]}{\partial x}dx, & b_{24}=-\dfrac{p_4d_{31}t_p}{\left(s_{11}^E+s_{12}^E\right)}\end{cases}$$

Finally, B_3^e denotes the inherent capacitance of the four PZTs and can be calculated by:

$$B_3^e=\begin{bmatrix}B_{31}&0&0&0\\0&\mathrm{B}_{32}&0&0\\0&0&\mathrm{B}_{33}&0\\0&0&0&\mathrm{B}_{34}\end{bmatrix},\quad B_{31}=B_{32}=B_{33}=B_{34}=\frac{w_bL_p\left[2{d_{31}}^2-\varepsilon_{33}^T\left(s_{11}^E+s_{12}^E\right)\right]}{t_p\left(s_{11}^E+s_{12}^E\right)}$$

Rearranging Eq. (4.1), the electrical relationship and dynamical motion relationship of one smart periodic cell in the frequency domain can also be obtained as:

$$\begin{cases}\left\{P^i\right\}=\left[A^e\right]\left\{d^i\right\}+\left[B_1^e\right]\left\{V_p^i\right\}\\ \left\{I_p^i\right\}=\left[j\omega B_2^e\right]\left\{d^i\right\}+\left[j\omega B_3^e\right]\left\{V_p^i\right\}\end{cases}\tag{4.2}$$

where $A^e\left(A^e=-\omega^2M^e+j\omega C^e+K^e\right)$ is the dynamic stiffness matrix, ω is the angular frequency, and I_p^i denotes the output current of the PZT in the i^{th} periodic cell.

In terms of dynamical relationships of the smart periodic cell in different cases, the piezoelectric voltage $\left\{{V_p}^i\right\}$ can be written as a function of the vector $\left\{d^i\right\}$ and yields:

$$\left\{{V_p}^i\right\}=\begin{cases}\left[B_4^e\right]\left\{d^i\right\}, & \text{for open circuit condition;}\\ \left[B_5^e\right]\left\{d^i\right\}, & \text{for purely resistive or linear resonant shunt;}\\ \left[B_6^e\right]\left\{d^i\right\}, & \text{for SSDI independent shunt.}\end{cases}\tag{4.3}$$

$$B_4^e = \begin{bmatrix} B_{41} \\ B_{42} \\ B_{43} \\ B_{44} \end{bmatrix}, \quad B_5^e = \begin{bmatrix} B_{51} \\ B_{52} \\ B_{53} \\ B_{54} \end{bmatrix}, \quad B_6^e = \begin{bmatrix} B_{61} \\ B_{62} \\ B_{63} \\ B_{64} \end{bmatrix}$$

$$\begin{cases} B_{41} = b_{41}\int_0^l \dfrac{\partial\left[N_\varphi(x)\right]}{\partial x}dx, \quad b_{41} = \dfrac{d_{31}{t_p}^2}{L_p\left[\varepsilon_{33}^T\left(s_{11}^E + s_{12}^E\right) - 2d_{31}^2\right]}; \\ B_{42} = b_{42}\int_0^l \dfrac{\partial\left[N_\varphi(x)\right]}{\partial x}dx, \quad b_{42} = \dfrac{d_{31}{t_p}^2}{L_p\left[\varepsilon_{33}^T\left(s_{11}^E + s_{12}^E\right) - 2d_{31}^2\right]}; \\ B_{43} = b_{43}\int_0^l \dfrac{\partial\left[N_\varphi(x)\right]}{\partial x}dx, \quad b_{43} = \dfrac{d_{31}{t_p}^2}{L_p\left[\varepsilon_{33}^T\left(s_{11}^E + s_{12}^E\right) - 2d_{31}^2\right]}; \\ B_{44} = b_{44}\int_0^l \dfrac{\partial\left[N_\varphi(x)\right]}{\partial x}dx, \quad b_{44} = \dfrac{d_{31}{t_p}^2}{L_p\left[\varepsilon_{33}^T\left(s_{11}^E + s_{12}^E\right) - 2d_{31}^2\right]}. \end{cases}$$

$$\begin{cases} B_{51} = \dfrac{j\omega Z_{ind}^{passive}\cdot B_{21}}{\left(1 - j\omega Z_{ind}^{passive}\cdot B_{31}\right)} \\ B_{52} = \dfrac{j\omega Z_{ind}^{passive}\cdot B_{22}}{\left(1 - j\omega Z_{ind}^{passive}\cdot B_{32}\right)} \\ B_{53} = \dfrac{j\omega Z_{ind}^{passive}\cdot B_{23}}{\left(1 - j\omega Z_{ind}^{passive}\cdot B_{33}\right)} \\ B_{54} = \dfrac{j\omega Z_{ind}^{passive}\cdot B_{24}}{\left(1 - j\omega Z_{ind}^{passive}\cdot B_{34}\right)} \end{cases}, \quad \begin{cases} B_{61} = \dfrac{j\omega Z_{ind}^{SSDI}\cdot B_{21}}{\left(1 - j\omega Z_{ind}^{SSDI}\cdot B_{31}\right)} \\ B_{62} = \dfrac{j\omega Z_{ind}^{SSDI}\cdot B_{22}}{\left(1 - j\omega Z_{ind}^{SSDI}\cdot B_{32}\right)} \\ B_{63} = \dfrac{j\omega Z_{ind}^{SSDI}\cdot B_{23}}{\left(1 - j\omega Z_{ind}^{SSDI}\cdot B_{33}\right)} \\ B_{64} = \dfrac{j\omega Z_{ind}^{SSDI}\cdot B_{24}}{\left(1 - j\omega Z_{ind}^{SSDI}\cdot B_{34}\right)} \end{cases}$$

where $Z_{ind}^{passive}$ denotes the purely resistive impedance or linear resonant impedance, Z_{ind}^{SSDI} denotes the SSDI electrical impedance as established in the previous chapter.

Furthermore, the dynamical relations in the i^{th} periodic cell under different electrical boundary conditions can be expressed as:

$$\left\{P^i\right\} = \begin{cases} \left[A^e\right]\left\{d^i\right\}, & \text{for short circuit condition} \\ \left[A_{EC}\right]\left\{d^i\right\}, & \text{for other electrical boundary conditions} \end{cases} \tag{4.4}$$

$$A_{EC} = \begin{cases} A_{open} = A^e + B_1^e \cdot B_4^e \\ A_{ind}^{passive} = A^e + B_1^e \cdot B_5^e \\ A_{ind}^{SSDI} = A^e + B_1^e \cdot B_6^e \end{cases}$$

In terms of the dynamical electromechanical relationships in the investigated interleaved cell (Figure 4.1 (b)), $V_{p1}^i, V_{p2}^i, V_{p3}^i, V_{p4}^i$ and I_{p1}^i , $I_{p2}^i, I_{p3}^i, I_{p4}^i$ are the output voltages and currents of the four PZTs (1,2,3,4) which are connected through the load Z_{int}. The electromechanical relationships of the interleaved periodic cell hold:

$$\begin{cases} V_{p1}^i - I_{M1} Z_{\text{int}} = V_{p3}^i \\ I_{p1}^i = -I_{p3}^i = I_{M1} \\ V_{p2}^i - I_{M2} Z_{\text{int}} = V_{p4}^i \\ I_{p2}^i = -I_{p4}^i = I_{M2} \\ \left\{P^i\right\} = \left[A^e\right]\left\{d^i\right\} + \left[B_1^e\right]\left\{V_p^i\right\} \\ \left\{I_p^i\right\} = \left[j\omega B_2^e\right]\left\{d^i\right\} + \left[j\omega B_3^e\right]\left\{V_p^i\right\} \end{cases} \tag{4.5}$$

$$I_p^i = \begin{bmatrix} I_{p1}^i \\ I_{p2}^i \\ I_{p3}^i \\ I_{p4}^i \end{bmatrix}, \quad V_p^i = \begin{bmatrix} V_{p1}^i \\ V_{p2}^i \\ V_{p3}^i \\ V_{p4}^i \end{bmatrix}$$

On the basis of Eq.(4.5), the piezoelectric voltage V_p^i in the interleaved periodic cell can be written as:

$$\left\{V_p^i\right\} = \left[B_8^e\right]\left\{d^i\right\} \tag{4.6}$$

$$B_8^e = \begin{bmatrix} \dfrac{-\left(\dfrac{B_{21}+B_{23}}{B_{31}}\right) + j\omega Z_{\text{int}} B_{21}}{2 - j\omega Z_{\text{int}} B_{31}} \\ \dfrac{-\left(\dfrac{B_{22}+B_{24}}{B_{31}}\right) + j\omega Z_{\text{int}} B_{22}}{2 - j\omega Z_{\text{int}} B_{31}} \\ -\left(\dfrac{B_{21}+B_{23}}{B_{31}}\right) - \dfrac{-\left(\dfrac{B_{21}+B_{23}}{B_{31}}\right) + j\omega Z_{\text{int}} B_{21}}{2 - j\omega Z_{\text{int}} B_{31}} \\ -\left(\dfrac{B_{22}+B_{24}}{B_{31}}\right) - \dfrac{-\left(\dfrac{B_{22}+B_{24}}{B_{31}}\right) + j\omega Z_{\text{int}} B_{22}}{2 - j\omega Z_{\text{int}} B_{31}} \end{bmatrix}$$

Therefore, dynamical relations of the i^{th} interleaved periodic cell can be expressed as:

$$\left\{P^i\right\}=\left[A_{\text{int}erleaved}\right]\left\{d^i\right\}=\left[A^e+B_1^eB_8^e\right]\left\{d^i\right\} \tag{4.7}$$

4.2.2 Electrical consumption analysis based on FEM methods

In order to make an electrical consumption comparison between the independent electrical case when using pure resistances / linear resonant shunts ($Z_{ind}^{passive}$) or SSDI shunts (Z_{ind}^{SSDI}) and the interleaved electrical case when using pure resistances / linear resonant shunts ($Z_{\text{int}}^{passive}$) or SSDI shunts (Z_{int}^{SSDI}), complex power in different cases is obtained in this section. For equitable comparison, unit periodic cell with different electrical networks includes the same number of minimal Bragg-type periodic cells for electrical consumption analysis (i.e., an interleaved periodic cell – composed of 4 minimal Bragg-type cells - is compared to 4 independent periodic cells).

In the investigated independent periodic cell including four minimal Bragg-type periodic cells, the complex power of four SSDI independent shunting branches can be obtained according to the following relationships:

$$\begin{cases}\left\{I_p^i\right\}=\left[j\omega B_2^e\right]\left\{d^i\right\}+\left[j\omega B_3^e\right]\left\{V_p^i\right\}\\ \left\{V_p^i\right\}=\left\{I_p^i\right\}\cdot Z_{ind},\quad Z_{ind}=Z_{ind}^{passive}\,or\;Z_{ind}^{SSDI}\\ Power_{ind}=\left\{V_p^i\right\}\cdot\left\{I_p^i\right\}^*\end{cases} \tag{4.8}$$

$$\left\{I_p^i\right\}=\begin{bmatrix}I_{p1}^i\\ I_{p2}^i\\ I_{p3}^i\\ I_{p4}^i\end{bmatrix}=E_{ind}d^i,\quad E_{ind}=\begin{bmatrix}\dfrac{-\omega^2B_{21}B_{31}Z_{ind}-j\omega B_{21}}{1+(\omega B_{31}Z_{ind})^2}\\ \dfrac{-\omega^2B_{22}B_{32}Z_{ind}-j\omega B_{22}}{1+(\omega B_{32}Z_{ind})^2}\\ \dfrac{-\omega^2B_{23}B_{33}Z_{ind}-j\omega B_{23}}{1+(\omega B_{33}Z_{ind})^2}\\ \dfrac{-\omega^2B_{24}B_{34}Z_{ind}-j\omega B_{24}}{1+(\omega B_{34}Z_{ind})^2}\end{bmatrix}$$

Therefore, the complex power $Power_{ind}$ can be given as:

$$Power_{ind} = \left\{V_p^{\ i}\right\} \cdot \left\{I_p^{\ i}\right\}^* = \begin{bmatrix} I_{p1}^i \cdot \left(I_{p1}^i\right)^* \cdot Z_{ind} \\ I_{p2}^i \cdot \left(I_{p2}^i\right)^* \cdot Z_{ind} \\ I_{p3}^i \cdot \left(I_{p3}^i\right)^* \cdot Z_{ind} \\ I_{p4}^i \cdot \left(I_{p4}^i\right)^* \cdot Z_{ind} \end{bmatrix} = \begin{bmatrix} \dfrac{\omega^4 Z_{ind}^3 B_{31}^2 + \omega^2 Z_{ind}}{\left(1+\omega^2 Z_{ind}^2 B_{31}^2\right)^2}\left(B_{21} d^i\right)^2 \\ \dfrac{\omega^4 Z_{ind}^3 B_{32}^2 + \omega^2 Z_{ind}}{\left(1+\omega^2 Z_{ind}^2 B_{32}^2\right)^2}\left(B_{22} d^i\right)^2 \\ \dfrac{\omega^4 Z_{ind}^3 B_{33}^2 + \omega^2 Z_{ind}}{\left(1+\omega^2 Z_{ind}^2 B_{33}^2\right)^2}\left(B_{23} d^i\right)^2 \\ \dfrac{\omega^4 Z_{ind}^3 B_{34}^2 + \omega^2 Z_{ind}}{\left(1+\omega^2 Z_{ind}^2 B_{34}^2\right)^2}\left(B_{24} d^i\right)^2 \end{bmatrix} \tag{4.9}$$

Similarly, in the investigated interleaved periodic cell including four minimal Bragg-type periodic cells, the complex power of two SSDI shunt branches can be obtained according to the following relationships based on Eq.(4.5):

$$\begin{cases} \begin{cases} I_{M\,\mathrm{int}} = \begin{Bmatrix} I_{M1} \\ I_{M2} \end{Bmatrix} = \begin{cases} \dfrac{-\omega^2 Z_{\mathrm{int}} B_{31} + j2\omega}{4+\omega^2 Z_{\mathrm{int}}^2 B_{31}^2}\left(B_{21} - B_{23}\right) d^i \\ \dfrac{-\omega^2 Z_{\mathrm{int}} B_{31} + j2\omega}{4+\omega^2 Z_{\mathrm{int}}^2 B_{31}^2}\left(B_{22} - B_{24}\right) d^i \end{cases} \\ V_{M\,\mathrm{int}} = \begin{Bmatrix} V_{M1} \\ V_{M2} \end{Bmatrix} = \begin{Bmatrix} V_{p1}^i - V_{p2}^i \\ V_{p3}^i - V_{p4}^i \end{Bmatrix} = I_{M\,\mathrm{int}} \cdot Z_{\mathrm{int}} \end{cases} \\ Power_{\mathrm{int}} = V_{M\,\mathrm{int}} \cdot I_{M\,\mathrm{int}}^*, \quad Z_{\mathrm{int}} = Z_{\mathrm{int}}^{passive} or\ Z_{\mathrm{int}}^{SSDI} \end{cases} \tag{4.10}$$

Therefore, the complex power $Power_{\mathrm{int}}$ in the investigated interleaved periodic cell can be given as:

$$Power_{\mathrm{int}} = V_{M\,\mathrm{int}} \cdot I_{M\,\mathrm{int}}^* = \begin{bmatrix} \left\{V_{M1}\right\} \cdot \left\{I_{M1}\right\}^* \\ \left\{V_{M2}\right\} \cdot \left\{I_{M2}\right\}^* \end{bmatrix} = \begin{bmatrix} \dfrac{\omega^4 Z_{\mathrm{int}}^3 B_{31}^2 + 4\omega^2 Z_{\mathrm{int}}}{\left(4+\omega^2 Z_{\mathrm{int}}^2 B_{31}^2\right)^2}\left(\left(B_{21} - B_{23}\right) d^i\right)^2 \\ \dfrac{\omega^4 Z_{\mathrm{int}}^3 B_{31}^2 + 4\omega^2 Z_{\mathrm{int}}}{\left(4+\omega^2 Z_{\mathrm{int}}^2 B_{31}^2\right)^2}\left(\left(B_{22} - B_{24}\right) d^i\right)^2 \end{bmatrix} \tag{4.11}$$

In summary, the total complex power $Power_{ind}^{Total}$ in the investigated independent periodic cell and the total complex power $Power_{\mathrm{int}}^{Total}$ in the investigated interleaved periodic cell can be obtained as:

$$\begin{cases} Power_{ind}^{Total} = \dfrac{\omega^4 Z_{ind}^3 B_{31}^2 + \omega^2 Z_{ind}}{\left(1+\omega^2 Z_{ind}^2 B_{31}^2\right)^2}\left(\left(B_{21}d^i\right)^2 + \left(B_{22}d^i\right)^2 + \left(B_{23}d^i\right)^2 + \left(B_{24}d^i\right)^2\right) \\ Power_{\text{int}}^{Total} = \dfrac{\omega^4 Z_{\text{int}}^3 B_{31}^2 + 4\omega^2 Z_{\text{int}}}{\left(4+\omega^2 Z_{\text{int}}^2 B_{31}^2\right)^2}\left(\left(\left(B_{21}-B_{23}\right)d^i\right)^2 + \left(\left(B_{22}-B_{24}\right)d^i\right)^2\right) \end{cases} \quad (4.12)$$

It is shown that in the independent / interleaved electrical connection configurations, two different kinds of total complex powers ($Power_{ind}^{Total}$, $Power_{\text{int}}^{Total}$) are determined for a given angular frequency ω. Electrical impedances (Z_{ind}, Z_{int}) are different, and displacement values ($B_{21}d^i, B_{22}d^i, B_{23}d^i, B_{24}d^i$) of the four PZTs in the four adjacent minimal Bragg-type periodic cells are also different from displacement difference values ($\left(B_{21}-B_{23}\right)d^i$, $\left(B_{22}-B_{24}\right)d^i$). Therefore, the complex power comparison between the independent case and the interleaved case does not show that the complex power of the independent case is greater than that of the interleaved case in the global frequency domain. In other words, the interleaved case has the theoretical possibility of outperforming the independent case on electrical consumption in some frequency domain.

4.3 Spectral analysis of the dispersion properties

Based on the experimental sample whose parameters are those used in Chapter 3, wave attenuation properties and group velocities of the proposed structure (Figure 4.2) are theoretically discussed and compared with periodic beam structure with independent electrical networks in this section. In addition, for FE modeling calculation based on Timoshenko beam theory, another compliance in short circuit is also used in this section: $s_{55}^E = 21.77\times10^{-12} m^2/N$. The dimension of a minimal Bragg-type periodic cell (Figure 4.2 (a)) is 22 mm. Each PZT is 10 mm long. For the sake of investigating the proposed structure, the interleaved periodic cell consisting of four minimal Bragg-type periodic cells as shown in Figure 4.2 (b), is decomposed into several FE elements. Based on the dynamical relationships of the periodic cell

(Eq.(4.7)), the transfer matrix linking the generalized displacements and forces on both sides of an interleaved periodic cell, similar with the global transfer matrix between adjacent independent periodic cells introduced in Chapter 3, is derived for propagation constant calculation. Only the positive direction is considered for wave propagation, and no structural damping is considered ($\mathbf{C}^e$= [0]).

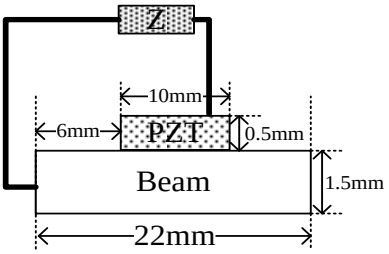

(a)

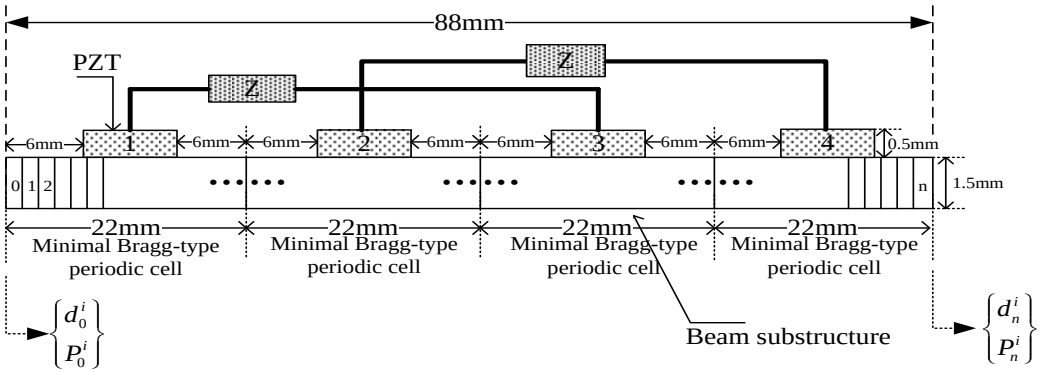

(b)

Figure 4.2 (a) A minimal Bragg-type periodic cell with independent electrical connection; (b) an interleaved periodic cell using different electrical shunts (*Z*: electronic impedance, 1234: PPPP, PPNN, PPNP (P: positive polarization direction; N: negative polarization direction)).

For investigating wave attenuation performance of smart periodic structure with different interleaved electrical networks (PPPP / PPNN / PPNP connections) using various electronic shunts (purely resistive shunts / resonant shunts / SSDI shunts), curves of real parts and imaginary parts of propagative wave and evanescent wave in different cases are plotted and compared in Figure 4.3 - Figure 4.11. For equitable comparison of wave attenuation performance, four minimal Bragg-type periodic cells using independent electrical networks are considered for one interleaved periodic cell for propagation constant calculation.

4.3.1 Purely resistive case

The applied pure resistances in the independent electrical network and the interleaved electrical network are all optimal and equal to Z_{ind}^{R} and Z_{int}^{R}, respectively, which can be given as:

$$Z_{ind}^{R} = \frac{1}{2\pi f C_0}, \quad Z_{\text{int}}^{R} = \frac{1}{\pi f C_0}$$

As shown in Figure 4.3, in the investigated frequency range ([0 kHz, 35 kHz]), elastic wave propagates with relatively large attenuation in two Bragg-type stop bands ([7.15 kHz, 8 kHz] and [29.4 kHz, 31.4 kHz]) in all cases, while primitive pass bands in the open circuit case become stop bands with minor attenuation due to influence of purely resistive electrical networks. Since propagative wave of each minimal Bragg-type periodic cell has two Bragg-type band gaps (in the curve of attenuation constant) corresponding to two inflexion areas (zero or π) of phase constant, wave propagated through four identical minimal Bragg-type periodic cells (with different polarization directions in the PPPP / PPNN / PPNP connections) attenuates four times more compared with propagation through one minimal Bragg-type periodic cell (within Bragg-type band gaps), and corresponding phase constant has 8 inflexion areas of which two main inflexion areas correspond to the locations of two Bragg-type band gaps. Specifically, as shown in Figure 4.3, the PPPP interleaved case has almost the same wave attenuation performance as the independent case in the frequency ranges

[0.8 kHz, 2.8 kHz]∪[16 kHz, 18 kHz], while in the other frequency domains except Bragg-type band gaps, the independent case has the broadest wave attenuation performance. However, in the two Bragg-type band gaps, the broadband resonance mechanism induced by the PPPP interleaved electrical connection, is not coupled effectively with Bragg scattering mechanism since the two Bragg-type band gaps are not affected. By comparison, the independent case and the PPNN / PPNP interleaved cases adversely attenuate the Bragg-type band gaps.

Attenuation constant of evanescent wave increases in all cases with the frequency, denoting the reflection at the interface between non-piezoelectric part and piezoelectric part. Compared with evanescent wave which has zero or nearly zero phase constant in open circuit condition and independent case, phase constant of evanescent wave in the interleaved case is not equal to zero as shown in Figure 4.4.

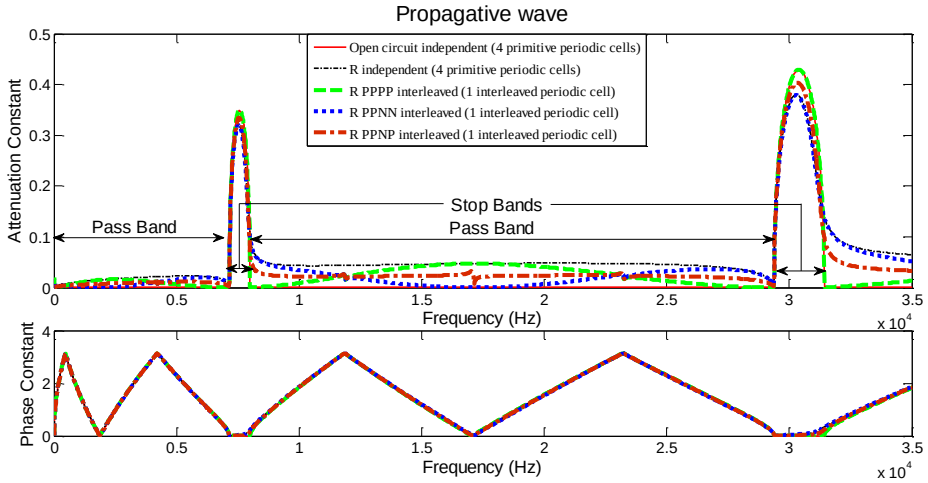

Figure 4.3 Propagation constant of propagative wave in different cases using purely resistive shunt and open circuit condition.

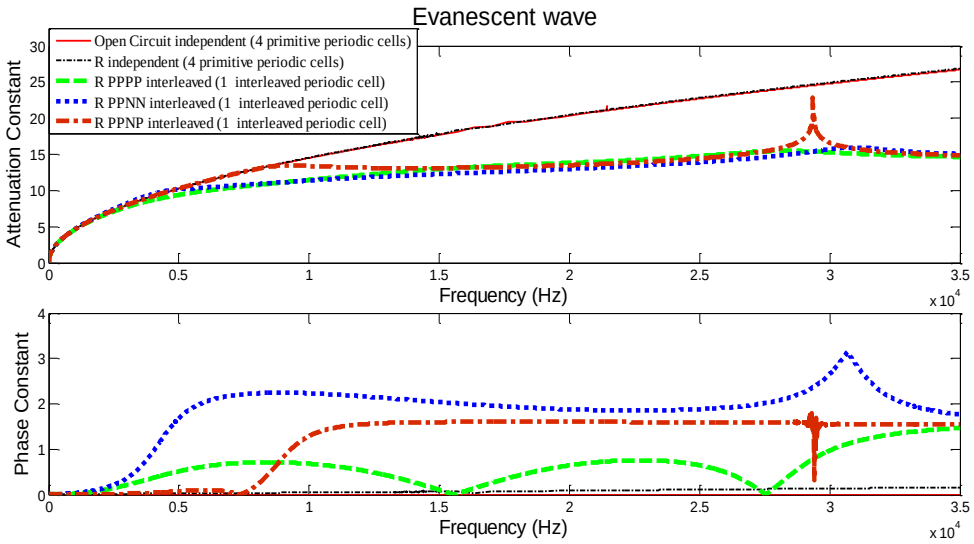

Figure 4.4 Propagation constant of evanescent wave in different cases using purely resistive shunt and open circuit condition.

4.3.2 Linear resonant (*RL*) case

For investigating wave attenuation performance of the proposed structure using linear resonant shunts, the single-mode series *RL* circuit [150] is adopted as an example as shown in Figure 4.1. The damping ratio ζ and the inductance L for single-mode tuning frequency ω_n can be calculated from the following equations:

$$\begin{cases} \zeta_1 = \dfrac{R_1}{2}\sqrt{\dfrac{C_0}{L_1}}, & \text{for one resonant shunt branch connected to one PZT} \\ \zeta_2 = \dfrac{R_2}{2}\sqrt{\dfrac{C_0}{2L_2}}, & \text{for one resonant shunt branch connected between two PZTs} \\ L_1 = \dfrac{1}{\omega_n^2 C_0}, & \text{for one resonant shunt branch connected to one PZT} \\ L_2 = \dfrac{2}{\omega_n^2 C_0}, & \text{for one resonant shunt branch connected between two PZTs} \end{cases} \tag{4.13}$$

In order to compare the attenuation performance of purely locally resonant bandgaps between the proposed structure and the structure with independent RL networks, assuming that the tuning frequency for locally resonant bandgaps is chosen to be 5 kHz (outside the primitive Bragg-type band gaps), with a damping ratio of 6% (the

system is assumed to be underdamped), according to Eq.(4.13), the inductance L and the resistance R in the RL-shunt can be obtained as:

$$\begin{cases} L_1 = 0.2H, R_1 = 782\Omega, & \text{for one resonant shunt branch connected to one PZT} \\ L_2 = 0.4H, R_2 = 1564\Omega, & \text{for one resonant shunt branch connected between two PZTs} \end{cases}$$

As shown in Figure 4.5, a resonant-type band gap ([4 kHz, 6 kHz]) is induced by different resonant cases, which can be predicted through conventionally local resonance mechanism. The interleaved cases with the same damping ratio show no superiority on wave attenuation performance compared with the independent case in the investigated frequency range. With the increase of damping ratio, the resonant-type band gap is still narrow, and its maximal attenuation amplitude is reduced (Figure 4.6 and Figure 4.7). Since locally resonant mechanism may not be used to predict the locations of locally resonant band gaps induced by complex electronic networks, the locations of resonant-type band gaps in the interleaved cases using linear resonant shunts, are investigated and compared with the independent case using linear resonant shunts by setting the same tuning frequency and the same damping ratio. Results show that locations of resonant-type band gaps can be predicted by locally resonant mechanism in the interleaved cases using single-mode linear series resonant shunts.

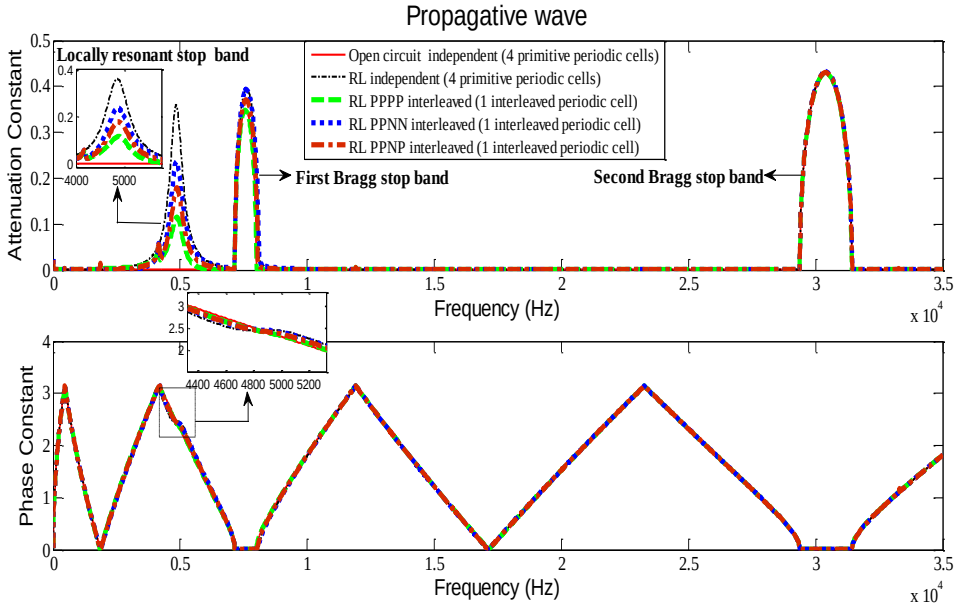

Figure 4.5 Propagation constant of propagative wave when using resonant shunt and open circuit condition.

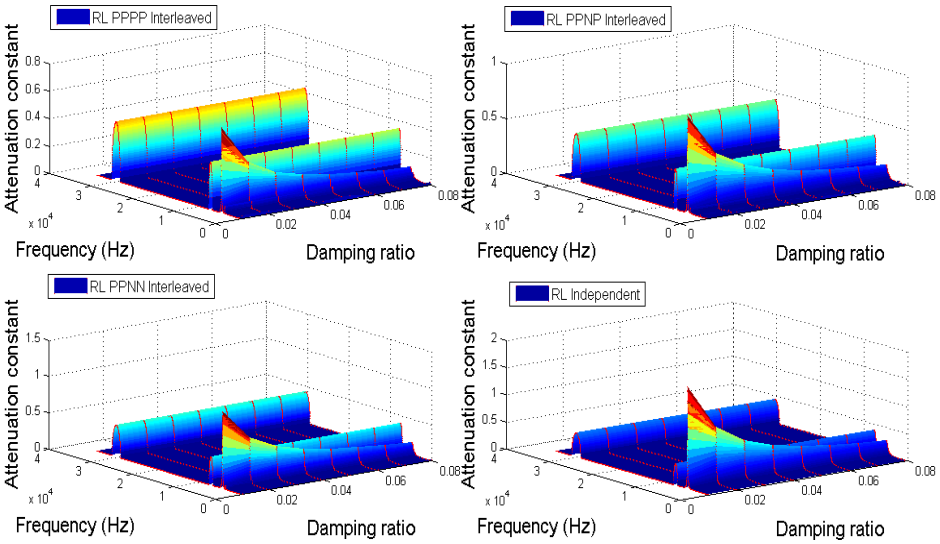

Figure 4.6 3D plots of attenuation constant of propagative wave versus damping ratio with different resonant electrical networks.

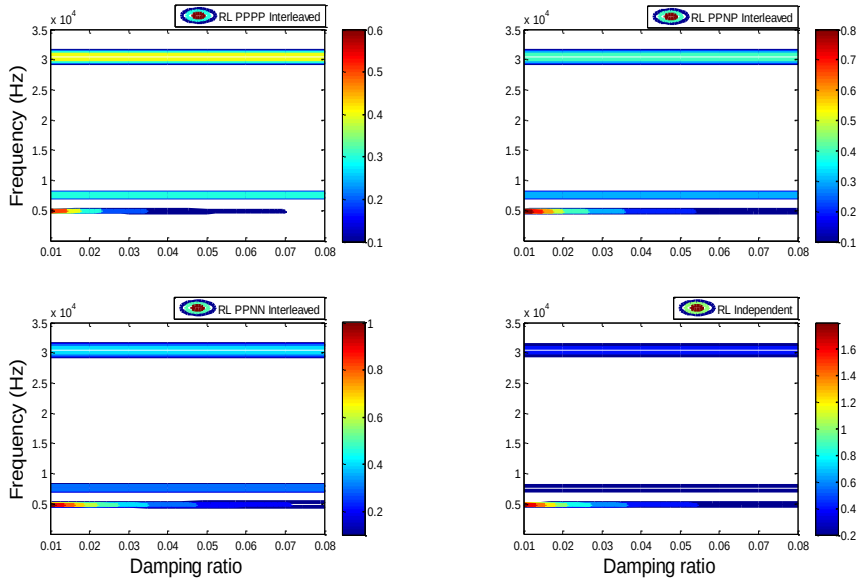

Figure 4.7 Contours of attenuation constant of propagative wave versus damping ratio in different resonant cases.

4.3.3 SSDI case

As shown in Figure 4.8, among different SSDI cases, the PPPP interleaved case shows the best attenuation performance in the frequency ranges ([0.7 kHz, 3.4 kHz] ∪ [13.5 kHz, 21.4 kHz]), and the PPNN interleaved case exhibits the best wave filtering capability over the frequency domains ([0 kHz, 0.2 kHz] ∪ [5.3 kHz, 10.5 kHz] ∪ [25.6 kHz, 35 kHz]). Therefore, similar to the SSDI Dual-connected case, the SSDI interleaved case not only has the technical simplicity of using two SSDI switching control devices for four minimal Bragg-type periodic cells (instead of four independent SSDI switching control devices in the SSDI independent case), but is also predominant in vibration reduction in low frequency range. However, in the whole investigated frequency domain, the PPNP interleaved case exhibits worse attenuation performance than that of the independent case. The possible explanation is that electrical configurations of two interleaved pairs of PZTs are different (PP and PN), so the attenuation predominance of PP or PN configuration (as introduced in section 3.2.2, PN better in the low frequency cases and PP better in the high frequency

cases) cannot be mutually reinforcing in the same frequency ranges in the PPNP interleaved case. By comparison, in the PPPP or PPNN interleaved cases, mutually reinforcing effect of such PP/PN attenuation superiority can be obtained in the same frequency ranges since two interleaved pairs of PZTs have the same electrical configurations (PP or PN).

In addition, the phase constant of evanescent wave in the SSDI interleaved cases (Figure 4.9) has similar changing trend with the interleaved cases using purely resistive shunts in the investigated frequency range excluding two Bragg-type stop bands.

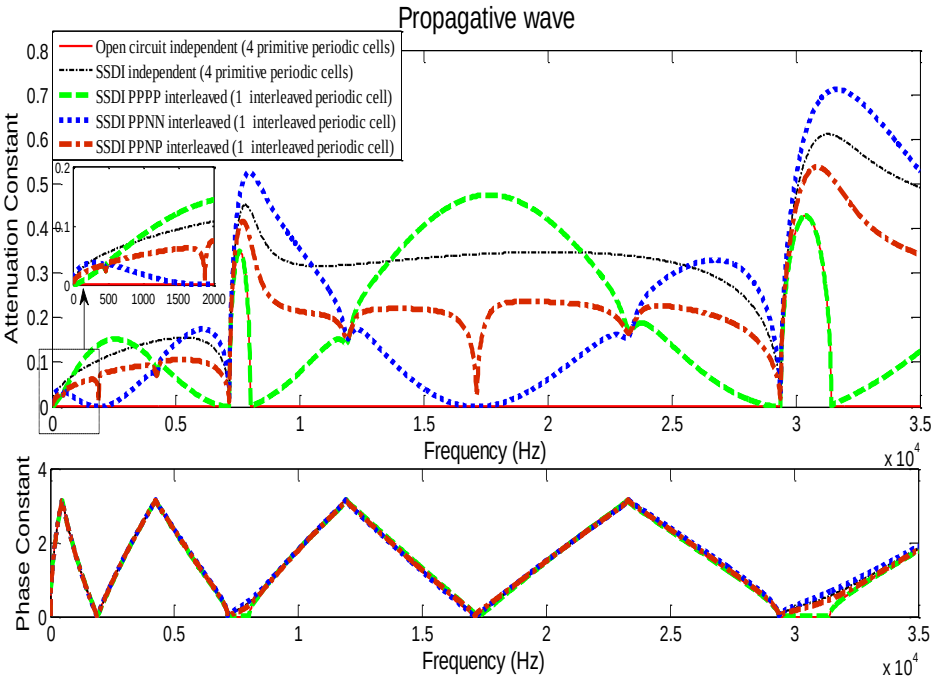

Figure 4.8 Propagation constant of propagative wave when using SSDI shunt and open circuit condition ($\gamma_{ind} = 0.5, \gamma_{\text{int}} = 0.6$).

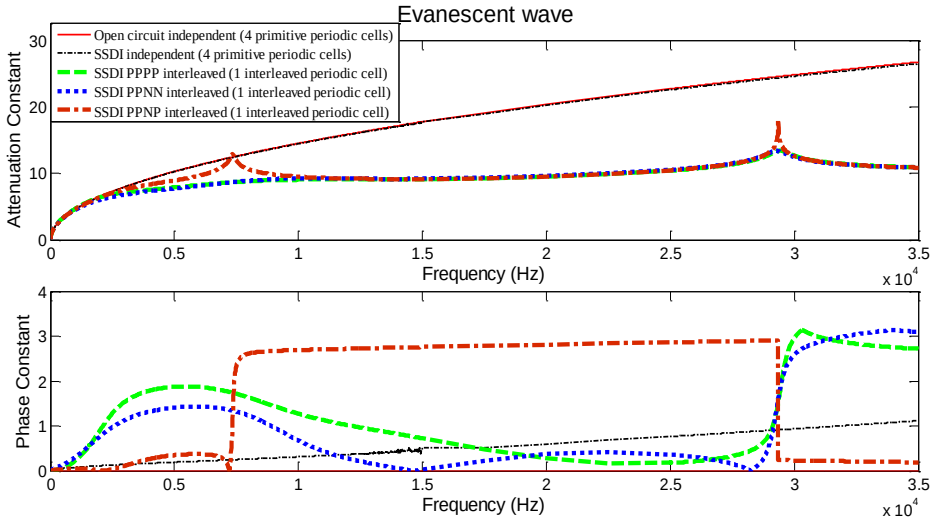

Figure 4.9 Propagation constant of evanescent wave in different SSDI cases and in open circuit condition ($\gamma_{ind} = 0.5, \gamma_{\text{int}} = 0.6$).

Furthermore, Figure 4.10 and Figure 4.11 show 3D plots and contours of attenuation constant of propagative wave in different SSDI cases versus inversion coefficient. Although the SSDI independent case has better global wave attenuation performance over the investigated frequency range as shown in the contours for the SSDI independent case and the SSDI PPNP interleaved case, the SSDI PPNP interleaved case is still an effective broadband attenuation method, and can be a cost-efficient choice for broadband wave attenuation applications using a significant number of active materials since it only requires half of the number of electronic switching devices compared with the SSDI independent case. Furthermore, the SSDI PPPP interleaved case and the SSDI PPNN interleaved case can be considered as comparatively effective narrow-band wave attenuation controllers. Wave attenuation performance near the peak of new resonant-type band gaps induced by the SSDI PPPP interleaved connection is locally predominant to that of resonant-type band gaps caused by the SSDI independent case. The SSDI PPNN interleaved case has better wave attenuation performance for broadening and enhancing the two Bragg-type band gaps ([7.15 kHz, 8 kHz] ∪ [29.4 kHz, 31.4 kHz]) than that of the SSDI independent

case. Especially, the SSDI PPPP interleaved case shows better wave attenuation performance than the SSDI independent case over the relatively broad low-frequency range (below 3.5 kHz), which is validated by the following experiments.

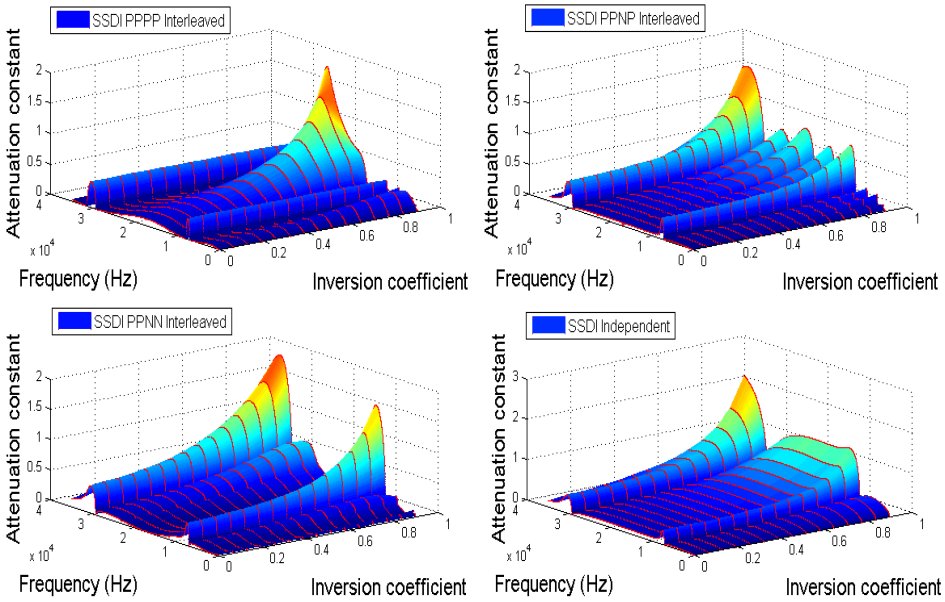

Figure 4.10 3D plots of attenuation constant of propagative wave versus inversion coefficient in different SSDI cases.

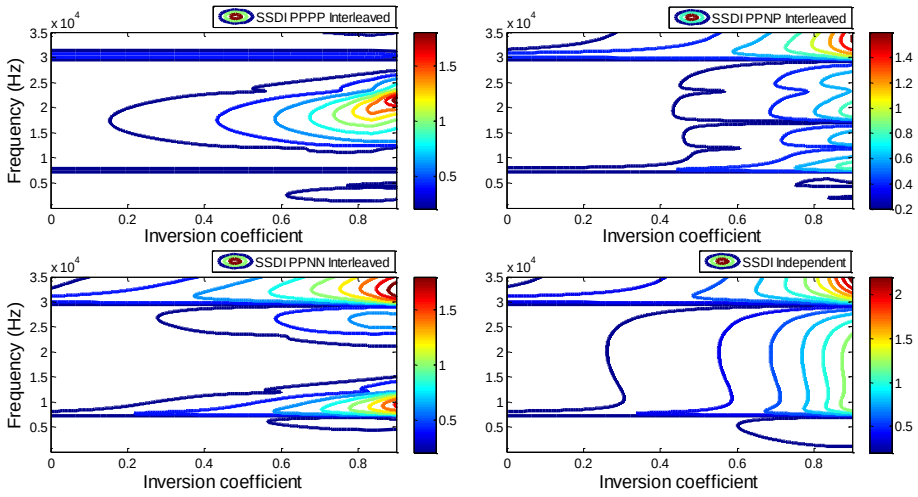

Figure 4.11 Contours of attenuation constant of propagative wave versus the inversion coefficient in different SSDI cases.

4.4 Group velocity estimation

The group velocities of propagative wave can be given by the real part of wavenumbers $\mathrm{Re}\{k_i(\omega_n)\}$ at each frequency step $\Delta\omega$ as follows [313]:

$$V_g(\omega_n) = \frac{\Delta\omega}{2}\left(\left|\frac{1}{\mathrm{Re}\{k_i(\omega_{n+1})\} - \mathrm{Re}\{k_i(\omega_n)\}}\right| + \left|\frac{1}{\mathrm{Re}\{k_i(\omega_n)\} - \mathrm{Re}\{k_i(\omega_{n-1})\}}\right|\right) \tag{4.14}$$

The group velocities associated with the propagative wave in different cases are shown in Figure 4.12 - Figure 4.14. As for the group velocities within the primitive pass bands ([0 kHz, 7.15 kHz] ∪ [8 kHz, 29.4 kHz] ∪ [31.4 kHz, 35 kHz]), there are six narrow-band frequency areas with high group velocities (at the frequency regions: [0.45 kHz, 0.55 kHz] ∪ [1.85 kHz, 1.95 kHz] ∪ [4.2 kHz, 4.32 kHz] ∪ [11.8 kHz, 12 kHz] ∪ [17 kHz, 17.2 kHz] ∪ [23.1 kHz, 23.4 kHz]) which correspond to six diminutive inflexion areas in the phase constant of propagative wave. Different purely resistive cases (Figure 4.12) have similar curves of the group velocity which are close to the curve of the group velocity in open circuit case. Moreover, high group velocities within the primitive six narrow-band areas for all of the SSDI cases decrease gradually with the increase of the inversion coefficient. Concerning the changing trends of the group velocities within the Bragg-type stop bands ([7.15 kHz, 8 kHz] ∪ [29.4 kHz, 31.4 kHz]), since phase constant of propagative wave within these bands for open circuit condition and purely resistant cases are respectively equal to a plateau constant (0 or π), the group velocity for the open circuit case is usually considered as zero [310], while it has very high value for purely resistive cases according to the expression of the group velocity (Eq.(4.14)). Physically, it can be illustrated by the difference of wave propagation velocity between the purely mechanical medium and the electrical medium in smart periodic beam structures. Normally, wave propagates faster through the electrical medium than through the mechanical one.

For group velocities in the resonant-type band gap for the linear resonant case (Figure 4.13), all the propagative waves for the interleaved cases have lower group velocity

than that of the independent case. With the inversion coefficient in the SSDI shunt increasing, the group velocities for all the SSDI cases (Figure 4.14) go down. Globally, propagative wave for the SSDI PPPP interleaved case ($\gamma_{ind}=0.5, \gamma_{\text{int}}=0.6$) has the highest group velocity (>4000 m/s) among all the SSDI cases, followed by the velocity for the SSDI PPNP interleaved case (3200 m/s), the SSDI independent case (2500 m/s) and finally the SSDI PPNN interleaved case (2000 m/s).

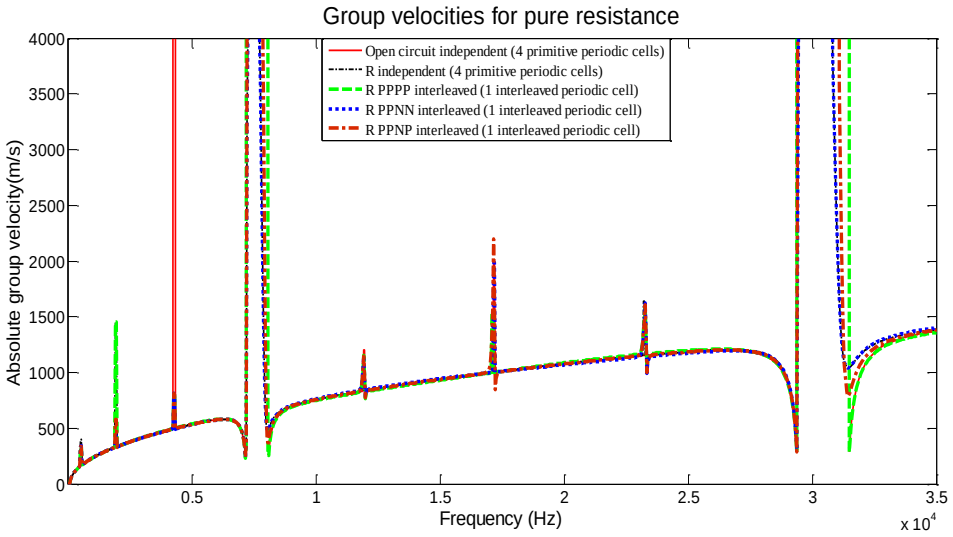

Figure 4.12 Group velocities for different purely resistive cases.

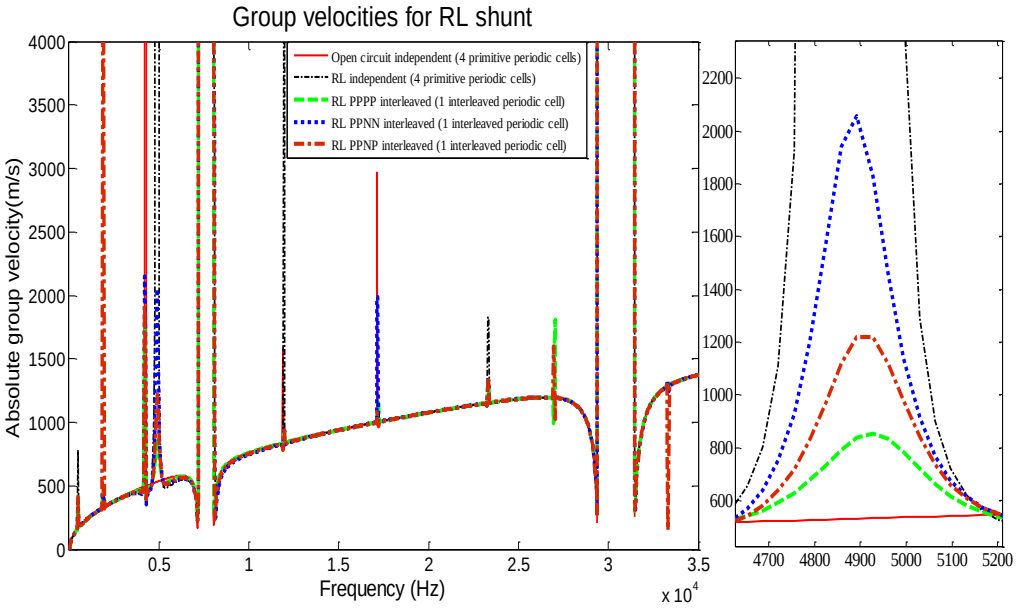

Figure 4.13 Group velocities for different linear resonant cases.

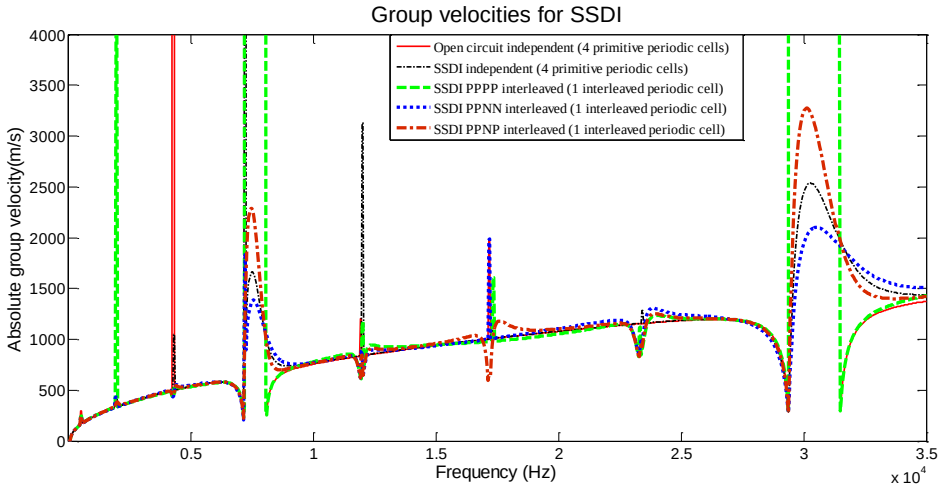

Figure 4.14 Group velocities for different SSDI cases ($\gamma_{ind} = 0.5, \gamma_{\text{int}} = 0.6$).

4.5 Experimental investigation

4.5.1 Experimental setup

In order to further validate vibration reduction performance of the proposed structure in low frequency domain, the sample of piezoelectric clamped-clamped periodic beam used in the experimental section of Chapter 3 is adopted in this section. Different SSDI interleaved networks coupled with the beam sample and the SSDI independent network coupled with the beam sample are shown in Figure 4.15. Based on frequency response to harmonic excitation for the clamped-clamped piezoelectric beam structure introduced in Chapter 3, experimental and theoretical frequency responses of the beam with different SSDI electrical networks are obtained and compared. Herein, for smart periodic structure composed of one kind of identical independent / interconnected periodic cells, the transfer matrix T is the same for every cell versus such periodic system, so the global transfer matrix of the system T_g can be obtained as:

$$T_g = [T]^n \tag{4.15}$$

where n is the number of identical periodic cells and T is the transfer matrix of the identical periodic cell.

For smart periodic structure composed of two kinds of identical periodic cells, the global transfer matrix for the structure can be given as:

$$T_g = [T_M]^n \cdot [T_{EM}]^m \left(\text{or } [T_{EM}]^m \cdot [T_M]^n \text{, depending on two directions of elastic wave propagation} \right) \tag{4.16}$$

where m is the number of one kind of electromechanical periodic cells and T_{EM} is the transfer matrix of the corresponding periodic cell; n is the number of minimal Bragg-type periodic cells without electrical shunt connections and T_M is the transfer matrix of the corresponding periodic cell.

Parameters of the beam and PZTs with same polarization directions are listed in Table 3.1 and Table 3.2. The experimental setup is depicted in Figure 4.16. When the PZT of one primitive periodic cell is in the open circuit condition, the primitive periodic

cell is considered as a minimal Bragg-type periodic cell (MB Cell) which is purely mechanical. When a minimal periodic cell with closed electrical boundary condition includes one PZT (or several PZTs) connected to single electrical shunt (or several electrical shunts with a unique connection), such periodic cell can be considered as an electromechanical periodic cell (EM Cell).

Two different SSDI interleaved-switched electrical cases including different number of SSDI interleaved periodic cells, as shown in Figure 4.15, are compared, together with three different SSDI independent electrical connections including different number of SSDI independent periodic cells. In the experiments, an external force, applied to the node between the 6^{th} and the 7^{th} minimal Bragg-type periodic cells, is generated by an electromagnet driven through an amplifier with the signal delivered by a function generator. Herein, the switching command is ensured by a dSPACE system for controlling dedicated switching circuits and achieving more precise experimental results. Practically, it is convenient to use integrated self-powered SSDI circuits [33, 34] to replace the dSPACE system for switch control. An inductive displacement sensor is used for monitoring the displacement of the node between the 7^{th} and the 8^{th} minimal Bragg-type periodic cells.

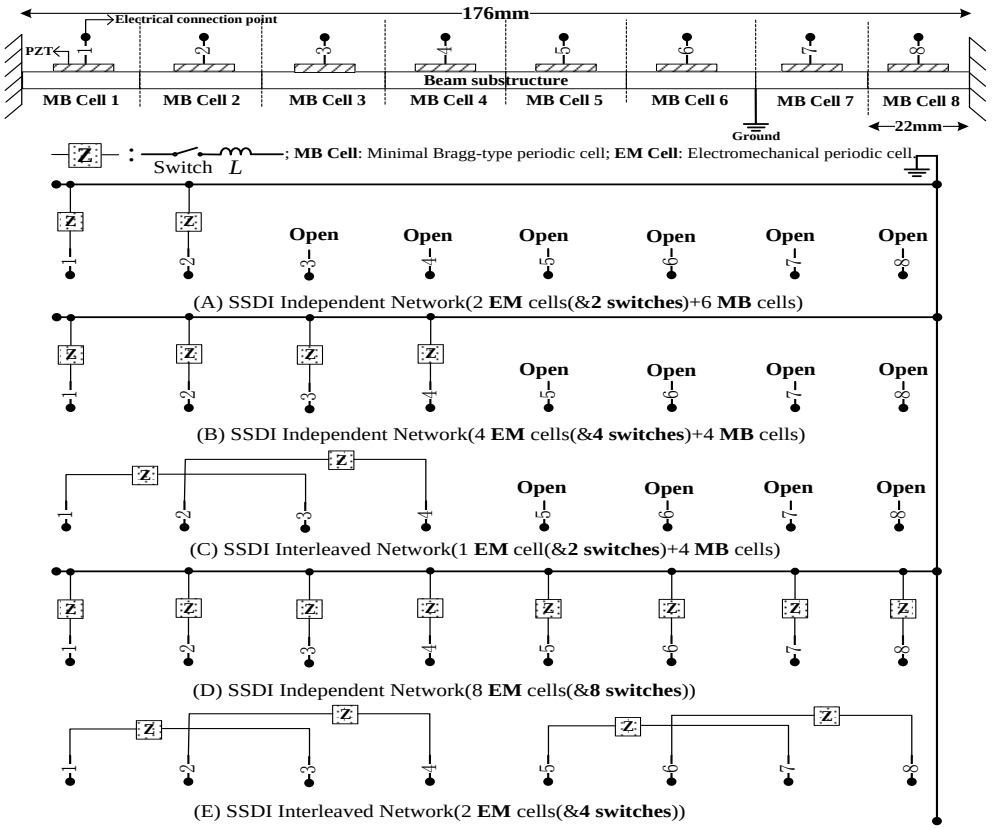

Figure 4.15 Periodic clamped-clamped piezoelectric beam with different SSDI electrical networks.

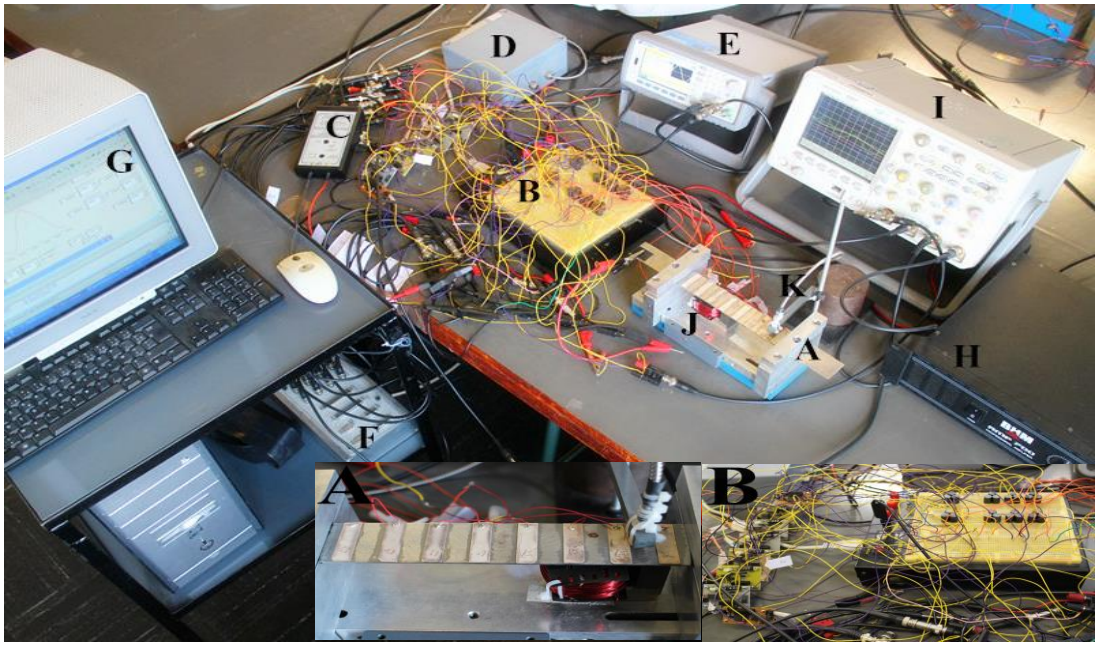

Figure 4.16 Experimental Setup: A: Host piezoelectric clamped-clamped periodic beam; B: SSDI switching circuits; C: differential voltage probe; D: displacement signal conditioner; E: function generator; F: dSPACE system; G: computer; H: power amplifier; I: oscilloscope; J: electromagnet; K: inductive vibrometer.

4.5.2 Theoretical and experimental results

In order to reflect real working conditions, structural damping is considered in the theoretical analysis. Herein, Rayleigh damping matrix C^e of one element as a function of the mass and stiffness matrices of a single element (respectively noted as M^e and K^e), is introduced. According to experimental measurements, the coefficient β_1 and β_2 in the damping matrix C^e can be given as:

$$\begin{cases} C^e = \beta_1 M^e + \beta_2 K^e \\ \beta_1 = 60\mathrm{s}^{-1}, \beta_2 = 13\times10^{-6}\mathrm{s} \end{cases}$$

In experiments, the inversion coefficient γ_{ind} in SSDI independent electrical networks and the inversion coefficient γ_{int} in SSDI interleaved-switched electrical networks are given by:

$$\gamma_{ind} = 0.5, \quad \gamma_{\text{int}} = 0.6$$

Theoretical normalized displacement and experimental normalized displacement of the clamped-clamped periodic beam with different SSDI electrical networks are plotted in Figure 4.17 and Figure 4.18, respectively. There are some small deviations between theoretical and experimental modal frequencies, similar with the experimental part of SSDI cases in Chapter 3. Both of predicted and measured results show that smart periodic structure with one SSDI interleaved-switched periodic cell (EM cell) and four adjacent minimal Bragg-type periodic cells (MB cell) has better vibration reduction performance than smart periodic structure with two adjacent SSDI independent periodic cells (EM cells) and six adjacent minimal Bragg-type periodic cells (MB cells), on condition that the same number of electrical switches is connected to PZTs bonded on the beam substructure is used, but also outperforms smart periodic structure with four adjacent SSDI independent periodic cells (EM cells) and four adjacent minimal Bragg-type periodic cells (MB cells) on condition that the same number of minimal Bragg-type periodic cells (MB cells) is fashioned into EM cells.

Vibration reduction superiority of the proposed structure is more distinct with the increase of the SSDI interleaved-switched periodic cells. As shown in Figure 4.18, experimental results demonstrate that the proposed structure with two adjacent SSDI interleaved-switched periodic cells using eight primitive periodic cells and four switches has much better attenuation performance than smart periodic structure with eight SSDI independent periodic cells using eight minimal Bragg-type periodic cells and eight switches. However, the corresponding theoretical results are not given in Figure 4.17 since theoretical normalized displacement of the proposed structure with two SSDI interleaved-switched periodic cells cannot be obtained correctly according to frequency response formulation to harmonic excitation for clamped-clamped

piezoelectric beam structure introduced in Chapter 3. This is explained by the fact that the proposed structure with two adjacent SSDI interleaved-switched periodic cells having 3 nodal points (2 fixed end points and 1 node point between two adjacent SSDI interleaved-switched periodic cells), neither the two fixed end points can be used to exert the external force because of clamped-clamped boundary condition, nor the nodal point in the middle of the clamped-clamped beam can be considered, therefore preventing frequency response prediction. Such performance of the approach can be explained by the introduction of some disorder within the structure, as such aperiodicity may enhance the vibration damping abilities [93].

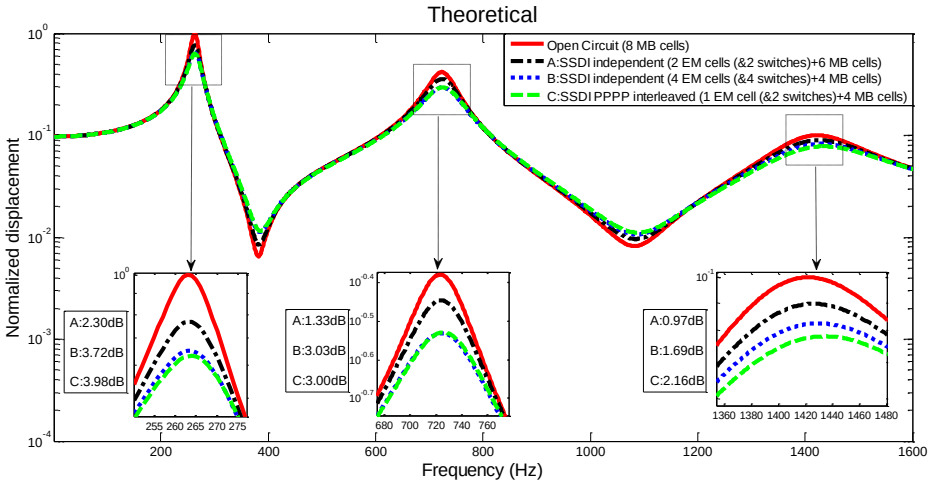

Figure 4.17 Predicted results of the periodic clamped-clamped beam with different SSDI electrical networks.

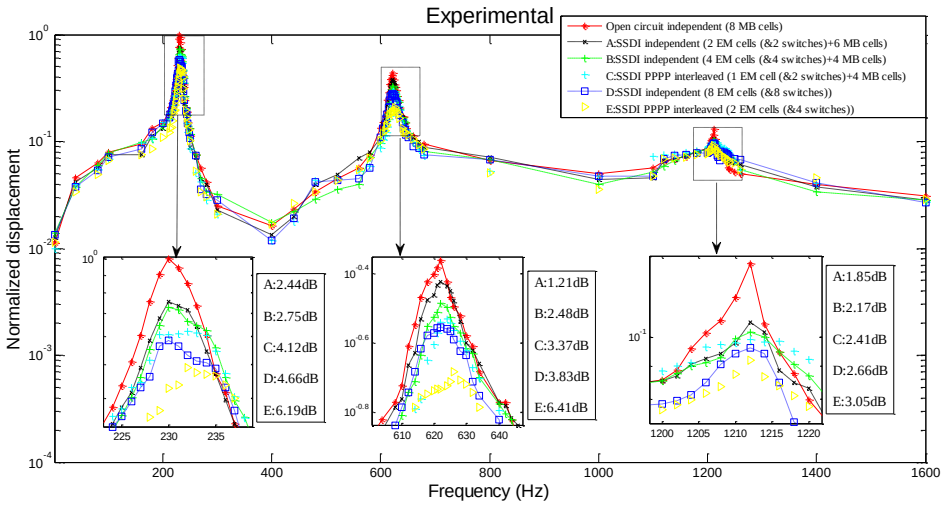

Figure 4.18 Measured results of the periodic clamped-clamped beam with different SSDI electrical networks.

4.6 Extension work - Smart periodic structure with nonlinear Tri-interleaved switched electric networks

Smart periodic structure with nonlinear SSDI Tri-interleaved piezoelectric topologies is proposed here as an extension for elastic wave control and effective low-frequency vibration reduction. A comparison of attenuation performance is made between piezoelectric periodic structure with SSDI independent electrical topologies and piezoelectric periodic structure with proposed electronic topologies. Compared with the previous smart periodic structure with SSDI independent electrical networks which achieves better band gap hybridization (near-coupling between Bragg scattering mechanism and wideband resonance mechanism induced by Synchronized Switch Damping networks in piezoelectric beam structures) than the previous SSDI interleaved electrical networks, theoretical results show that the proposed SSDI Tri-interleaved electronic topology exhibits better band gap hybridization over the investigated frequency domain. Furthermore, piezoelectric beam structure with proposed electronic topology generates a better resonant-type low-frequency broadband band gap, which is experimentally validated by measuring the harmonic

response of a piezoelectric periodic beam under clamped-clamped boundary conditions.

4.6.1 Overview of the investigated phononic beam structure

As shown in Figure 4.19, the proposed smart periodic beam structure with nonlinear Tri-interleaved electronic topologies is comprised of two sections: mechanical section and electrical section. Bragg-type band gap generation mechanism mainly depends on the mechanical section consisting of several identical PZTs periodically placed throughout the beam structure. By comparison, resonant-type band gap generation mechanism mainly relies on the electrical section. Electronic damping characteristics of resonant shunting circuits are combined with the dielectric properties of the PZTs, and hence affect physical properties of the whole smart periodic structure.

Herein, for an SSDI Tri-interleaved periodic cell, there are six adjacent PZTs (number of PZTs: 1^{st}, 2^{nd}, 3^{rd}, 4^{th}, 5^{th}, 6^{th}) uniformly distributed on the beam structure in the mechanical part, and one Tri-interleaved electronic topology including three independent SSDI control devices in the electrical part. The electromechanical coupling pattern consists in connecting the 1^{st} PZT and the 4^{th} PZT, the 2^{nd} PZT and the 5^{th} PZT, and the 3^{rd} PZT and the 6^{th} PZT as shown in Figure 4.19.

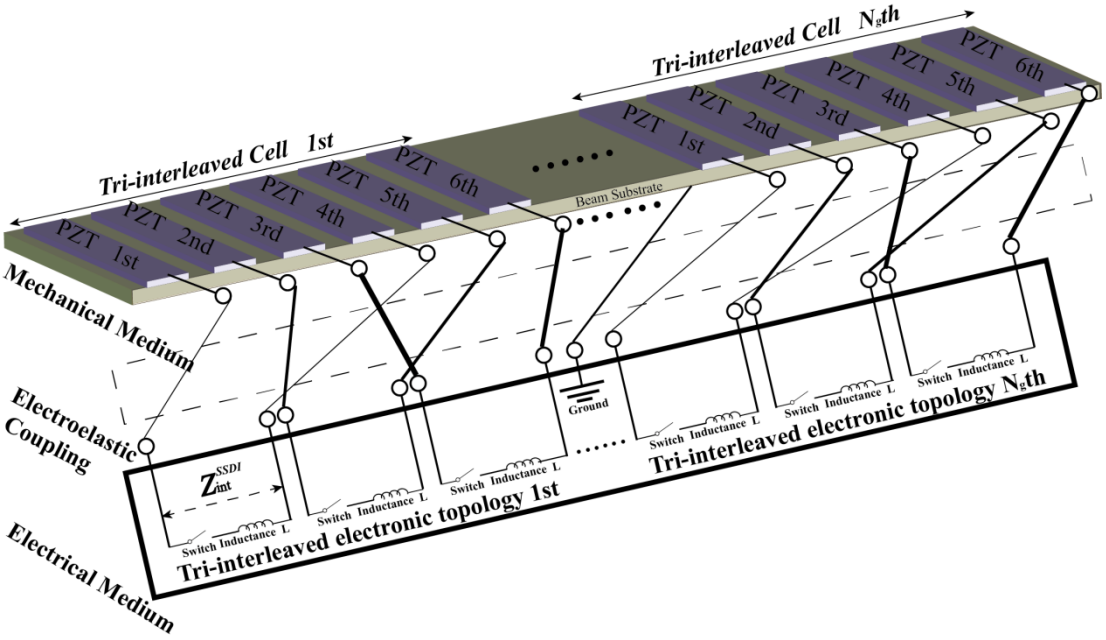

Figure 4.19 smart periodic beam structure carrying SSDI Tri-interleaved switched electronic topologies.

4.6.2 Electro-elastic relationships of a Tri-interleaved periodic cell

For investigating wave propagation properties of the proposed piezoelectric periodic beam structure, the dynamic electro-elastic relationships in a unit Tri-interleaved periodic cell are analyzed and demonstrated in this subsection. Herein, the piezoelectric periodic beam structure is assumed to follow Euler-Bernoulli beam assumptions. According to finite element modeling of the Euler-Bernoulli piezoelectric beam introduced in Chapter 2, if the i^{th} Tri-interleaved periodic cell $\left(1 \le i < N_g\right)$ of the proposed structure (composed of N_g Tri-interleaved periodic cells) can be divided into several finite elements, the fundamental electro-elastic relationships in a Tri-interleaved periodic cell in the frequency domain can be obtained as:

$$\begin{cases} \left[-\omega^2 M^e\right]\left\{d^i\right\}+\left[j\omega C^e\right]\left\{d^i\right\}+\left[K^e\right]\left\{d^i\right\}+\left[B_1^e\right]\left\{V_p^i\right\}=\left\{P^i\right\} \\ \left\{I_p^i\right\}=\left[j\omega B_2^e\right]\left\{d^i\right\}+\left[j\omega B_3^e\right]\left\{V_p^i\right\} \end{cases} \tag{4.17}$$

$$\begin{cases} \left[M^e\right]=\int_0^l\left[H\right]^T\rho A_c\left[H\right]dx,\ \left[K^e\right]=\int_0^l\left[H''\right]^T EI_s\left[H''\right]dx,\ \left[C^e\right]=\beta_1\left[M^e\right]+\beta_2\left[K^e\right] \\ \left[B_1^e\right]=\int_0^l b_1\left[H''\right]^T dx,\ \ \rho A_c=\begin{cases}\rho_b A_b, & \text{beam element without PZTs}\\ \rho_b A_b+\rho_p A_p, & \text{beam element with PZTs}\end{cases},\ \ EI_s=\begin{cases}E_b I_b, & \text{beam element without PZTs}\\ E_{eq} I_{eq}, & \text{beam element with PZTs}\end{cases} \end{cases}$$

where the matrices $\left[M^e\right],\left[C^e\right],\left[K^e\right]$ denote the mass, Rayleigh damping and short-circuit stiffness. l is the length of finite beam element. ω is the angular frequency. $\left[H\right]$ is the matrix of Hermitian shape function. $\left[H''\right]$ is the second order derivative of Hermitian shape functions. ρ is the mass density (ρ_b for the pure beam element, ρ_q for the piezoelectric material), A is the cross-sectional area (A_b for the pure beam element, A_q for the piezoelectric material), E the elastic modulus (E_b for the pure beam element, E_{eq} for the pure beam element with piezoelectric material), and I is the second moment of the cross-sectional area (I_b for the pure beam element, I_{eq} for the pure beam element with piezoelectric material). β_1, β_2 are the Rayleigh damping coefficients. $\left\{d^i\right\}$ and $\left\{P^i\right\}$ are the $2(n+1)$ by 1 matrices which respectively refer to the generalized nodal displacement vectors (displacement and slope vectors in the frequency domain) and the generalized nodal force vectors (force and moment vectors in the frequency domain). $\left\{V_p^i\right\}$ and $\left\{I_p^i\right\}$ with matrix size of 6 by 1 denote the piezoelectric voltages and output currents of the six identical PZTs in the investigated Tri-interleaved periodic cell. B_1^e is a $2(n+1)$ by 6 matrix which is given by:

$$B_1^e=\begin{bmatrix} B_{11} & B_{12} & B_{13} & B_{14} & B_{15} & B_{16}\end{bmatrix}$$

$$\begin{cases} B_{11}=b_{11}\int_0^l\left[H''\right]^T dx, b_{11}=-\dfrac{p_1 d_{31} w_b}{t_p\left(s_{11}^E+s_{12}^E\right)}\int_{t_b}^{t_b+t_p}\left(u_3-x_c\right)dx_3 \\ B_{12}=b_{12}\int_0^l\left[H''\right]^T dx, b_{12}=-\dfrac{p_2 d_{31} w_b}{t_p\left(s_{11}^E+s_{12}^E\right)}\int_{t_b}^{t_b+t_p}\left(u_3-x_c\right)dx_3 \\ B_{13}=b_{13}\int_0^l\left[H''\right]^T dx, b_{13}=-\dfrac{p_3 d_{31} w_b}{t_p\left(s_{11}^E+s_{12}^E\right)}\int_{t_b}^{t_b+t_p}\left(u_3-x_c\right)dx_3 \\ B_{14}=b_{14}\int_0^l\left[H''\right]^T dx, b_{14}=-\dfrac{p_4 d_{31} w_b}{t_p\left(s_{11}^E+s_{12}^E\right)}\int_{t_b}^{t_b+t_p}\left(u_3-x_c\right)dx_3 \\ B_{15}=b_{15}\int_0^l\left[H''\right]^T dx, b_{15}=-\dfrac{p_5 d_{31} w_b}{t_p\left(s_{11}^E+s_{12}^E\right)}\int_{t_b}^{t_b+t_p}\left(u_3-x_c\right)dx_3 \\ B_{16}=b_{16}\int_0^l\left[H''\right]^T dx, b_{16}=-\dfrac{p_6 d_{31} w_b}{t_p\left(s_{11}^E+s_{12}^E\right)}\int_{t_b}^{t_b+t_p}\left(u_3-x_c\right)dx_3 \end{cases}$$

$$B_2^e=\begin{bmatrix} B_{21} \\ B_{22} \\ B_{23} \\ B_{24} \\ B_{25} \\ B_{26} \end{bmatrix},\begin{cases} B_{21}=b_{21}\int_0^l\left[H''\right]dx,\ b_{21}=-\dfrac{p_1 d_{31} t_p}{\left(s_{11}^E+s_{12}^E\right)} \\ B_{22}=b_{22}\int_0^l\left[H''\right]dx,\ b_{22}=-\dfrac{p_2 d_{31} t_p}{\left(s_{11}^E+s_{12}^E\right)} \\ B_{23}=b_{23}\int_0^l\left[H''\right]dx,\ b_{23}=-\dfrac{p_3 d_{31} t_p}{\left(s_{11}^E+s_{12}^E\right)} \\ B_{24}=b_{24}\int_0^l\left[H''\right]dx,\ b_{24}=-\dfrac{p_4 d_{31} t_p}{\left(s_{11}^E+s_{12}^E\right)} \\ B_{25}=b_{25}\int_0^l\left[H''\right]dx,\ b_{25}=-\dfrac{p_5 d_{31} t_p}{\left(s_{11}^E+s_{12}^E\right)} \\ B_{26}=b_{26}\int_0^l\left[H''\right]dx,\ b_{26}=-\dfrac{p_6 d_{31} t_p}{\left(s_{11}^E+s_{12}^E\right)} \end{cases}$$

$$B_3^e=\begin{bmatrix} B_{31} & 0 & 0 & 0 & 0 & 0 \\ 0 & B_{32} & 0 & 0 & 0 & 0 \\ 0 & 0 & B_{33} & 0 & 0 & 0 \\ 0 & 0 & 0 & B_{34} & 0 & 0 \\ 0 & 0 & 0 & 0 & B_{35} & 0 \\ 0 & 0 & 0 & 0 & 0 & B_{36} \end{bmatrix}$$

$$B_{31}=B_{32}=B_{33}=B_{34}=B_{35}=B_{36}=\frac{w_b L_p\left[2{d_{31}}^2-\varepsilon_{33}^T\left(s_{11}^E+s_{12}^E\right)\right]}{t_p\left(s_{11}^E+s_{12}^E\right)}$$

with d_{31} the piezoelectric charge coefficient, ε_{33}^{T} the electrical permittivity under constant stress, $s_{ij}^{E}\left(s_{11}^{E}, s_{12}^{E}\right)$ the elastic constant under constant electric field. w_b, t_b and t_p, L_p respectively refer to the width and thickness of the beam substrate and thickness and length of a single PZT. u_3 is the displacement along the axis 3 and x_c denotes the neutral axis position. p_1, p_2, p_3, p_4, p_5, p_6 are the signs of piezoelectric constant determined by the polarization direction of the six PZTs within a Tri-interleaved periodic cell. Herein, all the six identical PZTs in one Tri-interleaved periodic cell are assumed to have positive polarization direction therefore the sign is equal to 1.

Similarly with the SSDI interleaved / interconnected cases, denoting the original (purely mechanical or short-circuited) dynamical stiffness matrix of such system $\left[A^e\right]$, which is equal to $\left[-\omega^2 M^e\right]+\left[j\omega C^e\right]+\left[K^e\right]$, the dynamical stiffness matrix of the system under different electrical boundary conditions is equal to:

$$\left\{P^i\right\}=\begin{cases}\left[A^e\right]\left\{d^i\right\}, & \text{for the short circuit condition}\\ \left[A_{EC}\right]\left\{d^i\right\}, & \text{for other electrial boundary conditions}\end{cases}$$
$$A_{EC}=\begin{cases}A_{open}=A^e+B_1^e\cdot B_4^e, & \text{for the open circuit condition}\\ A_{ind}^{SSDI}=A^e+B_1^e\cdot B_6^e, & \text{for the SSDI independent case}\end{cases} \tag{4.18}$$

where

$$B_4^e=\begin{bmatrix}B_{41}\\B_{42}\\B_{43}\\B_{44}\\B_{45}\\B_{46}\end{bmatrix},\begin{cases}B_{41}=b_{41}\int_0^l[H'']dx, b_{41}=\dfrac{d_{31}{t_p}^2}{L_p\left[\varepsilon_{33}^T\left(s_{11}^E+s_{12}^E\right)-2d_{31}^2\right]}\\B_{42}=b_{42}\int_0^l[H'']dx, b_{42}=\dfrac{d_{31}{t_p}^2}{L_p\left[\varepsilon_{33}^T\left(s_{11}^E+s_{12}^E\right)-2d_{31}^2\right]}\\B_{43}=b_{43}\int_0^l[H'']dx, b_{43}=\dfrac{d_{31}{t_p}^2}{L_p\left[\varepsilon_{33}^T\left(s_{11}^E+s_{12}^E\right)-2d_{31}^2\right]}\\B_{44}=b_{44}\int_0^l[H'']dx, b_{44}=\dfrac{d_{31}{t_p}^2}{L_p\left[\varepsilon_{33}^T\left(s_{11}^E+s_{12}^E\right)-2d_{31}^2\right]}\\B_{45}=b_{45}\int_0^l[H'']dx, b_{45}=\dfrac{d_{31}{t_p}^2}{L_p\left[\varepsilon_{33}^T\left(s_{11}^E+s_{12}^E\right)-2d_{31}^2\right]}\\B_{46}=b_{46}\int_0^l[H'']dx, b_{46}=\dfrac{d_{31}{t_p}^2}{L_p\left[\varepsilon_{33}^T\left(s_{11}^E+s_{12}^E\right)-2d_{31}^2\right]}\end{cases}$$

$$B_6^e=\begin{bmatrix}B_{61}\\B_{62}\\B_{63}\\B_{64}\\B_{65}\\B_{66}\end{bmatrix},\quad\begin{cases}B_{61}=\dfrac{j\omega Z_{ind}^{SSDI}\cdot B_{21}}{\left(1-j\omega Z_{ind}^{SSDI}\cdot B_{31}\right)};\\B_{62}=\dfrac{j\omega Z_{ind}^{SSDI}\cdot B_{22}}{\left(1-j\omega Z_{ind}^{SSDI}\cdot B_{32}\right)};\\B_{63}=\dfrac{j\omega Z_{ind}^{SSDI}\cdot B_{23}}{\left(1-j\omega Z_{ind}^{SSDI}\cdot B_{33}\right)};\\B_{64}=\dfrac{j\omega Z_{ind}^{SSDI}\cdot B_{24}}{\left(1-j\omega Z_{ind}^{SSDI}\cdot B_{34}\right)};\\B_{65}=\dfrac{j\omega Z_{ind}^{SSDI}\cdot B_{25}}{\left(1-j\omega Z_{ind}^{SSDI}\cdot B_{35}\right)};\\B_{66}=\dfrac{j\omega Z_{ind}^{SSDI}\cdot B_{26}}{\left(1-j\omega Z_{ind}^{SSDI}\cdot B_{36}\right)}.\end{cases}$$

where Z_{ind}^{SSDI} is the SSDI impedance of one SSDI shunt connected to both ends of a single PZT bonded on the structure which is introduced in Chapter 3.

As shown in Figure 4.20, $V_{p1}^i,V_{p2}^i,V_{p3}^i,V_{p4}^i,V_{p5}^i,V_{p6}^i$ and $I_{p1}^i,I_{p2}^i,I_{p3}^i,I_{p4}^i,I_{p5}^i,I_{p6}^i$ are the piezoelectric voltages and output currents of the six PZTs in a nonlinear switched Tri-interleaved periodic cell *i*. The SSDI Tri-interleaved periodic cell has the following dynamical electromechanical relationship:

$$\begin{cases} V_{p1}^i - I_{M1} Z_{\text{int}}^{SSDI} = V_{p4}^i \\ I_{p1}^i = -I_{p4}^i = I_{M1} \\ V_{p2}^i - I_{M2} Z_{\text{int}}^{SSDI} = V_{p5}^i \\ I_{p2}^i = -I_{p5}^i = I_{M2} \\ V_{p3}^i - I_{M3} Z_{\text{int}}^{SSDI} = V_{p6}^i \\ I_{p3}^i = -I_{p6}^i = I_{M3} \\ \left\{P^i\right\} = \left[A^e\right]\left\{d^i\right\} + \left[B_1^e\right]\left\{V_p^i\right\} \\ \left\{I_p^i\right\} = \left[j\omega B_2^e\right]\left\{d^i\right\} + \left[j\omega B_3^e\right]\left\{V_p^i\right\} \\ \left[A^e\right] = \left[-\omega^2 M^e\right] + \left[j\omega C^e\right] + \left[K^e\right] \\ Z_{\text{int}}^{SSDI} = \dfrac{\pi\left(1-\gamma_{\text{int}}\right)}{2\omega C_0\left(1+\gamma_{\text{int}}\right)} + \dfrac{2j}{\omega C_0} \end{cases} , \left\{I_p^i\right\} = \begin{bmatrix} I_{p1}^i \\ I_{p2}^i \\ I_{p3}^i \\ I_{p4}^i \\ I_{p5}^i \\ I_{p6}^i \end{bmatrix}, \left\{V_p^i\right\} = \begin{bmatrix} V_{p1}^i \\ V_{p2}^i \\ V_{p3}^i \\ V_{p4}^i \\ V_{p5}^i \\ V_{p6}^i \end{bmatrix} \tag{4.19}$$

where Z_{int}^{SSDI} is the SSDI impedance of one SSDI shunt connected between two PZTs bonded on the structure as discussed in Chapter 3.

Hence, the piezoelectric voltages of the PZTs in a nonlinear Tri-interleaved periodic cell *i* can be obtained as:

$$V_p^i = B_9^e d^i \tag{4.20}$$

$$B_9^e = \begin{bmatrix} \dfrac{-\left(\dfrac{B_{21}+B_{24}}{B_{31}}\right) + j\omega Z_{\text{int}}^{SSDI} B_{21}}{2 - j\omega Z_{\text{int}}^{SSDI} B_{31}} \\ \dfrac{-\left(\dfrac{B_{22}+B_{25}}{B_{31}}\right) + j\omega Z_{\text{int}}^{SSDI} B_{22}}{2 - j\omega Z_{\text{int}}^{SSDI} B_{31}} \\ \dfrac{-\left(\dfrac{B_{23}+B_{26}}{B_{31}}\right) + j\omega Z_{\text{int}}^{SSDI} B_{23}}{2 - j\omega Z_{\text{int}}^{SSDI} B_{31}} \\ -\left(\dfrac{B_{21}+B_{24}}{B_{31}}\right) - \dfrac{-\left(\dfrac{B_{21}+B_{24}}{B_{31}}\right) + j\omega Z_{\text{int}}^{SSDI} B_{21}}{2 - j\omega Z_{\text{int}}^{SSDI} B_{31}} \\ -\left(\dfrac{B_{22}+B_{25}}{B_{31}}\right) - \dfrac{-\left(\dfrac{B_{22}+B_{25}}{B_{31}}\right) + j\omega Z_{\text{int}}^{SSDI} B_{22}}{2 - j\omega Z_{\text{int}}^{SSDI} B_{31}} \\ -\left(\dfrac{B_{23}+B_{26}}{B_{31}}\right) - \dfrac{-\left(\dfrac{B_{23}+B_{26}}{B_{31}}\right) + j\omega Z_{\text{int}}^{SSDI} B_{23}}{2 - j\omega Z_{\text{int}}^{SSDI} B_{31}} \end{bmatrix}$$

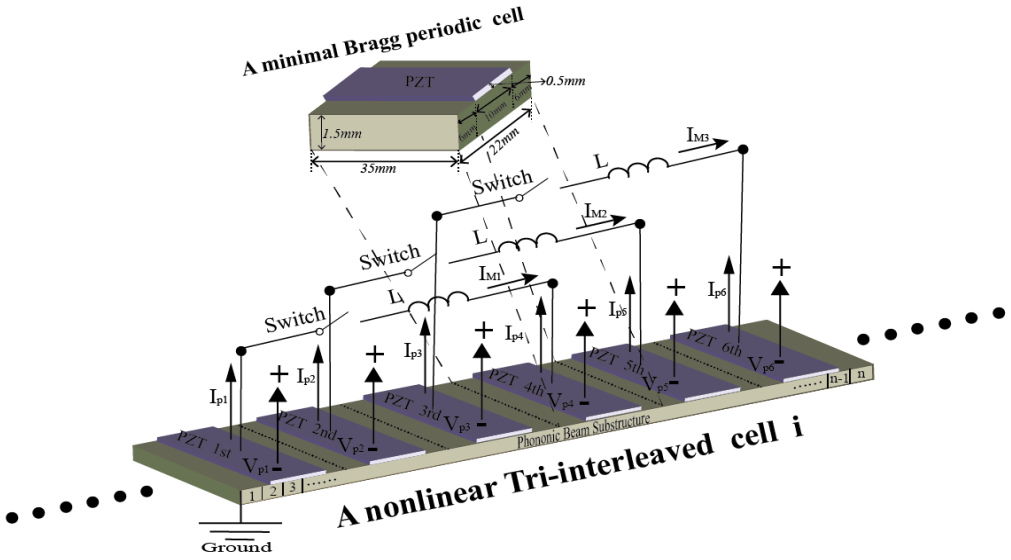

Figure 4.20 Nonlinear Tri-interleaved periodic cell.

Therefore, the dynamical relations of the nonlinear Tri-interleaved periodic cell *i* can be written as:

$$\left\{P^i\right\}=\left[A_{\text{Tri-interleaved}}\right]\left\{d^i\right\}=\left[A^e+B_1^eB_9^e\right]\left\{d^i\right\} \tag{4.21}$$

4.6.3 Theoretical results and discussion

For investigating wave propagation characteristics of the proposed piezoelectric periodic beam structure and wave localization properties within each nonlinear Tri-interleaved periodic cell, the transfer matrix for one nonlinear Tri-interleaved periodic cell (Figure 4.20) of the proposed 1D piezoelectric periodic beam structure (Figure 4.19) is obtained and analyzed in terms of localization factors and transmission factors.

Herein, the geometric and material parameters listed in Table 3.1 and Table 3.2, are used for numerical calculation. The dimension of the minimal Bragg-type periodic cell (Figure 4.20) is 22 mm. The PZT, which is 10 mm long, is bonded symmetrically in the minimal Bragg-type periodic cell. The investigated nonlinear Tri-interleaved periodic cell, including six adjacent minimal Bragg-type periodic cells, is decomposed into *n* finite elements. Similar to the previous theoretical discussions, it is assumed

that no structural damping is considered ($\left[C^e\right]=[0]$) and only the positive direction is taken into account in the following theoretical discussion.

As shown in Figure 4.19, the proposed piezoelectric beam structure is periodic since the transfer matrix is the same for every nonlinear Tri-interleaved periodic cell. However, the six adjacent minimal Bragg-type periodic cells within one nonlinear Tri-interleaved periodic cell (Figure 4.20) are disordered and aperiodic due to Tri-interleaved electronic topology. The transfer matrix for each minimal Bragg-type periodic cell in the nonlinear Tri-interleaved periodic cell is therefore irregular. For measuring the average attenuation constant per minimal Bragg-type periodic cell, localization factor, used to assess disordered systems [93], is introduced. The localization factor ϕ for irregular distribution of the electrical impedance in the nonlinear Tri-interleaved periodic cell can be defined as follows:

$$\phi=\frac{1}{6}In\left(\left|eig\left(T_{\text{Tri-interleaved}}\right)\right|\right)=\frac{1}{6}In\left(\left|e^{\mu}\right|\right) \tag{4.22}$$

where $T_{\text{Tri-interleaved}}$ is the transfer matrix of the nonlinear SSDI Tri-interleaved periodic cell. $eig\left(T_{\text{Tri-interleaved}}\right)$ is the eigenvalue of the transfer matrix $T_{\text{Tri-interleaved}}$. μ is a complex number, namely the averaged propagation constant. The real part $real(\phi)$ of the localization factor ϕ can be regarded as average attenuation constant per minimal Bragg-type periodic cell in the nonlinear Tri-interleaved periodic cell (the average logarithmic decay of the vibration amplitude of elastic wave propagating from one Bragg-type periodic cell to the next one). In addition, it should be noted that for the periodic beam structure in which each PZT has same electrical boundary condition (*i.e.*, in short / open circuit condition or SSDI independent control devices), the localization factor equals the attenuation constant since the attenuation constant for each minimal Bragg-type periodic cell is uniform.

Figure 4.21 (a) illustrates the comparison of average attenuation constant per minimal Bragg-type periodic cell among piezoelectric periodic beam structures with different

electrical networks (herein, $\gamma_{ind} = 0.5$, $\gamma_{\text{int}} = 0.6$, which accords with the following experimental validation). For the Tri-interleaved periodic cell in the open circuit condition, there is a Bragg-type band gap appearing in the frequency range [7.1 kHz, 8.1 kHz] over the investigated frequency domain. Compared with smart periodic beam structure with nonlinear SSDI independent networks which has broadband wave attenuation performance over the entire frequency domain, smart periodic beam structure with the proposed nonlinear SSDI Tri-interleaved topologies shows superiority in two aspects: 1. there is a relatively broadband low-frequency domain ([375 Hz, 1.51 kHz]) in which better wave attenuation capability is observed; 2. its band gap hybridization (electromechanical near-coupling between the Bragg scattering mechanism and the broadband resonance mechanism induced by nonlinear SSDI techniques) is superior to that of smart periodic beam structure with SSDI independent networks within the frequency range [6.05 kHz, 9.5 kHz].

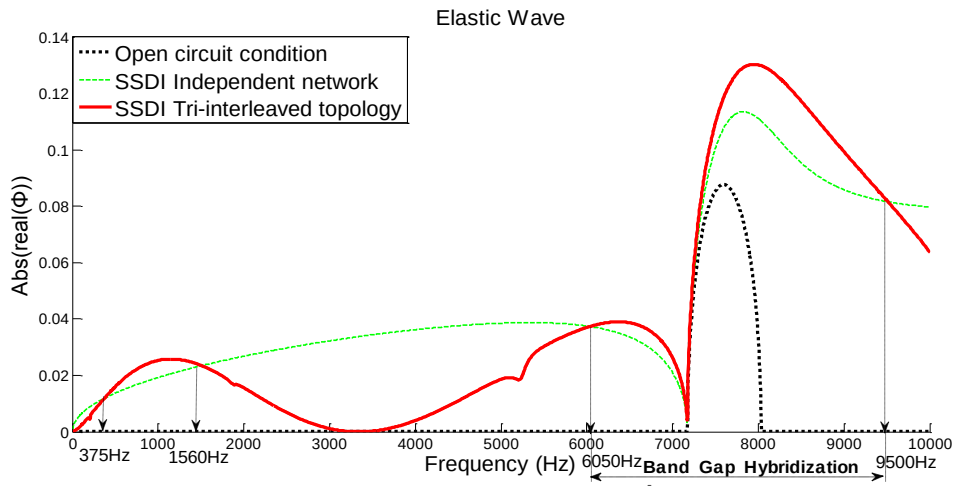

Figure 4.21 Localization factor of elastic waves in phononic beam metamaterial with different electrical boundary conditions.

Transmission factors of elastic wave in finite beam structures under proper boundary conditions and attenuation constants of smart periodic beam structure can be calculated by using transfer matrix method, which is introduced in Chapter 3. Specifically, a finite piezoelectric periodic beam structure composed of 8 minimal Bragg-type periodic cells under free-free boundary condition is chosen for the following transmission factor calculation under different electrical boundary conditions (Figure 4.22 (a), (b), (c)). The external force is placed on one side of the beam whose amplitude of the displacement is assumed to be equal to D_0, the amplitude of the other side of the beam is equal to D_8. Figure 4.22 (d) shows the transmission factor of finite free-free piezoelectric periodic beam structure with different electrical boundary conditions as depicted in Figure 4.22 (a, b, c). In the frequency ranges [500 Hz, 1.4 kHz] ∪ [6.05 kHz, 9.5 kHz], vibration reduction performance using the proposed SSDI Tri-interleaved topology is superior to that using the SSDI independent network, which matches well with the corresponding band gaps [375 Hz, 1.51 kHz] ∪ [6.5 kHz, 9.5 kHz].

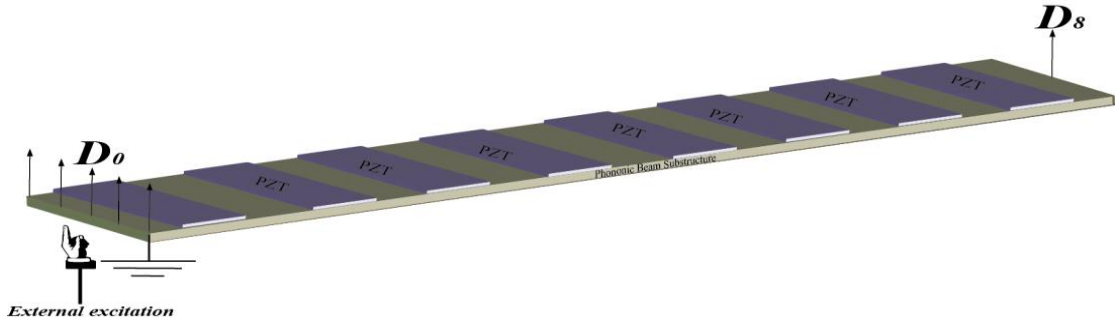

(a)

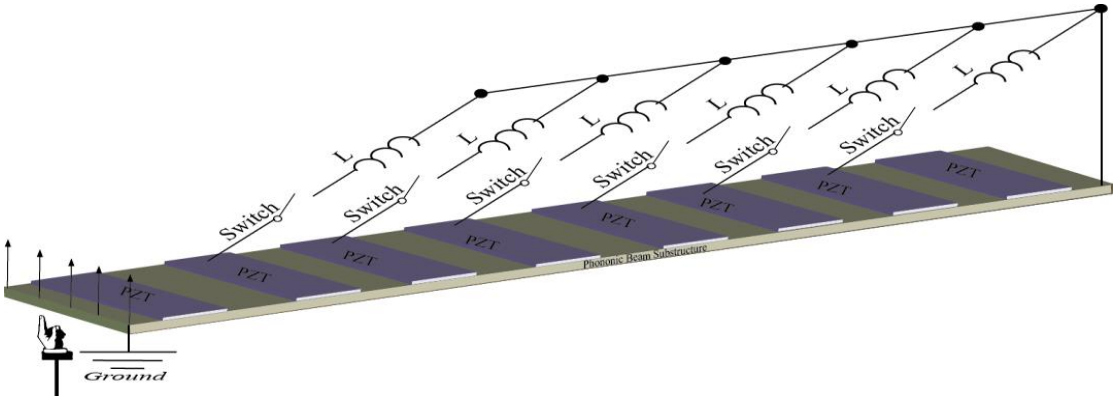

(b)

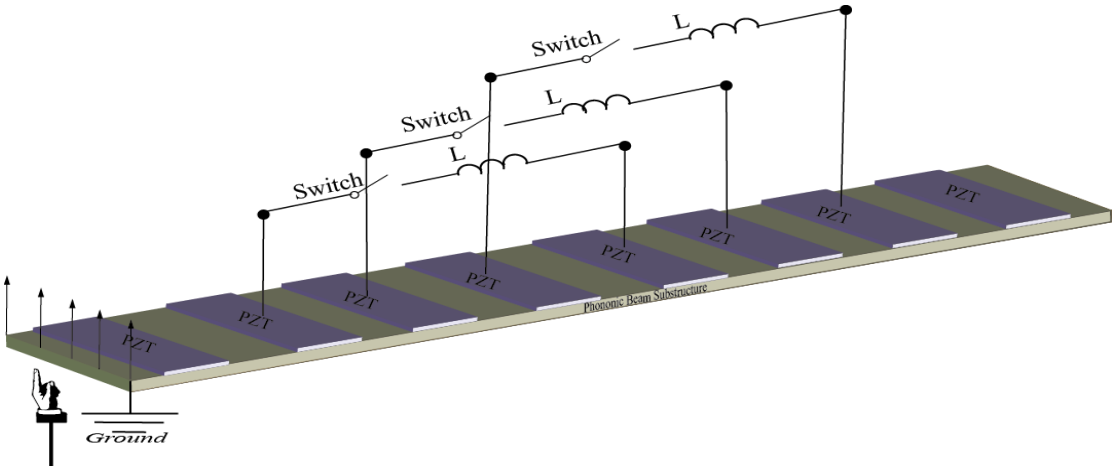

(c)

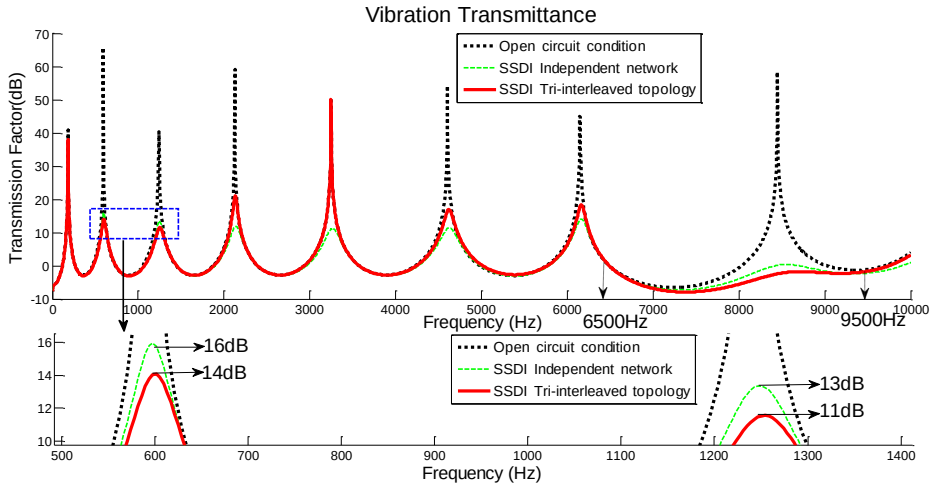

(d)

Figure 4.22 (a) Free-free piezoelectric periodic beam structure in open circuit condition; (b) free-free piezoelectric periodic beam structure with nonlinear SSDI independent networks; (c) free-free piezoelectric periodic beam structure with nonlinear SSDI Tri-interleaved electronic topology; (d) transmission factor of finite free-free periodic beam structure with different electrical boundary conditions (a, b, c).

Figure 4.23 depicts a comparison of the real part of the localization factor versus the voltage inversion coefficient between piezoelectric periodic beam structure with nonlinear SSDI independent networks and piezoelectric periodic beam structure with nonlinear SSDI Tri-interleaved topologies. It can be seen that wave attenuation efficiency of all the smart periodic beam structure with electrical SSDI networks becomes better and better with the increase of the voltage inversion coefficient. However, in the low-frequency area (< 2 kHz) and band gap hybridization area [6 kHz, 10 kHz], piezoelectric periodic beam structure with proposed SSDI Tri-interleaved topologies outperforms piezoelectric periodic beam structure with SSDI independent networks.

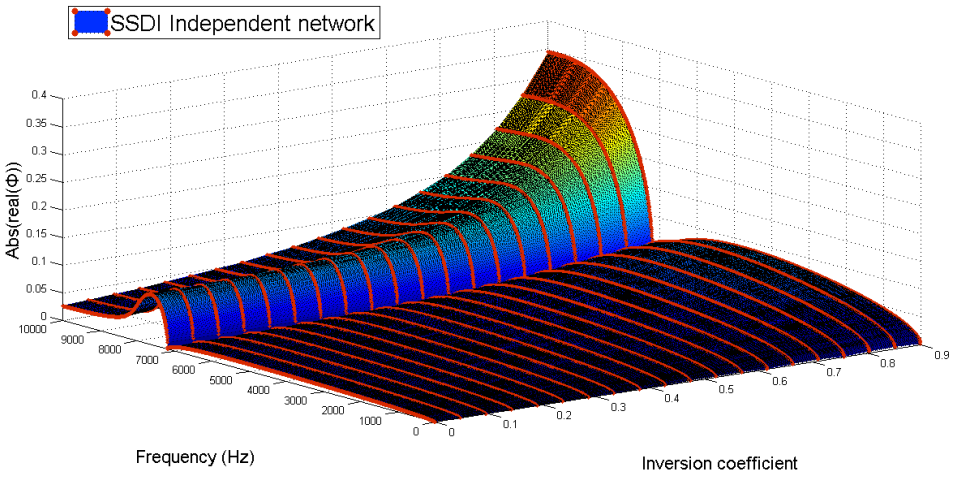

(a)

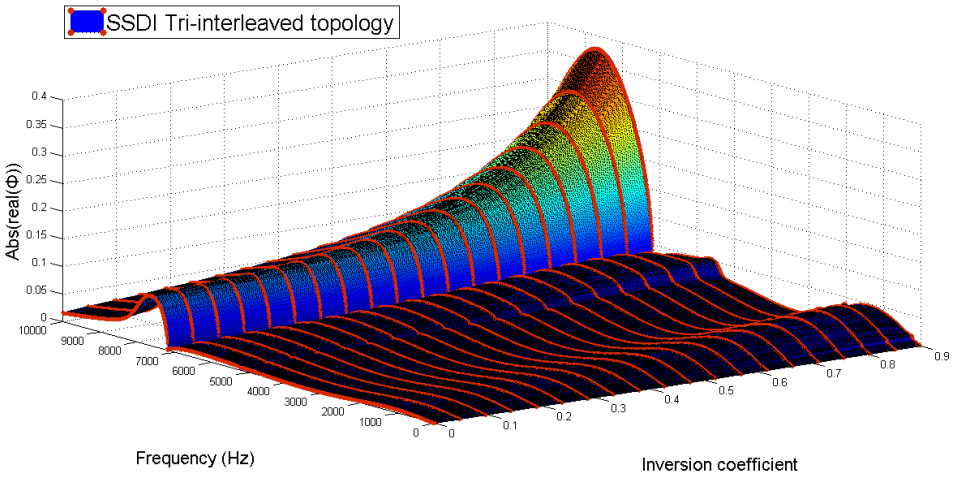

(b)

Figure 4.23 (a) 3D plot of real part of the localization factor of elastic wave versus the voltage inversion coefficient with different SSDI independent network; (b) 3D plot of real part of the localization factor of elastic wave versus the voltage inversion coefficient with SSDI Tri-interleaved topology (for equitable comparison, all the axis of inversion coefficient adopts the value of γ_{ind}).

4.6.4 Response to harmonic excitation for the clamped-clamped piezoelectric beam structure

The transfer matrix formulation can be applied to obtain the frequency response along the piezoelectric periodic beam for harmonic excitation. Since free-free periodic phononic beam structure cannot be infinite in practical applications, the clamped-clamped boundary condition is applied as an example at the beginning and end nodes of the investigated beam shown in Figure 4.22 (a) in the following experimental section (Figure 4.24). Since the SSDI Tri-interleaved periodic cell has closed electrical boundary condition, similar with the SSDI independent / interleaved periodic cell, the method for obtaining the frequency response along the piezoelectric periodic beam for harmonic excitation introduced in Chapter 3 can be used for the SSDI Tri-interleaved case.

Specifically, considering the investigated experimental structures of the following section, the overall transfer matrix for the periodic beam metamaterial with different electrical boundary conditions as shown in Figure 4.24 can be respectively given by:

$$T=\begin{cases} T_{open-global}=\left[T_{open}\right]^{8}, & \text{for the open circuit condition} \\ T_{IndSSDI-Type1}=T_{open}\cdot\left[T_{IndSSDI}\right]^{6}\cdot T_{open}, & \text{for A: the SSDI independent Type-1} \\ T_{TriSSDI-Type1}=T_{open}\cdot T_{TriSSDI}\cdot T_{open}, & \text{for B: the SSDI Tri-interleaved Type-1} \\ T_{TriSSDI-Type2}=T_{IndSSDI}\cdot T_{TriSSDI}\cdot T_{IndSSDI}, & \text{for C: the SSDI Tri-interleaved Type-2} \\ T_{IndSSDI-Type2}=\left[T_{IndSSDI}\right]^{8}, & \text{for D: the SSDI independent Type-2} \end{cases} \tag{4.23}$$

where T_{open} denotes the transfer matrix of the Bragg periodic cell in open circuit condition, $T_{IndSSDI}$ the transfer matrix of the periodic cell with the independent SSDI networks and $T_{TriSSDI}$ the transfer matrix of the periodic cell with the Tri-interleaved SSDI topology.

According to the above fundamental principle for deriving state vectors at any intermediate nodal point introduced in Chapter 3, and assuming that the external harmonic force *F* is applied to the node between the 1st minimal Bragg-type periodic

cell and the 2nd minimal Bragg-type periodic cell ($nf=1$), state vectors at the same node 1 (d^1, P^1) can be obtained as:

$$\begin{cases} \begin{Bmatrix} d^1 \\ P^1 \end{Bmatrix} = T_{open} \begin{Bmatrix} 0 \\ P^0 \end{Bmatrix} + \begin{Bmatrix} 0 \\ P_{ex}^1 \end{Bmatrix}, & \text{for} \begin{cases} \text{the open circuit condition;} \\ \text{A: the SSDI independent Type-1;} \\ \text{B: the SSDI Tri-interleaved Type-1} \end{cases} \\ \begin{Bmatrix} d^1 \\ P^1 \end{Bmatrix} = T_{IndSSDI} \begin{Bmatrix} 0 \\ P^0 \end{Bmatrix} + \begin{Bmatrix} 0 \\ P_{ex}^1 \end{Bmatrix}, & \text{for} \begin{cases} \text{C: the SSDI Tri-interleaved Type-2;} \\ \text{D: the SSDI independent Type-2} \end{cases} \end{cases} \tag{4.24}$$

$$\begin{cases} P^0 = -\left(t_{12}^{LG}\right)^{-1} t_{12}^{RG} P_{ex}^1, P^N = \left[-t_{22}^{LG} \left(t_{12}^{LG}\right)^{-1} t_{12}^{RG} + t_{22}^{RG} \right] P_{ex}^1 \\ T_{LG} = \begin{pmatrix} t_{11}^{LG} & t_{12}^{LG} \\ t_{21}^{LG} & t_{22}^{LG} \end{pmatrix}, \quad T_{RG} = \begin{pmatrix} t_{11}^{RG} & t_{12}^{RG} \\ t_{21}^{RG} & t_{22}^{RG} \end{pmatrix} \end{cases}$$

$$\begin{cases} T_{LG} = \left[T_{open} \right]^8, T_{RG} = \left[T_{open} \right]^7, & \text{for the open circuit condition} \\ T_{LG} = T_{open} \cdot \left[T_{IndSSDI} \right]^6 \cdot T_{open}, T_{RG} = T_{open} \cdot \left[T_{IndSSDI} \right]^6, & \text{for A: the independent SSDI Type-1} \\ T_{LG} = T_{open} \cdot T_{TriSSDI} \cdot T_{open}, T_{RG} = T_{open} \cdot T_{TriSSDI}, & \text{for B: the Tri-interleaved SSDI Type-1} \\ T_{LG} = T_{IndSSDI} \cdot T_{TriSSDI} \cdot T_{IndSSDI}, T_{RG} = T_{IndSSDI} \cdot T_{TriSSDI}, & \text{for C: the Tri-interleaved SSDI Type-2} \\ T_{LG} = \left[T_{IndSSDI} \right]^8, T_{RG} = \left[T_{IndSSDI} \right]^7, & \text{for D: the independent SSDI Type-2} \end{cases}$$

4.6.5 Experimental validation

The piezoelectric periodic beam sample depicted in Figure 4.22 (a) is chosen for the experimental investigation of low-frequency vibration reduction performance of the proposed structure. The corresponding parameters of the beam substructure and its PZTs with same polarization directions are listed in Table 3.1 and Table 3.2, respectively. The dimension of each minimal Bragg-type unit cell (Min Bragg Cell as shown in Figure 4.24) is depicted in Figure 4.20. Similarly, for demonstrating the low-frequency vibration damping advantage of the semi-passive nonlinear interface in smart periodic beam structures, only the first three vibration modes of the beam are considered. With regard to conventional passive piezoelectric vibration control, the value of the inherent PZT capacitance (Table 3.2) is too small to utilize small-dimension passive inductors with a large value for the linear multimodal *RL*-shunting technique for the first three modal vibration reduction. Practically, such

inductors with a large value are realized by active electronic components (*e.g.*, Operational Amplifiers). In addition, active electronic components are also unavoidable in the semi-active negative-capacitance vibration damping approaches. However, in such situation, semi-passive nonlinear SSDS / SSDI damping technique may remove the requirement of external energy supplies and further achieve broadband vibration damping performance, being even self-powered [33, 34].

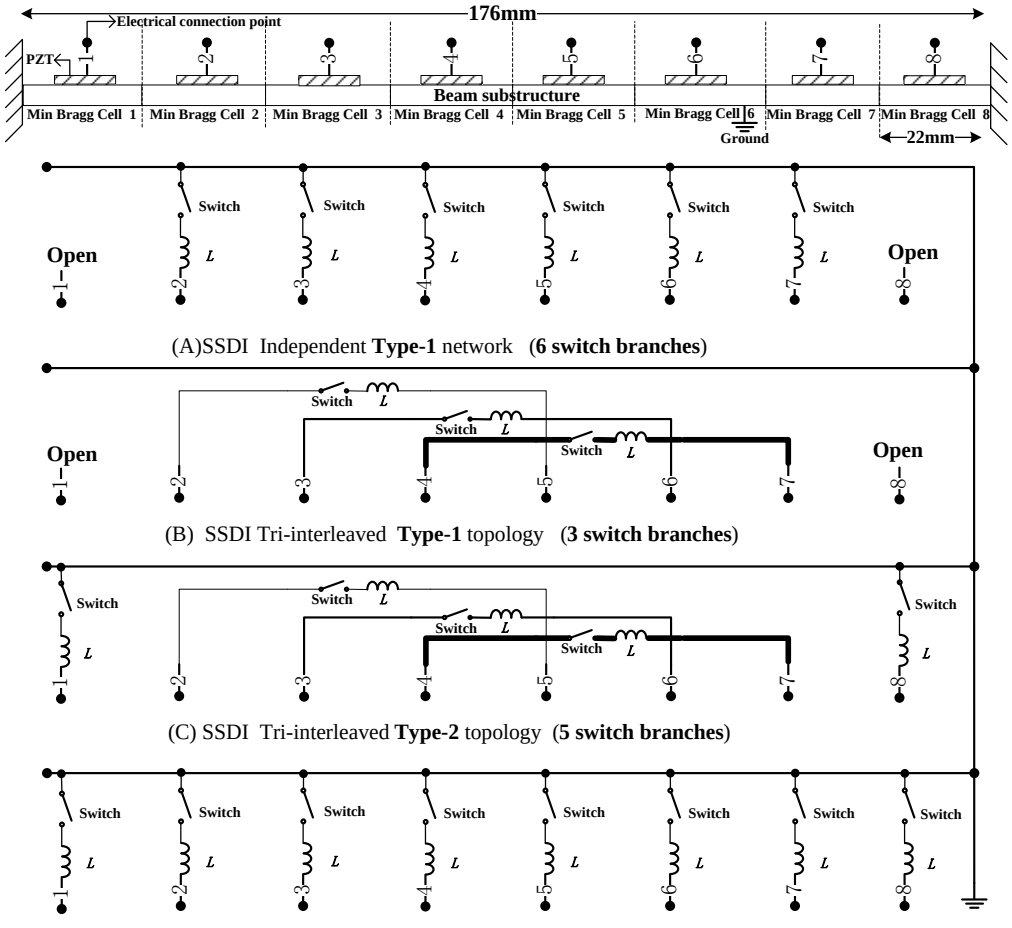

Figure 4.24 The piezoelectric periodic beam carrying different SSDI electronic networks under clamped-clamped boundary condition.

In this section, low-frequency vibration damping performance is compared experimentally and theoretically between the proposed piezoelectric periodic beam structure with SSDI Tri-interleaved electronic topologies and the piezoelectric periodic beam structure with SSDI independent electrical networks. The experimental setup is similar with that of the previous SSDI interconnected / interleaved cases. Clamped boundary conditions are also set on two sides of the investigated periodic beam. Four different electrical boundary conditions as shown in Figure 4.24 (A) - (D) are designed for the comparison of vibration damping performance between the SSDI Tri-interleaved case and the SSDI independent case.

In the experiments, an external force, generated by an electromagnet driven through an amplifier with the signal delivered by a function generator, is applied to the node between the 1st minimal Bragg-type periodic cell and the 2nd minimal Bragg-type periodic cell. A dSPACE system controlling dedicated switching circuits is used for generating switching commands. An inductive displacement sensor is for monitoring the displacement of the node between the 1st minimal Bragg-type periodic cell and the 2nd minimal Bragg-type periodic cell.

As shown in Figure 4.25, harmonic frequency response of the clamped-clamped piezoelectric periodic beam with / without different electronic networks (Figure 4.24) is investigated numerically (Figure 4.25 (a)) and experimentally (Figure 4.25 (b)), and the investigated frequency domain covers the predicted new-generated resonant-type low-frequency band gap (Figure 4.21). According to experimental measurements, the voltage coefficients in the SSDI independent electronic network and the SSDI Tri-interleaved electronic topology, and the coefficients (β_1, β_2) in the Rayleigh damping are determined as follows:

$$\begin{cases} \left[C^e\right] = \beta_1\left[M^e\right] + \beta_2\left[K^e\right] \\ \beta_1 = 67s, \beta_2 = 10^{-5}s^{-1} \\ \gamma_{ind} = 0.5, \quad \gamma_{\text{int}} = 0.6 \end{cases} \tag{4.25}$$

Figure 4.25 (a) shows the normalized theoretical displacement of the investigated periodic beam with different SSDI electronic networks. Specifically, the SSDI

Tri-interleaved Type-1 topologies with three electronic SSDI shunting branches (Figure 4.24 (B)) outperform the SSDI independent Type-1 networks with six electronic SSDI shunting branches (Figure 4.24 (A)) in all the first three vibration modes, and even have better damping performance than the SSDI independent Type-2 networks with eight electronic SSDI shunting branches (Figure 4.24 (D)) in the 2nd mode and the 3rd mode. The SSDI Tri-interleaved Type-2 topology with five electronic SSDI shunting branches (Figure 4.24 (C)) is the hybridization of one unit SSDI Tri-interleaved topology and two unit SSDI independent electrical networks. Its vibration damping effectiveness is obviously superior to that of other SSDI electronic connection in all the three modes. These numerical results are also well confirmed by the experimental results as shown in Figure 4.25 (b).

Furthermore, the attenuation performance of the SSDI Tri-interleaved Type-1 topology in the 2nd vibration mode is significantly better than that of the SSDI independent Type-1 network (7.04 dB *vs.* 4.51 dB in numerical results, 6.47 dB *vs.* 3.25 dB in experimental results), since the 2nd vibration mode is at the vicinity of the peak of the new resonant-type low-frequency band gap induced by the SSDI Tri-interleaved electronic topology (Figure 4.21). Similarly, it can be also observed that the SSDI Tri-interleaved Type-2 topology has distinctly better damping performance in the 2nd vibration mode (7.89 dB in numerical results, 7.43 dB in experimental results) than the SSDI independent Type-2 network (5.74 dB in numerical results, 4.32 dB in experimental results), owing to the damping abilities of a unit SSDI Tri-interleaved electronic topology of the SSDI Tri-interleaved Type-2 electrical topology.

Based on the above mutual validation between numerical and experimental results, it can be concluded that the irregular distribution of SSDI electronic impedance in a Tri-interleaved periodic cell may not only benefit to elastic wave attenuation and vibration damping performance, but also simplifies the nonlinear SSDI electrical networks coupled with the smart periodic beam structure through using less SSDI branches. If the unit SSDI interleaved / Tri-interleaved electronic topology is

introduced in smart periodic beam structure with SSDI independent electronic networks, original Bragg-type band gaps may be enhanced, and resonant-type low-frequency band gaps may be generated and practically targeted to the frequency domain of interest.

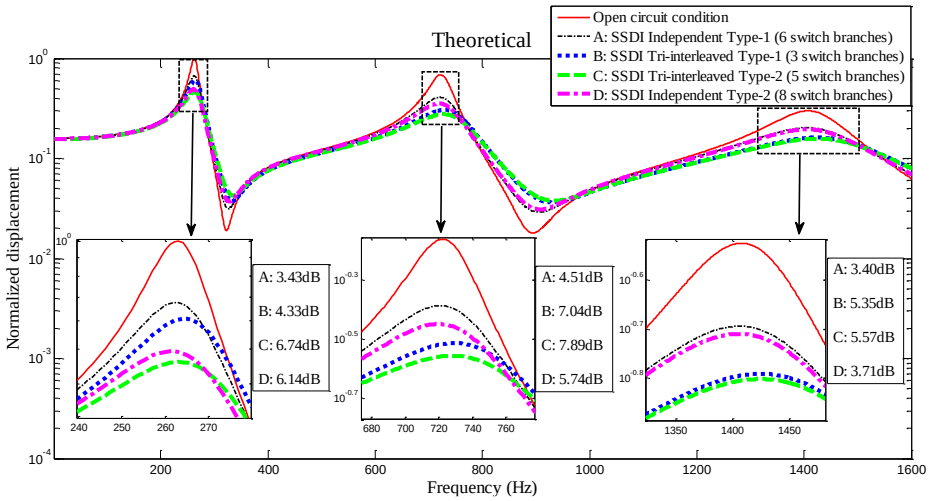

(a)

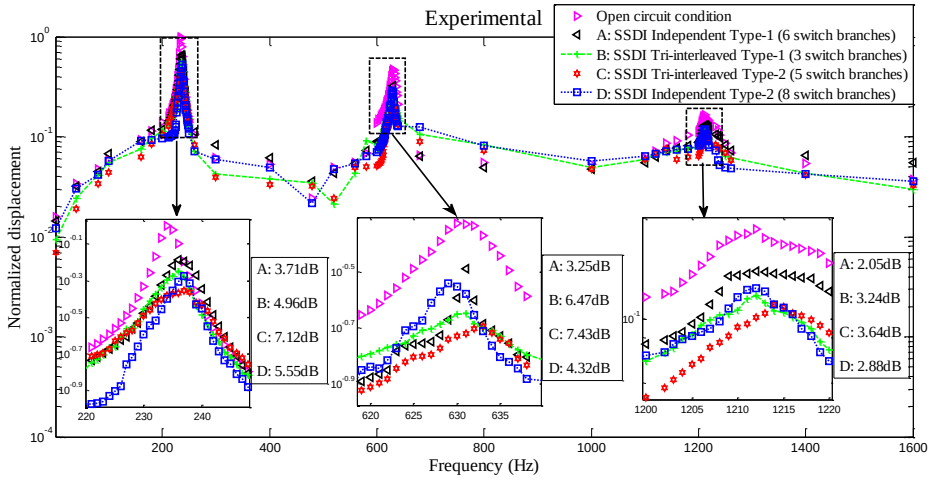

(b)

Figure 4.25 (a) Normalized theoretical displacement of the clamped-clamped beam structure with different SSDI electronic networks; (b) normalized experimental displacement of the clamped-clamped beam structure with different SSDI electronic networks.

4.7 Conclusion

Considering that the nonlinearity of the SSDI technique and the electronic irregularities of electrical networks coupled with smart periodic structure have the potential of enhancing Bragg-type band gaps and generating additional resonant-type band gaps on elastic wave propagation, two kinds of piezoelectric periodic beam structures with nonlinear SSDI interleaved / Tri-interleaved switched electrical networks are proposed and demonstrated for the resonant-type low-frequency band gap generation for low-frequency vibration reduction and the enhancement of Bragg-type band gaps.

In the proposed structures, nonlinear SSDI electrical networks in an interleaved-switching periodic cell have both unique electrical interleaved interconnection and nonlinear SSDI electrical characteristics, which results in electrical irregularities within an interleaved-switching periodic cell. Furthermore, such electrical irregularities within the interleaved-switching periodic cell, which further cause mechanical irregularities at the same time within the interleaved-switching periodic cell, are uniformly and periodically distributed in the proposed structures. Performance of the investigated structures is theoretically characterized by the methods of finite element modeling, wave propagation theory, and transfer matrix method which can be used to evaluate the occurrence of additional resonant-type band gaps and corresponding wave attenuation performance within such stop bands. Localization and transmission factors of the proposed structure have been obtained. Additionally, low-frequency vibration reduction performance of the proposed structure is also theoretically and experimentally validated and compared with the previously proposed periodic structure with SSDI independent electrical networks. Specifically, two different SSDI interleaved-switching electrical networks have been investigated:

A. PPPP / PPNN / PPNP interleaved switched electrical networks (purely resistive / linear resonant / SSDI interleaved-connection of 4 adjacent piezoelectric elements);
B. SSDI Tri-interleaved switched electrical network (SSDI interleaved-connection of 6 adjacent PZTs, the type can be named as 'PPPPPP' since all the PZTs has the same polarization direction in unit Tri-interleaved periodic cell).

Compared with smart periodic structure with SSDI independent electrical networks, the proposed structures have better elastic wave attenuation performance and vibration damping performance especially in a relatively broad low frequency range including typical structural modes of interest. In addition, in practical applications, it provides an economical way of reducing the number of electronic switches when a large number of cells are adopted in smart periodic structures.

Some conclusions can also be obtained from attenuation performance comparison between the SSDI interleaved case and the SSDI Tri-interleaved case: the SSDI interleaved case has broader resonant-type low-frequency band gaps than the SSDI Tri-interleaved case but has little beneficial effect on enhancing the primitive Bragg-type band gaps, while the SSDI Tri-interleaved case has better performance of band gap hybridization but relatively narrower resonant-type low-frequency band gaps. However, both cases show good damping performance for the first three vibration modes in the low frequency range, and the SSDI Tri-interleaved case has even better damping performance than the SSDI interleaved case since the resonant-type low-frequency band gap generated in the SSDI Tri-interleaved case is closer to the investigated frequency domain than the SSDI interleaved case.

In addition, if damping performance in some frequency ranges (especially resonant-type low-frequency band gaps and Bragg-type band gaps which are very interesting for practical applications) needs to be further enhanced in the piezoelectric periodic beam with SSDI independent networks, the independent networks of some adjacent Bragg-type periodic cells can be transformed into SSDI interleaved / Tri-interleaved electronic topologies. Therefore, such hybrid piezoelectric periodic beam structure contains two different types of SSDI periodic cells: the SSDI

independent periodic cells for the global broadband frequency ranges, and the SSDI interleaved / Tri-interleaved periodic cells for the more interesting narrowband frequency ranges.

Although the location and the bandwidth of new resonant-type band gaps induced by such nonlinear SSDI interleaved-switching electrical networks are difficult to predict due to the complexity of smart periodic structure with nonlinear electronic networks, which is similar to the SSDI independent / interconnected cases[3], the advantages and analytical methods for the proposed structures can be the base for investigating other smart periodic structures with nonlinear electronic networks, especially for smart periodic structures whose resonant-type band gap design is not confined to a unit minimal Bragg-type periodic cell analysis and also for low-frequency broadband passive vibration control.

[3] while according to the electronic resonance of the resonant shunt circuits, the locally resonant-type band gaps of smart periodic beam structure with linear resonant independent networks can be easily estimated

Chapter 5 Smart periodic structure with nonlinear interleaved-interconnected electrical networks

Abstract

In the continuity of the works exposed throughout this manuscript, a new class of smart periodic structure carrying a nonlinear multilevel interleaved-interconnected electronic network is proposed in this chapter. Its electro-elastic coupling between elastic wave (propagating through purely mechanical part of the structure) and electrical waves (propagating through the multilevel nonlinear interleaved-interconnected electronic network) is investigated, which is similar but more complex than that of the previous interconnected electronic case. Specifically, Section 5.1 introduces the overview of the proposed structure with nonlinear multilevel interleaved-interconnected electronic networks. Section 5.2 investigates the electro-elastic relationships in a k-level interleaved-interconnected periodic cell based on finite element method and basic knowledge introduced in Chapter 2. Transfer matrix formulation of the proposed smart periodic structure is obtained in Section 5.3. Section 5.4 presents theoretical results and discussions of the wave propagation properties of the investigated structure. Global relationship of the proposed structure under clamped-clamped case is given in Section 5.5. Some theoretical conclusions obtained in the low frequency range are validated experimentally through frequency response comparison in Section 5.6. Finally, Section 5.7 summarizes the conclusions of this chapter.

5.1 Overview of the proposed structure

The new piezoelectric periodic beam structure with nonlinear multilevel interleaved-interconnected electronic networks is depicted in Figure 5.1. The structure is composed of N_g primitive periodic cells. k denotes the level of the nonlinear interleaved-interconnected electronic networks of the proposed structure, which also denotes the number of primitive periodic cells composing a minimal

interleaved-interconnected periodic cell. m $(m=3,4,5...)$ is the total number of interleaved-interconnected periodic cells of the proposed structure, thus $N_g = m \cdot k$. Herein, in order to feature better wave attenuation performance for the proposed structure with SSDI interleaved-interconnected electrical networks, the minimum total number of interleaved-interconnected periodic cells is assumed to be equal to 3 since two electrical boundary conditions are required for the computation of the structural response.

In the middle of the proposed structure, the $i_{N_g}^{th}$ $\left(i_{N_g} \in \left(k,(m-1)\cdot k\right]\right)$ primitive periodic cell is interconnected to the adjacent $\left(i_{N_g} \pm k\right)^{th}$ primitive periodic cells using nonlinear SSDI shunts with estimated SSDI electronic impedance Z_{int}. Primitive periodic cells at the two extreme terminals of the beam structure $\left(i_{N_g}^{th} \in [1,k] \cup \left[(m-1)\cdot k+1, N_g\right]\right)$ are connected to the external electrical boundary conditions.

Figure 5.1 (b) shows that one interleaved-interconnected periodic cell *i* of the proposed periodic structure is composed of two electromechanical coupling sections: electrical and mechanical. The mechanical section includes several identical PZTs periodically placed throughout the elastic beam substrate. The nonlinear SSDI electrical networks composed of *k* nonlinear SSDI current branches $\left(I_1^k, I_2^k, ..., I_k^k\right)$, and the electrical and electromechanical characteristics of the PZTs contribute to the electrical section. Bragg-type band gap generation mechanism depends on the mechanical section, while resonance band gap generation mechanism is more related to the electrical section and electromechanical coupling. Herein, it should be noted that the extreme impedance value $\frac{Z}{2}$ of the interleaved-interconnected periodic cells represents $\frac{Z_{\text{int}}}{2}$ in the middle of the beam structure (Z_{int} is the impedance of the SSDI shunt between two PZTs).

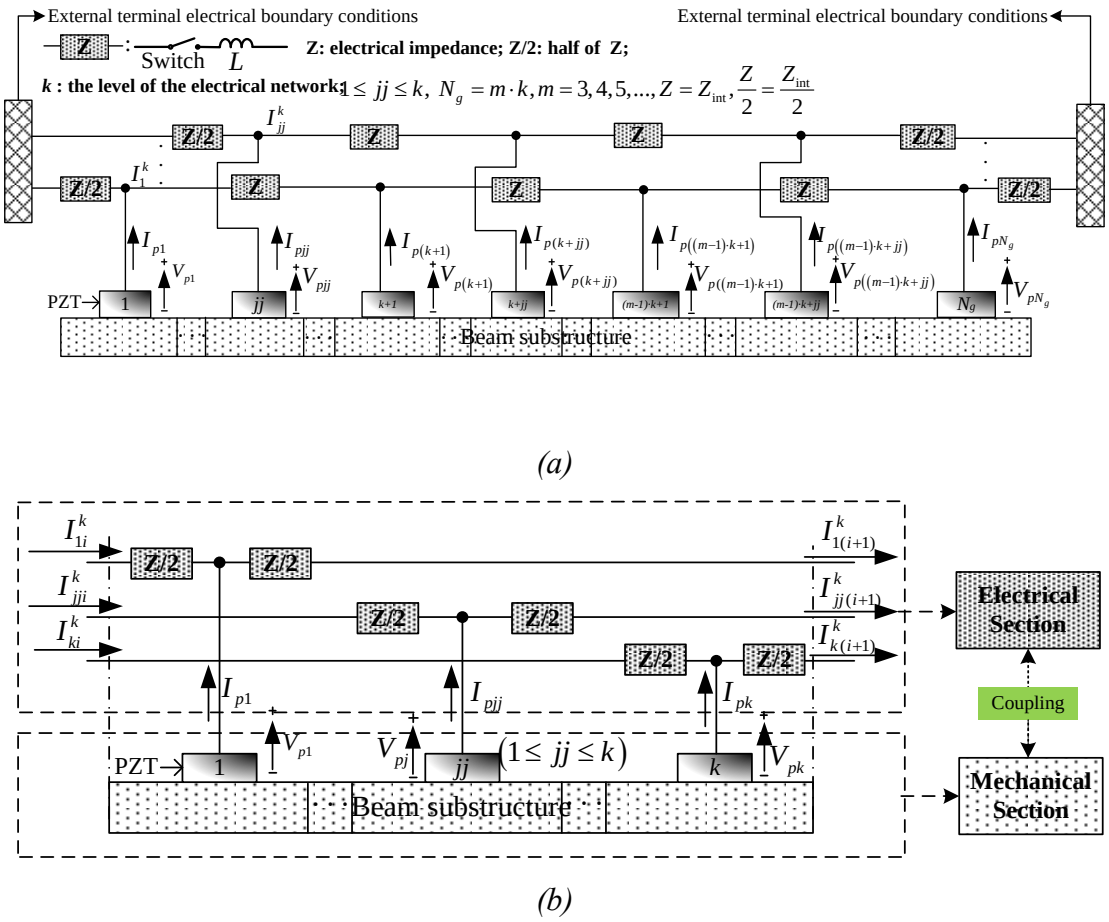

Figure 5.1 (a) Smart periodic beam structure with nonlinear *k*-level interleaved-interconnected electronic networks; (b) unit interleaved-interconnected periodic cell *i* of the structure.

In order to investigate common wave propagation characteristics of the above-mentioned electromechanical periodic structures, smart periodic structure with nonlinear *k*-level $(k = 1, 2, 3)$ interleaved-interconnected electronic networks as shown in Figure 5.2, Figure 5.3 and Figure 5.4, are investigated theoretically and experimentally. It can be noted that the 1-level structure is identical to the interconnected periodic structure investigated in Chapter 3.

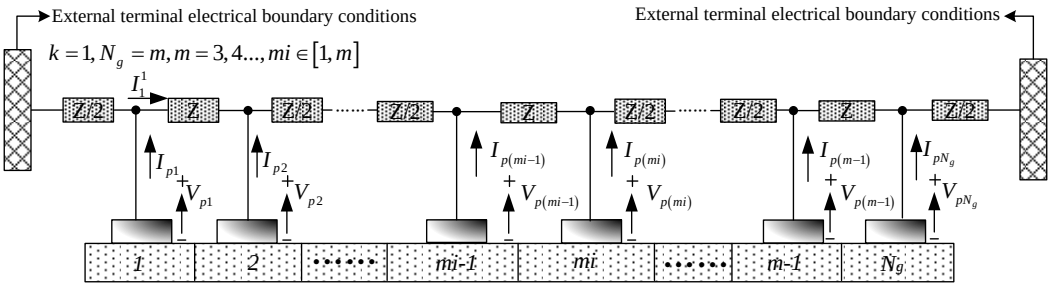

(a)

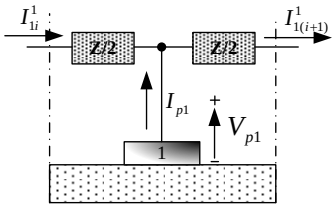

(b)

Figure 5.2 (a) Smart periodic structure with 1-level nonlinear interleaved-interconnected electronic networks; (b) one interleaved-interconnected periodic cell *i* of the structure.

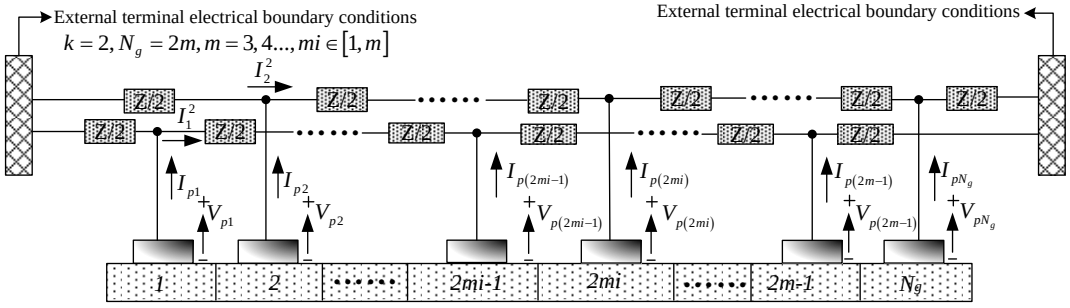

(a)

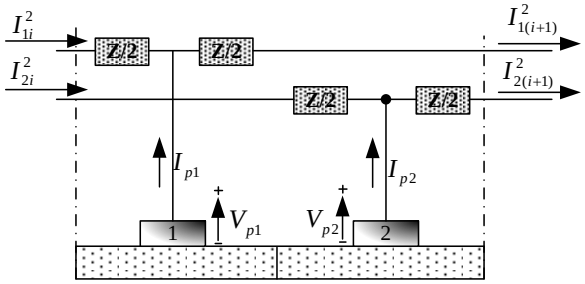

(b)

Figure 5.3 (a) Smart periodic structure with *2*-level nonlinear interleaved-interconnected electronic networks; (b) unit interleaved-interconnected periodic cell *i* of the structure.

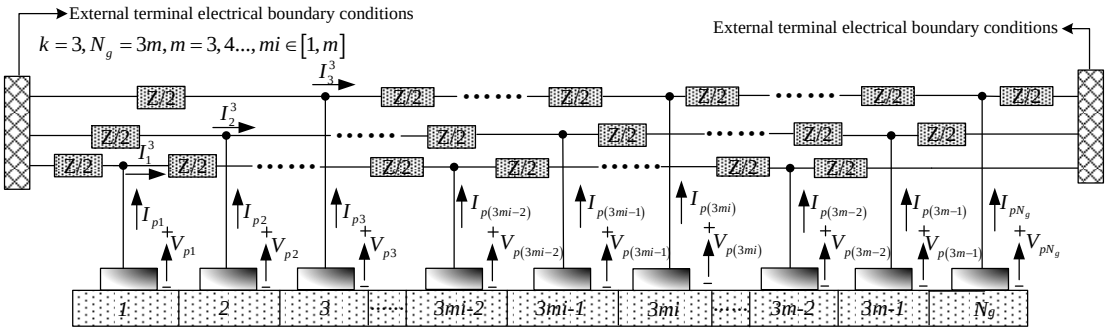

(a)

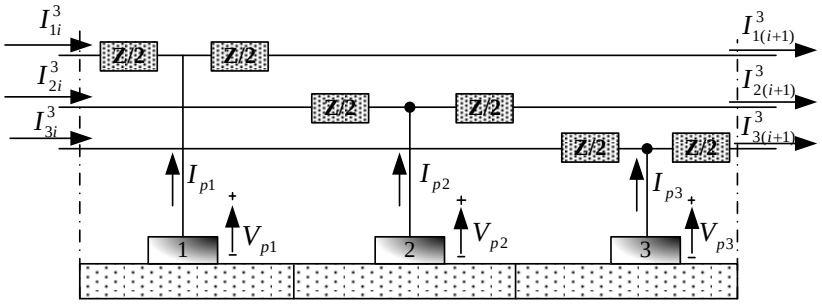

(b)

Figure 5.4 (a) Smart periodic structure with 3-level nonlinear interleaved-interconnected electronic networks; (b) unit interleaved-interconnected periodic cell *i* of the structure.

5.2 Electro-elastic relationships in an interleaved-interconnected periodic cell

Assuming that smart periodic structure follows Euler-Bernoulli beam hypotheses, and according to finite element modeling of the Euler-Bernoulli piezoelectric beam introduced in Chapter 3, if the i^{th} interleaved-interconnected periodic cell $\left(i\in[1,m]\right)$ of the proposed structure can be divided into several finite beam elements, the fundamental electromechanical relationships within unit interleaved-interconnect--ed periodic cell *i* in the frequency domain can be given by:

$$\begin{cases} \left[-\omega^2 M^e\right]\left\{d^i\right\}+\left[j\omega C^e\right]\left\{d^i\right\}+\left[K^e\right]\left\{d^i\right\}+\left[B_1^{k-level}\right]\left\{V_p^i\right\}=\left\{P^i\right\} \\ \left\{I_p^i\right\}=\left[j\omega B_2^{k-level}\right]\left\{d^i\right\}+\left[j\omega B_3^{k-level}\right]\left\{V_p^i\right\} \end{cases} \tag{5.1}$$

$$\left[M^e\right]=\int_0^l\left[H\right]^T\rho A_c\left[H\right]dx; \qquad \rho A_c=\begin{cases}\rho_b A_b, & \text{finite beam element without PZTs}\\ \rho_b A_b+\rho_p A_p, & \text{finite beam element with PZTs}\end{cases}$$

$$\left[K^e\right]=\int_0^l\left[H''\right]^T EI_s\left[H''\right]dx; \qquad EI_s=\begin{cases}E_b I_b, & \text{finite beam element without PZTs}\\ E_{eq} I_{eq}, & \text{finite beam element with PZTs}\end{cases}$$

$$\left[C^e\right]=\beta_1\left[M^e\right]+\beta_2\left[K^e\right];$$

where the matrices $\left[M^e\right],\left[C^e\right],\left[K^e\right]$ denote the mass, (Rayleigh) structural damping and short-circuit stiffness. *l* is the length of finite beam element. $\left[H\right]$ is the matrix of Hermitian shape function. $\left[H''\right]$ is the second order derivative of Hermitian shape functions. ρ is the mass density (ρ_b is the mass density of the pure beam substrate, ρ_p is the mass density of the piezoelectric materials), A_c is the cross-sectional area (A_b is the cross-sectional area of the pure beam element, A_p is the cross-sectional area of the piezoelectric material of the beam element with PZTs), E is the elastic modulus (E_b is the elastic modulus of the pure beam element, E_p is the elastic modulus of the piezoelectric material of the beam element with PZTs), and I_s is the second moment of the cross-sectional area (I_b is the second moment of the cross-sectional area of the pure beam element, I_{eq} is the second moment of the cross-sectional area of the beam element with PZTs). β_1, β_2 are the damping coefficient constants. $\left\{d^i\right\},\left\{P^i\right\}$ are $2(n+1)$ by *1* matrices respectively denoting the generalized nodal displacement vectors (displacement and slope vectors in the frequency domain) and the generalized nodal force vectors (force and moment vectors in the frequency domain). $\left\{V_p^i\right\},\left\{I_p^i\right\}$ denote the piezoelectric voltages and output currents of identical PZTs in the investigated periodic cell. The matrix size of

$\left\{V_p^i\right\},\left\{I_p^i\right\}$ is determined by the number of primitive periodic cells of the unit investigated periodic cell. Finally, ω refers to the angular frequency.

Assuming that the dynamical stiffness matrix of the mechanical section of one interleaved-interconnected periodic cell $\left[A_{mec}^e\right]$ is equal to $\left[-\omega^2 M^e\right]+\left[j\omega C^e\right]+\left[K^e\right]$, the dynamical stiffness matrix $\left[A^e\right]$ under different electrical boundary conditions is given as:

$$\left[A^e\right]=\begin{cases} A_{mec}^e, & \text{when each PZT is in short circuit condition;} \\ A_{mec}^e + A_{ele}^e, A_{ele}^e = B_1^{k-level}\cdot B_4^{k-level}, & \text{when each PZT is in open circuit condition.} \end{cases} \tag{5.2}$$

Herein, assuming that all the identical PZTs bonded on the beam substrate have positive polarization direction (sign assumed equal to 1), the value of $\left[B_1^{1-level}\right],\left[B_2^{1-level}\right],\left[B_3^{1-level}\right]$, and $\left[B_4^{1-level}\right]$ for the 1-level interleaved-interconnected periodic cell *i* (Figure 5.2), are given by:

$$\begin{cases} \left[B_1^{1-level}\right]=\left[B_1\right], & B_1 = b_1\int_0^l\left[H''\right]^T dx, b_1 = -\dfrac{d_{31}w_b}{t_p\left(s_{11}^E+s_{12}^E\right)}\displaystyle\int_{t_b}^{t_b+t_p}\left(u_3-x_c\right)dx_3 \\ \left[B_2^{1-level}\right]=\left[B_2\right], & B_2 = b_2\int_0^l\left[H''\right]dx,\ b_2 = -\dfrac{d_{31}t_p}{\left(s_{11}^E+s_{12}^E\right)} \\ \left[B_3^{1-level}\right]=\left[B_3\right], & B_3 = \dfrac{w_b L_p\left[2{d_{31}}^2-\varepsilon_{33}^T\left(s_{11}^E+s_{12}^E\right)\right]}{t_p\left(s_{11}^E+s_{12}^E\right)} \\ \left[B_4^{1-level}\right]=\left[B_4\right], & B_4 = b_4\int_0^l\left[H''\right]dx, b_4 = \dfrac{d_{31}{t_p}^2}{L_p\left[\varepsilon_{33}^T\left(s_{11}^E+s_{12}^E\right)-2d_{31}^2\right]} \end{cases} \tag{5.3}$$

Similarly, $\left[B_1^{2,3-level}\right]$, $\left[B_2^{2,3-level}\right]$, $\left[B_3^{2,3-level}\right]$ and $\left[B_4^{2,3-level}\right]$ for the 2-level or 3-level interleaved-interconnected periodic cell *i* (Figure 5.4 (b) and Figure 5.5 (b)) can be expressed as:

$$\begin{cases} \left[B_1^{2-level}\right]=\begin{bmatrix}B_1 & B_1\end{bmatrix}, \quad \left[B_2^{2-level}\right]=\begin{bmatrix}B_2\\ B_2\end{bmatrix} \\ \left[B_3^{2-level}\right]=\begin{bmatrix}B_3 & 0\\ 0 & B_3\end{bmatrix}, \quad \left[B_4^{2-level}\right]=\begin{bmatrix}B_4\\ B_4\end{bmatrix} \end{cases} \tag{5.4}$$

$$\begin{cases} \left[B_1^{3-level}\right]=\begin{bmatrix}B_1 & B_1 & B_1\end{bmatrix}, \quad \left[B_2^{3-level}\right]=\begin{bmatrix}B_2\\ B_2\\ B_2\end{bmatrix} \\ \left[B_3^{3-level}\right]=\begin{bmatrix}B_3 & 0 & 0\\ 0 & B_3 & 0\\ 0 & 0 & B_3\end{bmatrix}, \quad \left[B_4^{3-level}\right]=\begin{bmatrix}B_4\\ B_4\\ B_4\end{bmatrix} \end{cases} \tag{5.5}$$

in Eqs. (5.3) to (5.5) d_{31} is the piezoelectric charge coefficient, ε_{33}^{T} the electrical permittivity under constant stress, $s_{ij}^{E}\left(s_{11}^{E}, s_{12}^{E}\right)$ the elastic constant under constant electric field. w_b, t_b and t_p, L_p respectively refer to the width and thickness of the beam substrate, and thickness and length of a single PZT. u_3 is the displacement along the 3-axis and x_c denotes the neutral axis position. p_1, p_2, p_3 are the signs of piezoelectric constant depending on the polarization direction of the PZTs within the interleaved-interconnected periodic cell of smart periodic structure with nonlinear *k*-level interleaved-interconnected electronic networks (assumed equal to one in this study).

Figure 5.2 (b) , Figure 5.3 (b) and Figure 5.4 (b) respectively show the interleaved-interconnected periodic cell of the electromechanical PCs with 1-level, 2-level and 3-level nonlinear interleaved-interconnected electronic networks, $\left\{V_p^i\right\}$ and $\left\{I_p^i\right\}$ are the piezoelectric voltage and output current vectors of the piezoelectric element of the interleaved-interconnected periodic cell *i*. The periodic cell *i* with different interleaved-interconnected electronic networks has the following dynamical electromechanical relationships:

$$1\text{-}level:\begin{cases}\left\{I_p^i\right\}=\left[j\omega B_2^{1-level}\right]\left\{d^i\right\}+\left[j\omega B_3^{1-level}\right]\left\{V_p^i\right\}\\ \left[A_{mec}^e\right]\left\{d^i\right\}+\left[B_1^{1-level}\right]\left\{V_p^i\right\}=\left\{P^i\right\}\\ \left\{I_p^i\right\}=\left[I_{p1}^i\right],\quad \left\{V_p^i\right\}=\left[V_{p1}^i\right],\quad I_{p1}^i+I_{1i}^1=I_{1(i+1)}^1\\ V_{p1}^i-\dfrac{Z}{2}\cdot I_{1(i+1)}^1=V_{1(i+1)}^1,\quad V_{1i}^1-\dfrac{Z}{2}\cdot I_{1i}^1=V_{p1}^i\end{cases}\tag{5.6}$$

$$2\text{-}level:\begin{cases}\left\{I_p^i\right\}=\left[j\omega B_2^{2-level}\right]\left\{d^i\right\}+\left[j\omega B_3^{2-level}\right]\left\{V_p^i\right\}\\ \left[A_{mec}^e\right]\left\{d^i\right\}+\left[B_1^{2-level}\right]\left\{V_p^i\right\}=\left\{P^i\right\}\\ \left\{I_p^i\right\}=\left[I_{p1}^i\quad I_{p2}^i\right]^T,\quad \left\{V_p^i\right\}=\left[V_{p1}^i\quad V_{p2}^i\right]^T\\ V_{1i}^2-\dfrac{Z}{2}I_{1i}^2=V_{p1}^i,\quad I_{1i}^2+I_{p1}^i=I_{1(i+1)}^2\\ V_{p1}^i-\dfrac{Z}{2}I_{1(i+1)}^2=V_{1(i+1)}^2,\quad V_{2i}^2-\dfrac{Z}{2}I_{2i}^2=V_{p2}^i\\ I_{2i}^2+I_{p2}^i=I_{2(i+1)}^2,\quad V_{p2}^i-\dfrac{Z}{2}I_{2(i+1)}^2=V_{2(i+1)}^2\end{cases}\tag{5.7}$$

$$3\text{-}level:\begin{cases}\left\{I_p^i\right\}=\left[j\omega B_2^{3-level}\right]\left\{d^i\right\}+\left[j\omega B_3^{3-level}\right]\left\{V_p^i\right\}\\ \left[A_{mec}^e\right]\left\{d^i\right\}+\left[B_1^{3-level}\right]\left\{V_p^i\right\}=\left\{P^i\right\}\\ \left\{I_p^i\right\}=\left[I_{p1}^i\quad I_{p2}^i\quad I_{p3}^i\right]^T,\quad \left\{V_p^i\right\}=\left[V_{p1}^i\quad V_{p2}^i\quad V_{p3}^i\right]^T\\ V_{1i}^3-\dfrac{Z}{2}I_{1i}^3=V_{p1}^i,\quad I_{1i}^3+I_{p1}^i=I_{1(i+1)}^3\\ V_{p1}^i-\dfrac{Z}{2}I_{1(i+1)}^3=V_{1(i+1)}^3,\quad V_{2i}^3-\dfrac{Z}{2}I_{2i}^3=V_{p2}^i\\ I_{2i}^3+I_{p2}^i=I_{2(i+1)}^3,\quad V_{p2}^i-\dfrac{Z}{2}I_{2(i+1)}^3=V_{2(i+1)}^3\\ V_{3i}^3-\dfrac{Z}{2}I_{3i}^3=V_{p3}^i,\quad I_{3i}^3+I_{p3}^i=I_{3(i+1)}^3,\quad V_{p3}^i-\dfrac{Z}{2}I_{3(i+1)}^3=V_{3(i+1)}^3\end{cases}\tag{5.8}$$

Based on the above-mentioned relationships, the relationships of the mechanical variables and electrical variables at both sides of one interleaved-interconnected periodic cell *i* in different cases can be obtained as:

$$1\text{-}level:\begin{Bmatrix}P^i\\ V_{1(i+1)}^1\\ I_{1(i+1)}^1\end{Bmatrix}=\begin{bmatrix}A_{mec}^e & B_1 & -\dfrac{Z}{2}B_1\\ -j\omega\dfrac{Z}{2}B_2 & 1-j\omega\dfrac{Z}{2}B_3 & j\omega\dfrac{Z^2}{4}B_3-Z\\ j\omega B_2 & j\omega B_3 & 1-j\omega\dfrac{Z}{2}B_3\end{bmatrix}\begin{Bmatrix}d^i\\ V_{1i}^1\\ I_{1i}^1\end{Bmatrix}\tag{5.9}$$

$$2\text{-}level:\begin{Bmatrix} P^i \\ V^2_{2(i+1)} \\ I^2_{2(i+1)} \\ V^2_{1(i+1)} \\ I^2_{1(i+1)} \end{Bmatrix} = \begin{bmatrix} A^e_{mec} & B_1 & -\frac{Z}{2}B_1 & B_1 & -\frac{Z}{2}B_1 \\ -j\omega\frac{Z}{2}B_2 & 1-j\omega\frac{Z}{2}B_3 & j\omega\frac{Z^2}{4}B_3 - Z & 0 & 0 \\ j\omega B_2 & j\omega B_3 & 1-j\omega\frac{Z}{2}B_3 & 0 & 0 \\ -j\omega\frac{Z}{2}B_2 & 0 & 0 & 1-j\omega\frac{Z}{2}B_3 & j\omega\frac{Z^2}{4}B_3 - Z \\ j\omega B_2 & 0 & 0 & j\omega B_3 & 1-j\omega\frac{Z}{2}B_3 \end{bmatrix} \begin{Bmatrix} d^i \\ V^2_{2i} \\ I^2_{2i} \\ V^2_{1i} \\ I^2_{1i} \end{Bmatrix} \tag{5.10}$$

$$3\text{-}level:\begin{Bmatrix} P^i \\ V^3_{3(i+1)} \\ I^3_{3(i+1)} \\ V^3_{2(i+1)} \\ I^3_{2(i+1)} \\ V^3_{1(i+1)} \\ I^3_{1(i+1)} \end{Bmatrix} = \begin{bmatrix} A^e_{mec} & B_1 & -\frac{Z}{2}B_1 & B_1 & -\frac{Z}{2}B_1 & B_1 & -\frac{Z}{2}B_1 \\ -j\omega\frac{Z}{2}B_2 & 1-j\omega\frac{Z}{2}B_3 & j\omega\frac{Z^2}{4}B_3 - Z & 0 & 0 & 0 & 0 \\ j\omega B_2 & j\omega B_3 & 1-j\omega\frac{Z}{2}B_3 & 0 & 0 & 0 & 0 \\ -j\omega\frac{Z}{2}B_2 & 0 & 0 & 1-j\omega\frac{Z}{2}B_3 & j\omega\frac{Z^2}{4}B_3 - Z & 0 & 0 \\ j\omega B_2 & 0 & 0 & j\omega B_3 & -j\omega\frac{Z}{2}B_3 & 0 & 0 \\ -j\omega\frac{Z}{2}B_2 & 0 & 0 & 0 & 0 & 1-j\omega\frac{Z}{2}B_3 & j\omega\frac{Z^2}{4}B_3 - Z \\ j\omega B_2 & 0 & 0 & 0 & 0 & j\omega B_3 & -j\omega\frac{Z}{2}B_3 \end{bmatrix} \begin{Bmatrix} d^i \\ V^3_{3i} \\ I^3_{3i} \\ V^3_{2i} \\ I^3_{2i} \\ V^3_{1i} \\ I^3_{1i} \end{Bmatrix} \tag{5.11}$$

Therefore, the electromechanical relationships in the periodic cell i with k-level nonlinear interleaved-interconnected electronic networks can be obtained as follows:

$$k\text{-}level:\begin{Bmatrix} P^i \\ V^k_{k(i+1)} \\ I^k_{k(i+1)} \\ \cdots \\ V^k_{jj(i+1)} \\ I^k_{jj(i+1)} \\ \cdots \\ V^k_{1(i+1)} \\ I^k_{1(i+1)} \end{Bmatrix} = \begin{bmatrix} A^e_{mec} & B_1 & -\frac{Z}{2}B_1 & \cdots & B_1 & -\frac{Z}{2}B_1 & \cdots & B_1 & -\frac{Z}{2}B_1 \\ -j\omega\frac{Z}{2}B_2 & 1-j\omega\frac{Z}{2}B_3 & j\omega\frac{Z^2}{4}B_3 - Z & \cdots & 0 & 0 & \cdots & 0 & 0 \\ j\omega B_2 & j\omega B_3 & 1-j\omega\frac{Z}{2}B_3 & \cdots & 0 & 0 & \cdots & 0 & 0 \\ \cdots & \cdots & \cdots & \cdots & \cdots & \cdots & \cdots & \cdots & \cdots \\ -j\omega\frac{Z}{2}B_1 & 0 & 0 & \cdots & 1-j\omega\frac{Z}{2}B_3 & j\omega\frac{Z^2}{4}B_3 - Z & \cdots & 0 & 0 \\ j\omega B_2 & 0 & 0 & \cdots & j\omega B_3 & 1-j\omega\frac{Z}{2}B_3 & \cdots & 0 & 0 \\ \cdots & \cdots & \cdots & \cdots & \cdots & \cdots & \cdots & \cdots & \cdots \\ -j\omega\frac{Z}{2}B_1 & 0 & 0 & \cdots & 0 & 0 & \cdots & 1-j\omega\frac{Z}{2}B_3 & j\omega\frac{Z^2}{4}B_3 - Z \\ j\omega B_2 & 0 & 0 & \cdots & 0 & 0 & \cdots & j\omega B_3 & 1-j\omega\frac{Z}{2}B_3 \end{bmatrix} \begin{Bmatrix} d^i \\ V^k_{ki} \\ I^k_{ki} \\ \cdots \\ V^k_{jji} \\ I^k_{jji} \\ \cdots \\ V^k_{1i} \\ I^k_{1i} \end{Bmatrix} \tag{5.12}$$

5.3 Transfer matrix formulation of the proposed structure

In order to obtain the transfer matrix of the proposed structure with multilevel nonlinear interleaved-interconnected electrical networks, the following vectors can be assumed as:

$$\left\{P^i\right\}=\begin{Bmatrix}P_0^i\\P_J^i\\P_n^i\end{Bmatrix},\quad \left\{P_J^i\right\}=\begin{Bmatrix}P_1^i\\...\\P_{n-1}^i\end{Bmatrix},\quad \left\{d^i\right\}=\begin{Bmatrix}d_0^i\\d_J^i\\d_n^i\end{Bmatrix},\quad \left\{d_J^i\right\}=\begin{Bmatrix}d_1^i\\...\\d_{n-1}^i\end{Bmatrix},\quad \left\{U_i^k\right\}=\begin{Bmatrix}V_{ki}^k\\I_{ki}^k\\...\\V_{1i}^k\\I_{1i}^k\end{Bmatrix} \tag{5.13}$$

Furthermore, the dynamical responses for the interleaved-interconnected periodic cell *i* can be summarized as:

$$\begin{Bmatrix}P_0^i\\P_J^i\\P_n^i\\U_{i+1}^k\end{Bmatrix}=\begin{bmatrix}a_{00}&a_{0J}&a_{0n}&c_{00}\\a_{J0}&a_{JJ}&a_{Jn}&c_{J0}\\a_{n0}&a_{nJ}&a_{nn}&c_{n0}\\b_{00}&b_{0J}&b_{0n}&d_{00}\end{bmatrix}\begin{Bmatrix}d_0^i\\d_J^i\\d_n^i\\U_i^k\end{Bmatrix}=\begin{bmatrix}A_{11}&A_{12}\\A_{21}&A_{22}\end{bmatrix}\begin{Bmatrix}d_0^i\\d_J^i\\d_n^i\\U_i^k\end{Bmatrix} \tag{5.14}$$

where

$$A_{11}=\begin{bmatrix}a_{00}&a_{0J}&a_{0n}\\a_{J0}&a_{JJ}&a_{Jn}\\a_{n0}&a_{nJ}&a_{nn}\end{bmatrix}=A_{mec}^e,\quad A_{12}=\begin{bmatrix}c_{00}\\c_{J0}\\c_{n0}\end{bmatrix}=\begin{bmatrix}B_1&-\frac{Z}{2}B_1&...&B_1&-\frac{Z}{2}B_1\end{bmatrix}$$

$$A_{21}=\begin{bmatrix}b_{00}&b_{0J}&b_{0n}\end{bmatrix}=\begin{bmatrix}-j\omega\frac{Z}{2}B_2\\j\omega B_2\\...\\-j\omega\frac{Z}{2}B_2\\j\omega B_2\end{bmatrix},\quad A_{22}=\begin{bmatrix}d_{00}\end{bmatrix}=\begin{bmatrix}1-j\omega\frac{Z}{2}B_3&j\omega\frac{Z^2}{4}B_3-Z&...&0&0\\j\omega B_3&1-j\omega\frac{Z}{2}B_3&...&0&0\\...&...&...&...&...\\0&0&...&1-j\omega\frac{Z}{2}B_3&j\omega\frac{Z^2}{4}B_3-Z\\0&0&...&j\omega B_3&1-j\omega\frac{Z}{2}B_3\end{bmatrix}$$

According to Guyan's reduction, Eq.(5.14) of the terminal displacement, slope and electrical vectors can be further simplified as:

$$\begin{Bmatrix} P_0^i \\ P_n^i \\ U_{i+1}^k \end{Bmatrix} = S \begin{Bmatrix} d_0^i \\ d_n^i \\ U_i^k \end{Bmatrix}, S = A_{11} - A_{12} \cdot A_{22}^{-1} \cdot A_{21} = \begin{bmatrix} S_{11} & S_{12} & S_{13} \\ S_{21} & S_{22} & S_{23} \\ S_{31} & S_{32} & S_{33} \end{bmatrix} \tag{5.15}$$

where

$$\begin{cases} S_{11} = a_{00} - a_{0J} a_{JJ}^{-1} a_{J0}, & S_{12} = a_{0n} - a_{0J} a_{JJ}^{-1} a_{Jn}, & S_{13} = c_{00} - a_{0J} a_{JJ}^{-1} c_{J0} \\ S_{21} = a_{n0} - a_{nJ} a_{JJ}^{-1} a_{J0}, & S_{22} = a_{nn} - a_{nJ} a_{JJ}^{-1} a_{Jn}, & S_{23} = c_{n0} - a_{nJ} a_{JJ}^{-1} c_{J0} \\ S_{31} = b_{00} - b_{0J} a_{JJ}^{-1} a_{J0}, & S_{32} = b_{0n} - b_{0J} a_{JJ}^{-1} a_{Jn}, & S_{33} = d_{00} - b_{0J} a_{JJ}^{-1} c_{J0} \end{cases}$$

Thus,

$$\begin{Bmatrix} d_n^i \\ P_n^i \\ U_{i+1}^k \end{Bmatrix} = \begin{bmatrix} -S_{12}^{-1} \cdot S_{11} & S_{12}^{-1} & -S_{12}^{-1} \cdot S_{13} \\ S_{21} - S_{22} \cdot S_{12}^{-1} \cdot S_{11} & S_{22} \cdot S_{12}^{-1} & S_{23} - S_{22} \cdot S_{12}^{-1} \cdot S_{13} \\ S_{31} - S_{32} \cdot S_{12}^{-1} \cdot S_{11} & S_{32} \cdot S_{12}^{-1} & S_{33} - S_{22} \cdot S_{12}^{-1} \cdot S_{13} \end{bmatrix} \begin{Bmatrix} d_0^i \\ P_0^i \\ U_i^k \end{Bmatrix} \tag{5.16}$$

Since d^i (the displacement vectors and slope vectors) are continuous between finite beam elements in a periodic cell, and P_n^i (the force and moment exerted on the right side of the electromechanical periodic cell) are opposite to P_0^{i+1} (those exerted on the left side of the next electromechanical periodic cell), the transfer matrix T between interleaved-interconnected periodic cells can be given as:

$$\begin{Bmatrix} d_n^i \\ P_n^i \\ U_{i+1}^k \end{Bmatrix} = T \begin{Bmatrix} d_0^i \\ P_0^i \\ U_i^k \end{Bmatrix}, \quad T = \begin{bmatrix} -S_{12}^{-1} \cdot S_{11} & S_{12}^{-1} & -S_{12}^{-1} \cdot S_{13} \\ -S_{21} + S_{22} \cdot S_{12}^{-1} \cdot S_{11} & -S_{22} \cdot S_{12}^{-1} & -S_{23} + S_{22} \cdot S_{12}^{-1} \cdot S_{13} \\ S_{31} - S_{32} \cdot S_{12}^{-1} \cdot S_{11} & S_{32} \cdot S_{12}^{-1} & S_{33} - S_{22} \cdot S_{12}^{-1} \cdot S_{13} \end{bmatrix} \tag{5.17}$$

5.4 Theoretical results and discussions

Based on the experimental sample whose parameters are listed in Table 3.1 and Table 3.2, wave propagation properties of the structure with different levels of interleaved-interconnected electronic networks are investigated numerically through the FEM method in this section. As shown in Figure 5.5, the dimension of a minimal Bragg-type periodic cell is 22 mm long, the PZT centered at the minimal Bragg-type periodic cell is 10 mm long, and both of the beam substructure and the PZT has the same width (35 mm). In the following wave propagation analysis, only the positive direction is taken into account and no structural damping is considered.

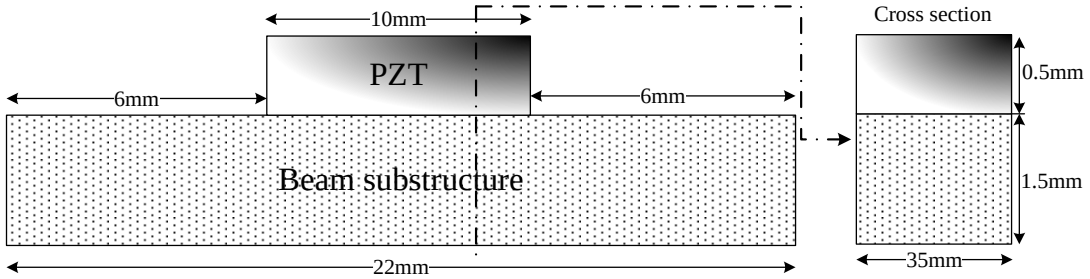

Figure 5.5 Dimension of a minimal Bragg periodic cell in the investigated metamaterial structure.

5.4.1 1-level interleaved-interconnected case

For investigating the wave propagation properties of the 1-level interleaved-interconnected case as shown in Figure 5.2, logarithmic decay and phase difference of the propagative wave in the investigated case ($\gamma_{\text{int}} = 0.6$) and open circuit condition are compared and plotted in Figure 5.6. There is a new resonant-type band gap ([1 kHz, 7 kHz]) generated within the pass band ([0 kHz, 7 kHz]). The peak of the new resonant-type band gap occurs near the 2 kHz, which is induced by electrical wave. However, the 1-level interleaved-interconnected nonlinear electrical networks weaken the original Bragg-type band gap ([7.1 kHz, 8.2 kHz]) which is corresponding to the inflexion area ($\beta = \pi$) of the phase constant of propagative wave. In addition, there is also an inflection point (2.05 kHz) in the phase constant of propagative wave corresponding to the peak of the new resonant-type band gap, but it is not obvious.

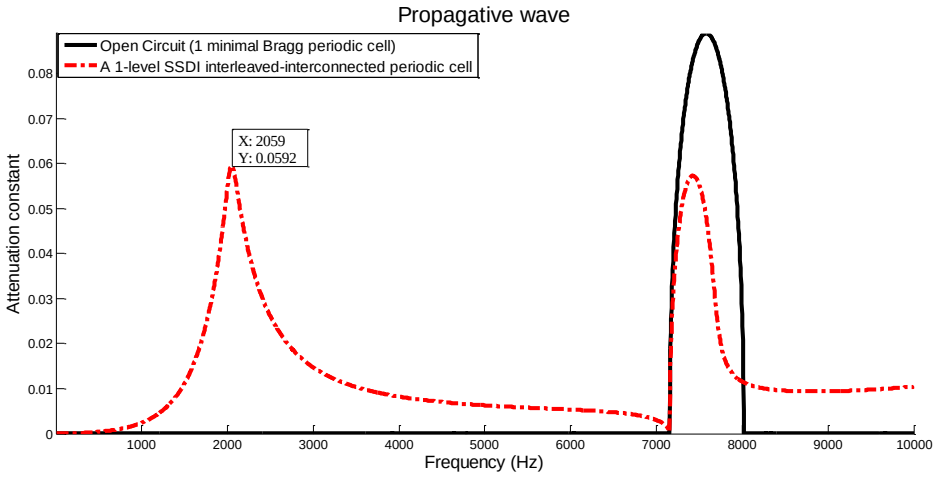

(a)

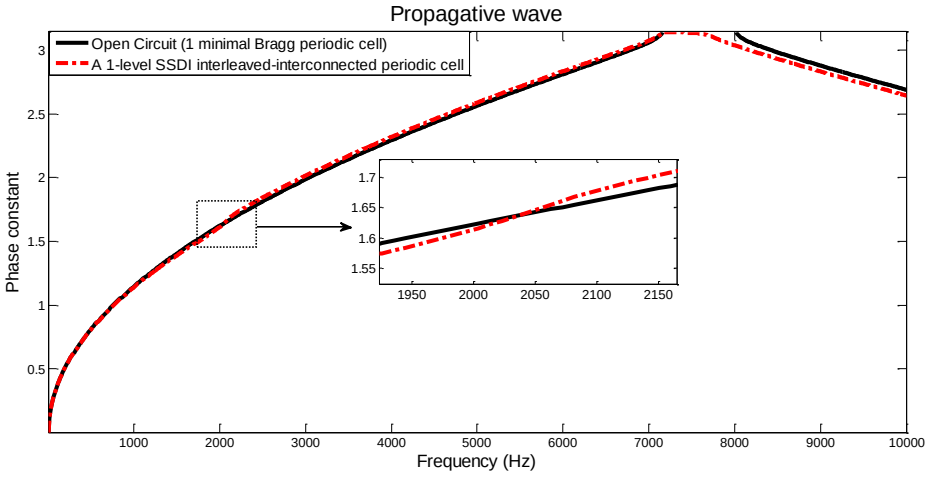

(b)

Figure 5.6 (a) Logarithmic decay of propagative wave in the 1-level nonlinear interleaved-interconnected case and open circuit condition; (b) phase difference of propagative wave in the 1-level nonlinear interleaved-interconnected case and open circuit condition.

Figure 5.7 shows evanescent wave and electrical wave in the investigated case and open circuit condition. Specifically, the attenuation constant of evanescent wave goes up with the frequency increasing, and the phase constant of evanescent wave is equal to zero within the whole investigated frequency range. It can be noted that the 2-level / 3-level nonlinear interleaved-interconnected cases have similar curves of evanescent waves with the 1-level nonlinear interleaved-interconnected case, and therefore will not be exposed in the following sections for the sake of clarity. In addition, the

inflection point (2 kHz around) of the attenuation constant of electrical wave corresponds to the peak of the new resonant-type band gap ([1 kHz, 7 kHz]), which may demonstrate wave propagation interaction between the continuous electrical medium and the continuous mechanical medium.

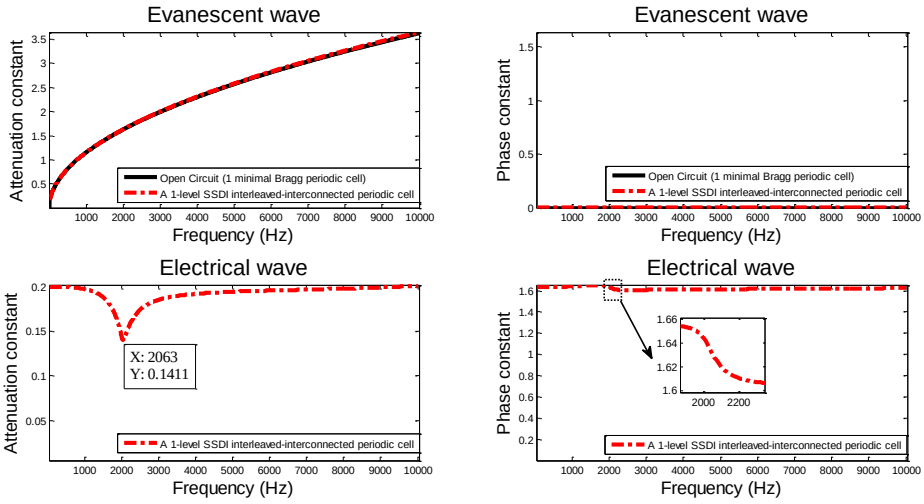

Figure 5.7 Evanescent wave and electrical wave in the investigated case and open circuit condition.

5.4.2 2-level interleaved-interconnected case

Figure 5.8 shows attenuation constant and phase constant of propagative wave in the 2-level nonlinear interleaved-interconnected case ($\gamma_{\text{int}} = 0.6$) and open circuit condition. There are two additional resonant-type band gaps in the attenuation constant of propagative wave: [200 Hz, 2 kHz] and [2 kHz, 6 kHz]. The 2-level nonlinear interleaved-interconnected case has little effect on the original Bragg-type band gap ([7.1 kHz, 8.2 kHz]) in the investigated frequency domain. Two inflexion areas ($\beta = 0$ or π) appear in the phase constant of propagative wave since wave propagated through a 2-level interleaved-interconnected periodic cell (composed of two minimal Bragg-type periodic cells) attenuates two times more compared with

propagation through one minimal Bragg-type periodic cell. One of the main inflexion area corresponds to the location of the Bragg-type band gap. There are other two inconspicuous inflection points (at 508 Hz and 4.06 kHz) in the phase constant of propagative wave corresponding to the peaks of two new resonant-type band gaps.

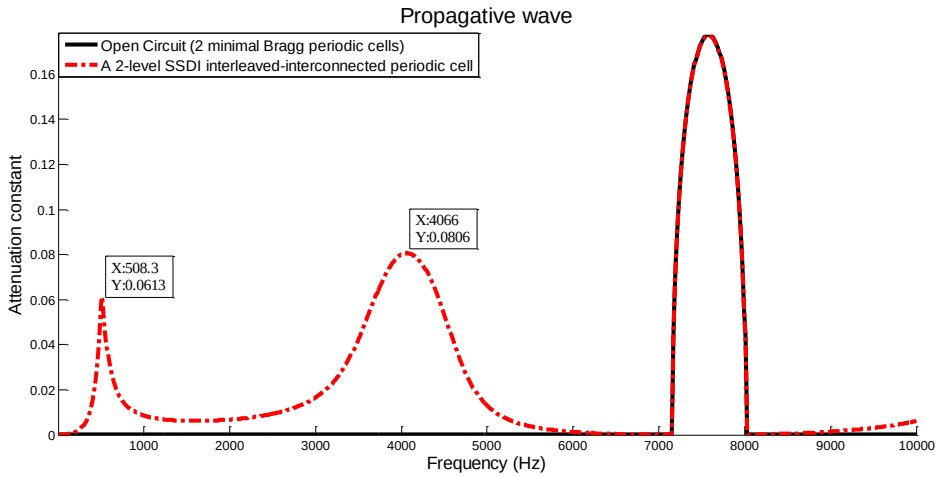

(a)

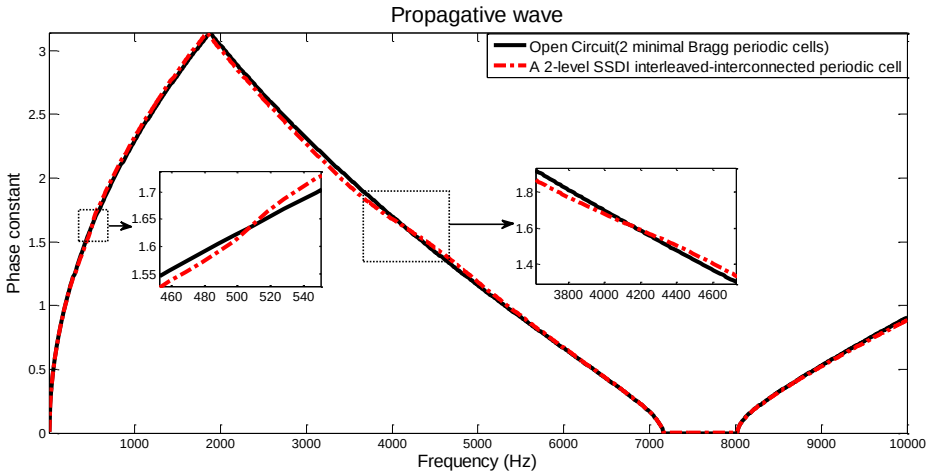

(b)

Figure 5.8 (a) Logarithmic decay of propagative wave in the 2-level nonlinear interleaved-interconnected case and open circuit condition; (b) Phase difference of propagative wave in the 2-level nonlinear interleaved-interconnected case and open circuit condition.

Two kinds of electrical waves are plotted in Figure 5.9. The peak (4.06 kHz) of attenuation constant of electrical wave 1 and the trough (508 Hz) of the attenuation constant of electrical wave 2 are respectively corresponding to the peaks (at 4.06 kHz and 508 Hz) of two new resonant-type band gaps. Therefore, two new resonant-type band gaps are likely to be induced by the peaks and troughs of attenuation constant of electrical waves.

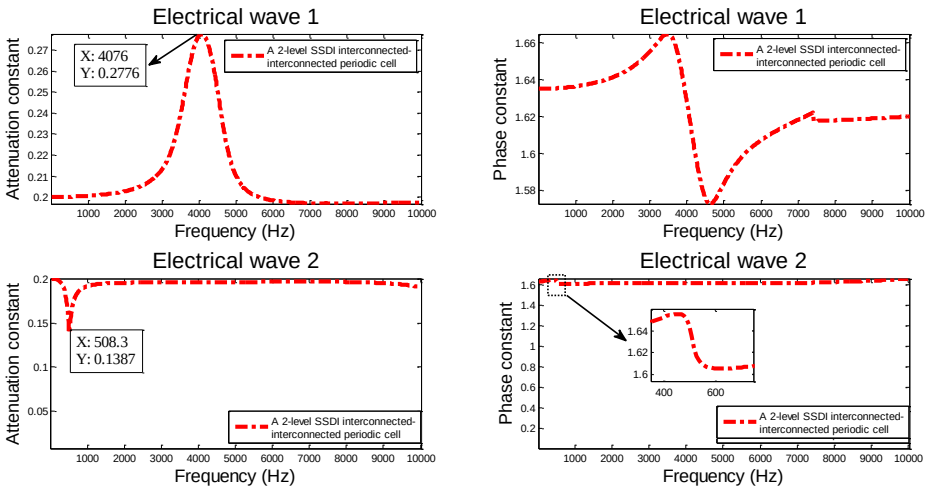

Figure 5.9 Two kinds of electrical waves in the investigated case.

5.4.3 3-level interleaved-interconnected case

Attenuation constant and phase constant of propagative wave in the 3-level interleaved-interconnected case ($\gamma_{\text{int}} = 0.6$) and open circuit condition are compared and plotted in Figure 5.10. Apart from the primitive Bragg-type band gap, three new resonant-type band gaps ([50 Hz, 700 Hz]$\cup$[700 Hz, 2.8 kHz]$\cup$[4 kHz, 7.15 kHz]) are generated and induced by three kinds of electrical waves. Similarly, there are three inflexion areas ($\beta = 0$ or π) appearing in the phase constant of propagative wave since elastic wave propagates through a 3-level interleaved-interconnected periodic cell composed of three minimal Bragg-type periodic cells, and three inflection points (224 Hz around, 1.8 kHz around and 5.3 kHz around) in the phase constant of propagative

wave are corresponding to the peaks of three new resonant-type PBGs (at 224 Hz, 1.8 kHz and 5.3 kHz). In addition, three kinds of electrical waves are plotted in Figure 5.11. The peak (1.8 kHz around) of electrical wave 1, the peak (5.3 kHz around) of electrical wave 2 and the peak (224 Hz around) of electrical wave 3 are respectively corresponding to the peaks of three new resonant-type band gaps (at 1.8 kHz, 5.3 kHz and 224 Hz).

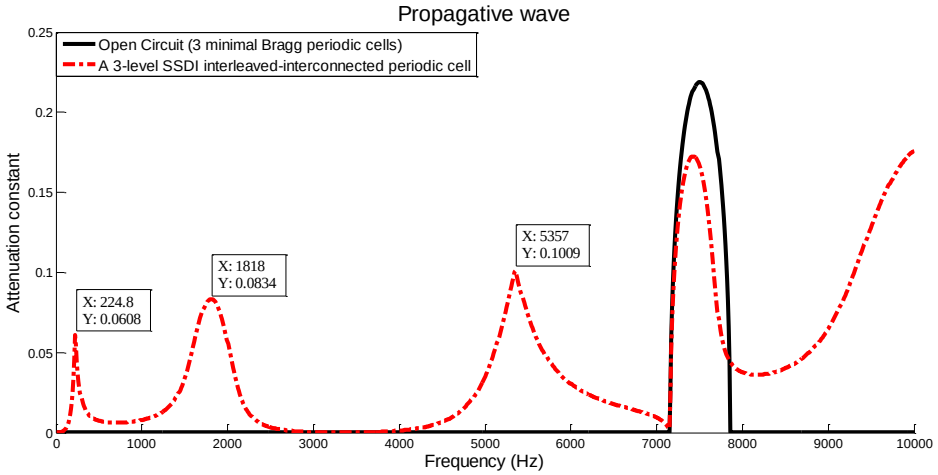

(a)

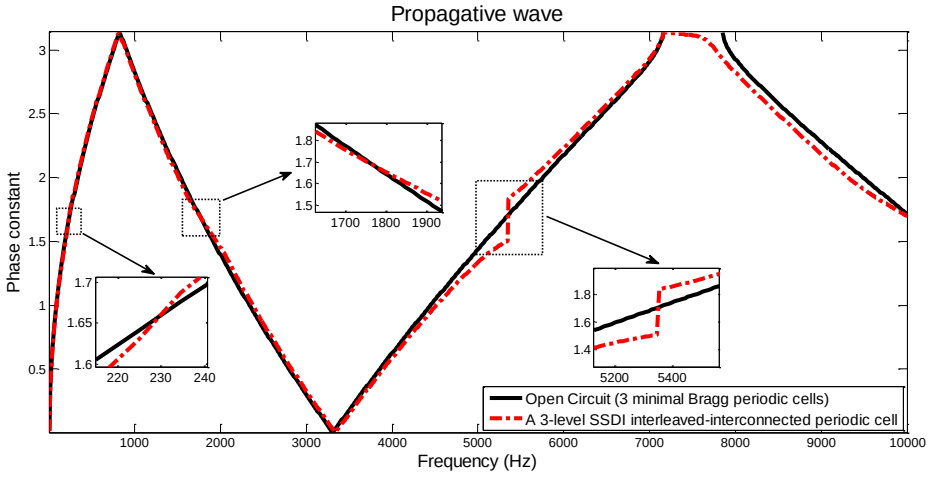

(b)

Figure 5.10 (a) Logarithmic decay of propagative wave in the 3-level nonlinear interleaved-interconnected case and open circuit condition; (b) phase difference of propagative wave in the 3-level nonlinear interleaved-interconnected case and open circuit condition.

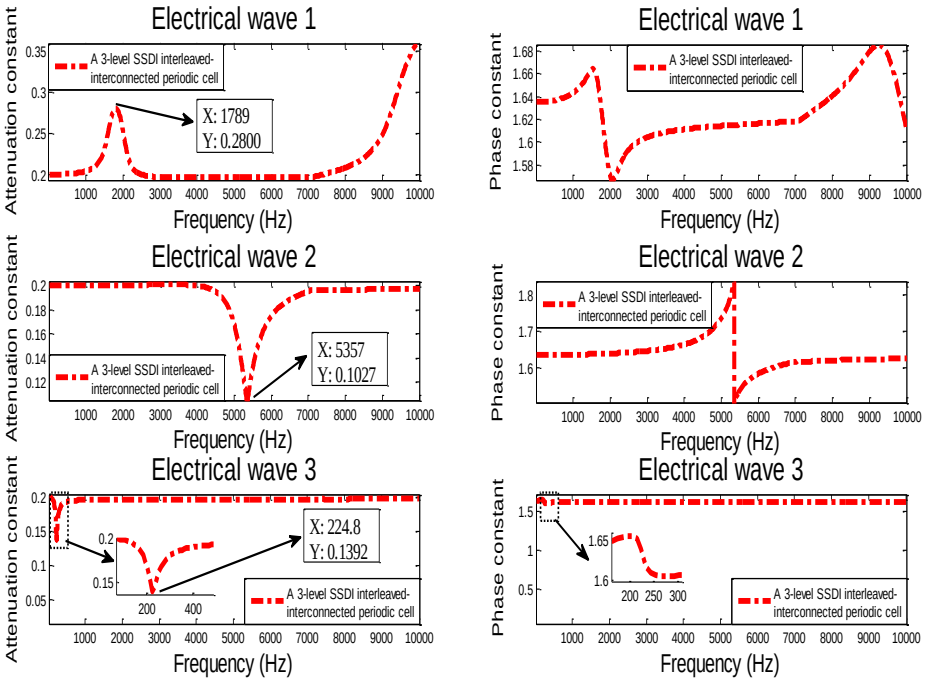

Figure 5.11 Three kinds of electrical waves in the investigated case.

As shown in Figure 5.12, localization factor ϕ introduced in section 4.6.3 is used for comparing attenuation performance among different interleaved-interconnected cases with the same inversion coefficient ($\gamma_{\text{int}} = 0.6$). It can be seen that with the increase of the level of SSDI interleaved-interconnected cases, the peak values of resonant-type band gaps induced by high level interleaved-interconnected case become lower than that of resonant-type band gaps induced by low level interleaved-interconnected case. In addition, the band width of resonant-type band gaps induced by the high level becomes relatively narrower than that of resonant-type band gaps induced by the low level.

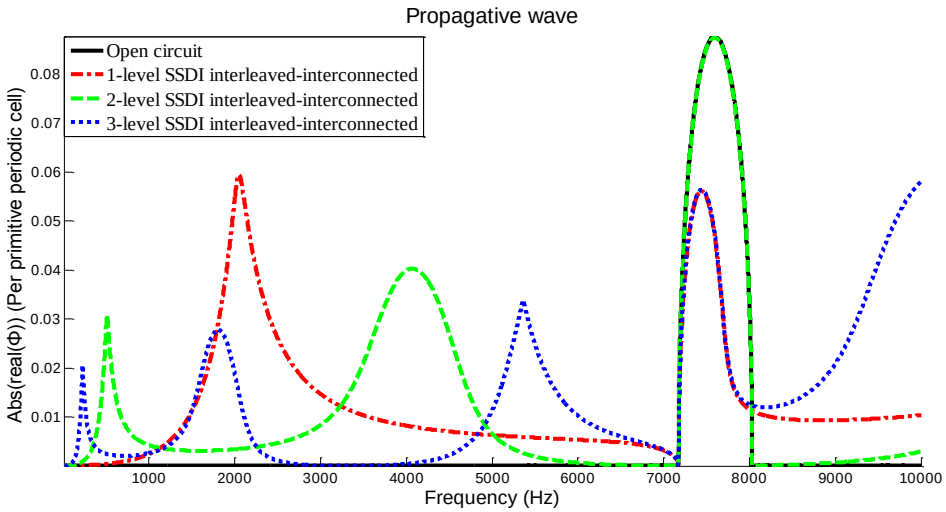

Figure 5.12 Localization factor in different SSDI interleaved-interconnected cases with the same inversion coefficient.

In order to further investigate the effect of inversion coefficient of SSDI technique on the wave propagation interaction between elastic wave and electrical wave of proposed electromechanical metamaterials, 2D plots of attenuation constant of propagative wave versus inversion coefficient with different SSDI interleaved -interconnected electrical networks are plotted in Figure 5.13. As shown in Figure 5.13, interesting frequency and inversion coefficient co-regions of the best wave attenuation performance, induced by the different nonlinear interleaved-interconnect--ed cases within the new resonant-type band gaps, appear in the following areas around:

$$\begin{cases} \text{1-level case: } (2000Hz:3000Hz, 0.4:0.8); \\ \text{2-level case: } (200Hz:400Hz, 0.4:0.8)\bigcup(3.5kHz:4.5kHz, 0.4:0.8); \\ \text{3-level case: } (50Hz:200Hz, 0.5:0.7)\bigcup(1.5kHz:2.5kHz, 0.4:0.8)\bigcup(5kHz:6kHz, 0.2:0.6) \end{cases} \quad (5.18)$$

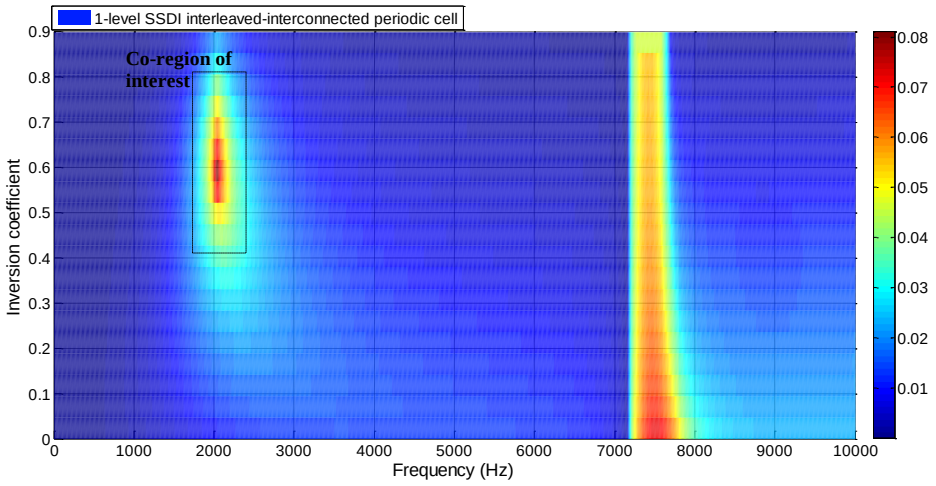

(a)

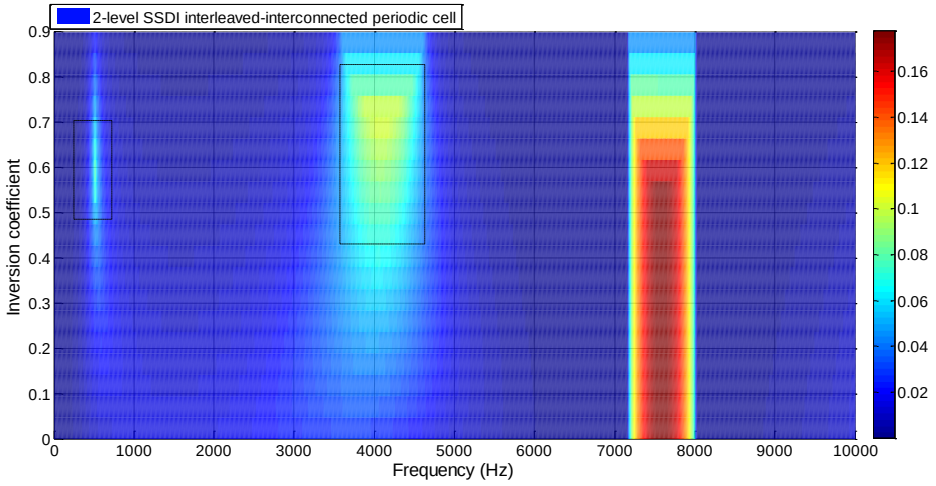

(b)

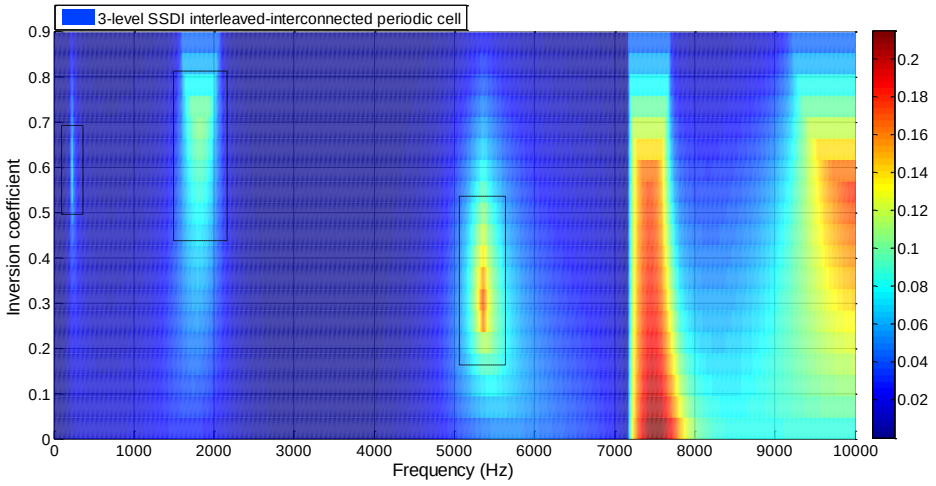

(c)

Figure 5.13 (a) 2D plot of attenuation constant of propagative wave versus inversion coefficient with SSDI interleaved-interconnected electrical networks: (a) 1-level; (b) 2-level; (c) 3-level.

With the increase of inversion coefficient, the original Bragg-type band gap in the l-level - 3-level nonlinear interleaved-interconnected cases is gradually attenuated as shown in Figure 5.13 (a)-(c). In addition, the 2-level nonlinear interleaved-interconne--cted electrical case has little effect on the original Bragg-type band gap when the value of inversion coefficient is between 0 and 0.6, but when inversion coefficient increases from the value of 0.6, the Bragg-type band gap is also gradually weakened as shown in Figure 5.13 (b).

5.5 Vibration transmittance comparison

Herein for brevity, vibration transmission factors of finite free-free periodic beam are compared only between the SSDI 1-level interleaved-interconnected case and the SSDI 2-level interleaved-interconnected case. Assuming that the two external terminal electrical are in open circuit condition, the external force is placed on one side of the investigated finite free-free beam whose amplitude of displacement is equal to D_0, and the amplitude of the other side of the beam is equal to D_8. Similar with the calculation method of transmission factor introduced in Chapter 3, transmission factor in different cases can be obtained.

Figure 5.14 (a) shows transmission factors of finite free-free periodic beam including 8 minimal Bragg-type periodic cells (as shown in Figure 5.5) in different cases. Specifically, there are 8 SSDI 1-level interleaved-interconnected periodic cells in the SSDI 1-level case, and 4 SSDI 2-level interleaved-interconnected periodic cells in the SSDI 2-level case. For the SSDI 1-level interleaved-interconnected case, transmission factor in the band gap B is damped by the first resonant-type band gap. For the SSDI 2-level interleaved-interconnected case, transmission factor in the band gap A and the band gap C is damped by the first resonant-type band gap and the second resonant-type band gap, respectively. Within the band gap D which is corresponding to the Bragg-type band gap, the SSDI 1-level interleaved-interconnected network weakens the original Bragg-type band gap, while the SSDI 2-level

interleaved-interconnected network has less effect on the original Bragg-type band gap.

Figure 5.14 (b) shows the transmission factors of finite free-free periodic beam including 10 minimal Bragg-type periodic cells in different cases. Specifically, there are 10 SSDI 1-level interleaved-interconnected periodic cells in the SSDI 1-level case, and 5 SSDI 2-level interleaved-interconnected periodic cells in the SSDI 2-level case. Compared with Figure 5.14 (a), since the number of periodic cells for calculating the transmission factor is increased and the vibration modes are also correspondingly altered, transmission factor for resonant-type band gaps induced by the SSDI interleaved-interconnected cases are further enhanced, especially in the band gap B and the band gap C.

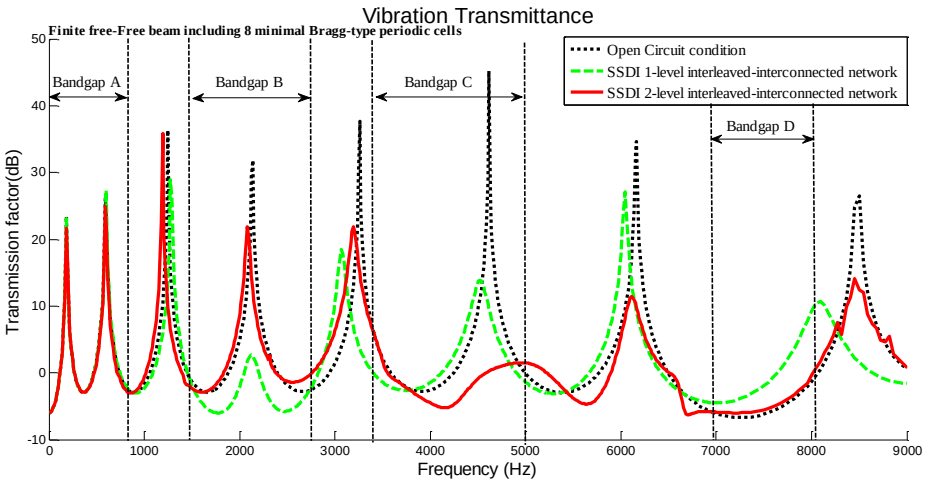

(a)

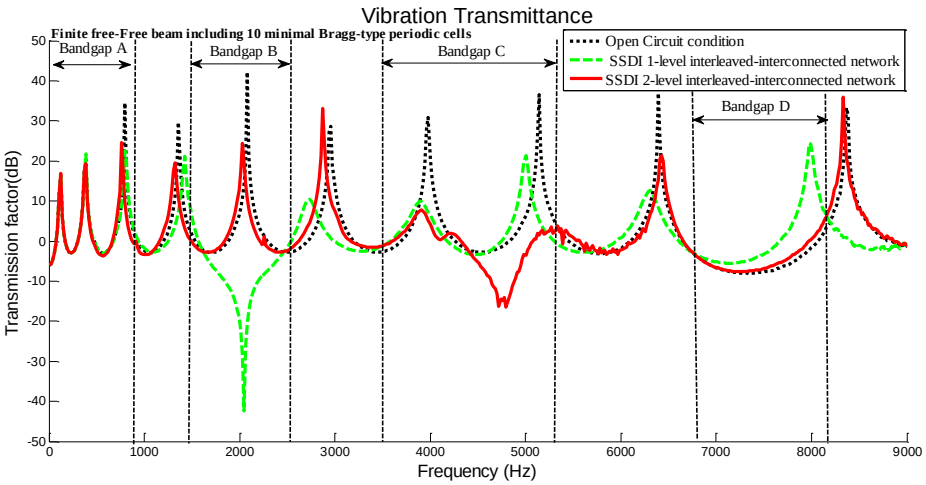

(b)

Figure 5.14 (a) Transmission factor of finite free-free periodic beam (including 8 minimal Bragg-type periodic cells) with SSDI 1-level and 2- level networks; (b) Transmission factor of finite free-free periodic beam (including 10 minimal Bragg-type periodic cells) with SSDI 1-level and 2-level networks. Band gap A, B, C and D respectively refer to the 1st resonant-type band gap in the SSDI 2-level, 1st resonant-type band gap in the SSDI 1-level, 2nd resonant-type band gap in the SSDI 2-level and 1st Bragg-type band gap in the SSDI 1-level / 2-level interleaved-interconnected cases.

5.6 Global relationship of the proposed smart periodic structure under the clamped-clamped case

In order to theoretically and experimentally investigate the damping performance of smart periodic structures with different multilevel SSDI interleaved-interconnected networks under clamped-clamped configuration, global relationship of the proposed periodic structure is firstly derived based on the transfer matrix method in this section. It is furthermore considered that the external force F is applied to the node between the nf^{th} and $(nf+1)^{th}$ primitive periodic cells, and the clamped-clamped boundary conditions enforce zero-value vectors of displacement and slope at the fixed ends. Hence, the two fixed ends exert external force and moment, respectively noted as:

$$P_0^0 = \begin{bmatrix} F^0 & M^0 \end{bmatrix}^t, \quad P_n^{N_g} = \begin{bmatrix} F^{N_g} & M^{N_g} \end{bmatrix}^t$$

where the vector P_0^0 ($resp.\ P_n^{N_g}$) denoting the force F^0 ($resp.\ F^{N_g}$) and moment M^0 ($resp.\ M^{N_g}$) applied by the clamp to the left (*resp.* right) end of the structure.

Therefore, the clamped-clamped boundary condition can be expressed as:

$$\begin{cases} d_0^0 = 0, \quad d_n^{N_g} = 0 \\ P_0^0 \neq 0, \quad P_n^{N_g} \neq 0 \end{cases} \tag{5.19}$$

where d_0^0, P_0^0 and $d_n^{N_g}$, $P_n^{N_g}$ respectively denote the generalized displacement and force vectors at the left end of the 1st periodic cell and at the right end of the N_g^{th} periodic cell.

In the k-level interleaved-interconnected case under clamped-clamped boundary condition, both electrical ends of the global structure are considered to be in open circuit condition. The currents $I_{10}^k,...,I_{k0}^k$ ($resp.\ I_{1N_g}^k,...,I_{kN_g}^k$) of the two ends are therefore equal to zero. Assuming that $V_{10}^k,...,V_{k0}^k$ ($resp.\ V_{1N_g}^k,...,V_{kN_g}^k$) are the voltages of the two ends, the following equation may be established according to the linearity of the system, considering open circuit condition for the extreme electrical nodes:

$$\begin{Bmatrix} 0 \\ P_n^{N_g} \\ U_{N_g}^k \end{Bmatrix} = [T]^{N_g} \begin{Bmatrix} 0 \\ P_0^0 \\ U_0^k \end{Bmatrix} + [T]^{(N_g - nf)} \begin{Bmatrix} 0 \\ P_{ex}^{nf} \\ 0 \end{Bmatrix} \tag{5.20}$$

The transfer matrix of an interleaved-interconnected periodic cell can be given as:

$$\begin{Bmatrix} d_n^i \\ P_n^i \\ U_{i+1}^k \end{Bmatrix} = T \begin{Bmatrix} d_0^i \\ P_0^i \\ U_i^k \end{Bmatrix}, \quad \{U_i^k\} = \begin{Bmatrix} V_{ki}^k \\ I_{ki}^k \\ \dots \\ V_{1i}^k \\ I_{1i}^k \end{Bmatrix} \tag{5.21}$$

Since it is not convenient to use above equations for obtaining the parameters of both ends, such as V_0^k ($resp.\ V_{N_g}^k$) and P_0^0 ($resp.\ P_n^{N_g}$), the transfer matrix T of a interleaved-interconnected periodic cell can be transformed into another form Tc:

$$\begin{Bmatrix} d_n^i \\ P_n^i \\ Uc_{i+1}^k \end{Bmatrix} = Tc \begin{Bmatrix} d_0^i \\ P_0^i \\ Uc_i^k \end{Bmatrix}, \quad \{Uc_i^k\} = \begin{Bmatrix} V_{ki}^k \\ \dots \\ V_{1i}^k \\ I_{ki}^k \\ \dots \\ I_{1i}^k \end{Bmatrix} \tag{5.22}$$

Thus, Eq.(5.20) can also be given as:

$$\begin{Bmatrix} 0 \\ P_n^{N_g} \\ Uc_{N_g}^k \end{Bmatrix} = [Tc]^{N_g} \begin{Bmatrix} 0 \\ P_0^0 \\ Uc_0^k \end{Bmatrix} + [Tc]^{(N_g - nf)} \begin{Bmatrix} 0 \\ P_{ex}^{nf} \\ 0 \end{Bmatrix} \tag{5.23}$$

where

$$Uc_{N_g}^k = \begin{Bmatrix} V_{kN_g}^k \\ \dots \\ V_{1N_g}^k \\ I_{kN_g}^k \\ \dots \\ I_{1N_g}^k \end{Bmatrix} = \begin{Bmatrix} V_{kN_g}^k \\ \dots \\ V_{1N_g}^k \\ 0 \\ \dots \\ 0 \end{Bmatrix} = \begin{Bmatrix} V_{N_g}^k \\ I_{N_g}^k \end{Bmatrix}, \quad \begin{cases} V_{N_g}^k = \begin{Bmatrix} V_{kN_g}^k \\ \dots \\ V_{1N_g}^k \end{Bmatrix} \\ I_{N_g}^k = \begin{Bmatrix} I_{kN_g}^k \\ \dots \\ I_{1N_g}^k \end{Bmatrix} = \begin{Bmatrix} 0 \\ \dots \\ 0 \end{Bmatrix} \end{cases}$$

$$Uc_0^k = \begin{Bmatrix} V_{k0}^k \\ \cdots \\ V_{10}^k \\ I_{k0}^k \\ \cdots \\ I_{10}^k \end{Bmatrix} = \begin{Bmatrix} V_{k0}^k \\ \cdots \\ V_{10}^k \\ 0 \\ \cdots \\ 0 \end{Bmatrix} = \begin{Bmatrix} V_0^k \\ I_0^k \end{Bmatrix}, \quad \begin{cases} V_0^k = \begin{Bmatrix} V_{k0}^k \\ \cdots \\ V_{10}^k \end{Bmatrix} \\ I_0^k = \begin{Bmatrix} I_{k0}^k \\ \cdots \\ I_{10}^k \end{Bmatrix} = \begin{Bmatrix} 0 \\ \cdots \\ 0 \end{Bmatrix} \end{cases}$$

Solving the above equations, dynamic responses based on the new form of transfer matrix under clamped-clamped condition can be obtained as:

$$V_0^k = \left(t_{42}^{\{N_g\}} \left(t_{12}^{\{N_g\}} \right)^{-1} t_{13}^{\{N_g\}} - t_{43}^{\{N_g\}} \right)^{-1} \left(t_{42}^{\{N_g - nf\}} - t_{42}^{\{N_g\}} \left(t_{12}^{\{N_g\}} \right)^{-1} t_{12}^{\{N_g - nf\}} \right) P_{ex}^{nf}$$

$$P_0^0 = \left(t_{12}^{\{N_g\}} \right)^{-1} \left(-t_{13}^{\{N_g\}} V_0^k - t_{12}^{\{N_g - nf\}} P_{ex}^{nf} \right)$$

$$V_{N_g}^k = t_{32}^{\{N_g\}} P_0^0 + t_{33}^{\{N_g\}} V_0^k + t_{32}^{\{N_g - nf\}} P_{ex}^{nf}$$

$$P_n^{N_g} = t_{22}^{\{N_g\}} P_0^0 + t_{23}^{\{N_g\}} V_0^k + t_{22}^{\{N_g - nf\}} P_{ex}^{nf}$$

$$[Tc]^{N_g} = \begin{bmatrix} t_{11}^{\{N_g\}} & t_{12}^{\{N_g\}} & t_{13}^{\{N_g\}} & t_{14}^{\{N_g\}} \\ t_{21}^{\{N_g\}} & t_{22}^{\{N_g\}} & t_{23}^{\{N_g\}} & t_{24}^{\{N_g\}} \\ t_{31}^{\{N_g\}} & t_{32}^{\{N_g\}} & t_{33}^{\{N_g\}} & t_{34}^{\{N_g\}} \\ t_{41}^{\{N_g\}} & t_{42}^{\{N_g\}} & t_{43}^{\{N_g\}} & t_{44}^{\{N_g\}} \end{bmatrix}, \quad [Tc]^{(N_g - nf)} = \begin{bmatrix} t_{11}^{\{N_g - nf\}} & t_{12}^{\{N_g - nf\}} & t_{13}^{\{N_g - nf\}} & t_{14}^{\{N_g - nf\}} \\ t_{21}^{\{N_g - nf\}} & t_{22}^{\{N_g - nf\}} & t_{23}^{\{N_g - nf\}} & t_{24}^{\{N_g - nf\}} \\ t_{31}^{\{N_g - nf\}} & t_{32}^{\{N_g - nf\}} & t_{33}^{\{N_g - nf\}} & t_{34}^{\{N_g - nf\}} \\ t_{41}^{\{N_g - nf\}} & t_{42}^{\{N_g - nf\}} & t_{43}^{\{N_g - nf\}} & t_{44}^{\{N_g - nf\}} \end{bmatrix}$$

Therefore, the generalized displacement and force vectors, voltage and current vectors at any node *i* may be obtained from:

$$\begin{Bmatrix} d_i \\ P_i \\ Uc_i^k \end{Bmatrix} = [Tc]^i \begin{Bmatrix} 0 \\ P_0^0 \\ Uc_0^k \end{Bmatrix} + [Tc]^{(i-nf)} \begin{Bmatrix} 0 \\ P_{ex}^{nf} \\ 0 \end{Bmatrix} \tag{5.24}$$

5.7 Experimental validation on low-frequency damping performance

As shown in Figure 5.15(a), the piezoelectric periodic beam sample under the clamped-clamped boundary condition is chosen for experimentally validating the damping performance of the proposed structure in the low frequency domain. The

parameters of the beam substructure and the bonded identical PZTs with same polarization directions are same as the parameters used in the theoretical sections. Considering the deficiency in the number of minimal Bragg-type periodic cells in the investigated beam sample for validating the damping performance of the SSDI 3-level interleaved-interconnected case, damping performance is only compared between the SSDI 1-level case and the SSDI 2-level case in this section.

Assuming that the external force is applied to the 3rd node; the displacement of the 7th node is used for frequency response calculation, both theoretical and experimental frequency responses to the beam sample under different electrical boundary conditions (Figure 5.15 (a), (b), (c) and (d)) are obtained as shown in Figure 5.16. It can be seen that the SSDI 2-level interleaved-interconnected case has better damping performance in the first two modes compared with the SSDI 1-level interleaved -interconnected case (theoretical: 5.35 dB *vs.* 0.45 dB for the 1st mode, 2.92 dB *vs.* 1.05 dB for the 2nd mode; experimental: 5.64 dB *vs.* 1.13 dB for the 1st mode, 3.03 dB *vs.* 2.04 dB for the 2nd mode) since the first two modes are closer to the first resonant-type band gap induced by the SSDI 2-level interleaved-interconnected electrical network than that of the SSDI 1-level case. While in the 3rd mode, the SSDI 1-level interleaved-interconnected case outperforms the SSDI 2-level interleaved-interconnected case (theoretical: 3.12 dB *vs.* 0.68 dB; experimental: 2.96 dB *vs.*1.06 dB) since the 3rd mode is at the vicinity of the first resonant-type band gap induced by the SSDI 1-level interleaved-interconnected electrical network in the investigated frequency domain.

In addition, compared with the SSDI independent case (theoretical: 5.19 dB in the 1st mode, 4.86 dB in the 2nd mode, 2.89 dB in the 3rd mode; experimental: 5.31 dB in the 1st mode, 3.80 dB in the 2nd mode, 2.60 dB in the 3rd mode), the 2-level SSDI interleaved-interconnected case shows slightly better damping performance in the 1st mode, but exhibits inferior damping efficiency in the 2nd mode and the 3rd mode. Same with the theoretical and experimental results obtained in Chapter 3 for the SSDI interconnected case (*i.e.*, the SSDI 1-level interleaved-interconnected case), the

1-level interleaved-interconnected case also shows better damping performance in the 3rd mode, but is worse in the 1st and the 2nd modes than the SSDI independent case.

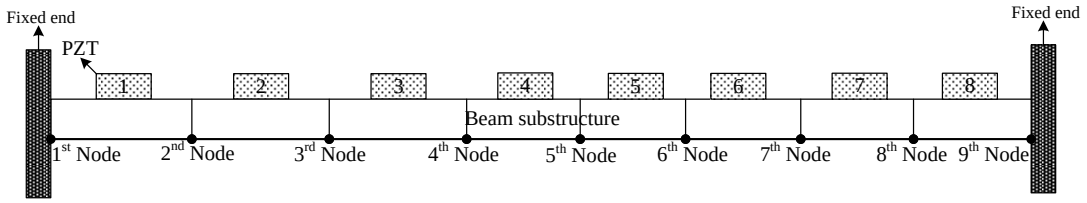

(a)

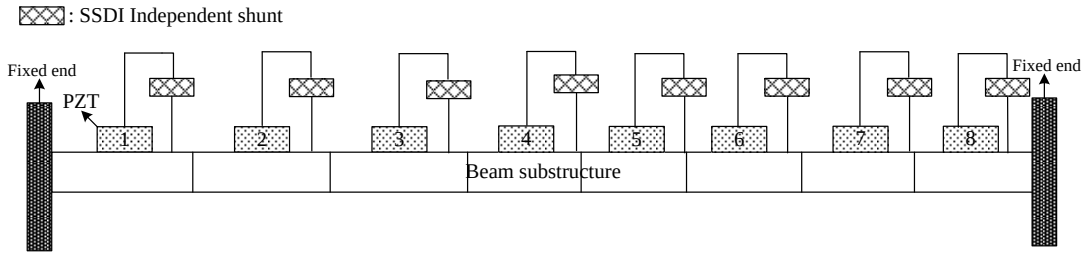

(b)

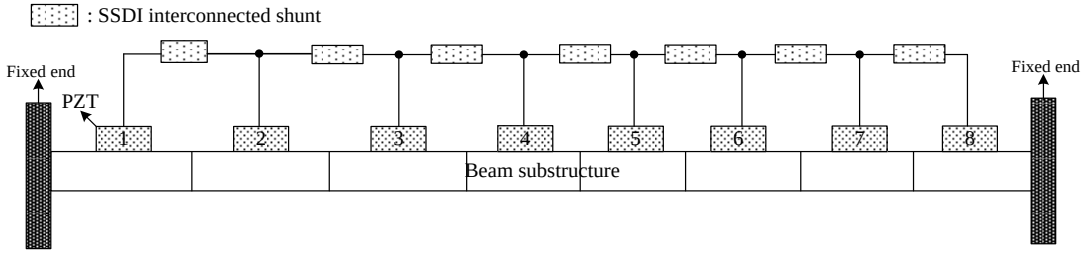

(c)

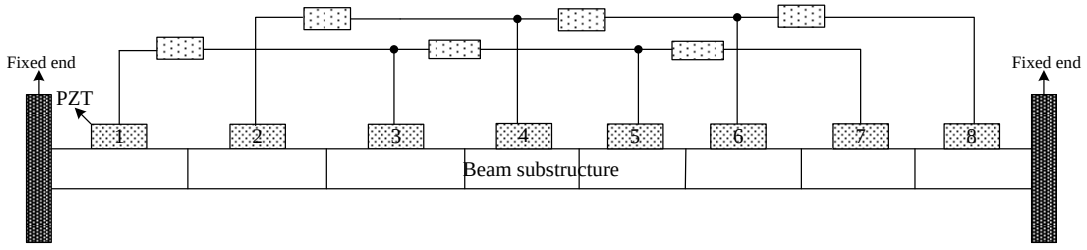

(d)

Figure 5.15 Clamped-clamped piezoelectric periodic beam (a) in open circuit condition; (b) with SSDI independent electrical networks; (c) with SSDI 1-level interleaved-interconnected electrical networks; (d) with SSDI 2-level interleaved -interconnected electrical networks.

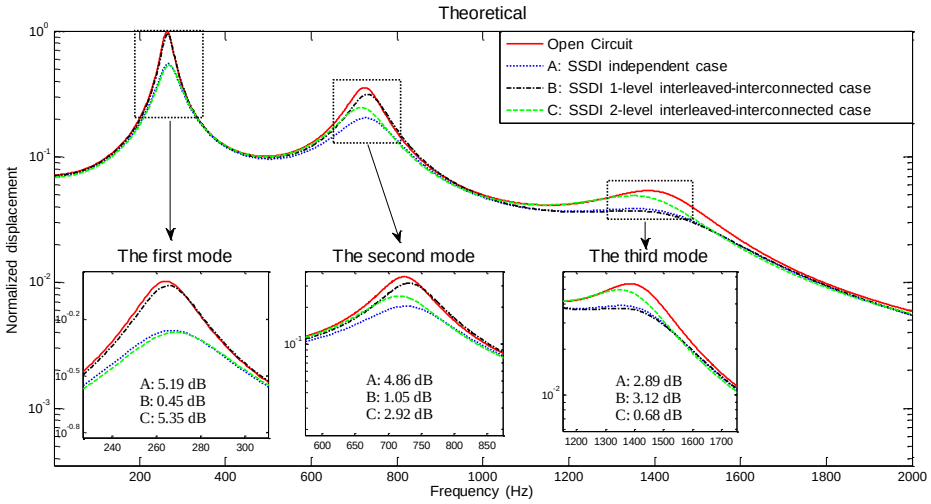

(a)

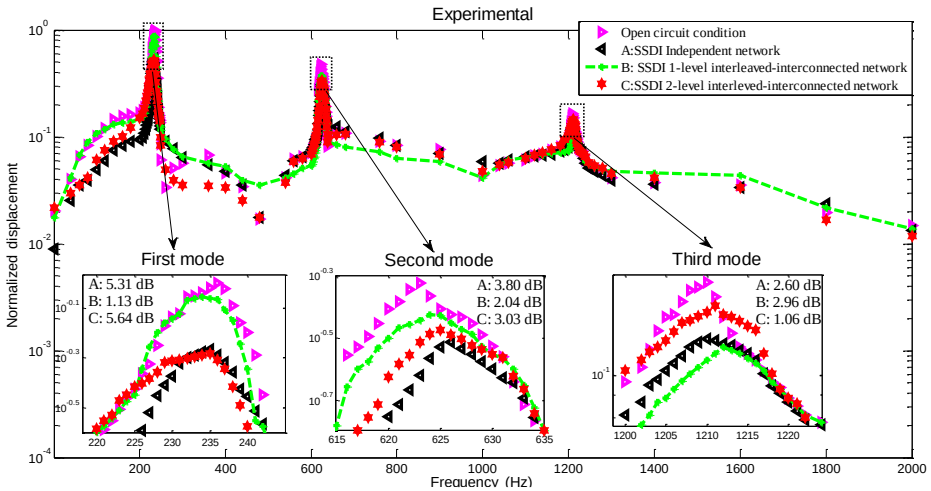

(b)

Figure 5.16 (a) Normalized theoretical displacement and (b) normalized experimental displacement of the clamped-clamped piezoelectric periodic beam with different SSDI interconnected electrical networks versus open circuit condition and SSDI independent electrical networks.

5.8 Conclusions

Smart periodic structures with nonlinear interleaved-interconnected electrical networks are investigated in this chapter. Based on finite element modeling, wave propagation theory, transfer matrix method and transmission factor analysis, wave attenuation performance and vibration damping performance of the structure were demonstrated in detail.

Different from the previous smart periodic structure with nonlinear interconnected electrical networks introduced in Chapter 3, the proposed structure has the feature of generating more than one resonant-type band gaps within each original pass band region thanks to the use of nonlinear multilevel interleaved-interconnected electrical networks. Especially, smart periodic structure with nonlinear interconnected electrical networks can be considered as smart periodic structure with 1-level interleaved-interc--onnected electrical networks. In addition, compared with smart periodic structure with nonlinear SSDI independent electrical networks which shows globally broadband wave attenuation performance, the proposed structure can achieve several discrete locally resonant-type band gaps, which increases wave attenuation control flexibility of smart periodic structure carrying nonlinear SSDI electrical networks for some particular practical applications. Furthermore, the locations of new resonant-type band gaps induced by multilevel interleaved-interconnected electrical networks can be altered by using the SSDI Hybrid Capacitance-Shunting interconnected electrical techniques introduced in Chapter 3.

In summary, compared with the traditional resonant-type band gap generation methodology using multimode damping techniques, this chapter proposed a new way of using nonlinear multilevel interleaved-interconnected electrical networks to induce more resonant-type band gaps in the investigated frequency domain. Especially, in the low frequency range, it is likely to generate several resonant-type band gaps without requiring large inductance for vibration reduction.

Chapter 6 Conclusions and future works

6.1 Conclusions

Overall, the thesis proposed different kinds of smart periodic structures with nonlinear electrical networks for achieving distributed, broadband vibration control devices, especially for the low frequency vibration control. Specifically, the originality of the work exposed here lies in the use of electromechanical periodic structures with nonlinear electronic interfaces that were implemented between piezoelectric elements, therefore adding another degree of freedom through the nonlinear energy exchange between transducers.

To do so, the first chapter presented the research background of the thesis. With the gradual introduction from the general concepts of vibration control systems to the specific concept of vibration damping techniques featuring piezoelectric periodic systems, the research value and significance of the thesis has been gradually set up. From this analysis, the feature of nonlinear SSDI electrical shunts and the unique characteristics of periodic structures emerged, allowing the development of new smart periodic structure with different nonlinear SSDI electrical networks that exhibit better wave attenuation and vibration damping performance, as outlined in Figure 6.1.

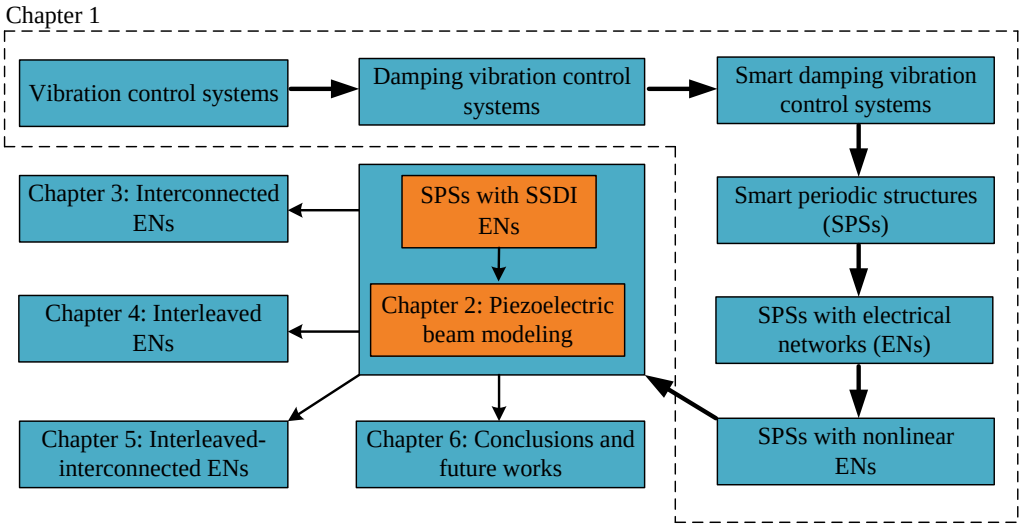

Figure 6.1 Summary of the thesis

For the theoretical modeling of the proposed technique and the theoretical evaluation of their performance, the Chapter 2 (Figure 6.2) aimed at exposing and developing finite element (FE) modeling methods for piezoelectric beam structures with passive / semi-passive electrical networks (PENs / SPENs). After a literature review on this particular topic which can be categorized into two types: impedance-based FE modeling and voltage-based FE modeling, a new voltage-based FE modeling method based on the Timoshenko beam theory is proposed for the mechanical and electrical domains featuring electromechanical connection. It has been shown that this approach has no effect on the electrical domain equations but ameliorates the mechanical domain analysis compared with voltage-based FE modeling based on the Euler-Bernoulli beam theory.

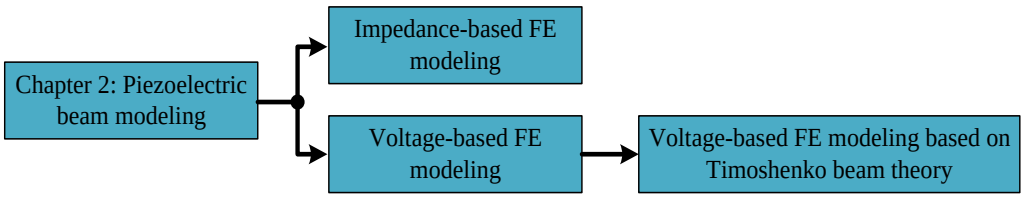

Figure 6.2 Summary of Chapter 2

Chapter 3 (Figure 6.3) is the first chapter to propose a particular nonlinear interfaced smart materials in periodic structures for vibration control. The chapter therefore studies smart periodic structures with nonlinear SSDI interconnected electrical networks based on voltage-based FE modeling, including PP interconnected electrical networks and PN interconnected electrical networks. For analyzing the electromechanical relationships of the proposed periodic cell, the SSDI independent/interconnected shunt is estimated with first harmonic approximation, allowing for demonstrating automatic impedance adaptation permitted by SSDI shunt. In addition, large inductance utilization can be avoided for the low frequency vibration reduction.

Compared with SSDI independent electrical networks attenuating the propagative waves over a broad frequency band, SSDI interconnected electrical networks are more effective in some specific frequency domains. Furthermore, SSDI PN interconnected electrical network is more likely to show better attenuation performance than SSDI PP interconnected electrical network in the low frequency range.

In addition, two extension works, smart periodic structure with SSDI Hybrid Capacitance-Shunting interconnected electrical networks and smart periodic structure with SSDI Dual-connected electrical networks, are proposed. Specifically, the additional capacitance in the SSDI HC-Shunting interconnected electrical networks can flexibly change the location of the new generated resonant-type band gap to frequency ranges of interest compared with smart periodic structure with SSDI interconnected electrical networks. Compared with SSDI independent electrical networks in the investigated frequency domain, SSDI PP Dual-connected electrical network is capable to use less SSDI switching devices yet obtain better wave attenuation performance near the Bragg-type band gaps, while SSDI PN Dual-connected electrical configuration exhibits better attenuation performance in the low frequency range.

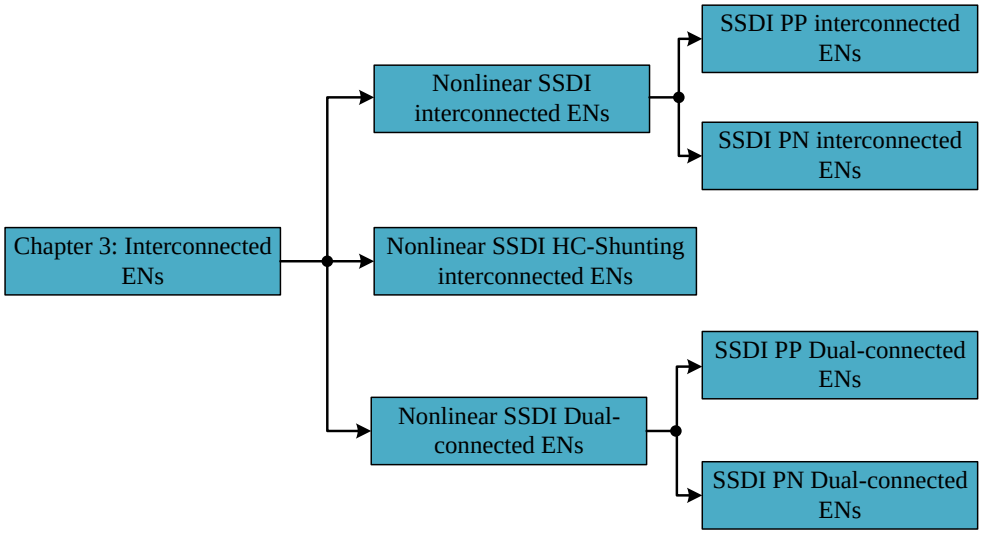

Figure 6.3 Summary of Chapter 3

Chapter 4 (Figure 6.4) proposed another way for electrically linking piezoelectric patches. More specificaaly, two kinds of piezoelectric periodic beam structures with nonlinear SSDI interleaved / Tri-interleaved switched electrical networks are proposed. Nonlinear SSDI interleaved / Tri-interleaved electrical networks, having both unique electrical interleaved interconnection and nonlinear SSDI electrical features, allow inducing electrical irregularities and further cause mechanical irregularities at the same time within an investigated periodic cell. Based on the methods of finite element modeling, wave propagation theory and transfer matrix method, wave attenuation performance and vibration damping performance of proposed structures were investigated.

Compared with SSDI independent electrical networks, the proposed electrical networks have better wave attenuation and damping performance especially in a relatively broad low frequency range. In addition, for the performance comparison between the SSDI interleaved electrical network (PPPP) and the SSDI Tri-interleaved electrical network (PPPPPP) in the investigated frequency domain, the SSDI interleaved electrical network has broader resonant-type low-frequency band gaps performance but has little beneficial effect on enhancing the primitive Bragg-type band gaps, while the SSDI Tri-interleaved electrical network has better performance

thanks to band gap hybridization but relatively narrower resonant-type low-frequency band gaps.

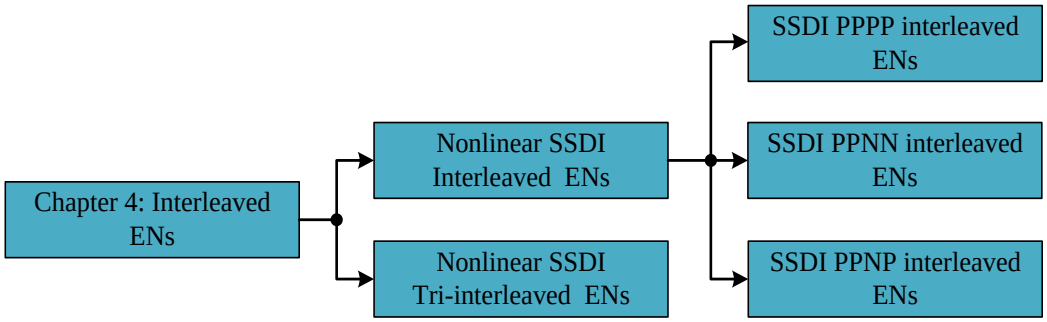

Figure 6.4 Summary of Chapter 4

Finally, Chapter 5 (Figure 6.5) proposed a new class of smart periodic structures taking advantages of the previously exposed interconnected and interleaved configurations, yielding nonlinear multilevel interleaved-interconnected electrical networks. Such unique configuration allows inducing more resonant-type band gaps in the primitive pass bands of purely mechanical periodic structures, which is different from resonant-type band gap generation mechanism relying on multi-modal resonant circuit design for smart periodic structures with independent electronic shunting networks.

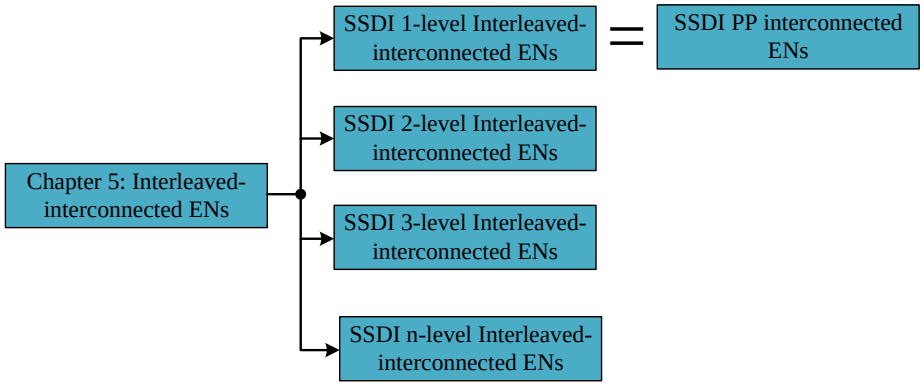

Figure 6.5 Summary of Chapter 5

6.2 Future works

Future works will include the following research directions (Figure 6.6):

a) Analysis of the underlying physical mechanisms of the proposed different electronic configurations, including detailed physical internal energy flow or mode shapes within the investigated periodic cell, should be further theoretically investigated in consideration of electronic nonlinearity and mechanical aperiodicity.

b) Other nonlinear SSD techniques, such as SSDV / adaptive SSDV and BSD techniques can be adopted into electrical domain design for smart periodic structures with semi-active electrical networks.

c) New electrical networks should be investigated for obtaining better resonant-type band gaps or achieving more kinds of wave attenuation properties for different practical applications.

d) Smart periodic structures with nonlinear electronic techniques can be extended to acoustic control.

e) The proposed nonlinear electronic networks can be used to more complex periodic structures such as plates.

f) Traditional damping techniques, such as viscoelastic damping, or Tuned Mass Dampers, can be utilized together with nonlinear electronic networks for designing smart periodic structures.

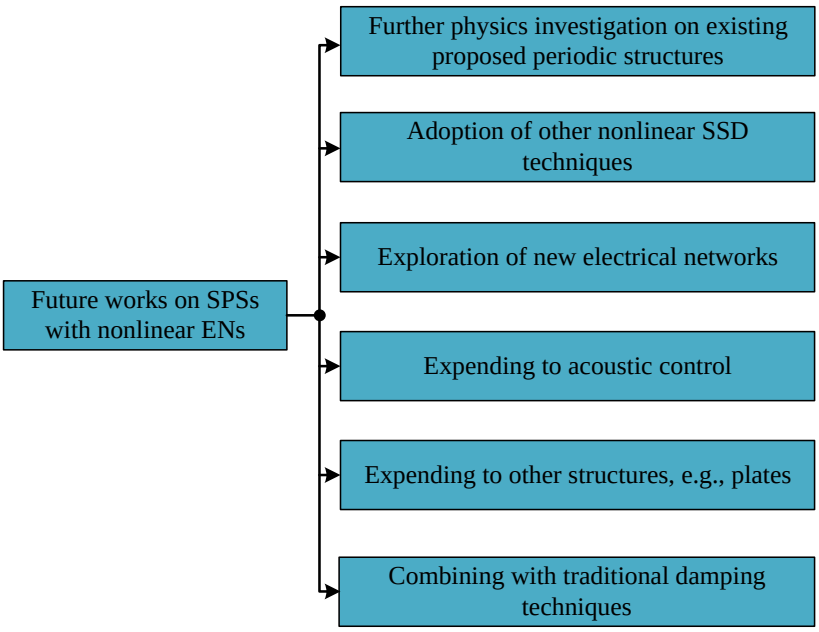

Figure 6.6 Future works

List of Figures

List of Tables

Appendix A: Shape Functions for Two Node Timoshenko Beam Finite Element Model

$$\left[N_u(x)\right]^T = \begin{bmatrix} \frac{1}{(1+\phi)}\left\{2\left(\frac{x}{L}\right)^3 - 3\left(\frac{x}{L}\right)^2 - \phi\left(\frac{x}{L}\right) + (1+\phi)\right\} \\ \frac{L}{(1+\phi)}\left\{\left(\frac{x}{L}\right)^3 - \left(2+\frac{\phi}{2}\right)\left(\frac{x}{L}\right)^2 + \left(1+\frac{\phi}{2}\right)\left(\frac{x}{L}\right)\right\} \\ -\frac{1}{(1+\phi)}\left\{2\left(\frac{x}{L}\right)^3 - 3\left(\frac{x}{L}\right)^2 - \phi\left(\frac{x}{L}\right)\right\} \\ \frac{L}{(1+\phi)}\left\{\left(\frac{x}{L}\right)^3 - \left(1-\frac{\phi}{2}\right)\left(\frac{x}{L}\right)^2 - \frac{\phi}{2}\left(\frac{x}{L}\right)\right\} \end{bmatrix}$$

$$\left[N_\varphi(x)\right]^T = \begin{bmatrix} \frac{6}{(1+\phi)L}\left\{\left(\frac{x}{L}\right)^2 - \left(\frac{x}{L}\right)\right\} \\ \frac{1}{(1+\phi)}\left\{3\left(\frac{x}{L}\right)^2 - (4+\phi)\left(\frac{x}{L}\right) + (1+\phi)\right\} \\ -\frac{6}{(1+\phi)L}\left\{\left(\frac{x}{L}\right)^2 - \left(\frac{x}{L}\right)\right\} \\ \frac{1}{(1+\phi)}\left\{3\left(\frac{x}{L}\right)^2 - (2-\phi)\left(\frac{x}{L}\right)\right\} \end{bmatrix}$$

$$\phi = \frac{12}{L^2}\left(\frac{EI_s}{\aleph GA}\right)$$

Bibliography

[1] Tulkoff, C., *Pad cratering : Prevention, mitigation, and detection strategies.* In APEX EXPO, 2013.

[2] Korenev, B.G.e. and L.M. Reznikov, *Dynamic vibration absorbers: theory and technical applications*. John Wiley & Sons,1993.

[3] Rana, R. and T. Soong, *Parametric study and simplified design of tuned mass dampers.* Engineering structures, 1998. **20**(3): 193-204.

[4] Samali, B. and K. Kwok, *Use of viscoelastic dampers in reducing wind-and earthquake-induced motion of building structures.* Engineering Structures, 1995. **17**(9): 639-654.

[5] Niederberger, D., *Smart damping materials using shunt control*. 2005: Diss., Eidgenössische Technische Hochschule ETH Zürich, Nr. 16043, 2006.

[6] Behrens, S., A. Fleming, and S. Moheimani, *A broadband controller for shunt piezoelectric damping of structural vibration.* Smart materials and structures, 2003. **12**(1): 18-28.

[7] Kwok, K. and B. Samali, *Performance of tuned mass dampers under wind loads.* Engineering Structures, 1995. **17**(9): 655-667.

[8] Setareh, M. and R.D. Hanson, *Tuned mass dampers to control floor vibration from humans.* Journal of Structural Engineering, 1992. **118**(3): 741-762.

[9] Kela, L. and P. Vähäoja, *Recent studies of adaptive tuned vibration absorbers/neutralizers.* Applied Mechanics Reviews, 2009. **62**(6): 060801.

[10] Zhang J, He L, Wang E, et al. *A LQR Controller Design for Active Vibration Control of Flexible Structures*// PACIIA 2008, Volume 1, 2008 IEEE Pacific-Asia Workshop on Computational Intelligence and Industrial Application, 19-20 December 2008, Wuhan, China. **2008**:127-132.

[11] Wills A G, Bates D, Fleming A J, et al. *Model Predictive Control Applied to Constraint Handling in Active Noise and Vibration Control*. IEEE Transactions on Control Systems Technology, 2008, **16**(1):3-12.

[12] Wang, R.L., H. Gu, and G. Song, *Adaptive robust sliding mode vibration control of a flexible beam using piezoceramic sensor and actuator: an experimental study.* Mathematical Problems in Engineering, 2014. **2014**(2):1-9.

[13] Hagood, N.W. and A. von Flotow, *Damping of structural vibrations with piezoelectric materials and passive electrical networks.* Journal of Sound and Vibration, 1991. **146**(2): 243-268.

[14] Uchino K, Ishii T. *Mechanical Damper Using Piezoelectric Ceramics*. Journal of the Ceramic Society of Japan, 1988. **96**(8): 863-867.

[15] Forward, R.L., *Electronic damping of vibrations in optical structures.* Applied optics, 1979. **18**(5): 690-697.

[16] Wu, S.-y. Wu S. *Piezoelectric shunts with a parallel R-L circuit for structural damping and vibration control*. Proceedings of SPIE - The International Society for Optical Engineering, 1996, **2720**:259-269.

[17] Baz, A., *Active control of periodic structures.* Journal of Vibration and Acoustics, 2001. **123**(4): 472-479.

[18] Reynolds, M. and S. Daley, *An active viscoelastic metamaterial for isolation applications.* Smart Materials and Structures, 2014. **23**(4): 045030.

[19] Reynolds, M. and S. Daley, *Enhancing the band gap of an active metamaterial.* Journal of Vibration and Control, 2015: 1077546315600330.

[20] Wu, S.-y. *Method for multiple-mode shunt damping of structural vibration using a single PZT transducer*. in *5th Annual International Symposium on Smart Structures and Materials*. International Society for Optics and Photonics, 1998.

[21] Hollkamp J J. *Multimodal Passive Vibration Suppression with Piezoelectric Materials and Resonant Shunts*. Journal of Intelligent Material Systems & Structures, 1994, **5**(5): 49-57.

[22] Behrens, S., S.R. Moheimani, and A. Fleming, *Multiple mode current flowing passive piezoelectric shunt controller.* Journal of Sound and Vibration, 2003. **266**(5): 929-942.

[23] Fleming A J, Behrens S, Moheimani S O R. *Reducing the inductance requirements of piezoelectric shunt damping systems*. Smart Materials & Structures, 2003, **12**(1): 57-64.

[24] Niederberger D, Fleming A, Moheimani S O R, et al. *Adaptive multi-mode resonant piezoelectric shunt damping*. Smart Materials & Structures, 2004, **13**(5): 1025-1035.

[25] Niederberger D. *Adaptive resonant shunted piezoelectric devices for vibration suppression*. Proceedings of SPIE - The International Society for Optical Engineering, 2003, **5056**: 213-224.

[26] Hollkamp, J.J. and T.F. Starchville, *A self-tuning piezoelectric vibration absorber.* Journal of Intelligent Material Systems and Structures, 1994. **5**(4): 559-566.

[27] Davis, C.L., G.A. Lesieutre, and J.J. Dosch. *Tunable electrically shunted piezoceramic vibration absorber.* Proceedings of SPIE - The International Society for Optical Engineering, 1997, 3045.

[28] Davis, C.L. and G.A. Lesieutre, *An actively tuned solid-state vibration absorber using capacitive shunting of piezoelectric stiffness.* Journal of sound and vibration, 2000. **232**(3): 601-617.

[29] Tylikowski, A., *Control of circular plate vibrations via piezoelectric actuators shunted with a capacitive circuit.* Thin-Walled Structures, 2001. **39**(1): 83-94.

[30] Lesieutre, G.A., *Vibration damping and control using shunted piezoelectric materials.* The Shock and Vibration Digest, 1998. **30**(3): 187-195.

[31] Richard, C., et al. *Semi-passive damping using continuous switching of a piezoelectric device*. in *1999 Symposium on Smart Structures and Materials*. 1999. International Society for Optics and Photonics. 1999, **3672**:104-111.

[32] Richard, C., et al. *Enhanced semi-passive damping using continuous switching of a piezoelectric device on an inductor*. Proceedings of SPIE - The International Society for Optical Engineering, 2000, **3989**:104-111.

[33] Richard, C., D. Guyomar, and E. Lefeuvre, *Self-powered electronic breaker with automatic switching by detecting maxima or minima of potential difference between its power electrodes.* FR2005/003000, publication number: WO/2007/063194, 2007.

[34] Lallart M, Élie Lefeuvre, Richard C, et al. *Self-powered circuit for broadband, multimodal piezoelectric vibration control*. Sensors & Actuators A Physical, 2008, **143**(2):377-382.

[35] Ji H, Qiu J, Cheng J, et al. *Application of a negative capacitance circuit in synchronized switch damping techniques for vibration suppression*. Journal of Vibration & Acoustics, 2011, **133**(4):041015-1.

[36] Shenck N S, Paradiso J A. *Energy Scavenging with Shoe-Mounted Piezoelectrics*. IEEE Micro, 2001, **21**(3):30-42.

[37] Fleming, A.J., S. Behrens, and S.R. Moheimani. *An autonomous piezoelectric shunt damping system*. Proceedings of SPIE-The International Society for Optical Engineering, 2003, **5052**:207-216.

[38] Ottman G K, Hofmann H F, Lesieutre G A. *Optimized piezoelectric energy harvesting circuit using step-down converter in discontinuous conduction mode*. IEEE Transactions on Power Electronics, 2002, **18**(2):1988-1994.

[39] Lesieutre, G.A., G.K. Ottman, and H.F. Hofmann, *Damping as a result of piezoelectric energy harvesting.* Journal of Sound and Vibration, 2004. **269**(3): 991-1001.

[40] Fleming, A.J., S. Behrens, and S.R. Moheimani. *Active LQR and H 2 shunt control of electromagnetic transducers*. IEEE Conference on Decision & Control. 2004: 2294 - 2299 Vol.3.

[41] Fleming A J, Moheimani S O R. *Control orientated synthesis of high-performance piezoelectric shunt impedances for structural vibration control*. IEEE Transactions on Control Systems Technology, 2005, **13**(1): 98-112.

[42] Bailey, T. and J. Ubbard, *Distributed piezoelectric-polymer active vibration control of a cantilever beam.* Journal of Guidance, Control, and Dynamics, 1985. **8**(5): 605-611.

[43] Hassan M, Dubay R, Li C, et al. *Active vibration control of a flexible one-link manipulator using a multivariable predictive controller.* Mechatronics, 2007. **17**(6): 311-323.

[44] Takács, G. and B. Rohaľ-Ilkiv, *Model Predictive Vibration Control: Efficient Constrained MPC Vibration Control for Lightly Damped Mechanical Structures*. Springer Science & Business Media, 2012.

[45] Ji J K, Lee D C, Sul S K. *LQG based speed controller for torsional vibration suppression in 2-mass motor drive system*. International Conference on Industrial Electronics, Control, and Instrumentation, 1993. Proceedings of the IECON. IEEE, 1993: 1157-1162 vol.2.

[46] Connolly A J, Green M, Chicharo J F, et al. The design of LQG and H∞ controllers for use in active vibration control and narrow band disturbance rejection. Decision and Control, 1995. Proceedings of the, IEEE Conference on. IEEE, 1995: 2982 - 2987.

[47] Han, J.-H., K.-H. Rew, and I. Lee, *An experimental study of active vibration control of composite structures with a piezo-ceramic actuator and a piezo-film sensor.* Smart Materials and Structures, 1997. **6**(5): 549-558.

[48] Edwards, C. and S. Spurgeon, *Sliding mode control: theory and applications*. 1998: CRC Press.

[49] Trindade, M., A. Benjeddou, and R. Ohayon, *Piezoelectric active vibration control of damped sandwich beams.* Journal of Sound and Vibration, 2001. **246**(4): 653-677.

[50] Yoshimura T, Kume A, Kurimoto M, et al. *Construction of an active suspension system of a quarter car model using the concept of sliding mode control.* Journal of Sound and Vibration, 2001. **239**(2): 187-199.

[51] Petersen, I.R. and H.R. Pota, *Minimax LQG optimal control of a flexible beam.* Control Engineering Practice, 2003. **11**(11): 1273-1287.

[52] Hu, Q. and G. Ma, *Variable structure control and active vibration suppression of flexible spacecraft during attitude maneuver.* Aerospace Science and Technology, 2005. **9**(4): 307-317.

[53] Utkin, V., J. Guldner, and J. Shi, *Sliding mode control in electro-mechanical systems*. Vol. 34. 2009: CRC press.

[54] Tang J, Wang K W. *Active-passive hybrid piezoelectric networks for vibration control: comparisons and improvement*. Smart Materials & Structures, 2001, **10**(4): 794-806.

[55] Trindade, M.A, A. Benjeddou, *Hybrid active-passive damping treatments using viscoelastic and piezoelectric materials: review and assessment.* Journal of Vibration and Control, 2002. **8**(6): 699-745.

[56] Forward R L. *Electromechanical transducer-coupled mechanical structure with negative capacitance compensation circuit*: US, US 4158787 A[P]. 1979.

[57] Browning D R, Wynn W D. *Vibration damping system using active negative capacitance shunt circuit with piezoelectric reaction mass actuator*: US, US 5558477 A[P]. 1996.

[58] Park, C.H. and A. Baz, *Vibration control of beams with negative capacitive shunting of interdigital electrode piezoceramics.* Journal of Vibration and Control, 2005. **11**(3): 331-346.

[59] Neubauer M, Oleskiewicz R, Popp K, et al. *Optimization of damping and absorbing performance of shunted piezo elements utilizing negative capacitance*. Journal of Sound & Vibration, 2006, **298**(1): 84-107.

[60] De Marneffe B, Preumont A. Vibration damping with negative capacitance shunts: theory and experiment. Smart Materials & Structures, 2008, **17**(17): 4006-4032.

[61] Riordan R H S. *Simulated inductors using differential amplifiers*. Electronics Letters, 1967, **3**(2):50-51.

[62] Antoniou A. *Realisation of gyrators using operational amplifiers, and their use in RC-active-network synthesis*. Electrical Engineers Proceedings of the Institution of, 1969, **116**(11): 1838-1850.

[63] Awad I A, Soliman A M. New CMOS realization of the CCII-. IEEE Transactions on Circuits & Systems II Analog & Digital Signal Processing, 1999, **46**(4): 460-463.

[64] Ferri G, Guerrini N. *High-valued passive element simulation using low-voltage low-power current conveyors for fully integrated applications*. IEEE Transactions on Circuits & Systems II Analog & Digital Signal Processing, 2001, **48**(4): 405-409.

[65] Clark W W. Vibration Control with State-Switched Piezoelectric Materials[J]. Journal of Intelligent Material Systems & Structures, 2000, **11**(4): 263-271.

[66] Cunefare K A, Rosa S D, Sadegh N, et al. State-Switched Absorber for SemiActive Structural Control. Journal of Intelligent Material Systems & Structures, 2000, **11**(4):300-310.

[67] Larson G D, Rogers P H, Munk W. *State switched transducers: A new approach to high-power, low-frequency, underwater projectors*. Journal of the Acoustical Society of America, 1998, **103**(3): 1428-1441.

[68] Ramaratnam, A., N. Jalili, and D.M. Dawson. *Semi-active vibration control using piezoelectric-based switched stiffness*. in *American Control Conference,* 2004: 5461-5466.

[69] Ramaratnam, A. and N. Jalili, *A switched stiffness approach for structural vibration control: theory and real-time implementation.* Journal of Sound and Vibration, 2006. **291**(1): 258-274.

[70] Lotfi-Gaskarimahalle, A. and C.D. Rahn. *Switched stiffness vibration controllers for fluidic flexible matrix composites*. in *ASME 2009 International Design Engineering Technical Conferences and Computers and Information in Engineering Conference*. 2009. American Society of Mechanical Engineers.

[71] Shen H, Qiu J, Ji H, et al. *A low-power circuit for piezoelectric vibration control by synchronized switching on voltage sources*. Sensors & Actuators A Physical, 2010, **161**(1–2): 245-255.

[72] Ji H, Qiu J, Xia P, et al. *The influence of switching phase and frequency of voltage on the vibration damping effect in a piezoelectric actuator*. Smart Materials & Structures, 2011, **20**(1): 15008-15023.

[73] Ji H, Qiu J, Badel A, et al. *Semi-active Vibration Control of a Composite Beam using an Adaptive SSDV Approach.* Journal of Intelligent Material Systems & Structures, 2009, **20**(20): 401-412.

[74] Lefeuvre E, Badel A, Petit L, et al. *Semi-passive Piezoelectric Structural Damping by Synchronized Switching on Voltage Sources*. Journal of Intelligent Material Systems & Structures, 2006, **17**(8-9): 653-660.

[75] Badel A, Sebald G, Guyomar D, et al. *Piezoelectric vibration control by synchronized switching on adaptive voltage sources: Towards wideband semi-active damping*. Journal of the Acoustical Society of America, 2006, **119**(5): 2815-2825.

[76] Neubauer M, Han X, Schwarzendahl S M. *Enhanced switching law for synchronized switch damping on inductor with bimodal excitation*. Journal of Sound & Vibration, 2011, **330**(12): 2707-2720.

[77] Chérif A, Richard C, Guyomar D, et al. *Simulation of multimodal vibration damping of a plate structure using a modal SSDI-Max technique*. Journal of Intelligent Material Systems & Structures, 2012, **23**(6): 675-689.

[78] Richard T, Magnet C, Richard C, et al. *Board multimodal vibration control using piezoelectric synchronised switch damping techniques*. Journal of Vibration & Control, 2010, **17**(6): 845-856.

[79] Collinger J C, Wickert J A. Adaptive Piezoelectric Vibration Control With Synchronized Switching. Journal of Dynamic Systems Measurement & Control, 2009, **131**(131): 1703-1712.

[80] Lallart M, Harari S, Petit L, et al. Blind switch damping (BSD): A self-adaptive semi-active damping technique. Journal of Sound & Vibration, 2009, **328**(1–2): 29-41.

[81] Ji H, Qiu J, Zhu K, et al. *Two-mode vibration control of a beam using nonlinear synchronized switching damping based on the maximization of converted energy*. Journal of Sound & Vibration, 2010, **329**(14): 2751-2767.

[82] Guyomar D, Richard C, Mohammadi S. *Semi-passive random vibration control based on statistics*. Journal of Sound & Vibration, 2007, **307**(3–5): 818-833.

[83] Fleming A J, Behrens S, Moheimani S O R. *Synthetic impedance for implementation of piezoelectric shunt-damping circuits*. Electronics Letters, 2000, **36**(18): 1525-1526.

[84] Matten G, Collet M, Cogan S, et al. *Synthetic Impedance for Adaptive Piezoelectric Metacomposite*. Procedia Technology, 2014, **15**: 84-89.

[85] Warkentin, D.J. and N.W. Hagood. *Nonlinear piezoelectric shunting for structural damping*. in *Smart Structures and Materials' 97*. 1997. International Society for Optics and Photonics. 3041: 747-757.

[86] Dell'Lsola F, Vescovo D D, Maurini C. Distributed electric absorbers of beam vibrations. Proceedings of SPIE-The International Society for Optical Engineering, 2003, **5052**:230-241.

[87] Dell'Isola F, Maurini C, Porfiri M. *Passive damping of beam vibrations through distributed electric networks and piezoelectric transducers: prototype design and experimental validation*. Smart Materials & Structures, 2004, **13**(2): 299-308.

[88] Maurini C, Dell'Isola F, Vescovo D D. Comparison of piezoelectronic networks acting as distributed vibration absorbers. Mechanical Systems & Signal Processing, 2004, **18**(5): 1243-1271.

[89] Bisegna P, Caruso G, Maceri F. Optimized electric networks for vibration damping of piezoactuated beams. Journal of Sound & Vibration, 2006, **289**(4–5): 908-937.

[90] Giorgio I, Culla A, Vescovo D D. *Multimode vibration control using several piezoelectric transducers shunted with a multiterminal network*. Archive of Applied Mechanics, 2009, **79**(9): 859-879.

[91] Lossouarn B, Aucejo M, Deü J F. *Multimodal vibration damping through a periodic array of piezoelectric patches connected to a passive network*. SPIE Smart Structures/nde. 2015.

[92] Ruzzene M, Baz A. *Control of Wave Propagation in Periodic Composite Rods Using Shape Memory Inserts*. Journal of Vibration & Acoustics, 2000, **122**(2): 151-159.

[93] Thorp O G, Ruzzene M, Baz A M. Attenuation and localization of wave propagation in rods with periodic shunted piezoelectric patches. Smart Materials & Structures, 2001, **18**(3): 657-696.

[94] Wang, G., S. Chen, and J. Wen, Wang G, Chen S, Wen J. *Low-frequency locally resonant band gaps induced by arrays of resonant shunts with Antoniou's circuit: experimental investigation on beams.* Smart Materials and Structures, 2010. **20**(1): 015026.

[95] Airoldi L, Ruzzene M. *Design of tunable acoustic metamaterials through periodic arrays of resonant shunted piezos*. New Journal of Physics, 2011, **13**(11): 746-754.

[96] Wang G, Wang J, Chen S, et al. *Vibration attenuations induced by periodic arrays of piezoelectric patches connected by enhanced resonant shunting circuits.* Smart Materials and Structures, 2011. **20**(12): 125019.

[97] Chen S, Wang G, Wen J, et al. *Wave propagation and attenuation in plates with periodic arrays of shunted piezo-patches*. Journal of Sound & Vibration, 2013, **332**(6): 1520-1532.

[98] Bergamini A, Delpero T, Simoni L D, et al. *Phononic Crystal with Adaptive Connectivity*. Advanced Materials, 2014, **26**(9): 1343-1347.

[99] Wang G, Chen S. *Large low-frequency vibration attenuation induced by arrays of piezoelectric patches shunted with amplifier–resonator feedback circuits*. Smart Materials & Structures, 2016, **25**(1): 015004.

[100] Beck B, Cunefare K A, Ruzzene M. *Broadband Vibration Suppression Assessment of Negative Impedance Shunts*. ASME 2008 Conference on Smart Materials, Adaptive Structures and Intelligent Systems. 2008: 491-500.

[101] Beck B S, Cunefare K A, Ruzzene M, et al. *Experimental Analysis of a Cantilever Beam with a Shunted Piezoelectric Periodic Array*. Journal of Intelligent Material Systems & Structures, 2010, **22**(22):1177-1187.

[102] Chen Y Y, Huang G L, Sun C T. *Band gap control in an active elastic metamaterial with negative capacitance piezoelectric shunting.* Journal of Vibration and Acoustics, 2014. **136**(6): 061008.

[103] Huang T, Ichchou M, Collet M, et al. *Wave propagation control in smart structures with shunted piezoelectric patches.* ISMA 2012 conference on Noise and Vibration Engineering. 2012.

[104] Tateo F, Collet M, Ouisse M, et al. *Design variables for optimizing adaptive metacomposite made of shunted piezoelectric patches distribution*. Journal of Vibration & Control, 2014: 1077546314545100.

[105] Tateo F, Collet M, Ouisse M, et al. *Experimental characterization of a bi-dimensional array of negative capacitance piezo-patches for vibroacoustic control*. Journal of Intelligent Material Systems and Structures, 2014: 1045389X14536006.

[106] Casadei F, Beck B S, Cunefare K A, et al. *Vibration control of plates through hybrid configurations of periodic piezoelectric shunts*. Journal of Intelligent Material Systems & Structures, 2012, **23**(10): 1169-1177.

[107] Zhang, H., Wen J -H, Chen S -B, et al. *Flexural wave band-gaps in phononic metamaterial beam with hybrid shunting circuits.* Chinese Physics B, 2015. **24**(3): 269-274.

[108] Lallart M, Yan L, Richard C, et al. Damping of periodic bending structures featuring nonlinearly interfaced piezoelectric elements. Journal of Vibration & Control, 2015: 1077546314567724.

[109] Yan, L., *Broadband vibration control using nonlinearly interfaced piezoelectric elements*. Diss. INSA de Lyon, 2013.

[110] Guyomar D, Badel A. *Nonlinear semi-passive multimodal vibration damping: An efficient probabilistic approach.* Journal of Sound and Vibration, 2006. **294**(1): 249-268.

[111] Lallart M, Magnet C, Richard C, et al. *New Synchronized Switch Damping methods using dual transformations.* Sensors and Actuators A: Physical, 2008. **143**(2): 302-314.

[112] Joannopoulos J D, Johnson S G, Winn J N, et al. *Photonic crystals: molding the flow of light*. Princeton university press, 2011.

[113] Pendry J B, Holden A J, Stewart W J, et al. *Extremely low frequency plasmons in metallic mesostructures*. Physical Review Letters, 1996, **76**(25): 4773-4776.

[114] Vlasov Y A, Bo X Z, Sturm J C, et al. *On-chip natural assembly of silicon photonic bandgap crystals*. Nature, 2001, **414**(6861): 289-293.

[115] Brillouin L. *Wave Propagation in Periodic Structures: Electric Filters and Crystal Lattices*. McGraw-Hill Book Company, Inc. New York, 1946(4026): 926.

[116] Lee J, Singer J P, Thomas E L. *Micro-/Nanostructured Mechanical Metamaterials*. Advanced Materials, 2012, **24**(36): 4782-4810.

[117] Maldovan, M., *Sound and heat revolutions in phononics.* Nature, 2013. **503**(7475): 209-217.

[118] Liu Z, Zhang X, Mao Y, et al. *Locally resonant sonic materials.* Science, 2000. **289**(5485): 1734-1736.

[119] Sharma B, Sun C T. *Local resonance and Bragg bandgaps in sandwich beams containing periodically inserted resonators.* Journal of Sound and Vibration, 2016. **364**: 133-146.

[120] Dai L, Jiang S, Lian Z, et al. *Locally resonant band gaps achieved by equal frequency shunting circuits of piezoelectric rings in a periodic circular plate*. Journal of Sound and Vibration, 2015, **337**: 150-160.

[121] Xiao Y, Wen J, Wang G, et al. *Theoretical and experimental study of locally resonant and Bragg band gaps in flexural beams carrying periodic arrays of beam-like resonators*. Journal of Vibration and Acoustics, 2013, **135**(4): 041006.

[122] Xiao Y, Wen J, Wen X. *Broadband locally resonant beams containing multiple periodic arrays of attached resonators*. Physics Letters A, 2012, **376**(16): 1384-1390.

[123] Xiao Y, Wen J, Yu D, et al. *Flexural wave propagation in beams with periodically attached vibration absorbers: band-gap behavior and band formation mechanisms*. Journal of Sound and Vibration, 2013, **332**(4): 867-893.

[124] Croënne C, Lee E J S, Hu H, et al. *Band gaps in phononic crystals: Generation mechanisms and interaction effects*. AIP Advances, 2011, **1**(4): 041401.

[125] Li F M, Wang Y S, Hu C, et al. *Localization of elastic waves in randomly disordered multi-coupled multi-span beams*. Waves in random media, 2004, **14**(3): 217-227.

[126] Bouzit D, Pierre C. *Wave localization and conversion phenomena in multi-coupled multi-span beams.* Chaos, Solitons & Fractals, 2000. **11**(10): 1575-1596.

[127] Bendiksen O O. *Mode localization phenomena in large space structures*. AIAA journal, 1987, **25**(9): 1241-1248.

[128] Collet M, Cunefare K A, Ichchou M N. *Wave Motion Optimization in Periodically Distributed Shunted Piezocomposite Beam Structures*. Journal of Intelligent Material Systems & Structures, 2009, **20**(7): 787-808.

[129] Collet M, Ouisse M, Ichchou M, et al. *Semi-active optimization of 2D wave's dispersion into shunted piezocomposite systems for controlling acoustic interaction*. ASME 2011 Conference on Smart Materials, Adaptive Structures and Intelligent Systems. American Society of Mechanical Engineers, 2011: 79-87.

[130] Collet M, Ouisse M, Ichchou M N. *Structural energy flow optimization through adaptive shunted piezoelectric metacomposites*. Journal of Intelligent Material Systems and Structures, 2012, **23**(15): 1661-1677.

[131] Huang T L, Ichchou M N, Bareille O A, et al. *Traveling wave control in thin-walled structures through shunted piezoelectric patches*. Mechanical Systems and Signal Processing, 2013, **39**(1): 59-79.

[132] Huang T, Ichchou M N, Bareille O, et al. *Multimodal wave propagation in smart composite structures with shunted piezoelectric patches*. Journal of Intelligent Material Systems and Structures, 2013: 1045389X13480571.

[133] Livet S, Collet M, Berthillier M, et al. *Structural multi-modal damping by optimizing shunted piezoelectric transducers*. European Journal of Computational Mechanics/Revue Européenne de Mécanique Numérique, 2011, **20**(1-4): 73-102.

[134] Yamada K, Matsuhisa H, Utsuno H. *Enhancement of efficiency of vibration suppression using piezoelectric elements and LR circuit by amplification of electrical resonance*. Journal of Sound and Vibration, 2014, **333**(5): 1281-1301.

[135] Airoldi L, Ruzzene M. *Wave propagation control in beams through periodic multi-branch shunts*. Journal of Intelligent Material Systems and Structures, 2011: 1045389X11408372.

[136] Duhamel D, Mace B R, Brennan M J. Finite element analysis of the vibrations of waveguides and periodic structures[J]. Journal of sound and vibration, 2006, **294**(1): 205-220.

[137] Houillon L, Ichchou M N, Jezequel L. *Wave motion in thin-walled structures*. Journal of Sound and Vibration, 2005, **281**(3): 483-507.

[138] Mace B R, Duhamel D, Brennan M J, et al. *Finite element prediction of wave motion in structural waveguides*. The Journal of the Acoustical Society of America, 2005, **117**(5): 2835-2843.

[139] Ichchou M N, Mencik J M, Zhou W. *Wave finite elements for low and mid-frequency description of coupled structures with damage*. Computer methods in applied mechanics and engineering, 2009, **198**(15): 1311-1326.

[140] Mencik J M, Ichchou M N. *Multi-mode propagation and diffusion in structures through finite elements*. European Journal of Mechanics-A/Solids, 2005, **24**(5): 877-898.

[141] Challa V R, Prasad M G, Shi Y, et al. *A vibration energy harvesting device with bidirectional resonance frequency tunability*. Smart Materials and Structures, 2008, **17**(1): 015035.

[142] Beranek L L, Ver I L. *Noise and vibration control engineering-principles and applications*. Noise and vibration control engineering-Principles and applications John Wiley & Sons, Inc., 1992.

[143] Koopmann G H, Fox D J, Neise W. *Active source cancellation of the blade tone fundamental and harmonics in centrifugal fans*. Journal of sound and vibration, 1988, **126**(2): 209-220.

[144] Rivin E I, Rivin E I. Passive vibration isolation. New York: Asme press, 2003.

[145] Karnopp D. *Active and semi-active vibration isolation*. Journal of Vibration and Acoustics, 1995, **117**(B): 177-185.

[146] Kalaycıoğlu T, Özgüven H N. *Nonlinear structural modification and nonlinear coupling*. Mechanical Systems and Signal Processing, 2014, **46**(2): 289-306.

[147] Khot N S, Venkayya V B, Eastep F E. *Optimal structural modifications to enhance the active vibration control of flexible structures*. AIAA journal, 1986, **24**(8): 1368-1374.

[148] Deymier, Pierre A., ed. Acoustic metamaterials and phononic crystals. Vol. 173. Springer Science & Business Media, 2013.

[149] Noda S, Tomoda K, Yamamoto N, et al. *Full three-dimensional photonic bandgap crystals at near-infrared wavelengths*. Science, 2000, **289**(5479): 604-606.

[150] Zhou W, Wu Y, Zuo L. *Vibration and wave propagation attenuation for metamaterials by periodic piezoelectric arrays with high-order resonant circuit shunts*. Smart Materials and Structures, 2015, **24**(6): 065021.

[151] Soto M G, Adeli H. *Tuned mass dampers*. Archives of Computational Methods in Engineering, 2013, **20**(4): 419-431.

[152] Bonello P. *Adaptive tuned vibration absorbers: design principles, concepts and physical implementation*. INTECH Open Access Publisher, 2011.

[153] Vonflotow A H, Beard A, Bailey D. *Adaptive tuned vibration absorbers: tuning laws, tracking agility, sizing, and physical implementations*.Noise Con 1994: Proceedings of the 1994 National Conference on Noise Control Engineering. 1994, **1**: 437-454.

[154] Brennan M J, Dayou J. *Global control of vibration using a tunable vibration neutralizer*. Journal of Sound and Vibration, 2000, **232**(3): 585-600.

[155] Brennan M J. *Vibration control using a tunable vibration neutralizer*. Proceedings of the Institution of Mechanical Engineers, Part C: Journal of Mechanical Engineering Science, 1997, **211**(2): 91-108.

[156] Frahm H. *Device for damping vibrations of bodies*: U.S. Patent 989,958[P]. 1911-4-18.

[157] Ormondroyd J. *Theory of the dynamic vibration absorber*. Transaction of the ASME, 1928, **50**: 9-22.

[158] Den Hartog J P. *Mechanical vibrations*. Courier Corporation, 1985.

[159] Kidner M, Brennan M J. *Improving the performance of a vibration neutraliser by actively removing damping*. Journal of Sound and Vibration, 1999, **221**(4): 587-606.

[160] Zuo L, Nayfeh S A. *Minimax optimization of multi-degree-of-freedom tuned-mass dampers*. Journal of Sound and Vibration, 2004, **272**(3): 893-908.

[161] Zuo L, Nayfeh S A. *Optimization of the individual stiffness and damping parameters in multiple-tuned-mass-damper systems*. Journal of Vibration and Acoustics, 2005, **127**(1): 77-83.

[162] Marano G C, Quaranta G. *Robust optimum criteria for tuned mass dampers in fuzzy environments.* Applied Soft Computing, 2009. **9**(4): 1232-1243.

[163] Zuo L. *Effective and robust vibration control using series multiple tuned-mass dampers*. Journal of Vibration and Acoustics, 2009, **131**(3): 031003.

[164] Tigli O F. *Optimum vibration absorber (tuned mass damper) design for linear damped systems subjected to random loads*. Journal of Sound and Vibration, 2012, **331**(13): 3035-3049.

[165] Marano G C, Greco R, Chiaia B. *A comparison between different optimization criteria for tuned mass dampers design.* Journal of Sound and Vibration, 2010. **329**(23): 4880-4890.

[166] Hoang N, Fujino Y, Warnitchai P. *Optimal tuned mass damper for seismic applications and practical design formulas*. Engineering structures, 2008, **30**(3): 707-715.

[167] Bekdaş G, Nigdeli S M. *Estimating optimum parameters of tuned mass dampers using harmony search*. Engineering Structures, 2011, **33**(9): 2716-2723.

[168] Hrovat D, Barak P, Rabins M. *Semi-active versus passive or active tuned mass dampers for structural control*. Journal of Engineering Mechanics, 1983, **109**(3): 691-705.

[169] Fujii K, Tamura Y, Sato T, et al. *Wind-induced vibration of tower and practical applications of tuned sloshing damper*. Journal of Wind Engineering and Industrial Aerodynamics, 1990, **33**(1-2): 263-272.

[170] Balendra T, Wang C M, Cheong H F. *Effectiveness of tuned liquid column dampers for vibration control of towers*. Engineering Structures, 1995, **17**(9): 668-675.

[171] Jalili N, Knowles IV D W. *Structural vibration control using an active resonator absorber: modeling and control implementation*. Smart Materials & Structures, 2004, **13**(5):998-1005.

[172] Bonello P, Brennan M J, Elliott S J, et al. *Designs for an adaptive tuned vibration absorber with variable shape stiffness element*. Proceedings of the Royal Society of London A: Mathematical, Physical and Engineering Sciences. The Royal Society, 2005, **461**(2064): 3955-3976.

[173] Kim S M, Wang S, Brennan M J. *Dynamic analysis and optimal design of a passive and an active piezo-electrical dynamic vibration absorber*. Journal of sound and vibration, 2011, **330**(4): 603-614.

[174] Tso M H, Yuan J, Wong W O. *Suppression of random vibration in flexible structures using a hybrid vibration absorber*. Journal of sound and vibration, 2012, **331**(5): 974-986.

[175] Kareem A, Kline S. *Performance of multiple mass dampers under random loading*. Journal of structural engineering, 1995, **121**(2): 348-361.

[176] Bonello P, Brennan M J, Elliott S J. *Vibration control using an adaptive tuned vibration absorber with a variable curvature stiffness element*. Smart Materials & Structures, 2005, **14**(5): 1055–1065.

[177] Weber F, Boston C, Maślanka M. *An adaptive tuned mass damper based on the emulation of positive and negative stiffness with an MR damper*. Smart Materials and Structures, 2010, **20**(1): 015012.

[178] Kerwin Jr, E.M., *Damping of flexural waves by a constrained viscoelastic layer.* The Journal of the Acoustical society of America, 1959. **31**(7): 952-962.

[179] Ross D, Ungar E E, Kerwin E M. *Damping of plate flexural vibrations by means of viscoelastic laminae*. Structural damping, 1959, **3**: 44-87.

[180] Lall A K, Asnani N T, Nakra B C. *Damping analysis of partially covered sandwich beams*. Journal of sound and vibration, 1988, **123**(2): 247-259.

[181] Kung S W, Singh R. V*ibration analysis of beams with multiple constrained layer damping patches*. Journal of Sound and Vibration, 1998, **212**(5): 781-805.

[182] Nakra, B., *Vibration control in machines and structures using viscoelastic damping.* journal of Sound and Vibration, 1998, **211**(3):449-466.

[183] Kung S W, Singh R. *Development of approximate methods for the analysis of patch damping design concepts*. Journal of Sound and Vibration, 1999, **219**(5): 785-812.

[184] Hu Y C, Huang S C. *The frequency response and damping effect of three-layer thin shell with viscoelastic core*. Computers & Structures, 2000, **76**(5): 577-591.

[185] Jones D I G. *Response and damping of a simple beam with tuned dampers*. The journal of the acoustical society of America, 1967, **42**(1): 50-53.

[186] Rao M D. *Recent applications of viscoelastic damping for noise control in automobiles and commercial airplanes*. Journal of Sound and Vibration, 2003, **262**(3): 457-474.

[187] Rashid A, Nicolescu C M. *Design and implementation of tuned viscoelastic dampers for vibration control in milling*. International Journal of Machine Tools and Manufacture, 2008, **48**(9): 1036-1053.

[188] Ghoneim H. Electromechanical surface damping using constrained layer and shunted piezoelectric.1993 North American Conference on Smart Structures and Materials. International Society for Optics and Photonics, 1993: 78-89.

[189] Park C H, Baz A. *Vibration control of bending modes of plates using active constrained layer damping*. Journal of Sound and vibration, 1999, **227**(4): 711-734.

[190] Chantalakhana C, Stanway R. *Active constrained layer damping of clamped-clamped plate vibrations*. Journal of Sound and Vibration, 2001, **241**(5): 755-777.

[191] Ray M C, Baz A. *Control of nonlinear vibration of beams using active constrained layer damping*. Journal of Vibration and Control, 2001, **7**(4): 539-549.

[192] Xu Z, Wang M Y, Chen T. *Particle damping for passive vibration suppression: numerical modelling and experimental investigation.* Journal of Sound and Vibration, 2005, **279**(3): 1097-1120.

[193] YASUDA K, TOYODA M. *The damping effect of an impact damper*. Bulletin of JSME, 1978, **21**(153): 424-430.

[194] Ema S, Marui E. *A fundamental study on impact dampers*. International Journal of Machine Tools and Manufacture, 1994, **34**(3): 407-421.

[195] Butt A S, Akl F A. *Numerical model of impact-damped continuous systems*. Journal of engineering mechanics, 1997, **123**(4): 384-392.

[196] Papalou A, Masri S F. *An experimental investigation of particle dampers under harmonic excitation*. Journal of vibration and control, 1998, **4**(4): 361-379.

[197] Wu C J, Liao W H, *Wang M Y. Modeling of granular particle damping using multiphase flow theory of gas-particle*. Journal of vibration and acoustics, 2004, **126**(2): 196-201.

[198] Liu W, Tomlinson G R, Rongong J A. *The dynamic characterisation of disk geometry particle dampers*. Journal of Sound and Vibration, 2005, **280**(3): 849-861.

[199] Marhadi K S, Kinra V K. *Particle impact damping: effect of mass ratio, material, and shape*. Journal of sound and vibration, 2005, **283**(1): 433-448.

[200] Bai X M, Keer L M, Wang Q J, et al. *Investigation of particle damping mechanism via particle dynamics simulations*. Granular Matter, 2009, **11**(6): 417-429.

[201] Friend R D, Kinra V K. *Particle impact damping*. Journal of Sound and Vibration, 2000, **233**(1): 93-118.

[202] Masri S F. *General motion of impact dampers*. The Journal of the Acoustical Society of America, 1970, **47**(1B): 229-237.

[203] Saluena C, Poeschel T, Esipov S E. *Dissipative properties of vibrated granular materials*. Physical Review E, 1998, **59**(59):4422-4425.

[204] Papalou A, Masri S F. *Response of impact dampers with granular materials under random excitation*. Earthquake engineering & structural dynamics, 1996, **25**(3): 253-267.

[205] Mcelhaney J M, Palazzolo A, Kascak A. *Modeling and simulation methods for MDOF structures and rotating machinery with impact dampers*. Journal of Engineering for Gas Turbines & Power, 1995, **119**(2): 436-446.

[206] Popplewell N, Semercigil S E. *Performance of the bean bag impact damper for a sinusoidal external force*. Journal of Sound and Vibration, 1989, **133**(2): 193-223.

[207] Cempel C, Lotz G. *Efficiency of vibrational energy dissipation by moving shot*. Journal of Structural Engineering, 1993, **119**(9): 2642-2652.

[208] Mao K, Wang M Y, Xu Z, et al. *DEM simulation of particle damping*. Powder Technology, 2004, **142**(2): 154-165.

[209] Weiss K D, Carlson J D, Nixon D A. *Viscoelastic properties of magneto-and electro-rheological fluids*. Journal of Intelligent Material Systems and Structures, 1994, **5**(6): 772-775.

[210] Stanway R, Sproston J L, Stevens N G. *Non-linear modelling of an electro-rheological vibration damper*. Journal of Electrostatics, 1987, **20**(2): 167-184.

[211] Stanway R, Sproston J L, Elwahed A K. *Applications of electro-rheological fluids in vibration control: a survey*. Smart Materials & Structures, 1996, **5**(4):464-482.

[212] Sasaki M, Ishii T, Haji K. Electro rheological fluid: U.S. Patent 5,679,280[P]. 1997-10-21.

[213] Khanicheh A, Mintzopoulos D, Weinberg B, et al. *Evaluation of electrorheological fluid dampers for applications at 3-T MRI environment*. IEEE/ASME Transactions on Mechatronics, 2008, **13**(3): 286-294.

[214] Jolly M R, Carlson J D, Muñoz B C. *A model of the behaviour of magnetorheological materials*. Smart Materials & Structures, 1996, **5**(5): 607-614.

[215] Dyke S J, Spencer B F, Sain M K, et al. *Modeling and control of magnetorheological dampers for seismic response reduction*. Smart Materials & Structures, 1996, **5**(5): 565-575.

[216] de Vicente J, Klingenberg D J, Hidalgo-Alvarez R. *Magnetorheological fluids: a review*. Soft Matter, 2011, **7**(8): 3701-3710.

[217] Carlson J D, Catanzarite D M, St. Clair K A. *Commercial magneto-rheological fluid devices*. International Journal of Modern Physics B, 1996, **10**(23n24): 2857-2865.

[218] Ashour O, Rogers C A, Kordonsky W. *Magnetorheological fluids: materials, characterization, and devices.* Journal of intelligent material systems and structures, 1996. **7**(2): 123-130.

[219] Damjanovic D, Newnham R E. *Electrostrictive and piezoelectric materials for actuator applications*. Journal of intelligent material systems and structures, 1992, **3**(2): 190-208.

[220] Galvagni, J. *Electrostrictive actuators and their use in optical applications.* Optical Engineering, 1990. **29**(11): 1389-1391.

[221] Lallart M, Wang L, Richard C, et al. *Lumped model of bending electrostrictive transducers for energy harvesting*. Journal of Applied Physics, 2014, **116**(12): 124106.

[222] Lee F S. *Modeling of actuator systems using multilayer electrostrictive materials*. Control Applications, 1999. Proceedings of the 1999 IEEE International Conference on. IEEE, 1999, **2**: 1406-1411.

[223] Liu Y, Ren K L, Hofmann H F, et al. *Investigation of electrostrictive polymers for energy harvesting*. ieee transactions on ultrasonics, ferroelectrics, and frequency control, 2005, **52**(12): 2411-2417.

[224] Wang L, Lallart M, Petit L, et al. *Low-cost charge of electrostrictive polymers for efficient energy harvesting*. Journal of Intelligent Material Systems and Structures, 2015, **26**(16): 2123-2136.

[225] Song G, Ma N, Li H N. *Applications of shape memory alloys in civil structures*. Engineering structures, 2006, **28**(9): 1266-1274.

[226] Otsuka K, Wayman C M. Shape memory materials[M]. Cambridge university press, 1999.

[227] Lagoudas, D.C., *Shape memory alloys.* Science and Business Media, LLC, 2008.

[228] Hartl D J, Lagoudas D C. *Aerospace applications of shape memory alloys.* Proceedings of the Institution of Mechanical Engineers, Part G: Journal of Aerospace Engineering, 2007. **221**(4): 535-552.

[229] Baz A, Imam K, McCoy J. *Active vibration control of flexible beams using shape memory actuators*. Journal of Sound and Vibration, 1990, **140**(3): 437-456.

[230] Auricchio F, Taylor R L. *Shape-memory alloys: modelling and numerical simulations of the finite-strain superelastic behavior.* Computer methods in applied mechanics and engineering, 1997. **143**(1): 175-194.

[231] Block H, Kelly J P, Qin A, et al. *Materials and mechanisms in electrorheology.* Langmuir, 1990. **6**(1): 6-14.

[232] Tonoli A, Silvagni M, Amati N. *Electromechanical dampers for vibration control of structures and rotors*. INTECH Open Access Publisher, 2010.

[233] Sodano H A, Bae J S, Inman D J, et al. *Concept and model of eddy current damper for vibration suppression of a beam*. Journal of Sound and Vibration, 2005, **288**(4): 1177-1196.

[234] Meisel J. *Principles of electromechanical-energy conversion*. Krieger Pub Co, 1984.

[235] Kim H Y, Lee C W. D*esign and control of active magnetic bearing system with Lorentz force-type axial actuator.* Mechatronics, 2006, **16**(1): 13-20.

[236] Crandall S H. *Dynamics of mechanical and electromechanical systems*. McGraw-Hill, 1968.

[237] Bae J S, Hwang J H, Kwag D G, et al. *Vibration Suppression of a Large Beam Structure Using Tuned Mass Damper and Eddy Current Damping*. Shock & Vibration, 2014, **2014**(1):1-10.

[238] Fink D G, McKenzie A A. *Electronics engineers' handbook*. New York: McGraw-Hill, 1975, edited by Fink, Donald G.; McKenzie, Alexander A., 1975, 1.

[239] Graves K E, Toncich D, Iovenitti P G. *Theoretical comparison of motional and transformer EMF device damping efficiency*. Journal of Sound and Vibration, 2000, **233**(3): 441-453.

[240] Nagaya K, Kojima H. *On a Magnetic Damper Consisting of a Circular Magnetic Flux and a Conductor of Arbitrary Shape. Part I: Derivation of the Damping Coefficients*. Journal of dynamic systems, measurement, and control, 1984, **106**(1): 46-51.

[241] Ikeda T. *Fundamentals of piezoelectricity*. Oxford university press, 1996.

[242] Jaffe B. *Piezoelectric ceramics*. Elsevier, 2012.

[243] Olson H F. *Electronic control of noise, vibration, and reverberation*. The Journal of the Acoustical Society of America, 1956, **28**(5): 966-972.

[244] Agnes G S, Napolitano K. Active constrained layer viscoelastic damping. AIAA/ASME/ASCE/AHS/ASC 34th Structures, Structural Dynamics, and Materials Conference. 1993: 3499-3506.

[245] Azvine B, Tomlinson G R, Wynne R J. *Use of active constrained-layer damping for controlling resonant vibration*. Smart Materials and Structures, 1995, **4**(1): 1-6.

[246] Lam M J, Inman D J, Saunders W R. *Vibration control through passive constrained layer damping and active control*. Journal of Intelligent Material Systems and Structures, 1997, **8**(8): 663-677.

[247] Lam M J, Inman D J, Saunders W R. Variations of hybrid damping. 5th Annual International Symposium on Smart Structures and Materials. International Society for Optics and Photonics, 1998: 32-43.

[248] Park C H. *Dynamics modelling of beams with shunted piezoelectric elements*. Journal of Sound and Vibration, 2003, **268**(1): 115-129.

[249] Horowitz P, Hill W, Robinson I. *The art of electronics*. Cambridge: Cambridge university press, 1980.

[250] Wu S Y. *Broadband piezoelectric shunts for structural vibration control*: U.S. Patent 6,075,309[P]. 2000-6-13.

[251] Berardengo, M., *Innovative vibration control systems based on smart materials for light structures*. Diss. Italy, 2016.

[252] Guyomar D, Lallart M, Monnier T. *Stiffness tuning using a low-cost semiactive nonlinear technique*. IEEE/ASME Transactions on Mechatronics, 2008, **13**(5): 604-607.

[253] Lallart M, Badel A, Guyomar D. *Nonlinear Semi-active Damping using Constant or Adaptive Voltage Sources: A Stability Analysis*. Journal of Intelligent Material Systems & Structures, 2008, **19**(10):1131-1142.

[254] Niederberger D, Morari M. *An autonomous shunt circuit for vibration damping*. Smart Materials & Structures, 2006, **15**(2): 359-364.

[255] Ji H, Qiu J, Xia P, et al. *Coupling analysis of energy conversion in multi-mode vibration structural control using a synchronized switch damping method*. Smart Materials and Structures, 2011, **21**(1): 015013.

[256] Sigalas M M, Economou E N. *Comment on "Acoustic band structure of periodic elastic composites"*. Physical Review Letters, 1995, **75**(19): 3580.

[257] Martinezsala R, Sancho J, Sánchez J V, et al. *Sound-attenuation by sculpture*. nature, 1995, **378**(6554): 241-241.

[258] Sigalas M, Economou E N. *Band structure of elastic waves in two dimensional systems*. Solid State Communications, 1993, **86**(3): 141-143.

[259] Wu T T, Huang Z G, Tsai T C, et al. *Evidence of complete band gap and resonances in a plate with periodic stubbed surface*. Applied Physics Letters, 2008, **93**(11): 111902.

[260] Maldovan, M., *Narrow low-frequency spectrum and heat management by thermocrystals.* Physical review letters, 2013. **110**(2): 025902.

[261] Maldovan, M., *Phonon wave interference and thermal bandgap materials.* Nature materials, 2015. **14**(7): 667-674.

[262] Economou E N, Sigalas M. *Stop bands for elastic waves in periodic composite materials*. The Journal of the Acoustical Society of America, 1994, **95**(4): 1734-1740.

[263] Kushwaha M S, Halevi P. *Band-gap engineering in periodic elastic composites*. Applied Physics Letters, 1994, **64**(9): 1085-1087.

[264] Sigalas M M, Economou E N. *Elastic waves in plates with periodically placed inclusions*. Journal of Applied Physics, 1994, **75**(6): 2845-2850.

[265] Bragg W H, Bragg W L. *The reflection of X-rays by crystals*. Proceedings of the Royal Society of London. Series A, Containing Papers of a Mathematical and Physical Character, 1913, **88**(605): 428-438.

[266] Yu D, Wen J, Zhao H, et al. *Vibration reduction by using the idea of phononic crystals in a pipe-conveying fluid*[J]. Journal of Sound and vibration, 2008, **318**(1): 193-205.

[267] Kafesaki M, Economou E N. *Multiple-scattering theory for three-dimensional periodic acoustic composites.* Physical review B, 1999. **60**(17): 11993.

[268] García-Pablos D, Sigalas M, Espinosa F R M D, et al. *Theory and experiments on elastic band gaps*. Physical Review Letters, 2000, **84**(19):4349-4352.

[269] Langlet P, Hladky‐Hennion A, Decarpigny J. *Analysis of the propagation of plane acoustic waves in passive periodic materials using the finite element method*. Journal of the Acoustical Society of America, 1995, **98**(5): 2792-2800.

[270] Wang G, Wen X, Wen J, et al. *Two-dimensional locally resonant phononic crystals with binary structures*. Physical Review Letters, 2004, **93**(15):9587-9602.

[271] Goffaux C, Sánchez-Dehesa J, Yeyati A L, et al. *Evidence of fano-like interference phenomena in locally resonant materials*. Physical review letters, 2002, **88**(22): 225502.

[272] Wang G, Yu D, Wen J, et al. *One-dimensional phononic crystals with locally resonant structures*. Physics Letters A, 2004, **327**(5): 512-521.

[273] Wang G, Wen X, Wen J, et al. *Quasi-one-dimensional periodic structure with locally resonant band gap*. Journal of Applied Mechanics, 2006, **73**(1): 167-170.

[274] Vidoli S, Dell'Isola F. *Modal coupling in one-dimensional electromechanical structured continua.* Acta Mechanica, 2000, **141**(1-2): 37-50.

[275] Fuller C C, Elliott S, Nelson P A. *Active control of vibration*. Academic Press, 1996.

[276] Kim Y, Baz A M. *Active control of a two-dimensional periodic structure*. Smart Structures and Materials. International Society for Optics and Photonics, 2004: 329-339.

[277] Li F, Song Z. *Vibration analysis and active control of nearly periodic two-span beams with piezoelectric actuator/sensor pairs*. Applied Mathematics and Mechanics, 2015, **36**(3): 279-292.

[278] Rao M S, Narayanan S. *Active control of wave propagation in multi-span beams using distributed piezoelectric actuators and sensors*. Smart Materials & Structures, 2007, **16**(6):2577-2594.

[279] Singh A, Pines D J, Baz A. *Active/passive reduction of vibration of periodic one-dimensional structures using piezoelectric actuators*. Smart Materials & Structures, 2004, **13**(4):698-711.

[280] Hansen C, Snyder S, Qiu X, et al. *Active control of noise and vibration*. CRC Press, 2012.

[281] Vasques C M A, Rodrigues J D. *Active vibration control of smart piezoelectric beams: Comparison of classical and optimal feedback control strategies*. Computers & Structures, 2006, **84**(22–23):1402-1414.

[282] Courant R, Hilbert D. *Methods of Mathematical Physics*, Vol. I. Physics Today, 2009, **30**(1): 139-140.

[283] Collet M, Fan Y, Ichchou M. *Periodically distributed piezoelectric patches optimization for waves attenuation and vibrations damping*. The Journal of the Acoustical Society of America, 2015, **138**(3): 1920-1920.

[284] Huang T L, Ichchou M N, Bareille O A, et al. *Multi-modal wave propagation in smart structures with shunted piezoelectric patches*. Computational Mechanics, 2013, **52**(3): 721-739.

[285] Wen J, Chen S, Wang G, et al. *Directionality of wave propagation and attenuation in plates with resonant shunting arrays*. Journal of Intelligent Material Systems and Structures, 2014: 1045389X14560361.

[286] Bergamini A E, Zündel M, Parra E A F, et al. *Hybrid dispersive media with controllable wave propagation: A new take on smart materials*. Journal of Applied Physics, 2015, 118(15): 154310.

[287] Degraeve S, Granger C, Dubus B, et al. *Bragg band gaps tunability in an homogeneous piezoelectric rod with periodic electrical boundary conditions*. Journal of applied Physics, 2014, **115**(19): 194508.

[288] Kutsenko A A, Shuvalov A L, Poncelet O, et al. *Tunable effective constants of the one-dimensional piezoelectric phononic crystal with internal connected electrodes*. The Journal of the Acoustical Society of America, 2015, **137**(2): 606-616.

[289] Mencik J M, Ichchou M N. *A substructuring technique for finite element wave propagation in multi-layered systems*. Computer Methods in Applied Mechanics and Engineering, 2008, **197**(6): 505-523.

[290] Becker J, Fein O, Maess M, et al. *Finite element-based analysis of shunted piezoelectric structures for vibration damping*. Computers & structures, 2006, **84**(31): 2340-2350.

[291] Mead D J. *A general theory of harmonic wave propagation in linear periodic systems with multiple coupling*. Journal of Sound and Vibration, 1973, **27**(2): 235-260.

[292] Mead D J. *Wave propagation and natural modes in periodic systems: I. Mono-coupled systems*. Journal of Sound and Vibration, 1975, **40**(1): 1-18.

[293] Zhong W X, Williams F W. *On the direct solution of wave propagation for repetitive structures*. Journal of Sound and Vibration, 1995, **181**(3): 485-501.

[294] Hao Z, Ji-Hong W, Sheng-Bing C, et al. *Flexural wave band-gaps in phononic metamaterial beam with hybrid shunting circuits.* Chinese Physics B, 2015. **24**(3): 036201.

[295] Jian-Wei W, Gang W, Sheng-Bing C, et al. *Broadband attenuation in Phononic Beams induced by periodic arrays of feedback shunted piezoelectric patches*. Chinese Physics Letters, 2012, **29**(6): 064302.

[296] Sheng-Bing C, Ji-Hong W, Dian-Long Y, et al. *Band gap control of phononic beam with negative capacitance piezoelectric shunt*. Chinese Physics B, 2011, **20**(1): 014301.

[297] Sheng-Bing C, Ji-Hong W, Gang W, et al. *Locally resonant gaps of phononic beams induced by periodic arrays of resonant shunts*. Chinese Physics Letters, 2011, **28**(9): 094301.

[298] Wang G, Chen S, Wen J. *Low-frequency locally resonant band gaps induced by arrays of resonant shunts with Antoniou's circuit: experimental investigation on beams*. Smart Materials and Structures, 2010, **20**(1): 015026.

[299] Kwon Y W, Bang H. *The finite element method using MATLAB*. CRC press, 2000.

[300] Cesari L. *Functional analysis and Galerkin's method*. The Michigan Mathematical Journal, 1964, **11**(4): 385-414.

[301] Allik H, Hughes T J R. *Finite element method for piezoelectric vibration*. International journal for numerical methods in engineering, 1970, **2**(2): 151-157.

[302] Casadei F, Ruzzene M, Dozio L, et al. *Broadband vibration control through periodic arrays of resonant shunts: experimental investigation on plates*. Smart materials and structures, 2009, **19**(1): 015002.

[303] Spadoni A, Ruzzene M, Cunefare K. *Vibration and wave propagation control of plates with periodic arrays of shunted piezoelectric patches*. Journal of Intelligent Material Systems and Structures, 2009, **20**(8): 979-990.

[304] Tzou H S, Tseng C I. *Distributed piezoelectric sensor/actuator design for dynamic measurement/control of distributed parameter systems: a piezoelectric finite element approach*. Journal of sound and vibration, 1990, **138**(1): 17-34.

[305] Yan L, Lallart M, Guyomar D. *Hybrid time-domain and spatial filtering nonlinear damping strategy for efficient broadband vibration control*. Journal of Intelligent Material Systems and Structures, 2016, **27**(2): 261-277.

[306] Kaneko T. *On Timoshenko's correction for shear in vibrating beams*. Journal of Physics D: Applied Physics, 1975, **8**(16): 1927-1936.

[307] Friedman Z, Kosmatka J B. *An improved two-node Timoshenko beam finite element*. Computers & structures, 1993, **47**(3): 473-481.

[308] Ji H, Qiu J, Zhu K. *Vibration control of a composite beam by an adaptive semi-active method based on LMS algorithm*, Piezoelectricity, Acoustic Waves, and Device Applications, 2008. SPAWDA 2008. Symposium on. IEEE, 2008: 193-198.

[309] Park J, Palumbo D L. *A new approach to identify optimal properties of shunting elements for maximum damping of structural vibration using piezoelectric patches*. INTER-NOISE and NOISE-CON Congress and Conference Proceedings. 2004.

[310] Bardell N S, Langley R S, Dunsdon J M, et al. T*he effect of period asymmetry on wave propagation in periodic beams*. Journal of sound and vibration, 1996, **197**(4): 427-445.

[311] Aköz Y, Aksoydan M. *Transfer Stiffnes Matrix for Timoshenko Beams on Elastic Foundations*. ARI The Bulletin of the Istanbul Technical Univercity, 2004, **54**: 1-15.

[312] Wei S T, Pierre C. *Statistical analysis of the forced response of mistuned cyclic assemblies*. AIAA journal, 1990, **28**(5): 861-868.

[313] Ichchou M N, Akrout S, Mencik J M. *Guided waves group and energy velocities via finite elements*. Journal of Sound and Vibration, 2007, **305**(4): 931-944.

Scientific Production

Journal Papers

[1] L. Yan, **B. Bao**, D. Guyomar and M. Lallart, *Periodic Structure with Interconnected Nonlinear Electrical Networks*, J. Intell. Mat. Syst. Struct., *in press.* Available online at http://jim.sagepub.com/content/early/2016/06/10/1045389X16649448.abstract

[2] **B. Bao**, D. Guyomar and M. Lallart, *Vibration reduction for smart periodic structures via periodic piezoelectric arrays with nonlinear interleaved-switched electronic networks*, Mech. Syst. Sig. Proc., *in press.* Available online at http://www.sciencedirect.com/science/article/pii/S0888327016301066

[3] **B. Bao**, D. Guyomar and M. Lallart, *Electron-phonon metamaterial featuring nonlinear Tri-interleaved piezoelectric topologies and its application in low-frequency vibration control*, Smart Mater. Struct., *accepted*.

International Conferences

[1] **B. Bao**, M. Lallart and D. Guyomar, *Nonlinear Vibration Damping in Mechanical/Electrical Periodic Structures Featuring Switched Piezoelectric Elements*, 5th International Conference on Smart and Multifunctional Materials, Structures and Systems, CIMTEC 2016, Session E-1 - Physics and Modelling of Metamaterials Systems, Perugia, Italy, June 5-9, 2016.

FOLIO ADMINISTRATIF

THESE DE L'UNIVERSITE DE LYON OPEREE AU SEIN DE L'INSA LYON

NOM : BAO DATE de SOUTENANCE : 23rd Septembre 2016
(avec précision du nom de jeune fille, le cas échéant)

Prénoms : Bin

TITRE : Systèmes de contrôle de vibrations distribué large bande utilisant des approches non-linéaires

NATURE : Doctorat Numéro d'ordre : 2016LYSEI086

Ecole doctorale : Electronique, Electrotechnique et Automatique

Spécialité : Génie Electrique

RESUME : L'amélioration du confort des usagers ainsi que l'augmentation du niveau de sécurité des structures requièrent le développement de techniques permettant de limiter efficacement les vibrations. Dans cette optique, les travaux exposés ici proposent le développement et l'analyse de méthodes de contrôle vibratoire pour des structures de faibles dimensions et utilisant peu d'énergie. Afin de satisfaire à ces deux critères, il est ici proposé d'utiliser des éléments piézoélectriques électriquement interfacés de manière non-linéaire et périodiquement distribués sur la structure-cible à contrôler. Ainsi, l'approche proposée permet de bénéficier à la fois des avantages des techniques de contrôle non-linéaires appliquées aux matériaux intelligents de type piézoélectrique, offrant des performances remarquables tout en étant peu consommatrices d'énergie, avec ceux des structures périodiques exhibant des bandes fréquentielles interdites présentant de fortes atténuations de la propagation d'onde.
Plus particulièrement, ce mémoire s'intéresse à différentes architectures d'interconnexion des interfaces électriques non-linéaires permettant un bon compromis entre la bande fréquentielle contrôlée et les performances en termes d'atténuation des vibrations. Ainsi, trois architectures principales sont proposées, allant de structures totalement périodiques, tant au niveau mécanique qu'électrique (interconnexions), à des structures présentant un certain degré d'apériodicité sur le plan électrique (entrelacement), impactant ainsi la propagation de l'onde acoustique en élargissant la bande de contrôle, pour enfin proposer une architecture hybride entre interconnexion et entrelacement conduisant à des systèmes large bande performants.

MOTS-CLES : vibration, amortissement, piézoélectrique, non-linéaire, structures périodiques, propagation

Laboratoire (s) de recherche : LGEF - Laboratoire de Génie Electrique et Ferroélectricité-INSA Lyon

Directeur de thèse : Pr. Daniel GUYOMAR
Co-directeur de thèse : Dr. Mickaël LALLART

Président de jury : Pr. Claude RICHARD

Composition du jury : Pr. Yves BERNARD, Pr. Morvan OUISSE, Dr. Adrien BADEL, Assoc. Prof. Stefano MANZONI, Pr. Claude RICHARD, Pr. Daniel GUOYMAR, Dr. Mickaël LALLART